

*NASA Conference Publication 10066
Part 2*

Aerospace Applications of Magnetic Suspension Technology

*Edited by
Nelson J. Groom
Langley Research Center
Hampton, Virginia*

*Colin P. Britcher
Old Dominion University Research Foundation
Norfolk, Virginia*

Proceedings of a workshop held at
NASA Langley Research Center
Hampton, Virginia
September 25-27, 1990

MARCH 1991

(NASA-CP-10066-Pt-2) AEROSPACE APPLICATIONS
OF MAGNETIC SUSPENSION TECHNOLOGY, PART 2
(NASA) 394 p CSCL 22B

N91-21203

--THRU--

N91-21212

Unclass

G3/18 0007579



National Aeronautics and
Space Administration

Langley Research Center
Hampton, Virginia 23665-5225

CONTENTS

Part 1*

INTRODUCTION	vii
--------------------	-----

TECHNICAL PROGRAM (*presenters indicated in Italics*)

Session 2 - Pointing and Isolation Systems

Chairman - Claude R. Keckler, NASA Langley Research Center

1. MAGNETIC SUSPENSION SYSTEMS for SPACE APPLICATIONS	1
D.G. Havenhill, <i>P.J. Wolke</i> , Honeywell Inc.	

2. ADVANCED MAGNETIC SUSPENSIONS for VIBRATION ISOLATION and	27
FAST-ATTITUDE CONTROL of SPACE-BASED GENERIC POINTING MOUNTS	
<i>R.W. Bosley</i> , A.N. Trivedi, AiResearch-Los Angeles Division, Allied-Signal Corp	

3. A SUPERCONDUCTING LARGE-ANGLE MAGNETIC SUSPENSION	57
<i>J. Downer</i> , J. Goldie, R. Torti, SatCon Technology Corporation	

Session 3 - Microgravity and Vibration Isolation I

Chairman - Duncan C. McCallum, Charles Stark Draper Laboratory

4. CONTROL ISSUES of MICROGRAVITY VIBRATION ISOLATION	77
<i>C.R. Knospe</i> , R.D. Hampton, University of Virginia	

5. SLIDING MODE CONTROL of MAGNETIC SUSPENSIONS for PRECISION	143
POINTING and TRACKING APPLICATIONS	
K.M. Misovec, F.J. Flynn, <i>B.G. Johnson</i> , SatCon Technology Corporation	
J.K. Hedrick, University of California at Berkeley	

Session 4 - Bearing Applications

Chairman - Patrick J. Wolke, Honeywell, Inc.

6. MAGNETIC BEARINGS with ZERO BIAS	165
<i>G.V. Brown</i> , C.M. Grodsinsky, NASA Lewis Research Center	

*Published under separate cover.

7. MAGNETIC BEARINGS for a SPACEFLIGHT OPTICAL DISK RECORDER	183
<i>R. Hockney, V. Gondhalekar, T. Hawkey, SatCon Technology Corporation</i>	

8. FIVE-DEGREE-of-FREEDOM CONTROL of an ULTRA-PRECISION	199
MAGNETICALLY-SUSPENDED LINEAR BEARING	
<i>D.L. Trumper, University of North Carolina at Charlotte</i>	
<i>A.H. Slocum, Cranfield Institute of Technology</i>	

<p><i>Session 5 - Wind Tunnel Model Suspension Systems</i></p> <p>Chairman - Robert A. Kilgore, NASA Langley Research Center</p>
--

9. MAGNETIC SUSPENSION and BALANCE SYSTEM ADVANCED STUDY	225
- 1989 DESIGN	
<i>R.W. Boom, Y.M. Eyssa, M.K. Abdelsalam, G.E. McIntosh</i>	
<i>Madison Magnetics Incorporated.</i>	

10. PROPULSION SIMULATOR for MAGNETICALLY-SUSPENDED	249
WIND TUNNEL MODELS	
<i>P.B. Joshi, C.L. Goldey, G.P. Sacco, Physical Sciences Inc.</i>	
<i>P. Lawing, NASA Langley Research Center</i>	

11. A SOLID-STATE CONTROLLABLE POWER SUPPLY for a MAGNETIC	281
SUSPENSION WIND TUNNEL	
<i>T.S. Daniels, J.S. Tripp, NASA Langley Research Center</i>	

<p><i>Session 6 - Large Gap Magnetic Suspension Systems</i></p> <p>Chairman - Sharon S. Welch, NASA Langley Research Center</p>

12. DESCRIPTION of the LARGE-GAP MAGNETIC SUSPENSION SYSTEM	303
(LGMS) GROUND BASED EXPERIMENT	
<i>N.J. Groom, NASA Langley Research Center.</i>	
13. LARGE GAP MAGNETIC SUSPENSION SYSTEM	325
<i>M.K. Abdelsalam, Y.M. Eyssa, Madison Magnetics Incorporated</i>	

14. STABILITY CONSIDERATIONS for MAGNETIC SUSPENSION SYSTEMS USING 355
ELECTROMAGNETS MOUNTED in a PLANAR ARRAY

N.J. Groom, NASA Langley Research Center, *C.P. Britcher*, Old Dominion University

Part 2

Session 7 - Controls

Chairman - James A. Downer, SatCon Corporation

15. NONLINEAR COMPENSATION TECHNIQUES for MAGNETIC 377
SUSPENSION SYSTEMS

D.L. Trumper, University of North Carolina at Charlotte.

16. A TIME DELAY CONTROLLER for MAGNETIC BEARINGS 389

K. Youcef-Toumi, S. Reddy, Massachusetts Institute of Technology.

17. MICROGRAVITY VIBRATION ISOLATION: An OPTIMAL CONTROL LAW 413
for the ONE-DIMENSIONAL CASE

R.D. Hampton, University of Virginia

C.M. Grodsinsky, NASA Lewis Research Center

P.E. Allaire, D.W. Lewis, C.R. Knospe, University of Virginia

18. MEASUREMENT and CALCULATION of FORCES in a MAGNETIC 477
JOURNAL BEARING ACTUATOR

J. Knight, E. McCaul, Z. Xia, Duke University

Session 8 - Rotating Machinery

Chairman - Paul E. Allaire, University of Virginia

19. DYNAMIC MODELLING and ANALYSIS of a MAGNETICALLY SUSPENDED 499
FLEXIBLE ROTOR

D.C. McCallum, Charles Stark Draper Laboratory

20. CRITICAL SPEEDS and FORCED RESPONSE SOLUTIONS for ACTIVE 539
MAGNETIC BEARING TURBOMACHINERY, Part I

J. Keesee, D. Rawal, *R.G. Kirk*, Virginia Polytechnic Institute and State University

21. CRITICAL SPEEDS and FORCED RESPONSE SOLUTIONS for ACTIVE 559
MAGNETIC BEARING TURBOMACHINERY, Part II

D. Rawal, J. Keesee, *R.G. Kirk*, Virginia Polytechnic Institute and State University

Session 9 - Science and Applications of Superconductivity

• Chairman - Pierce L. Lawing, NASA Langley Research Center

22. REDUCTION in BEARING SIZE due to SUPERCONDUCTORS in MAGNETIC BEARINGS 583

D.K. Rao, P. Lewis, J.F. Dill, Mechanical Technology Incorporated

23. CHEMICAL SPRAY PYROLYSIS of Tl-Ba-Ca-Cu-O HIGH- T_c SUPERCONDUCTORS 607
for HIGH-FIELD BITTER MAGNETS

L.P. de Rochemont, J.G. Zhang, M.R. Squillante, Radiation Monitoring Devices

A.M. Hermann, H.M. Duan, University of Colorado

R.J. Andrews, Rome Air Development Center

W.C. Kelliher, NASA Langley Research Center

Session 10 - PANEL DISCUSSION-Applications of Superconductivity

Chairman - Dantam K. Rao, Mechanical Technology Incorporated

Panel Members - G.V. Brown, NASA Lewis Research Center 629

M.K. Abdelsalam, Madison Magnetics Incorporated

D. Eisenhaure, SatCon Technology Incorporated

W. Kelliher, NASA Langley Research Center

Session 11 - Microgravity and Vibration Isolation II

Chairman - Colin P. Britcher, Old Dominion University

24. DEVELOPMENT and DESIGN of a MAGNETIC INERTIALLY REFERENCED 643
ISOLATION SYSTEM for MICROGRAVITY EXPERIMENTATION

K. Logsdon, C.M. Grodsinsky, NASA Lewis Research Center

25. ACTIVE VIBRATION ISOLATION MOUNTS	655
---	-----

H.M. Chen, R. Dorman, D. Wilson, Mechanical Technology Incorporated

presented by J. Hurley, MTI

26. VIBRATION ISOLATION of SCIENCE EXPERIMENTS in SPACE	679
---	-----

- DESIGN of a LABORATORY TEST SETUP

B.B. Banerjee, P.E. Allaire, C.R. Knospe, University of Virginia

Session 12 - Sensors

Chairman - Nelson J. Groom, NASA Langley Research Center

27. DEVELOPMENT of a SUITABLE INDUCTIVE SENSOR for MAGNETIC BEARINGS	705
--	-----

D.P. Plant, FARE Incorporated

R.B. Zmood, Royal Melbourne Institute of Technology

J. A. Kirk, University of Maryland

28. The NEW ELECTRO-OPTICAL DISPLACEMENT MEASURING SYSTEM	721
---	-----

for the 13 inch MSBS

T.D. Schott, P. Tchong, NASA Langley Research Center

29. The OPTICAL POSITION MEASUREMENT SYSTEM for a LARGE-GAP SUSPENSION SYSTEM (LGMSS)	731
--	-----

S.S. Welch, NASA Langley Research Center

J.I. Clemmons Jr., Vigyan Research Associates

APPENDIX - LIST OF ATTENDEES	767
------------------------------------	-----

N91-21204

NONLINEAR COMPENSATION TECHNIQUES for MAGNETIC SUSPENSION SYSTEMS

David L. Trumper
University of North Carolina at Charlotte
Department of Electrical Engineering
Charlotte
NC 28223

Nonlinear Compensation Techniques for Magnetic Suspension Systems

David L. Trumper
Dept. of Electrical Engineering
Univ. of N. Carolina at Charlotte
Charlotte, NC 28223

1 Introduction

In aerospace applications, magnetic suspension systems may be required to operate over large variations in air-gap. Thus the nonlinearities inherent in most types of suspensions will have a significant effect. Specifically, large variations in operating point may make it difficult to design a linear controller which gives satisfactory stability and performance over a large range of operating points.

One way to address this problem is through the use of nonlinear compensation techniques such as feedback linearization. In the last decade, this area has seen a great deal of research effort among system theorists [6], [7], [8], and has been successfully used in flight control applications [9], but has yet to be widely used in the area of magnetic suspensions.

Nonlinear compensators have received limited attention in the magnetic suspension literature. In [11] the control system design for suspension of a 1-ton, 4-passenger vehicle is presented. A flux sensor is located on the pole-face of the suspension magnet. A minor feedback loop is closed on flux which linearizes the dependence of magnetic force on position. The force goes as the square of flux, so an additional square root linearization is required. The idea of using an analog multiplier to compute the ratio i/x is mentioned, which would allow elimination of the flux sensor. However, this technique is reported as prone to drift and noise, and was abandoned. This flux-feedback scheme is described in more detail in [12]. In [13] a nonlinear correction law is used to correct the inverse square law magnet behavior in a flywheel suspension. The nonlinear compensation is implemented with analog multiplier and square root circuits. Microprocessor-based linearizing transformations are reported in [14] in the context of a demonstration system.

In recent years, progress has been made in the theory of nonlinear control systems, and in the sub-area of feedback linearization. Here, [6] is of fundamental importance in that it presents the conditions under which a system may be linearized. In [7] these results are globally extended, and in [8] the theory is developed for multi-input/multi-output systems. In a subsequent section the results of [6] are applied to a third order suspension example. However, for a simple system, it is often possible to construct the linearizing transformations by inspection. We start then by demonstrating the idea of feedback linearization using a second order suspension system. In the context of the second order suspension, sampling rate issues in the implementation of feedback linearization are examined through simulation. The system which is studied is presented in the next section.

2 Nonlinear Suspension Model

In this section, the open-loop dynamics for a simple one-degree-of-freedom suspension are presented. This system exhibits the essential issues faced in the design of tractive type suspensions, that is, suspensions which operate as variable reluctance devices. The example is drawn from [10] pgs. 22-23, 84-86, and 193-200. The only change is that the system is inverted such that gravity acts to open the air-gap. This system is shown in Figure 1.

The details of the electromagnetics are worked out in [10]; for the present purposes, the important details are the coil voltage

$$v_c = \frac{2w d \mu_0 N^2}{g_0 + x} \frac{di}{dt} - \frac{2w d \mu_0 N^2 i}{(g_0 + x)^2} \frac{dx}{dt} + iR \quad (1)$$

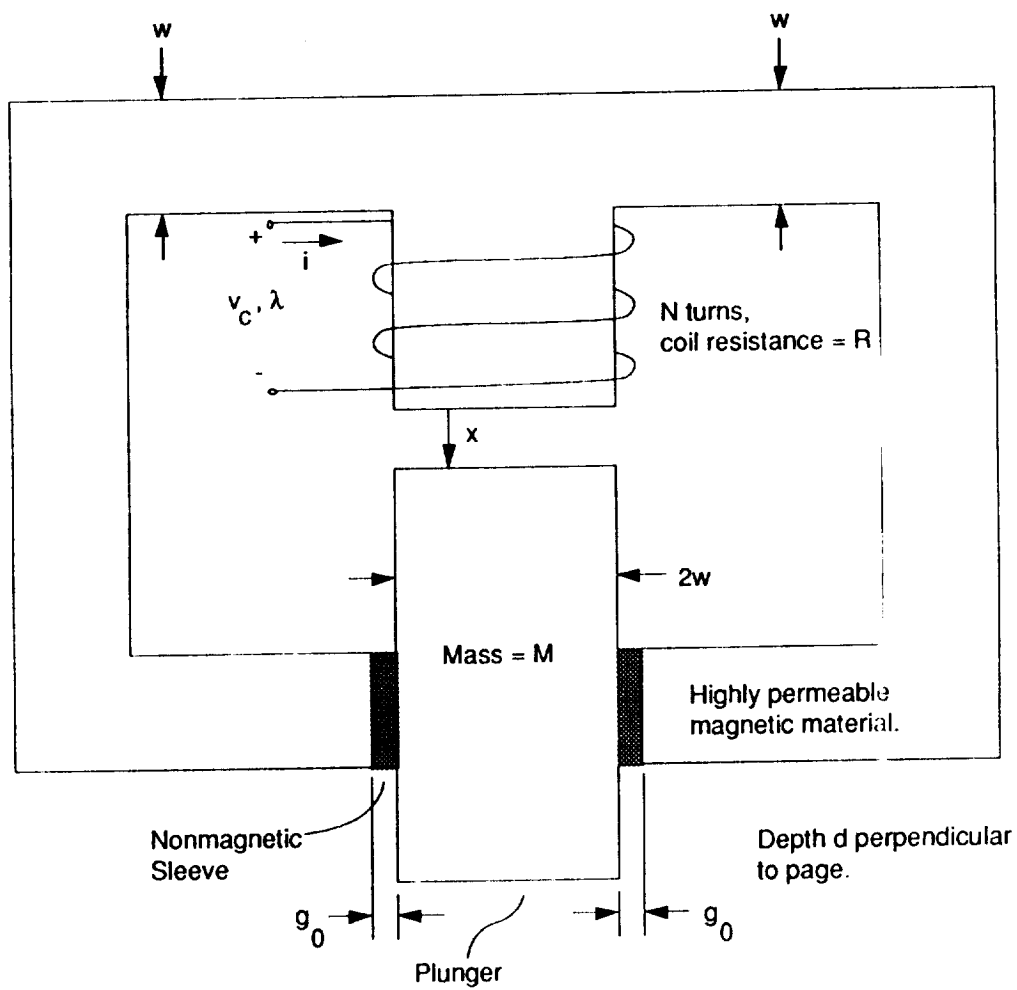


Figure 1: Single degree of freedom suspension.

and the force on the plunger

$$f_x = -wd\mu_0 N^2 \left(\frac{i}{g_0 + x} \right)^2 + Mg - f_d, \quad (x > 0) \quad (2)$$

where the first term is the electromagnet force, the second term is the gravitational force on the plunger, and the third term is a disturbance force acting on the plunger in the direction the electromagnet force. The nonmagnetic sleeve is assumed to exert no frictional forces on the plunger.

If we define

$$\begin{aligned} u &= v_c \\ C &= wd\mu_0 N^2 \\ x_1 &= x + g_0, \quad (x_1 > g_0) \\ \dot{x}_1 &= x_2 \end{aligned}$$

then the state equations for the open-loop suspension are

$$\begin{aligned} \dot{x}_1 &= x_2 \\ \dot{x}_2 &= -\frac{C}{M} \left(\frac{i}{x_1} \right)^2 + g - \frac{f_d}{M} \\ \dot{i} &= \frac{ix_2}{x_1} - \frac{Rx_1 i}{2C} + \frac{x_1 u}{2C}. \end{aligned} \quad (3)$$

2.1 Second order system

If the coil current is assumed to be the control input, then the suspension state equations are reduced to second order.

$$\begin{aligned} \dot{x}_1 &= x_2 \\ \dot{x}_2 &= -\frac{C}{M} \left(\frac{i}{x_1} \right)^2 + g - \frac{f_d}{M} \end{aligned} \quad (4)$$

These equations will adequately model the system if the coil current is controlled by a high-bandwidth current loop with sufficiently high voltage-drive capabilities. In applications, it is most typical to drive the coil with such a current loop, as this essentially eliminates the dependence of position-loop performance upon the electromagnet coil resistance and inductance.

3 Linearization of second-order suspension

The basic idea of feedback linearization is to define transformations on the states and input(s) such that the nonlinear system appears linear and operating-point invariant in terms of the transformed representation. Then a controller can be designed for the transformed variables. This allows the closed-loop system stability to be made independent of operating point.

For the second-order equations (4), a transformation on the input is all that is required to linearize the system. This transformation may be derived by inspection without using any formal mathematical machinery; this is the approach taken in [11], [12], [13], and [14]. That is, if the coil current i is made to vary as

$$i = x_1 \sqrt{\frac{-vM}{C}} \quad (5)$$

then the suspension is globally linearized in terms of the new input v . The notation for the auxiliary input v has been chosen to match the notation in [6].

Specifically, substituting from (5) into (4), the system state equations become

$$\begin{aligned} \dot{x}_1 &= x_2 \\ \dot{x}_2 &= v + g - \frac{f_d}{M} \end{aligned} \quad (6)$$

These equations are linear, with an input v , and disturbance terms g and f_d .

Here, v is a signal internal to the compensator which may be thought of as a setpoint for acceleration in the direction of increasing airgap. In operation, the signal v will be computed within the compensator, and constrained to be less than or equal to zero. Since the magnet can only supply accelerations in the direction of decreasing air gap it would not be physically meaningful to ask for acceleration in the direction of *increasing* air gap by setting v greater than zero. Thus the term $-v$ in (5) will always be greater than or equal to zero, and the square root will yield a real number.

The plant appears linear in terms of the new input v . This compensation of the nonlinear term does not however stabilize the plant. To stabilize the system, the nonlinear compensator is preceded by a linear compensator. The resulting closed-loop system is shown in Figure 2. The compensator may be thought of as having two parts, a nonlinear compensation section and a linear compensation section. It is the function of the nonlinear section to implement (5) in order to adjust i as a function of x_1 and v , such that the acceleration of the plunger is equal to v . It is the function of the linear section to specify the value of v as a function of the error between the position setpoint and the measured position such that the linearized plant is robustly stabilized and has good disturbance rejection and settling time properties. The signal v forms the connection between the linear and nonlinear sections of the compensator.

This combination of linear and nonlinear compensation sections stabilizes the plant such that the loop dynamics are independent of operating point. Such operating point independence is the main advantage of using a nonlinear compensator. Note that as viewed from the input to the nonlinear section, the incremental relationship between v and x_1 is equal to $1/s^2$, independent of operating point. Thus, the linear compensator can be designed to control a double integrator via standard linear techniques. If it is desirable to reject static disturbance forces with no position error, then the linear compensator can be designed to include an integral term. This integral term will adjust the value of v to balance gravity and any low-frequency components of the disturbance f_d .

In applications where large excursions or disturbance forces are anticipated, the additional complexity of the nonlinear compensation approach is justified. The major caveat is that we are assuming that the suspension model is accurate. For the electromagnetics an accurate model can readily be developed, and thus nonlinear compensation techniques are applicable. The nonlinear compensation technique was used in the construction of a class demonstration system which is described below.

4 Classroom demonstration implementing linearization

In the Spring of 1988, the author constructed a single degree of freedom levitation system for use as a classroom demonstration which implemented the nonlinear compensation technique described in the previous section. As developed there, if the plant state equations are given by (4), then applying the nonlinear compensation law (5) results in a system which appears to be linear in terms of the intermediate signal v . The demonstration system uses a high-bandwidth current-drive to regulate the electromagnet current, and thus (4) is applicable.

In the demonstration system, a one inch steel ball bearing is suspended below an electromagnet consisting of 3100 turns of #22 magnet wire wound on an 1 inch diameter by 4 inch length steel core. The coil current is controlled by a Bose-type switching regulator, with a half-scale current switching frequency of 10 kHz, and a full scale current of 2 Amperes. The operating point current is about 0.4 Amperes at a typical operating point air gap of 1 cm. The system is digitally controlled by an 8088/8087-based single-board computer and data acquisition system at a 400 Hz sampling rate. The control law for the nonlinear compensation section uses (5) to linearize the magnetic force relationship. This allows the stability of the closed-loop system to be essentially independent of the operating point. The control law for the linear compensation section is then developed via classical techniques applied in the discrete-time domain. The position of the ball is sensed optically, and nonlinearities in the sensor output versus position are compensated for in software.

In order to apply the nonlinear compensation technique, an accurate model of the plant is required. For the classroom demonstration, this model is developed by measuring the force on the ball as a function of current and position. This measurement is accomplished by using a balance beam for measuring the magnetic force on the ball. A 1 inch ball bearing is glued into one end of an aluminum balance beam of rectangular tubular cross-section measuring 1 inch wide by 0.75 inches deep by 12 inches long. The

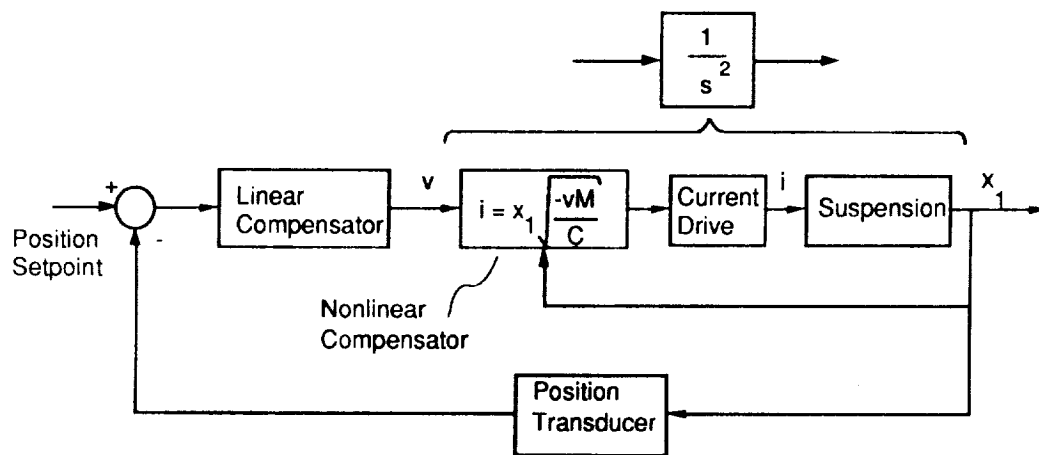


Figure 2: Nonlinear compensation of second-order magnetic suspension system.

beam pivots at the center on a thin wire which is held by fixed side supports. Balance pans are hung from the beam on both sides of the pivot midway between the pivot and the ends of the beam. These pans are used to add or subtract weight carried by the suspension. At the end of the beam opposite the ball, a micrometer is positioned to push against the beam and thus provide a position reference.

The idea here is that the ball glued into the end of the beam can be placed into suspension and the beam thus provides a handle by which the force applied to the ball can be varied. This is accomplished by putting weights into the balance pans on either side of the pivot. The beam is made of aluminum, and thus does not interact with the electromagnet at low frequencies. At the ball end, the beam is made thin so as not to interfere with the optical measurement. The ball is attached to the bottom of the thinned end of the beam such that it interacts with the optical sensor in the same fashion as a freely suspended ball.

The force relationship (2) was well fit by the experimental data with the parameters $C = 4.43 \times 10^{-4} \text{ Nm}^2/\text{A}^2$ and $g_0 = 0.25\text{cm}$. The mass of the ball is 67 grams. These parameters are used in the nonlinear compensation law (5). The only deviation from the relationship (2) is at high currents ($> 1\text{A}$), where the effects of magnetic saturation are apparent.

The optical position sensor is constructed as follows. A 24 volt, 5 watt incandescent lamp is used as the source, and a piece of cadmium sulfide photo-cell is used as the sensor, in what is a standard position sensor for magnetic suspensions. Using the balance beam described above, the sensor output is measured for a number of ball positions. When the shadow-line cast on the sensor is in the central region of the sensor, the sensor output is essentially linear with ball position. However, as the shadow-line approaches the upper or lower edge of the photo-cell, the sensor sensitivity begins to decrease. This nonlinearity in the relation between ball position and sensor output is corrected in software in the section of code which inputs the sensor voltage. The corrected position measurement is then linear with actual ball position. It is this corrected position measurement which is passed to the rest of the control loop.

The position sensor was found to have several defects which limit the system performance. First, the incandescent bulb output decreases significantly as a function of time. This is believed to be due to the evaporation of the filament. Material driven off of the filament is deposited on the inside of the glass envelope, thereby decreasing the bulb brightness. The second problem is that the cadmium sulfide sensor is sensitive to any light falling on its surface, independent of the source. Thus ambient lighting is indistinguishable from the light emitted by the bulb.

Both of these effects cause problems in the nonlinear compensation law (5) and in the correction of the sensor nonlinearities. First, the decrease in bulb intensity and any changes in average ambient light act as offset terms which drive the system to incorrect points on the sensor correction curve and in the magnet nonlinearity correction law (5). This offset deteriorates the system stability. Secondly, the ambient light has a large component at twice the power line frequency, especially in rooms with fluorescent lighting. This signal at 120 Hz acts as a large noise source which causes error motions in the ball position.

The above problems can be solved as follows. First, the light source needs to be made more constant with time. This can be achieved by using a more specialized incandescent bulb, or by switching to a semiconductor light source such as an infra-red light emitting diode. The ambient lighting offset and noise problems can be solved by either or both of two approaches which are classical. The first is to make the system narrow-band. Commonly available IR diodes emit a relatively narrow-band optical signal; laser diodes are narrower. In this case, an optical band-pass filter can be placed in front of the sensor, so that only the emitted frequencies are sensed, and the ambient lighting is greatly attenuated. The second approach is to switch the light-source on and off at a high frequency and use synchronous detection to reject signals which are not at the same frequency and phase as the source. The frequency of switching must be made much higher than the cross-over frequency of the position control loop, perhaps on the order of 10 kHz switching frequency. This rate is easily within the capabilities of available electronics.

The results derived in the previous section for the nonlinear compensation laws assume that these are implemented in continuous time. For discrete-time implementation, the issue of sampling rate becomes important. This issue is investigated in the next section.

4.1 Sampling rate issues

Due to the complexity of the transformations it is most likely that a linearizing compensator will be implemented in discrete time. As an introduction to one issue involved in discrete-time implementation, the effect of sampling rate on the second-order suspension system (4) is investigated by simulation. For this example, the suspension parameters have been given the values developed for the class demonstration system described above. These values are $M = 67$ grams, and $C = 4.43 \times 10^{-4} \text{ Nm}^2/\text{Amp}^2$.

The system is simulated assuming a nonlinear compensation law of the form (5). The four graphs shown in Figure 3 indicate the system behavior when a net 0.05g acceleration ($v = -0.05$ in (5)) is specified. The lines labelled 'ideal' show that if the nonlinear compensation was perfectly implemented, the force on the ball would be constant, and the graph of velocity vs. time would be a straight line. However, with any finite sampling rate this is not the case. The system is open-loop unstable, and uncontrolled between sampling instants. Thus it 'runs away' during the interval in which the control current is held constant. The graphs show the result of this process for sampling rates of 1 kHz and 200 Hz. To get reasonable behavior, it can be seen that a sampling rate on the order of 1 kHz is required. In the class demo, due to computational speed limitations a 400 Hz sampling rate is used. This is found to be adequate as long as the ball is not allowed to approach too close to the pole face.

Another way to look at the effect of sampling rate is to examine the system behavior under closed-loop position control. To this end, a linear proportional plus lead compensator is designed in discrete-time to stabilize the nominal plant which would result if the nonlinear compensation were perfect. That is, in the ideal case, the nonlinear compensated system appears as a double integrator independent of operating point. In the finite sampling time implementation, the quality of this approximation deteriorates as the air gap closes. This can be seen in Figure 4 which displays simulated step responses for the closed-loop system at four nominal operating points and for the two sampling rates. Note that the system with 200 Hz sampling goes unstable at the 0.5 cm and smaller air gaps, whereas the behavior of the 1000 Hz sampled system only begins to deteriorate when the air gap approaches 0.3 cm. The unstable response for 200 Hz sampling is not shown for the 0.3 cm air gap.

This example shows that the practical implementation of linearizing transformations may require very high sampling rates. Also, what may be considered a satisfactory sampling rate depends on the range of operating points which are encountered in system operation. Certainly, the issue of discrete-time implementation merits further study.

Experience with this simple nonlinear compensation system provided the impetus toward an understanding of feedback linearization techniques in more generality. A description of the application of feedback linearization to the third order suspension system is given in the next section.

4.2 Linearization of third-order suspension

For more complex plants it may be difficult to develop linearizing transformations by inspection. The results of [6] provide a general approach to this problem. A good introduction to these ideas is presented in [4] and [5]. These references assume no more than an undergraduate background in control theory and are thus a good place to start for someone new to this area.

Without reviewing the results from the above references, if the plant satisfies a controllability condition and a condition on the existence of solutions to a set of partial differential equations, then transformations $z_1 = T_1(x), \dots, z_n = T_n(x), v = T_{n+1}(x, u)$ can be constructed such that in the z - v space the system appears linear. Here, x is the state-vector of the nonlinear system, z is the state-vector of the linearized system, and n is the system order. Under these transformations, the nonlinear system is mapped to the controllability canonical form

$$\frac{d}{dt} \begin{pmatrix} z_1 \\ \vdots \\ z_{n-1} \\ z_n \end{pmatrix} = \begin{pmatrix} z_2 \\ \vdots \\ z_n \\ 0 \end{pmatrix} + \begin{pmatrix} 0 \\ \vdots \\ 0 \\ 1 \end{pmatrix} v. \quad (7)$$

For the system (3), the required conditions are satisfied, and the results of [6] yield the linearizing transformations $z_1 = x_1$, $z_2 = x_2$, $z_3 = -(C/M)(i/x_1)^2$, and $z_4 = \frac{i}{Mx_1}(Ri - u)$. Thus the system

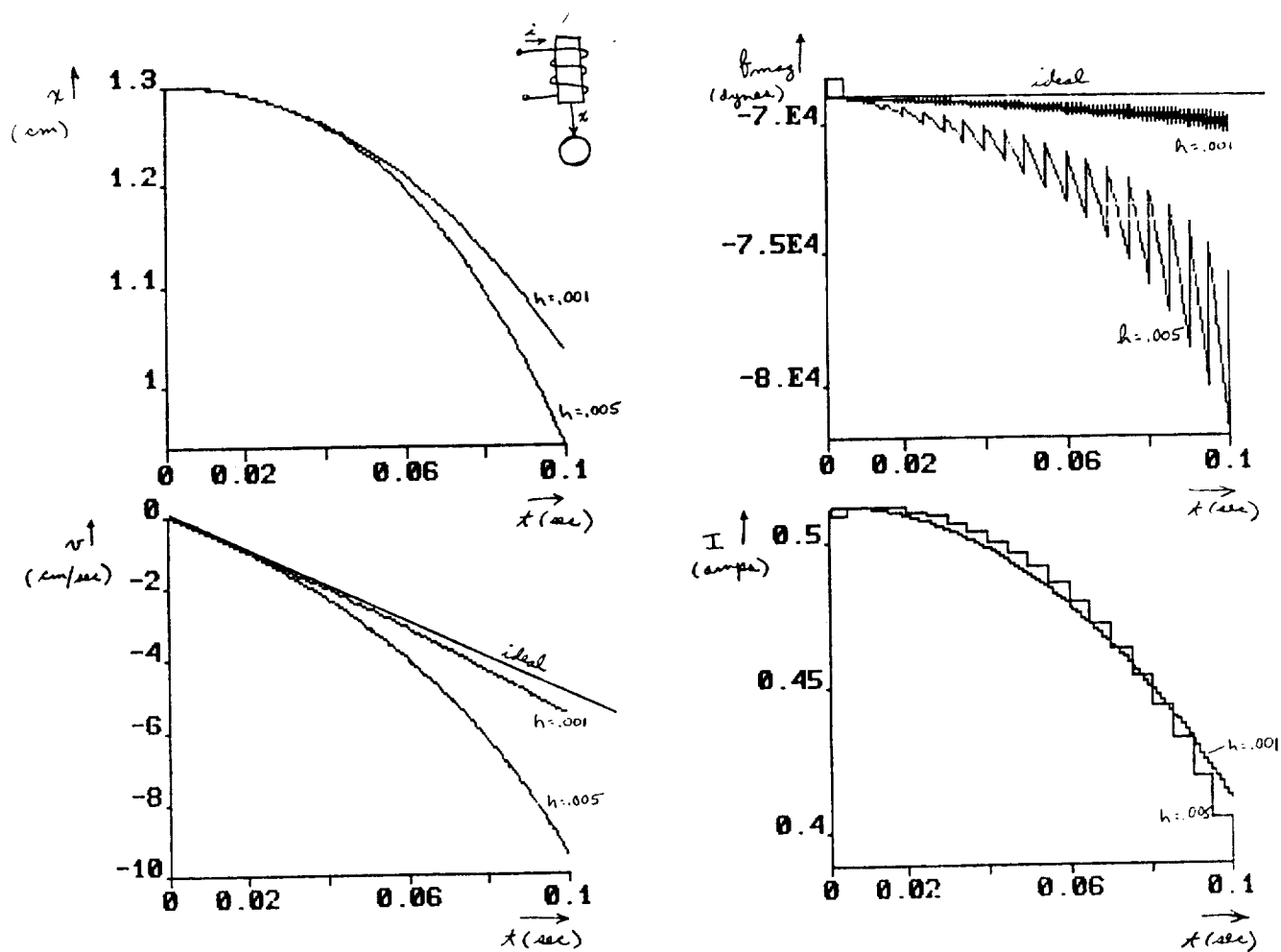


Figure 3: The open-loop system with nonlinear compensation showing its performance with sampling periods h of 1 and 5 milliseconds. Position x is in cm separation from the pole face, velocity v is in cm/sec, force on the ball is in dynes, and current I is in amps.

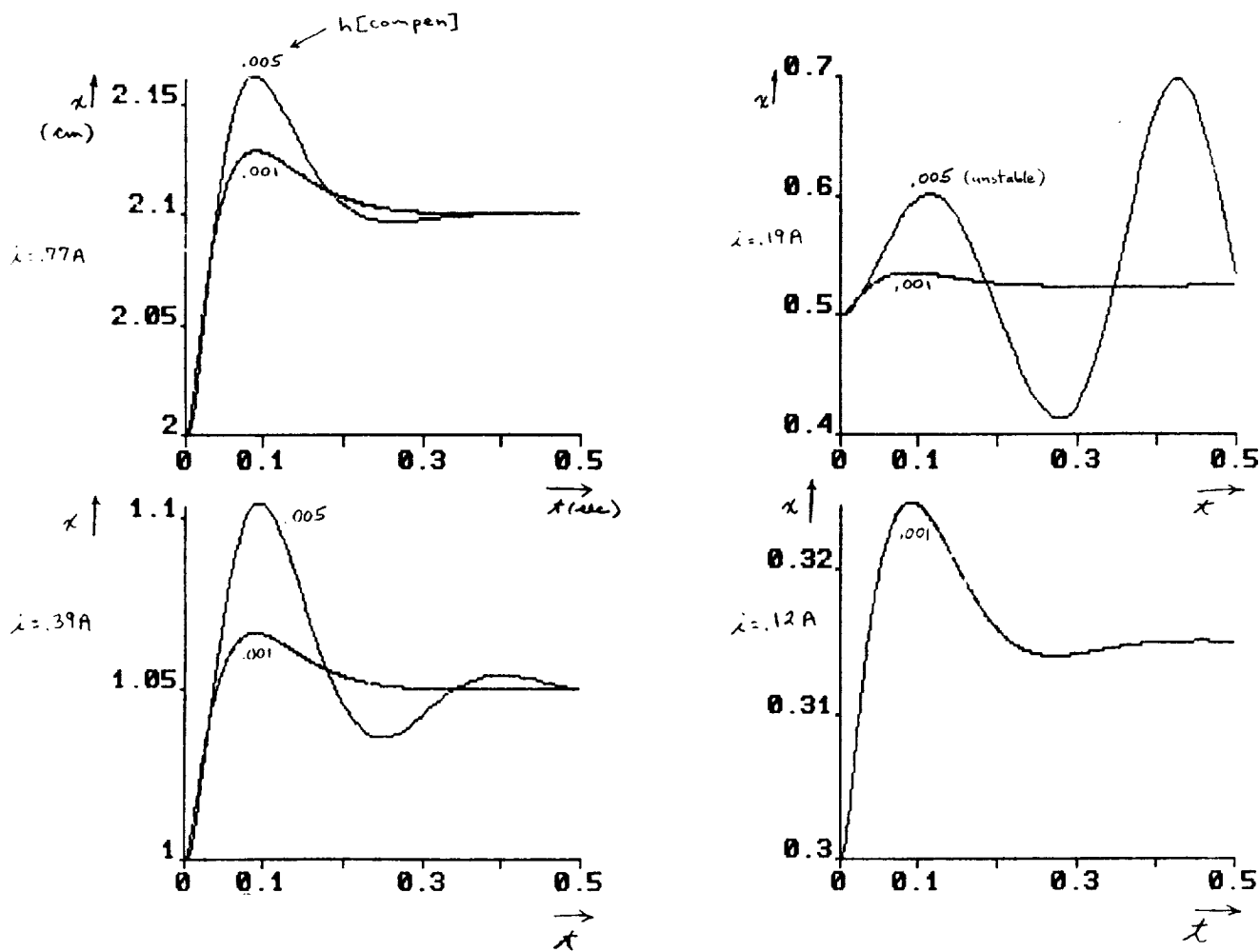


Figure 4: The closed-loop system with nonlinear compensation showing its performance with sampling periods h of 1 and 5 milliseconds as the operating point position is moved towards the pole face. Position x is in cm separation from the pole face. The nominal operating points are 2, 1, 0.5, and 0.3 cm respectively.

appears linear in terms of state variables z_1 , z_2 , and z_3 , and with a properly redefined input v . The states z_1 and z_2 are simply the original position and velocity. State z_3 is the acceleration applied to the suspended member. Thus it makes physical sense that the suspension will appear linear in z_3 . The suspension force happens to vary nonlinearly with the untransformed state and input, but Newton's law guarantees linearity in terms of a transformed state variable which is proportional to acceleration. In an implementation, the voltage drive u must be computed in terms of v :

$$u = -\frac{Mx_1v}{i} + iR. \quad (8)$$

Since v drives the derivative of z_3 , we can think of v as being a setpoint for the *slope* of the acceleration. Note that the coil resistance voltage drop iR is directly added to the input u .

Thus we have found a set of linearizing transformations. However the transformations are not unique. Direct substitution will verify that the transformations $T_1 = x_1^2$, $T_2 = 2x_1x_2$,

$$T_3 = 2x_2^2 - \frac{2Ci^2}{Mx_1} \quad (9)$$

and

$$T_4 = -\frac{6Cx_2i^2}{Mx_1^2} + \frac{2i}{M}(Ri - u) \quad (10)$$

though more complex than the first set, do indeed globally linearize the system. Actually, there are an infinity of such transformations which linearize this system. This is a consequence of the nature of nonlinear systems. It is clear however that the first set has the greatest physical meaning, and thus would be chosen in any practical context. Note also that in the first set the transformed state z_3 need never be computed. This is so because the system is linear between the transformed input v and the original position state variable x_1 . Further, note that the input transformation (8) depends only upon position x_1 and current i . Both of these quantities may be readily measured.

5 Conclusions

As we have seen in the magnetic suspension examples, the technique of feedback linearization is of great utility in designing control loops for nonlinear systems such that the closed-loop systems are well-behaved despite large variations in operating point or disturbance forces. Sampling rates for discrete-time implementations have been shown to be critical, especially at small air gaps. For practical applications, the most important area which we have overlooked is that of robustness with respect to plant modeling errors. This is an area which has also been a topic of current research [5]. In [3] it is noted that the electromagnet nonlinearity results in nonlinear cross-coupling terms in the control of five degrees of freedom of a precision linear bearing suspension. Thus it will be advantageous to implement nonlinear compensation laws for this and other multivariable suspension systems.

6 Acknowledgements

This work forms part of a thesis submitted by the author to the Department of Electrical Engineering and Computer Science at M.I.T. in partial fulfillment of the requirements for the degree of Doctor of Philosophy [2]. The authors gratefully acknowledge the assistance of Van Pham, Tim Hawkey, Eric Heatzig, Dave Gessel, and Art Rudolf at M.I.T., and Carl Much, Mike Johnson, Pete Rossini, Paul Mitiguy, and Hardy Prince at M.I.T. Lincoln Laboratory. This work was sponsored by the Department of the Air Force, and performed at the M.I.T. Lincoln Laboratory.

7 References

- [1] Slocum, A.H., and Eisenhaure, D.B., "Design Considerations for Ultra-Precision Magnetic Bearing Supported Slides," NASA Magnetic Suspension Technology Conference, Hampton, Va. Feb. 2-4, 1988.

- [2] Trumper, D.L., "Magnetic Suspension Techniques for Precision Motion Control," Ph.D. Thesis, Dept. of Elec. Eng. and Comp. Sci., M.I.T., Camb., Mass., Sept., 1990.
- [3] Trumper, D.L., "Five-Degree-of-Freedom Control of an Ultra-Precision Magnetically-Suspended Linear Bearing," NASA Workshop on Aerospace Applications of Magnetic Suspension Technology, Hampton, VA, Sept. 25-27, 1990.
- [4] Slotine, and Li, preliminary notes for text on nonlinear control, to be published Jan., 1991. Used as course notes for MIT class 2.152.
- [5] Spong, M., and Vidyasagar, M., *Robot Dynamics and Control*, Wiley, 1989, pp. 259-283.
- [6] Su, R., "On the linear equivalents of nonlinear systems," *Systems and Control Letters*, vol. 2, No. 1, pp. 48-52, July, 1982.
- [7] Hunt, L.R., Su, R., and Meyer, G., "Global Transformations of Nonlinear Systems," *IEEE Transactions on Automatic Control*, Vol. AC-28, No. 1, Jan., 1983.
- [8] Hunt, L.R., Su, R., and Meyer, G., "Design for Multi-Input Nonlinear Systems," in *Differential Geometric Control Theory*, Brockett, Millman, and Sussmann, eds., *Progress in Mathematics*, Vol. 27, pp. 268-298, Birkhauser, Boston, 1983.
- [9] Meyer, G., Su, R., and Hunt, L.R., "Application of Nonlinear Transformations to Automatic Flight Control," *Automatica*, Vol. 20, No. 1, pp. 103-107, 1984.
- [10] Woodson, H.H., and Melcher, J.R., *Electromechanical Dynamics - Part I*, John Wiley and Sons, 1968.
- [11] Jayawant, B.V., Hodkinson, R.L., Wheeler, A.R., and Whorlow, R.J., "Transducers and Their Influence in the Design of Magnetically Suspended Vehicles," *I.E.E. Conf. on Control Aspects of New Forms of Guided Land Transport*, I.E.E. Publication No. 117, Aug., 1974, pp. 200-206.
- [12] Jayawant, B.V., Sinha, P.K., Wheeler, A.R., and Whorlow, R.J., "Development of 1-ton Magnetically Suspended Vehicle Using Controlled D.C. Electromagnets," *Proc. I.E.E.*, Vol. 123, No. 9, Sept., 1976.
- [13] Groom, N.J., and Waldeck, G.C., "Magnetic Suspension System for a Laboratory Model Annular Momentum Control Device," *AIAA Paper No. 79-1755*, 1979.
- [14] Traxler, A., Meyer, F., and Murbach, H., "Fast Digital Control of a Magnetic Bearing with a Microprocessor," *International Kongress Mikroelektronik*, Munich, Nov 13-15, 1984, pp 94-102.

N 9 1 - 2 1 2 0 5

A TIME DELAY CONTROLLER for MAGNETIC BEARINGS

**K. Youcef-Toumi, S. Reddy
Massachusetts Institute of Technology
Department of Electrical Engineering
Room 35-233
77 Massachusetts Avenue
Cambridge
MA 02139**

1990 Workshop On Aerospace Applications
of Magnetic Suspension Technology

A TIME DELAY CONTROLLER
FOR MAGNETIC BEARINGS

K. Youcef-Toumi, Associate Professor, and S. Reddy, Graduate Student

Department of Mechanical Engineering
Massachusetts Institute of Technology
Cambridge, MA 02139
U.S.A.

Abstract

The control of systems with unknown dynamics and unpredictable disturbances has raised some challenging problems. This is particularly important when high system performance is to be guaranteed at all times. Recently, the Time Delay Control has been suggested as an alternative control scheme. The proposed control system does not require an explicit plant model nor does it depend on the estimation of specific plant parameters. Rather, it combines adaptation with past observations to directly estimate the effect of the plant dynamics.

This paper formulates a control law for a class of dynamic systems and then presents a sufficient condition for control system stability. The derivation is based on the bounded input-bounded output stability approach using L_∞ function norms. The control scheme is implemented on a five degrees-of-freedom high speed and high precision magnetic bearing. The control performance is evaluated using step responses, frequency responses and disturbance rejection properties. The experimental data show an excellent control performance despite the system complexity.

1 Introduction

Some classical control methods deal with well known linear time-invariant systems. In many applications, however, some relevant part of the system maybe unknown, time varying, or nonlinear. Controlled systems are thus often limited to operating in only a small portion of their available range. For example, servo motors must operate in the linear part of their range for accurate control. Restrictions such as these have led to the development of control techniques that deal with such complexities.

Several types of modern control strategies have been developed to deal with nonlinear, time-variant systems. One of the first methods to accommodate nonlinear systems was Model Reference Control. This technique employs a model of the system and uses the difference between the model response and the plant response as the input signal to the plant [18]. The model is either a physical model or a simulated system on a computer. Although it has no variable parameters, it is very useful for either specifying desired performance or for the observation of unaccessible states. A drawback in this technique is that it requires knowledge of the full dynamic model and system limitations. When perfect cancellation of the system nonlinearities is not achieved due to imperfect modeling or inaccurate parameter values, the dynamic performance of the plant may be degraded to the point of closed loop instability [22].

Another advanced technique is Adaptive Control. An adaptive system measures a certain index of performance which is a function of the inputs, states and/or outputs of the system. From the comparison of the measured index of performance with a set of given ones, the adaptation mechanism modifies the parameters of the controller or the set of given ones [4,14,16,21]. There are several classes of adaptive control. A very common variation uses a desired reference model as a basis for comparison and is termed Model Reference Adaptive Control (MRAC). In the direct MRAC, no attempt is made to identify the plant parameters. Controller parameters are directly updated. In Self-Tuning control, plant model parameters are identified/modified and the controller action is automatically updated according to a

fixed regulator design. Another approach generates the control action in part by an adaptive feedforward controller which "behaves" as the "inverse" of the plant [22]. All adaptive controllers share the distinguishing feature of system identification followed by variation of parameters to maintain desired performance. A drawback of adaptation is that it is generally slow and computationally intense. Often the environment changes faster than the system, causing performance degradation or even instability. Other references on adaptive control include [8,9,11,12,19,20,24].

Other control methods, such as Variable Structure Controllers, take totally different strategies to achieve stability in nonlinear systems. This type of controller utilizes state feedback in a control law which switches the structure of the closed loop system between trajectories which may themselves be unstable or marginally stable but when combined by the control law in a switching technique, result in a system which is stable. A method of switching called "sliding mode", described in [23,26,27,37], arranges the switching so that ideally the system remains on one of the switching lines (or surfaces) as it "slides" stably toward the origin of the phase plane. Real systems, however, take time to switch trajectories, resulting in periods of infinite frequency, or no control, as the system switches from one trajectory to another while attempting to remain on the switching line. This high frequency chattering undesirably excites high frequency dynamics.

Systems which are capable of recognizing the familiar features and patterns of a situation and which use past experiences in behaving in an optimal fashion are called Learning Systems. A learning system, when presented with a novel situation, learns how to behave by an adaptive approach. Then if the system experiences the same situation, it will recognize and behave optimally without going through the same adaptive approach. An advantage is that the system need not be identified in every environmental situation, making the response time faster under situations that have already been learned. A drawback is that such systems often require repetitive trial and error to bring them into an operating state [1,25]. A large list of references on methods of control mentioned above can be found in [13] and [17].

Another method, Time Delay Control (TDC) proposed in references [30,31,32,33], depends neither on estimation of specific parameters, repetitive actions, infinite switching frequencies, or discontinuous control. It employs, rather, direct estimation of the effect of the plant dynamics through the use of time delay. The controller uses the gathered information to cancel the unknown dynamics and disturbances simultaneously and then inserts the desired dynamics into the plant. The TDC employs past observation of the system response and control inputs to directly modify the control actions rather than adjust the controller gains. It updates its observation of the system every sampling period, therefore, estimation of the plant dynamics is dependent upon the sampling frequency. The TDC has a similar feature as the learning control algorithm proposed in reference [10]. This learning control algorithm is applicable for nonlinear systems with linear input action. It updates the control action in each learning trial by comparing the state derivative of the actual trajectory with that of the desired reference trajectory in the previous trial. Time Delay Control differs from this approach in that the control action is updated at each instant based on recent past. This paper uses the concepts developed in references [30,31,32,33] to explore the potentials and limitations of the TDC approach.

The TDC control algorithm leads to systems that have a similar form to that of time delay systems. These systems, which are also referred to as time-lag or retarded systems, are systems in which time delay exists between the cause and effect. In time delay systems, these delays arise as a result of delays existing in the hardware components or computation [5]. In our case, the time delay is a feature of the control algorithm. The mathematical formulation for such time delay systems leads to delayed differential equations. A special class of these equations are referred to as integral-differential equations which were studied by Volterra [29]. Volterra was the first to study such systems and developed the theory to investigate the consequences of time delay. Several other researchers have contributed to the development of the general theory of the Volterra type. Reference [15] provides several references of contributors to delayed differential equations including historical perspective of control theory and developments of time delay.

The Time Delay Control was originally formulated in [30] for a class of nonlinear systems with linear input action. The control algorithm has been applied to robot manipulators and servo systems with very satisfactory results even under large system parameter variations and disturbances [30,31,32,33,35]. Stability and convergence analysis was also performed for linear SISO systems [34].

This paper formulates a control law for a class of dynamic systems with nonlinear input action and then presents a sufficient condition for control system stability. The derivation is based on the bounded input-bounded output stability approach using L_∞ function norms. The control scheme is implemented on a five degrees-of-freedom high speed and high precision magnetic bearing. The control performance is evaluated using step responses, frequency responses and disturbance rejection properties. The experimental data show an excellent control performance despite the system complexity.

2 Time Delay Control

In this paper we are concerned with a class of systems described by the following differential equations,

$$\dot{\mathbf{x}}(t) = \mathbf{F}(\mathbf{x}, t) + \mathbf{G}(\mathbf{x}, \mathbf{u}, t) + \mathbf{D}(t) \quad (1)$$

where $\mathbf{x}(t) \in \mathcal{R}^n$ and $\mathbf{u}(t) \in \mathcal{R}^r$ are the system state vector and control input vector respectively. $\mathbf{F}(\mathbf{x}, t)$, $\mathbf{G}(\mathbf{x}, \mathbf{u}, t)$ and $\mathbf{D}(t)$ are vector functions with appropriate dimensions and represent respectively known dynamics, unknown dynamics and disturbances. The variable t represents time. In order to transform the system into a familiar form, Equ.(1) can be written as

$$\dot{\mathbf{x}}(t) = \mathbf{F}(\mathbf{x}, t) + \mathbf{H}(\mathbf{x}, \mathbf{u}, t) + \mathbf{B}\mathbf{u}(t) \quad (2)$$

where the new term $\mathbf{H}(\mathbf{x}, \mathbf{u}, t)$ is defined as

$$\mathbf{H}(\mathbf{x}, \mathbf{u}, t) = \mathbf{G}(\mathbf{x}, \mathbf{u}, t) + \mathbf{D}(t) - \mathbf{B}\mathbf{u}(t) \quad (3)$$

and \mathbf{B} is a matrix to be selected by the designer. A reference model that generates the desired trajectory is chosen as a linear time invariant system,

$$\dot{\mathbf{x}}_m(t) = \mathbf{A}_m \mathbf{x}_m(t) + \mathbf{B}_m \mathbf{r}(t) \quad (4)$$

where $\mathbf{x}_m(t) \in \mathcal{R}^n$ is a reference model state vector, $\mathbf{r}(t) \in \mathcal{R}^r$ is a reference input. \mathbf{A}_m and \mathbf{B}_m are constant matrices with appropriate dimensions.

The class of systems considered in this paper includes systems that satisfy a matching condition. It was shown in references [30,32,33] that systems in a special canonical form satisfy the matching condition. These systems can be partitioned as follows

$$\mathbf{x} = \begin{bmatrix} \mathbf{x}_q \\ \dots \\ \mathbf{x}_r \end{bmatrix}; \quad \mathbf{F}(\mathbf{x}, t) = \begin{bmatrix} \mathbf{x}_s \\ \dots \\ \mathbf{F}_r(\mathbf{x}, t) \end{bmatrix}$$

$$\mathbf{H}(\mathbf{x}, \mathbf{u}, t) = \begin{bmatrix} \mathbf{0} \\ \dots \\ \mathbf{H}_r(\mathbf{x}, \mathbf{u}, t) \end{bmatrix}; \quad \mathbf{B} = \begin{bmatrix} \mathbf{0} \\ \dots \\ \mathbf{B}_r \end{bmatrix}$$

where the partial states are $\mathbf{x}_q \in \mathcal{R}^{n-r}$, $\mathbf{x}_r \in \mathcal{R}^r$, $\mathbf{x}_s = [\mathbf{x}_{r+1}, \mathbf{x}_{r+2}, \dots, \mathbf{x}_n]^T \in \mathcal{R}^{n-r}$. The vector functions have the following dimensions $\mathbf{F}_r(\mathbf{x}, t)$, $\mathbf{H}_r(\mathbf{x}, \mathbf{u}, t) \in \mathcal{R}^r$, $\mathbf{B} \in \mathcal{R}^{n \times r}$ and $\mathbf{B}_r \in \mathcal{R}^{r \times r}$ is of rank r . The matrices involved in the reference model of Equ. (4) are also partitioned in the same manner,

$$\mathbf{A}_m = \begin{bmatrix} \mathbf{0} & | & \mathbf{I}_q \\ \dots & & \mathbf{A}_{mr} \end{bmatrix}, \quad \mathbf{B}_m = \begin{bmatrix} \mathbf{0} \\ \dots \\ \mathbf{B}_{mr} \end{bmatrix}$$

where $\mathbf{I}_q \in \mathcal{R}^{(n-r) \times (n-r)}$, $\mathbf{A}_{mr} \in \mathcal{R}^{r \times n}$, $\mathbf{B}_{mr} \in \mathcal{R}^{r \times r}$, $\mathbf{B}_m \in \mathcal{R}^{n \times r}$ and $\mathbf{r}(t) \in \mathcal{R}^r$. Furthermore assume a feedback matrix \mathbf{K} of the form,

$$\mathbf{K} = \begin{bmatrix} \mathbf{0} \\ \dots \\ \mathbf{K}_r \end{bmatrix}$$

where $\mathbf{K} \in \mathcal{R}^{n \times n}$ and $\mathbf{K}_r \in \mathcal{R}^{r \times n}$. The objective is to generate a control action \mathbf{u} that forces the error to vanish according to

$$\dot{\mathbf{e}} = (\mathbf{A}_m + \mathbf{K})\mathbf{e} = \mathbf{A}_e \mathbf{e} \quad (5)$$

The control action that combines past observations with adaptation for systems described by Equ. (2) is given by

$$\mathbf{u}(t) = \mathbf{B}^+ [-\dot{\mathbf{x}}(t-L) + \mathbf{F}(\mathbf{x}, t-L) - \mathbf{F}(\mathbf{x}, t) \\ + \mathbf{A}_m \mathbf{x}(t) + \mathbf{B}_m \mathbf{r}(t) + \mathbf{B}\mathbf{u}(t-L) - \mathbf{K}\mathbf{e}(t)] \quad (6)$$

where the parameter L represents the time delay [30,32,33], the error vector \mathbf{e} is defined as the difference between the plant and the reference model state vectors,

$$\mathbf{e} = \mathbf{x}_m - \mathbf{x} \quad (7)$$

The term \mathbf{B}^+ is the pseudo-inverse matrix defined as $\mathbf{B}^+ = (\mathbf{B}^T \mathbf{B})^{-1} \mathbf{B}^T$. For the special canonical form considered, \mathbf{B}^+ is given by

$$\begin{aligned} \mathbf{B}^+ &= (\mathbf{B}^T \mathbf{B})^{-1} \mathbf{B}^T = \left\{ \begin{bmatrix} 0 \\ \vdots \\ \mathbf{B}_r \end{bmatrix}^T \begin{bmatrix} 0 \\ \vdots \\ \mathbf{B}_r \end{bmatrix} \right\}^{-1} [0 : \mathbf{B}_r^T] \\ &= (\mathbf{B}_r^T \mathbf{B}_r)^{-1} [0 : \mathbf{B}_r^T] = \mathbf{B}_r^{-1} [0 : \mathbf{I}_r] = [0 : \mathbf{B}_r^{-1}] \end{aligned}$$

The control action now reduces to

$$\begin{aligned} \mathbf{u}(t) &= \mathbf{B}_r^{-1} [-\dot{\mathbf{x}}_r(t-L) + \mathbf{F}_r(\mathbf{x}, t-L) - \mathbf{F}_r(\mathbf{x}, t) + \mathbf{A}_{mr} \mathbf{x}(t) \\ &\quad + \mathbf{B}_r \mathbf{u}(t-L) + \mathbf{B}_{mr} \mathbf{r}(t) - \mathbf{K}_r \mathbf{e}(t)] \end{aligned} \quad (8)$$

Note that this control law is a special case of a general algorithm which uses convolutions for estimating unknown system dynamics [36].

The objective of this research is to be able to control such systems and guarantee performance despite the presence of large dynamic variations in $\mathbf{G}(\mathbf{x}, \mathbf{u}, t)$ and large unexpected disturbances in $\mathbf{D}(t)$.

As described in [31], each term in Equ.(8) has the following meaning: (1) \mathbf{B}_r^{-1} , cancels the control matrix \mathbf{B}_r , (2) the term $-\mathbf{F}_r(\mathbf{x}, t) - \dot{\mathbf{x}}(t-L) + \mathbf{F}_r(\mathbf{x}, t-L) + \mathbf{B}_r \mathbf{u}(t-L)$ attempts to cancel the undesired known nonlinear dynamics $\mathbf{F}(\mathbf{x}, t)$, the unknown nonlinear dynamics and the unexpected disturbances $\mathbf{H}(\mathbf{x}, t)$, (3) the term $\mathbf{A}_{mr} \mathbf{x} + \mathbf{B}_{mr} \mathbf{r}$ inserts the desired dynamics of the reference model, and (4) the error feedback term $-\mathbf{K}_r \mathbf{e}$ adjusts the error dynamics. Thus this controller observes the current state, the state derivatives (estimates) and the inputs of the system at time $t-L$, one step into the past, and determines the best control action that should be commanded at time t . The scheme used in the time delay control is reminiscent of numerical methods used to solve differential equations.

3 Stability Analysis

3.1 Error dynamics

As indicated in [32,33], the stability of such control systems using time delay depends on the delay parameter L , the control gains \mathbf{K} , the speed of the response of the plant and the speed of response of the reference trajectory. The method used to perform this analysis is based on the bounded input bounded output stability procedure. In what follows, we discuss the stability analysis for two situations pertaining to whether the control distribution matrix $\frac{\partial \mathbf{G}}{\partial \mathbf{u}}$ is constant and known or unknown. In order to perform the stability analysis, we formulate the governing equations for the error dynamics. First using the control action of Equ.(8), the plant equations of Equ.(1) become

$$\begin{aligned} \dot{\mathbf{x}}(t) &= \begin{bmatrix} \mathbf{x}_s \\ \vdots \\ \mathbf{F}_r(\mathbf{x}, t) + \mathbf{H}_r(\mathbf{x}, \mathbf{u}, t) + [-\dot{\mathbf{x}}_r(t-L) + \mathbf{F}_r(\mathbf{x}, t-L) - \mathbf{F}_r(\mathbf{x}, t) \\ + \mathbf{B}_r \mathbf{u}(t-L) + \mathbf{A}_{mr} \mathbf{x}(t) + \mathbf{B}_{mr} \mathbf{r}(t) - \mathbf{K}_r \mathbf{e}(t)] \end{bmatrix} \\ &= \begin{bmatrix} \mathbf{x}_s \\ \vdots \\ \mathbf{H}_r(\mathbf{x}, \mathbf{u}, t) - \mathbf{H}_r(\mathbf{x}, \mathbf{u}, t-L) + \mathbf{A}_{mr} \mathbf{x}(t) + \mathbf{B}_{mr} \mathbf{r}(t) - \mathbf{K}_r \mathbf{e}(t) \end{bmatrix} \end{aligned}$$

The previously defined error \mathbf{e} of Equ.(7) is now governed by

$$\dot{\mathbf{e}}(t) = (\mathbf{A}_m + \mathbf{K})\mathbf{e}(t) + \mathbf{H}(\mathbf{x}, \mathbf{u}, t-L) - \mathbf{H}(\mathbf{x}, \mathbf{u}, t) \quad (9)$$

where the second and third terms are forcing functions due to the unknown system dynamics and unpredictable disturbances.

Rewriting Equ. (9) as

$$\dot{\mathbf{e}}(t) = (\mathbf{A}_m + \mathbf{K})\mathbf{e}(t) + \mathbf{p}(t) \quad (10)$$

where

$$\mathbf{p}(t) = \begin{bmatrix} 0 \\ - \\ - \\ \mathbf{p}_r(t) \end{bmatrix}$$

and

$$\mathbf{p}_r(t) = \mathbf{H}_r(\mathbf{x}, \mathbf{u}, t - L) - \mathbf{H}_r(\mathbf{x}, \mathbf{u}, t)$$

One may ask the question: what conditions does the vector $\mathbf{p}(t)$ have to satisfy for the system to be stable? A sufficient condition for stability will be derived in the next section.

3.2 Sufficient conditions for stability

This section presents a general solution to this multi-input multi-output control problem. We will use the bounded input-bounded output approach based on L_∞ norms in order to derive sufficient conditions for stability. We now consider the governing differential of the error as given by Equ.(10) and its corresponding time response,

$$\mathbf{e}(t) = e^{(\mathbf{A}_m + \mathbf{K})t} \mathbf{e}(0) + \int_0^t e^{(\mathbf{A}_m + \mathbf{K})(t-\tau)} \mathbf{p}(\tau) d\tau$$

We will use $\|(\cdot)_T\|$ to indicate the norm of the time truncated function (\cdot) and $\|(\cdot)\|_i$ for the induced matrix norm. Taking the norm of the error [28],

$$\begin{aligned} \|\mathbf{e}_T\| &\leq \| (e^{(\mathbf{A}_m + \mathbf{K})t})_T \|_i \|\mathbf{e}(0)\| + \sup_{t \in [0, T]} \int_0^t \|e^{(\mathbf{A}_m + \mathbf{K})(t-\tau)}\|_i \|\mathbf{p}(\tau)\| d\tau \\ &\leq \| (e^{(\mathbf{A}_m + \mathbf{K})t})_T \|_i \|\mathbf{e}(0)\| + \|\mathbf{p}_T\| \sup_{t \in [0, T]} \int_0^t \|e^{(\mathbf{A}_m + \mathbf{K})(t-\tau)}\|_i d\tau \end{aligned}$$

The desired error dynamics given by $(\mathbf{A}_m + \mathbf{K})$ are always chosen to be asymptotically stable. This implies that there exist finite positive constants m, λ such that

$$\|e^{(\mathbf{A}_m + \mathbf{K})(t-\tau)}\|_i \leq m e^{-\lambda(t-\tau)} \quad \forall \tau, t > \tau$$

which implies

$$\sup_{t \in [0, T]} \int_0^t \|e^{(\mathbf{A}_m + \mathbf{K})(t-\tau)}\|_i d\tau \leq \sup_{t \in [0, T]} \frac{m}{\lambda} (1 - e^{-\lambda t}) = \frac{m}{\lambda}$$

$$\begin{aligned} \|(e^{(\mathbf{A}_m + \mathbf{K})t})_T\|_i &= \sup_{t \in [0, T]} \|(e^{(\mathbf{A}_m + \mathbf{K})t})\|_i \\ &\leq \sup_{t \in [0, T]} m e^{-\lambda t} = m \end{aligned}$$

Therefore, the norm of the error is bounded

$$\|\mathbf{e}_T\| \leq \alpha + \beta \|\mathbf{p}_T\| \quad (11)$$

where

$$\alpha = m \|\mathbf{e}(0)\|, \quad \beta = \frac{m}{\lambda}$$

In order to be more specific on these stability conditions, we need to expand the forcing term $\mathbf{p}(t)$. We can rewrite $\mathbf{p}_r(t)$ as

$$\begin{aligned}
\mathbf{p}_r(t) &= \mathbf{H}_r(\mathbf{x}(t-L), \mathbf{u}(t-L), t-L) - \mathbf{H}_r(\mathbf{x}(t), \mathbf{u}(t-L), t) \\
&\quad + \mathbf{H}_r(\mathbf{x}(t), \mathbf{u}(t-L), t) - \mathbf{H}_r(\mathbf{x}(t), \mathbf{u}(t), t) \\
\|[\mathbf{p}(t)]_T\| &= \|[\mathbf{p}_r(t)]_T\| \leq \|[\mathbf{H}_r(\mathbf{x}(t-L), \mathbf{u}(t-L), t-L) \\
&\quad - \mathbf{H}_r(\mathbf{x}(t), \mathbf{u}(t-L), t)]_T\| \\
&\quad + \|[\mathbf{H}_r(\mathbf{x}(t), \mathbf{u}(t-L), t) - \mathbf{H}_r(\mathbf{x}(t), \mathbf{u}(t), t)]_T\|
\end{aligned} \tag{12}$$

Assuming that the function $\mathbf{H}_r(\mathbf{x}, \mathbf{u}, t)$ is continuous and differentiable, the Mean Value Theorem yields [6]

$$\begin{aligned}
&\|[\mathbf{H}_r(\mathbf{x}(t-L), \mathbf{u}(t-L), t-L) - \mathbf{H}_r(\mathbf{x}(t), \mathbf{u}(t-L), t)]_T\| \\
&\leq \left\| \left[\left(\frac{\partial \mathbf{H}_r}{\partial t} + \frac{\partial \mathbf{H}_r}{\partial \mathbf{x}} \dot{\mathbf{x}} \right) (\mathbf{x}(\zeta), \mathbf{u}(t-L), \zeta) \right]_T \right\| L
\end{aligned} \tag{13}$$

$$\begin{aligned}
&\|[\mathbf{H}_r(\mathbf{x}(t), \mathbf{u}(t-L), t) - \mathbf{H}_r(\mathbf{x}(t), \mathbf{u}(t), t)]_T\| \\
&\leq \left\| \left[\frac{\partial \mathbf{H}_r}{\partial \mathbf{u}} (\mathbf{x}(t), \delta, t) (\mathbf{u}(t) - \mathbf{u}(t-L)) \right]_T \right\|
\end{aligned} \tag{14}$$

where $\zeta \in (t-L, t)$ and $\delta \in (\mathbf{u}(t-L), \mathbf{u}(t))$.

Equations (13) and (14) involve terms in \mathbf{x} and \mathbf{u} . To express them in terms of \mathbf{e} , the following expressions are used,

$$\frac{\partial \mathbf{H}_r}{\partial t} + \frac{\partial \mathbf{H}_r}{\partial \mathbf{x}} \dot{\mathbf{x}} = \frac{\partial \mathbf{H}_r}{\partial t} + \frac{\partial \mathbf{H}_r}{\partial \mathbf{x}} \dot{\mathbf{x}}_m - \frac{\partial \mathbf{H}_r}{\partial \mathbf{x}} \dot{\mathbf{e}} \tag{15}$$

$$\begin{aligned}
\mathbf{u}(t) - \mathbf{u}(t-L) &= \mathbf{B}_r^{-1} [-\dot{\mathbf{x}}_r(t-L) + \mathbf{F}_r(\mathbf{x}, t-L) - \mathbf{F}_r(\mathbf{x}, t) \\
&\quad + \mathbf{A}_{mr} \mathbf{x}(t) + \mathbf{B}_{mr} \mathbf{r}(t) - \mathbf{K}_r \mathbf{e}(t)] \\
&= \mathbf{B}_r^{-1} [-\dot{\mathbf{x}}_{mr}(t-L) + \dot{\mathbf{e}}_r(t-L) + \mathbf{F}_r(\mathbf{x}, t-L) - \mathbf{F}_r(\mathbf{x}, t) \\
&\quad + \dot{\mathbf{x}}_{mr}(t) - (\mathbf{A}_{mr} + \mathbf{K}_r) \mathbf{e}(t)]
\end{aligned} \tag{16}$$

since $\dot{\mathbf{e}}_r = \dot{\mathbf{x}}_{mr} - \dot{\mathbf{x}}_r$ and $\dot{\mathbf{x}}_{mr}(t) = \mathbf{A}_{mr} \mathbf{x}_m(t) + \mathbf{B}_{mr} \mathbf{r}(t)$. Substitution of (13), (14), (15) and (16) in (12) and some algebraic manipulation yields,

$$\begin{aligned}
\|\mathbf{p}_T\| &\leq \left\| \frac{\partial \mathbf{H}_r}{\partial t} + \frac{\partial \mathbf{H}_r}{\partial \mathbf{x}} \dot{\mathbf{x}}_m \right\| L + \left\| \frac{\partial \mathbf{H}_r}{\partial \mathbf{x}} \right\|_i L \|\dot{\mathbf{e}}_T\| \\
&\quad + \left\| \frac{\partial \mathbf{H}_r}{\partial \mathbf{u}} \mathbf{B}_r^{-1} (\mathbf{A}_{mr} + \mathbf{K}_r) \right\|_i \|\mathbf{e}_T\| \\
&\quad + \left\| \frac{\partial \mathbf{H}_r}{\partial \mathbf{u}} \mathbf{B}_r^{-1} \right\|_i \|(\dot{\mathbf{x}}_{mr}(t) - \dot{\mathbf{x}}_{mr}(t-L))\| \\
&\quad + \left\| \frac{\partial \mathbf{H}_r}{\partial \mathbf{u}} \mathbf{B}_r^{-1} \right\|_i \|\dot{\mathbf{e}}_T\| \\
&\quad + \left\| \frac{\partial \mathbf{H}_r}{\partial \mathbf{u}} \mathbf{B}_r^{-1} \right\|_i \|[\mathbf{F}_r(\mathbf{x}, t-L) - \mathbf{F}_r(\mathbf{x}, t)]_T\|
\end{aligned} \tag{17}$$

$$\begin{aligned}
\|[\mathbf{F}_r(\mathbf{x}, t-L) - \mathbf{F}_r(\mathbf{x}, t)]_T\| &\leq \left\| \left[\left(\frac{\partial \mathbf{F}_r}{\partial t} + \frac{\partial \mathbf{F}_r}{\partial \mathbf{x}} \dot{\mathbf{x}} \right) (\mathbf{x}(\xi), \xi) \right]_T \right\| L \\
&\leq \left\| \frac{\partial \mathbf{F}_r}{\partial t} + \frac{\partial \mathbf{F}_r}{\partial \mathbf{x}} \dot{\mathbf{x}}_m \right\| L + \left\| \frac{\partial \mathbf{F}_r}{\partial \mathbf{x}} \right\|_i L \|\dot{\mathbf{e}}_T\|
\end{aligned} \tag{18}$$

where $\xi \in (t-L, t)$. Substituting Equ. (18) in Equ. (17) yields

$$\|\mathbf{p}_T\| \leq c_1 + c_2 \|\mathbf{e}_T\| + c_3 \|\dot{\mathbf{e}}_T\| \quad (19)$$

where the constants c_1, c_2 and c_3 can be identified as

$$\begin{aligned} c_1 &= \left\| \frac{\partial \mathbf{H}_r}{\partial \mathbf{u}} \mathbf{B}_r^{-1} \right\|_i \left[L \left\| \frac{\partial \mathbf{F}_r}{\partial t} + \frac{\partial \mathbf{F}_r}{\partial \mathbf{x}} \dot{\mathbf{x}}_m \right\| + \|\dot{\mathbf{x}}_{mr}(t) - \dot{\mathbf{x}}_{mr}(t-L)\| \right] \\ &\quad + L \left\| \frac{\partial \mathbf{H}_r}{\partial t} + \frac{\partial \mathbf{H}_r}{\partial \mathbf{x}} \dot{\mathbf{x}}_m \right\| \\ c_2 &= \left\| \frac{\partial \mathbf{H}_r}{\partial \mathbf{u}} \mathbf{B}_r^{-1} (\mathbf{A}_{mr} + \mathbf{K}_r) \right\|_i \\ c_3 &= \left\| \frac{\partial \mathbf{H}_r}{\partial \mathbf{x}} \right\|_i L + \left\| \frac{\partial \mathbf{H}_r}{\partial \mathbf{u}} \mathbf{B}_r^{-1} \right\|_i + \left\| \frac{\partial \mathbf{H}_r}{\partial \mathbf{u}} \mathbf{B}_r^{-1} \right\|_i \left\| \frac{\partial \mathbf{F}_r}{\partial \mathbf{x}} \right\|_i L \end{aligned}$$

We will assume later that the terms in the right hand side of the three equations listed above are bounded and hence the parameters c_1, c_2 and c_3 will be bounded. The norm of the error in Equ.(11) can now be evaluated and is found to be,

$$\|\mathbf{e}_T\| \leq \alpha + \beta \|\mathbf{p}_T\| \leq \alpha + \beta c_1 + \beta c_2 \|\mathbf{e}_T\| + \beta c_3 \|\dot{\mathbf{e}}_T\|$$

or

$$\|\mathbf{e}_T\| \leq \frac{\alpha + \beta c_1 + \beta c_3 \|\dot{\mathbf{e}}_T\|}{(1 - \beta c_2)} \quad \text{if } \beta c_2 < 1 \quad (20)$$

The above equation relates the norms of the error and the error derivative. To obtain absolute bounds on the error another equation of this form is needed. The norm of the derivative of the error $\dot{\mathbf{e}}$, can be found from Eqs. (10) and (19),

$$\begin{aligned} \|\dot{\mathbf{e}}_T\| &\leq \|\mathbf{A}_m + \mathbf{K}\|_i \|\mathbf{e}_T\| + \|\mathbf{p}_T\| \\ &\leq [\|\mathbf{A}_m + \mathbf{K}\|_i + c_2] \|\mathbf{e}_T\| + c_1 + c_3 \|\dot{\mathbf{e}}_T\| \end{aligned} \quad (21)$$

This condition can be stated as,

$$\|\dot{\mathbf{e}}_T\| \leq \frac{c_1}{(1 - c_3)} + \frac{[\|\mathbf{A}_m + \mathbf{K}\|_i + c_2]}{(1 - c_3)} \|\mathbf{e}_T\| \quad \text{if } c_3 < 1 \quad (22)$$

and substituting Equ.(20) one obtains

$$\begin{aligned} &[\|\mathbf{A}_m + \mathbf{K}\|_i + c_2] (\alpha + \beta c_1 + \beta c_3 \|\dot{\mathbf{e}}_T\|) \\ &\quad + (1 - \beta c_2) c_1 \\ \|\dot{\mathbf{e}}_T\| &\leq \frac{}{(1 - c_3)(1 - \beta c_2)} \end{aligned}$$

or

$$\|\dot{\mathbf{e}}_T\| \leq \frac{\|\mathbf{A}_m + \mathbf{K}\|_i (\alpha + \beta c_1) + c_1 + c_2 \alpha}{[1 - \beta c_2 - c_3 - \beta c_3 \|\mathbf{A}_m + \mathbf{K}\|_i]}$$

if $c_3 + \beta(c_2 + c_3 \|\mathbf{A}_m + \mathbf{K}\|_i) < 1$ is satisfied. Using the expressions for the constants c_1, c_2 and c_3 , we have

$$\begin{aligned}
& \left(\left\| \frac{\partial \mathbf{H}_r}{\partial \mathbf{x}} \right\|_i L + \left\| \frac{\partial \mathbf{H}_r}{\partial \mathbf{u}} \mathbf{B}_r^{-1} \right\|_i + \left\| \frac{\partial \mathbf{H}_r}{\partial \mathbf{u}} \mathbf{B}_r^{-1} \right\|_i \left\| \frac{\partial \mathbf{F}_r}{\partial \mathbf{x}} \right\|_i L \right) \\
& \left[1 + \frac{m}{\lambda} \|\mathbf{A}_m + \mathbf{K}\|_i \right] \\
& + \left\| \frac{\partial \mathbf{H}_r}{\partial \mathbf{u}} \mathbf{B}_r^{-1} (\mathbf{A}_{mr} + \mathbf{K}_r) \right\|_i \frac{m}{\lambda} < 1
\end{aligned} \tag{23}$$

Based on the foregoing analysis and relations between the vector functions \mathbf{H}_r , \mathbf{G}_r , and \mathbf{B}_r given by

$$\frac{\partial \mathbf{H}_r}{\partial \mathbf{x}} = \frac{\partial \mathbf{G}_r}{\partial \mathbf{x}} \text{ and } \frac{\partial \mathbf{H}_r}{\partial \mathbf{u}} = \frac{\partial \mathbf{G}_r}{\partial \mathbf{u}} - \mathbf{B}_r$$

the following sufficient condition follows,

Theorem 1 :

If the functions $\mathbf{F}(\mathbf{x}, t)$, $\mathbf{G}(\mathbf{x}, \mathbf{u}, t)$, $\mathbf{D}(t)$ are continuous and differentiable, and

If the Jacobian matrices $\frac{\partial \mathbf{F}_r}{\partial \mathbf{x}}$, $\frac{\partial \mathbf{G}_r}{\partial \mathbf{x}}$, $\frac{\partial \mathbf{G}_r}{\partial \mathbf{u}}$, and the vector functions $\frac{\partial \mathbf{F}_r}{\partial t}$, $\frac{\partial \mathbf{G}_r}{\partial t}$, $\frac{\partial \mathbf{D}_r}{\partial t} \in L_\infty$, and

If the eigenvalues of the matrix $(\mathbf{A}_m + \mathbf{K})$ are in the left-half plane, and

If the following stability condition is satisfied

$$\begin{aligned}
& \left[1 + \frac{m}{\lambda} \|\mathbf{A}_m + \mathbf{K}\|_i \right] \left[\left\| \frac{\partial \mathbf{G}_r}{\partial \mathbf{x}} \right\|_i L \right. \\
& + \left\| \frac{\partial \mathbf{G}_r}{\partial \mathbf{u}} \mathbf{B}_r^{-1} - \mathbf{I} \right\|_i \left(1 + \left\| \frac{\partial \mathbf{F}_r}{\partial \mathbf{x}} \right\|_i L \right) \\
& + \left\| \left(\frac{\partial \mathbf{G}_r}{\partial \mathbf{u}} \mathbf{B}_r^{-1} - \mathbf{I} \right) (\mathbf{A}_{mr} + \mathbf{K}_r) \right\|_i \frac{m}{\lambda} < 1
\end{aligned} \tag{24}$$

Then the time delay controller is stable, and

the resultant bounds on the norms of the error, \mathbf{e} , and its derivative $\dot{\mathbf{e}}$ are

$$\begin{aligned}
\|\mathbf{e}\| & \leq \frac{\alpha + \beta c_1 - \alpha c_3}{[1 - \beta c_2 - c_3 - \beta c_3 \|\mathbf{A}_m + \mathbf{K}\|_i]} \\
\|\dot{\mathbf{e}}\| & \leq \frac{\|\mathbf{A}_m + \mathbf{K}\|_i (\alpha + \beta c_1) + c_1 + c_2 \alpha}{[1 - \beta c_2 - c_3 - \beta c_3 \|\mathbf{A}_m + \mathbf{K}\|_i]}
\end{aligned} \tag{25}$$

The constants c_1 , c_2 , c_3 , α and β are,

$$\begin{aligned}
c_1 & = \left\| \left(\frac{\partial \mathbf{G}_r}{\partial \mathbf{u}} \mathbf{B}_r^{-1} - \mathbf{I} \right) \right\|_i \left[L \left\| \frac{\partial \mathbf{F}_r}{\partial t} + \frac{\partial \mathbf{F}_r}{\partial \mathbf{x}} \dot{\mathbf{x}}_m \right\| + \|\dot{\mathbf{x}}_{mr}(t) - \mathbf{x}_{mr}(t - L)\| \right] \\
& + L \left\| \frac{\partial \mathbf{G}_r}{\partial t} + \frac{\partial \mathbf{G}_r}{\partial \mathbf{x}} \dot{\mathbf{x}}_m \right\| \\
c_2 & = \left\| \left(\frac{\partial \mathbf{G}_r}{\partial \mathbf{u}} \mathbf{B}_r^{-1} - \mathbf{I} \right) (\mathbf{A}_{mr} + \mathbf{K}_r) \right\|_i \\
c_3 & = \left\| \frac{\partial \mathbf{G}_r}{\partial \mathbf{x}} \right\|_i L + \left\| \frac{\partial \mathbf{G}_r}{\partial \mathbf{u}} \mathbf{B}_r^{-1} - \mathbf{I} \right\|_i \left(1 + \left\| \frac{\partial \mathbf{F}_r}{\partial \mathbf{x}} \right\|_i L \right) \\
\alpha & = m \|\mathbf{e}(0)\| \\
\beta & = \frac{m}{\lambda}
\end{aligned}$$

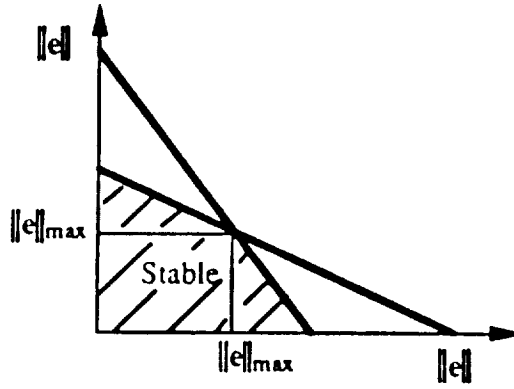


Figure 1: Region of Stability in the $\|e\| - \|\dot{e}\|$ space

Condition (ii) implies that the rate of change of the functions F_r , G_r and D_r with respect to t , x and u are bounded. Condition (iii) implies that the desired error dynamics are chosen to be stable. Condition (iv) relates the time delay L , the rates of change of F_r and G_r with respect to x and u , and the desired error dynamics specified by $(A_m + K)$.

The bounds on the norms of the error, e and its derivative \dot{e} are shown graphically in Figure 1. Equ. (20) yields a straight line as the boundary between stable and unstable regions. Similarly, Equ. (22) yields another straight line. The common region bounded by the two straight lines is the region of stability as shown. The absolute bounds $\|e\|_{max}$ and $\|\dot{e}\|_{max}$ shown in Figure 1 correspond to those given by Equ. (25).

3.3 Special cases and discussions

Condition (iv) stated in the proposition 1 can be rewritten in a more convenient and usable form. This simplified and convenient condition, however, is more conservative. Starting with condition (24) and after some algebraic manipulations we obtain,

$$\left\| \frac{\partial G_r}{\partial u} B_r^{-1} - I \right\|_i < \frac{\left\{ 1 - \left\| \frac{\partial G_r}{\partial x} \right\|_i L \left[1 + \frac{m}{\lambda} \|A_m + K\|_i \right] \right\}}{\left\{ \begin{array}{l} (1 + \left\| \frac{\partial F_r}{\partial x} \right\|_i L) \\ + \frac{m}{\lambda} [\|A_{mr} + K_r\|_i \\ + \|A_m + K\|_i (1 + \left\| \frac{\partial F_r}{\partial x} \right\|_i L)] \end{array} \right\}} \quad (26)$$

The condition (26) implies a bound on the variation of $\frac{\partial G_r}{\partial u}$ relative to the controller gain matrix B_r . The size of this bound is dependent on the delay time L , the norms of $\left\| \frac{\partial G_r}{\partial x} \right\|_i$ and $\left\| \frac{\partial F_r}{\partial x} \right\|_i$, and the desired characteristics of error dynamics given by $(A_m + K)$. The smaller the delay time is and the smaller the bounds on $\left\| \frac{\partial G_r}{\partial x} \right\|_i$ and $\left\| \frac{\partial F_r}{\partial x} \right\|_i$ are, then the larger the allowable size of bound is on the range of $\frac{\partial G_r}{\partial u}$ relative to B_r .

In the case of first order SISO systems the vector functions reduce to scalar functions $G_r = g$, $B_r = b$ and $F_r = f$. Some interesting results are stated below for this class of systems. For first order SISO systems, we have

$$\|e^{(A_m + K)(t-\tau)}\|_i = |e^{(a_m + k)(t-\tau)}| = e^{(a_m + k)(t-\tau)}$$

$$m = 1$$

$$\lambda = -(a_m + k)$$

$$\|\mathbf{A}_{mr} + \mathbf{K}_r\|_i = \|\mathbf{A}_m + \mathbf{K}\|_i = |a_m + k| = -(a_m + k)$$

the stability condition (26) becomes

$$\left\| \frac{\partial \mathbf{G}_r}{\partial \mathbf{u}} \mathbf{B}_r^{-1} - \mathbf{I} \right\|_i = \left\| \frac{\frac{\partial g}{\partial u}}{b} - 1 \right\|_i < \frac{\left(1 - 2\left\| \frac{\partial g}{\partial x} \right\| L\right)}{\left(3 + 2\left\| \frac{\partial f}{\partial x} \right\| L\right)} \quad (27)$$

The above condition implies

$$1 - \frac{\left(1 - 2\left\| \frac{\partial g}{\partial x} \right\| L\right)}{\left(3 + 2\left\| \frac{\partial f}{\partial x} \right\| L\right)} < \frac{\left(\frac{\partial g}{\partial u}\right)}{b} < 1 + \frac{\left(1 - 2\left\| \frac{\partial g}{\partial x} \right\| L\right)}{\left(3 + 2\left\| \frac{\partial f}{\partial x} \right\| L\right)} \quad (28)$$

with the lower bound on $\frac{\left(\frac{\partial g}{\partial u}\right)}{b}$ being always positive. For the case where $\frac{\partial g}{\partial u} = b$ the stability condition (28) becomes,

$$\left\| \frac{\partial g}{\partial x} \right\| L < \frac{1}{2} \quad (29)$$

This implies that as $\left\| \frac{\partial g}{\partial x} \right\|$ becomes large, the delay time L must be decreased to maintain stability which makes intuitive sense. From (28), it can be observed that for "sufficiently" small L ($L \rightarrow 0$), the condition is reduced to the following limiting case,

$$\begin{aligned} \left\| \frac{\frac{\partial g}{\partial u}}{b} - 1 \right\|_i &< \frac{1}{3} \\ \frac{2}{3} &< \frac{\frac{\partial g}{\partial u}}{b} < \frac{4}{3} \end{aligned} \quad (30)$$

The result indicates that stability is maintained for a variation of 66% of $\frac{\partial g}{\partial u}$ with respect to b .

When the control distribution matrix $\frac{\partial \mathbf{G}_r}{\partial \mathbf{u}}$ is a constant and known, the controller gain matrix \mathbf{B}_r may be chosen such that $\frac{\partial \mathbf{G}_r}{\partial \mathbf{u}} = \mathbf{B}_r$. This enables exact cancellation of the known dynamics \mathbf{F}_r and approximate cancellation of unknown dynamics and disturbances [33]. The stability condition (26) then reduces to a bound on delay time L in terms of $\frac{\partial \mathbf{G}_r}{\partial \mathbf{x}}$ and $(\mathbf{A}_m + \mathbf{K})$. The known dynamics \mathbf{F}_r , the control distribution matrix $\frac{\partial \mathbf{G}_r}{\partial \mathbf{u}}$ and the controller gain matrix \mathbf{B}_r do not enter the stability condition because of exact cancellation.

4 Application: Control of a high speed and high precision magnetic bearing system

The magnetic system under consideration is a turbo molecular pump, a device used to create vacuum in special environments such as integrated circuit manufacturing. A schematic diagram of this pump is shown in Figure 2. The pump action is produced once the rotor, with blades attached to it, is spun by an induction motor. In order to minimize impurities and particle generation, the rotor is suspended magnetically in the X, Y and Z directions shown in the figure. Some information relevant to this design are summarized in Table 1. This system has five degrees which may be described by a differential equation of the form,

$$\frac{d}{dt} \begin{bmatrix} \mathbf{x}_q \\ \vdots \\ \mathbf{x}_r \end{bmatrix} = \begin{bmatrix} \mathbf{x}_r \\ \vdots \\ \mathbf{F}_r(\mathbf{x}, t) \end{bmatrix} + \begin{bmatrix} 0 \\ \vdots \\ \mathbf{G}_r(\mathbf{x}, \mathbf{u}, t) \end{bmatrix} + \begin{bmatrix} 0 \\ \vdots \\ \mathbf{D}_r(t) \end{bmatrix} \quad (31)$$

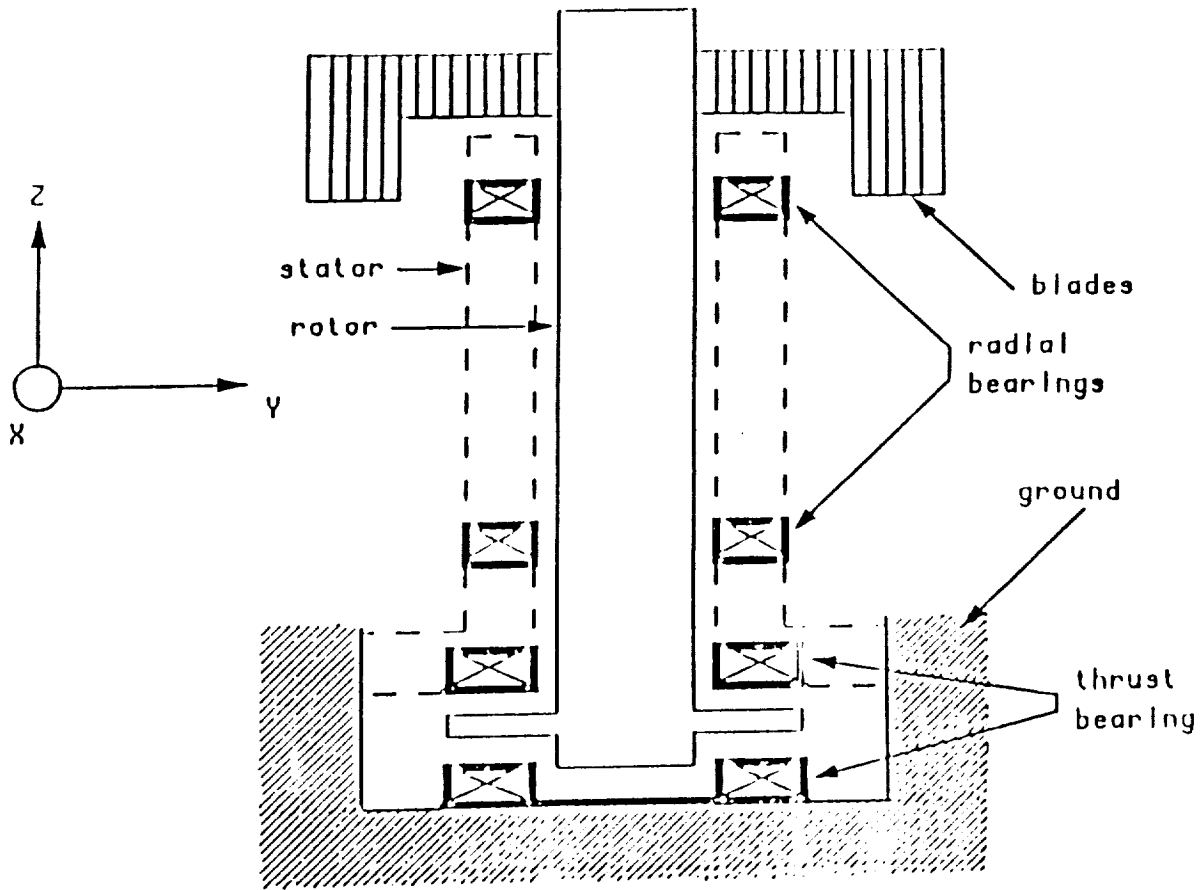


Figure 2: A five-axis magnetic bearing

Rotor Mass	=	2.2 Kg
Air gap for thrust bearing	=	400 μm
Air gap for radial bearing	=	250 μm
Maximum current to bearings	=	10 Amp.
Maximum rotational speed	=	45,000 RPM

Table 1: Relevant system parameters

where $\mathbf{x}_q \in \mathcal{R}^5$ and $\mathbf{x}_r \in \mathcal{R}^5$ represent displacements and velocities of the rotor with respect to the bearing stators respectively. The current inputs to the electromagnets are represented by the vector $\mathbf{u} \in \mathcal{R}^5$. The control objective is to levitate the rotor and maintain stability. Also, the control system must reject disturbances under spinning and nonspinning conditions of the rotor.

This plant is multi-input, multi-output with all five degrees of freedom unstable open loop. Disturbances and coupling include forces due to gravity, magnetic actions, unbalance and gyroscopic effects. All of these effects will show up in the vector function \mathbf{G}_r . Note that since the magnetic force is proportional to the current squared and inverseley proportional to the gap distance squared the function $\mathbf{G}_r(\mathbf{x}, \mathbf{u})$ is a nonlinear function dependent on the state \mathbf{x} and the control action \mathbf{u} .

The variation of the component of \mathbf{G}_r in the Z direction in terms of the gap x and control current u are shown in Figures 3, 4, and 5. Figure 3 shows that for a gap of 0.15 mm, the rotor acceleration corresponds to 30 m/sec² and 110 m/sec² for control currents of 1 and 2 amps respectively. Also, for the same gap opening and with currents levels of 1 and 2 amps, $\frac{\partial g}{\partial x}$ changes from about $0.22 \times 10^6 \frac{1}{\text{sec}^2}$ to about $0.88 \times 10^6 \frac{1}{\text{sec}^2}$, and $\frac{\partial g}{\partial u}$ changes from about 32 m/amp-sec² to about 112 m/amp-sec². It is clear that this particular device experiences drastic dynamic changes. Therefore, such dynamic information would be necessary if a conventional control system is used; otherwise the system performance may be acceptable only for some specific operating conditions.

The control algorithm was implemented on a DSP chip as shown in Figure 6. In this experimental setup, we have the option of controlling the system using either a linear analog controller which resides in the compensation block,

or a time delay controller implemented digitally in the DSP board. The position signal for the Time Delay controller is obtained through the test points TP2 and/or TP3 and this signal is then sent into an analog to digital converter (A/D converter) which is linked to the DSP board. The A/D board has an adjustable built in low pass filter where the position signal can be filtered. The control voltage signal is sent out through the D/A converter which has a low pass filter with adjustable cutoff frequency.

The program was written in C and assembly language. The sampling frequency used was around 5 KHz. The computation time for the control algorithm was about $70\mu\text{sec}$. The cutoff frequency of the filter for the position signal was kept at 7.2 KHz since the signal from the sensor is already bandlimited to 1 KHz. The position signals are then obtained by the DSP board and the control actions representing currents are sent out through the D/A converter. The D/A converter has a low pass filter with a cutoff frequency set to 1.5 KHz. Although a sampling rate of 5 KHz was adequate for this system, the sampling frequency could be increased up to 15 KHz. This sampling rate could further be increased by optimizing the program code and hence reducing the computation time for the Time Delay Control law.

In this section, we will use the control procedure described earlier to maintain a desired performance. The model reference for the thrust bearing position was chosen as a second order system with a natural frequency of 200 rad/sec and a damping ratio of .707. The experimental data shown in Figure 7 indicate that the actual position response tracks the reference model response very closely. In this case, the position of the rotor moves from $200\mu\text{m}$ to $0\mu\text{m}$ which corresponds to the suspended configuration. The error between the desired and actual position trajectories is shown in the same figure and has about less than 10% maximum error. The control current necessary to produce this response is also shown in that same figure with a maximum current of about 1.75 amps. This is an excellent performance considering that the controller has no detailed information about the system. Figure 8 shows the closed-loop frequency response between the reference position and actual position of the thrust bearing. In this case it is clear that the magnitude and phase characteristics are close to those of the reference model selected. In order to check the disturbance rejection properties of the control system, an additional current is injected through the drive amplifiers (Auxiliary input 2 in Figure 6) to create an intentional disturbance force. The frequency of this input is then varied from 0.1 Hz to 10 KHz (sine sweep). In order to check the disturbance rejection properties, we measured the frequency response from the additional current to the position of the rotor. The disturbance rejection properties of the thrust bearing are shown in Figure 9. This curve represents a compliance curve. The controller rejects disturbances up to the bandwidth which is again around 200 rad/sec. The static stiffness is about 100 MN/m and the minimum stiffness is about 300 KN/m at the frequency of 200 rad/sec.

Figure 10 shows the closed loop frequency response for a radial bearing. Again, this response is between the reference position and actual rotor position. This is very similar to that of the reference model. Figure 11 shows the disturbance rejection of the radial bearing when the rotor is at rest and while it is spinning at 10900 RPM, 20100 RPM, 30400 RPM and 34800 RPM. When the rotor is not spinning, the static stiffness is about 200 MN/m and the minimum stiffness is about 500 KN/m. It is clear that the disturbance rejection properties are almost the same for these different operating conditions. Figure 12 shows the effect of using a lower bandwidth of 100 rad/sec. In this case, the disturbance rejection curve moves up indicating a lower stiffness. These data demonstrate that such a control scheme possesses excellent robustness properties.

5 Conclusion

The time delay controller algorithm uses past observations for adaption in controlling systems with unknown dynamics and unpredictable disturbances. The time delay control law is formulated for a class of nonlinear systems with nonlinear input action. The result of stability analysis performed based on the bounded input-bounded output stability approach are presented and interpreted. The control scheme is implemented on a five-degree-of-freedom magnetic bearing. The control performance, evaluated using step responses and disturbance rejection properties, is shown to be excellent despite the complex nonlinearities in the system.

Acknowledgements

The authors gratefully acknowledge the support of Ebara Research Corporation, Ltd. of Japan, and especially the continuous assistance of Dr. Y. Kanemitsu.

References

- [1] Arimoto, S., Kawamura, S. and Miyazaki, F. "Can Mechanical Robots Learn by Themselves?" Proceeding of Second International Symposium on Robotics Research, Kyoto, Japan, August, 1984.
- [2] Asada, H. and Youcef-Toumi, K. "Analysis and Design of a Direct-Drive Arm with a Five-Bar-Link Parallel Drive Mechanism", ASME Journal of Dynamic Systems Measurement and Control, vol. 106, No. 3 pp. 225-230 Sept., 1984.
- [3] Astrom, K.J. and Wittenmark, B. "On Self-Tuning Regulators" Automatica, Vol. 9, pp. 185-199, 1973.
- [4] Astrom, K. J. and Wittenmark, B. Adaptive Control, Addison Wesley, 1989.
- [5] Bahill, A. T. "A Simple Adaptive Smith Predictor for Controlling Time Delay Systems", IEEE Control System Magazine, vol 3, pp. 16-22, 1983
- [6] Bartle, R. G., The Elements of Real Analysis, John Wiley & Sons, Inc., New York, 1976.
- [7] Brogan, W.L. Modern Control Theory, 1985.
- [8] Craig, J.J., Hsu, P. and Sastry, S.S. "Adaptive Control of Mechanical Manipulators", Proceeding of the IEEE International Conference on Robotic and Automation, April 7-10, 1986.
- [9] Dubowsky, S. and DesForges, D.T., "The Application of Model Reference Adaptive Control to Robotic Manipulators" ASME Journal of Dynamic Systems, Measurement and Control, 101:193-200, 1979.
- [10] Hauser, John E. "Learning Control for a Class of Nonlinear Systems", Proceedings of the 28th Conference on Decision and Control, pp.859-860, December 1987.
- [11] Hsia, T.C. "Adaptive Control of Robot Manipulators - A Review" Proceeding of the IEEE International Conference on Robotics and Automation, April 7-10, 1986.
- [12] Ih, C.C. and Wang, S. J. "Dynamic Modelling and Adaptive Control for Space Stations" JPL Publication 85-57, July, 1985.
- [13] Ljung, L. Editor "Control Theory 1984-1986, A Progress Report from IFAC's Technical Committee on Theory", Presented at IFAC, 1987.
- [14] Landau, Y. D. Adaptive Control, Marcel Dekker Inc., New York, NY, 1979.
- [15] Malek-Zavarei M., and M. Jamshidi Time-Delay Systems Analysis, Optimization and Application, North-Holland Systems and Control Series, Vol. 9, 1987.
- [16] Narendra, K. S. and Annaswamy, A. M. Stable Adaptive Systems, Pentice-Hall, 1989.
- [17] Ogata Katsuhiko Modern Control Engineering, Prentice-Hall, Inc., Englewood Cliffs, NJ, 1970.
- [18] Ogata Katsuhiko Discrete-Time Control Systems, Prentice-Hall, Inc., Englewood Cliffs, NJ, 1987.
- [19] Sadegh, N., Horowitz, R., "Stability Analysis of an Adaptive Controller for Robotic Manipulators," Proceedings of the IEEE International Conference on Robotics and Automation, pp. 1223-1239, Raleigh, North Carolina, March 1987.
- [20] Sadegh, N., Horowitz, R., Kao, W.-W., and Tomizuka, M., "A Unified Approach to the Design of Adaptive and Repetitive Controllers for Robotic Manipulator," Proceedings of USA-Japan Symposium on Flexible Automation, Minneapolis, MN, July 1988.
- [21] Sastry, S. and Bodson, M. Adaptive Control Stability, Convergence, and Robustness Prentice Hall, 1989.
- [22] Seraji, H. "A New Approach to Adaptive Control of Manipulators", Journal of Dynamic Systems, Measurement and Control, Vol. 109, pp. 193-202, 1987.
- [23] Slotine, J. J.E. and Sastry, S.S. "Tracking Control of Nonlinear Systems Using Sliding Surfaces with Applications to Robot Manipulators" International Journal of Control, 38-2, 465-492, 1983.

- [24] Tomizuka, M. and Horowitz, R. "Model Reference Adaptive Control of Mechanical Manipulators", IFAC Adaptive Systems in Control and Signal Processing, San Francisco, CA, 1983.
- [25] Uchiyama, M. "Formulation of High-Speed Motion Pattern of a Mechanical Arm by Trial", Transaction of Society of Instrument and Control Engineering of Japan, Vol. 14, No. 6, pp. 706-712, December, 1978.
- [26] Utkin, V.I. "Equations of Sliding Mode in Discontinuous Systems" Automation and Remote Control I(II), 1972.
- [27] Utkin, V.I. "Variable Structure Systems with Sliding Modes", IEEE Trans. on Automatic Control, Vol. 22, pp. 212-222, 1977.
- [28] Vidyasagar, M., Nonlinear Systems Analysis Prentice-Hall, Inc. 1978.
- [29] Volterra, V. "Lecons sur les equation integrales et les equations integro-differentielles", Gauthier-Villars, Paris, 1913. Also see "Sur la Theorie mathematique des phenomenes Hereditaires", F. Math. Paris, Vol. 7, fasc. III, pp. 249-298, 1928.
- [30] Youcef-Toumi, K. and Ito, O. "On Model Reference Control Using Time Delay for Nonlinear Plants with Unknown Dynamics", M.I.T. Report, LMP/RBT 86-06, June, 1986.
- [31] Youcef-Toumi, K. and Ito, O. "Controller Design for Systems with Unknown Dynamics" Proceeding of American Control Conference, Minneapolis, MN, June, 1987.
- [32] Youcef-Toumi, K. and Ito, O. "Model Reference Control Using Time Delay for Nonlinear Plants with Unknown Dynamics", Proceeding of Inter National Federation of Automatic Control World Congress, Munich, Federal Republic of Germany, July, 1987.
- [33] Youcef-Toumi, K. and Ito, O. "Controller Design for Systems with Unknown Dynamics" Proceeding of American Control Conference, Atlanta, GA, June, 1988. Also in the ASME Journal of Dynamic Systems, Measurement and Control, Vol. , No. , pp. , March 1990.
- [34] Youcef-Toumi, K. and Leung, Y.F. "Analysis of Time Delay Controllers for Linear SISO Systems", Proceedings of 1988 USA-Japan Symposium on Flexible Automation.
- [35] Youcef-Toumi, K. and Fuhlbrigge, T. "Application of a Decentralized Time Delay Controller to Robot Manipulators", Proceedings of the 1989 IEEE Conference on Robotics and Automation.
- [36] Youcef-Toumi, K. "The Control of Systems with Unknown Dynamics with Application to Robot Manipulators," M.I.T. Laboratory for Manufacturing and Productivity, Report No. 90-003, March 1990.
- [37] Young, K.-K.D. "Controller Design for a Manipulator Using Theory of Variable Structure Systems", IEEE Transactions, SMC 8-2, pp. 101-109, 1978.

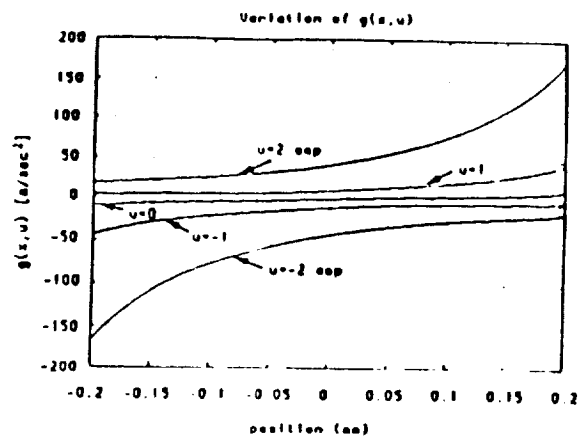


Figure 3: Dynamic changes of the function $g(x,u)$

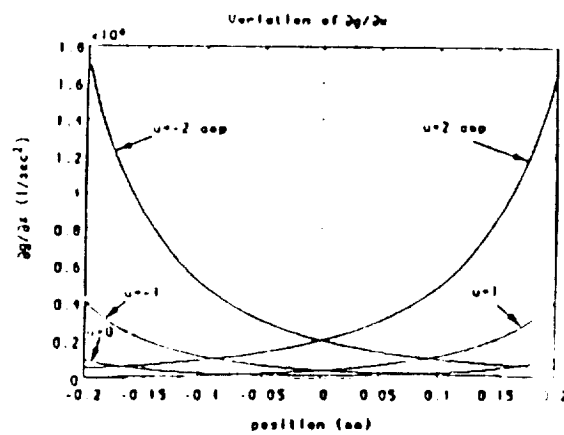


Figure 4: Dynamic changes of the function $\frac{\partial g(x,u)}{\partial x}$

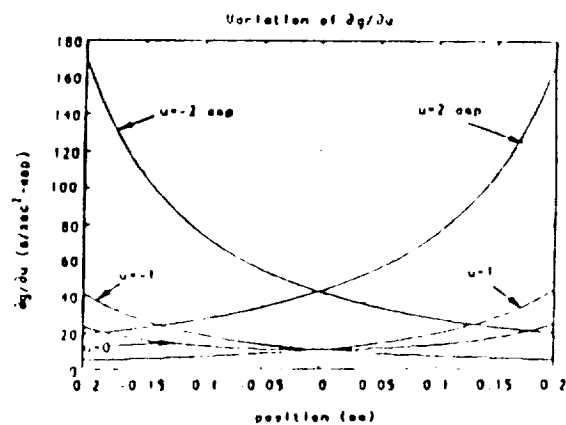


Figure 5: Dynamic changes of the function $\frac{\partial g(x,u)}{\partial u}$

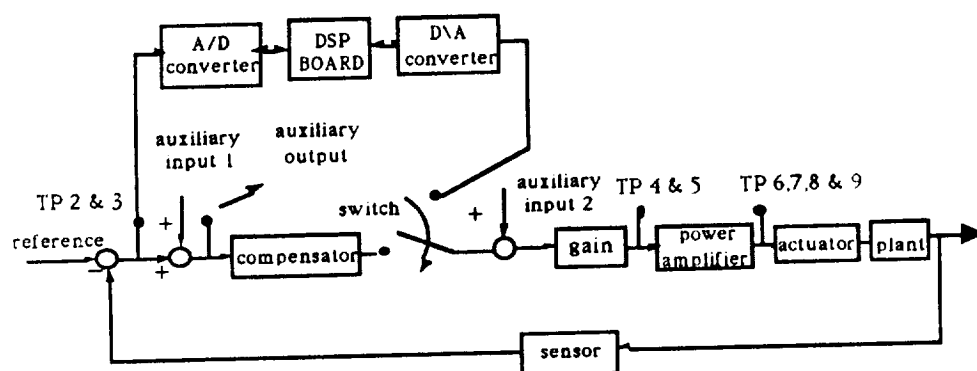


Figure 6: Block diagram representation

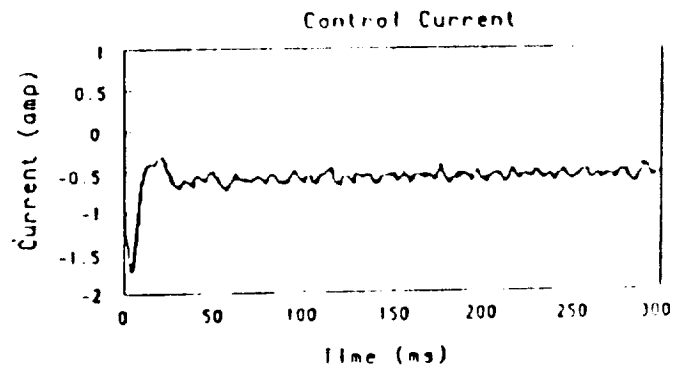
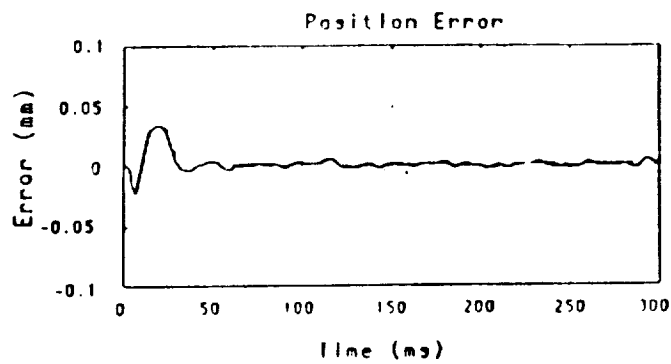
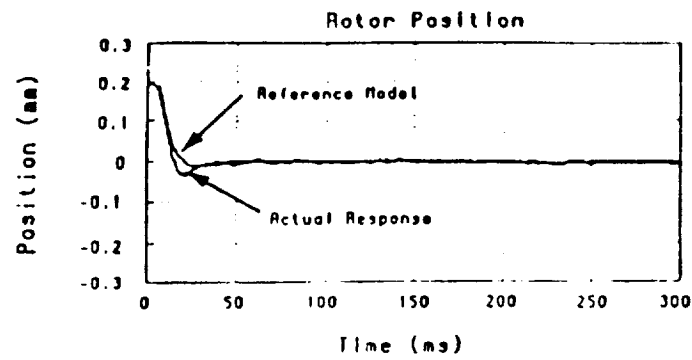


Figure 7: Experimental time response data of the thrust bearing

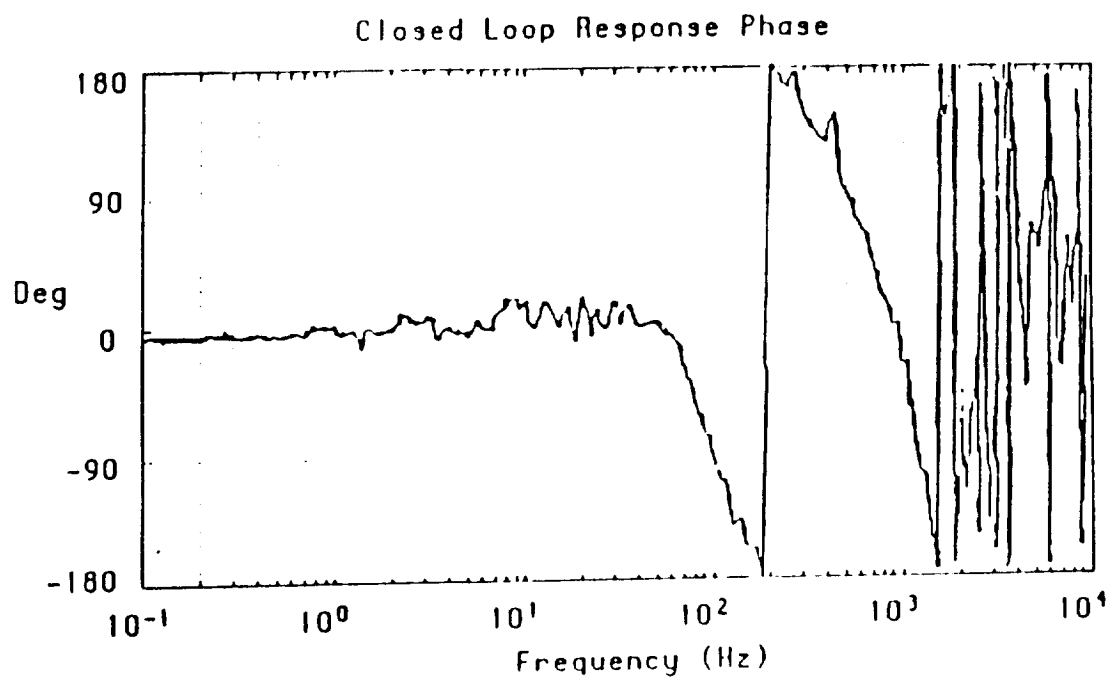
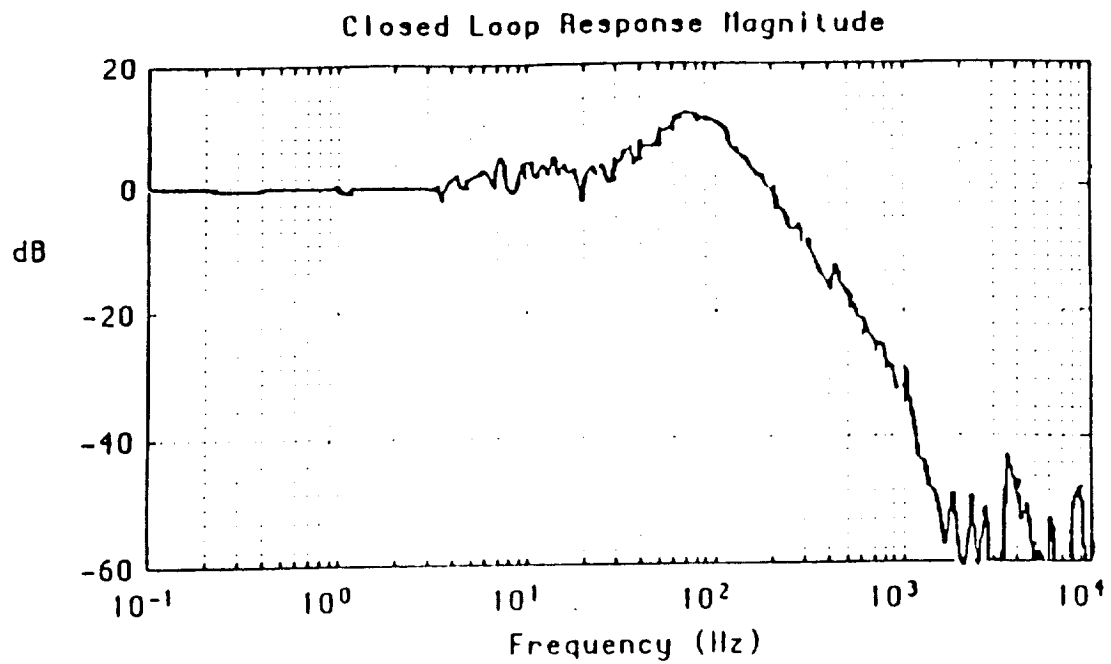


Figure 8: Closed loop frequency response of thrust bearing

Disturbance Compliance Magnitude

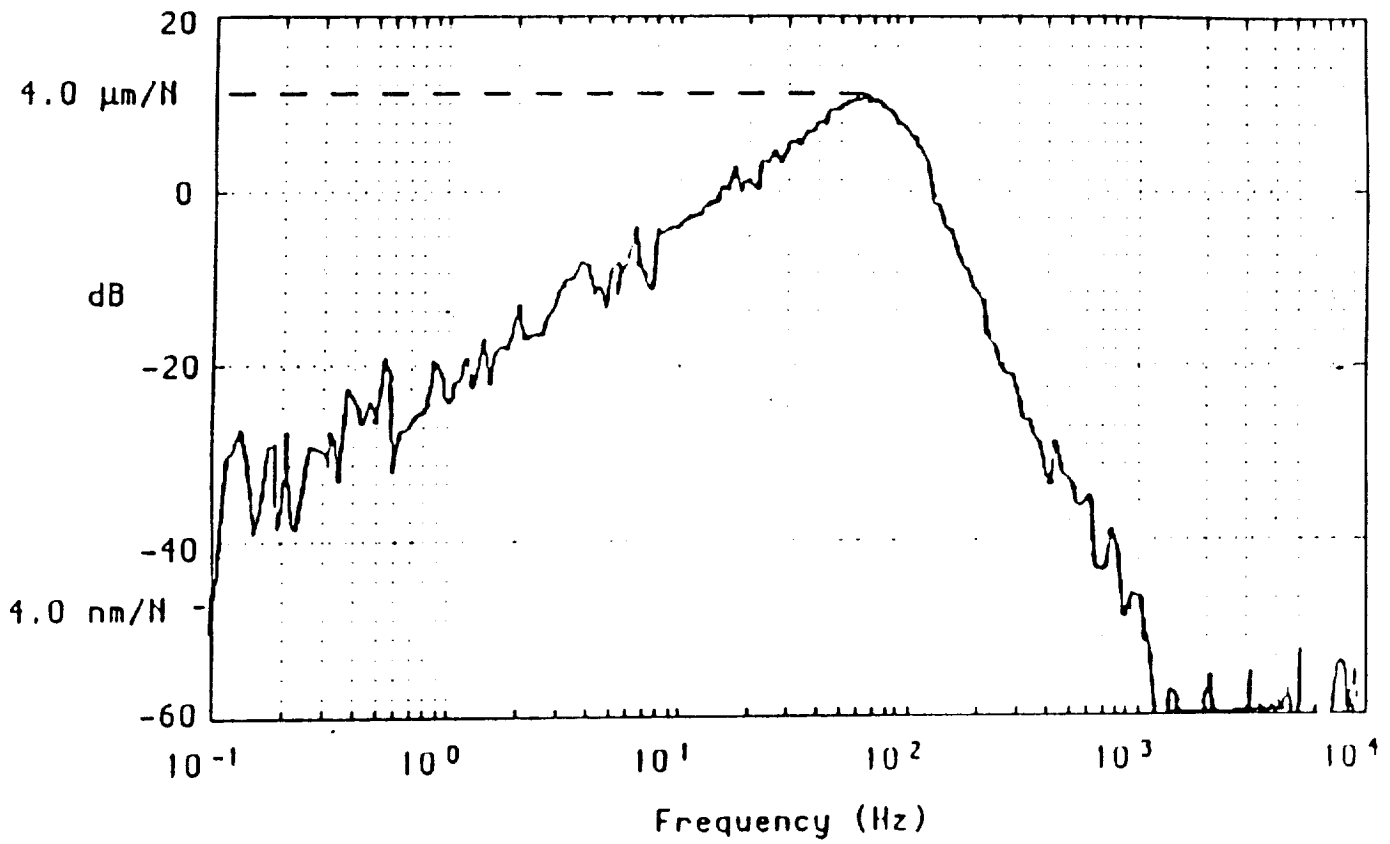


Figure 9: Disturbance rejection of thrust bearing bearing

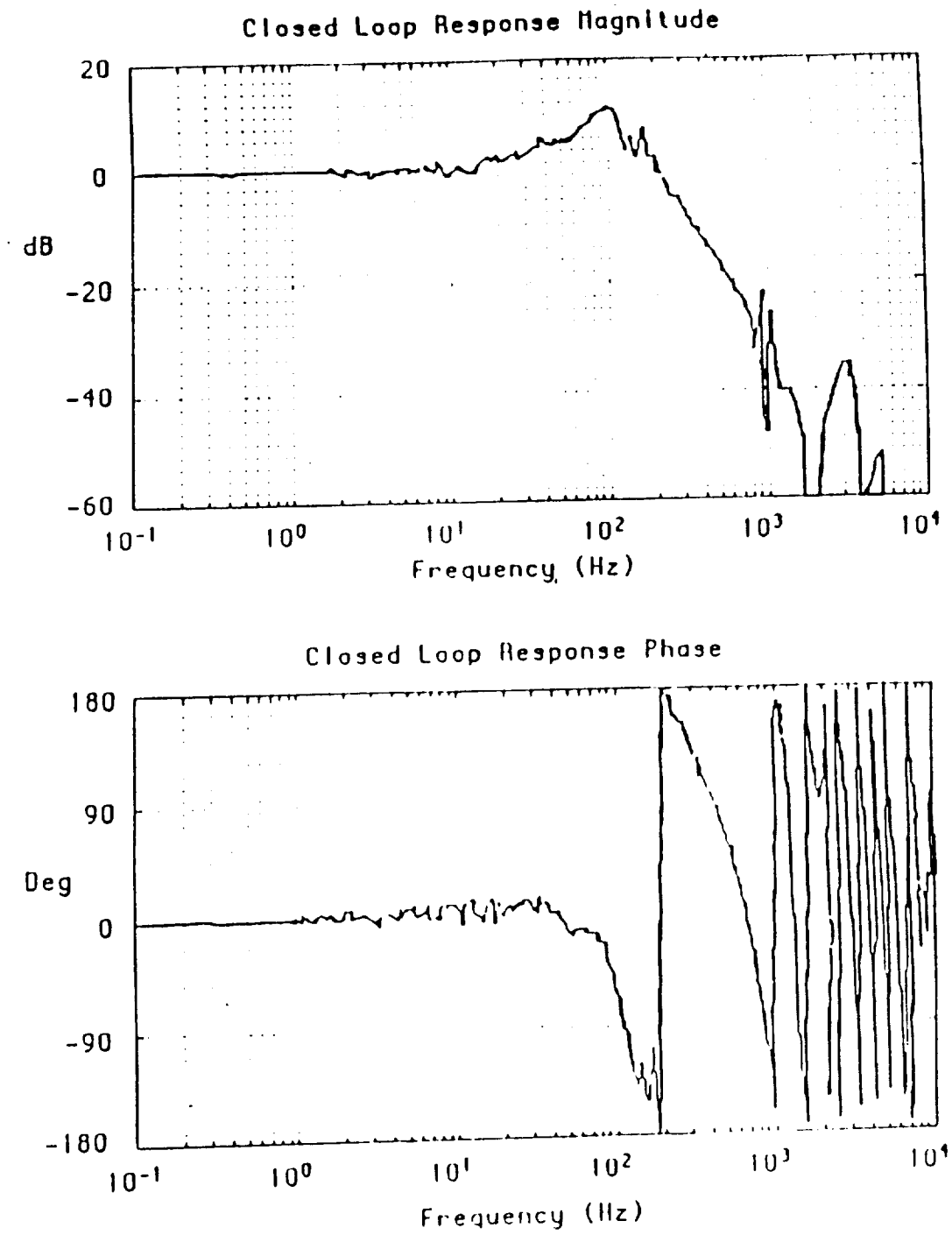


Figure 10: Closed loop frequency response of radial bearing

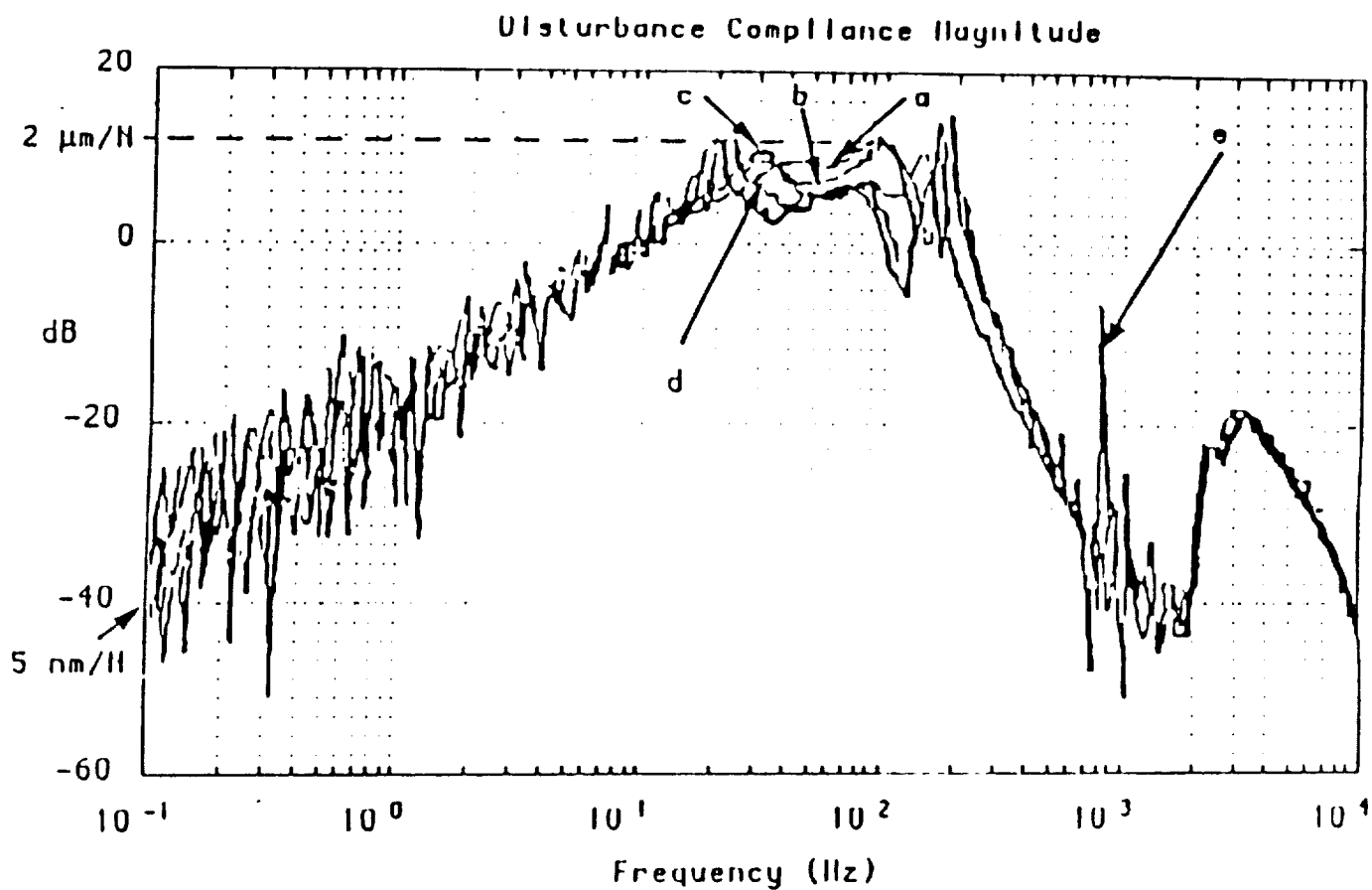


Figure 11: Disturbance rejection of radial bearing: (a) at rest, (b) 10,900 rpm, (c) 20,100 rpm, (d) 30,400 rpm, (e) 34,800 rpm.

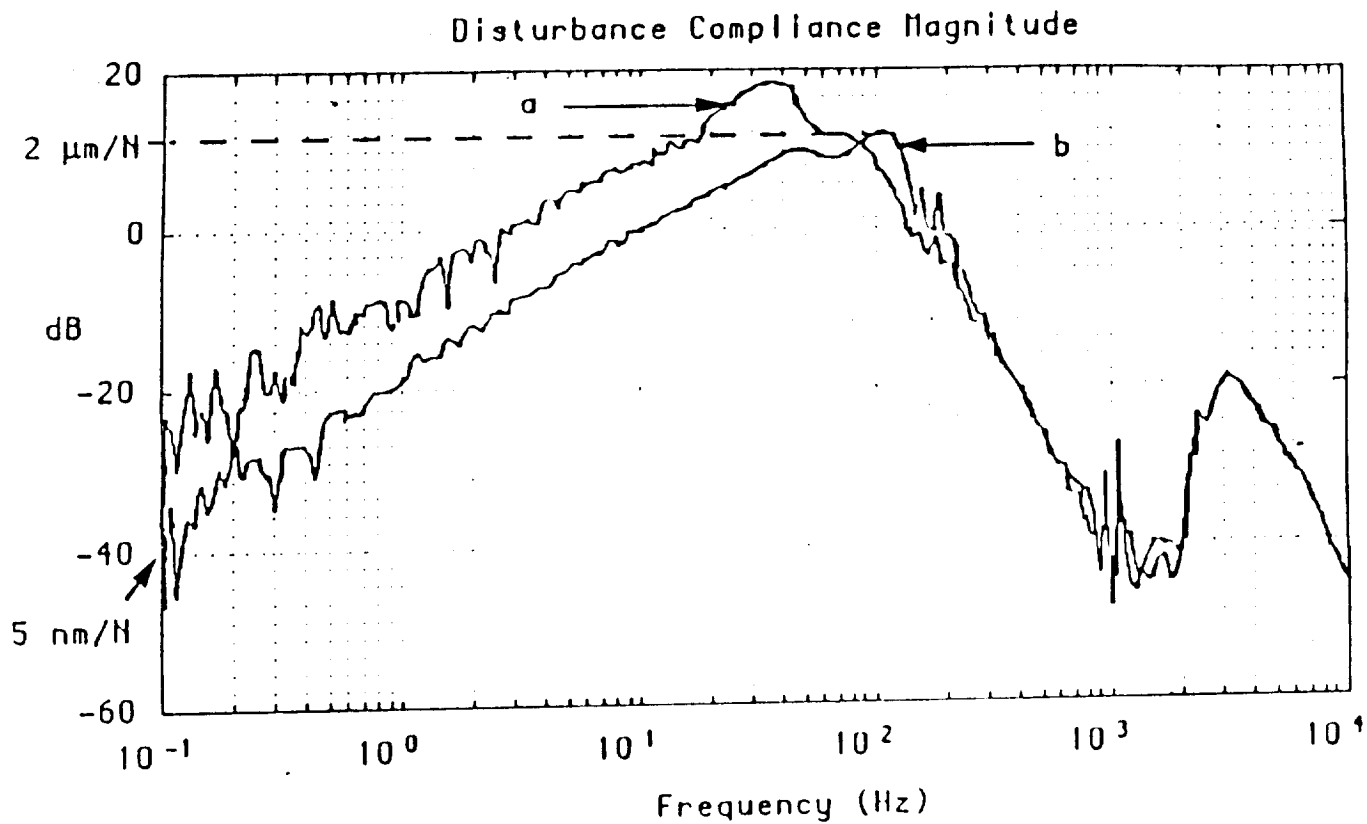


Figure 12: Disturbance rejection of radial bearing with nonspinning rotor (a) bandwidth = 100 rad/sec, (b) bandwidth = 200 rad/sec

N91-21206

**MICROGRAVITY VIBRATION ISOLATION: An OPTIMAL CONTROL LAW
for the ONE-DIMENSIONAL CASE**

**Richard D. Hampton
University of Virginia
Thornton Hall, McCormick Road
Charlottesville
VA 22901**

**Carlos M. Grodsinsky
NASA Lewis Research Center
Mail Stop 23-3
Cleveland
OH 44135**

**Paul E. Allaire, David W. Lewis, Carl R. Knospe
University of Virginia
Thornton Hall, McCormick Road
Charlottesville
VA 22901**

ABSTRACT

Certain experiments contemplated for space platforms must be isolated from the accelerations of the platform. In this paper an optimal active control is developed for microgravity vibration isolation, using constant state feedback gains (identical to those obtained from the Linear Quadratic Regulator [LQR] approach) along with constant feedforward (preview) gains.

The quadratic cost function for this control algorithm effectively weights external accelerations of the platform disturbances by a factor proportional to $(1/\omega)^4$. Low frequency accelerations (less than 50 Hz) are attenuated by greater than two orders of magnitude. The control relies on the absolute position and velocity feedback of the experiment and the absolute position and velocity feed-forward of the platform, and generally derives the stability robustness characteristics guaranteed by the LQR approach to optimality.

The method as derived is extendable to the case in which only the relative positions and velocities and the absolute accelerations of the experiment and space platform are available.

1. INTRODUCTION

A space platform experiences local, low frequency accelerations (0.01–30 Hz) due to equipment motions and vibrations, and to crew activity [1]. Certain experiments, such as the growth of isotropic crystals, require an environment in which the accelerations amount to only a few micro-g's [2]. Such an environment is not presently available on manned space platforms.

Since the experiment and space platform centers of gravity do not coincide, a means is needed to prevent the experiment from drifting into its own orbital motion and into the space platform wall. Additionally, some experiments require umbilicals to provide power, experiment control, coolant flow, communications linkage, or other services. Unfortunately, such measures also mean that unwanted platform accelerations will be transmitted to the experiments. This necessitates experiment isolation. Passive isolators, however, cannot compensate for umbilical stiffness, nor can they achieve low enough corner frequencies even if umbilicals are absent. Active isolation is therefore essential.

The problem, then, is to design an active isolation system to minimize these undesired acceleration transmissions, while achieving adequate stability margins and system robustness. Spatial and control energy limitations must also be accommodated.

2. MATHEMATICAL MODEL

The general problem has three translational and three rotational degrees of freedom. For simplicity, however, this analysis will consider only the one-dimensional problem. The general problem could be treated in an analogous manner. Let the experiment be modeled as a mass m , with position $x(t)$. Assume that the space station has position $d(t)$, and that umbilicals with stiffness k and damping c connect the experiment and space station. Suppose further that a magnetic actuator applies a control force proportional to the applied current $i(t)$, with proportionality constant α . Such a model is shown in Figure 1.

The system equation of motion is

$$m\ddot{x} + c(\dot{x}-\dot{d}) + k(x-d) + \alpha i = 0 \quad (1)$$

Division by m and rearrangement yields

$$\ddot{x} = -\frac{k}{m}(x-d) - \frac{c}{m}(\dot{x}-\dot{d}) - \frac{\alpha}{m}i \quad (2)$$

In state space notation this becomes

$$\dot{\underline{x}} = \underline{A} \underline{x} + \underline{b} u + \underline{f} \quad (3)$$

where

$$\underline{x} = \begin{Bmatrix} x_1 \\ x_2 \end{Bmatrix} = \begin{Bmatrix} x \\ \dot{x} \end{Bmatrix}, \quad \dot{\underline{x}} = \begin{Bmatrix} \dot{x}_1 \\ \dot{x}_2 \end{Bmatrix} = \begin{Bmatrix} \dot{x} \\ \ddot{x} \end{Bmatrix},$$

$$\underline{A} = \begin{bmatrix} 0 & 1 \\ -\frac{k}{m} & -\frac{c}{m} \end{bmatrix}, \quad \underline{b} = \begin{bmatrix} 0 \\ -\frac{\alpha}{m} \end{bmatrix},$$

$$\mathbf{u} = \mathbf{i} \quad , \quad \mathbf{f} = \begin{Bmatrix} 0 \\ \frac{k}{m} \mathbf{d} + \frac{c}{m} \dot{\mathbf{d}} \end{Bmatrix}$$

The objective is to minimize the acceleration $\ddot{\mathbf{x}}(t)$.

3. OPTIMAL CONTROL PROBLEM

The optimal control problem is that of determining the control current $u(t) = i$ which minimizes a suitable performance index

$$J = J(\underline{x}, u, t) \quad (4)$$

for the system described by Eqn. (3) subject to the state variable conditions

$$\underline{x}(0) = \underline{x}_0 \quad (5a)$$

$$\lim_{t \rightarrow \infty} \underline{x}(t) = \underline{0} \quad (5b)$$

Another reasonable assumption is that $\underline{f}(t)$ is bounded, and it will be found mathematically advantageous (and only minimally restrictive) to assume that $\underline{f}(t)$ is also a dwindling function:

$$\lim_{t \rightarrow \infty} \underline{f}(t) = \underline{0} \quad (5c)$$

A quadratic performance index

$$J = \frac{1}{2} \int_0^{\infty} [\underline{x}^T W_1 \underline{x} + w_3 u^2] dt \quad (6)$$

has been chosen, as one that lends itself well to the variational approach to optimal controls, since an analytical solution is desired. The upper limit of the definite integral has been selected so as to yield a time-invariant controller. Here W_1 is a square 2x2 constant weighting matrix while w_3 is a weighting constant.

Although, W_1 could be a full 2x2 matrix, for this problem a diagonal form has been employed for the sake of simplicity.

$$W_1 = \begin{bmatrix} w_{1a} & 0 \\ 0 & w_{1b} \end{bmatrix} \quad (7)$$

The performance index consequently reduces to

$$J = \frac{1}{2} \int_0^{\infty} [w_{1a} \dot{x}_1^2 + w_{1b} \dot{x}_2^2 + w_3 u^2] dt \quad (8)$$

so that each state is weighted independently.

If sinusoidal motion of the experiment is considered, so that

$$x(t) = B \sin \omega t$$

and $\ddot{x}(t) = \omega^2 x(t)$, the cost function can be expressed in terms of the acceleration and control as

$$J = \frac{1}{2} \int_0^{\infty} \left[\left(\frac{w_{1a}}{\omega^4} + \frac{w_{1b}}{\omega^2} \right) B^2 \ddot{x}^2 + w_3 u^2 \right] dt \quad (9)$$

It is apparent that this performance index conveniently weights acceleration - at low frequencies much more than at higher frequencies.

4. SOLUTION

Finding the optimal control to minimize Eqn. (4) is a variational problem of Lagrange, for which the initial steps of the solution are well-known (e.g., Elbert [4]). The variational approach is outlined below, following which the complications added by the nonhomogeneous term $\underline{f}(t)$ will be addressed. Current optimal controls texts either assume that $\underline{f}(t) \equiv 0$ (e.g., [4], p. 262) or require that it have a restricted range space (e.g., [6], p. 238). The solution that follows provides an analytical optimal without imposing such restrictions.

The argument of the cost function J from Eqn. (4) is augmented by the Lagrange multiplier $\underline{\lambda}$ times the system equation of motion Eqn. (3) where

$$\underline{\lambda} = \begin{Bmatrix} \lambda_1 \\ \lambda_2 \end{Bmatrix} \quad (10)$$

The result \hat{J} can be expressed as

$$\hat{J} = \int_0^\infty H \, dt \quad (11)$$

where the Hamiltonian H is

$$H = \frac{1}{2} (\underline{x}^T \underline{W}_1 \underline{x} + w_3 u^2) + \underline{\lambda}^T (\dot{\underline{x}} - \underline{A}\underline{x} - \underline{b}u - \underline{f}) \quad (12)$$

It is desired to obtain an optimal solution $u = u^*$ which minimizes \hat{J} .

The first variation of $\hat{J}(\underline{x}, u, \dot{\underline{x}})$ is

$$\delta \hat{J} = \int_0^\infty \left[\frac{\partial H}{\partial \underline{x}} \delta \underline{x} + \frac{\partial H}{\partial u} \delta u + \frac{\partial H}{\partial \dot{\underline{x}}} \delta \dot{\underline{x}} \right] dt$$

which is set equal to zero to minimize \hat{J} . However, integrating by parts,

$$\int_0^\infty \left(\frac{\partial H}{\partial \underline{\dot{x}}} \delta \underline{\dot{x}} \right) dt = - \int_0^\infty \underline{\dot{\lambda}}^T \delta \underline{x} dt$$

so that the above expression for $\delta \hat{J}$ becomes

$$\delta \hat{J} = \int_0^\infty \left[\left(\frac{\partial H}{\partial \underline{\dot{x}}} - \underline{\dot{\lambda}}^T \right) \delta \underline{\dot{x}} + \frac{\partial H}{\partial u} \delta u \right] dt = 0 \quad (13)$$

Both $\delta \underline{\dot{x}}$ and δu are arbitrary variations, so $\delta \hat{J} = 0$ only if

$$\frac{\partial H}{\partial \underline{\dot{x}}} = \underline{\dot{\lambda}}^T \quad (14a)$$

$$\frac{\partial H}{\partial u} = 0 \quad (14b)$$

The conditions given by Equ. (5) still apply.

Solving Eqs. (14a) and (14b) yields

$$\underline{\dot{\lambda}} = W_1 \underline{x} - A \underline{\lambda} \quad (15a)$$

$$u^* = \frac{1}{w_3} \underline{b}^T \underline{\lambda} \quad (15b)$$

Temporarily eliminating u^* produces the result

$$\begin{Bmatrix} \dot{\underline{x}} \\ \dot{\underline{\lambda}} \end{Bmatrix} = \hat{A} \begin{Bmatrix} \underline{x} \\ \underline{\lambda} \end{Bmatrix} + \begin{Bmatrix} \underline{f} \\ \underline{0} \end{Bmatrix} \quad (16)$$

where

$$\hat{A} = \begin{bmatrix} A & \frac{1}{w_3} b b^T \\ w_1 & -A^T \end{bmatrix}$$

If Eqn. (16) is now solved for $\underline{\lambda}$ in terms of \underline{x} and \underline{f} , Eqn. (15b) will then furnish an expression for the optimal control u^* .

As noted before, optimal control texts generally treat the homogeneous problem (where $\underline{f}(t) \equiv 0$), but they do not provide an analytical solution to the nonhomogeneous system described by (5) and (16). Salukvadze has treated the nonhomogeneous problem [4,5], but his difficult treatment seems largely to have remained either uncomprehended or under-appreciated. This method is especially well-suited to low-frequency disturbance rejection, and has been applied below to the present problem.

The homogeneous solution to Eqn. (15), where $\underline{f} = \underline{0}$, is

$$\begin{Bmatrix} \underline{x} \\ \underline{\lambda} \end{Bmatrix}_h = e^{\hat{A}t} \begin{Bmatrix} \underline{x}_0 \\ \underline{\lambda}_0 \end{Bmatrix} \quad (17)$$

The four eigenvalues of \hat{A} may be found to be, in ascending order of real parts,

$$\mu_1 = - \left[\frac{-\beta_1 + (\beta_1^2 - 4\beta_2)^{1/2}}{2} \right]^{1/2} \quad (18a)$$

$$\mu_2 = - \left[\frac{-\beta_1 - (\beta_1^2 - 4\beta_2)^{1/2}}{2} \right]^{1/2} \quad (18b)$$

$$\mu_3 = -\mu_1 \quad (18c)$$

$$\mu_4 = -\mu_2 \quad (18d)$$

where β_1 and β_2 are defined as follows:

$$\beta_1 = \frac{2k}{m} - \frac{c^2}{m^2} - \frac{\alpha w_{1b}}{m w_3} \quad (19a)$$

and

$$\beta_2 = \beta_1^2 - 4 \left[\frac{\alpha^2 w_{1a}}{m^2 w_3} + \frac{k}{m^2} \right] \quad (19b)$$

The eigenvectors of \hat{A} corresponding to the respective eigenvalues μ_k may be chosen to be

$$p_k = \left\{ \begin{array}{c} 1 \\ \mu_k \\ \frac{\gamma_4}{\mu_k} + \frac{\gamma_1^2}{\gamma_3 \mu_k} + \frac{\gamma_1(\gamma_2 + \mu_k)}{\gamma_3} \\ \frac{\gamma_1 + (\gamma_2 + \mu_k)\mu_k}{\gamma_3} \end{array} \right\} \quad (20a)$$

where γ_1 , γ_2 , γ_3 , and γ_4 are defined below:

$$\gamma_1 = \frac{k}{m} \quad (20b)$$

$$\gamma_2 = \frac{c}{m} \quad (20c)$$

$$\gamma_3 = \frac{\alpha^2}{m^2 w_3} \quad (20d)$$

$$\gamma_4 = w_{1a} \quad (20e)$$

Using Eqs. (18) through (20) with (17) the solution to the homogeneous system is

$$\begin{Bmatrix} \underline{x} \\ \underline{\lambda} \end{Bmatrix}_h = \begin{Bmatrix} c_1 e^{\mu_1 t} p_{1,1} + c_2 e^{\mu_2 t} p_{2,1} + c_3 e^{-\mu_1 t} p_{3,1} + c_4 e^{-\mu_2 t} p_{4,1} \\ c_1 e^{\mu_1 t} p_{1,2} + c_2 e^{\mu_2 t} p_{2,2} + c_3 e^{-\mu_1 t} p_{3,2} + c_4 e^{-\mu_2 t} p_{4,2} \end{Bmatrix} \quad (21)$$

with $p_k = \begin{Bmatrix} p_{k,1} \\ p_{k,2} \end{Bmatrix}$, $k = 1, \dots, 4$ and where c_1, \dots, c_4 are arbitrary constants.

Application of the variation of parameters method with terminal conditions (Eqs. 5b,c) leads to the general solution of the non-homogeneous system, with two constants of integration yet undetermined.

If the two constants of integration are eliminated by solving for $\underline{\lambda}$ in terms of \underline{x} and \underline{f} , the general solutions for λ_1 and λ_2 become:

$$\lambda_1 = \xi_1 x_1 + \xi_2 x_2 + \xi_3 e^{-\mu_1 t} + \xi_4 e^{-\mu_2 t} \quad (22a)$$

$$\lambda_2 = \xi_5 x_1 + \xi_6 x_2 + \xi_7 e^{-\mu_1 t} + \xi_8 e^{-\mu_2 t} \quad (22b)$$

in which the ξ_i 's are functions of the eigenvalues and eigenvectors of \dot{A} , and of the disturbance $\underline{f}(t)$.

The Solution Form

Using the fact that

$$\underline{u}^*(t) = \frac{1}{w_3} \underline{\Delta}^T \underline{b} \quad [\text{cf. Eqn. (15b)}] \quad (23)$$

the optimal control is found to be

$$\underline{u}^*(t) = \eta_1 x_1 + \eta_2 x_2 + \eta_3 e^{-\mu_1 t} \int e^{\mu_1 t} f_2(t) dt + \eta_4 e^{-\mu_2 t} \int e^{\mu_2 t} f_2(t) dt \quad (24a)$$

where

$$\eta_1 = \frac{-m}{\alpha} \left(\frac{k}{m} - \mu_1 \mu_2 \right) \quad (24b)$$

$$\eta_2 = \frac{-m}{\alpha} \left(\frac{c}{m} + \mu_1 + \mu_2 \right) \quad (24c)$$

$$\eta_3 = \frac{m}{\alpha} \left(\frac{1}{\mu_1 - \mu_2} \right) (\mu_1^2 + \frac{c}{m} \mu_1 + \frac{k}{m}) \quad (24d)$$

$$\eta_4 = -\frac{m}{\alpha} \left(\frac{1}{\mu_1 - \mu_2} \right) (\mu_2^2 + \frac{c}{m} \mu_2 + \frac{k}{m}) \quad (24e)$$

(It should be noted that the feedback gains η_1 and η_2 are those which would result from applying standard LQR theory to the homogeneous system equation $\dot{\underline{x}} = \underline{A}\underline{x} + \underline{b}\underline{u}$). In Eqns. (24) μ_1, μ_2 are the eigenvalues of \dot{A} with negative real parts, [see Eqns. (18a,b)] and

$$f_2(t) = \frac{k}{m} d + \frac{c}{m} \dot{d} \quad (24f)$$

By repeated application of the method of integration by parts, the control may be re-expressed in terms of an infinite sum:

$$u^*(t) = \eta_1 x_1 + \eta_2 \dot{x}_2 + \eta_3 \left[\sum_{r=0}^{\infty} \frac{(-1)^r f_2^{(r)}(t)}{\mu_1^{r+1}} \right] + \eta_4 \left[\sum_{r=0}^{\infty} \frac{(-1)^r f_2^{(r)}(t)}{\mu_2^{r+1}} \right] \quad (25)$$

Rewriting f_2 in terms of d and \dot{d} , the control function becomes

$$\begin{aligned} u^*(t) = & \eta_1 x(t) + \eta_2 \dot{x}(t) + \left[\frac{k}{m} \left(\frac{\eta_3}{\mu_1} + \frac{\eta_4}{\mu_2} \right) \right] d(t) \\ & + \sum_{i=1}^{r-1} \left[(-1)^{i-1} \frac{c}{m} \left(\frac{\eta_3}{\mu_1^i} + \frac{\eta_4}{\mu_2^i} \right) + (-1)^i \frac{k}{m} \left(\frac{\eta_3}{\mu_1^{i+1}} + \frac{\eta_4}{\mu_2^{i+1}} \right) \right] d^{(i)}(t) \\ & + [(-1)^{n-1} \frac{c}{m} \left(\frac{\eta_3}{\mu_1^n} + \frac{\eta_4}{\mu_2^n} \right)] d^{(n)}(t) + \text{higher order terms} \end{aligned} \quad (26)$$

This may be written in a more appealing form as

$$u^*(t) = c_p x(t) + c_v \dot{x}(t) + c_{d0} d(t) + c_{d1} \dot{d}(t) + \text{higher order terms} \quad (27)$$

in which the constant coefficients c_p , c_v , c_{d0} , and c_{d1} may be defined from Eqns. (24) and (26). Clearly, if the infinite sums converge rapidly enough, the optimal control can be approximated by

$$u^*(t) = c_p x(t) + c_v \dot{x}(t) + c_{d0} d(t) + c_{d1} \dot{d}(t) \quad (28)$$

For very low frequency disturbances the higher order terms in Eqn. (26) are negligibly small, and the control (Eqn. (28)) closely approximates the optimal. If, in fact, the second- and higher-order derivatives of $d(t)$ are identically zero, the approximation is exact. It can be shown that for the critically damped closed loop system the eigenvalues are real and equal, and that the convergence is more rapid than for the overdamped system. Further, as the closed-loop system eigenvalues become more negative the convergence speed goes up as well.

5. CONTROL EVALUATION

Physical Realizability of the Control

The control, Eqn. (25), is physically realizable, if the states and sufficient derivatives of $d(t)$ are accessible (or estimable by an observer), and if the higher order terms are negligible. It is not necessary that the eigenvalues be real, although the proof of this requires a more general linear-algebra or state-transition-matrix approach.

If values are assigned to the system parameters, associated controller gains can be evaluated. Suppose that $m = 100$ lbm, $k = 0.3$ lbf/ft, $c = 0$ lbf-sec/ft, and $\alpha = 10$ lbf/Amp. With w_3 arbitrarily set at 1 and w_{1b} varied, associated integer values of w_{1a} can be found below which the eigenvalues μ_1 and μ_2 will always be real. Such values are tabulated in Table 1. Stated otherwise, the tabulated values of the weights w_{1a} and w_{1b} are those integer values (for the sake of simplicity) for which the closed loop system is closest to being critically damped without being underdamped. Corresponding controller feedback and feed-forward gains (for the first five derivatives) are also included.

The states $x(t)$ and $\dot{x}(t)$ and the derivatives $d^{(0)}(t)$, $d^{(1)}(t)$ and $d^{(2)}(t)$ are clearly available for an earth-based system. However, in space, the only absolute measurements which can be directly available are $\ddot{x}(t)$ and $\ddot{d}(t)$, from which $\dot{x}(t)$, $\dot{d}(t)$ and $x(t)$, $d(t)$ are obtainable only by successive integration(s). Rearrangement of (28) into

$$u^*(t) = (c_p + c_{d0})x(t) + (c_v + c_{d1})\dot{x}(t) - c_{d0}[x(t) - d(t)] - c_{d1}[\dot{x}(t) - \dot{d}(t)] \quad (29)$$

or

$$u^*(t) = (c_p + c_{d0})d(t) + (c_v + c_{d1})\dot{d}(t) + c_p[x(t) - d(t)] + c_v[\dot{x}(t) - \dot{d}(t)] \quad (30)$$

obviates the need for one accelerometer, but one accelerometer plus two integrations remain necessary for either the platform or the experiment. Since $[x(t)-d(t)]$ (or one of its integrals) has not been weighted in the performance index J , experiment drift will be a problem that must be corrected either by another control loop or by a change of system states. The latter could be accomplished by incorporating an accelerometer attached to the experiment into the state equation. Alternatively, one could append an integrator to the plant, include the current $i(t)$ as a third state, and optimize the control di/dt . But for the sake of simplicity (i.e., fewer states) the former has been assumed (without development) in this paper.

The higher order terms of the control [Eqns. (25) and (26)] can be neglected, for low frequencies, if the eigenvalues μ_1 and μ_2 are of sufficient modulus. These eigenvalues, in turn, are under the control of the designer, determined by his choice of weights w_{1a} , w_{1b} , and w_3 . It is apparent from Eqn. (25) that $u^*(t)$ essentially reduces to two alternating power series. For a sinusoidal disturbance of frequency ω the series form of the control converges for $|\omega/\mu_i| < 1$ ($i = 1, 2$). It can be shown that each alternating power series converges like $\sum_{r=0}^{\infty} (-1)^r (\frac{\omega}{\mu})^{2r}$. With "low" frequency disturbances (i.e., small relative to system closed loop eigenvalues) a control formed by series truncation very closely approximates the optimal.

For example, suppose that the normalized frequencies $|\omega/\mu_i|$ for a sinusoidal disturbance are less than $1/5$, and that only the feedforward control terms $c_{d0}d(t)$ and $c_{d1}\dot{d}(t)$ are included with the feedback terms. Even so, the feedforward portion of the truncated control, at any time t , will be a current that is still within 4% [i.e., $(1/5)^2$] of the feedforward portion of the actual optimal. If the normalized frequencies are below $1/10$, this approximation error will be less than 1%. Table 1 shows that the gains c_{di} of higher order derivatives $d^{(i)}(t)$ [see Eqn. (26) for algebraic representations] are, in fact, quite small.

In some circumstances there may be design constraints which prevent the designer from selecting weights that will lead to sufficiently rapid convergence. However, since convergence occurs rapidly even for eigenvalues of relatively small modulus ($|\omega/\mu_1| < 1/3$), in a great many cases the designer will have much latitude in his choice of weights. For "low" frequency disturbances, in these cases, a control which includes only one or two feedforward terms will be "close" to the optimal. These frequencies will be well-attenuated.

Higher frequency disturbances will also be well-attenuated, provided the input-to-output transfer function(s) are at least strictly proper in the Laplace Transform variable s . This will not be the case for the present problem if more than three feedforward gains (c_{d0} , c_{d1} , c_{d2}) are included in the control. Practically, this means that only proportional and first-derivative feedforward [Eqn. (25) with $r = 0,1$ or Eqn. (26) with $n = 2$] should be added to the feedback control terms. As will be seen shortly, however, adding even the proportional feedforward term(s) can dramatically improve the disturbance rejection over that afforded by LQR feedback alone.

Transfer Function and Block Diagram

Neglecting the higher order terms, the transfer function between input and output accelerations or displacements is

$$\frac{s^2 X(s)}{s^2 D(s)} = \frac{X(s)}{D(s)} = \frac{(\frac{c}{\alpha} - c_{d1})s + (\frac{k}{\alpha} - c_{d0})}{(\frac{m}{\alpha})s^2 + (\frac{c}{\alpha} + c_v)s + (\frac{k}{\alpha} + c_p)} \quad (31)$$

and a block diagram of the controlled system can be drawn as in Figure 2.

Control Stability, Stability Robustness, and General Robustness

Since the control feedback gains are the same as those obtained by solution of the standard Linear Quadratic Regulator (LQR) problem, the closed loop system is stable and enjoys the stability robustness characteristics guaranteed by the (LQR) approach to optimality, viz., a minimum of 60° phase margin, infinite positive gain margin, and 6 dB negative gain margin [6]. Additionally, numerical checks indicate that it enjoys substantial insensitivity, or general robustness to uncertainties in k , c , and m , as indicated by Table 2 and Figures 3 through 10. By comparing the Bode plots of Figures 3, 5, 7, and 9 (corresponding to controls using both LQR F/B and proportional F/F) with those of Figures 4, 6, 8, and 10, respectively (corresponding to controls using LQR F/B only), one can see that adding feed-forward substantially improves disturbance rejection at low frequencies. For example a comparison of Figures 3 with Figure 4 indicates that the optimal control method described above can lead to acceleration reductions of greater than four orders of magnitude for all frequencies. This reduction is more than two orders of magnitude below that afforded by LQR feedback alone at the lower frequencies, i.e., those most heavily weighted in the performance index.

The order of the reduction is eventually limited by control cost, of course, probably in terms either of actuator-related limitations (such as heat-removal or force-generation requirements) or of power limitations (especially in a space-station environment). The control also leads to displacement reductions of the same magnitude, limited in this case by actuator-stroke or spatial limitations. Providing a unit transmissibility for very low frequencies and weighting $(x-d)$ and/or $\dot{f}(x-d)$ in the performance index J would be steps toward addressing these latter limitations.

Computational Aspects

A significant amount of algebra was required to solve the two-state problem of this paper, and the labor involved increases dramatically with each additional state. However, such symbolic manipulators as MACSYMA may be used to ease the workload if a symbolic solution is desired. Further, well-known numerical methods exist (i.e., Potter's method [7] or Laub's method [8]) for solving the solution to the homogeneous system. These can readily provide the feedback gains in numerical form, even for problems with many states. It might be anticipated, then, that a numerical method also exists for finding the desired feed-forward gains. Such is the case, as will be shown in a later paper.

6. CONCLUSIONS

This paper has applied an existing method for obtaining an optimal control to the microgravity platform isolation problem, for which the disturbances to be rejected are low-frequency accelerations. The system was assumed to be representable in the form $\dot{\underline{x}} = \underline{A} \underline{x} + \underline{b} u + \underline{f}$, with quadratic cost function $J = \frac{1}{2} \int_0^\infty (\underline{x}^T \underline{W}_1 \underline{x} + w_3 u^2) dt$ and diagonal weighting matrix \underline{W}_1 . The resultant control law was found to be simple, stable, robust, and physically realizable. Further it was shown to have excellent acceleration- and displacement-attenuation characteristics, and to be frequency-weighted toward the low end of the acceleration spectrum.

The method is extendable to the case for which only relative positions and velocities, and absolute accelerations, are available; and can be applied so as to weight relative displacements in the performance index.

The approach as presented is algebraically intensive, but symbolic manipulators can be used to ease the algebraic labors. Further, since the method produces feedback gains identical to those obtained by the LQR approach to optimality, numerical computation of those gains is easily accomplished, even for large systems. The feed-forward gains can be found numerically with comparable ease.

7. ACKNOWLEDGEMENTS

The authors would like to recognize NASA for partial funding of this work. Eric Maslen at the University of Virginia for his many helpful control-related suggestions at problem points and regarding future work, and Dr. Gerald Brown of NASA Lewis for his insights into the microgravity isolation problem in an orbital environment.

8. REFERENCES

1. Hamacher, H., Jilg, R., and Merbold, U., "Analysis of Microgravity Measurements Performed During DI," 6th European Symposium on Materials Sciences Under Microgravity Conditions, Bordeaux, December 2–5, 1986.
2. Alexander, J. Irwan D., "Experiment Sensitivity: Determination of Requirements for Vibration Isolation," Vibration Isolation Technology Workshop, NASA Lewis Research Center, September 28–29, 1988.
3. Elbert, Theodore F. Estimation and Control of Systems. New York: Van Nostrand Reinhold Company Inc., 1984. Chapter 6: "Optimal Control of Dynamic Systems."
4. Salukvadze, M. E., "Analytic Design of Regulators (Constant Disturbances)," translated in Automation and Remote Control, Vol. 22, No. 10, pp. 1147–1155, October 1961. Originally published in Avtomatika i Telemekhanika, Vol. 22, No. 10, pp. 1279–1287, February 1961.
5. Salukvadze, M. E., "The Analytical Design of an Optimal Control in the Case of Constantly Acting Disturbances," translated in Automation and Remote Control, Vol. 23, No. 6, pp. 657–667, June 1962. Originally published in Avtomatika i Telemekhanika, Vol. 23, No. 6, pp. 721–731, July 1962.
6. Anderson, B. D. O. and Moore, J. B. Linear Optimal Control. Englewood Cliffs, New Jersey: Prentice Hall, 1971. pp. 70–74.
7. Potter, J. E., "Matrix Quadratic Solutions," SIAM Journal of Applied Mathematics, Vol. 14, No. 3, May 1966, pp. 496–501.
8. Laub, A. J., "A Schur method for solving algebraic Riccati equations," IEEE Transactions on Automatic Control, Vol. AC-24, pp. 913–921.

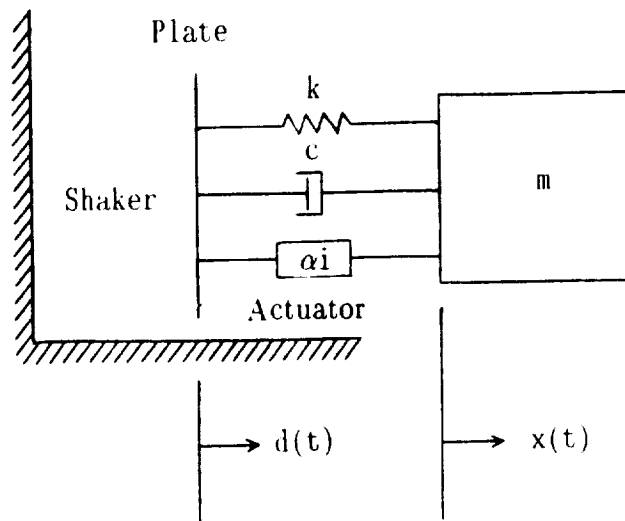


Figure 1. System Model

Table 1. Optimal F/F and F/B Gains for Selected State Variable and Control Weightings.

System Parameters:

$m = 100 \text{ lbm}$ $k = 0.3 \text{ lbf/ft}$
 $c = 0.000622 \text{ lbf-sec/ft}$ ($\zeta = 0.1\%$)
 $\alpha = 10 \text{ lbf/amp}$

Weights			F/B Gains		F/F Gains					
w_{1a}	w_{1b}	w_3	C_p	C_v	C_{d0}	C_{d1}	C_{d2}	C_{d3}	C_{d4}	C_{d5}
2	1	1	1.3845	1.3637	0.0294	-0.0006	-0.0070	-0.0067	-0.0049	-0.0032
10	2	1	3.1324	1.9863	0.0297	-0.0001	-0.0030	-0.0019	-0.0009	-0.0004
23	3	1	4.7659	2.4414	0.0298	-0.0000	-0.0020	-0.0010	-0.0004	-0.0001
41	4	1	6.3732	2.8210	0.0299	0.0000	-0.0015	-0.0007	-0.0002	-0.0001
64	5	1	7.9701	3.1544	0.0299	0.0000	-0.0012	-0.0005	-0.0001	-0.0000
92	6	1	9.5617	3.4552	0.0299	0.0000	-0.0010	-0.0004	-0.0001	-0.0000
126	7	1	11.1950	3.7354	0.0299	0.0000	-0.0008	-0.0003	-0.0001	-0.0000
165	8	1	12.8153	3.9949	0.0299	0.0000	-0.0007	-0.0002	-0.0001	-0.0000
209	9	1	14.4269	4.2480	0.0299	0.0000	-0.0006	-0.0002	-0.0000	-0.0000
258	10	1	16.0324	4.4674	0.0299	0.0000	-0.0006	-0.0002	-0.0000	-0.0000
581	15	1	24.0710	5.1729	0.0300	0.0001	-0.0004	-0.0001	-0.0000	-0.0000
1034	20	1	32.1259	6.3209	0.0300	0.0001	-0.0003	-0.0001	-0.0000	-0.0000
1617	25	1	40.1819	7.0680	0.0300	0.0001	-0.0002	-0.0000	-0.0000	-0.0000
2329	30	1	48.2297	7.7441	0.0300	0.0001	-0.0002	-0.0000	-0.0000	-0.0000
3171	35	1	56.2816	8.3610	0.0300	0.0001	-0.0002	-0.0000	-0.0000	-0.0000
4143	40	1	64.3361	8.9420	0.0300	0.0001	-0.0001	-0.0000	-0.0000	-0.0000
9325	60	1	96.5360	10.9526	0.0300	0.0001	-0.0001	-0.0000	-0.0000	-0.0000
16581	80	1	128.7372	12.6475	0.0300	0.0001	-0.0001	-0.0000	-0.0000	-0.0000
25911	100	1	160.9389	14.1407	0.0300	0.0001	-0.0001	-0.0000	-0.0000	-0.0000

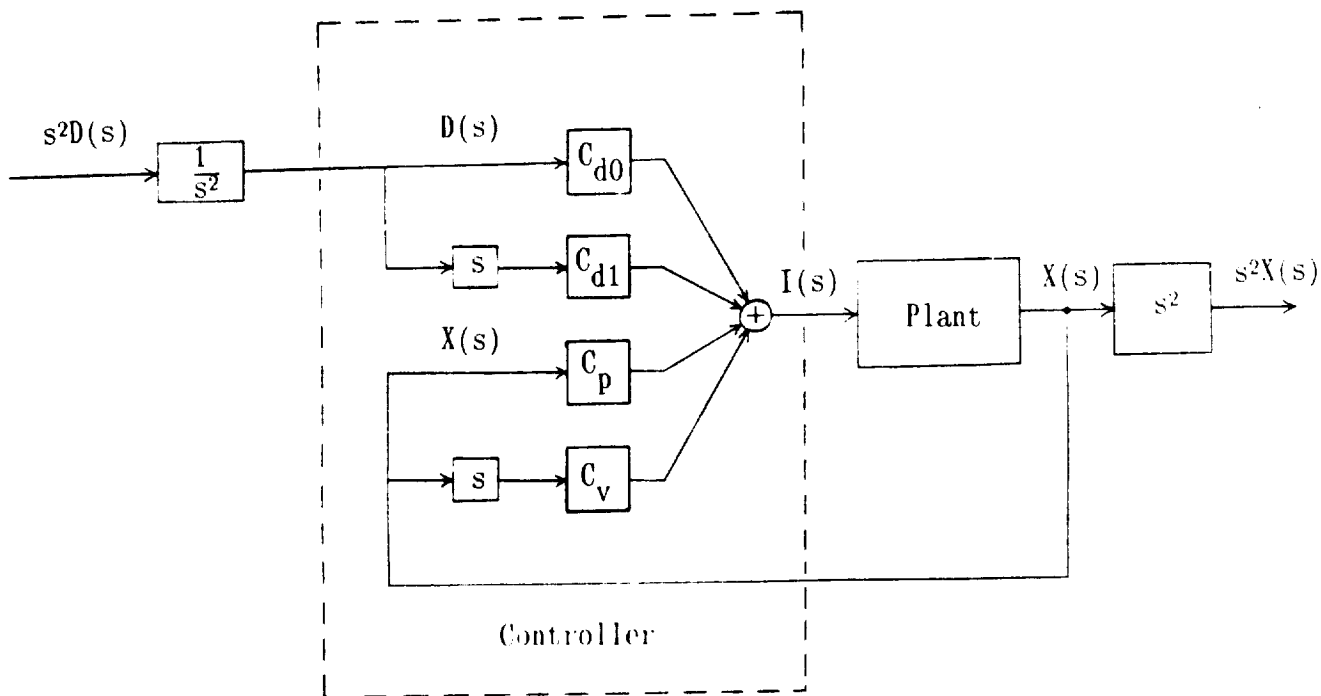


Figure 2. Block Diagram

Table 2. Closed loop transfer functions for system with design parameter values of $k = 0.3$, $c = 0.000622$, and $m = 100$; but with actual parameter values as shown. G1, G3, G5, and G7 include both LQR F/B and proportional F/F; G2, G4, G6, and G8 include LQR F/B alone. Weighting parameters used were $w_{1a} = 258$, $w_{1b} = 10$, $w_3 = 1$ (see Table 1).

System Parameters			Closed Loop Transfer Function
$k \left(\frac{\text{lb f}}{\text{ft}} \right)$	$c \left(\frac{\text{lb f-sec}}{\text{ft}} \right)$	$m \text{ (lbm)}$	$\frac{s^2 X(s)}{s^2 D(s)}$
0.3	0.000622 ($\zeta=0.1\%$)	100	$G1(s) = \frac{0.0000622s + 0.0001}{0.31056s^2 + 4.4675s + 16.0624}$
0.3	0.000622	100	$G2(s) = \frac{0.0000622s + 0.0300}{0.31056s^2 + 4.4675s + 16.0624}$
0.45	0.000622	100	$G3(s) = \frac{0.0000622s + 0.0151}{0.31056s^2 + 4.4675s + 16.0774}$
0.45	0.000622	100	$G4(s) = \frac{0.0000622s + 0.0450}{0.31056s^2 + 4.4675s + 16.0774}$
0.3	0.00622	100	$G5(s) = \frac{0.000622s + 0.0001}{0.31056s^2 + 4.4680s + 16.0624}$
0.3	0.00622	100	$G6(s) = \frac{0.000622s + 0.0300}{0.31056s^2 + 4.4680s + 16.0624}$
0.45	0.00622	90	$G7(s) = \frac{0.000622s + 0.0151}{0.27950s^2 + 4.4680s + 16.0774}$
0.45	0.00622	90	$G8(s) = \frac{0.000622s + 0.0450}{0.27950s^2 + 4.4680s + 16.0774}$

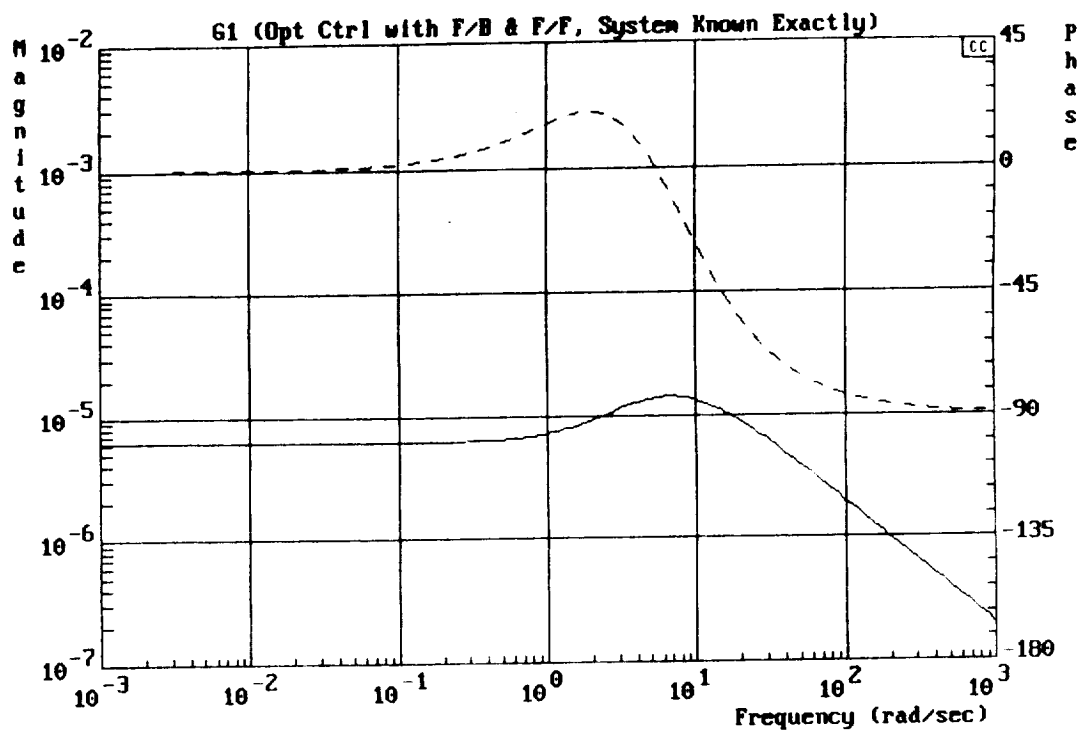


Figure 3

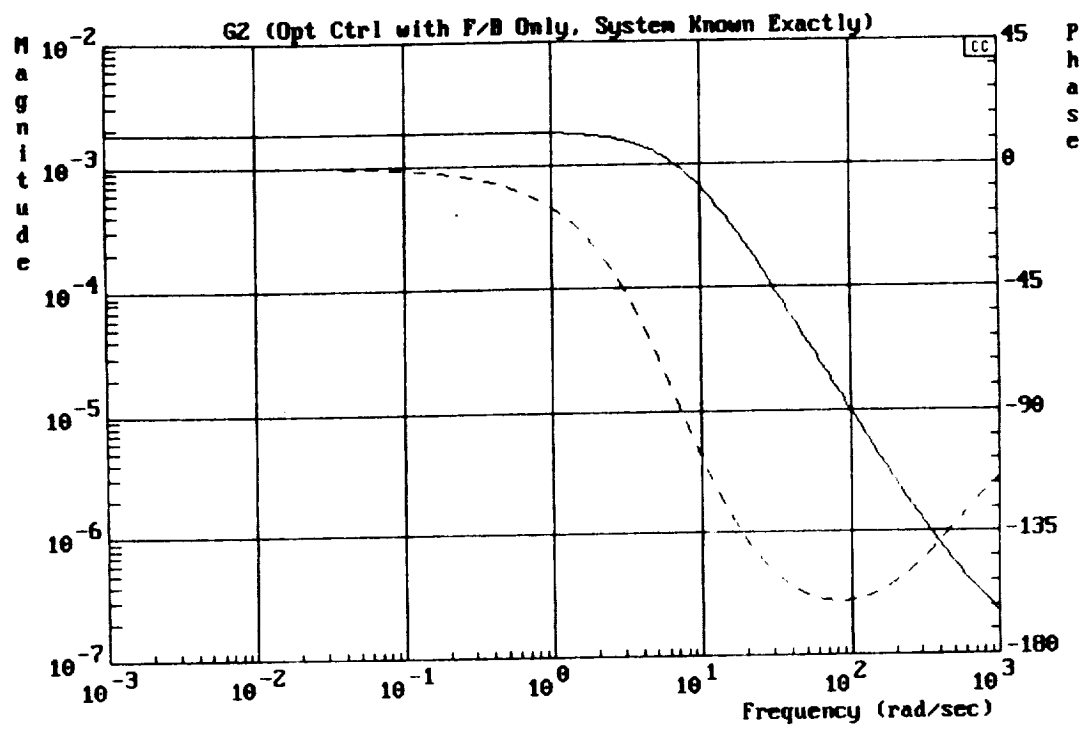


Figure 4

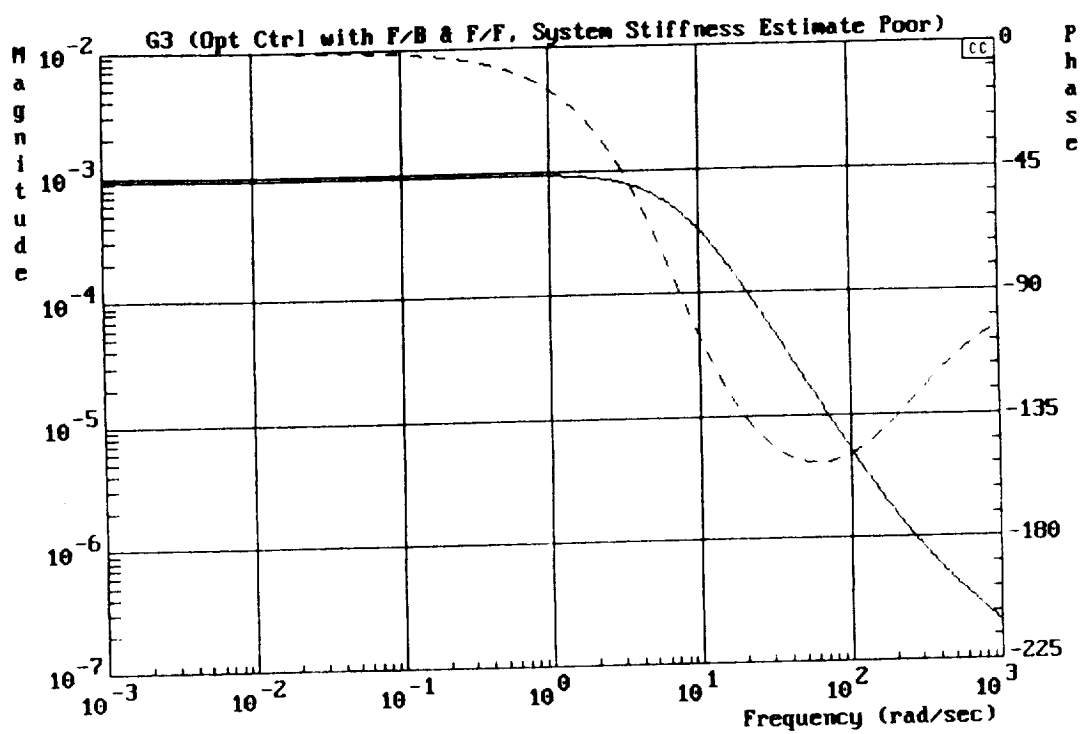


Figure 5

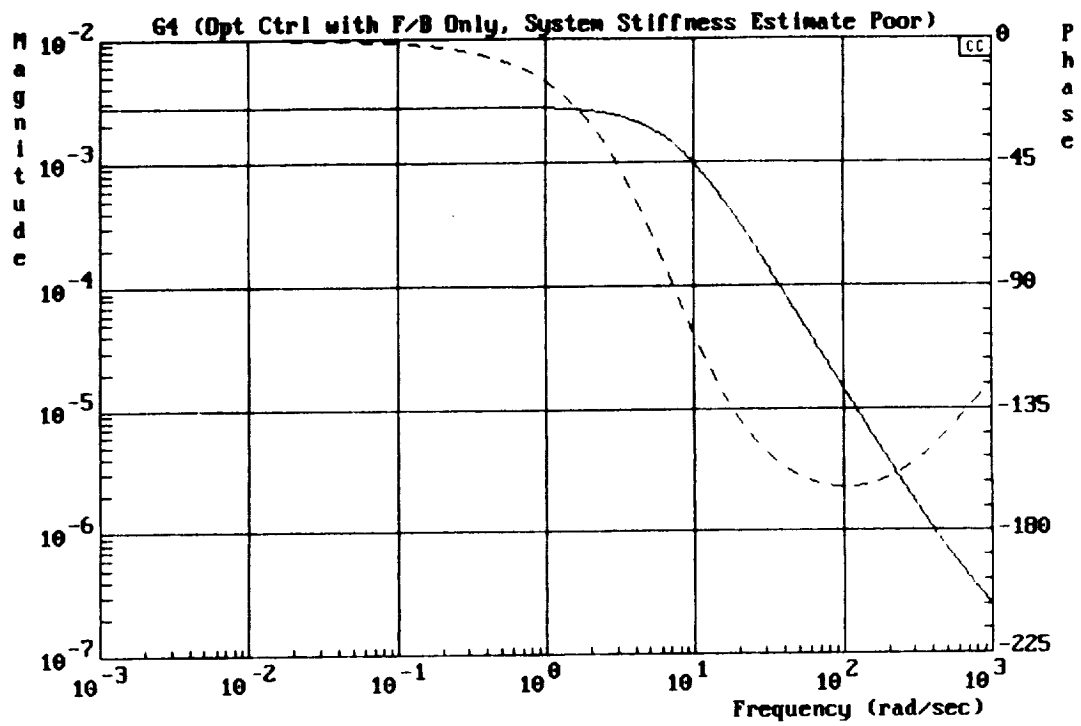


Figure 6

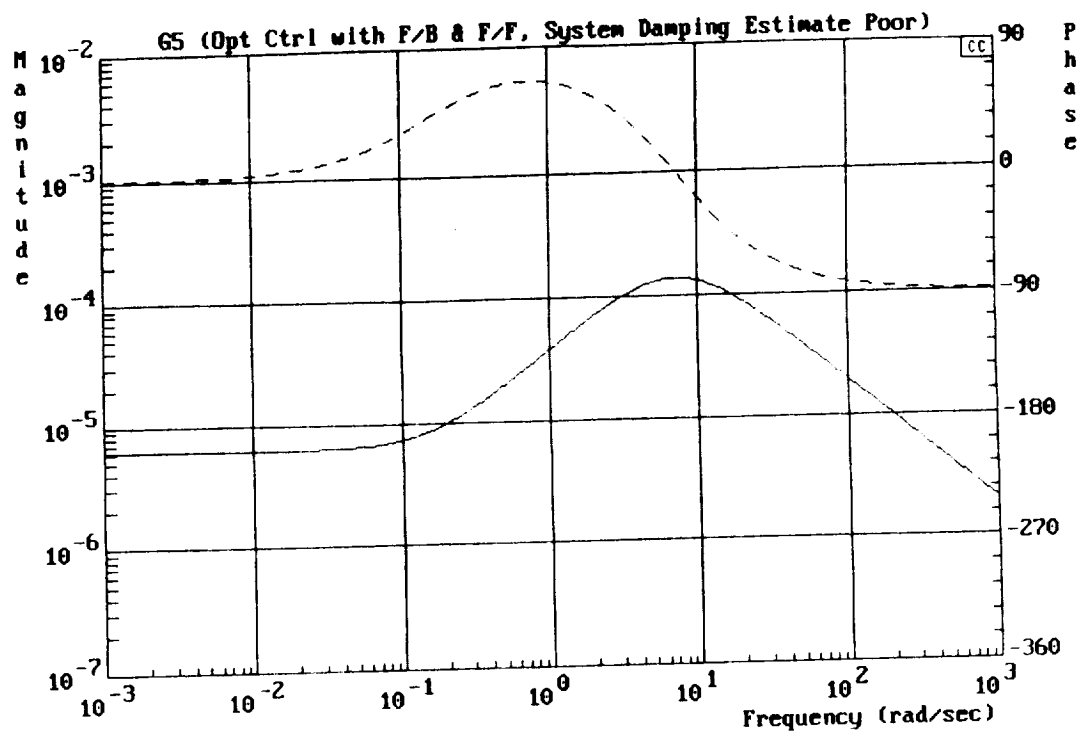


Figure 7

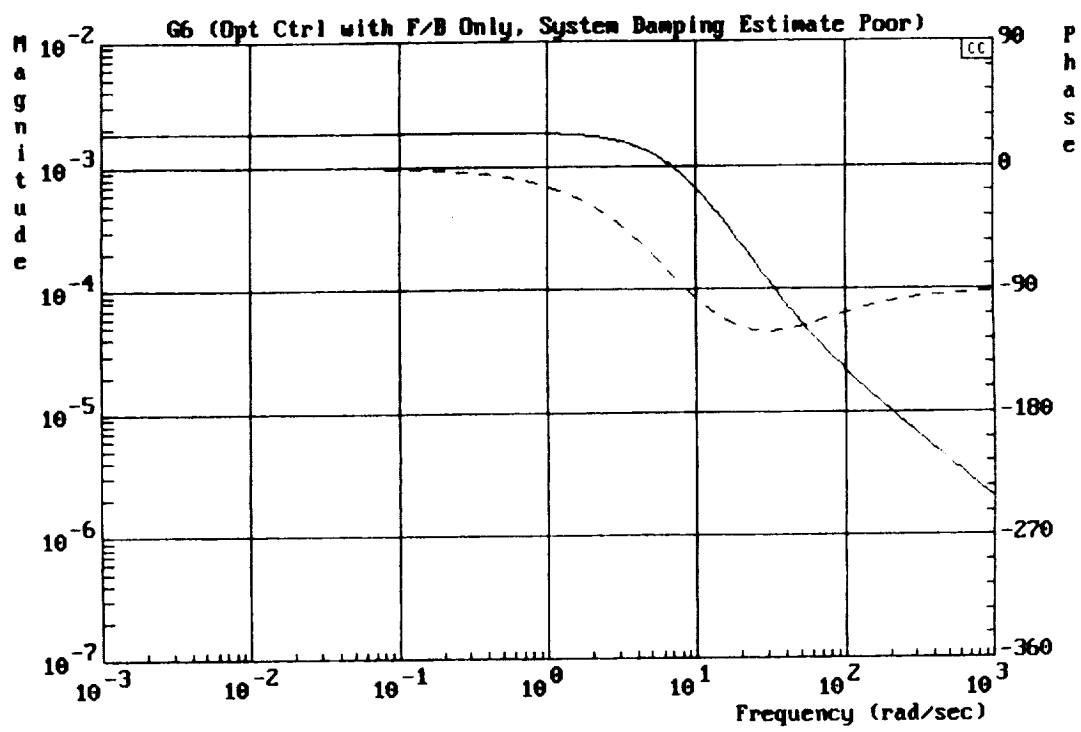


Figure 8

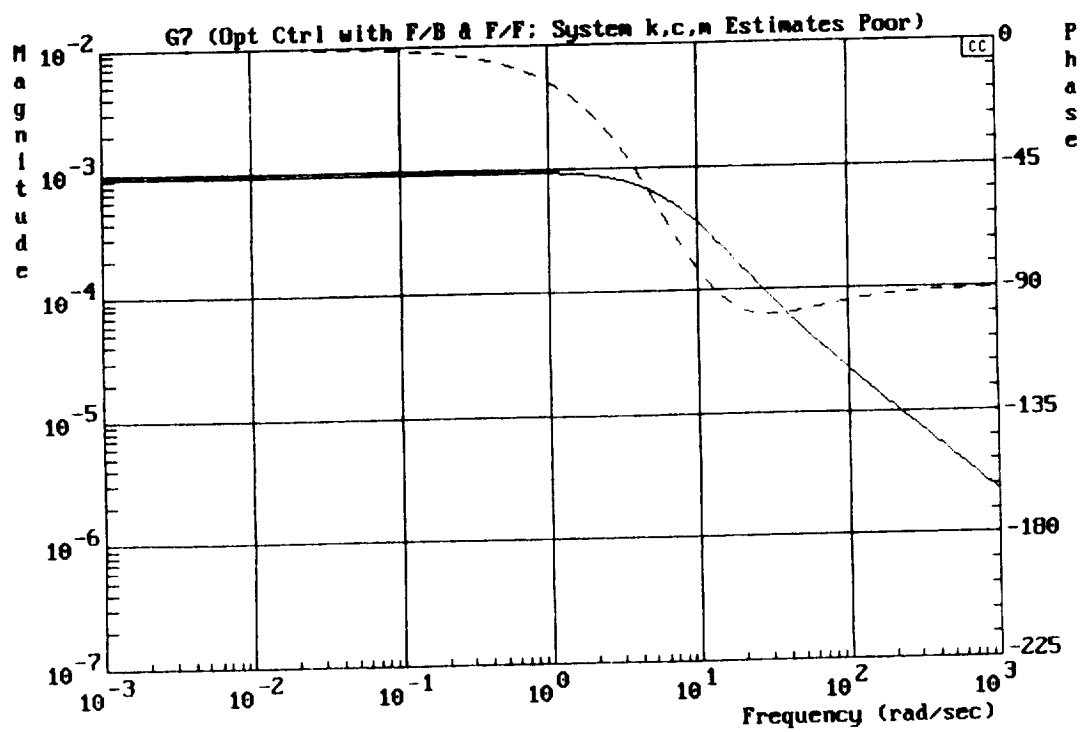


Figure 9

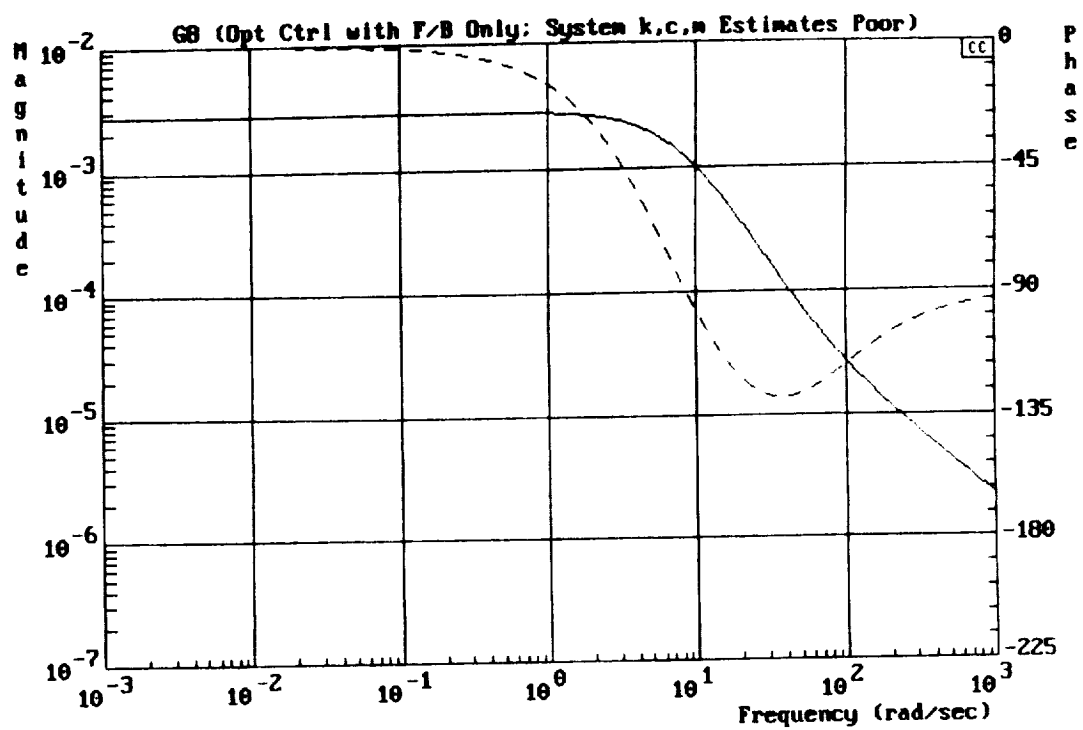
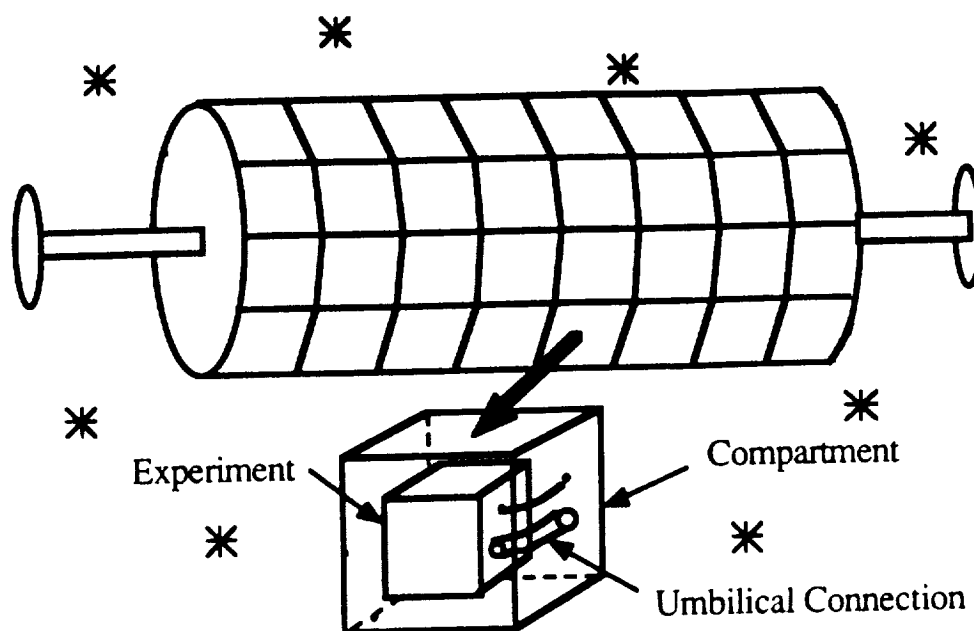


Figure 10



Scientific Experiment in Spacecraft

**DISTURBANCE LEVELS****Quasi-Steady or "DC" Accelerations**

<u>Relative Gravity</u>	<u>Frequency (Hz)</u>	<u>Source</u>
<i>1E-7</i>	<i>0 to 1E-3</i>	<i>Aerodynamic Drag</i>
<i>1E-8</i>	<i>0 to 1E-3</i>	<i>Light Pressure</i>
<i>1E-7</i>	<i>0 to 1E-3</i>	<i>Gravity Gradient</i>

Periodic Accelerations

<u>Relative Gravity</u>	<u>Frequency (Hz)</u>	<u>Source</u>
<i>2E-2</i>	<i>9</i>	<i>Thruster Fire (orbital)</i>
<i>2E-3</i>	<i>5 to 20</i>	<i>Crew Motion</i>
<i>2E-4</i>	<i>17</i>	<i>Ku Band Antenna</i>

Non-Periodic Accelerations

<u>Relative Gravity</u>	<u>Frequency (Hz)</u>	<u>Source</u>
<i>1E-4</i>	<i>1</i>	<i>Thruster Fire (Attitudinal)</i>
<i>1E-4</i>	<i>1</i>	<i>Crew Push-Off</i>

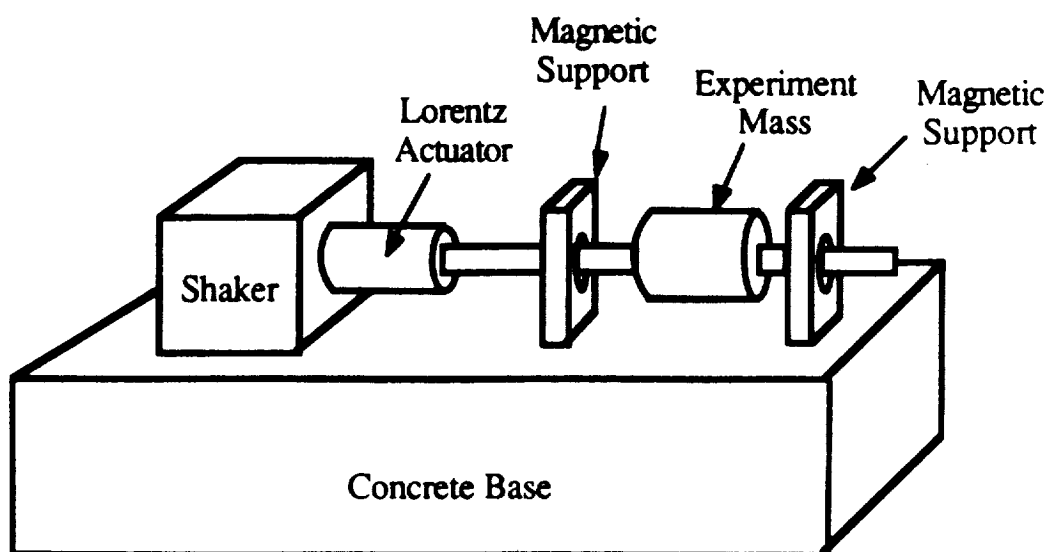


General Problem:

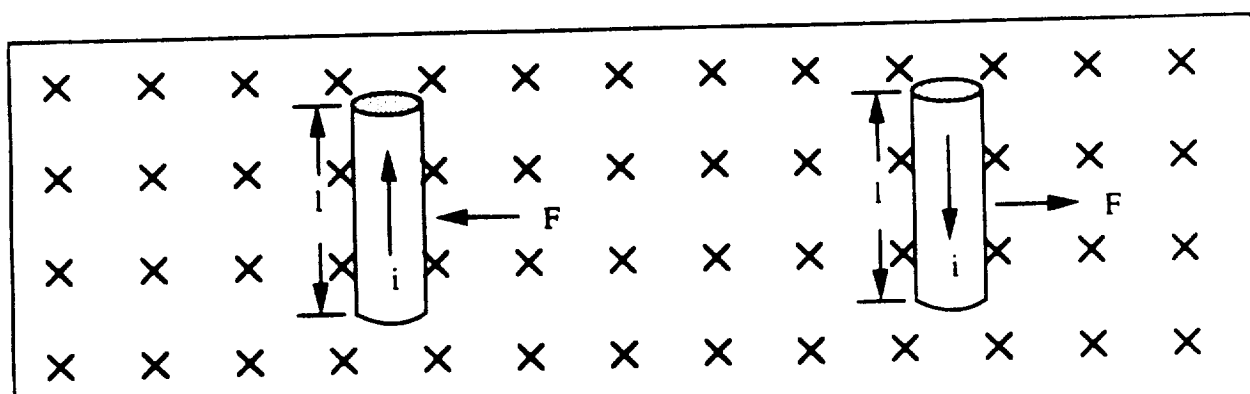
In the upcoming space station, planned by NASA for completion in the 1990's, minimize the low frequency accelerations transmitted from the space station to an experimental platform contained on (inside) the space station.

"minimize": reduce to $\sim 10^{-6} g$ if possible

"low frequency": 0.001 to 20 Hz



Control Law Validation Apparatus



The Lorentz Equation: $F = il \times B$

F = Force

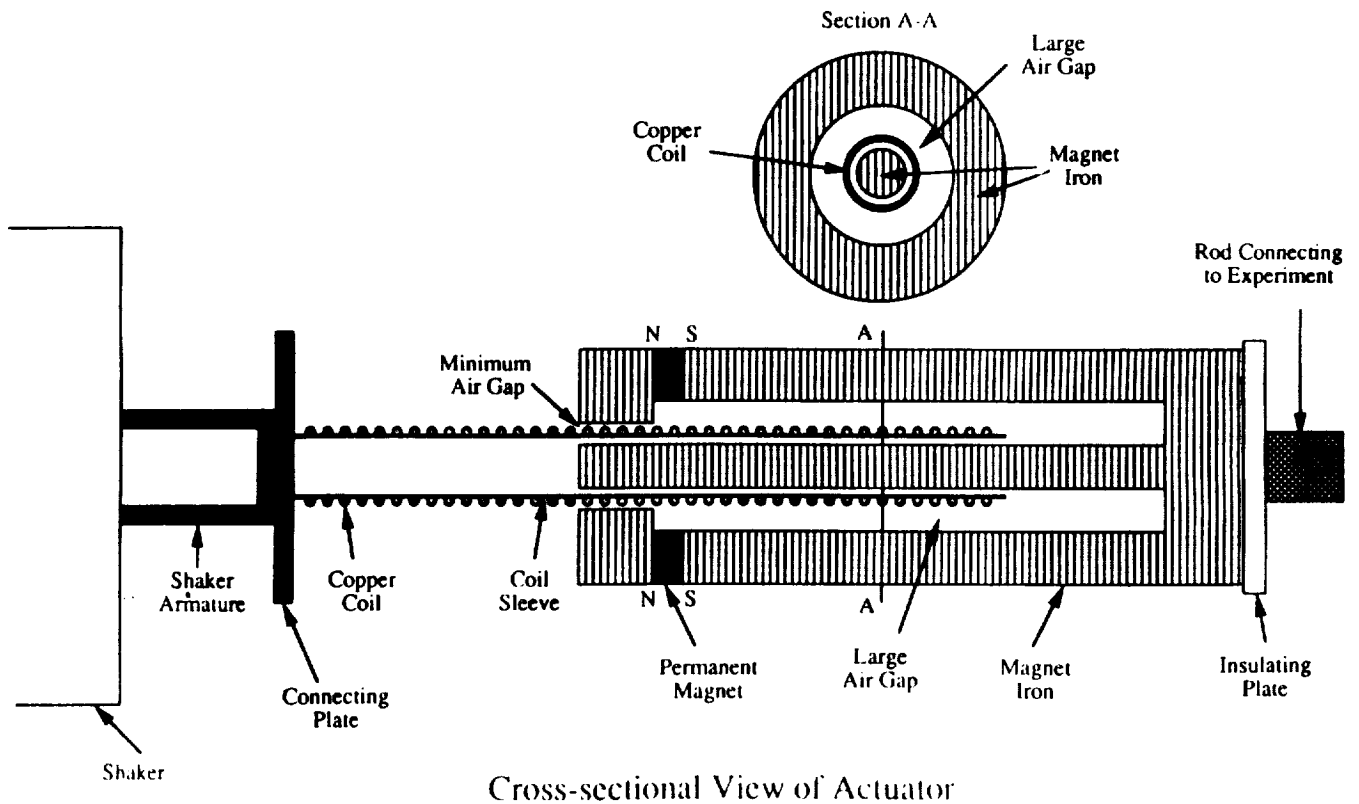
l = length of wire

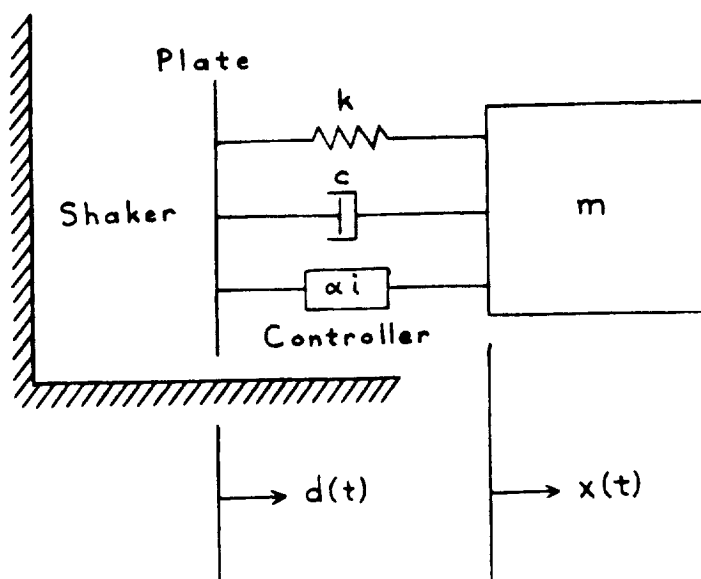
i = current

\times Represents the tail feathers of a magnetic field B vector into the page



Lorentz Actuator Design





System Model



Objective:

Find the “best” $i(t)$,
to minimize $\ddot{x}(t)$.



Equation of Motion:

$$\ddot{x}(t) = \frac{-k}{m} [x(t) - d(t)] \\ - \frac{c}{m} [\dot{x}(t) - \dot{d}(t)] - \frac{\alpha}{m} i(t)$$



State Equations:

$$\begin{Bmatrix} \dot{x}_1 \\ \dot{x}_2 \end{Bmatrix} = \begin{bmatrix} 0 & 1 \\ -\frac{k}{m} & -\frac{c}{m} \end{bmatrix} \begin{Bmatrix} x_1 \\ x_2 \end{Bmatrix} + \begin{Bmatrix} 0 \\ \frac{1}{m} \alpha \end{Bmatrix} i + \begin{Bmatrix} 0 \\ \frac{k}{m} d + \frac{c}{m} \dot{d} \end{Bmatrix}$$

OR

$$\dot{\underline{x}} = A \underline{x} + \underline{b} u + \underline{f}$$

$$\text{where } \underline{x} = \begin{Bmatrix} x_1 \\ x_2 \end{Bmatrix} = \begin{Bmatrix} x(t) \\ \dot{x}(t) \end{Bmatrix}$$

$$A = \begin{bmatrix} 0 & 1 \\ -\frac{k}{m} & -\frac{c}{m} \end{bmatrix}$$

$$\underline{b} = \begin{Bmatrix} 0 \\ \frac{1}{m} \alpha \end{Bmatrix}$$

$$\underline{f} = \begin{Bmatrix} f_1 \\ f_2 \end{Bmatrix} = \begin{Bmatrix} 0 \\ \frac{k}{m} d + \frac{c}{m} \dot{d} \end{Bmatrix}$$



Problem Statement:

Determine the control $\underline{u}(t)$ which minimizes the performance index

$$J = \frac{1}{2} \int_0^{\infty} (\underline{x}^T W_1 \underline{x} + \underline{u}^T W_3 \underline{u}) dt$$

for the system

$$\dot{\underline{x}} = A \underline{x} + B \underline{u} + \underline{f}$$

subject to the conditions

$$\underline{x}(0) = \underline{x}_0$$

$$\lim_{t \rightarrow \infty} \underline{x}(t) = \underline{0}$$

$$\lim_{t \rightarrow \infty} \underline{f}(t) = \underline{0}$$



Solution Method (Differential Equations Approach):

1. Augment the performance index J with the state equations using Lagrange multipliers.
2. Take the 1st variation $\delta \bar{J}$ of the augmented performance index \bar{J} and set it equal to zero:

$$\delta \bar{J} = \int_0^{\infty} \left[\frac{\partial H}{\partial \underline{x}} \delta \underline{x} + \frac{\partial H}{\partial \underline{u}} \delta \underline{u} + \frac{\partial H}{\partial \dot{\underline{x}}} \delta \dot{\underline{x}} \right] dt = 0$$

$$\text{where } H = \frac{1}{2} (\underline{x}^T W_1 \underline{x} + \underline{u}^T W_3 \underline{u}) + \underline{\lambda}^T (\dot{\underline{x}} - A \underline{x} - B \underline{u} - \underline{f})$$

3. Integrate the third term of the integrand by parts, combine terms, and set coefficients of the arbitrary variations $\delta \underline{x}$ and $\delta \underline{u}$ equal to zero.

$$\text{Result: } \begin{aligned} \dot{\underline{\lambda}} &= W_1 \underline{x} - A^T \underline{\lambda} \\ \underline{u} &= W_3^{-1} B^T \underline{\lambda} \end{aligned}$$

4. Substitute for \underline{u} in the state equations, to yield

$$\begin{Bmatrix} \dot{\underline{x}} \\ \dot{\underline{\lambda}} \end{Bmatrix} = \begin{bmatrix} A & B W_3^{-1} B^T \\ W_1 & -A^T \end{bmatrix} \begin{Bmatrix} \underline{x} \\ \underline{\lambda} \end{Bmatrix} + \begin{Bmatrix} \underline{f} \\ \underline{0} \end{Bmatrix}$$



The solution (i.e., the optimal control $\underline{u} = \underline{u}^*$) is now $\underline{u}^* = W_3^{-1} B^T \underline{\lambda}$ where $\underline{\lambda}$ is found by solving the system

$$\begin{Bmatrix} \dot{\underline{x}} \\ \dot{\underline{\lambda}} \end{Bmatrix} = \begin{bmatrix} A & BW_3^{-1}B^T \\ W_1 & -A^T \end{bmatrix} \begin{Bmatrix} \underline{x} \\ \underline{\lambda} \end{Bmatrix} + \begin{Bmatrix} \underline{f} \\ \underline{0} \end{Bmatrix}$$

subject to

$$\underline{x}(0) = \underline{x}_0$$

$$\lim_{t \rightarrow \infty} \underline{x}(t) = \underline{0}$$

$$\lim_{t \rightarrow \infty} \underline{f}(t) = \underline{0}$$

5. Find the solution of the homogeneous system,

i.e., of
$$\begin{Bmatrix} \dot{\underline{x}} \\ \dot{\underline{\lambda}} \end{Bmatrix} = \begin{bmatrix} A & BW_3^{-1}B^T \\ W_1 & -A^T \end{bmatrix} \begin{Bmatrix} \underline{x} \\ \underline{\lambda} \end{Bmatrix}$$

6. Use the variation of parameters method to find the general solution of the nonhomogeneous system, i.e., of

$$\begin{Bmatrix} \dot{\underline{x}} \\ \dot{\underline{\lambda}} \end{Bmatrix} = \begin{bmatrix} A & BW_3^{-1}B^T \\ W_1 & -A^T \end{bmatrix} \begin{Bmatrix} \underline{x} \\ \underline{\lambda} \end{Bmatrix} + \begin{Bmatrix} \underline{f} \\ \underline{0} \end{Bmatrix}$$

7. Apply the terminal conditions on $\underline{x}(t)$, to conclude that n of the $2n$ arbitrary constants in the general solution are equal to zero.



8. Solve for $\underline{\lambda}(t)$ in terms of $\underline{x}(t)$ in a manner such that the remaining n arbitrary constants are eliminated.
9. Use the equation

$$\underline{u}^* = W_3^{-1} B^T \underline{\lambda}$$

to find \underline{u}^* in terms of \underline{x} .

Result:

$$\underline{u}^*(t) = \left(W_3^{-1} B^T X_{21} X_{11}^{-1} \right) \underline{x} + \left(W_3^{-1} B^T X_{22}^{(-1)-1} \right) e^{-\Lambda t} \int e^{\Lambda t} X_{21}^{(-1)} \underline{f}(t) dt$$

where $\begin{bmatrix} \Lambda & 0 \\ 0 & -\Lambda \end{bmatrix}$ is the Jordan

Canonical Form of the Hamiltonian matrix $\begin{bmatrix} A & B W_3^{-1} B^T \\ W_1 & -A^T \end{bmatrix}$,

where Λ contains only the negative eigenvalues of the Hamiltonian matrix, corresponding to the eigenvalues of the closed-loop system (assuming $\{A, B\}$ controllable),

where $X = \begin{bmatrix} X_{11} & X_{12} \\ X_{21} & X_{22} \end{bmatrix}$ is the eigenvector matrix which leads to the above J. C. F.,



where $X^{-1} = \begin{bmatrix} X_{11}^{(-1)} & X_{12}^{(-1)} \\ X_{21}^{(-1)} & X_{22}^{(-1)} \end{bmatrix},$

and where integration of the indefinite integral requires constants of integration that are all identically zero.

10. Integrating repeatedly by parts and using the facts that

$$X_{22}^{(-1)T} \Lambda^T X_{22}^{(-1)-T} = X_{11} \Lambda X_{11}^{-1} = \bar{A} = A - BW_3^{-1}B^T P$$

where $P = -X_{21} X_{11}^{-1}$ [P is the solution to the well-known Algebraic Riccati Equation],

develop equivalent forms for $\underline{u}^*(t)$:

$$\begin{aligned} \underline{u}^*(t) &= -W_3^{-1}B^T P \underline{x} + W_3^{-1}B^T X_{22}^{(-1)-1} e^{-\Lambda t} \int e^{\Lambda \tau} X_{21}^{(-1)} \underline{f}(\tau) d\tau \\ &= -W_3^{-1}B^T P \underline{x} - W_3^{-1}B^T X_{22}^{(-1)-1} \sum_{r=0}^{\infty} (-\Lambda^{-1})^{r+1} X_{21}^{(-1)} \underline{f}^{(r)} \\ &= -W_3^{-1}B^T P \underline{x} - W_3^{-1}B^T \sum_{r=0}^{\infty} (-\bar{A}^{-T})^{r+1} P \underline{f}^{(r)} \\ &= -W_3^{-1}B^T P \underline{x} - W_3^{-1}B^T X_{11}^{-T} \sum_{r=0}^{\infty} (-\Lambda^{-T})^{r+1} X_{21}^T \underline{f}^{(r)} \end{aligned}$$

Note: A state transition matrix approach yields

$$\underline{u}^*(t) = -W_3^{-1}B^T P \underline{x} - W_3^{-1}B^T X_{22}^{(-1)-1} e^{-\Lambda t} \int_t^{\infty} e^{\Lambda \tau} X_{21}^{(-1)} \underline{f}(\tau) d\tau$$

Solution:

$$\begin{aligned}
\underline{u}^*(t) &= -W_3^{-1} B^T P \underline{x} + W_3^{-1} B^T X_{22}^{(-1)-1} e^{-\Lambda t} \int_0^t e^{\Lambda \tau} X_{21}^{(-1)} \underline{f}(\tau) d\tau \\
&= -W_3^{-1} B^T P \underline{x} - W_3^{-1} B^T X_{22}^{(-1)-1} e^{-\Lambda t} \int_t^\infty e^{\Lambda \tau} X_{21}^{(-1)} \underline{f}(\tau) d\tau \\
&= -W_3^{-1} B^T P \underline{x} - W_3^{-1} B^T X_{22}^{(-1)-1} \sum_{r=0}^{\infty} (-\Lambda^{-1})^{r+1} X_{21}^{(-1)} \underline{f}^{(r)} \\
&= -W_3^{-1} B^T P \underline{x} - W_3^{-1} B^T \sum_{r=0}^{\infty} (-\bar{A}^{-T})^{r+1} P \underline{f}^{(r)} \\
&= -W_3^{-1} B^T P \underline{x} - W_3^{-1} B^T X_{11}^{-T} \sum_{r=0}^{\infty} (-\Lambda^{-1})^{r+1} X_{21}^T \underline{f}^{(r)}
\end{aligned}$$

Dropping higher order terms (for $r > 0$):

$$\begin{aligned}
^{(a)} \underline{\tilde{u}}^*(t) &= -W_3^{-1} B^T P \underline{x} + W_3^{-1} B^T X_{22}^{(-1)-1} \Lambda^{-1} X_{21}^{(-1)} \underline{f} \\
&= -W_3^{-1} B^T P \underline{x} + W_3^{-1} B^T X_{22}^{(-1)-1} \Lambda^{-1} X_{22}^{(-1)} P \underline{f} \\
&= -W_3^{-1} B^T P \underline{x} + W_3^{-1} B^T X_{11}^{-T} \Lambda^{-T} X_{11}^T P \underline{f} \\
&= -W_3^{-1} B^T P \underline{x} + W_3^{-1} B^T X_{11}^{-T} \Lambda^{-T} X_{21}^T \underline{f}
\end{aligned}$$

$$^{(a)} \underline{\tilde{u}}^*(t) = -W_3^{-1} B^T P \underline{x} + W_3^{-1} B^T \bar{A}^{-T} P \underline{f}$$

$$\begin{aligned}
\text{where } \bar{A}^{-T} &= -P(PA + W_1)^{-1} = (A - BW_3^{-1}B^TP)^{-T} \\
&= (X_{11} \Lambda X_{11}^{-1})^{-T} = X_{22}^{(-1)-1} \Lambda^{-1} X_{22}^{(-1)}
\end{aligned}$$

These are several forms for the control law.



Solution:

$$\begin{aligned} {}^{(o)} \tilde{\underline{u}}^*(t) = & \left(-W_3^{-1} B^T P \right) \underline{x}(t) \\ & + \left(W_3^{-1} B^T \bar{A}^{-T} P \right) \underline{f}(t) \end{aligned}$$

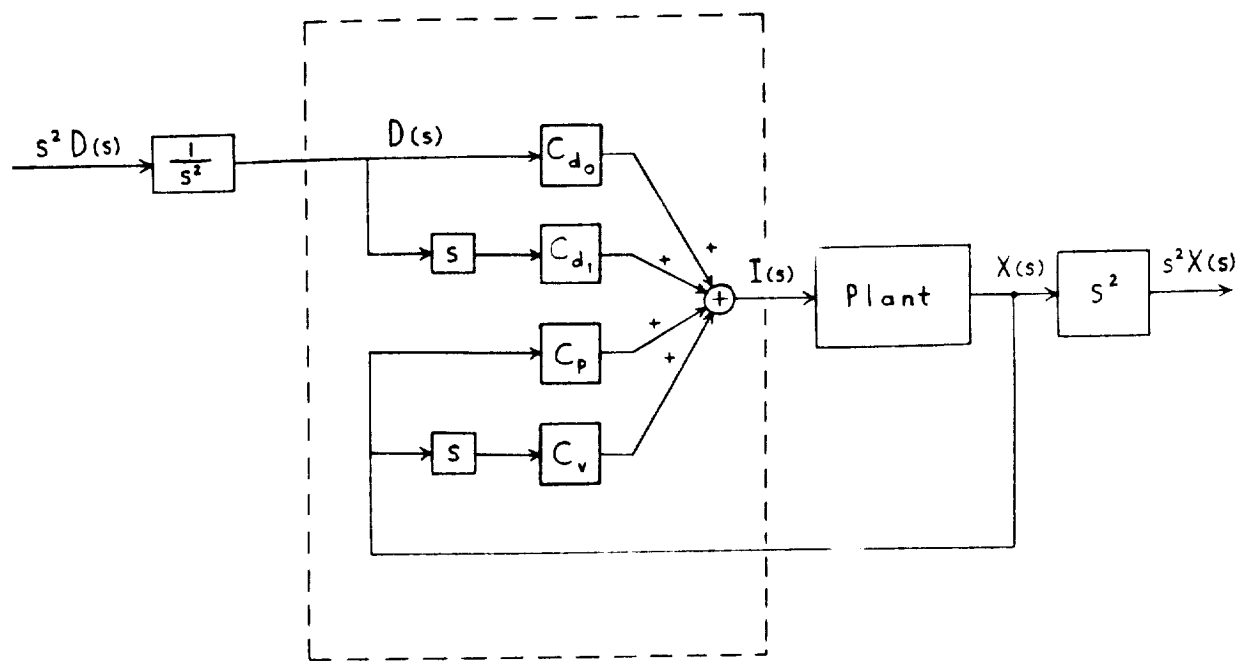
$$\text{where } \bar{A} = A - BW_3^{-1}B^TP$$



Application to our specific problem:

$$i(t) = C_p x(t) + C_v \dot{x}(t) \\ + C_{d_o} d(t) + C_{d_i} \dot{d}(t)$$

where C_p , C_v , C_{d_o} , and C_{d_i}
are constant gains.



Block Diagram



Table 1 Optimal F/F and F/B Gains for Selected State Variable and Control Weightings.

System Parameters:

$m = 100 \text{ lbm}$ $k = 0.3 \text{ lbf/ft}$
 $c = 0.000622 \text{ lbf-sec/ft}$ ($\zeta = 0.1\%$)
 $\alpha = 10 \text{ lbf/amp}$

Weights			F/B Gains		F/F Gains					
w_{1a}	w_{1b}	w_3	C_p	C_v	C_{d0}	C_{d1}	C_{d2}	C_{d3}	C_{d4}	C_{d5}
2	1	1	1.3845	1.3637	0.0294	-0.0006	-0.0070	-0.0067	-0.0019	-0.0032
10	2	1	3.1324	1.9863	0.0297	-0.0001	-0.0030	-0.0019	-0.0009	-0.0004
23	3	1	4.7659	2.4413	0.0298	-0.0000	-0.0020	-0.0010	-0.0004	-0.0001
41	4	1	6.3732	2.8210	0.0299	0.0000	-0.0015	-0.0007	-0.0002	-0.0001
64	5	1	7.9701	3.1544	0.0299	0.0000	-0.0012	-0.0005	-0.0001	-0.0000
92	6	1	9.5617	3.4552	0.0299	0.0000	-0.0010	-0.0004	-0.0001	-0.0000
126	7	1	11.1950	3.7354	0.0299	0.0000	-0.0008	-0.0003	-0.0001	-0.0000
165	8	1	12.8153	3.9949	0.0299	0.0000	-0.0007	-0.0002	-0.0001	-0.0000
209	9	1	14.4260	4.2380	0.0299	0.0000	-0.0006	-0.0002	-0.0000	-0.0000
258	10	1	16.0324	4.4674	0.0299	0.0000	-0.0006	-0.0002	-0.0000	-0.0000
581	15	1	24.0740	5.4729	0.0300	0.0001	-0.0004	-0.0001	-0.0000	-0.0000
1034	20	1	32.1259	6.3209	0.0300	0.0001	-0.0003	-0.0001	-0.0000	-0.0000
1617	25	1	40.1819	7.0680	0.0300	0.0001	-0.0002	-0.0000	-0.0000	-0.0000
2329	30	1	48.2297	7.7431	0.0300	0.0001	-0.0002	-0.0000	-0.0000	-0.0000
3171	35	1	56.2816	8.3640	0.0300	0.0001	-0.0002	-0.0000	-0.0000	-0.0000
4113	40	1	64.3361	8.9420	0.0300	0.0001	-0.0001	-0.0000	-0.0000	-0.0000
9325	60	1	96.5360	10.9526	0.0300	0.0001	-0.0001	-0.0000	-0.0000	-0.0000
16581	80	1	128.7372	12.6475	0.0300	0.0001	-0.0001	-0.0000	-0.0000	-0.0000
25911	100	1	160.9389	14.1407	0.0300	0.0001	-0.0001	-0.0000	-0.0000	-0.0000



Table 2. Closed loop transfer functions for system with design parameter values of $k = 0.3$, $c = 0.000622$, and $m = 100$; but with actual parameter values as shown. G1, G3, G5, and G7 include both LQR F/B and proportional F/F; G2, G4, G6, and G8 include LQR F/B alone. Weighting parameters used were $w_{1a} = 258$, $w_{1b} = 10$, $w_3 = 1$ (see Table 1).

System Parameters			Closed Loop Transfer Function
$k \left(\frac{\text{lbf}}{\text{ft}} \right)$	$c \left(\frac{\text{lbf-sec}}{\text{ft}} \right)$	$m \text{ (lbm)}$	$\frac{s^2 X(s)}{s^2 D(s)}$
0.3	0.000622 ($\zeta=0.1\%$)	100	$G1(s) = \frac{0.0000622s + 0.0001}{0.31056s^2 + 4.4675s + 16.0624}$
0.3	0.000622	100	$G2(s) = \frac{0.0000622s + 0.0300}{0.31056s^2 + 4.4675s + 16.0624}$
0.45	0.000622	100	$G3(s) = \frac{0.0000622s + 0.0151}{0.31056s^2 + 4.4675s + 16.0774}$
0.45	0.000622	100	$G4(s) = \frac{0.0000622s + 0.0450}{0.31056s^2 + 4.4675s + 16.0774}$
0.3	0.00622	100	$G5(s) = \frac{0.000622s + 0.0001}{0.31056s^2 + 4.4680s + 16.0624}$
0.3	0.00622	100	$G6(s) = \frac{0.000622s + 0.0300}{0.31056s^2 + 4.4680s + 16.0624}$
0.45	0.00622	90	$G7(s) = \frac{0.000622s + 0.0151}{0.27950s^2 + 4.4680s + 16.0774}$
0.45	0.00622	90	$G8(s) = \frac{0.000622s + 0.0450}{0.27950s^2 + 4.4680s + 16.0774}$

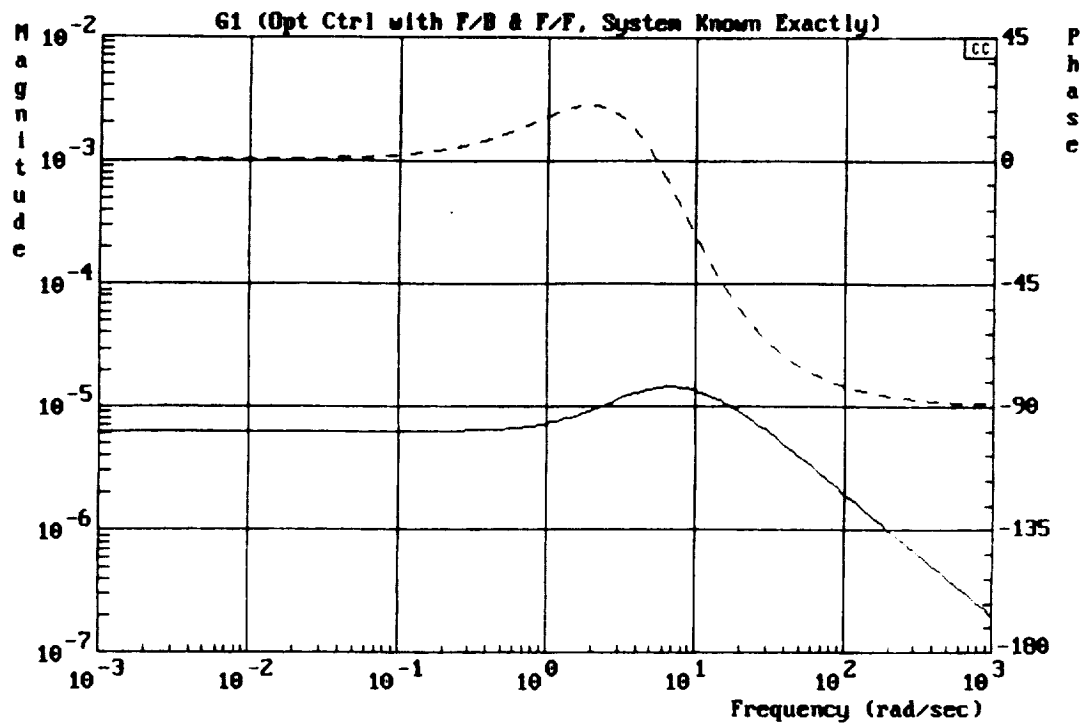


Figure 3

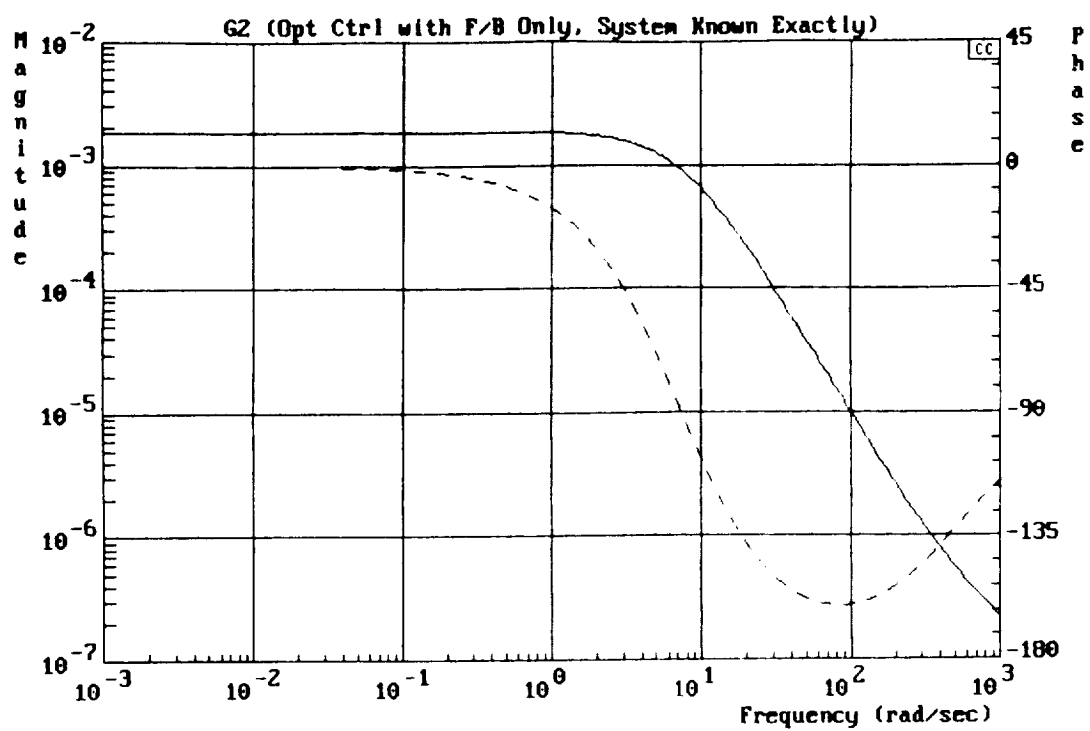


Figure 4

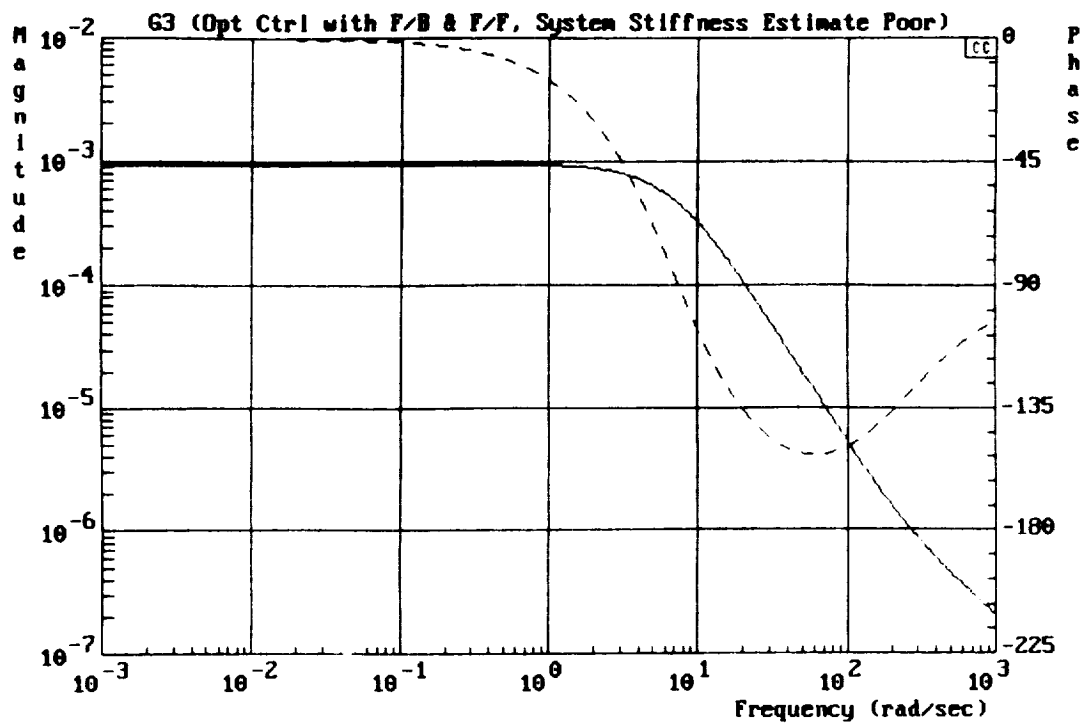


Figure 5

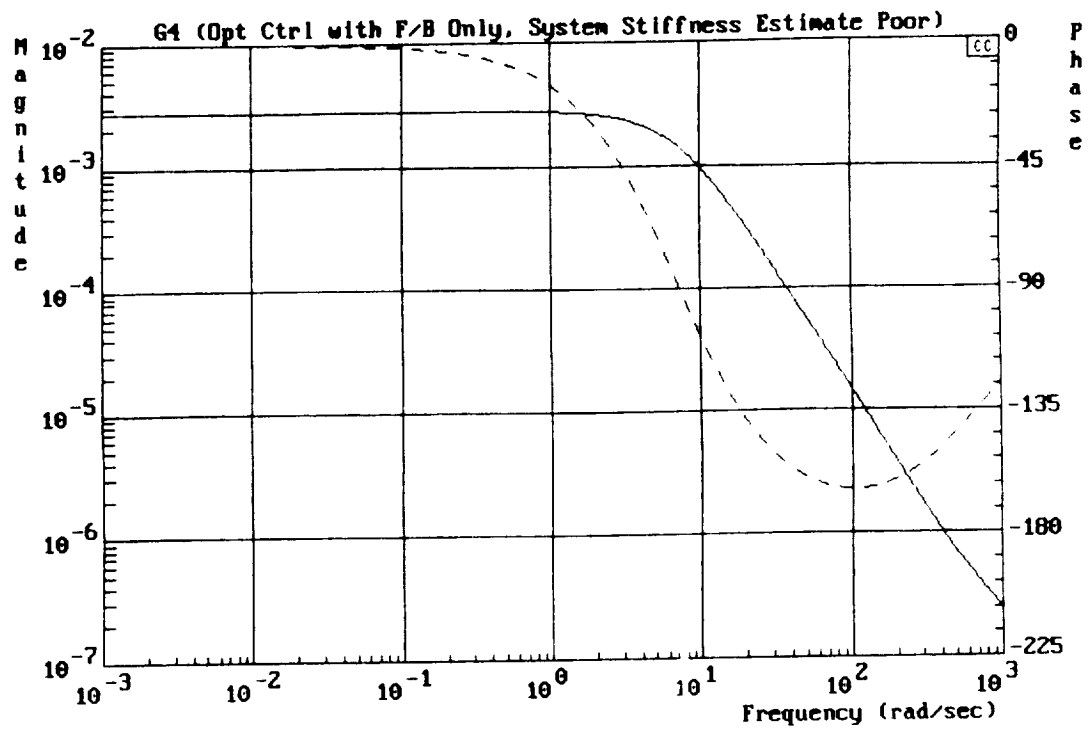


Figure 6

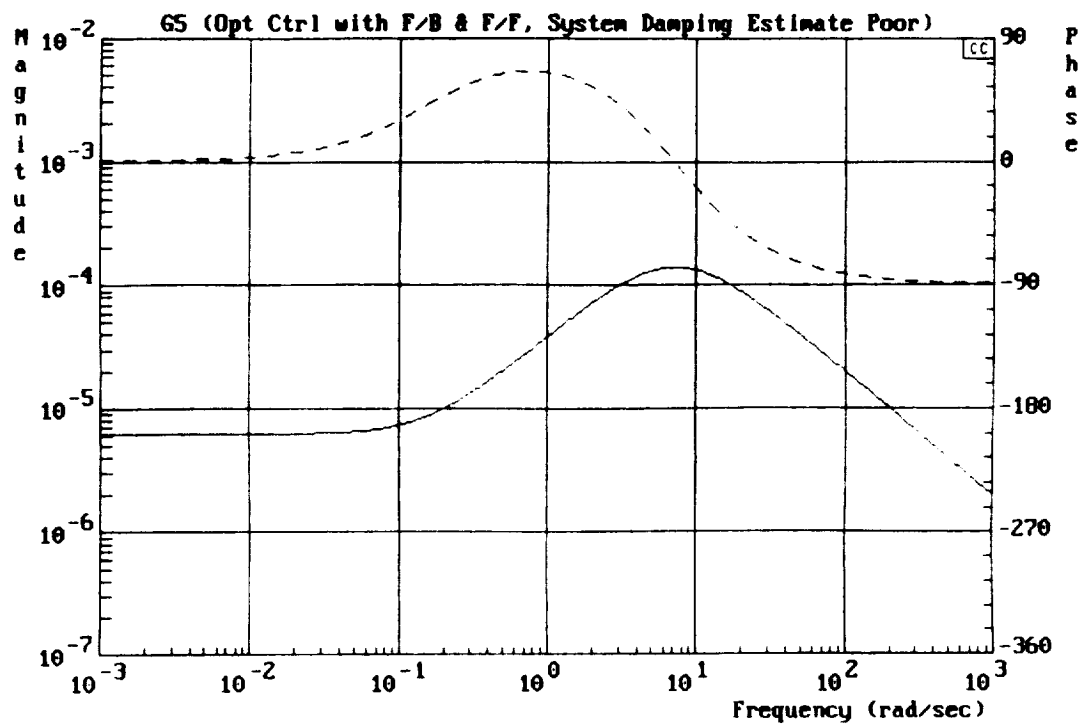


Figure 7

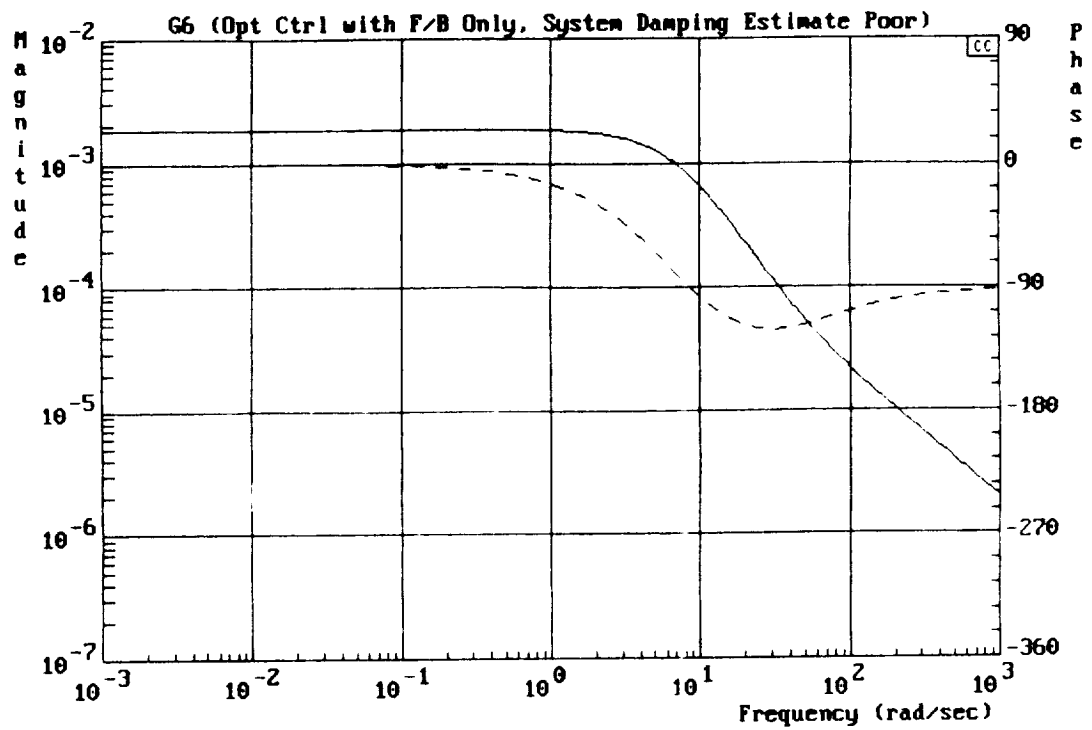


Figure 8

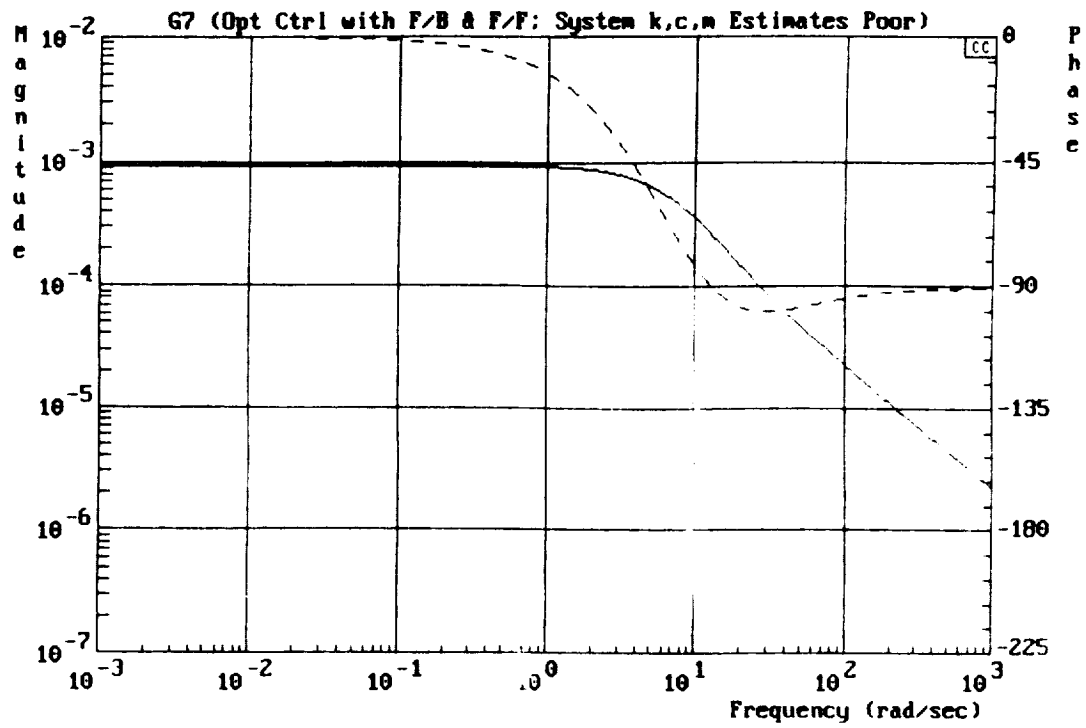


Figure 9

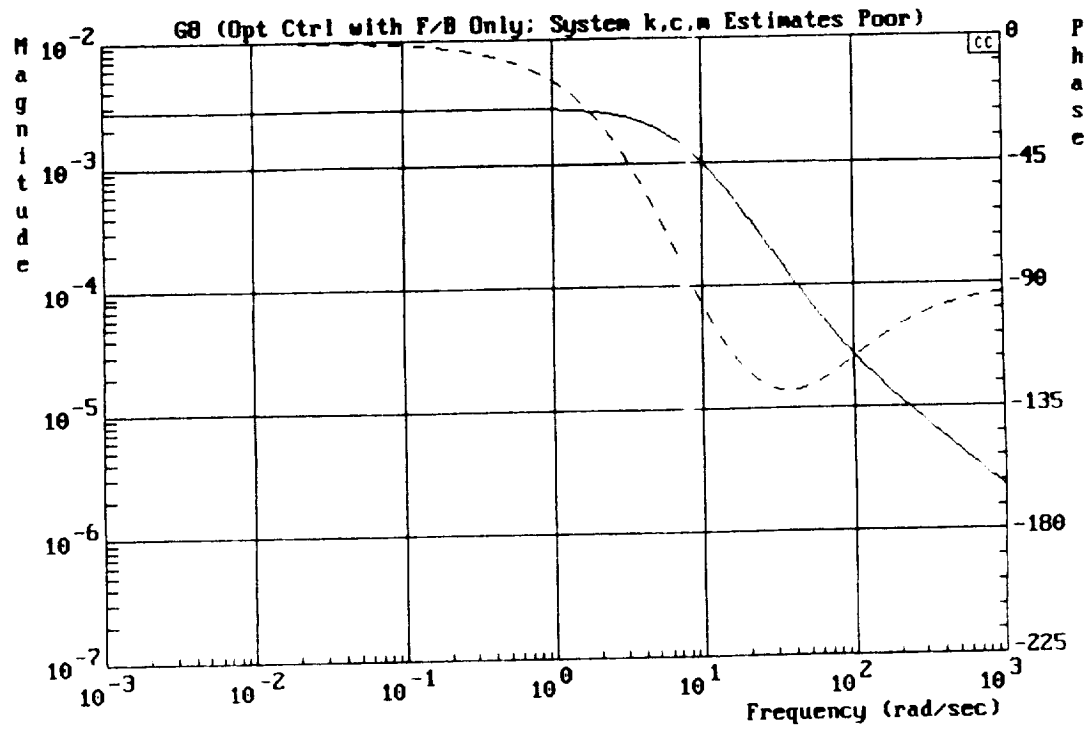


Figure 10



Conclusions:

1. An optimal control has been determined for the nonhomogeneous LQR problem.
2. An approximation to this optimal control has been found which uses constant feedback and feedforward gains.
3. The optimal control has the following advantages:
 - a. The gains can be easily determined.
 - b. The control is very robust (60° phase margin, infinite positive gain margin, 6 dB negative gain margin).
 - c. The control is applicable to a wide range of problems.
 - d. The control offers substantial improvement in disturbance rejection over that afforded by LQR feedback alone.
 - e. The control can be easily implemented.

N91-21207

**MEASUREMENT and CALCULATION of FORCES in a MAGNETIC
JOURNAL BEARING ACTUATOR**

Josiah Knight, Edward McCaul, Zule Xia

Duke University

Department of Mechanical Engineering and Materials Science

Durham

NC 27706

Measurement and Calculation of Forces in a Magnetic Journal Bearing Actuator

**Josiah Knight
Assistant Professor**

**Edward McCaul
Zule Xia
Graduate Assistants**

**Department of Mechanical Engineering
and Materials Science
Duke University
Durham, North Carolina**

**funded by
NASA Lewis Research Center**

**presented at
NASA Workshop on Aerospace Applications
of Magnetic Suspension
Langley Research Center**

September 1990

Abstract

Numerical calculations and experimental measurements of forces from an actuator of the type used in active magnetic journal bearings are presented. The calculations are based on solution of the scalar magnetic potential field in and near the gap regions. The predicted forces from a single magnet with steady current are compared with experimental measurements in the same geometry. The measured forces are smaller than calculated ones in the principal direction but are larger than calculated in the normal direction. This combination of results indicates that material and spatial effects other than saturation play roles in determining the force available from an actuator.

1. Introduction

Recently, there has been much interest in the use of active magnetic bearings to replace or augment traditional bearings in turbomachinery. Magnetic bearings offer a number of potential advantages, including low power loss, suitability for harsh environments, and the ability to change the bearing characteristics to minimize vibration.

This paper presents data on calculation and measurement of forces from a magnetic actuator similar to those that are used in magnetic journal bearings. The data are for open-loop, steady conditions only and are part of the development of models for active bearings.

Much research has recently been devoted to magnetic bearings. No extensive literature survey is attempted in this paper, but from a sampling of the published papers on the topic [1-9], and the proceedings of the two international symposia on magnetic bearings [10,11], it is clear that the concentration is on control aspects. Although the development of robust control strategies is important in optimizing magnetic bearing characteristics, particularly stability characteristics, it is also necessary to understand the forces arising from actuators in order to optimize fully a magnetic bearing system. This is expected to become increasingly important when the requirements for peak force and for force to weight ratio are stringent, which may be expected in aerospace applications. Better understanding of the characteristics of the journal bearing actuator is necessary in order to take advantage of all available parameters, including gap size, shape and material selection in a system optimization. This paper presents preliminary results of work toward this goal.

2. Theory

A computer program has been written that calculates the force exerted on the journal by a magnet having a steady current in its coils. The force is found by calculating the energy stored in the air gaps between the magnet and the journal, then performing a numerical perturbation to obtain a central difference of the energy change per unit position change. This gives the force in the direction of the perturbation. The force for a magnet at an arbitrary location can be calculated.

The algorithm includes the following assumptions:

- i. The permeability of the metal is infinite compared to that of the gaps, which is assumed equal to that of free space. This implies that all the energy is stored in the gaps.
- ii. All magnetic flux closes the path through both metal parts. Expansion or fringing of the field near the gaps is allowed, however.
- iii. The coil current, therefore the MMF, is constant over a perturbation.

In an isotropic domain not containing currents, where time variations are only of low frequency, the magnetic field can be represented as the gradient of a scalar field $\phi(x,y)$.

The energy contained in the domain is

$$\sigma = \int_V \bar{\mathbf{B}} \cdot \bar{\mathbf{B}} dV \quad (1)$$

where the flux density \mathbf{B} is given by

$$\bar{\mathbf{B}} = -\nabla\phi \quad (2)$$

and the potential ϕ satisfies the governing equation

$$\nabla^2\phi = 0 \quad (3)$$

with the boundary conditions

$$\frac{\partial\phi}{\partial n} = 0 \text{ on free boundaries} \quad (4)$$

and, because of assumption (i) above

$$\begin{aligned} \phi &= \Phi_1 \text{ on pole face 1} \\ \phi &= \Phi_2 \text{ on pole face 2} \\ \phi &= 0 \text{ on journal surface,} \end{aligned} \quad (5)$$

as shown in Figure 1.

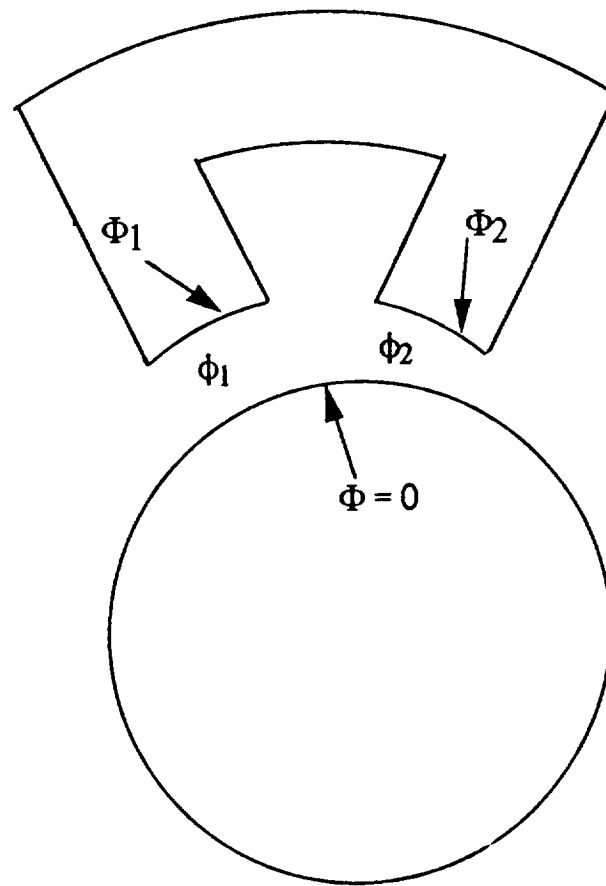
Initially the boundary values of ϕ on the pole faces, Φ_1 and Φ_2 , are not known, but must be determined in relation to the datum of $\phi=0$ on the journal surface. The problem is made tractable by the fact that the governing equation is a linear one, so that the values of ϕ internally are determined within a multiplicative constant even for an arbitrary choice of boundary condition values. The fact that the flux must be the same through the two gaps allows the ratio

$$\kappa = \frac{\Phi_2}{\Phi_1} \quad (6)$$

to be determined. Then the fact that the difference between the two potentials is the magnetomotive force,

$$\Phi_1 - \Phi_2 = \zeta \quad (7)$$

allows determination of the actual surface potentials.



ϕ scalar potential field

Φ boundary value of scalar potential

Figure 1. Boundary conditions for solution of magnetic scalar potential.

2.1. Computer Program

The algorithm above is embodied in a FORTRAN computer program, GAPFOR1, which uses the finite element method for calculating the magnetic potential in two dimensions. For a given journal position the program calculates the gap height as a function of angular location and generates a finite element mesh for each gap. Flux fringing is allowed by extending the finite element domain beyond the edges of each pole face. Then the journal position is perturbed four times, first with positive dx and negative dx , then with positive dy and negative dy . At each step the mesh is regenerated and the energies are recalculated. The central difference analog to the derivative of energy is then computed, which is equal to the force in the perturbation direction.

To achieve rapid computational speed and efficiency, a dedicated finite element program was written for this application. It includes a grid generation routine as well as a banded gauss elimination solver for the assembled equations.

Forces from one magnet of a bearing

The computer program has been used to predict the forces from one magnet acting on the journal at various positions of the journal within the clearance space. The geometry corresponds to that of the experimental apparatus described in Section 3. Half of the entire clearance space is mapped, since all positions of the journal with respect to a single magnet can be represented in terms of positions in this half plane. Figures 2 and 3 show a map of force versus x,y position. The magnet is the upper vertical magnet, and a steady current of 1 ampere through the coils is used. The dimensions and other parameters are the same as those of the experimental apparatus described below. The figure indicates that the force in the y -direction (the principal force) varies between 6 and 180 N as the journal is moved along the y axis between $-0.7 < y/c < 0.7$. When the journal is also given an x -direction eccentricity, the y -force increases somewhat.

Except at $x=0$, there is also an x , or normal, component to the force, as shown in Figure 3. This normal force increases rapidly as x is made larger. At $x/c = 0.7$ it is 12% of the principal force.

3. Experiment

3.1 Design of Apparatus

The apparatus for force measurement is shown in an exploded view in Figure 4. Each magnet is independent and is wound with 400 turns capable of carrying current of 2.0 A in the steady state. In the steady force measurement mode, the rotor is held stationary by

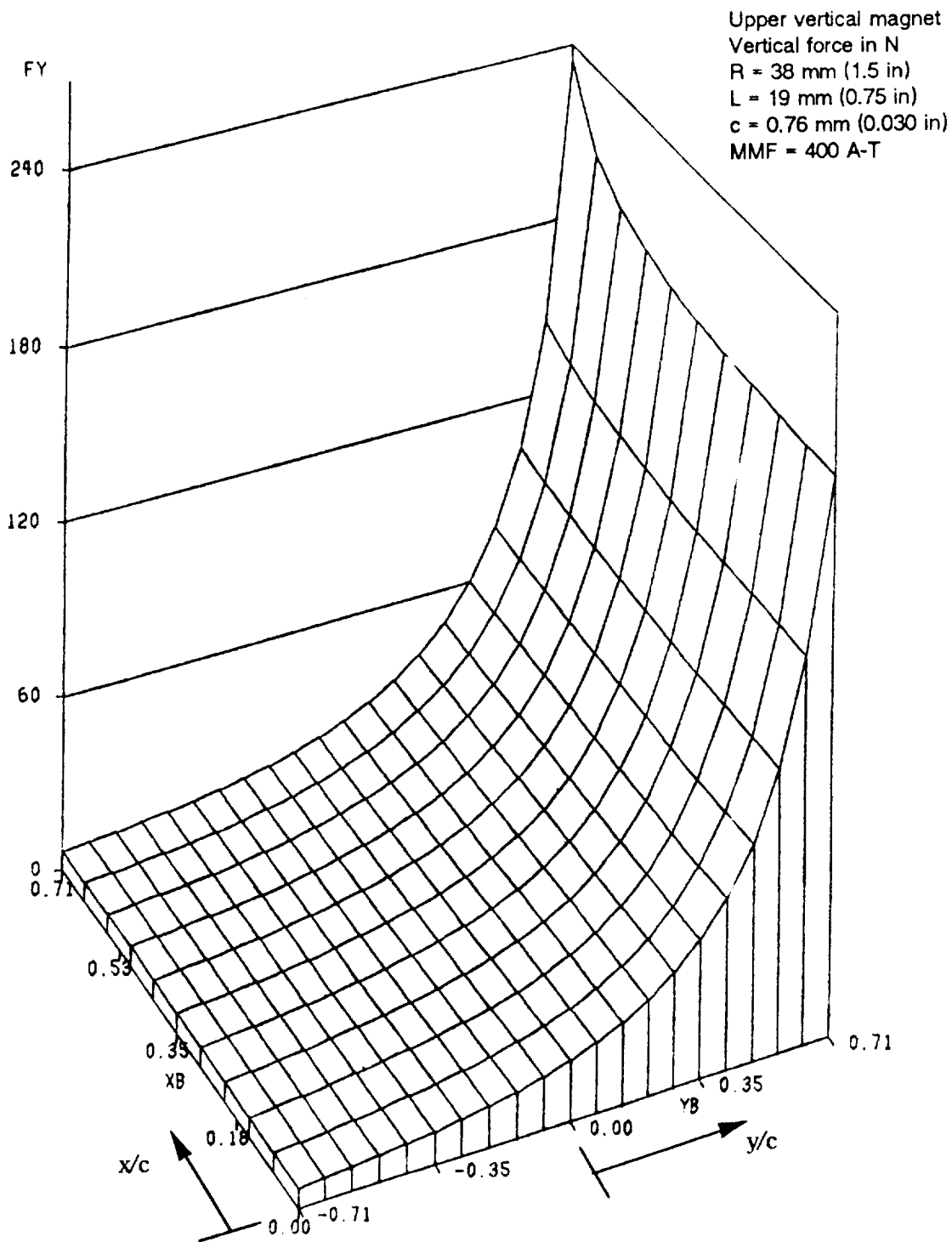


Figure 2. Attractive force from one magnet in principal direction.

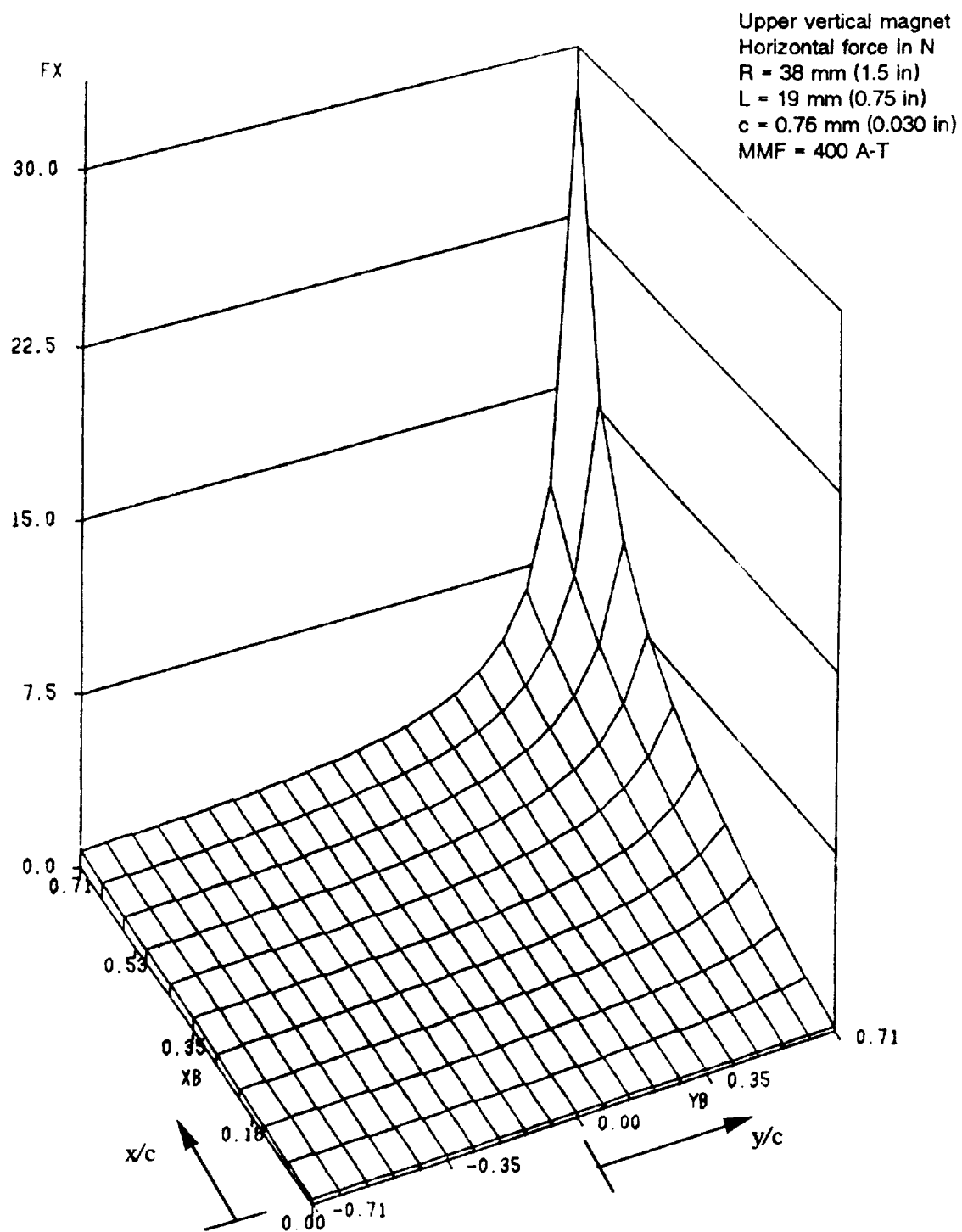


Figure 3. Attractive force from one magnet in normal direction.

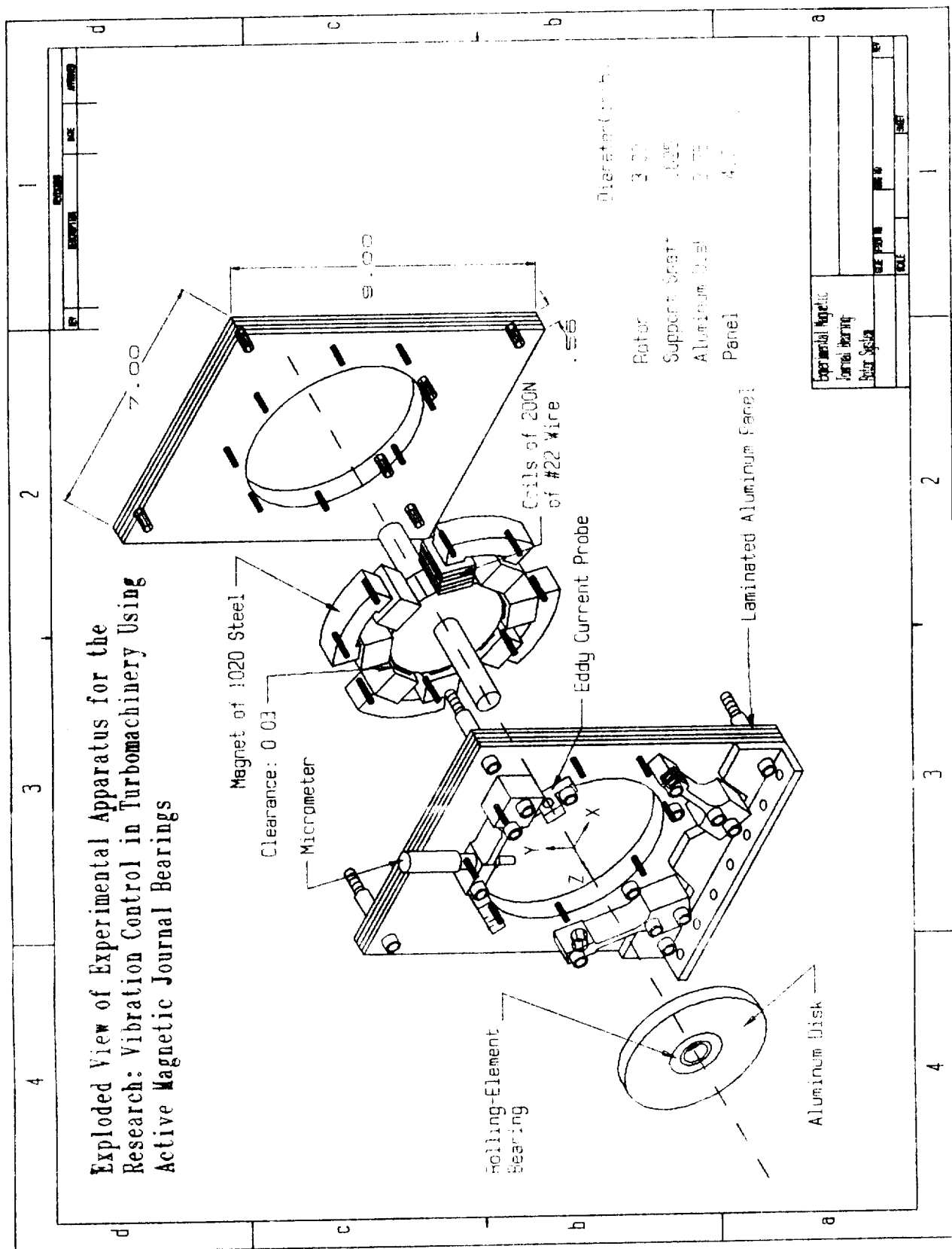


Figure 4. Assembly drawing of force measurement apparatus.

pressure from six micrometer heads (three on each end) that are in turn held by cantilever arms instrumented with strain gauge bridges. Thus all mechanical force on the rotor passes through the micrometer pushers and the strain gauge arm transducers. To minimize any tangential force on the pusher ends Teflon ball sockets with steel spheres were used between the pusher micrometers and the support disks. A full assessment of the uncertainty due to friction has not been completed.

3.2 Results of Measurements

Forces were measured at several locations and for several values of steady current. The figures referred to below display dimensional data as measured, with forces in Newtons plotted against y/c , the eccentricity ratio in the vertical direction. All of the forces presented are from the lower vertical magnet, so the vertical forces are in the negative y -direction. The eccentricities in the x -direction are all positive. Three traverses of the y -direction were made, at x/c positions of approximately 0.0, 0.24, and 0.45. Assessments of the errors in measurement are not complete; however, it is expected that the error in position measurement is no greater than plus or minus 0.05 in y/c and x/c , and that the error in force measurement is no greater than plus or minus 5 N. Errors in current level control are within 0.1 A. A larger series of measurements that were made before the addition of the ball/socket contacts was eventually discarded because the measurement error due to friction appeared to be significant.

The data support some of the anticipated relationships among the position, current and force variables but appear to disagree with other aspects of the present theory. Figure 5 shows the vertical force as a function of y/c for several values of current. The force tends to increase roughly as the inverse square of the gap. The magnitudes of the forces, however, are considerably lower than those predicted either by the linear finite element theory or by the traditional theory based on assumption of uniform gaps, and the ratio between measured and predicted forces is not constant. Figure 6 is a comparison of the measured forces with those predicted by the finite element calculation. The results indicate that at large gap and/or small current the ratio between the measured and predicted forces is about 1.5, but at smaller gaps and/or higher currents this ratio increases, eventually exceeding 2.0 for all the three values of current that are plotted.

Several mechanisms may be operating to cause these discrepancies, including flux leakage, non-uniform permeability of the materials and magnetic saturation. Some part of the disagreement is likely the result of measurement errors, but the differences appear to be significant even after allowing for reasonable experimental error. These disagreements reinforce the need for additional work, already planned, on force calculation.

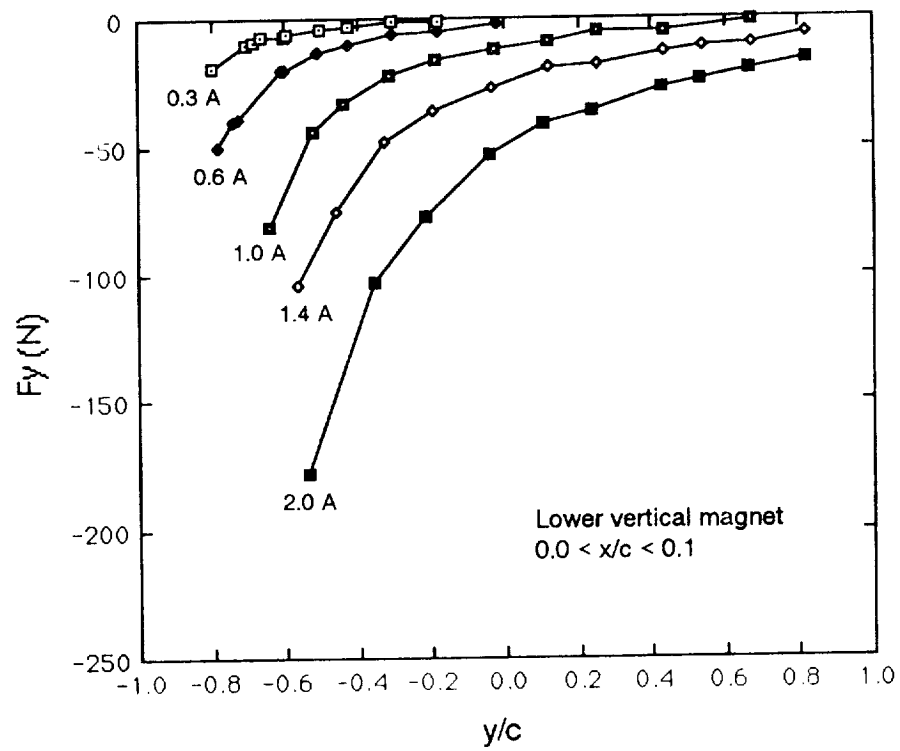


Figure 5. Vertical force from lower vertical magnet at different values of current.

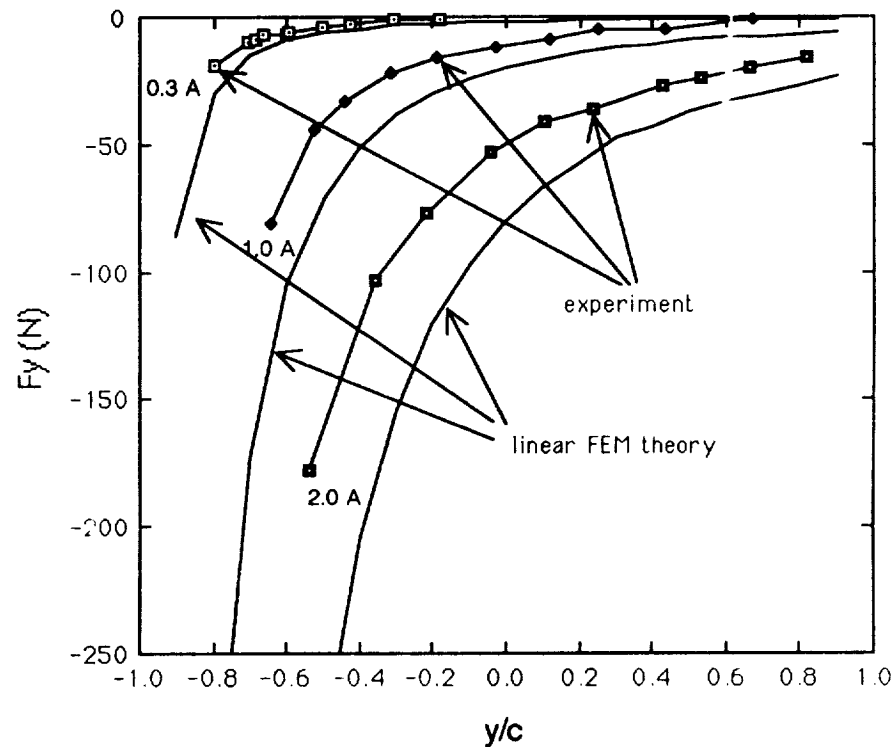


Figure 6. Measured forces and forces predicted by linear FEM calculation.

The linear finite element theory predicts the existence of forces from a magnet that are normal to its axis of symmetry when the rotor is displaced from this symmetry axis, but the forces that are measured are considerably stronger than those predicted by calculation. Figure 7 shows the x component of force when the rotor is placed as closely as possible on the y-axis. The normal force appears to be somewhat stronger at higher current levels but all these forces are small, on the order of 5 % or less of the principal force, so it is difficult to attribute much significance to this ratio in view of the experimental uncertainty. At higher values of x/c , however, the normal force becomes much more significant. Figures 8 through 11 show the vertical and horizontal components of force when the x/c value is 0.24 or 0.45, and Figure 12 shows the value of the x force as a function of position for several values of x/c while the current is held constant at 1.0 A. In general it appears that the normal force increases significantly with increasing x/c , and at $x/c = 0.24$ and 0.45 the horizontal force is about 10 % of the principal force. Theory predicts a ratio of about 2 % to 4 %.

Figure 13 indicates that within measurement uncertainty there are not significant differences in the y-components of force at the three different values of x/c . This is in general agreement with the theoretical predictions, which show some increase in the y-component of force as the x-eccentricity is increased.

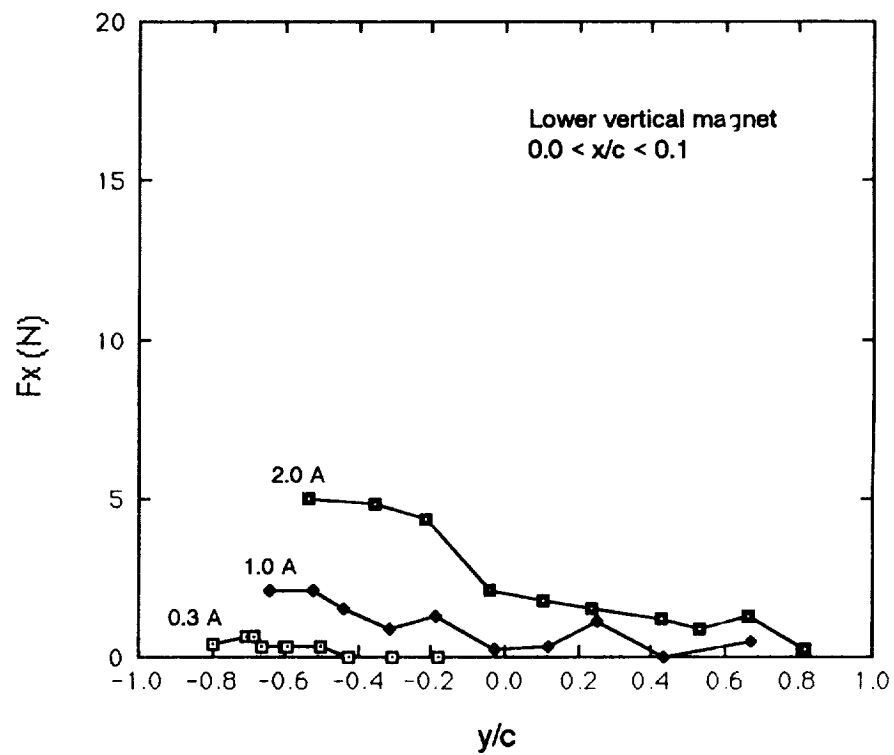


Figure 7. Horizontal force from lower vertical magnet at different values of current.

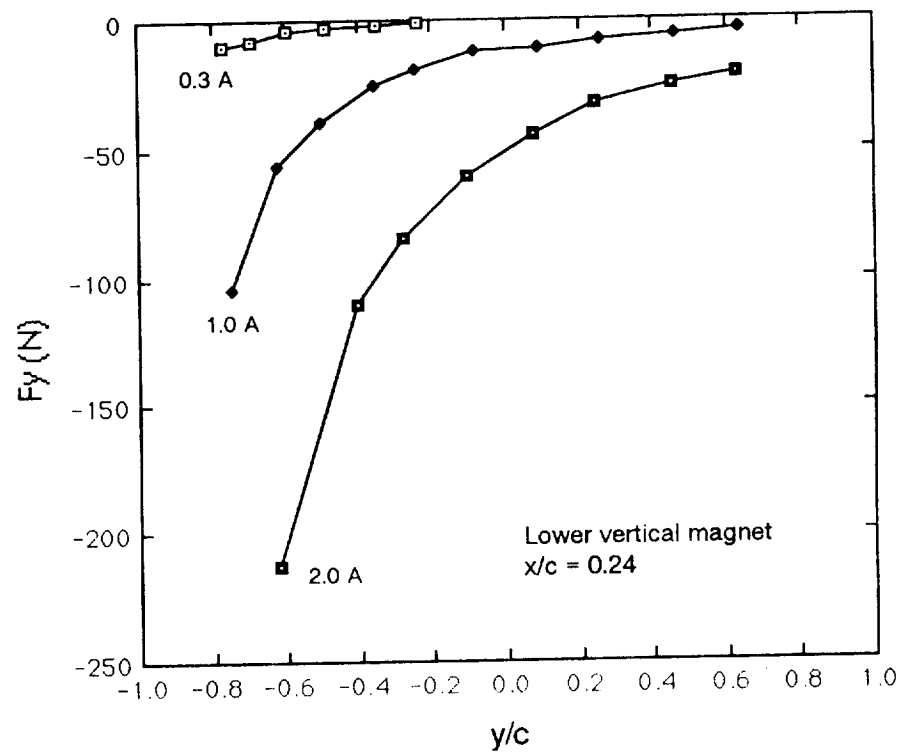


Figure 8. Vertical force from lower vertical magnet when $x/c = 0.24$.

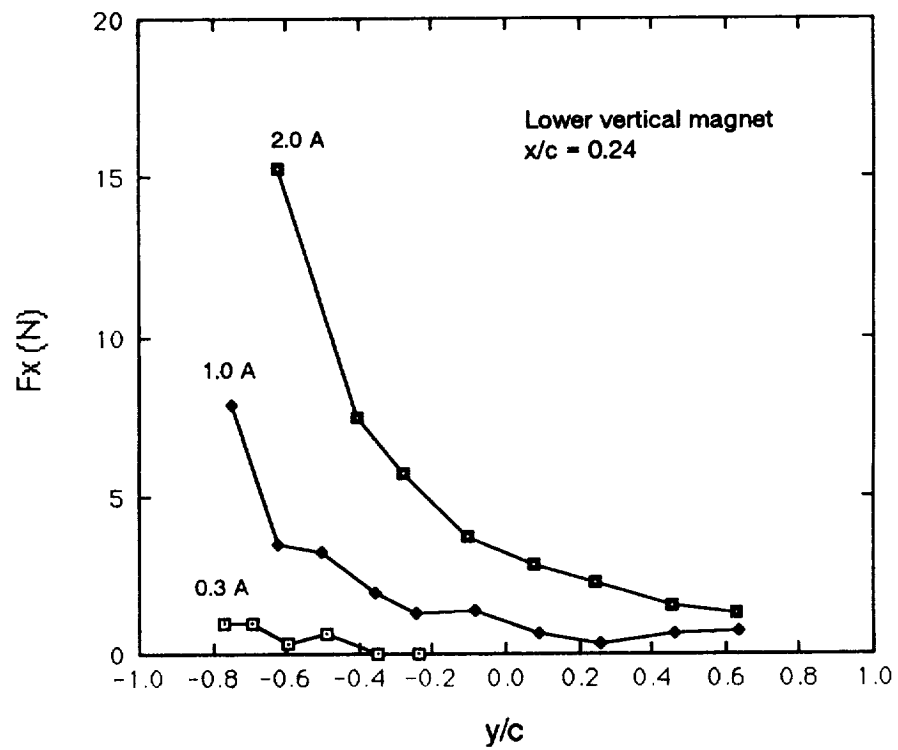


Figure 9. Horizontal force from lower vertical magnet when $x/c = 0.24$.

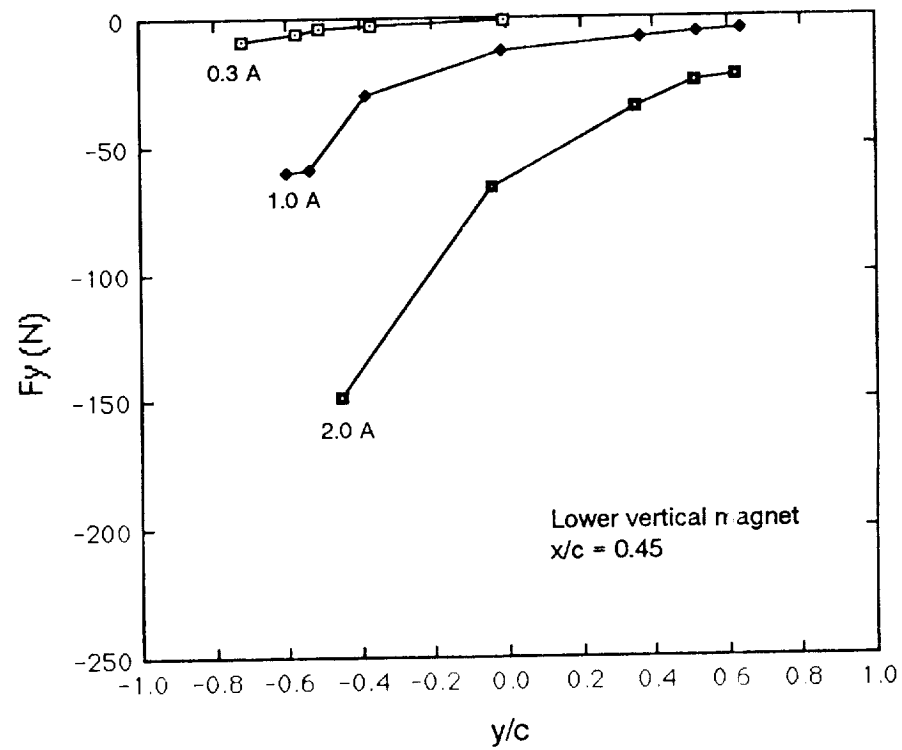


Figure 10. Vertical force from lower vertical magnet when $x/c = 0.45$.

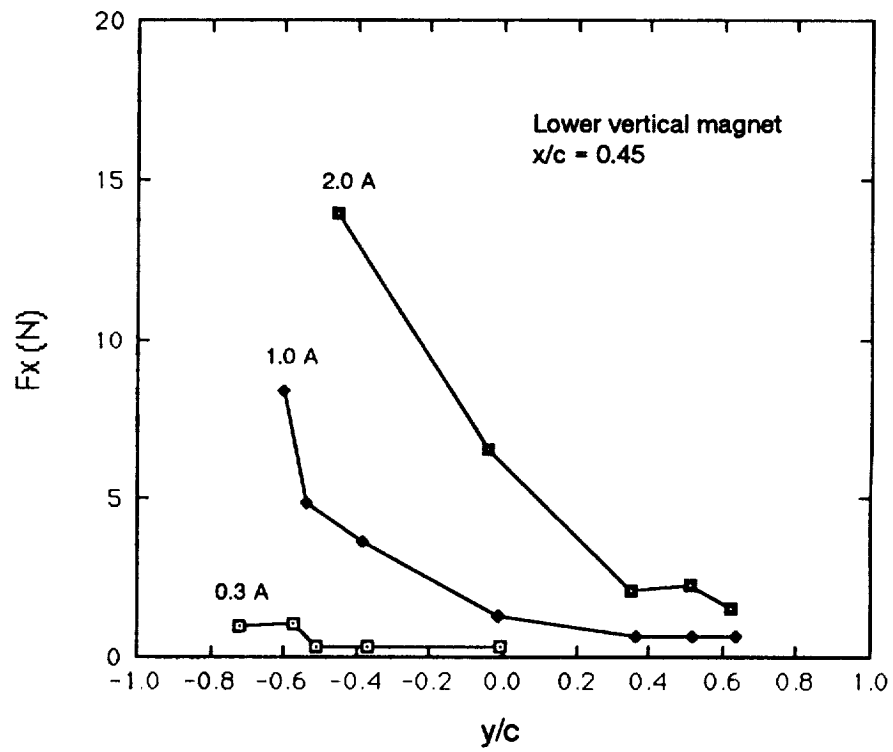


Figure 11. Horizontal force from lower vertical magnet when $x/c = 0.45$.

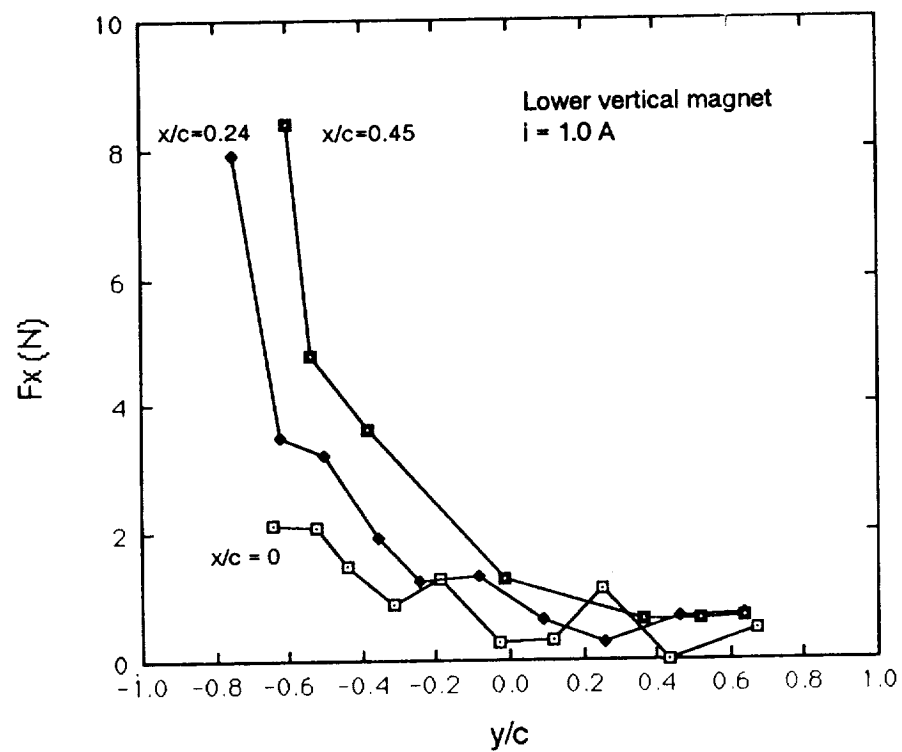


Figure 12. Horizontal force at different x positions with 1.0 A current.

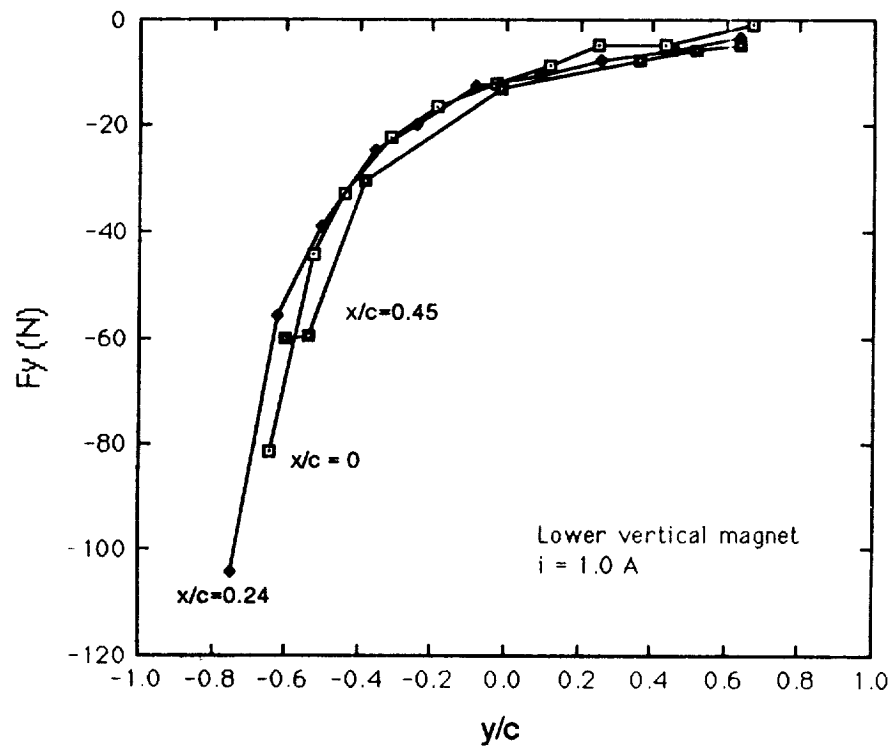


Figure 13. Vertical force at different x positions with 1.0 A current.

4. Conclusion

Numerical calculations and experimental measurements of forces in a magnetic journal bearing actuator are presented.

In summary, the general trends of the measured principal forces agree with the predictions of the theory while the magnitudes of forces are somewhat smaller than those predicted. The measured forces in the normal direction appear to be significantly larger than those predicted by theory when the rotor has an x eccentricity. The accuracy of the measured results has not been firmly established, and these conclusions should be reexamined as later measurements are made. It appears, however, that these effects will be significant even after considering experimental uncertainty, and both of these phenomena warrant further study.

Additional work is planned that will include force calculations considering the finite permeability of metals, and further force measurements using other materials. A new apparatus is being constructed that will allow more precise position control and force measurement.

5. Acknowledgments

The authors gratefully acknowledge the support of this work by NASA Lewis Research Center under research grant NAG 3-968, and the advice and assistance of the grant technical officer, Dr. G. V. Brown.

5. REFERENCES

1. Habermann, H. and Liard, G., "An Active Magnetic Bearing System," *Tribology International*, April 1980, pp. 85-89.
2. Schweitzer, G. and Lange, R., "Characteristics of a Magnetic Rotor Bearing for Active Vibration Control," *First International Conference on Vibrations in Rotating Machinery*, Institution of Mechanical Engineers, London, Cambridge, 1980.
3. Nikolajsen, J. L., Holmes, R., and Gondhalekar, V., "Investigation of an Electromagnetic Damper for Vibration Control of a Transmission Shaft," *Institution of Mechanical Engineers*, Vol. 193, No. 31, 1979, pp. 331-336.
4. Allaire, P. E., Lewis, D. W., and Knight, J. D., "Active Vibration Control of the Single Mass Rotor on Flexible Supports," *Journal of the Franklin Institute*, Vol. 315, 1983, pp. 211-222.
5. Kelm, R. D., "Analysis and Testing of a Magnetic Bearing for Flexible Rotors," M.S. Thesis, University of Virginia, 1986.
6. Chen, H. M. and M. S. Darlow, "Magnetic Bearing with Rotating Force Control," *ASME Jnl. of Tribology*, paper 87-Trib-7.
7. Walowit, J. A. and Pinkus, O., "Analytical and Experimental Investigation of Magnetic Support Systems. Part 1: Analysis," *ASME Jnl. of Lubrication Technology*, Vol. 104, No. 2, July 1982, pp. 418-428.
8. Albrecht, P. R., Walowit, J. and Pinkus, O., "Analytical and Experimental Investigation of Magnetic Support Systems. Part 2: Experimental Investigation," *ASME Jnl. of Lubrication Technology*, Vol. 104, No. 2, July 1982, pp. 429-437.
9. Keith, F. J., Williams, Rd. D. and Allaire, P. E., "Digital Control of Magnetic Bearings Supporting a Multimass Flexible Rotor," *STLE preprint* 89-AM-1B-3.
10. Schweitzer, G., (ed), Magnetic Bearings: Proceedings of the First International Symposium, ETH Zurich, Switzerland, June 6-8, 1988, Springer-Verlag, Berlin, 1989.
11. Higuchi, T. (ed), "Proceedings of the Second International Symposium on Magnetic Bearings," Tokyo, July 1990.

N91-21208

**DYNAMIC MODELLING and ANALYSIS of a MAGNETICALLY SUSPENDED FLEXIBLE
ROTOR**

Duncan C. McCallum
Charles Stark Draper Laboratory
Mail Stop #4-C
555 Technology Avenue
Cambridge
MA 02139

Abstract

A 12-state lumped-element model is presented for a flexible rotor supported by two attractive force electromagnetic journal bearings. The rotor is modelled as a rigid disk with radial mass unbalance mounted on a flexible, massless shaft with internal damping (Jeffcott rotor). The disk is offset axially from the midspan of the shaft. Bearing dynamics in each radial direction are modelled as a parallel combination of a negative (unstable) spring and a linear current-to-force actuator. The model includes translation and rotation of the rigid mass and the first and second bending models of the flexible shaft, and is unique in that it simultaneously includes internal shaft damping, gyroscopic effects, and the unstable nature of the attractive force magnetic bearings.

The model is used to analyze the dependence of the system transmission zeros and open-loop poles on system parameters. The dominant open-loop poles occur in stable/unstable pairs with bandwidth dependent on the ratios of bearing (unstable) stiffnesses to rotor mass and damping dependent on the shaft spin rate. The zeros occur in complex conjugate pairs with bandwidth dependent on the ratios of shaft stiffnesses to rotor mass and damping dependent on the shaft spin rate. Some of the transmission zeros are non-minimum phase when the spin rate exceeds the shaft critical speed.

The transmission zeros and open-loop poles impact the design of magnetic bearing control systems. The minimum loop cross-over frequency of the closed-loop system is the speed of the unstable open-loop poles. And for super-critical shaft spin rates, the presence of non-minimum phase zeros limits the disturbance rejection achievable at frequencies near or above the shaft critical speed. Since non-minimum phase transmission zeros can only be changed by changing the system inputs and/or outputs, closed-loop performance will be limited for super-critical spin rates unless additional force or torque actuators are added.

This paper reports work performed as part of the author's master's thesis [McCallum 1988], which was completed in the winter of '87 and spring of '88. This work was funded under Draper Lab I.R.&D.

Motivation

- The use of modern control system design methodologies for magnetic bearing applications is the focus of current research.
- In many applications, rotors spin above the first and second critical speeds
 - e.g. - jet engines, momentum wheels
- The application of modern design techniques to the active control of high-speed rotors requires a linear state-space model that is simple to use yet includes all important dynamics -
 - shaft flexibility, and *the effects of internal shaft damping*
 - angular dynamics and gyroscopic effects
 - coupling between translational and angular dynamics
 - variation of rotor dynamics with spin rate
 - unstable nature of attractive-force magnetic bearings



The application of modern, multi-input multi-output (MIMO) control system design methodologies to the control of flexible rotors is the focus of current research. These methodologies include: linear quadratic gaussian (LQG) control; LQG/LTR (Linear Quadratic Gaussian/Loop Transfer Recovery); and H-infinity optimal control.

In many magnetic bearing applications, such as aircraft engines, the suspended rotor spins at speeds exceeding the first and second critical speeds. The application of modern design techniques to the control of these high speed rotors requires a linear system model that is simple yet includes all dynamic effects that are important at high speeds.

When rotors spin above their critical speed(s), rotor flexible body modes can be excited. When the rotor flexes, internal damping can serve as a mechanism of instability [Crandall 1980, Johnson 1986]. Thus, the model used for control design should include rotor flexibility (first and second bending modes) and the effects of internal shaft damping. Angular dynamics are also important at high spin rates since gyroscopic coupling between input axes can be large for high speed rotors. Gyroscopic effects are particularly important for jet engines, where the rotor-bearing system can be subject to relatively large rotation rates. Coupling between angular dynamics and translational dynamics can be significant, and should be included in the model. Finally, the unstable nature of attractive-force magnetic bearings should also be included.

This paper presents a model that simultaneously includes first and second mode bending, gyroscopic effects, the effects of internal shaft damping, and the unstable nature of attractive-force magnetic bearings. The model is used to determine system open-loop poles and transmission zeros and their dependence on spin rate. The paper concludes with a brief discussion of the implications for control system design.

The model presented here is intended to bridge the gap between models available in the literature when the author's thesis research was performed and models used for detailed rotor dynamic analysis. In practice, the model presented here should be augmented with finite element or experimental analyses in a magnetic bearing control system development effort.

Outline

- *Motivation*
- *Outline*
- Model Description
- Analysis
 - Open-loop eigenvalues (poles)
 - Transmission zeros
- Conclusions - implications for control
- Appendices - linearized equations of motion, bibliography

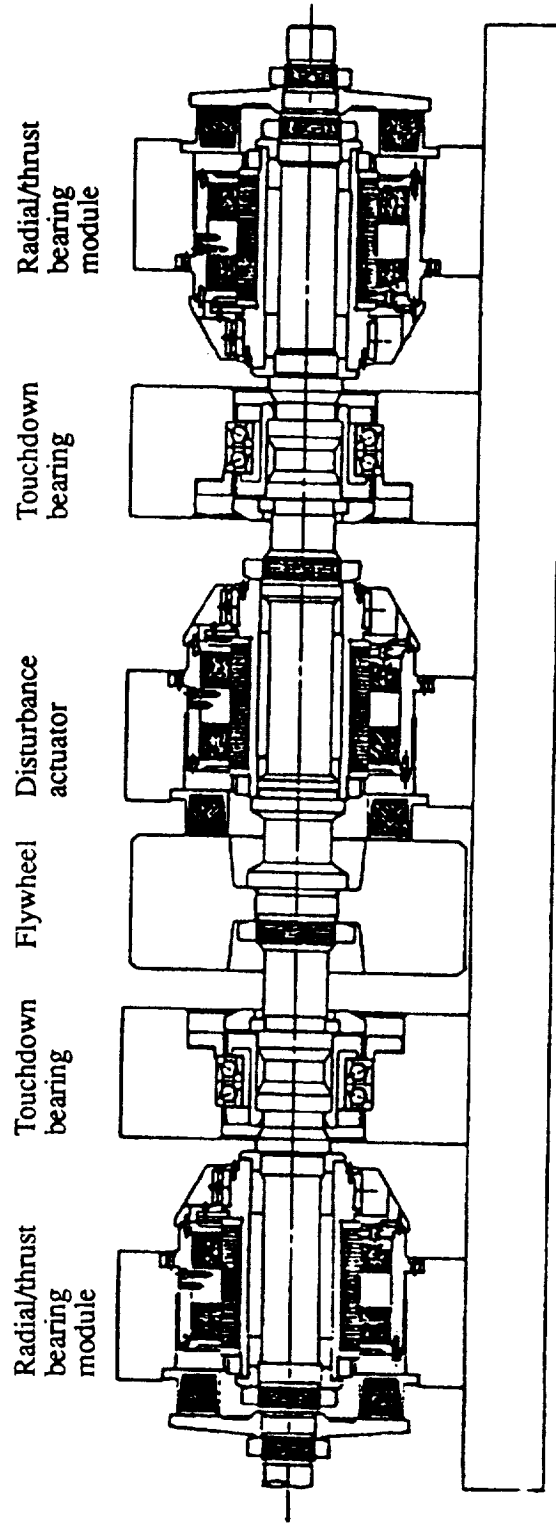


The remainder of this paper is composed of three sections and two appendices. A description of the lumped-element model is presented first. A discussion of the open-loop eigenvalues and transmission zeros, and their variation with shaft spin rate, is then presented. The paper concludes with a brief discussion of the implications of the system dynamics for control.

Linearized equations of motion for the model are presented in the appendix. A complete derivation of these equations, and a more thorough analysis of the dynamics, can be found in [McCallum 1988]. A bibliography also appears in an appendix.

Model Description

- The parameters used in the model are for a testbed designed at Draper Lab. The testbed employs two attractive-force, permanent magnet-biased electromagnetic journal bearings. A similar testbed is now under construction.
- The model includes only radial dynamics. Axial dynamics decouple (to first order).



Parameters used in the modelling effort are from a testbed designed at Draper Lab in 1987-1988. A testbed similar to the one shown above is now under construction.

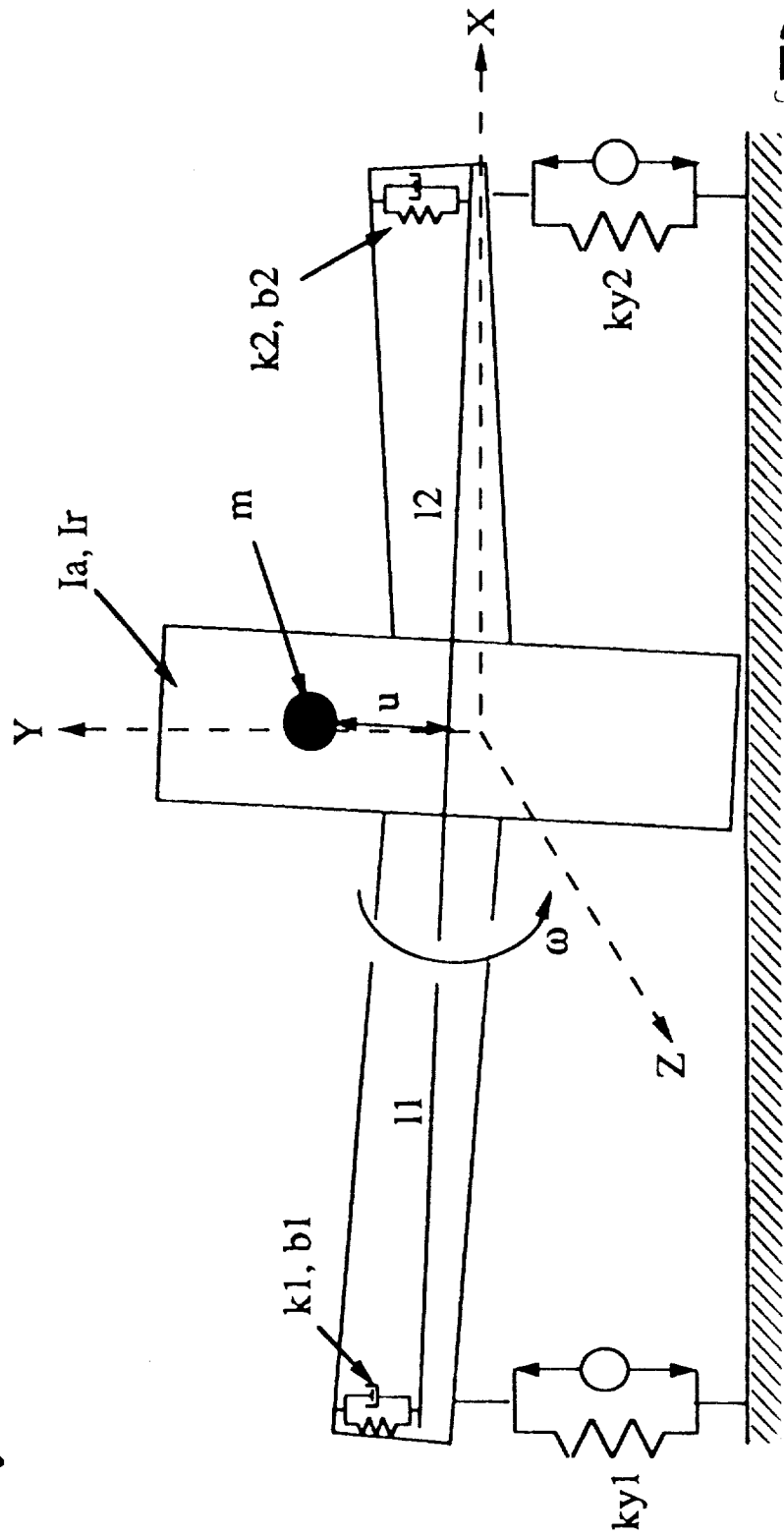
The testbed consists of a flexible rotor supported at its ends by two attractive-force, permanent magnet biased, electro-magnetic journal bearings. Inputs to the testbed are the bearing currents in each axis. Measurements of the shaft-end positions are used for control.

Although model parameters are from the Draper testbed, the model and results presented here can be generalized to other actively-controlled rotors.

The model presented here considers only radial dynamics (radial translation and rotation about shaft radii). Axial dynamics decouple from the radial dynamics to first order.

Model Description (cont.)

- The 12 state, lumped-element model includes radial translation of the flywheel and shaft ends and rotation of the flywheel about its radii.



The rotor is modelled as a rigid flywheel with radial mass unbalance mounted on a flexible, massless shaft with internal damping. In the model, the flywheel is allowed to translate in radial directions and rotate about its radii. Each end of the shaft is modelled by a rigid rod of appropriate length, with a parallel combination of a spring and a damper acting between the rod end and the shaft wall in each of two perpendicular radial directions. The shaft ends are allowed to move (independent of flywheel and of each other) in shaft radial directions.

As desired, this rotor model includes gyroscopic effects, first and second mode bending, the effects of static mass unbalance, and internal shaft damping. Note that, since the rigid rods are not necessarily of equal length, the effects of coupling between angular and translational dynamics are also included.

Assumptions used in modelling the rotor are -

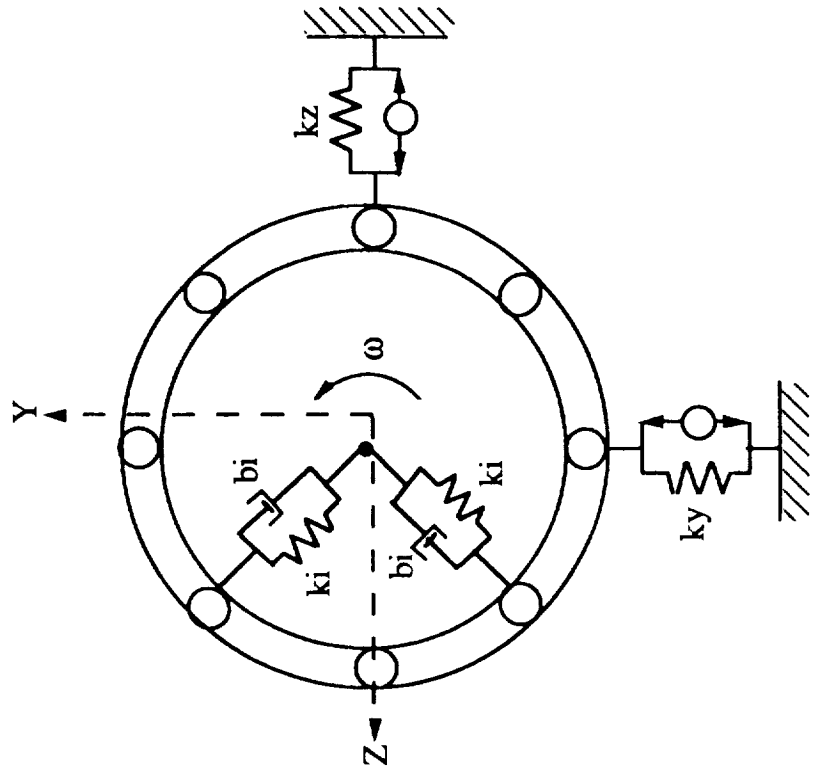
- the rigid flywheel is dynamically balanced
- the shaft ends are axisymmetric, so that stiffness and damping are the same in all radial directions
- shaft stress is linearly dependent on strain-rate (linear internal shaft damping)
- axial dynamics decouple from the radial dynamics

Dynamics of each bearing in each radial direction are modelled by a parallel combination of an unstable spring and a linear current to force actuator. Losses and high frequency roll-off are ignored in the bearing model. Past magnetic bearing designs have demonstrated input current to output force frequency responses that are flat to high frequencies [Traxler 1984, Ulbrich 1984, Maslen, 1988]. This bearing model has appeared often in the literature [ex. Downer 1986].

System inputs are the currents in coils for each axis of the two bearings. It is assumed that (only) shaft end positions at the bearing are available. The measurements and bearing forces are assumed to be in the same radial plane of the shaft - the effects of noncollocation are not considered here.

Model Description (cont.)

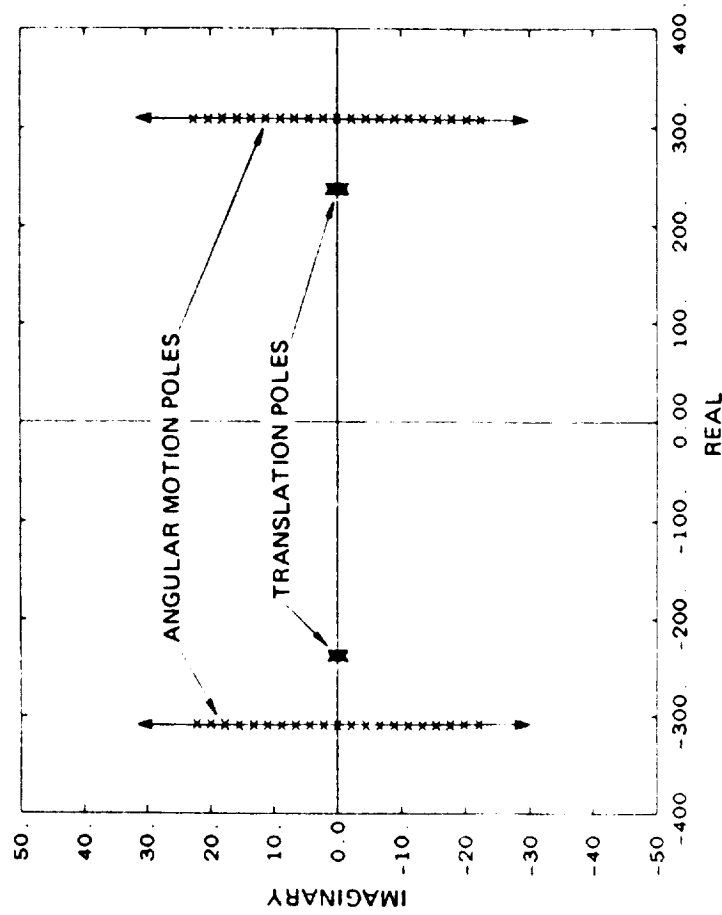
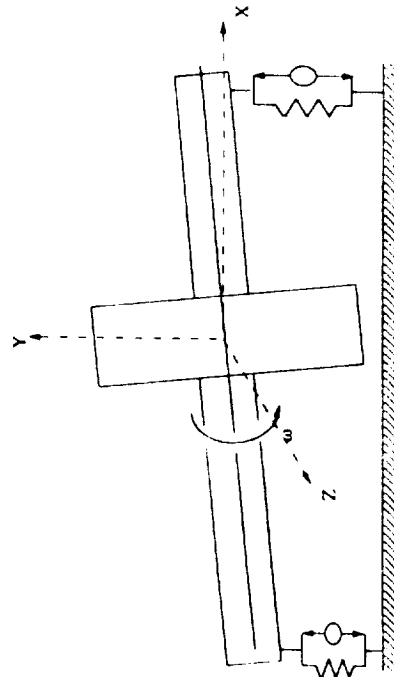
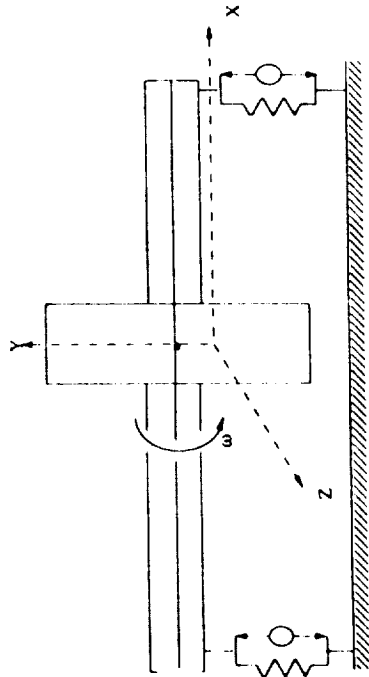
- The equivalent shaft springs and dampers rotate with the shaft (Jeffcott rotor). This is important for modelling flexible body modes, where modal damping varies with the spin rate and is dependent on the direction of whirl.



The figure above shows an end view of the model. Note that the shaft equivalent springs and dampers rotate with the shaft. This model is sometimes called the Jeffcott rotor in the literature [Johnson 1986]. Rotation of the dampers with the shaft is important for modelling shaft whirl modes, since the equivalent damping of forward and backward whirl modes is different for non-zero spin rates. In fact, the combination of shaft spin and internal damping can add energy to the system for supercritical spin rates.

Analysis - open-loop eigenvalues

- The model predicts 12 eigenvalues.
- 4 eigenvalue pairs correspond to rigid body rotation.



Linearized equations of motion are derived in detail in [McCallum 1988], and are presented in the appendix of this paper. The model that results for this system has 12 states, and predicts dynamics that are a function of shaft spin rate.

The linearized equations of motion were used to analyze the dependence of system eigenvalues (poles) and transmission zeros on system parameters (stiffness, damping, spin rate). Only the dependence on spin rate is discussed in this paper.

The model predicts 12 eigenvalues. 4 pair of eigenvalues correspond to rigid body motion of the suspended rotor.

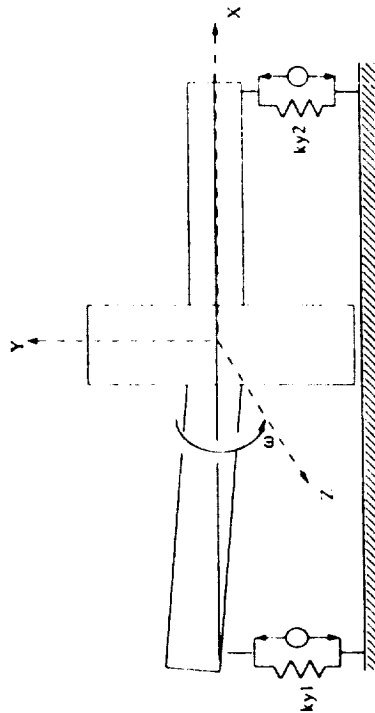
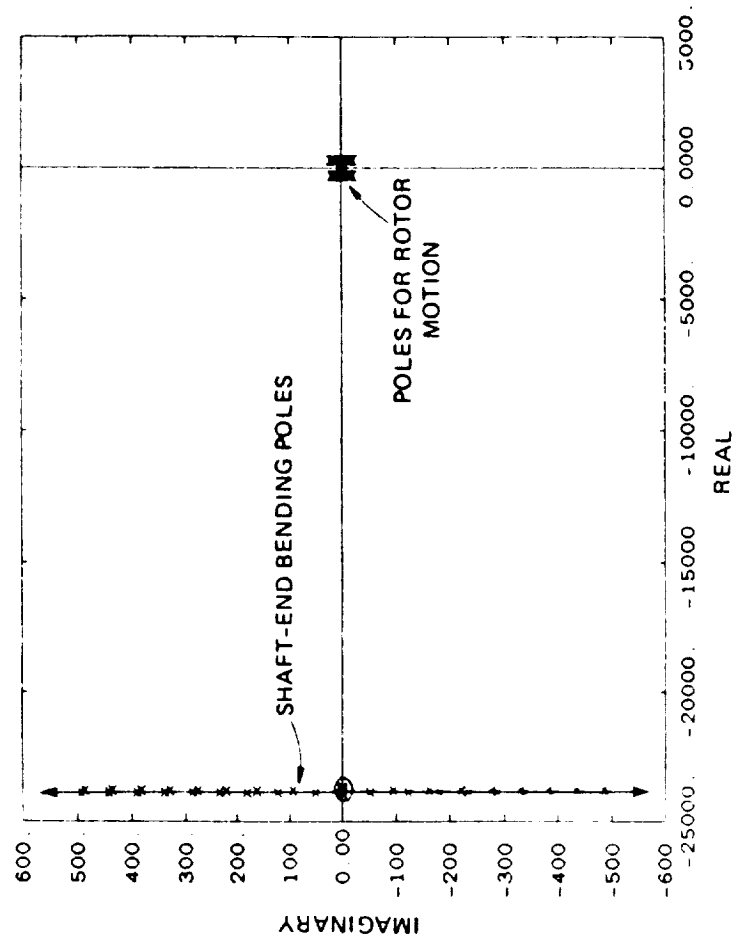
The first 4 rigid body poles correspond to angular motion of the flywheel. These poles occur in 2 stable/unstable pairs. Since the shaft is much stiffer than the bearings, the speed of these poles is dependent on the ratio of the equivalent rotational stiffness of the bearings to the radial moment of inertia of the flywheel. For zero spin rate, these poles lie on the real axis. As spin rate increases, the imaginary component of these poles increases due to gyroscopic coupling.

4 poles correspond to translational motion of the flywheel. These poles occur in 2 stable/unstable pairs, each pair corresponding to displacement of the flywheel in the horizontal or vertical direction. The speed of these poles is dependent on the ratio of the bearing (unstable) stiffness to the rotor mass. For zero spin rate, these poles lie on the real axis. As the spin rate increases, the translational poles have a small imaginary component due to coupling with the angular rotational mode. If the flywheel were in the shaft center, the translational motion poles would be independent of spin rate.

As the flywheel moves away from the center, coupling between the angular and translational open-loop modes increases. In these cases, all rigid body modes will be a combination of angular and translational motion.

Analysis - open-loop eigenvalues (cont.)

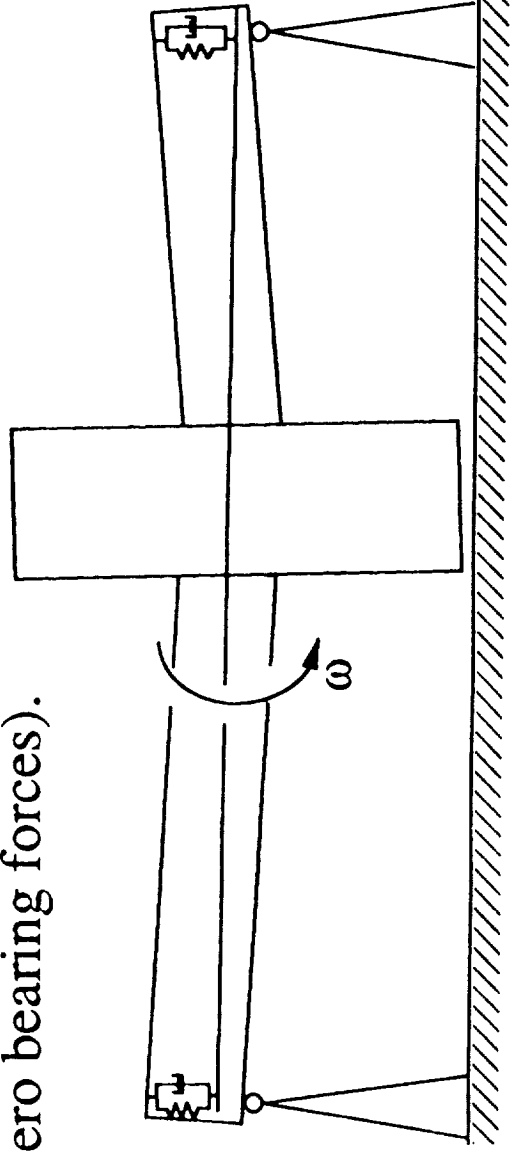
- 2 eigenvalue pairs correspond to shaft-end bending.



The 4 remaining poles correspond to shaft-end bending. These poles occur in pairs, each pair corresponding to bending of one shaft end. The speed of these poles is the ratio of the equivalent shaft end stiffness to the shaft end damping. For zero spin rate, these poles lie on the real axis. As spin rate increases, the shaft-end bending poles have an imaginary component equal to the shaft spin rate. This is because the projection of the shaft-end deflection in the lab frame changes as the shaft rotates.

Analysis - transmission zeros

- A transmission zero corresponds to a natural system motion where the output vector is zero for a non-zero input.
- Outputs = shaft end positions
- Inputs = coil currents, proportional to bearing force when shaft ends do not move
- Frequencies and (part of) directions of transmission zeros are the eigenvalues and eigenvectors the rotor would have if mounted in perfectly rigid bearings (no shaft end motion, non-zero bearing forces).



Transmission zeros occur when, for some initial condition, a natural motion of the system exists for which the output vector is zero for a non-zero input vector.

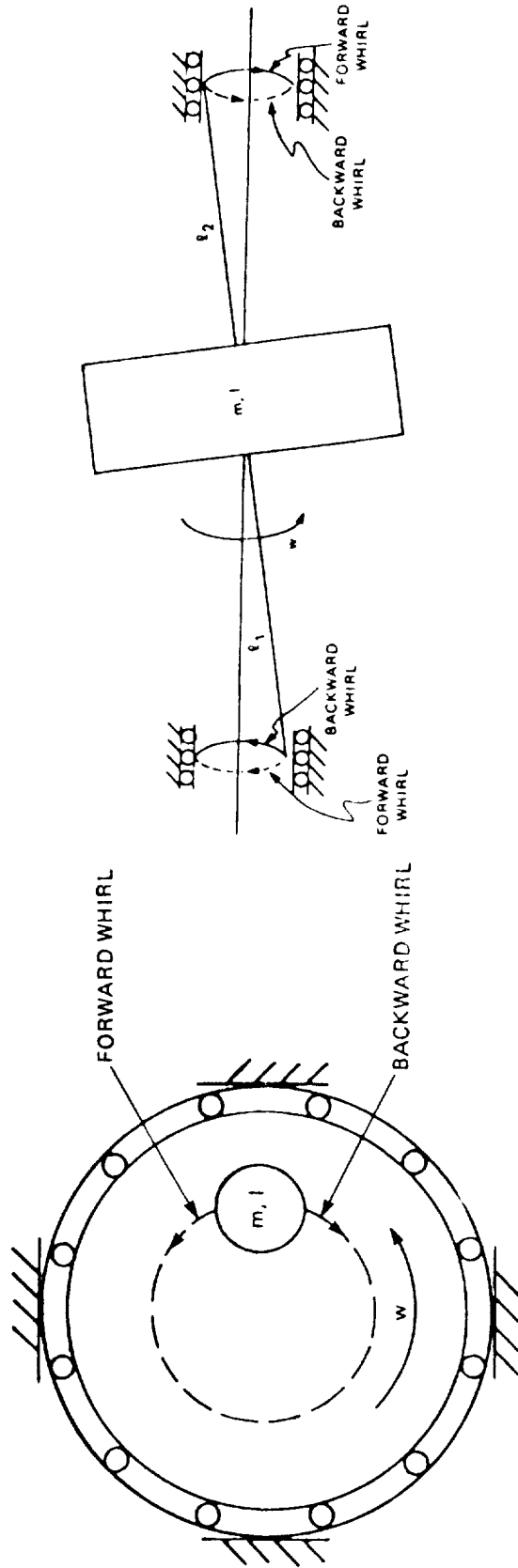
For our model, the outputs are the shaft-end positions and the inputs are the bearing currents. For a transmission zero to exist, the shaft-ends must be stationary. And if the shaft ends are stationary, bearing current is directly proportional to bearing force. Thus, for this model a transmission zero occurs if and only if there is a natural motion of the system where the shaft-ends remain fixed for non-zero bearing forces.

These natural motions correspond to motions the rotor would have if mounted in perfectly rigid bearings. Thus, the frequencies and (part of) the directions of transmission zeros are the same as the eigenvalues and eigenvectors of the rotor with both ends fixed.

The extensive literature on the dynamics of rotors in stiff bearings can be used to predict transmission zeros. Any rotor that is unstable in stiff bearings will have non-minimum phase transmission zeros.

Analysis - transmission zeros (cont.)

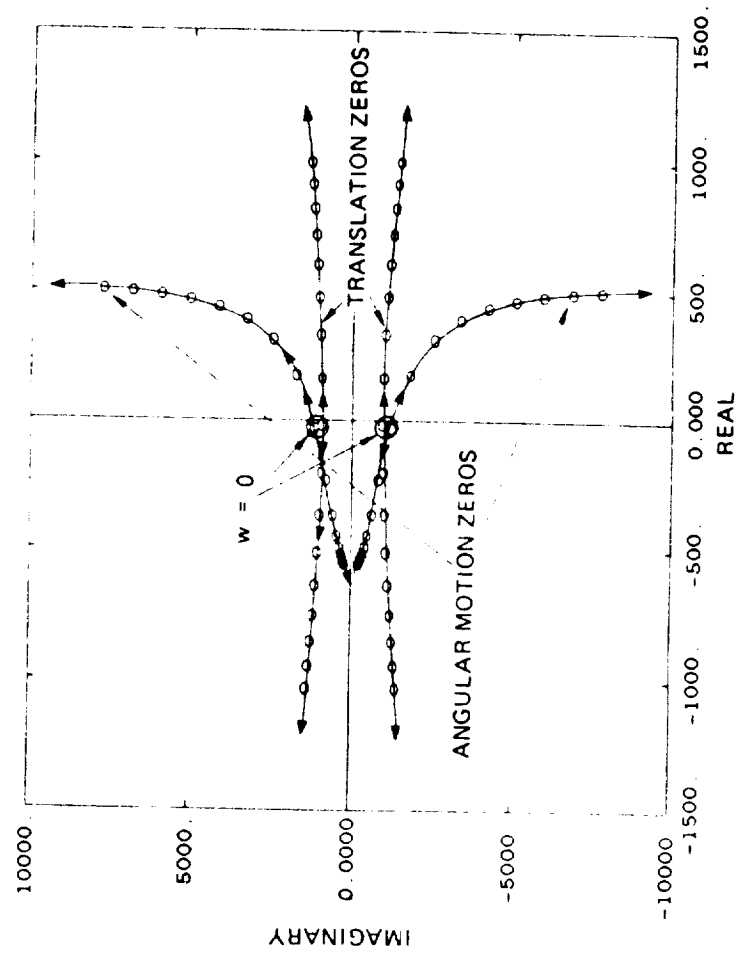
- The model predicts 4 pair of transmission zeros.
 - 2 pair correspond to first-mode bending (translational whirl)
 - 2 pair correspond to second-mode bending (rotational whirl)



The model predicts 4 pair of transmission zeros. The first 2 pair correspond to translational whirl (first-mode bending). 1 pair corresponds to forward translational whirl. 1 pair corresponds to backward translational whirl. Forward whirl is defined as a circular rotor motion in the same direction as the rotor spin. Backward whirl is defined as circular rotor motion in the direction opposite the rotor spin. Forward and backward translational whirl are illustrated in above.

The second 2 pair of transmission zeros correspond to rotational whirl (second-mode bending). Again, 1 pair corresponds to forward whirl, the other pair correspond to backward whirl. For the rotational whirl case, forward whirl corresponds to motions where the ends of the equivalent rigid rods move in circles in the same direction as the shaft spin. Backward whirl is the opposite motion.

Analysis - transmission zeros (cont.)



The above figure shows the transmission zeros as a function of spin rate.

The translational motion transmission zeros have a frequency equal to the first critical speed. The frequency of these zeros is only a weak function of rotational speed. However, the damping of these zeros is a strong function of spin rate. Damping of the backward whirl zeros increases with spin rate, while the damping of the forward whirl zeros decreases with spin rate. The forward translational whirl zeros become non-minimum phase for all spin rates exceeding the first critical speed (the translational resonance frequency).

At zero speed, the rotational motion transmission zeros has a frequency equal to the second critical speed. The frequency of these zeros is a strong function of spin rate, with forward whirl zeros asymptotically approaching the gyroscopic whirl frequency. The damping of the forward whirl zeros is a decreasing function of rotational speed - for spin rates exceeding the second critical speed, the forward whirl zeros are non-minimum phase. The damping of the backward rotational whirl zeros increases with spin rate, with the frequency of these zeros asymptotically approaching zero.

Conclusions - implications for control

- The minimum loop cross-over frequency of the closed-loop system is the speed of the unstable open-loop poles.
- When the spin rate reaches a critical speed, a complex-conjugate zero pair will become non-minimum phase, contributing 180 deg. of phase lag (rather than phase lead). This transition plane explains stability problems encountered when spinning through shaft critical speeds.
- Non-minimum phase zeros limit the achievable closed-loop disturbance rejection at frequencies near or above the shaft critical speeds.
- Zeros can only be changed by changing the system inputs or outputs, i.e. adding additional actuators or sensors.
Limitations imposed by n.m.p. zeros are physical limitations that cannot be overcome through feedback.



The open-loop system dynamics impact the design and achievable performance of magnetic bearing control systems.

The minimum loop cross-over frequency of the closed-loop system is the speed of the unstable open-loop poles associated with rigid body motion. This result has appeared in the literature [Groom 1979, Downer 1986].

For spin rates at or above the rotors critical speed, the transmission zeros become non-minimum phase. As a result, the achievable disturbance rejection of the closed-loop system is limited at frequencies near or above the shaft critical speeds (the frequencies of the zeros). In addition, when the transmission zeros become non-minimum phase, each complex conjugate pair contributes 180 deg. of phase lag rather than phase lead. This transition explains stability problems encountered when spinning a magnetically suspended rotor through its critical speeds (as for systems with notch filters).

Non-minimum phase zeros cannot be changed through active control. Canceling right-half plane zeros with compensator poles results in a system that it is internally unstable. Zeros can only be changed by changing the system inputs or outputs, i.e. by adding additional actuators or sensors. The limitations imposed by non-minimum phase zeros are physical limitations that cannot be overcome through feedback.

Appendix A - Equations of Motion

This appendix presents linearized equations of motion for a magnetic bearing - suspended rotor system. Included are a summary of the assumptions used in deriving the equations, descriptions of reference frames, and a list of symbols. A detailed derivation of the equations of motion can be found in [McCallum 1988].

A.1 Summary of assumptions

The magnetically-suspended rotor is modelled as a rigid flywheel with radial mass unbalance mounted on a flexible, massless shaft with internal damping. In the model, the flywheel is allowed to translate in radial directions and rotate about its radii. The shaft ends are allowed to move (independent of the flywheel and of each other) in radial directions. The mass is not assumed to be at the midspan of the shaft, so that the forces at the shaft ends are not equal. The rotor model includes: gyroscopic effects; the first and second bending modes; the effects of internal shaft damping; and differences in bearing loads. The rotor model excludes the effects of axial torque and axial translation. Further, the shaft is assumed to be axially symmetric so that the shaft stiffness and damping are the same in all radial directions. Also, the rotor is assumed to be configured such that the spin axis is aligned with the axial principal axis of the rotor (i.e., the rotor is dynamically balanced) and the radial moment of inertia is the same in all directions.

The magnetic bearings are modelled as a parallel combination of an unstable spring and a linear current-force actuator in each direction¹, i.e.,

$$F_{yi} = K_{yi} Y_i + K_i \delta i_{Y1} \quad (\text{A.1.1})$$

Bearing losses and high frequency dynamics are ignored.

It is assumed that (only) measurements of the shaft end positions are available. Sensor dynamics are excluded. In addition, it is assumed that the bearing forces and the sensor measurements are at the same points on the shaft - non-colocation effects are ignored. Justifications for the assumptions listed here can be found in [McCallum 1988].

¹This model appears often in the literature.

A.2 Reference frames

The system state is described by the position and velocity of the flywheel's geometric center, the positions of the shaft ends, and rotations of the flywheel about its radii. Positions and velocities are described in the cartesian reference frame XYZ shown in Figure A.1. This frame is fixed to "ground" with its origin at the force-free equilibrium position of the flywheel's geometric center. The X -axis is horizontal and coincident with the centerline of the shaft when the system is in force-free equilibrium. The Y -axis of the frame is vertical. The Z -axis is horizontal and coincident with a radius of the flywheel at equilibrium. Figure A.1 also shows the frames xyz and 123 , which are used in [McCallum 1988] to derive the equations of motion. The rotational motions of the flywheel are described in terms of the gyroscopic coordinates illustrated in Figures A.2 and A.3.

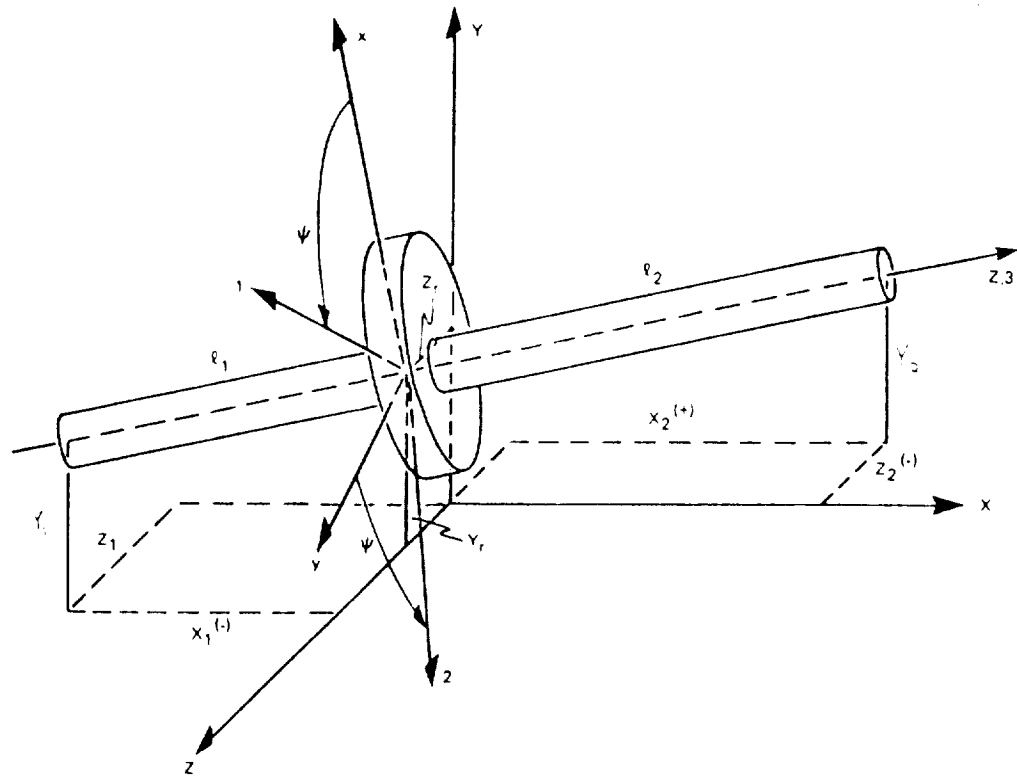


Figure A.1 - Reference frames

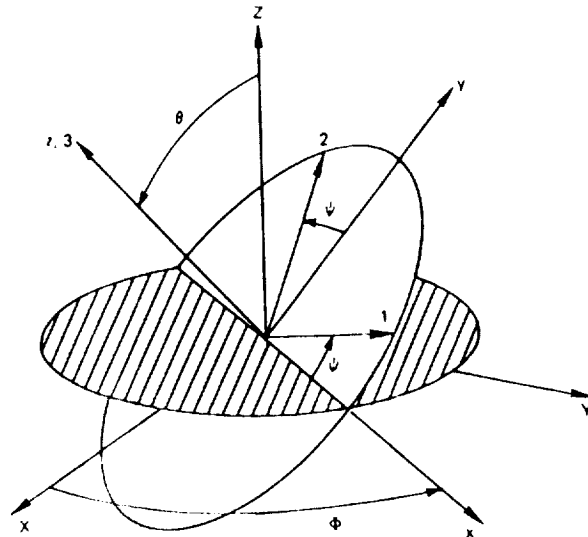


Figure A.2 - Euler angles

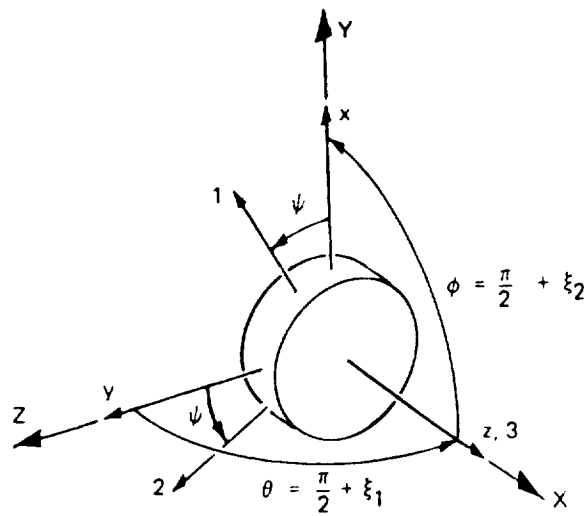


Figure A.3 - Gyroscopic coordinates

A.3 Equations of Motion

The system states (\mathbf{x}) are chosen as the flywheel translational and rotational positions and velocities and the positions of the shaft ends

$$\mathbf{x} = \left[Y_r \quad \dot{Y}_r \quad Z_r \quad \dot{Z}_r \quad \xi_1 \quad \dot{\xi}_1 \quad \xi_2 \quad \dot{\xi}_2 \quad Y_1 \quad Z_1 \quad Y_2 \quad Z_2 \right]^T \quad (\text{A.3.1})$$

System inputs are the changes in bearing coil currents from their equilibrium values

$$\mathbf{u} = [i_{Y1} \ i_{Z1} \ i_{Y2} \ i_{Z2}]^T \quad (\text{A.3.2})$$

System outputs are the positions of the shaft ends

$$\mathbf{y} = [Y_1 \ Z_1 \ Y_2 \ Z_2]^T \quad (\text{A.3.3})$$

Linearized equations of motion for the rotor-bearing system can be written in state-space form as:

$$\dot{\mathbf{x}} = \mathbf{A}(\omega) \mathbf{x} + \mathbf{B} \mathbf{u} + \mathbf{d} \quad (\text{A.3.4})$$

$$\mathbf{y} = \mathbf{C} \mathbf{x} + \mathbf{D} \mathbf{u} + \mathbf{n} \quad (\text{A.3.5})$$

where

$$\mathbf{d} = \begin{bmatrix} 0 \\ u \dot{\omega} \sin(\omega t + \theta_0) + u \omega^2 \cos(\omega t + \theta_0) - g + \frac{dY_r}{M} \\ 0 \\ -u \dot{\omega} \cos(\omega t + \theta_0) + u \omega^2 \sin(\omega t + \theta_0) + \frac{dZ_r}{M} \\ 0 \\ \frac{d\xi_1}{l_r} \\ 0 \\ \frac{d\xi_2}{l_r} \\ \frac{dY_1}{b1} \\ \frac{dZ_1}{b1} \\ \frac{dY_2}{b2} \\ \frac{dZ_2}{b2} \end{bmatrix} \quad (\text{A.3.6})$$

$$A = \begin{bmatrix} 0 & 1 & 0 & 0 & 0 & 0 & 0 & 0 & 0 & 0 & 0 & 0 \\ 0 & 0 & 0 & 0 & 0 & 0 & 0 & 0 & \frac{Ky1}{M} & 0 & \frac{Ky2}{M} & 0 \\ 0 & 0 & 0 & 1 & 0 & 0 & 0 & 0 & 0 & 0 & 0 & 0 \\ 0 & 0 & 0 & 0 & 0 & 0 & 0 & 0 & 0 & \frac{Kz1}{M} & 0 & \frac{Kz2}{M} \\ 0 & 0 & 0 & 0 & 0 & 1 & 0 & 0 & 0 & 0 & 0 & 0 \\ 0 & 0 & 0 & 0 & 0 & 0 & 0 & -\frac{\omega Ia}{I_r} & 0 & \frac{Kz1 \cdot l1}{M} & 0 & -\frac{Kz2 \cdot l2}{M} \\ 0 & 0 & 0 & 0 & 0 & 0 & 0 & 1 & 0 & 0 & 0 & 0 \\ 0 & 0 & 0 & 0 & 0 & \frac{\omega Ia}{I_r} & 0 & 0 & -\frac{Ky1 \cdot l1}{M} & 0 & \frac{Ky2 \cdot l2}{M} & 0 \\ \frac{k1}{b1} & 1 & \omega & 0 & l1 \omega & 0 & -\frac{k1 \cdot l1}{b1} & -l1 & \frac{Ky1 - k1}{b1} & -\omega & 0 & 0 \\ -\omega & 0 & \frac{k1}{b1} & 1 & \frac{k1 \cdot l1}{b1} & l1 & l1 \omega & 0 & \omega & \frac{Kz1 - k1}{b1} & 0 & 0 \\ \frac{k2}{b2} & 1 & \omega & 0 & -l2 \omega & 0 & \frac{k2 \cdot l2}{b2} & l2 & 0 & 0 & \frac{Ky2 - k2}{b2} & -\omega \\ -\omega & 0 & \frac{k2}{b2} & 1 & -\frac{k2 \cdot l2}{b2} & -l2 & -l2 \omega & 0 & 0 & 0 & \omega & \frac{Kz2 - k2}{b2} \end{bmatrix}$$

(A.3.7)

$$B = \begin{bmatrix} 0 & 0 & 0 & 0 \\ \frac{Ki}{M} & 0 & \frac{Ki}{M} & 0 \\ 0 & 0 & 0 & 0 \\ 0 & \frac{Ki}{M} & 0 & \frac{Ki}{M} \\ 0 & 0 & 0 & 0 \\ 0 & \frac{Ki \cdot l1}{I_r} & 0 & -\frac{Ki \cdot l2}{I_r} \\ 0 & 0 & 0 & 0 \\ -\frac{Ki \cdot l1}{I_r} & 0 & \frac{Ki \cdot l2}{I_r} & 0 \\ \frac{Ki}{b1} & 0 & 0 & 0 \\ 0 & \frac{Ki}{b1} & 0 & 0 \\ 0 & 0 & \frac{Ki}{b2} & 0 \\ 0 & 0 & 0 & \frac{Ki}{b2} \end{bmatrix}$$

(A.3.8)

$$\mathbf{C} = \begin{bmatrix} 0 & 0 & 0 & 0 & 0 & 0 & 0 & 0 & 1 & 0 & 0 & 0 \\ 0 & 0 & 0 & 0 & 0 & 0 & 0 & 0 & 0 & 1 & 0 & 0 \\ 0 & 0 & 0 & 0 & 0 & 0 & 0 & 0 & 0 & 0 & 1 & 0 \\ 0 & 0 & 0 & 0 & 0 & 0 & 0 & 0 & 0 & 0 & 0 & 1 \end{bmatrix} \quad (\text{A.3.9})$$

$$\mathbf{D} = [0_{(4 \times 4)}] \quad (\text{A.3.10})$$

Note that, in this representation, radial mass unbalance is modelled as an input force disturbance. The effects of dynamic balance could be included similarly. The effects of measurement center offset could be added to this model as additive measurement noise.

A.4 List of Symbols

b_i	= equivalent damping of shaft end i
\mathbf{d}^2	= vector of input disturbances
$d\xi_1$	= torque disturbance acting on the rotor in the ξ_1 -direction
$d\xi_2$	= torque disturbance acting on the rotor in the ξ_2 -direction
dY_i	= force disturbance acting on shaft end i in the Y-direction
dY_r	= force disturbance acting on the rotor in the Y-direction
dZ_i	= force disturbance acting on shaft end i in the Z-direction
dZ_r	= force disturbance acting on the rotor in the Z-direction
I_a	= axial moment of inertia
I_r	= radial moment of inertia
i_{Yi}	= current in the Y-coil(s) at shaft end i
i_{Zi}	= current in the Z-coil(s) at shaft end i
k_i	= equivalent stiffness of shaft end i
K_{Yi}	= equivalent (unstable) stiffness of bearing at shaft end i in the Y-direction
K_{Zi}	= equivalent (unstable) stiffness of bearing at shaft end i in the Z-direction
l_i	= equivalent length of shaft end i
M	= rotor mass
\mathbf{n}	= sensor noise
\mathbf{u}	= control inputs
u	= radial mass unbalance distance
ω	= shaft spin rate

²**Bold** denotes a vector.

\mathbf{x} = state vector
 ξ_1 = gyroscopic coordinate, approximately equal to rotation about the +Y-axis
 ξ_2 = gyroscopic coordinate, approximately equal to rotation about the +Z-axis
 \mathbf{y} = system outputs
 Y_i = displacement of shaft end i in the Y-direction
 Y_r = displacement of the rigid rotor in the Y-direction
 Z_i = displacement of shaft end i in the Z-direction
 Z_r = rotor displacement in the Z-direction
 t = time
 θ_0 = orientation of the radial unbalance vector with respect to the +1 axis
 θ, ϕ, ψ = Euler angles describing rotor orientation

Appendix B - Bibliography

Adams, M.L. and J. Padovan. [1981] **Insights Into Linearized Rotor Dynamics.** Journal of Sound and Vibration, 76, n 1 (1981).

Adams, M.L. ed. [1983] **Rotor Dynamics Instability.** American Society of Engineers, Applied Mechanics Symposia Series: AMD Vol. 55, papers presented at the Applied Mechanics, Bioengineering, and Fluids Engineering Conference, Houston, Texas, June 20-22, 1983.

Akishita, S., et. al. [1990] **Vibration Control of Magnetically Suspended Flexible Rotor by the Use of Optimal Regulator.** Second International Symposium on Magnetic Bearings. Tokyo, Japan: July 12-14, 1990, pp. 147-154.

Alberg, H. [1982] **Rotor Dynamics of Non-Symmetrical Rotor-Bearing-Frame Systems.** Conference on Rotordynamic Problems in Power Plants, Rome, Italy, September 28-October 1, 1982.

Allaire, P.E., R. Humphris, and L. Barrett. [1986] **Critical Speeds and Unbalance Response of a Flexible Rotor in Magnetic Bearings.** Proceedings of First European Turbomachinery Symposium, Brunel University, London, England, October 27-28, 1986.

Allaire, P.E., R. Humphris, M. Kasarda, and M. Koolman. [1987] **Magnetic Bearing/Damper Effects on Unbalance Response of Flexible Rotors.** Proceedings of AIAA Conference, Philadelphia, PA, August 10-14, 1987.

Anton, E. and H. Ulbrich. [1985] **Active Control of Vibrations in the Case of Asymmetrical High-Speed Rotors by Using Magnetic Bearings.** ASME Design Engineering Technical Conference, Cincinnati, OH, September 10-13, 1985.

Beams, J. [1964] **Magnetic Bearings.** SAE 810A, January 1964.

Beatty, R. [1985] **Notch Filter Control of Magnetic Bearings to Improve Rotor Synchronous Response.** S.M. Thesis, Massachusetts Institute of Technology, May 1988.

Bleuler, H. and G. Schweitzer. [1983] **Dynamics of Magnetically Suspended Rotor with Decentralized Control.** Proceedings of the IASTED Symposium on Applied Control and Identification, Copenhagen: June 28-July 1, 1983.

Crandall, S.H. [1980] **Physical Explanation of the Destabilizing Effect of Damping in Rotating Parts.** In Rotordynamic Instability Problems in High Performance Turbomachinery, NASA CP 2133, May 1980, pp. 369-382.

Crandall, S.H. [1983] **The Physical Nature of Rotor Instability Mechanisms.** In Rotor Dynamical Instability, ed. M.L. Adams, ASME Special Publication AMD 55 (1983): 1-18.

Downer, J. [1980] **Analysis of a Single Axis Magnetic Suspension System.** S.M. Thesis, Massachusetts Institute of Technology, January 1980.

Downer, J. [1986] **Design of Large-Angle, Magnetic Suspensions.** Sc.D. Thesis, Massachusetts Institute of Technology, May 1986.

Fermantal, D., P. LaRocca, and E. Cusson [1990] **Decentralized Control of Flexible Rotors.** Second International Symposium on Magnetic Bearings. Tokyo, Japan: July 12-14, 1990.

Fermantal, D., P. LaRocca, and E. Cusson [1990] **The Jeffcott Rotor: It's Decomposition and Control.** Draper Lab Report #P-2920, February 1990.

Freudenberg, J. and D. Looze, [1985] **Right Half Plane Poles and Zeros and Design Tradeoffs in Feedback Systems.** IEEE Transactions on Automatic Control, v AC-30, n 6, June 1985, pp. 555-565.

Friedland, B. [1986] **Control System Design - An Introduction to State-Space Methods.** New York: McGraw-Hill Book Company, 1986.

Fujita, M., et. al. [1990] **H-infinity Control Design for a Magnetic Suspension System.** Second International Symposium on Magnetic Bearings. Tokyo, Japan: July 12-14, 1990, pp. 349-356.

Groom, N.J. [1979] **Magnetic Suspension System for a Laboratory Model Annular Momentum Control Device.** AIAA Guidance and Control Conference, Boulder, Colorado. AIAA Paper No. 19-1755 (1979).

Groom, N.J. [1984] **Overview of Magnetic Bearing Control and Linearization Approaches for Annular Magnetically Suspended Devices.** An Assessment of Integrated Flywheel System Technology, Conference Proceedings, Huntsville, Alabama: February 7-9, 1984: 297-306. NASA Conference Publication 2346.

Habermann, H. and M. Brunet. [1984] **The Active Magnetic Bearing Enables Optimum Damping of Flexible Rotors.** ASME International Gas Turbine, 84-GT-117, June 1984.

Hendrickson, C., J. Lyman, and P. Studer. [1974] **Magnetically Suspended Momentum Wheels for Spacecraft Stabilization.** 12th AIAA Aerospace Sciences Meeting, January 1974.

Hendrickson, T.A., J. Leonard, and D. Weise. [1987] **Application of Magnetic Bearing Technology for Vibration Free Machinery.** Naval Engineers Journal, May 1987.

Herzog, R., and H. Bleuler [1990] **Stiff AMB Control using and H-infinity Approach.** Second International Symposium on Magnetic Bearings. Tokyo, Japan: July 12-14, 1990, pp. 343-348.

Hubbard, M. and P. McDonald. [1980] **Feedback Control Systems for Flywheel Radial Instabilities.** 1980 Flywheel Technology Symposium Proceedings, Scottsdale, Arizona: October 1980.

Hustak, J., Kirk, R. and K. Schoeneck. [1986] **Analysis and Test Results of Turbocompressors Using Active Magnetic Bearings.** American Society of Lubrication Engineers, Preprint No. 86-AM-1A-1, Presented at 41st Annual Meeting, Toronto, May 12-15, 1986.

Jeffcott, H.H. [1919] **The Lateral Vibrations of Loaded Shafts in the Neighbourhood of a Whirling Shaft - The Effect of Want of Balance.** Philosophy Magazine, 6, n 37 (1919): 304-314.

Johnson, B. [1985] **Active Control of a Flexible Rotor.** S.M. Thesis, Massachusetts Institute of Technology, February 1985.

Johnson, B. [1986] **Active Control of a Flexible, Two-Mass Rotor: The Use of Complex Notation.** Sc.D. Thesis, Massachusetts Institute of Technology, September 1986.

Johnson, B. [1987] **Stability Constraints on the Control of Flexible Rotors.** Published by AIAA, 1987.

Keith, F., R. Williams, P. Allaire, and R. Schafer. [1988] **Digital Control of Magnetic Bearings Supporting a Multimass Flexible Rotor.** Presented at the NASA Workshop on Magnetic Suspension Technology, February 2-4, 1988.

Kimball, A.L. [1925] **Internal Friction as a Cause of Shaft Whirling.** Philosophy Magazine, 6, n 49, (1925): 724-727.

Kwakernaak, H. and R. Sivan. [1972] **Linear Optimal Control Systems.** New York: John Wiley and Sons, 1972.

La Rocca, P. [1988] **A Multivariable Controller for an Electromagnetic Bearing - Shaft System.** S.M. Thesis, Massachusetts Institute of Technology, May 1988.

Malsen, E., P. Hermann, M. Scott, and R. Humphris. [1988] **Practical Limits to the Performance of Magnetic Bearings: Peak Force, Slew Rate, and Displacement Sensitivity.** Presented at the NASA Workshop on Magnetic Suspension Technology, February 2-4, 1988.

Matsumura, F., et. al. [1990] **Modeling and Control of Magnetic Bearing Systems Achieving a Rotation Around the Axis of Inertia.** Second International Symposium on Magnetic Bearings. Tokyo, Japan: July 12-14, 1990, pp. 273-280.

McCallum, D. [1987] **Dynamic Model for Large Angle Magnetic Suspension - Control Moment Gyro (LAMS-CMG).** (unpublished) Draper Lab Internal Memorandum #MSD-2052-87: April 15, 1987.

McCallum, D. [1988] **Dynamic Modelling and Control of a Magnetic Bearing - Suspended Rotor System.** S.M. Thesis, Massachusetts Institute of Technology, May 1988.

McDonald, P. and M. Hubbard. [1985] **An Actively Controlled Pendulous Flywheel with Magnetic Bearings.** Proceedings of the 20th Intersociety Energy Conversion Engineering Conference, Miami Beach, Fl: August 18-23: 2.525-2.520.

Miki, M., et. al. [1990] **Single Axis Active Magnetic Bearing System with Mechanical Dampers for High Speed Rotors.** Second International Symposium on Magnetic Bearings. Tokyo, Japan: July 12-14, 1990, pp. 183-187.

Moore, J., D. Lewis, and J. Heinzman. [1980] **Feasibility of Active Feedback Control of Rotordynamic Instability.** In Rotordynamic Instability Problems of High-Performance Turbomachinery, NASA CP-2133, May 1980: pp. 467-476.

Nikolajsen, J.L., R.L. Holmes, and V. Gondhalekar. [1979] **Investigation of an Electromagnetic Damper for Vibration Control of a Transmission Shaft.** Proceedings of the Institution of Mechanical Engineers. 193, (1979): 331-336.

Orpwood, R.D. and D.R. Britton. [1976] **A Magnetically Suspended Flywheel for Spacecraft Control.** Proceedings of the 7th Symposium on Automatic Control in Space. Rottach-Egern, West Germany: May 17-21, 1976.

Sabnis, A.J., J. Dendy, and F. Schmidt. [1975] **Magnetically Suspended Large Momentum Wheel.** Journal of Spacecraft and Rockets, 12, July 1975: pp. 420-427.

Salm, J. and G. Schweitzer. [1984] **Modelling and Control of a Flexible Rotor with Magnetic Bearings.** Proceedings of the Third International Conference on Vibrations in Rotating Machinery, University of York, England: September 11-13, 1984, p. 553.

Sasaki, S. [1987] **Stabilization of Precession-Free Rotors Supported by Magnets.** Journal of Applied Physics, v 62, n 7, October 1987, pp. 2610-15.

Schweitzer, G. [1974] **Stabilization of Self-Excited Rotor Vibrations by an Active Damper.** In Dynamics of Rotors, ed., F.I. Niordson, Springer-Verlag, New York: 1975.

Schweitzer, G. and A. Traxler. [1984] **Design of Magnetic Bearings.** Proceedings of the International Symposium on Design and Synthesis, Tokyo, Japan: July 11-13, 1984.

Schweitzer, G. and H. Ulbrich. [1980] **Magnetic Bearings - A Novel Type of Suspension.** Second International Conference on Vibrations in Rotating Machinery. Cambridge, U.K.: September 1-4, 1980, pp. 151-156.

Schweitzer, G., and R. Lange. [1976] **Characteristics of a Magnetic Rotor Bearing for Active Vibration Control.** Proceedings of the International Conference on Vibration in Rotational Machinery, Cambridge, U.K.: 1976, pp. 301-306.

Stroh, C.G. [1985] **Rotordynamic Stability - A Simplified Approach.** Proceedings of the Fourteenth Turbomachinery Symposium, Houston, Texas: October 22-24, 1985.

Swann, M. and W. Michaud [1990] **Active Magnetic Bearing Performance Standard Specification.** Second International Symposium on Magnetic Bearings. Tokyo, Japan: July 12-14, 1990, pp. 79-86.

Traxler, A. and G. Schweitzer. [1984] **Measurement of the Force Characteristics of a Contactless Electromagnetic Rotor Bearing.** Proceedings from Symposium on Measurement and Estimation, Bressanone, Italy, May 8-12, 1984.

Ulbrich, H.G. and E. Anton. [1984] **Theory and Application of Magnetic Bearings with Integrated Displacement and Velocity Sensors.** Proceedings of the Third International Conference on Vibrations in Rotating Machinery, University of York, England: September 11-13, 1984, p. 543-551/

Weise, D. [1985a] **Magnetic Bearings and Their Industrial Applications.** Fifth Annual Rotating Machinery and Controls Industrial Research Conference, June 1985.

Weise, D. [1985b] **Active Magnetic Bearings Provide Closed Loop Servo Control for Enhanced Dynamic Response.** 27th IEEE Machine Tool Conference, October 1985.

Zmood, R., D. Anand, and J. Kirk. [1987] **The Design of Magnetic Bearing for High Speed Shaft Driven Applications.** Copyright American Institute of Aeronautics and Astronautics, Inc., 1987.

N91-21209

**CRITICAL SPEEDS and FORCED RESPONSE SOLUTIONS of ACTIVE
MAGNETIC BEARING TURBOMACHINERY, Part I**

**J. Kecsee, D. Rawal, R. Gordon Kirk
Virginia Polytechnic Institute and State University
Department of Mechanical Engineering
Randolph Hall
Blacksburg
VA 24061-0238**

**CRITICAL SPEEDS AND FORCED RESPONSE SOLUTIONS
FOR ACTIVE ACTIVE MAGNETIC BEARING TURBOMACHINERY
PART I**

J. Keesee, Research Assistant
D. Rawal, Research Assistant
R. G. Kirk, Associate Professor

Virginia Polytechnic Institute and State University
Blacksburg, VA

ABSTRACT

The prediction of critical speeds and forced response of active magnetic bearing turbomachinery is of great interest due to the increased use of this new and promising technology. Calculating the system undamped critical speeds and forced response is important to all those who are involved in the design of the active magnetic bearing system. This paper is the first part of a two part paper which presents the theory and results of an investigation into the influence of sensor location on the undamped critical speeds and forced response of the rotor and bearing system.

Part I of this paper concentrates on an extended Jeffcott model which was used as an approximate solution to a more accurate transfer matrix procedure. Theory behind a two-degree-of-freedom extended Jeffcott model will be presented. Results of the natural frequency calculation will be shown followed by the results of the forced response calculation. The system response was predicted for two types of forcing. A constant magnitude excitation with a wide frequency variation was applied at the bearings as one forcing function. The normal unbalance force at midspan was the second source of excitation. The results of this extended Jeffcott solution gives useful design guidance for the influence of the first and third modes of a symmetric rotor system.

NOMENCLATURE

- A shaft relative motion max amplitude for 1st mode (cm)
- a mass eccentricity of imbalance (cm)
- B shaft relative motion max amplitude for 3rd mode (cm)
- C ratio of bearing damping to shaft damping (dim)
- C_1 damping of AMB (N-s/cm)

C_2 damping of flexible shaft (N-s/cm)
 F_ϕ constant magnitude force applied to journal mass (N)
 i square root of -1, complex variable (dim)
 K ratio of bearing stiffness to shaft stiffness (dim)
 K_1 stiffness of AMB (N/cm)
 K_2 stiffness of flexible shaft (N/cm)
 K_{11} row 1, column 1 of stiffness matrix in Jeffcott solution
 K_{12} row 1, column 2 of stiffness matrix in Jeffcott solution
 K_{21} row 2, column 1 of stiffness matrix in Jeffcott solution
 K_{22} row 2, column 2 of stiffness matrix in Jeffcott solution
 L bearing span (cm)
 M ratio of bearing journal mass to rotor midspan mass (dim)
 M_1 equivalent bearing journal mass (kg)
 M_2 equivalent rotor midspan mass (kg)
 R shaft absolute displacement (cm)
 X shaft maximum displacement in the X-direction (cm)
 r_1 shaft deflection at bearing journal location (cm)
 r_2 shaft deflection at midspan mass (cm)
 r_s shaft deflection at AMB sensor location (cm)
 z axial distance along rotor (cm)
 z_s axial distance to AMB sensor (cm)
 α sensor relative position to midspan (dim)
 β normalized shaft motion at sensor location (dim)
 ω angular velocity of shaft (rad/s)
 Ω natural frequency normalized to rigid bearing critical speed (dim)

INTRODUCTION

The evaluation of critical speeds and forced response for turbomachinery with fluid-film and antifriction bearings is now standard design practice for many manufacturers. The standard transfer matrix solution technique (Myklestad, 1944; Prohl, 1945) is the current industry standard for evaluation of rotor response and undamped critical speeds. More recently interest in improved forced response and stability of high pressure compressors and pumps have forced designers to consider active magnetic bearings (AMBs) for either retrofit or new machinery application. The initial application of magnetic bearings to centrifugal compressor was evaluated using standard critical speed codes without consideration for sensor location (Hustak et al., 1987; Schoeneck and Hustak, 1987). The comparisons of predicted response and critical speed placement to actual test and field results (Hustak et al., 1987; Schoeneck and Hustak, 1987; Kirk et al., 1988) have drawn attention to possible improvements in the analytical representation of the magnetic bearings.

This paper is the first of a two part paper which presents an evaluation of the effect of sensor location on the predicted undamped critical speeds and forced response of turbomachinery. This paper concentrates on the solution of a two-degree-of-freedom model developed by extending the original Jeffcott model to include bearing stiffness and damping, journal mass and accounting for non-colocation of bearing and sensor. The second paper will discuss the evaluation of a modified transfer matrix solution and will present results of a typical rotor bearing system analysis.

The extended Jeffcott model will be considered to have sensors either inboard or outboard of the bearing centerline. The system response is calculated for two different types of forcing functions. The first excitation force is the usual unbalance located at the midspan mass. The second is a constant magnitude excitation applied at the journal mass while the excitation frequency is varied. The second type of rotor excitation is available in an actual active magnetic bearing and rotor system.

PRINCIPLE OF ACTIVE MAGNETIC BEARING OPERATION

The AMB is composed of two major mechanical parts, the rotor and the stator. Both are made of ferromagnetic laminations. The rotor laminations are placed on the machine shaft at the selected journal location. The stator laminations are slotted and include windings to provide the magnetic levitation and position control. For each degree of freedom, two electromagnets are required since they operate by attraction only. Figure 1 shows the stator

lamination construction of a radial bearing and sensor with the rotor lamination sleeve in the background.

Rotor position is monitored by sensors and this signal is compared to a nominal reference signal with a closed loop controller which supplies a command signal to the power amplifiers. These amplifiers provide power to the electromagnets to resist rotor movement from the nominal position. The design of the control loop gives the option to select the effective bearing stiffness and damping. The details of this design procedure are not the subject of this paper but the values of stiffness and damping must be carefully selected to give the rotor system the desired optimum dynamic response and stability.

Before power is applied to the bearings, the rotor is supported on two auxiliary ball bearings located in close proximity to the AMB. The clearance between the rotor and the inner race of the ball bearing is selected to prevent rotor contact with the AMB pole pieces or the internal seals of the compressor while the rotor is at rest or during an emergency shutdown. When power is applied to the electronic controls, the electromagnets levitate the rotor in the magnetic field and rotation by the driving source, such as a motor or turbine, can be started. The sensors and control system regulate the strength and direction of the magnetic fields to maintain exact rotor position by continually adjusting to the changing forces on the rotor. Should both the main and redundant features of the AMB fail simultaneously, the auxiliary bearing and rotor system are designed to permit safe deceleration.

When the turbomachine is running the rotor shaft may take a dynamic mode shape such that the displacement at the sensor location may not be the same as the magnetic bearing centerline displacement. The command signal is taken from the sensor location but the actuator applies the force through the coil such that the average force acts at the bearing centerline. This variation in command signal and actuator location is unique to the active magnetic bearings and may be used to the advantage of the designer to help place critical speeds. The performance of the AMB supported machinery may be more accurately predicted if proper account is taken for sensor location. This requires a modified, iterative solution strategy for current standard state-of-the-art computer codes for critical speeds, forced response, and stability. To initially evaluate the influence of the sensor placement, a modified extended Jeffcott rotor model will be developed with an assumed deformation to study the sensitivity of rotor bending modes and response to sensor location.

AMB EXTENDED JEFFCOTT MODEL

The original rotor model developed by H. H. Jeffcott consists of a single mass on a flexible shaft supported by rigid bearings. Kirk and Gunter (1972) modified this model to study the effect of support flexibility and damping on the synchronous response of the single mass flexible rotor. This paper extends the original Jeffcott model by assuming the existence of AMB supports. The extended model adds journal mass, bearing stiffness and damping at bearing locations, and assumes rigid bearing pedestals. The AMB extended Jeffcott model is shown in Figure 2.

To develop the extended Jeffcott model the disk mass plus the two center quarters of the shaft mass are lumped at midspan, M_2 . The journal and shaft end quarter masses are lumped at bearing locations and modeled as $M_1/2$. The model is assumed to be symmetric; therefore, it can be simplified to a two-degree-of-freedom (2DOF) system as shown in Figure 3. An unbalance force is shown at M_2 , and a constant magnitude excitation force is shown acting on M_1 .

The equations of motion (EOM) for the 2DOF system are written as follows:

$$M_2 \ddot{r}_2 = M_2 \omega^2 a e^{i\omega t} - C_2 (\dot{r}_2 - \dot{r}_1) - K_2 (r_2 - r_1) \quad [1]$$

$$M_1 \ddot{r}_1 = F_0 e^{i\omega t} + C_2 (\dot{r}_2 - \dot{r}_1) + K_2 (r_2 - r_1) - C_1 \dot{r}_s - K_1 r_s \quad [2]$$

In equations [1] and [2] the deflections at M_1 and M_2 are defined as r_1 and r_2 respectively. The deflection at the AMB sensor location is defined as r_s . It is indicated by the EOM that the bearing forces are proportional to the sensor location deflection - not the bearing location deflection, as would be the case with conventional fluid-film or antifriction bearings.

The sensor location deflection is calculated after assuming mode shapes of a half-period of a sine wave. These mode shapes, modeling the first and third modes, are shown in Figure 4. Using Figure 4, the equation for the sensor location deflection is written as follows:

$$r_s = r_1 + (r_2 - r_1) \sin(\pi\alpha/2) \quad [3]$$

where,

$$\alpha = z_s / (L/2). \quad [4]$$

Equation [4] defines the value α as the ratio between the sensor offset and the shaft half-span.

After substitution of equation [3], equations [1] and [2] can be written in matrix form as follows:

$$\begin{bmatrix} M_1 & 0 \\ 0 & M_2 \end{bmatrix} \begin{bmatrix} \ddot{r}_1 \\ \ddot{r}_2 \end{bmatrix} + \begin{bmatrix} C_1 & 0 \\ 0 & C_2 \end{bmatrix} \begin{bmatrix} \dot{r}_1 \\ \dot{r}_2 \end{bmatrix} + \begin{bmatrix} K_1 & 0 \\ 0 & K_2 \end{bmatrix} \begin{bmatrix} r_1 \\ r_2 \end{bmatrix} = \begin{bmatrix} F\phi e^{i\omega t} \\ M_2\omega^2 a e^{i\omega t} \end{bmatrix} \quad [5]$$

By assuming a solution of $r = Re^{i\omega t}$, the matrix equation [5] can be written in the following form:

$$\begin{bmatrix} K_{11} & K_{12} \\ K_{21} & K_{22} \end{bmatrix} \begin{bmatrix} R_1 \\ R_2 \end{bmatrix} = \begin{bmatrix} F\phi \\ M_2\omega^2 \end{bmatrix} \quad [6]$$

where,

$$K_{11} = (K_1(1-\beta) + K_2 - M_1\omega^2) + i\omega(C_2 + C_1(1-\beta))$$

$$K_{12} = (K_1\beta - K_2) + i\omega(C_1\beta - C_2)$$

$$K_{21} = -K_1 - i\omega C_2$$

$$K_{22} = (K_2 - M_2\omega^2) + i\omega C_2$$

$$\beta = \sin \pi\alpha/2.$$

INFLUENCE OF SENSOR LOCATION ON UNDAMPED NATURAL FREQUENCY

The influence of sensor location on the critical speeds of the AMB rotor system is initially investigated by calculating the natural frequencies of the extended Jeffcott Model. The sensor location is varied inboard and outboard of the bearing centerline by as much as 20% of half-span.

Eliminating damping terms, C_1 and C_2 , from equation [6]; and solving for the determinant of the resulting stiffness matrix, results in the following equation for the natural frequencies:

$$\omega^4 - (1 - \beta)\frac{K_1}{M_1} + \frac{(M_1 + M_2)}{M_1 M_2} K_2\omega^2 + \frac{K_1 K_2}{M_1 M_2} = 0. \quad [7]$$

Equation [7] can be written in the following non-dimensional form:

$$\Omega^2 - \left(1 - \frac{K}{M}\right)(1 + K(1 - \beta))\Omega + \frac{K}{M} = 0 \quad [8]$$

where,

$$M = M_1/M_2$$

$$K = K_1/K_2$$

$$\Omega = \omega^2/(K_2/M_2)$$

Results from Natural Frequency Analysis of AMB Extended Jeffcott Model

To show how sensor location influences the first and third natural frequencies of various geometries of the extended Jeffcott model, the solution of equation [8] was graphed for alpha values ranging from -2.0 to 2.0. This exemplifies sensor separations of 20% of half-span both inboard and outboard of the bearing centerline. The results are shown for mass ratios, M , of 1.0 (Figure 5), and 0.25 (Figure 6). The stiffness ratio, K , varies from 0.1 up to 10 in each analysis.

The results are similar for both mass ratios. The sensitivity to non-colocation of bearing and sensor is increased in two different situations. An increase in sensitivity occurs as stiffness ratios increase. This is attributed to the fact that when the bearing stiffness increases relative to the shaft stiffness there is more bending energy in the rotor. This causes a greater difference between bearing and sensor deflection at higher stiffness ratios. The sensitivity also increases as sensor-bearing separation increases. This also results in greater differences between bearing and sensor deflections.

The direction in which the criticals move depends on whether the sensor, at an inboard or outboard location, gives more or less response than the normal bearing centerline. For the first mode, the inboard sensors have a greater deflection than the bearings; therefore, the critical increases due to higher bearing forces. Outboard sensors detect less deflection than at the bearing, thus decreasing bearing forces and lowering the critical frequency. The opposite occurs at the third mode. The inboard sensors detect less deflection, while the outboard sensors detect more deflection than at the bearing centerline. This lowers the third critical frequency for inboard sensors and raises it for outboard sensors.

INFLUENCE OF SENSOR LOCATION ON FORCED RESPONSE SOLUTION

The response is calculated for two forms of excitation applied independently to the AMB extended Jeffcott model equations. In order to calculate the response, the matrix equation [6] is solved for R_1 and R_2 using Cramer's Rule (Anton, 1984). The solution has the following form:

$$R_1 = \frac{F\phi K_{22} - K_{12}(M_2 a \omega^2)}{K_{11} K_{22} - K_{12} K_{21}} \quad [9]$$

$$R_2 = \frac{K_{11}(M_2 a \omega^2) - F\phi K_{21}}{K_{11} K_{22} - K_{12} K_{21}} \quad [10]$$

The resulting response is complex, thus there exists an amplitude and a phase angle associated with both R_1 and R_2 . The phase angles can be obtained from the following equations:

$$\theta_1 = \cos^{-1} \left[\frac{\text{real}(R_1)}{\sqrt{(\text{real}(R_1))^2 + (\text{imag}(R_1))^2}} \right] \quad [11]$$

$$\theta_2 = \cos^{-1} \left[\frac{\text{real}(R_2)}{\sqrt{(\text{real}(R_2))^2 + (\text{imag}(R_2))^2}} \right] \quad [12]$$

It must be noted at this point that the unbalance force and the constant excitation force are never applied at the same time as this introduces additional complexities not accounted for by the Jeffcott model. Physically, the constant magnitude excitation force is applied in one plane only, therefore the motion of the masses is in one plane only. However, for computational and analytical simplicity, it will be assumed that the constant magnitude excitation force acts in two mutually perpendicular planes in a manner similar to the unbalance force. The correct solution for the constant magnitude excitation force plane, is then, simply the real part of the deflections R_1 and R_2 shown above. However, since the motion is assumed to be circular, the maximum amplitudes in the X-direction, X_1 and X_2 , will be the same as R_1 and R_2 , for masses M_1 and M_2 . Similarly, the phase angles calculated from R_1 and R_2 are also valid for motion in one plane. Thus, regardless of whether an unbalance force or a constant magnitude excitation force is applied, the solution technique and the solution itself will remain the same.

Results from Forced Response Analysis of AMB Extended Jeffcott Model

The results that are to be shown are of the bearing journal response. Similar results occur for the mid-span mass response; therefore, they are omitted.

The response amplitude at the bearing location is plotted versus shaft frequency in Figure 7. The excitation causing this response is due to an imbalance at mid-span resulting from an eccentricity of 0.076 mm at M_2 . In this case $M = 1.0$, $K = 2.0$, and the bearing damping is set to 0.283 N-s/mm. The shaft damping is assumed negligible. The value of α , being varied as in the critical speed solution, ranges from -0.2 to 0.2.

In Figure 7 it can be seen that the first mode peak resonance frequencies increase from the colocation case, $\alpha = 0$, when inboard sensors, $\alpha > 0$, are used. The peak frequencies are shown to decrease with outboard sensor, $\alpha < 0$, use. For the third mode, the peak frequencies are lower with inboard sensor use, and raised for outboard sensor use. These results are very consistent with the results shown from the influence of sensor location on natural frequencies. The same reasoning can be used to explain both sets of results.

The results from the case using a constant magnitude excitation at the bearing location shows the same tendencies as the unbalance case. Shown in Figure 8 are the results of the bearing location excitation case.

CONCLUSIONS

This preliminary investigation into the effect of sensor location on the rotor dynamic performance of AMB turbomachinery gives very useful results. The natural frequency and forced response results from the AMB extended Jeffcott model could give the rotor-bearing system designer greater confidence in the proper selection of sensor location.

From the test run of the AMB extended Jeffcott model the following specific conclusions were made:

1. For inboard sensors, as the sensor is moved away from the bearing, the first mode critical frequency goes higher. For outboard sensors, as the sensor is moved away from the bearing, the first mode critical frequency goes lower.
2. For inboard sensors, as the sensor is moved away from the bearing the third mode critical frequency decreases. However for outboard sensors, as the sensor is moved away from the

bearing the third mode critical frequency increases.

3. The vibrational characteristics of the two mass rotor system did not vary when a constant excitation force was used instead of a rotating unbalance.

4. The effect of the sensor position on the critical frequencies was considerable, when the stiffness ratio was high.

5. Higher mass ratios led to increased sensitivity of third mode critical frequency to changing sensor positions. Vice versa, low mass ratios led to increased damping effects in the third mode, making the rotor relatively insensitive to changing sensor locations.

RECOMMENDATIONS

The AMB extended Jeffcott model is a simple but very useful approximation of a much more complex rotor-bearing system. The following recommendations are made for extending the current approximate analysis:

1. The addition of pedestal stiffness and damping should be included in this model.

2. A method for accounting for sensor location should be included in the transfer matrix codes that are used to calculate forced response.

3. This research should be extended to a stability analysis in order to improve prediction capability for AMB turbomachinery.

4. Experimental test results must be generated for comparison and verification of the analyses developed.

REFERENCES

Hustak, J. F., R. G. Kirk, and K. A. Schoeneck, 1987, "Analysis and Test Results of Turbocompressors Using Active Magnetic Bearings," Lubrication Engineering, Vol. 43, No. 5, pp. 356-362.

Kirk, R. G., J. F. Hustak and K. A. Schoeneck, 1988, "Analysis and Test Results of Two Centrifugal Compressors Using Active Magnetic Bearings," Vibrations in Rotating Machinery, I. Mech. E. Proceedings of 4th International Conference, Edinburg, pp. 93-100.

Kirk, R. G., and E. J. Gunter, Jr., 1972, "The Effect of Support Flexibility and Damping on the Synchronous Response of a Single-Mass Flexible Rotor," ASME Trans., J. of Engrg. for Industry, Vol. 94, Series B, No. 1.

Myklestad, N. O., 1944, "A New Method of Calculating Natural Modes of Uncoupled Bending Vibration of Airplane Wings and Other Types of Beams," J. of Aeronautical Sciences, pp. 153-162.

Prohl, M. A., 1945, "A General Method for Calculating Critical Speeds of Flexible Rotors," J. of Applied Mechanics, pp. 142-148.

Schoeneck, K. A., and J. F. Hustak, 1987, "Comparison of Analytical and Field Experience for a Centrifugal Compressor Using Active Magnetic Bearings," I. Mech. E. Conference Proceedings, The Hague, Netherlands, May 18-20.

ACKNOWLEDGMENT

This work has been sponsored by a joint industry/Virginia Center for Innovative Technology Research Grant No. CAE-89-015, with matching funds from Dresser-Rand Co. and Magnetic Bearings, Inc. The authors are especially grateful for the support given by Dr. Ira Jacobson, Director of the Institute of Computer Aided Engineering, Charlottesville, Virginia.

ORIGINAL PAGE
BLACK AND WHITE PHOTOGRAPH

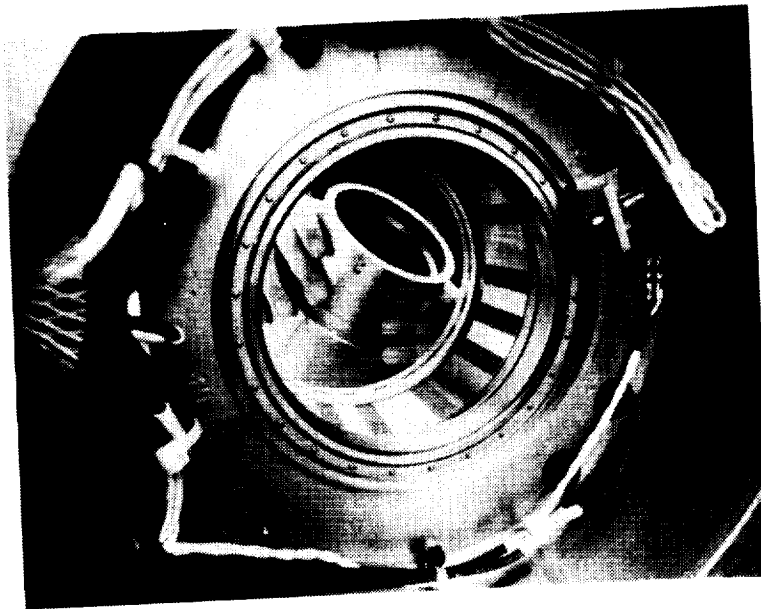


Figure 1. Picture of active magnetic bearing

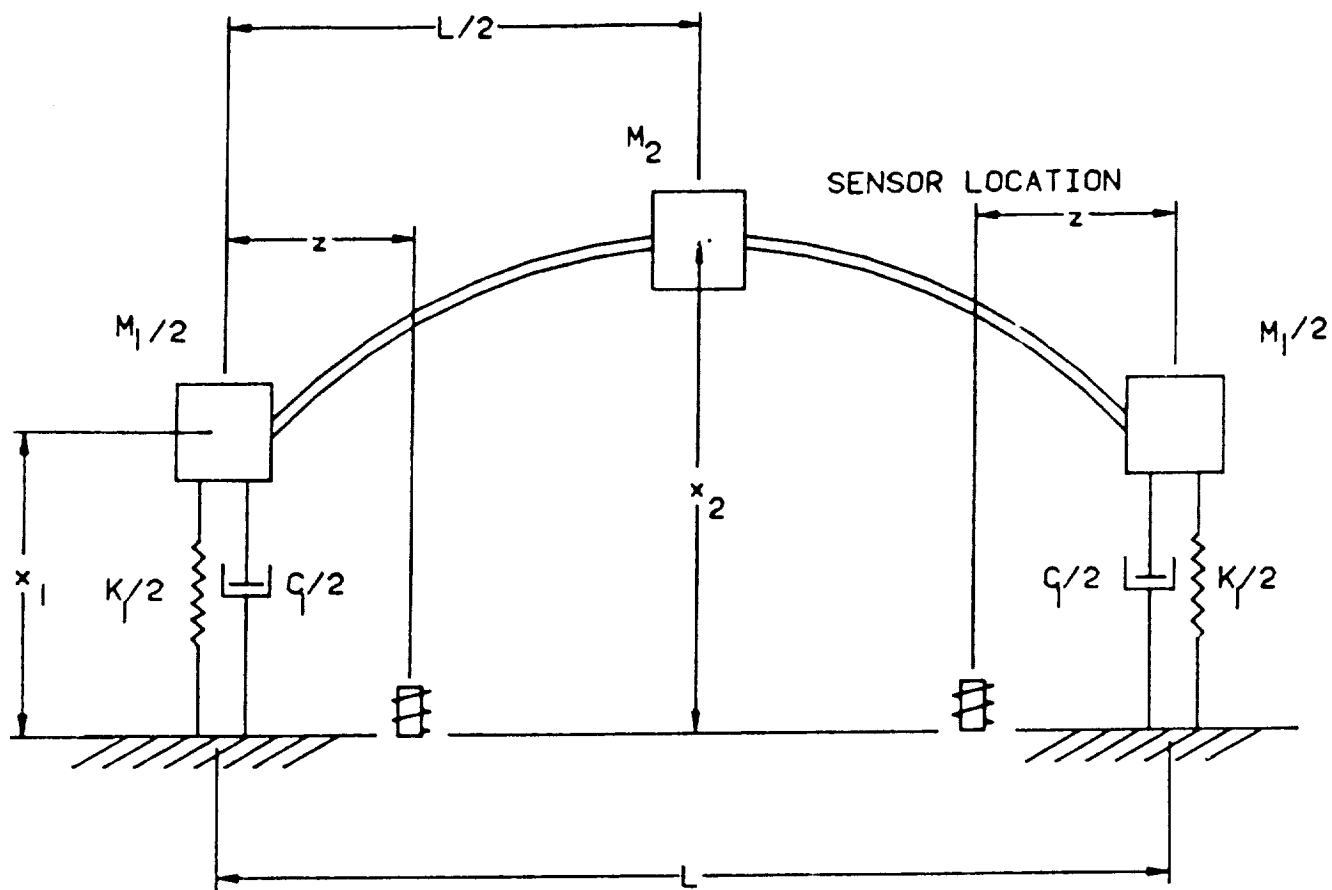


Figure 2. The modified Jeffcott model

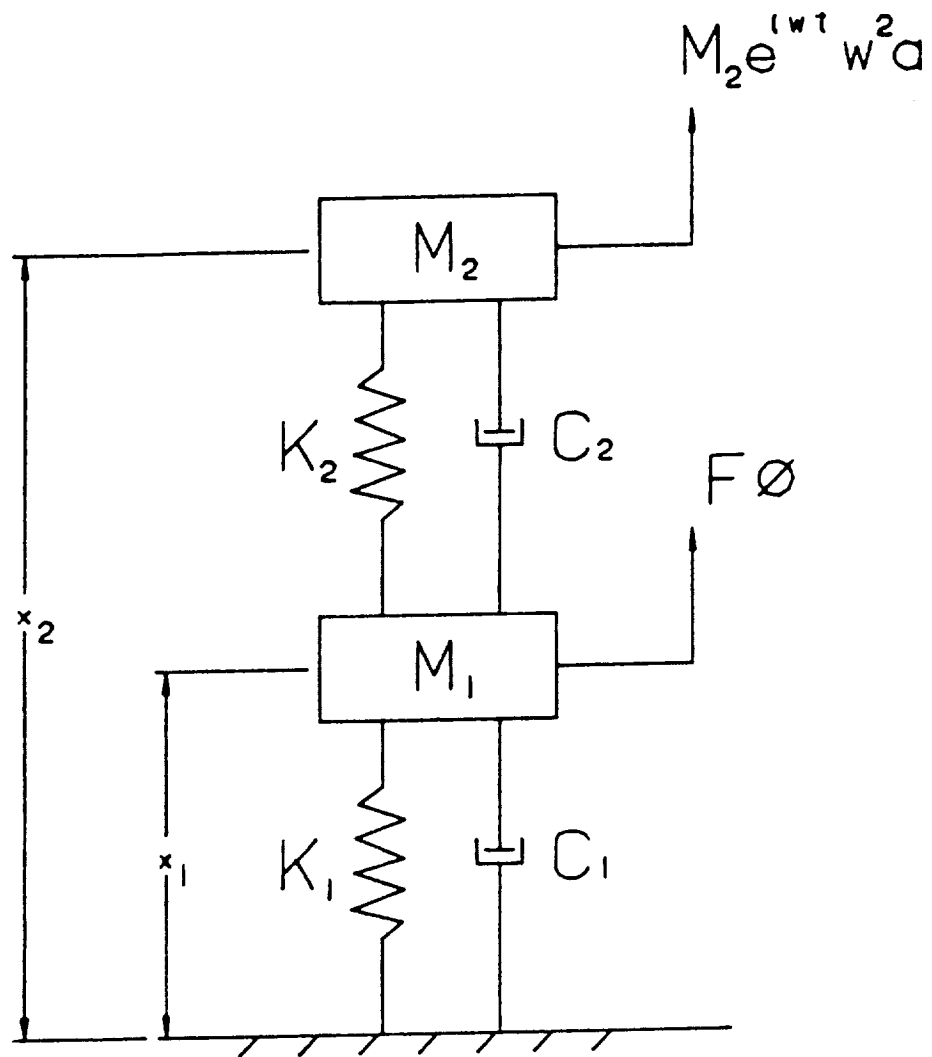


Figure 3. Reduced two DOF representation of the modified Jeffcott model

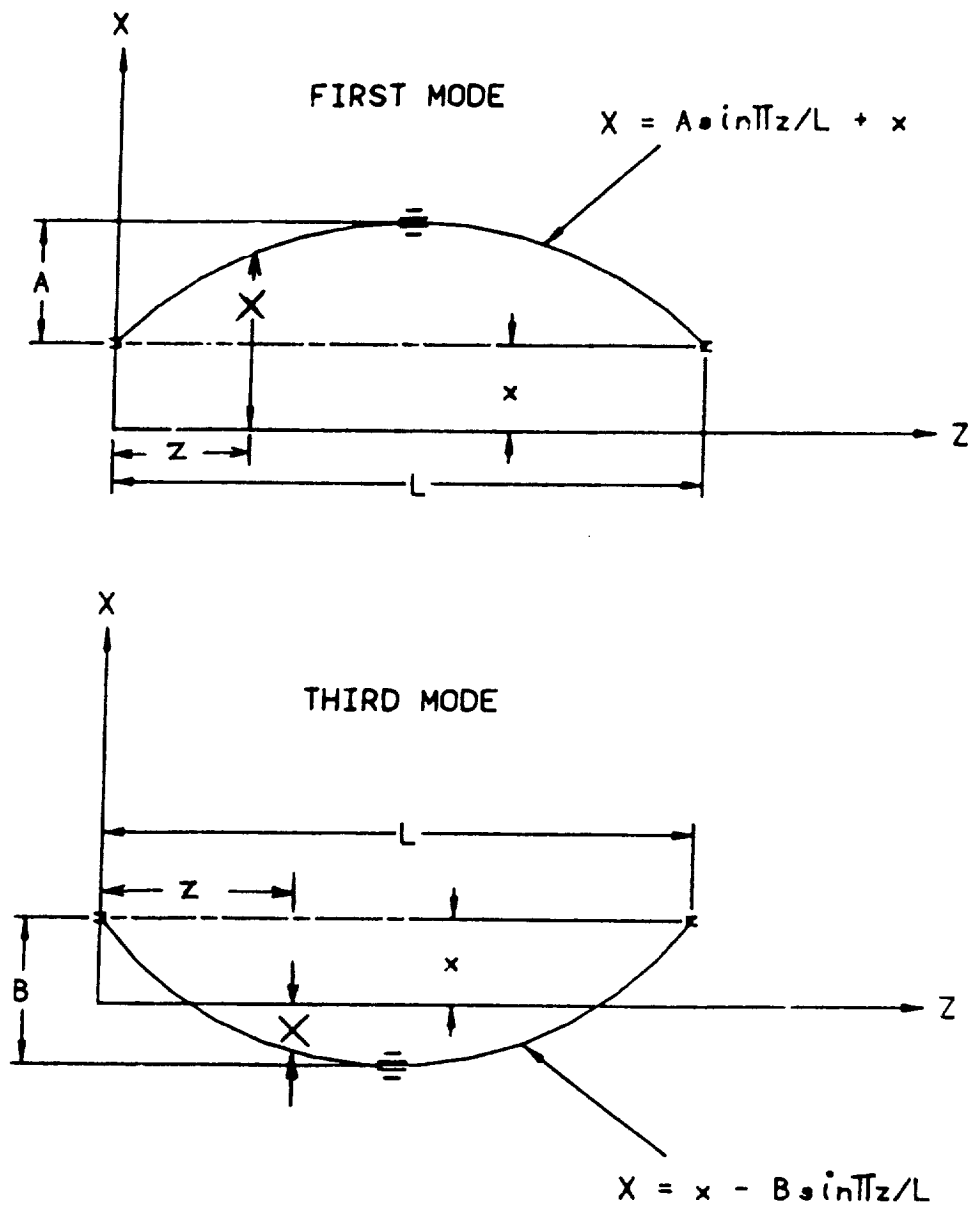


Figure 4. Mode shapes for the modified Jeffcott model

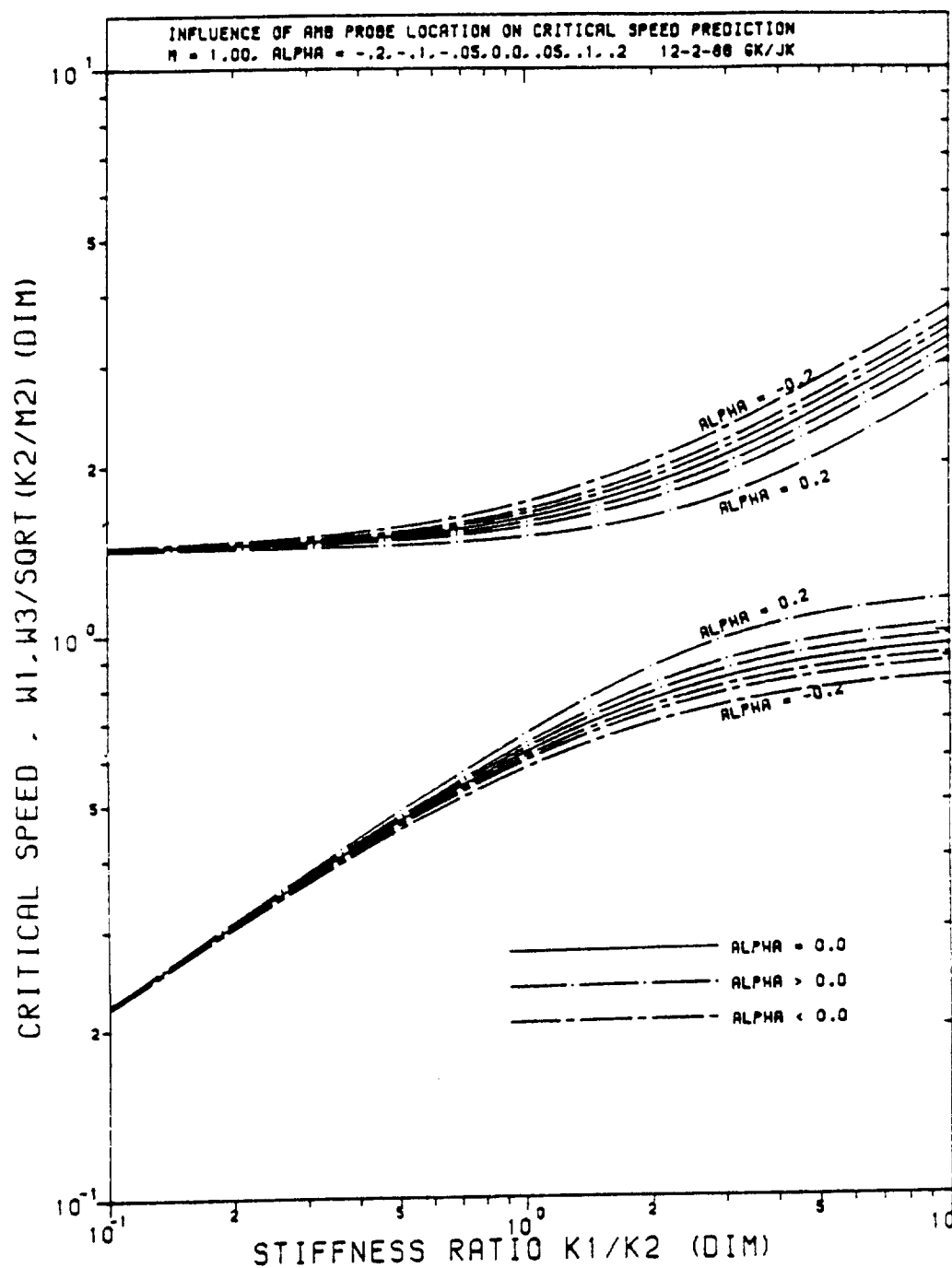


Figure 5. Critical speed map for $M = 1.0$ from AMB modified Jeffcott analysis

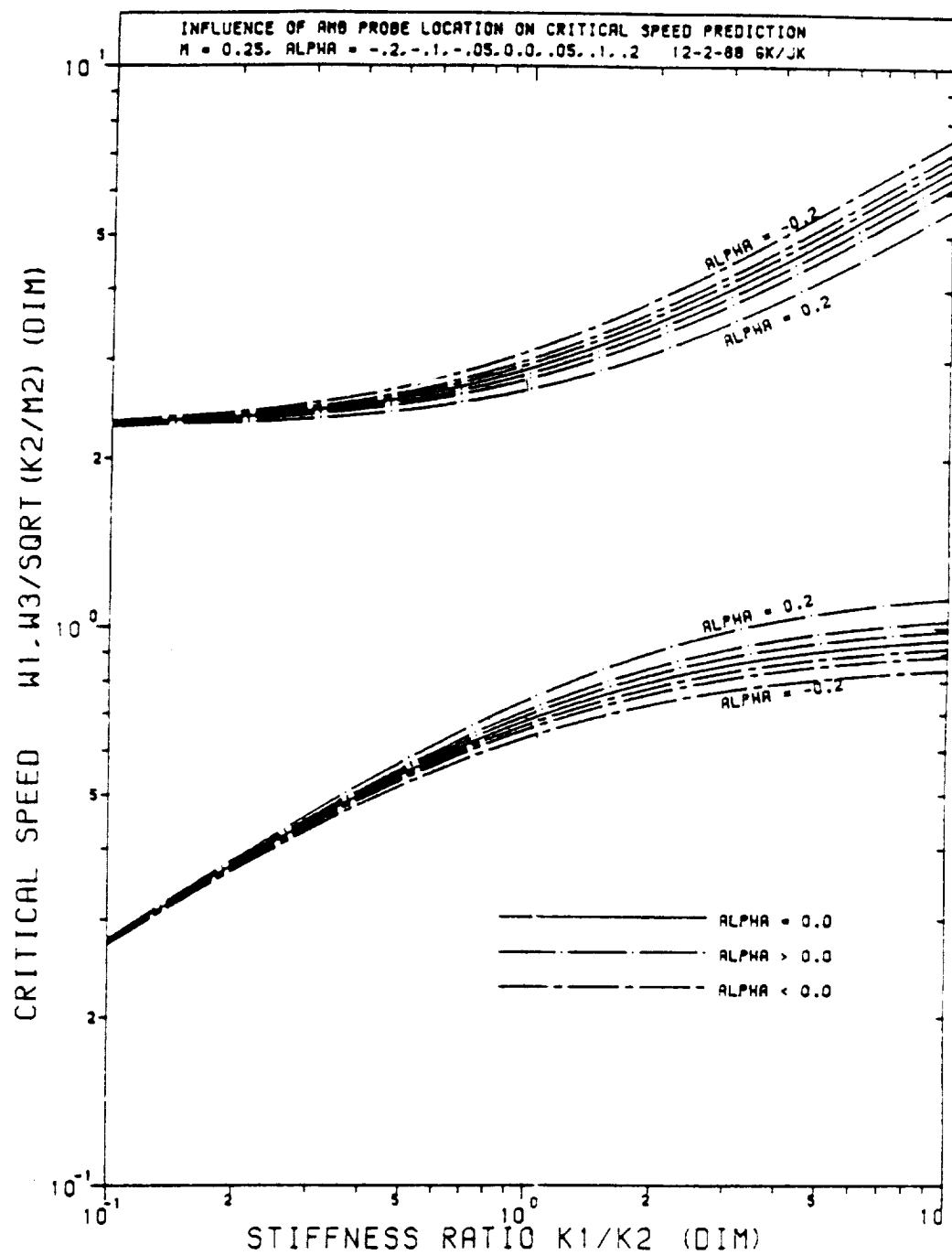


Figure 6. Critical speed map for $M = 0.25$ from AMB modified Jeffcott analysis

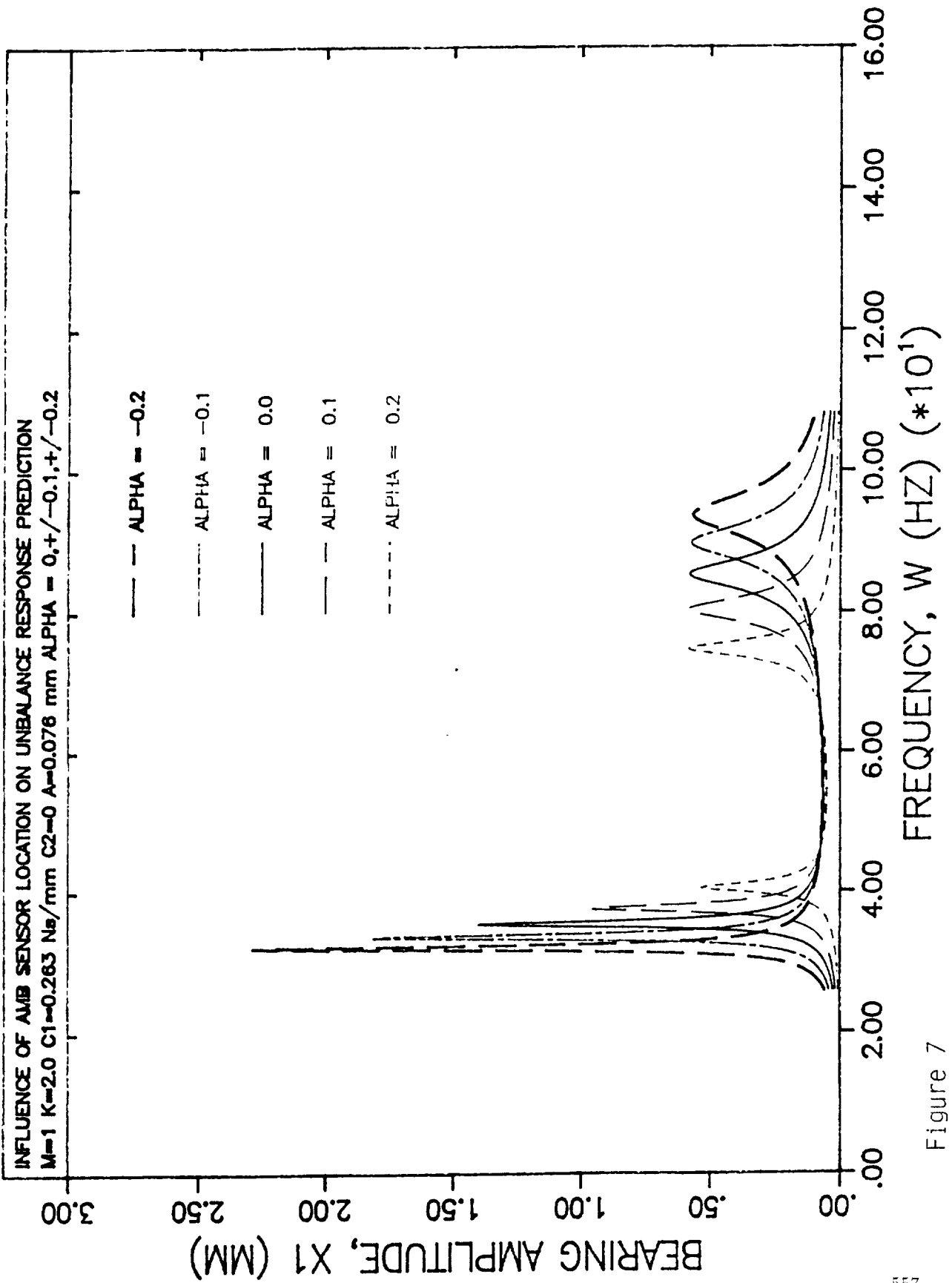


Figure 7

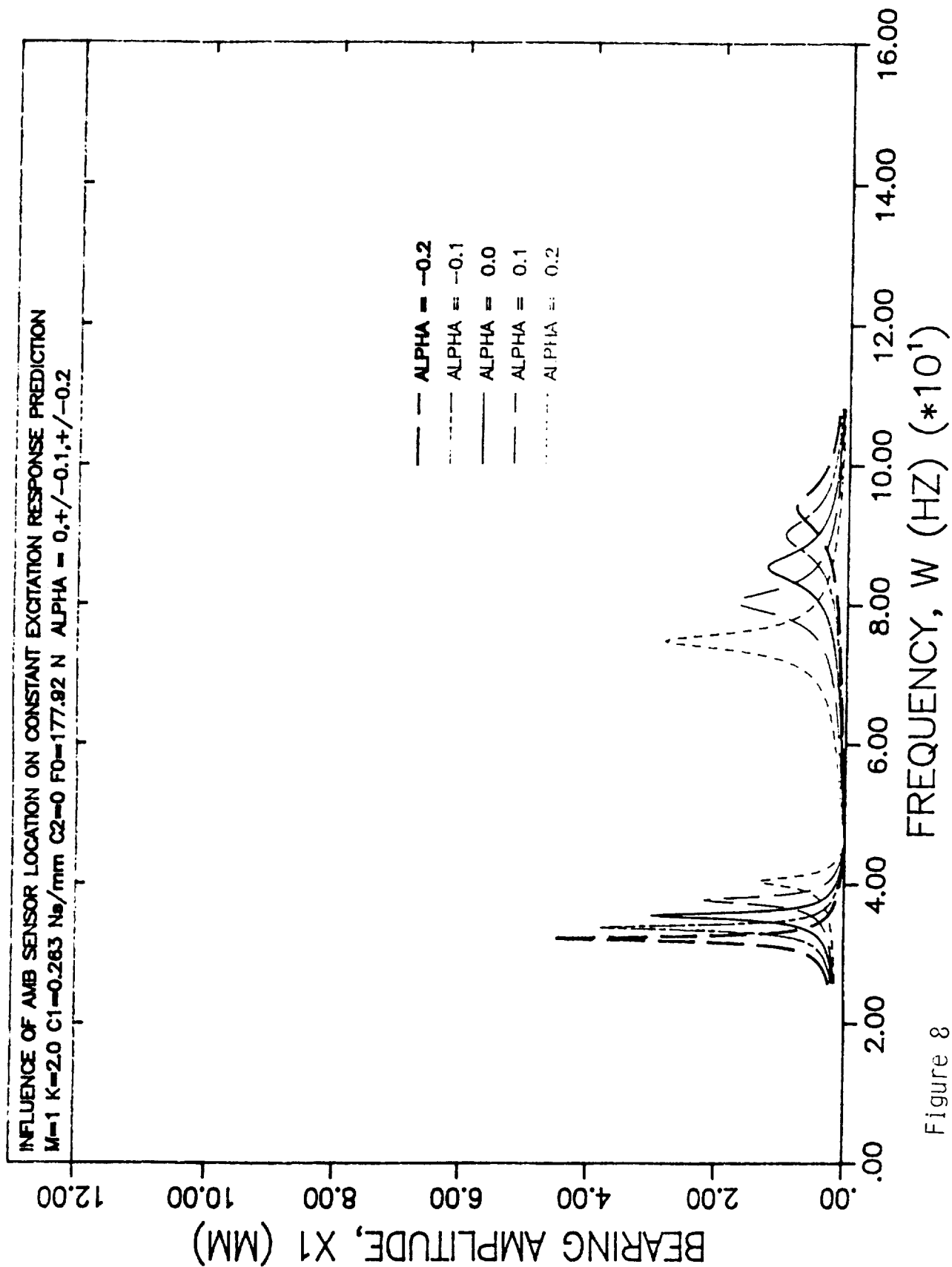


Figure 8

N91-21210

**CRITICAL SPEEDS and FORCED RESPONSE SOLUTIONS for ACTIVE
MAGNETIC BEARING TURBOMACHINERY, Part II**

**D. Rawal, J. Keesee, R. Gordon Kirk
Virginia Polytechnic Institute and State University
Department of Mechanical Engineering
Randolph Hall
Blacksburg
VA 24061-0238**

CRITICAL SPEEDS AND FORCED RESPONSE SOLUTIONS FOR ACTIVE MAGNETIC BEARING TURBOMACHINERY PART II

D. Rawal, Research Assistant
J. Keesee, Research Assistant
R. G. Kirk, Associate Professor

Virginia Polytechnic Institute and State University
Blacksburg, VA

ABSTRACT

The need for better performance of turbomachinery with active magnetic bearings has necessitated a study of such systems for accurate prediction of their vibrational characteristics. This is the second part of a two part paper on the effect of sensor location on the forced response characteristics of AMB turbomachinery. This paper presents a modification of existing transfer matrix methods for rotor analysis, to predict the response of rotor systems with active magnetic bearings. The position of the magnetic bearing sensors is taken into account and the effect of changing sensor position on the vibrational characteristics of rotor systems is studied. The modified algorithm is validated using a simpler Jeffcott model described in part I of this paper. The effect of changing from a rotating unbalance excitation to a constant excitation in a single plane is also studied. A typical eight stage centrifugal compressor rotor is analysed using the modified transfer matrix code. The results for a two mass Jeffcott model are presented in part I of this paper. The results obtained by running this model with the transfer matrix method have been compared with the results of the Jeffcott analysis for purposes of verification. Also included, are plots of amplitude vs frequency for the eight stage centrifugal compressor rotor. These plots will demonstrate the significant influence that sensor location has on the amplitude and critical frequencies of the rotor system.

NOMENCLATURE

E	Modulus of elasticity (N/mm ²)
I	Moment of inertia of massless shaft (mm ⁴)
I_p	Polar moment of inertia (mm ⁴)
I_t	Transverse moment of inertia (mm ⁴)
K	Stiffness ratio, k_1/k_2 (dim)
	Stiffness in transfer matrix equations (N/mm)
k_1	AMB stiffness (N/mm)
k_2	Shaft stiffness (N/mm)
M	Mass ratio, m_1/m_2 (dim)
M_{xc}	Moment component in transfer matrix equation (N-mm ²)
M_{xs}	Moment component in transfer matrix equation (N-mm ²)
V_{xc}	Shear component in transfer matrix equation (N)
V_{xs}	Shear component in transfer matrix equation (N)
a_x	Eccentricity component in transfer matrix equation (mm)
a_y	Eccentricity component in transfer matrix equation (mm)
C	Damping (N-sec/mm)
e	Exponential constant = 2.7182818 (dim)
i	Complex constant (dim)
l	Length of massless shafts in transfer matrix equation (mm)
m_i	Point masses in transfer matrix equations (Kg)
xc	Deflection component in transfer matrix equations (mm)
xs	Deflection component in transfer matrix equations (mm)
θ_{xc}	Slope component in the transfer matrix equation (rad)
θ_{xs}	Slope component in the transfer matrix equation (rad)
$F\phi$	Constant excitation force in Jeffcott model (N)
F_{xc}	Constant excitation force component in the transfer matrix equations (N)
F_{xs}	Constant excitation force component in the transfer matrix equations (N)
α	Ratio of the distance between bearing centerline and sensor to half-span of the rotor (dim)
ω	Frequency of shaft excitation (rad/sec)

s

Frequency of shaft rotation (rad/sec)

Subscripts

i

Rotor station number in transfer matrix equations

INTRODUCTION

The use of active magnetic bearings in turbomachinery is a comparatively new development but one which has shown great promise for better control of rotating equipment. The idea behind these bearings is not new however. The use of magnetic attraction to levitate the rotor shaft free of the bearing had been tried before, but because the system is inherently unstable unless a real-time control system is used, the use was not successful. The first actively controlled bearing was developed in the 1950's. Since then the use of active magnetic bearings has gained widespread acceptance particularly in North America and Canada. Weise [2] has given some examples of the varied uses to which active magnetic bearings have been applied. Kirk [5] lists a number of turbomachinery installations where active magnetic bearings have been used. Magnetic bearings possess a number of advantages compared to conventional bearings. They give an almost unlimited control over rotor vibrational characteristics due to adjustable stiffness and damping. Automatic balancing is possible by allowing the rotor to spin on its inertial axis. This leads to decreased vibrations and noise. Active magnetic bearings do not require lubrication, and since they are non-contact bearings, they eliminate the possibility of wear and tear of the stator and rotor surfaces. Weise [2] demonstrates the tolerance of magnetic bearings to a wide range of temperatures and also their insensitivity to hostile environments. Żlotykamien [1] gives a good description of the various advantages of active magnetic bearings.

Most of the research in active magnetic bearings has been in the control systems used. Schweitzer [7] shows a method for controlling an elastic rotor so that it can be represented by a low order model amenable to control techniques. Williams, Keith and Allaire [6] have developed theoretical relationships to relate the characteristics of a controller transfer function to the stiffness and damping properties of an active magnetic bearing. Burrows and Sahinkaya [8] have evaluated various strategies for applying a magnetic bearing to control the synchronous vibration of a flexible rotor. Kirk et al [5] have presented results of shop tests on a high speed eight stage centrifugal compressor supported by active magnetic bearings along with some design recommendations. Keesee [3] has examined the effects of sensor position on the critical frequencies of rotors with active magnetic bearing. This work is an extension of Keesee's work to include sensor position effect on forced response vibration amplitudes, using the modified transfer matrix method.

RESEARCH OBJECTIVE

As stated before in the introduction, the sensors are not located at the place where the attraction forces are applied on the rotor shaft, but at some distance away along the axis of the shaft. Due to this "non-colocation" of the sensors from the bearing position, the deflection sensed by the sensors is not the same as the actual deflection at the bearing but differs from it by some magnitude, dictated by the mode shape of the rotor shaft. Because of this, the stiffness and damping forces of the active magnetic bearing depend not on the deflection at the bearing location, but on the deflection at the sensor location. For such cases, the vibrational characteristics of the rotor system is different from that obtained using conventional analysis programs. The objective of this research is to take into account, the effect of sensor non-colocation on the vibrational characteristics of rotors with active magnetic bearings.

This research is an extension of the work done by Keesee [3] and involves the modification of an existing transfer matrix code to account for sensor non-colocation. But whereas Keesee's research was limited to studying the effect of sensor non-colocation on critical frequencies, this work also considers sensor non-colocation effects on forced response amplitudes. The other objective of this research was to compare the vibrational characteristics of rotor systems, when they are subject to unbalance excitation with circular synchronous shaft rotation, and constant excitation in one plane with no shaft rotation or whirling. The effect of changing mass ratios and stiffness ratios was also studied.

The modification of the transfer matrix program was validated by comparing its results for the two mass model with the results obtained from a simple program written to specifically analyse the two

mass model described in part I of this paper. A typical eight stage centrifugal compressor rotor model was also analysed using the modified transfer matrix method and its results were compared with the results of the Jeffcott model to verify the trend of behaviour of the rotor system with varying sensor locations.

THE MODIFIED TRANSFER MATRIX METHOD

The first analytical study of flexible rotors using the transfer matrix method was presented by Myklestad and Prohl. The rotor is divided into several discrete masses called stations and these masses are joined by massless flexible shafts. The response of the system is computed by using influence coefficients, and formulating a set of equations. The equations are solved and a final sweep is made to obtain the solution. J. W. Lund analysed the equations involved in the transfer matrix method for the case of elliptic non-synchronous response of the rotor system and wrote a program using these equations to study the vibrational characteristics of rotor systems. The program was subsequently simplified to analyse circular synchronous response of rotor systems. This paper describes the modification of precisely this simplified transfer matrix program written by E. J. Gunter Jr. and R. G. Kirk at the University of Virginia, Charlottesville, Virginia. The modification was done to take into account the non-colocation of sensors in active magnetic bearings.

To understand the classical transfer matrix method, consider a typical rotor section element assumed to be composed of a point mass and a massless elastic shaft to its right.

Consider the forces acting on the mass to formulate the equations required for equilibrium. Referring to figure 1

$$V_{xic}^R = V_{xic}^L + (m_i \omega^2 - K_i)x_{ic} - C_i \omega x_{is} + FXC_i + a_{x_i} m_i \omega^2 \quad [1]$$

$$V_{xis}^R = V_{xis}^L + C_i \omega x_{ic} + (m_i \omega^2 - K_i)x_{is} + FXS_i - a_{y_i} m_i \omega^2 \quad [2]$$

$$M_{yic}^R = M_{yic}^L + (I_p - I_T) \omega^2 \theta_{xic}^L \quad [3]$$

$$M_{yis}^R = M_{yis}^L + (I_p - I_T) \omega^2 \theta_{xis}^L \quad [4]$$

$$\theta_{xic}^R = \theta_{xic}^L \quad [5]$$

$$\theta_{xis}^R = \theta_{xis}^L \quad [6]$$

$$x_{ic}^R = x_{ic}^L \quad [7]$$

$$x_{is}^R = x_{is}^L \quad [8]$$

The solution in the Y direction can be obtained from the solution in the X direction since it is assumed that the motion of the shaft is circular. Hence equations in the Y direction are not required. Now consider the equations for the massless elastic shaft of station i. From figure 2

$$V_{xi+1c}^L = V_{xic}^R \quad [9]$$

$$V_{xi+1s}^L = V_{xis}^R \quad [10]$$

$$M_{yi+1c}^L = M_{yic}^R + l_i V_{xic}^R \quad [11]$$

$$M_{yi+1s}^L = M_{yis}^R + l_i V_{xis}^R \quad [12]$$

$$\theta_{xi+1c}^L = \theta_{xic}^R + \frac{l_i^2}{2EI} V_{xic}^R + \frac{l_i}{EI} M_{yic}^R \quad [13]$$

$$\theta_{xi+1s}^L = \theta_{xis}^R + \frac{l_i^2}{2EI} V_{xis}^R + \frac{l_i}{EI} M_{yis}^R \quad [14]$$

$$x_{i+1c}^I = x_{ic}^R + l_i \theta_{xic}^R + \left(\frac{l_i^3}{6EI} - GN_i \right) V_{xic}^R + \frac{l_i^2}{2EI} M_{yic}^R \quad [15]$$

$$x_{i+1s}^L = x_{is}^R + l_i \theta_{xis}^R + \left(\frac{l_i^3}{6EI} - GN_i \right) V_{xis}^R + \frac{l_i^2}{2EI} M_{yis}^R \quad [16]$$

These equations can be presented in matrix form and the matrices are called transfer matrices. As can be seen from this matrix, a correction to account for the shear deformation effect has also been included. The terms of this correction factor are explained below

$$GN_i = \frac{l_i}{a_i \cdot G_i \cdot sf_i} \quad [17]$$

a_i = area of section i

G_i = shear modulus of section i

$$sf_i = \frac{[(7. + .6\mu)(1. + dr^2)^2 + (20. + 12.\mu)dr^2]}{[6.(1. + \mu)(11. + dr^2)^2]} \quad [18]$$

μ is poissons ratio = $E_i/2G_i - 1$

dr_i is the diameter ratio = inner diameter/outer diameter

MODIFICATION FOR SENSOR NON-COLOCATION

Due to sensor non-colocation, at the station representing the bearing location, equations [3.1] and [3.2] are modified as follows

$$V_{xic}^R = V_{xic}^L + m_i \omega^2 x_{ic} - K_i x_{ic_{sen}} - C_i \omega x_{is_{sen}} + FXC_i + a_{x_i} m_i \omega^2 \quad [19]$$

$$V_{xis}^R = V_{xis}^L + C_i \omega x_{ic_{sen}} + m_i \omega^2 x_{is} - K_i x_{is_{sen}} + FXS_i - a_{y_i} m_i \omega^2 \quad [20]$$

The bearing stiffness is multiplied by the deflection sensed at the sensor location instead of the actual deflection at the bearing.

ALGORITHM FOR MODIFICATION DUE TO SENSOR NON-COLOCATION

The modification in the point matrix for the bearing station, due to the sensor non-colocation has already been discussed. However a straight forward sweep of the rotor is possible only in certain cases of sensor location. Upon examination, three cases of sensor location relative to the bearing location can be listed.

1. One sensor before the bearing
2. One sensor after the bearing
3. Two sensors, one each on either side of the bearing.

Case 1

For case 1, the sensor deflections are saved in the sweeping process and then used at the bearing station. The sweeping process is straightforward. Refer figures 3.

Case 2

In this case, since the sensor comes after the bearing, the sensor deflections are not known when the sweeping process reaches the bearing. Thus the sensor deflections are assumed to be some arbitrary value. Generally, the deflections at the station before the bearing are used as these arbitrary values. The sweeping process is then continued until the sensor location is reached. Here a comparison is made between the assumed sensor deflection and the sensor deflection calculated by the sweeping process. If the two quantities agree to within a certain margin of error, the sweeping process is continued from the sensor station onwards. If the two quantities do not lie within the error margin, the program iterates back to the bearing location and uses the sensor deflections calculated by the current sweeping process. These sensor deflections are used, as explained before, in

the bearing station point matrix calculations and the sweep process is continued. This leads to a series of iterations between the bearing station and the sensor station and these iterations are continued until the sensor deflections used at the bearing station agree with the sensor deflections calculated at the sensor station by the sweeping process, i.e. convergence is obtained. refer figures 3.

Case 3

With two sensors, one each before and after the bearing, the case can be split up into two cases one resembling case one and the other resembling case two. Refer figures 3. When the sensor before the bearing is reached, the sensor deflections are saved. These are used, the first time the bearing location is reached. The sweep process is then continued and the sensor after the bearing is dealt with in a manner similar to case two.

DISCUSSION OF THE CONVERGENCE PROCESS

To aid the process of convergence to the correct values of sensor deflections, the Taylors series convergence technique in two variables was used. This method was the most suitable one since there is cross-coupling between the stiffness and damping terms. However, due to the very low magnitude derivatives involved, the convergence process fails and leads to divergence from the correct solution.

When the cross-coupling of the stiffness and damping terms was ignored, and the Secant method of convergence was used to converge on the sensor deflections along the two axes independently, the algorithm converged with diminishing oscillations. However the number of iterations required were more than those required, when no convergence algorithm was used.

Thus simply using the sensor deflections obtained from the sweeping process, back at the bearing location, gave the fastest convergence. Refer table 1.

MODIFICATION TO SEPARATE GYROSCOPIC STIFFNESS FROM TRANSVERSE STIFFNESS

When the rotor is subjected to an external vibrational force assuming no unbalance to be present, the gyroscopic stiffness will depend only on the rotor spinning speed and not on the frequency of excitation. Considering the rotor spinning frequency to be "s", equations [3.3] and [3.4] are modified as follows

$$M_{yic}^R = M_{yic}^L + \omega(sI_p - \omega I_T)\theta_{xic} \quad [21]$$

$$M_{yis}^R = M_{yis}^L + \omega(sI_p - \omega I_T)\theta_{xis} \quad [22]$$

Here ω is the frequency of excitation.

COMPARISON OF THE RESULTS OF THE 2 MASS ROTOR SYSTEM, FOR THE JEFFCOTT MODEL AND THE TRANSFER MATRIX METHOD

The results of the 2 mass rotor system as obtained by the Jeffcott Model program have already been shown and discussed in part I of this paper. The same rotor system data was used with the modified transfer matrix method program, so as to compare the results with the Jeffcott model and thus validate the correctness of the modifications. The Jeffcott model is important, but because of its simplicity, its results are of limited use. Also it does not model a complex rotor system composed of many disk masses and possibly different shaft cross-sections along the rotor length. Hence, it is the transfer matrix method that is more useful for application purposes, and the Jeffcott model will serve for the purpose of comparison only.

Tables 2 and 3 give the comparison between the two programs. As can be seen from the tables, there is a fairly close agreement between the results obtained from the two programs. The agreement in the critical frequency values is much better than that between amplitude values and again, amplitude values agree better than phase angle values. This is because, the critical frequencies of a rotor system depends mostly on its mass and stiffness properties, both of which are accounted for in a similar manner in the two programs. The amplitude and phase angle values show greater disagreement due to the fact that the Jeffcott code assumes a sine-wave shape for the mode shapes and this assumption is only an approximation of the actual mode shape. It can be seen from the tables, that the Jeffcott code underestimates amplitude values in most cases. Also, amplitude values show a

higher disagreement when a constant force excitation is applied instead of an unbalance force excitation.

THE EIGHT STAGE CENTRIFUGAL COMPRESSOR ROTOR SYSTEM MODEL

To obtain a more realistic idea of the influence of sensor position, an eight stage centrifugal compressor rotor system was used with the transfer matrix code. This rotor system is illustrated in figure 4 and its design parameters are given in table 4.

The program was run with all the four cases of sensor positions, namely sensor colocation, inboard sensors, outboard sensors and two sensors on each side of the bearing. α values of -0.18, 0 and 0.18 were used, as is indicated by the sensor locations.

RESULTS OBTAINED FROM THE EIGHT STAGE COMPRESSOR ROTOR SYSTEM

The results obtained from the eight stage compressor rotor system are summarized below and illustrated in figures 5 to 11.

1. The first mode critical frequency increases as the sensor is moved from the direction of the outboard location in the direction of the inboard location. This is in agreement with the results obtained from the two mass rotor system.
2. A significant difference between these plots and those of the two mass model, is the higher amplitudes exhibited by the compressor rotor system when the sensors are moved inboard. To verify this deviation, an approximate two mass model of the compressor rotor system was run with the Jeffcott program. The results obtained with this approximate model are shown in figures 7 and 8, and show agreement with the results obtained by the transfer matrix program with the compressor rotor system data as input. The reason for this behaviour will become clear when the mode shape shown in figures 9 is examined.
The deflection at the sensor location is less compared to the deflection at the bearing location. Due to this, a lesser stiffness and damping force is applied at the bearing location and this leads to higher amplitudes of the rotor system. For a certain inboard sensor location, the deflection at the sensor location is reduced to zero and this condition will produce the largest amplitudes in the rotor system. The peculiar first mode shape that produces this phenomenon is similar to that observed in the third mode, and seems to be the result of the high bearing damping values. It has been observed that as sensors are moved inboard, the first critical frequency increases and the third critical frequency decreases. This is shown in figure 10. High bearing damping may bring the first and third critical frequencies together in such a case and thus produce a first mode shape similar to the third mode shape.
3. Additionally, it was observed that when the mass ratio was increased, the maximum amplitudes occurred with inboard sensor locations nearer to the bearing location. Refer figures 11. This can also be explained from the plots of the mode shapes. The maximum amplitude is observed when the deflection at the sensor location is zero. In such a case, the stiffness and damping forces at the bearing location are reduced to zero and the rotor system essentially exhibits free-free vibration. Due to this, the deflection along the rotor longitudinal axis will depend only on the mass distribution of the rotor system and not on the bearing stiffness and damping. A higher mass ratio means greater mass at the bearing location and therefore, lesser deflection in free-free vibration than that at midspan. In such a case, the point of zero deflection occurs nearer to the bearing location and a sensor placed at this point will produce the maximum amplitude of vibration of the rotor system.

CONCLUSIONS

The modification of the rotor dynamics codes to account for sensor non-colocation show a definite change in the vibrational characteristics when the sensors are moved away from the bearing location. The following conclusions can be drawn from this research:

1. The first mode critical frequency increases as the sensor is moved from the outboard to the inboard direction. This is due to the fact that for the first mode, the sensors sense a greater deflection as they move inboard and away from the bearing location. This increases the effective stiffness of the active magnetic bearing and results in higher critical frequencies. Because of this effect, it is possible to bypass the first critical by using the inboard sensors while starting the rotor and when the rotational frequency nears the first critical, switching to the outboard

sensors. This has been suggested by Keesee [3]. The higher critical frequencies can be handled similarly.

2. The amplitudes at the first critical will be higher with outboard sensors and decrease as the sensors are moved inboard and away from the bearing. However, this is not true in certain cases where the first and third mode coincide. In such a case, the amplitudes at the first critical increase as the sensors are moved inboard upto a certain point and then decrease again. The reason for such behaviour can be traced to the presense of high damping values along with the condition of inboard sensors. The behaviour of the critical frequencies and amplitudes, with regard to changes in the sensor position, can be predicted by examining the mode shape of the rotor shaft at or near the critical frequencies.
3. The results indicate a fairly close agreement between the Jeffcott model and the transfer matrix model. The comparison indicates greater differences in amplitude values compared to critical frequency values and greater deviation in phase angle values compared to amplitude values.
4. The behaviour of the rotor system, with respect to changes in sensor location, does not indicate any significant deviation when a constant force excitation is used instead of an unbalance force excitation.
5. The effect of sensor location on first mode critical frequency increases with higher stiffness ratios. This has been explained in the second chapter. Higher mass ratios lead to increased damping effects in the third mode and hence lower the amplitudes considerably.

The following recommendations can be made for future work in this area:

1. The transfer matrix model modified for this work, does not consider the effect of pedestal stiffness and damping, *ie* it assumes a rigid foundation. The program can easily be modified to take this factor into account.
2. The existing transfer matrix code can only handle circular synchronous rotation of the rotor system. It can be extended to analyse non-circular and non-synchronous motion of the shaft.
3. The constant force excitation in the transfer matrix program is applied as a force function, directly on the journal mass. The behaviour of the rotor system, when the constant force excitation is applied as a displacement function, and on the bearing or pedestal mass, needs to be investigated.
4. The modified transfer matrix code assumes that no couplings are present in the rotor longitudinal cross-section. The code can be modified for the presence of a coupling, which then, would only transfer displacements and shears across the connection, but would not transfer the moments.

BIBLIOGRAPHY

1. Zlotykamien H., "The Active Magnetic Bearing enables Optimum Control of Machine Vibrations," *International Conference on Vibrations in Rotating Machinery, Proc. of the Institution of Mechanical Engineers*, Sept. 1988
2. Weise D. A., "Present Industrial Applications of Active Magnetic Bearings," *22nd Intersociety Energy Conversion Engineering Conference, American Institute of Aeronautics and Astronautics*, Aug. 1987.
3. Keesee J. M., "Influence of Active Magnetic Bearing Sensor Location on the Calculated Critical Speeds of Turbomachinery," *Masters Thesis, Virginia Polytechnic Institute and State University*, June 1989.
4. Hustak J., Kirk R.G., and Schoeneck K. A., "Active Magnetic Bearings for Optimum Turbomachinery Design," *Instability in Rotating Machinery, NASA Conference Publication 2409*, June 1985

5. Kirk R. G., and Hustak J. F., "Analysis and Test Results of two Centrifugal Compressors using Active Magnetic Bearings," *International Conference on Vibrations in Rotating Machinery, Proc. of the Institution of Mechanical Engineers*, Sept. 1988
6. Williams R. D., Keith F. J., and Allaire P.E., "Digital control of Active Magnetic Bearings," *IEEE Transactions on Industrial Electronics*, Vol. 37, No. 1, Feb. 1990.
7. Schweitzer G., "Magnetic Bearings for Vibration Control," *Instability in Rotating Machinery, NASA Conference Publication 2409*, June 1985.
8. Burrows C. R., and Sahinkaya M. N., "Control Strategies for use with Magnetic Bearings," *International Conference on Vibrations in Rotating Machinery, Proc. of the Institution of Mechanical Engineers*, Sept. 1988.
9. Kirk R.G., and Gunter E. J., "The Effect of Support Flexibility and Damping on the Synchronous Response of a Single-Mass Flexible Rotor," *ASME Transactions, Journal of Engineering for Industry*, Vol. 94, Series B, No. 1, 1972.
10. Lund J. W., "Stability and Damped Critical Speeds of a Flexible Rotor in Fluid-Film Bearings," *ASME Transactions, Paper No. 73-Det-103*, 1973.

ACKNOWLEDGMENT

This work has been sponsored by a joint industry/Virginia Center for Innovative Technology Research Grant No. CAE-89-015, with matching funds from Dresser-Rand Co. and Magnetic Bearings, Inc. The authors are especially grateful for the support given by Dr. Ira Jacobson, Director of the Institute of Computer Aided Engineering, Charlottesville, Virginia.

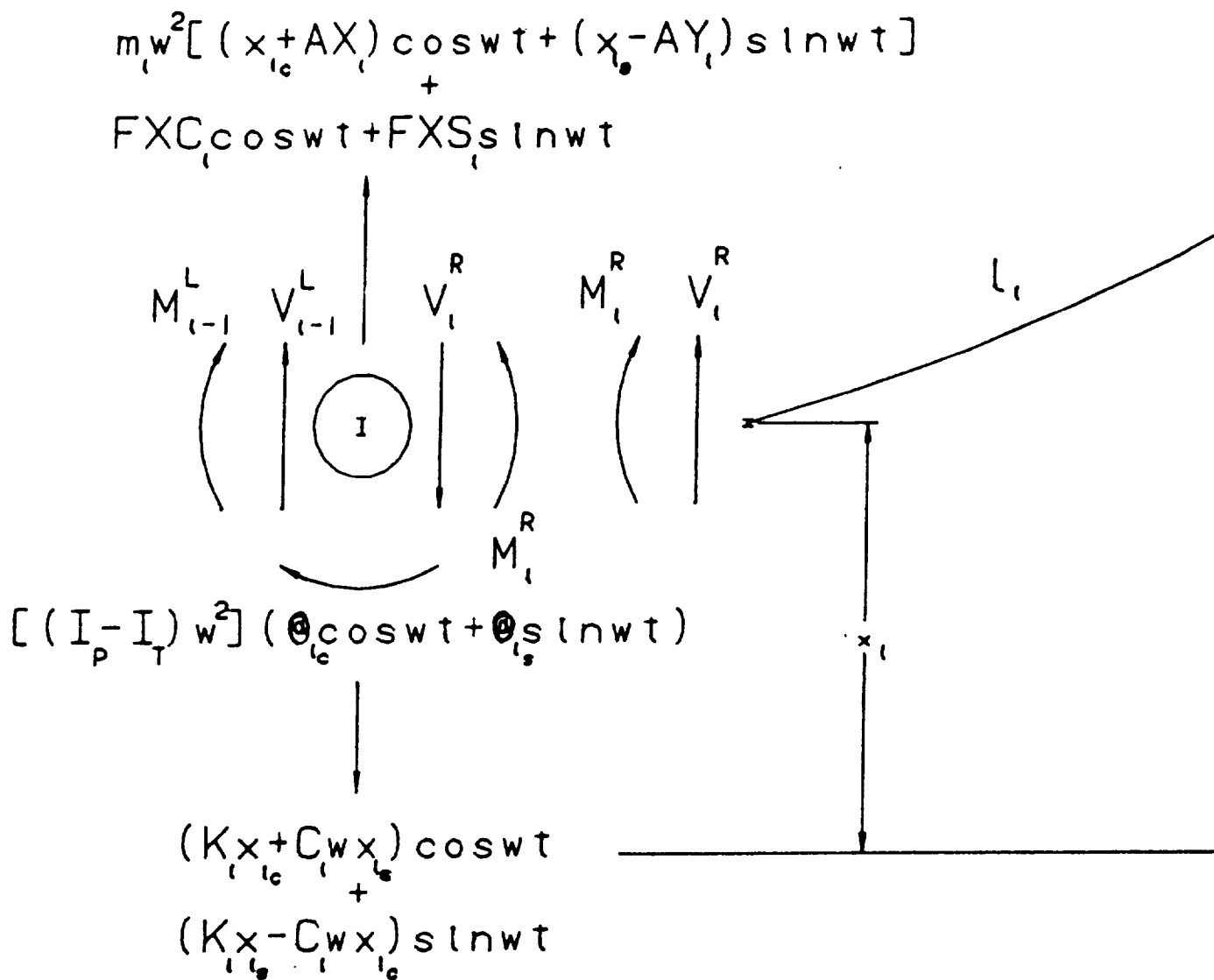


Figure 1. Forces acting on the point mass

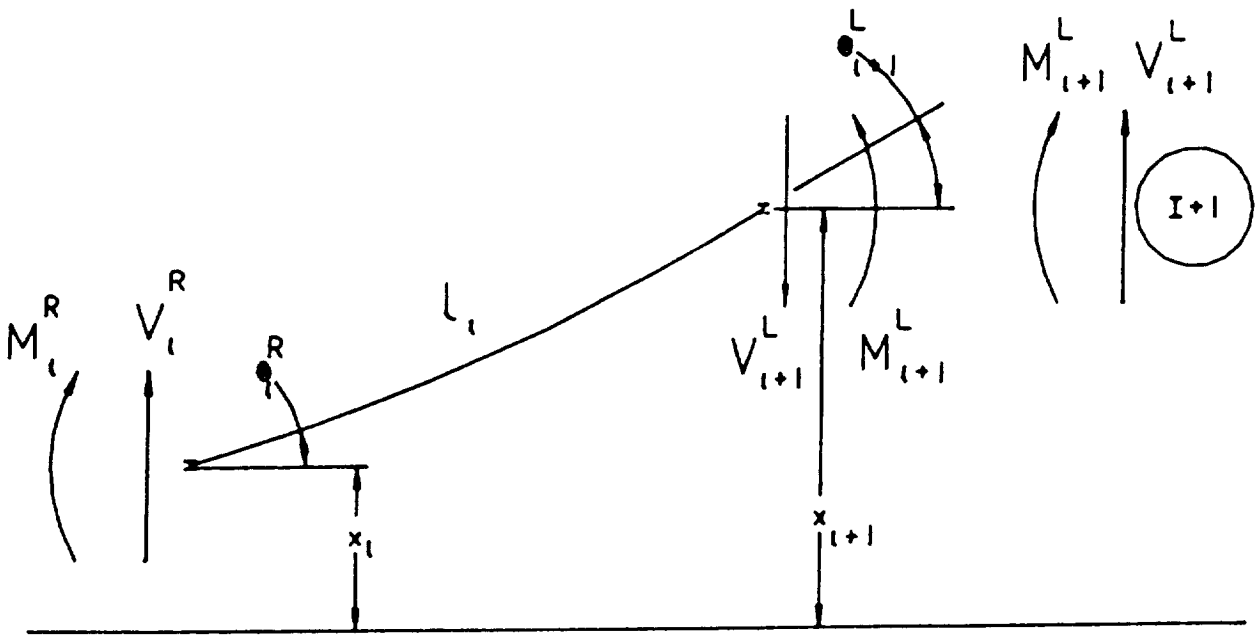


Figure 2. Forces acting on the massless elastic shaft

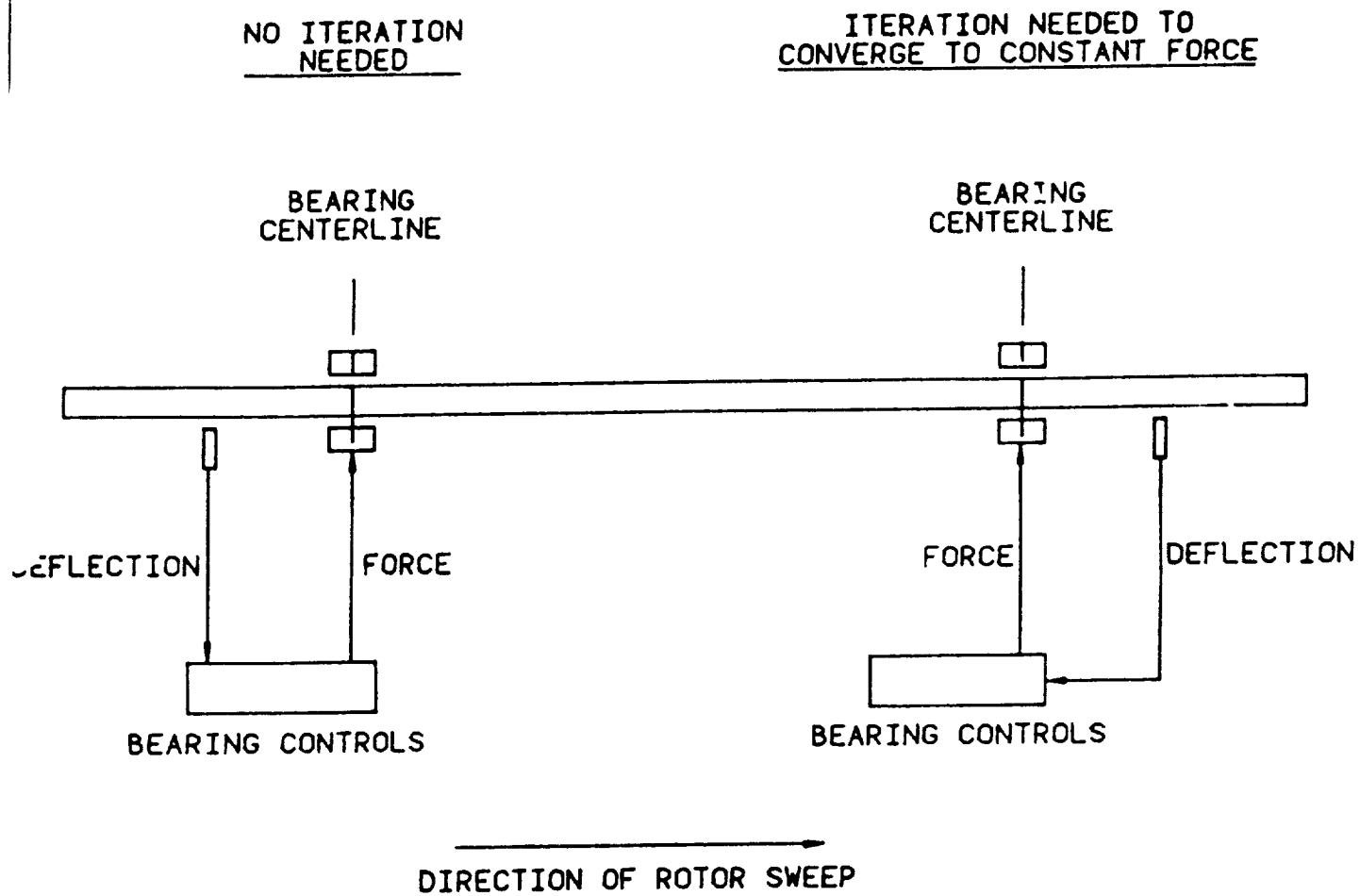


Figure 3. Different sensor locations

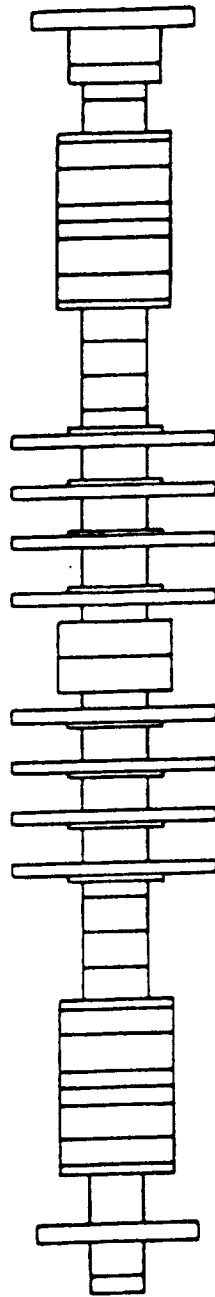


Figure 4. The eight stage centrifugal compressor rotor system

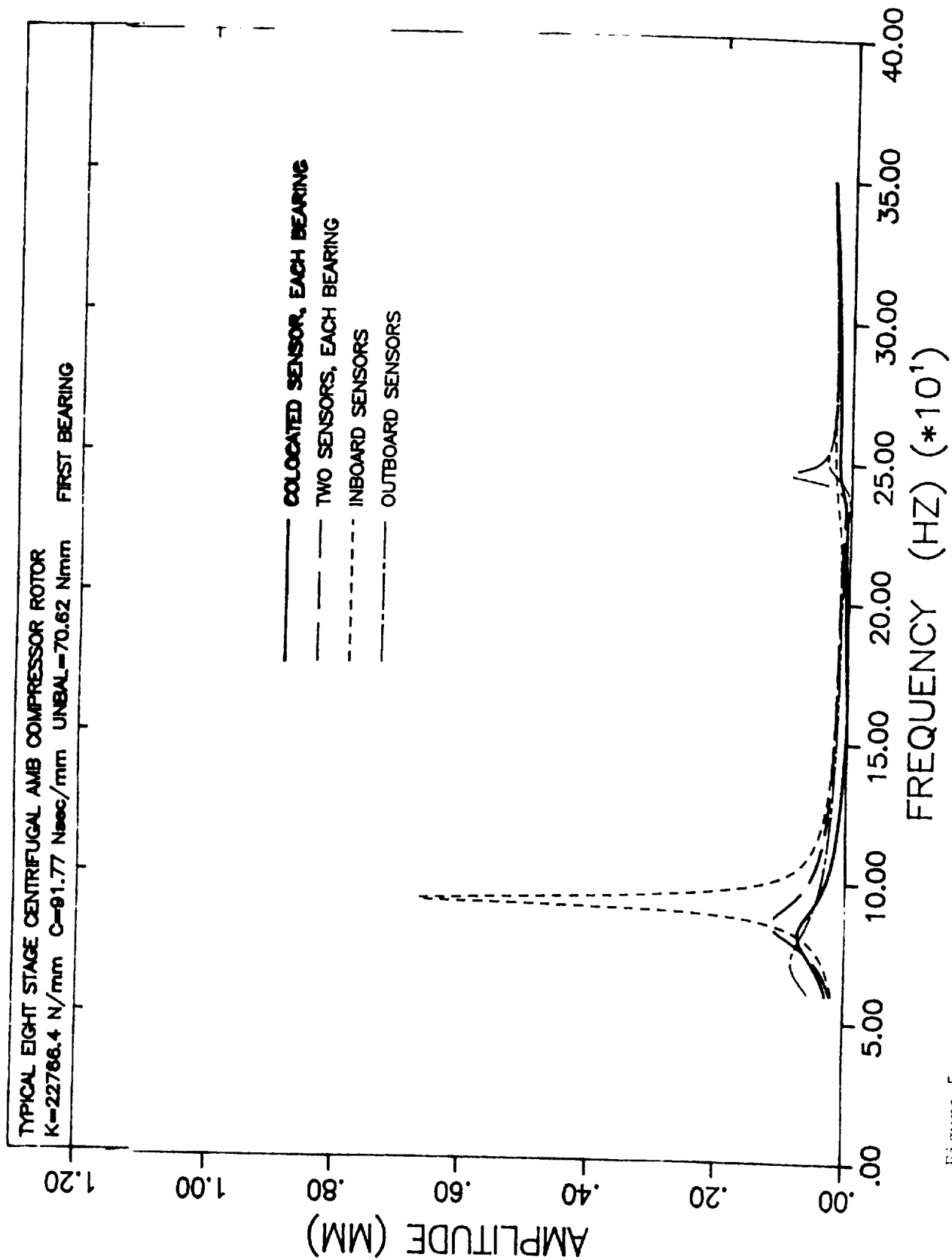


Figure 5

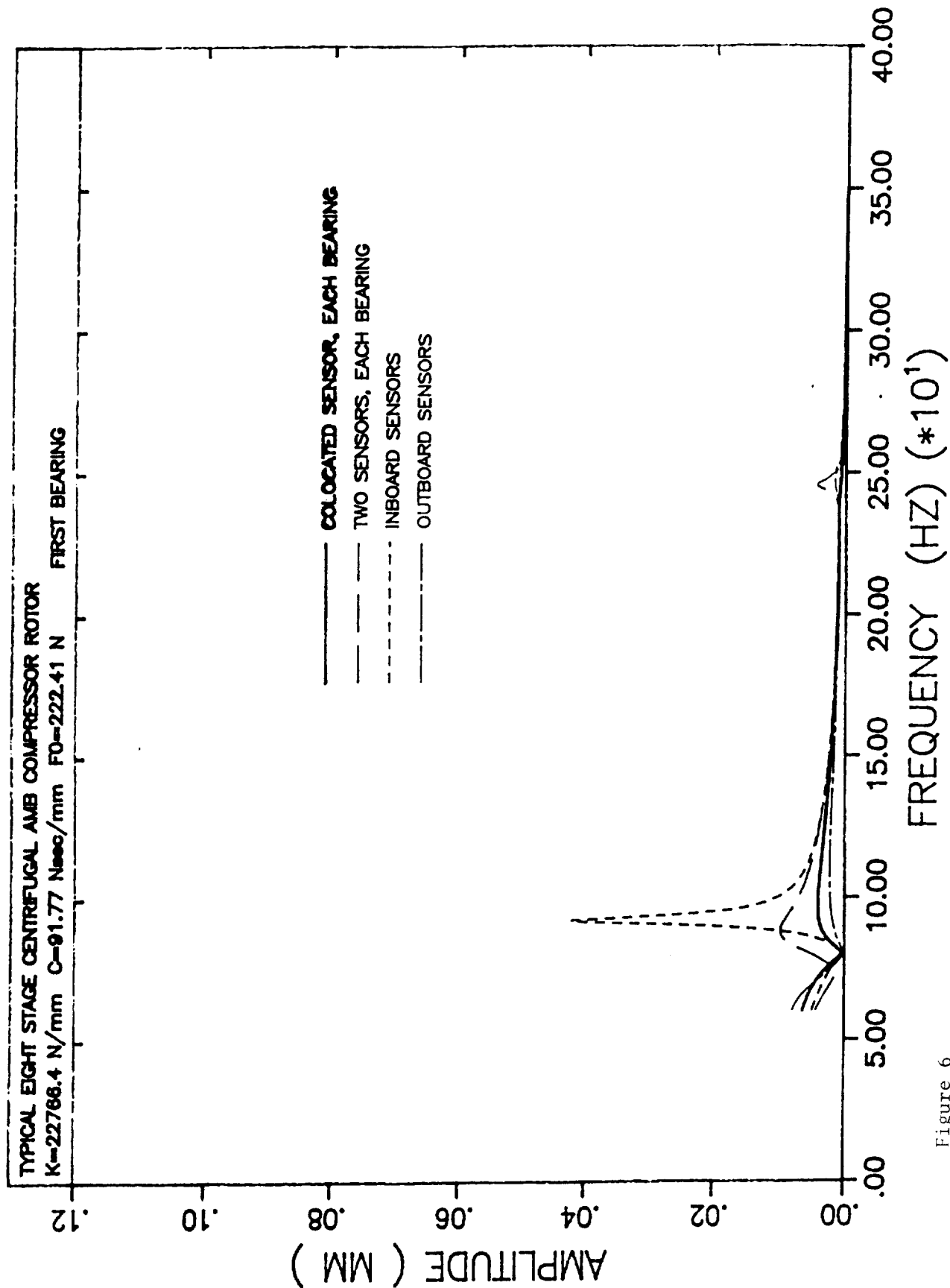


Figure 6

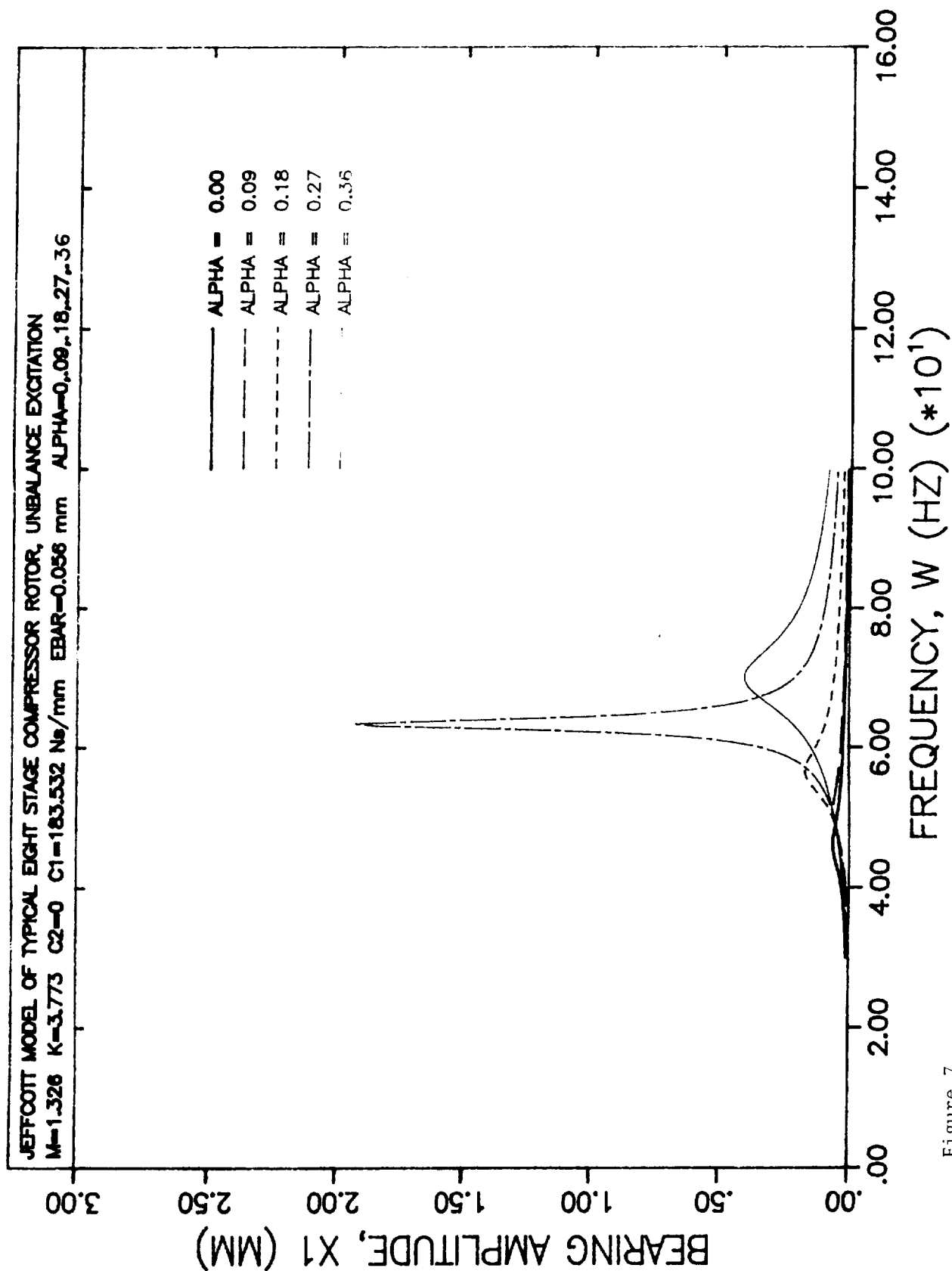


Figure 7

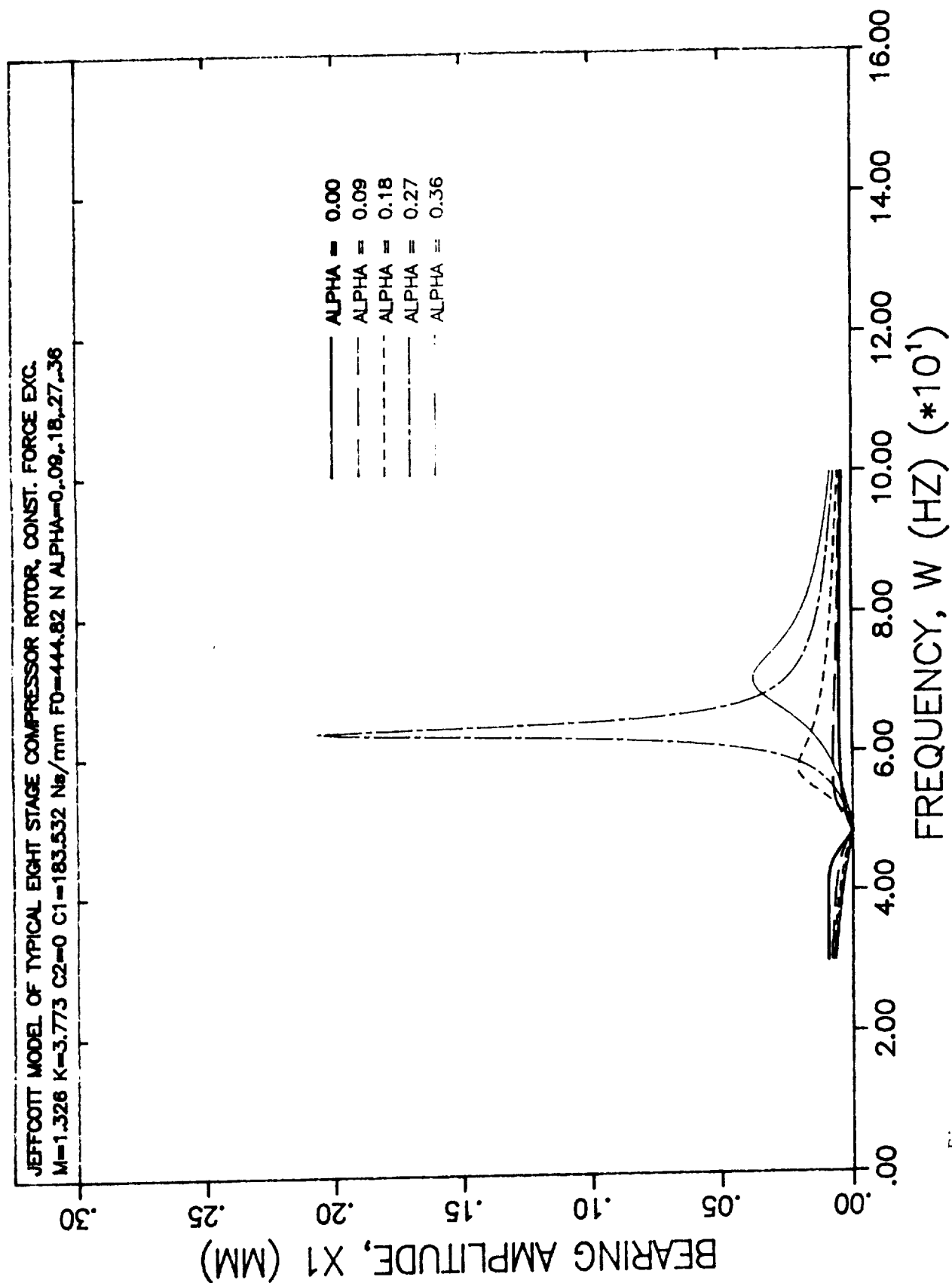


Figure 8

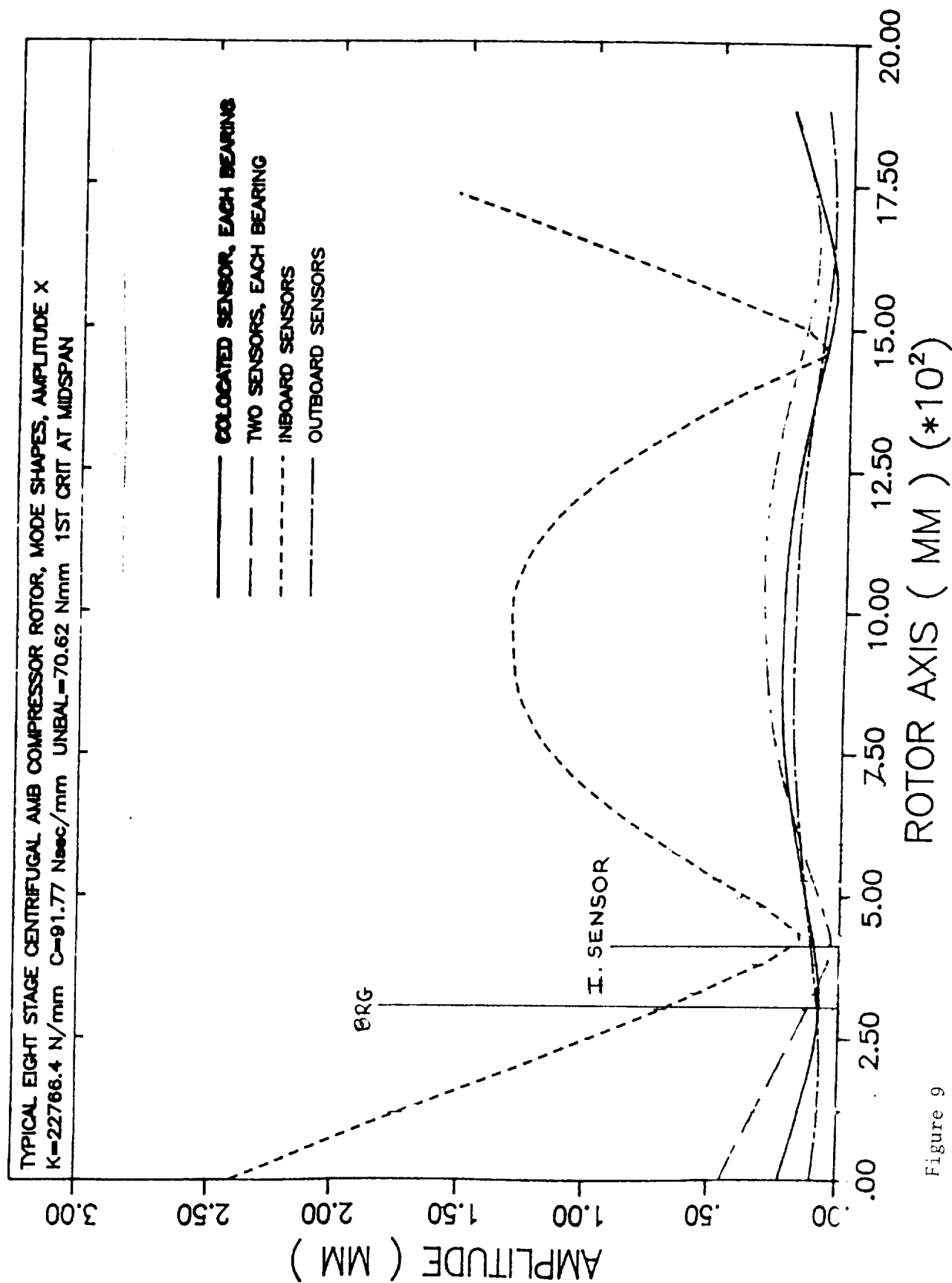


Figure 9

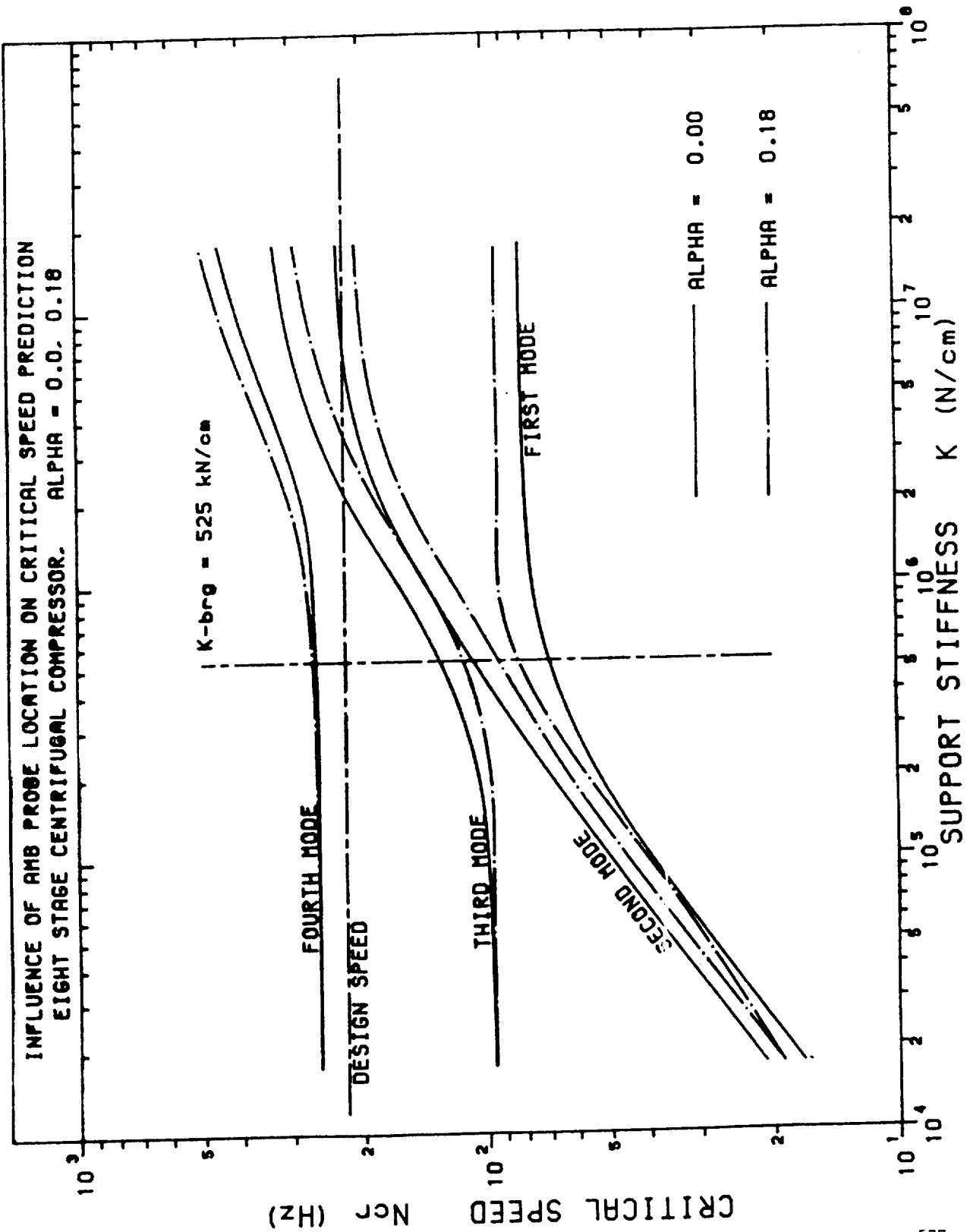


Figure 10

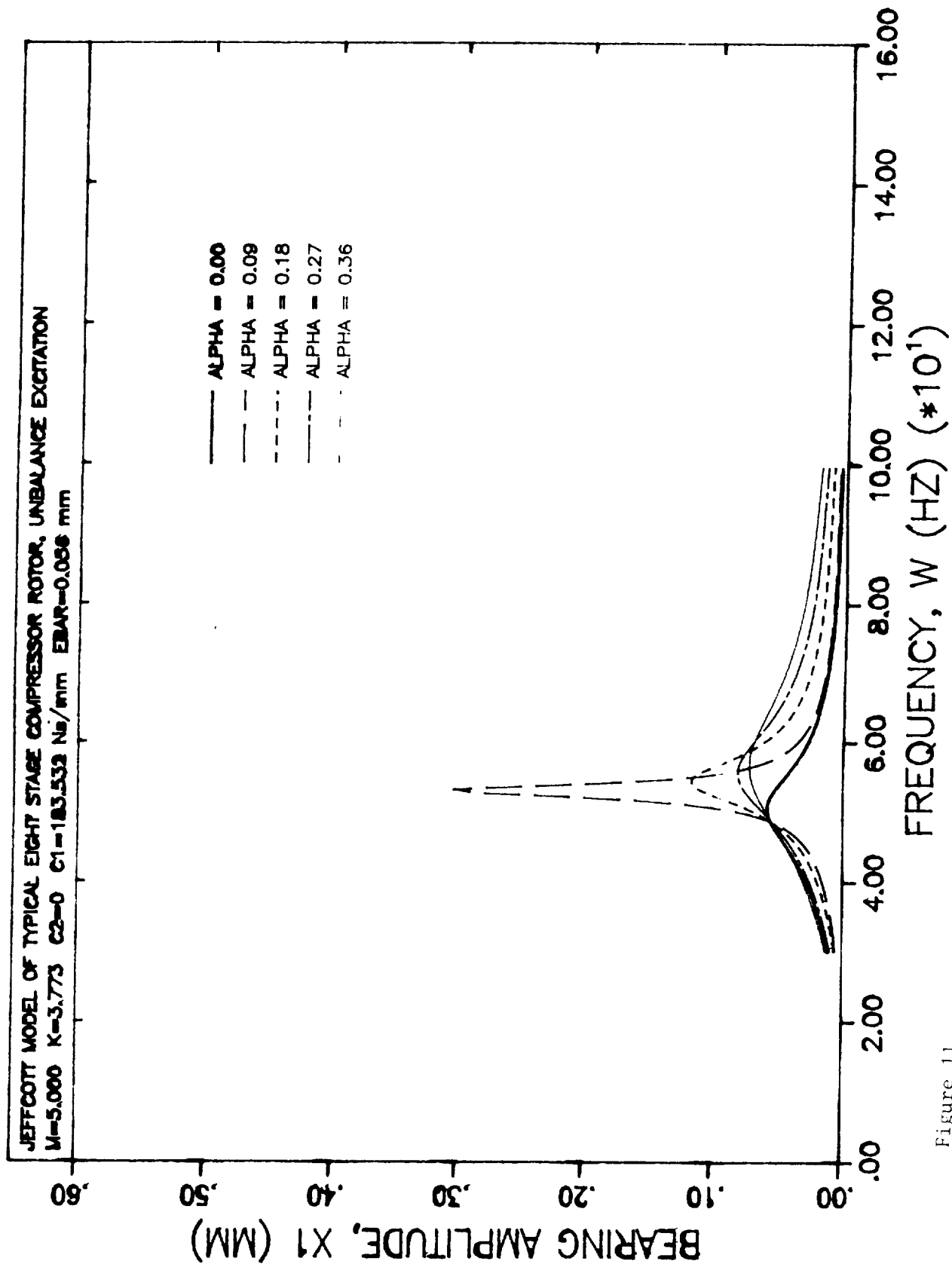


Figure 11

2 MASS MODEL, UNBALANCE EXCITATION, M = 1, K = 2, ALPHA = 0.3 FREQ = 130 HZ, CONVERGENCE TO XC, TRUE SOLUTION = 7.649442						
No. of Iter.	Taylor's series Convergence	% Diff. from true Soln.	Secant method Convergence	% Diff. from true Soln.	Simple Iteration	% Diff. from true Soln.
1	3.500004	54.24	3.500004	54.24	3.500004	54.24
2	8.051951	-5.26	8.051951	-5.26	8.051951	-5.26
3	7.737319	-1.15	7.737319	-1.15	7.737319	-1.15
4	7.581234	0.89	7.930811	-3.68	7.628863	0.27
5	7.849375	-2.61	7.605373	0.576	7.648726	0.0094
6	3.625942	52.60	7.642738	0.088	7.650135	-0.0091
7	69.54724	-809.2	7.655252	-0.076	7.649398	0.00058
8	-959.629	12645.1	7.650030	-0.0077	7.649425	0.00022
9	15109.55	-197425	7.649057	0.0050	7.649445	-0.00004
10	-235777.3	3082381	7.649363	0.001	7.649442	0.0
11	3681287.0	-48124809	7.649458	-0.00021	7.649442	0.0
12	---	---	7.649447	-0.000065	7.649442	0.0
13	---	---	7.649434	0.0001	7.649442	0.0
14	---	---	7.649441	0.000013	7.649442	0.0
15	---	---	7.649443	-0.000013	7.649442	0.0
16	---	---	7.649442	0.0	7.649442	0.0
17	---	---	7.649441	0.000013	7.649442	0.0
18	---	---	7.649441	0.000013	7.649442	0.0
19	---	---	7.649442	0.0	7.649442	0.0

Table 1. Comparison of different convergence schemes

FIRST MODE, UNBALANCE EXCITATION, M = 1, K = 2, BEARING/(MIDSPAN)			
	Jeffcott Code	Transfer matrix Code	% Difference
$\alpha = -0.2$ Critical Frequency Amplitude Phase Angle	32.167 / (32.167) 2.285 / (4.425) 103.48 / (102.57)	32.167 / (32.167) 2.302 / (4.482) 86 / (85.1)	0 / (0) -0.74 / (-1.29) 16.89 / (17.03)
$\alpha = 0.0$ Critical Frequency Amplitude Phase Angle	35.333 / (35.333) 1.408 / (3.401) 90.214 / (88.398)	35.333 / (35.333) 1.408 / (3.402) 91.6 / (89.8)	0 / (0) 0 / (-0.03) -1.54 / (-1.59)
$\alpha = 0.2$ Critical Frequency Amplitude Phase Angle	40.333 / (40.333) 0.539 / (2.281) 92.571 / (86.391)	40.167 / (40.000) 0.571 / (2.310) 104.1 / (81.8)	0.41 / (0.83) -5.94 / (-1.27) -12.45 / (5.31)

Table 2. Comparison of the results of the 2 mass rotor system, for the Jeffcott model and the transfer matrix method

FIRST MODE, CONSTANT FORCE EXCITATION, M = 1, K = 2, BEARING/(MIDSPAN)			
	Jeffcott Code	Transfer matrix Code	% Difference
$\alpha = -0.2$ Critical Frequency Amplitude Phase Angle	32.167 / (32.167) 4.577 / (8.896) 104.24 / (104.24)	32.167 / (32.167) 5.410 / (10.522) 86.8 / (86.8)	0 / (0) -18.20 / (-18.28) 16.73 / (16.73)
$\alpha = 0.0$ Critical Frequency Amplitude Phase Angle	35.333 / (35.333) 3.045 / (7.352) 90.214 / (90.214)	35.333 / (35.333) 3.262 / (7.882) 91.6 / (91.6)	0 / (0) -7.13 / (-7.21) -1.54 / (-1.54)
$\alpha = 0.2$ Critical Frequency Amplitude Phase Angle	40.333 / (40.333) 1.335 / (5.643) 88.527 / (88.527)	40.000 / (40.000) 1.420 / (5.709) 83.9 / (83.9)	0.83 / (0.83) -6.37 / (-1.17) 5.23 / (5.23)

Table 3. Comparison of the results of the 2 mass rotor system, for the Jeffcott model and the transfer matrix method

ROTOR SYSTEM PROPERTY	SI UNITS	ENGLISH UNITS
<i>Total rotor length</i>	<i>1879.6 mm</i>	<i>74.0 in</i>
<i>Distance to bearing 1 centerline</i>	<i>304.8 mm</i>	<i>12.0 in</i>
<i>Distance to sensor at bearing 1:</i>		
<i>Outboard sensor</i>	<i>190.5 mm</i>	<i>7.5 in</i>
<i>Inboard sensor</i>	<i>419.1 mm</i>	<i>16.5 in</i>
<i>Distance to bearing 2 centerline</i>	<i>1574.8 mm</i>	<i>62.0 in</i>
<i>Distance to sensor at bearing 2:</i>		
<i>Inboard sensor</i>	<i>1460.5 mm</i>	<i>57.5 in</i>
<i>Outboard sensor</i>	<i>1689.1 mm</i>	<i>66.5 in</i>
<i>Mid-span diameter</i>	<i>177.8 mm</i>	<i>7.0 in</i>
<i>Journal diameter</i>	<i>177.8 mm</i>	<i>7.0 in</i>
<i>Journal length</i>	<i>254.0 mm</i>	<i>10.0 in</i>
<i>Total rotor weight</i>	<i>2.95 KN</i>	<i>663.2 lb_f</i>
<i>Reaction at bearing 1</i>	<i>1.41 KN</i>	<i>317.0 lb_f</i>
<i>Reaction at bearing 2</i>	<i>1.54 KN</i>	<i>346.2 lb_f</i>

Table 4. Data for eight stage centrifugal rotor system model

N 9 1 - 2 1 2 1 1

REDUCTION in BEARING SIZE due to SUPERCONDUCTORS in MAGNETIC BEARINGS

Dantam K. Rao, Paul Lewis, James F. Dill

Mechanical Technology Incorporated

968 Albany-Shaker Road

Latham

NY 12110

Overview

This presentation assesses a design concept that reduces the size of magnetic bearings. The small size will enable magnetic bearings to fit into limited available bearing volume of cryogenic machinery.

The design concept, called SUPERC, uses (high Tc) superconductors or high-purity aluminum conductors in windings instead of copper. The relatively high-current density of these conductors reduces the slot radial thickness for windings, which reduces the size of the bearings.

MTI developed a sizing program called SUPERC that translates the high-current density of these conductors into smaller sized bearings. We used this program to size a superconducting bearing to carry a 500-lb load. The sizes of magnetic bearings needed by various design concepts are as follows:

- SUPERC design concept = 3.75 in.
- Magnet-bias design concept = 5.25 in. [2]
- All electromagnet design concept = 7.0 in. [2]

These results indicate that the SUPERC design concept can significantly reduce the size of the bearing. This reduction, in turn, reduces the weight and yields a lighter bearing. Since the superconductors have inherently near-zero resistance, they are also expected to save power needed for operation considerably.

OVERVIEW

Objective: Assess a Concept to Reduce the Size of Magnetic Bearings

Design Concept

- Utilize High-Current Density of Hyperconductors or Superconductors to Reduce Size

Accomplishments

- Computer Program SUPERC Developed to Size Superconducting Bearings and Controls
- 500-lb Magnetic Bearing Sized Per Various Concepts:
 - SUPERC Design Concept = 3.75 in.
 - Magnetic Bias Design Concept = 5.25 in.
 - All Electromagnet Design Concept = 7.0 in.

***Superconducting Bearings Are Smaller and, Hence,
Suitable for Cryogenic Aerospace Applications***

Mechanical Technology Incorporated

Approaches to Long-Life Cryogenic Bearings

Currently, rolling element bearings are being used to support rotors in high-performance cryogenic turbopumps such as the SSME. The life of these bearings is limited due to wear under high-load conditions. Hence, there is a need to remove the contact/wear environment in cryogenic rotor support systems.

The options to remove the wear environments are fluid film and magnetic suspension. The challenge to both technologies is to achieve the required load capacity within limited available volume with least power consumption.

We selected to study the magnetic bearing option because it can meet load requirements without any physical contact. The fluid-film bearing, on the other hand, needs contact by fluids. Its performance is sensitive to the lubrication capability of cryogenic fluids, which is known to be low at cryogenic temperatures.

Mechanical Technology Incorporated

APPROACHES TO LONG-LIFE CRYOGENIC BEARINGS

- Rolling Element Bearings — Life Limited Due to Wear
- Remove Contact/Wear Environment
- Options:
 - Fluid Film
 - Magnetic
- Challenge — Achieve Required Load Capacity in
 - Limited Available Volume
 - Least Power Consumption
- Selected Magnetic Bearings
 - No Solid or Fluid Contact Required
 - Lower Power Dissipation

The Problem

Magnetic bearings are fundamentally limited by the magnetic, electric, and mechanical strength of materials used. The mechanism by which magnetic strength (flux density) limits the load capacity is well understood [2]. The mechanism by which the electric strength (current density) limits the size of the bearing is not very well understood. The challenge is therefore to understand how current density controls the size of the bearing.

The Solution

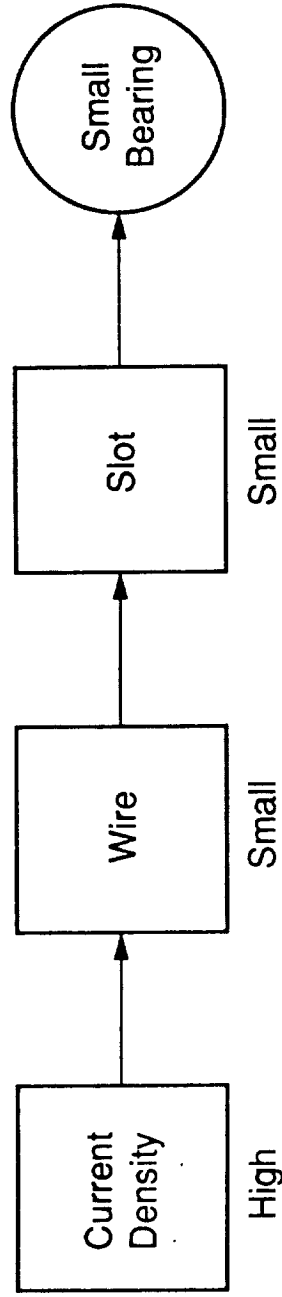
The SUPERC design concept consists of replacing copper winding (present in conventional magnetic bearings) by hyperconducting or superconducting windings. These conductors are known to carry currents at densities one or two orders of magnitude higher than that of copper (1000 A/mm^2 vs. 10 A/mm^2).

The higher current density reduces the size of wire to carry the same ampere turns. The smaller wire requires a smaller slot. By reducing the radial thickness of the slot by an order of magnitude, the SUPERC design concept reduces the size of the bearing.

Alternatively, the magnet bias design concept [6, 7] saves the size by replacing the volume occupied by bias currents with that of permanent magnets. As per [6], the resulting bearing is smaller as the electromagnet coil window is smaller because coils are sized to carry control currents only.

THE PROBLEM

The Problem: Understand How Higher Current Density Reduces Bearing Size



The Solution: SUPERC Design Concept. High Current Density Leads to Smaller Wire, Smaller Slot, and Hence Smaller Bearing

Operating Principle of SUPERC Design Concept

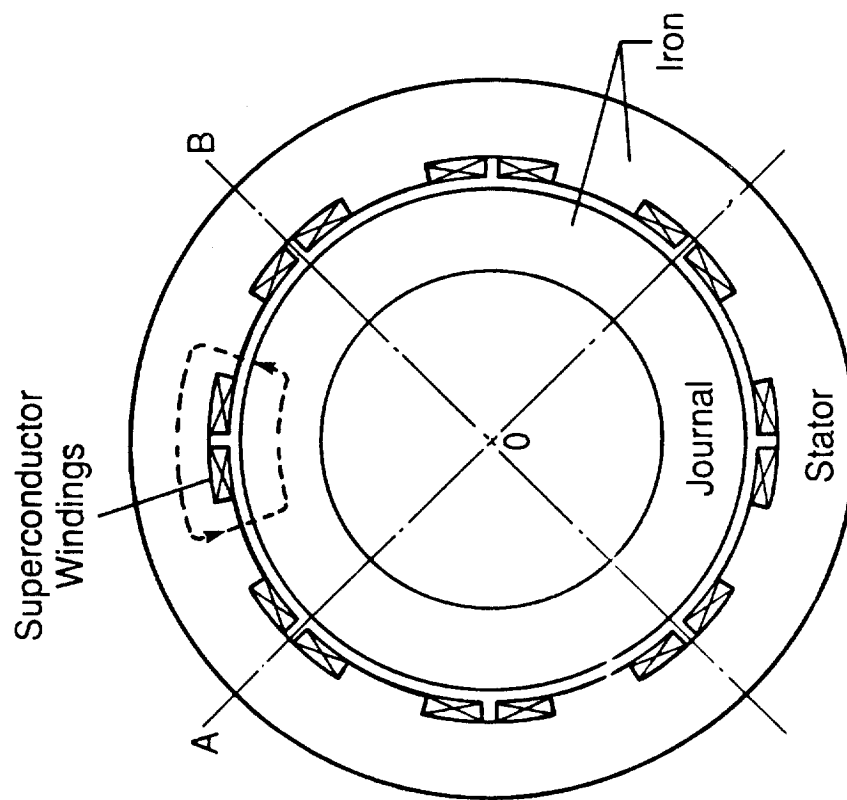
The SUPERC design concept [5] consists of a ferromagnetic journal mounted on a shaft which is attracted by controlled electromagnets in the housing. If the forces due to operation of a machine causes the rotor to move up, the current in the top electromagnet is decreased to reduce the upward attraction force.

The servo system that regulates the current consists of a sensor, controller, and power amplifier. The sensor converts the mechanical position of the rotor into an electrical voltage signal. The controller converts this sensor signal into a control signal that can stabilize the rotor. The power amplifier converts the control signal into control currents that drive the electromagnets.

The housing is sized to carry iron, windings, and sensors. The iron is needed to channel flux, and its size is dictated by the flux saturation. The windings energize the electromagnets, and its size is dictated by current density needed to generate the required ampere turns.

[The weight of electronics needed to generate bias currents could be saved by using persistent currents.]

ACTIVE SUPERCONDUCTING BEARING CONCEPT



Sizing Analysis

The bearing diameter, D , is estimated by the formula:

$$D = d + 2g + 2t_j + 2t_r + 2t_s \quad (1)$$

where the shaft diameter, d , and the magnetic gap, g , are fixed by application. The radial thickness of the journal, return path, and slot (t_j , t_r , t_s) are estimated as follows:

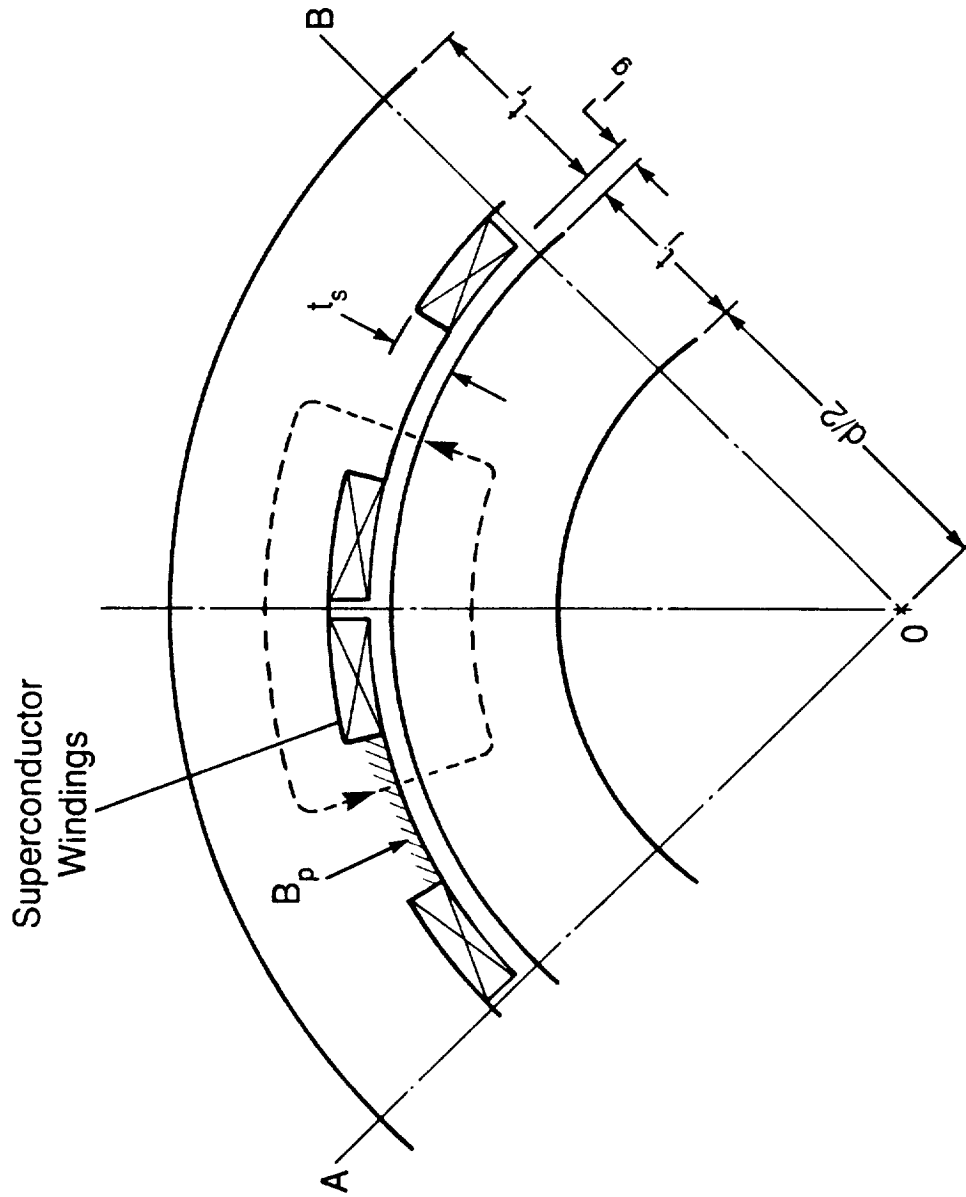
Iron Area (Magnetic Path)

- Estimate the total pole area, A , needed to equalize the mechanical pressure due to given force, P , with the saturation pressure $B_s^2/2\mu_0$ that can saturate the magnetic material.
- Estimate the individual pole width, b_p , from the total pole area, A , number of poles, n , and axial flux length, L .
- Estimate the thickness of journal and return paths by assuming that all cross sections normal to flux paths have an area equal to individual pole area, so that $t_j = t_r = b_p$.

Winding Area (Electric Path)

- Estimate the ampere turn, NI , needed to generate the flux density, B , in the magnetic gap from the magnetic circuit analysis.
- Compute the winding area, A' , needed to generate this ampere turn, NI , from a conductor of current density, J , and fill factor, J' .
- Estimate the slot width, b_s , as the difference between the pole pitch and pole width, b_p .
- Estimate the slot thickness, t_s , from the total winding area divided by the slot width.

SIZING ANALYSIS



Computer Program to Size SUPERC Bearings

The program sizes the bearing housing as well as the control system from given load requirements and B-H curve of flux path material.

The program outputs include geometric, dynamic, thermal, and electric variables. Sample parameters outputted are:

Geometric	Dynamic	Thermal	Electrical
Housing Diameter	Shaft Orbits	Temperature Rise	Currents
Pole Dimensions	Stiffness	Heat Generated	Inductance
Slot Dimensions	Damping		Resistance
Journal Dimensions	Mass		Back emf

In addition, the program allows for several secondary effects such as core reluctance, leakage flux, fringe flux, lamination thickness, pole angle, and temperature coefficient of resistance. These effects combine to degrade the load capacity considerably and, hence, are needed for accurate sizing.

COMPUTER PROGRAM TO SIZE SUPERCONDUCTING BEARINGS

Input: Load, Flux Density, Current Density

Output: • Geometric

- Dynamic
- Thermal
- Electrical
- Control System

Included Secondary Effects

- Core Reluctance
- Leakage Flux
- Fringe Flux
- Lamination Thickness
- Pole Angles
- Temperature Coefficient of Resistance

Mechanical Technology Incorporated

Estimated Performance Parameters

In addition to sizing, the program estimates the performance capability of the bearing by a set of seven parameters:

System	Load
Bearing Size	Magnetic Pressure
Bearing Weight	Load Capacity (Static)
Power Loss	Load Capacity (Dynamic)
	Load Efficiency

The bearing size is quantified by the outer diameter of the housing. The bearing weight includes that of the housing and journal, but excludes that of the support electronics. The power loss is estimated from ohmic losses in the windings.

The magnetic pressure is defined as $B^2/2 \mu_o$. The static load capacity is computed as the output force per unit projected area of the bearing. The dynamic load capacity is computed as the dynamic load transmitted to the housing for specified shaft orbital amplitude at specified speed.

The load efficiency is computed as the ratio of output force (lb) and the weight of the bearing needed to generate this force. This output force is computed as maximum force that can be generated along a single axis.

ESTIMATED PERFORMANCE PARAMETERS

Bearing

- Size
- Weight
- Power

Load

- Magnetic Pressure
- Load Capacity (Static)
- Load Capacity (Dynamic)
- Load Efficiency

Performance Comparison

Based on the analysis, the performance of a 500-lb magnetic bearing are compared to the following design approaches:

- SUPERC
- Magnet bias
- All electromagnet

The following parameters are kept constant as a basis for comparison:

- Radial load: 500 lb (2230 N)
- Shaft diameter: 2 in. (50.8 mm)
- Journal diameter: 3 in. (76.2 mm)
- Flux density limit: 1.6 tesla
- Axial length of flux: 4.3 in. (109 mm)

A 24-pole design with a current density of 100 A/mm^2 was used in the SUPERC design concept.

This table indicates that the SUPERC design concept yields bearings that are smaller in size, lighter in weight, and delivers higher load (lb) per each pound of bearing weight.

PERFORMANCE COMPARISON OF MAGNETIC BEARING DESIGN CONCEPT

Performance Parameter	Design Concept		
	SUPERC	Magnet Bias	All Electromagnet (Vandium Permeandur)
Load Capacity Per Axis (lb)	500	500	500
Journal Diameter (in.)	3	3	3
Axial Flux Path Length (in.)	4.3	4.3	4.3
Size/Outer Diameter (in.)	3.75	5.25	7.0
Weight/Stator and Journal (lb)	9.5	21.4	43.8
Load Efficiency (lb/lb)	52.6	23.4	11.4
Remarks	<ul style="list-style-type: none"> • Smaller Size • Lighter Weight 	<ul style="list-style-type: none"> • Medium Size • Medium Weight 	<ul style="list-style-type: none"> • Large Size • Large Weight

Size Comparison

To give a physical feel for the bearing size, the accompanying figure compares the actual size of the bearing per various design concepts.

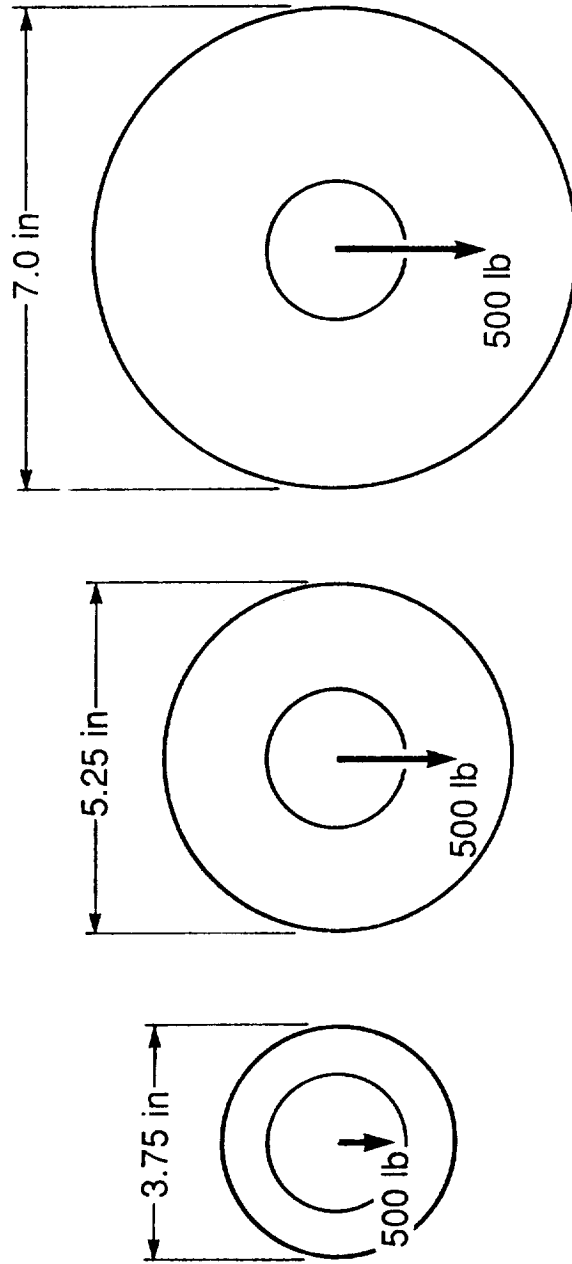
The SUPERC bearing is half the size of all electromagnetic (vanadium permendur) designs. It is 30% smaller than the magnet bias bearing. This small size is due to the higher current density which reduces the slot size and, hence, needs smaller sized electromagnets.

The SUPERC bearing is about 4.6 times lighter than all electromagnetic (vanadium permendur) designs and about 2.2 times lighter than magnet bias design. The lighter weight is attributed to the reduced size afforded by higher current densities.

For the same lb of bearing, the SUPERC design can carry a load that is double that of the magnet bias design and four times that of all electromagnetic designs.

These numbers indicate that introduction of superconductors can substantially improve the performance of the magnetic bearings.

SIZE COMPARISON



SUPERC	Magnet Bias	All Electromagnet
Design Concept	Design Concept [2]	Design Concept [3]

Effect of Current Density on Size Reduction

The minimal housing diameter needed for a 500-lb bearing with a 3-in. diameter journal is calculated as per the preceding analysis for various current densities. This analysis yields the following size reduction table:

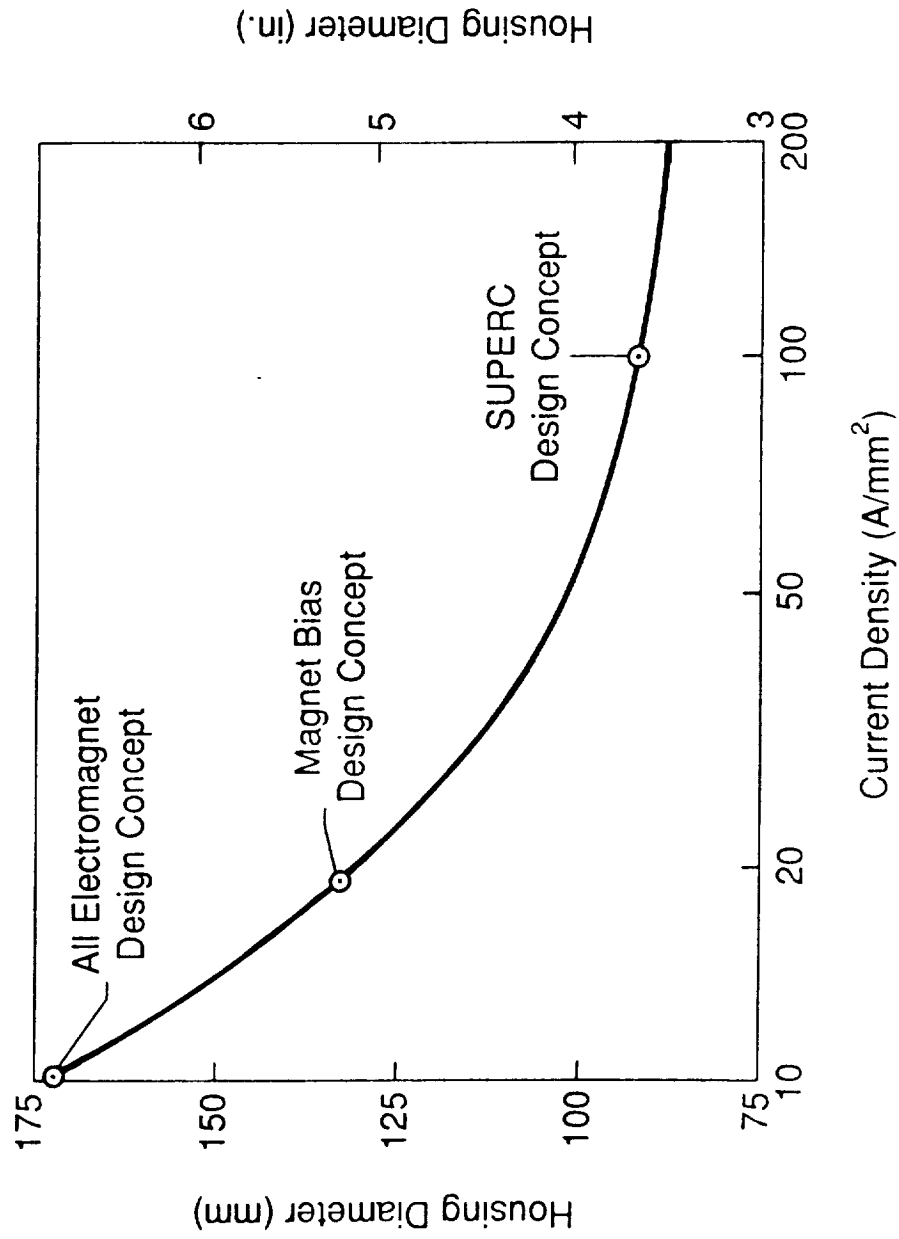
	Current Density (A/mm ²)	Multiplier	Minimal Housing Diameter (mm)	% Reduction
Copper	10	x1	172	--
	20	x2	128	25
	50	x5	101	41
	100	x10	93	46
Superconductor	200	x20	88	49

From the current density vs housing diameter plot, it is clear that the payoff of current density (size reduction) is initially high when the current density is increased by a factor of 2 to 5 (from 10 to 50 A/mm²). Further increase in current density does not automatically payoff as a proportional size reduction. Beyond 200 A/mm², the current density does not have any appreciable payoff.

The magnet bias design equals the performance of SUPERC bearings at a current density of 20 A/mm². A current density of 50 A/mm² would then result in a bearing better than the magnet bias design.

Mechanical Technology Incorporated

EFFECT OF CURRENT DENSITY ON SIZE REDUCTION



CONCLUSIONS

- The Analysis Presented Herein Indicates That the SUPERC Concept, Which Utilizes Superconductors, Can Reduce the Size of Magnetic Bearings by As Much As 30% Compared to the Most Recent Magnet Bias Design Concept.
- It Can Also Carry Double the Load Per lb of Bearing Weight.
- These Results Indicate That the SUPERC Design Concept Is Attractive As a Small-Size, High-Load Bearing for Cryogenic Turbomachines in Aerospace Applications.

REFERENCES

1. Rao, D. K. and J. F. Dill. "Identification of Potential Candidates for Superconducting Bearings in SDI Systems." MTI Technical Report 90TR28, prepared for SDIO, May 1990.
2. Meeks, C., E. DiRusso, and G. V. Brown. "Development of a Compact, Lightweight Magnetic Bearing." Presented at the 26th Annual AIAA/SAE/ASME/ASEE Joint Propulsion Conference in Orlando, Florida, July 16-18, 1990.
3. Anonymous. "Magnetic Bearings Catalog Data Sheet." MBI, Redford, Virginia.
4. Rao, D. K. and J. F. Dill. "Comparative Assessment of Single-Axis Force Generation for Superconducting Suspensions." Presented at the 25th IECEC Conference, Reno, Nevada, August 1990.
5. Dill, J. F., D. K. Rao, and R. Decher. "A Feasibility Study for the Application of High-Temperature Superconducting Bearings in Rocket Engine Turbopumps." Presented at the 1990 Conference on Advanced Earth-to-Orbit Propulsion Technology, Huntsville, Alabama, March 15-17, 1990.
6. Meeks, C., S. D. Schwartz, V. Spencer, and A. Kascak. "Design of a Highly Efficient Magnetic Bearing for Cryogenic Applications." Presented at the 1990 Conference on Advanced Earth-to-Orbit Propulsion Technology, Huntsville, Alabama, May 15-17, 1990.
7. McCarty, L. H. "Hybrid Design Lightens Magnetic Bearing." Design News, vol. 46, no. 11, pp 156-157, June 11, 1990.
8. Haberman, H. and G. L. Liard. "An Active Magnetic Bearing System." Tribology International, vol. 13, no. 2, pp 85-89, April 1980.
9. Maslen, E., P. Hermann, M. Scott, and R. R. Humphris. "Practical Limits to Performance of Magnetic Bearings: Force, Slew Rate, and Power Requirements." Presented in Magnetic Bearing Technology Workshop, NASA Langley Research Center, Hampton, Virginia, February 1988.

N91-21212

CHEMICAL SPRAY PYROLYSIS of Ti-Ba-Ca-Cu-O HIGH- T_c SUPERCONDUCTORS
for HIGH-FIELD BITTER MAGNETS

L. Pierre. de Rochemont, John G. Zhang, Michael R. Squillante

Radiation Monitoring Devices

44 Hunt Street

Watertown

MA 02172

A.M. Hermann, H.M. Duan

University of Colorado at Boulder

Department of Physics

Boulder

CO 80309

Robert J. Andrews, Rome Air Development Center

Solid State Sciences Directorate

Hanson Air Force Base

MA 01731

Warren C. Kelliher

Mail Stop 416A

NASA Langley Research Center

Hampton

VA 23665-5225

I. INTRODUCTION.

This research is part of a NASA program to investigate the feasibility of applying high- T_c superconducting ceramics to the development of a high-field (5-6 Tesla) magnet, with an ultimate objective of utilizing these materials in a liquid nitrogen cooled wind tunnel magnetic suspension balance. The current state of the high- T_c superconducting ceramics inhibits their immediate application to high-field magnets for a number of reasons. Their superconducting properties are strongly anisotropic, with preferential critical performance perpendicular to the perovskite c-axis, i.e., in the a-b plane of the crystal. As a consequence, the bulk ceramics, which have largely random crystal orientations are not suitable for optimal engineering. Epitaxial films can be prepared in which the c-axis is parallel to the plane of the substrate, i.e., perpendicular to the substrate surface. However, since the design and demonstration of a high- T_c superconducting high-field magnet will require preferential c-axis orientation over a large topological surface, many of the vacuum epitaxial deposition techniques are not suited for this application because of the limited surface areas which can be coated.

These issues can be circumvented by advancing chemical spray pyrolysis as a means to deposit large area films on to a tape wire which can then be configured into the geometry necessary to drive the magnetic field. Chemical spray pyrolysis has a number of advantages. It is inexpensive. It can produce good quality films over very large areas. It is an open system deposition technique so continuous strips of film can be prepared, and it has already demonstrated feasibility in a number of electronics applications, particularly in the field of solar cell fabrication.

This paper reports on the deposition of Tl-Ba-Ca-Cu-O thick films by spray pyrolyzing a Ba-Ca-Cu-O precursor film and diffusing thallium into the film to form the superconducting phase. This approach was taken to reduce exposure to thallium and its health and safety hazards. The Tl-Ba-Ca-Cu-O system was selected because it has very attractive features which make it appealing to device and manufacturing engineering. Tl-Ba-Ca-Cu-O will accommodate a number of superconducting phases. This attribute makes it very forgiving to stoichiometric fluctuations in the bulk and film. It has excellent thermal and chemical stability, and appears to be relatively insensitive to chemical impurities. Oxygen is tightly bound into the system, consequently there is no orthorhombic (conductor) to tetragonal (insulator) transition which would affect a component's lifetime. More significantly, the thallium based superconductors appear to have harder magnetic properties than the other high- T_c oxide ceramics. Estimates using magnetoresistance measurements, [1], indicate that at 77 K $Tl_2Ba_2CaCu_2O_{10}$ will have an upper critical field, H_{c2} , of 26 Tesla for applied fields parallel to the c-axis and ≈ 1000 Tesla for fields oriented in the a-b plane. [2]

Results to date have shown that superconducting films can be reproducibly deposited on 100 oriented MgO substrates. One film had a zero resistance temperature of 111.5 K. Furthermore, x-ray diffraction analysis of the films showed preferential c-axis orientation parallel to the plane of the substrate. These results have now made it possible to consider the manufacture of a superconducting tape wire which can be configured into a topology useful for high-field magnet designs. This paper will review the research which lead to the preparation of these films and plans for further development.

II. EXPERIMENTAL RESULTS.

In chemical spray pyrolysis soluble salts of the metallic components of the superconducting ceramic are dissolved in solution in stoichiometric amounts. In this work the nitrate precursors of barium, calcium, and copper, $(Ba(NO_3)_2, Ca(NO_3)_2, Cu(NO_3)_2)$, were used. Once thoroughly mixed this solution can be sprayed onto a surface which is hot enough to volatilize the transport fluid and then allow the salts to decompose, oxidize and

form a polycrystalline ceramic. Ultrasonic techniques were used to nebulize the solution into droplets. The sprayed surface is thermally treated in the presence of oxygen, air is suitable, to decompose the nitrates into their respective oxides. Once a Ba-Ca-Cu-O oxide precursor film had been formed thallium was diffused into the film which was then thermally processed to produce the superconductive Tl-Ba-Ca-Cu-O phase.

Stoichiometric control is crucial to the electromagnetic performance of high- T_c superconducting ceramics. Thus a primary objective of the Phase I effort is to tune the spray process to produce Ba-Ca-Cu-O precursor thin/thick films with stoichiometric control and uniformity. A second objective of the program is to fuse all the individual metallic ions into a uniform polycrystalline ceramic prior to thallium diffusion processing. Oxides of Ba and Ca fused into crystalline copper oxide structures are less likely to outgas during subsequent thermal annealing and thallium diffusion processing than would amorphous barium or calcium oxides loosely distributed in the film. Furthermore, a fused crystal structure will have better order and chemical uniformity.

It is therefore a fundamental objective of this program to eliminate single species clustering or agglomerations in the films, enhance grain alignment, and to promote superior microstructure. This can be achieved by using a suitable chemical "binder" in the solution which favors thorough dissolution, intermixing and complexation of the different reactants prior to deposition. Ideally, this solvent should enhance mutual reactivity of the salts during the crystal fusion process.

A. PRECURSOR DEVELOPMENT AND STOICHIOMETRIC CONTROL.

To develop stoichiometric control over the process and to avoid single component clustering in the films the effect of solution solvent and substrate temperature on metal ion incorporation, surface morphology and chemical uniformity were evaluated. The thermal behavior of each of the individual nitrate compounds was measured. These measurements were then used to evaluate the effect of a particular solvent by comparison to thermal analysis on a dried residue of that solution in which the nitrates were mixed in stoichiometric amounts.

Since nitrate compounds are generally hygroscopic and their molecular weights can be altered by ambient humidity conditions, stock solutions of each nitrate were prepared. Stock solution concentration was measured using Atomic Absorption spectroscopy, (AA), by Northern Analytical Laboratory, Amherst, NH.

1. Metallic Nitrate Precursor Denitration/Decomposition

The denitration of the individual cation precursors was studied by drying $\text{Ba}(\text{NO}_3)_2$, $\text{Ca}(\text{NO}_3)_2$, and $\text{Cu}(\text{NO}_3)_2$ water solutions on alumina substrates. The thin film material was scratched off the surface and analyzed using differential thermogravimetric analysis, (DTGA). These measurements were performed by Robert J. Andrews with the Solid State Sciences Directorate, of the Rome Air Development Center, Hanscom AFB, MA using a Perkin-Elmer Delta Series TGA7 Thermal Analyzer.

a. Thermal Denitration/Decomposition of $\text{Cu}(\text{NO}_3)_2$ in Water Solution.

X-ray diffraction spectra on sprayed films shows that $\text{Cu}(\text{NO}_3)_2$ in an aqueous environment breaks down at elevated temperatures to form $\text{Cu}_2(\text{OH})_3\text{NO}_3$. DTGA analysis of the dried $\text{Cu}(\text{NO}_3)_2$ -water complex, shown in Figure 1, indicates that the temperature for maximal denitration/dehydration of the $\text{Cu}(\text{NO}_3)_2$ is 265°C . All thermal analysis measurements were done in oxygen atmospheres. It appears that between 10° and 210°C residual water is driven from the film residue. A very sharp transition is observed between 210°C and 310°C which is attributed to the denitration/dehydration of $\text{Cu}_2(\text{OH})_3\text{NO}_3$. The 33.7% percentage weight change between 210°C and 1010°C agrees

favorably with the formation of CuO from $\text{Cu}_2(\text{OH})_3\text{NO}_3$, on the basis of the following fractional weight percents:

	$\text{Cu}_2(\text{OH})_3\text{NO}_3$	\longrightarrow	CuO	+	oxides of nitrogen.
fractional wt%	100%		66.2%		33.8%

The chemical stability of CuO in oxygen at higher temperatures is evident.

b. Thermal Denitration/Decomposition of $\text{Ca}(\text{NO}_3)_2$ in Water Solution.

Analysis on $\text{Ca}(\text{NO}_3)_2$, (see Figure 2), shows dehydration below 200° C, and a percentage weight change of 66.1% between 400° C and 750° C. Unlike the cuprous reaction, a series of weaker outgassing peaks are observed in the first derivative spectra prior to a very pronounced rate of weight loss at 733° C. This data agrees quite favorably with the formation CaO through the following path:

	$\text{Ca}(\text{NO}_3)_2$	\longrightarrow	CaO	+	oxides of nitrogen
fractional wt%	100%		34.16%		65.84%.

CaO appears to be stable in oxygen above 740° C, after denitration.

c. Thermal Denitration/Decomposition of $\text{Ba}(\text{NO}_3)_2$ in Water Solution.

The barium nitrates, $\text{Ba}(\text{NO}_3)_2$, are the most stable of the starting compounds. (See Figure 3). First derivative spectra indicates pyrolytic phenomena starts above 600° C. A stable regime is noted between 800° and 900° C. This stability breaks down above 900° C, but first derivative spectra shows the film tends towards stability again above 1010° C. The percentage weight change between room temperature and 1010° is 40.4%, which is close to the fractional weight which would be lost in the formation of BaO:

	$\text{Ba}(\text{NO}_3)_2$	\longrightarrow	BaO	+	oxides of nitrogen
fractional wt%	100%		58.65%		41.35%

The stable oxynitrate phase observed in the $\text{Ba}(\text{NO}_3)_2$ derivative between 800° and 900° C can not be identified at this time. The $\text{Ba}(\text{NO}_3)_2$ DTGA data suggests that unless the presence of the other nitrates, $(\text{Cu}(\text{NO}_3)_2$ and its derivatives, or $\text{Ca}(\text{NO}_3)_2$), can accelerate conversion of $\text{Ba}(\text{NO}_3)_2$ to BaO at lower temperatures, annealing above 1000 C will be required to completely denitrate the BaCaCuO precursor films.

2. Effects of Solvents and Chemical Binders on Nitrate Denitration/Decomposition in Mixed Precursor Solutions.

To study identify optimal solution chemistry and chemical binder activity the nitrate precursors were mixed in stoichiometric ratios of 2:1:2 Ba:Ca:Cu and dissolved in:

- A) A water-only solution
- B) An ethanol-(20% vol)/water solution
- C) A glycerol-(20% vol)/water solution

Each solution was dried on a hot (120° to 230° C depending on solvent volatility) alumina substrate. DTGA scans were run to observe effects of the solvents and the other nitrates on chemical reactivity during denitration. Ethanol solutions were considered to reduce

Ba(NO₃)₂ precipitation from solution. Glycerol solutions were considered to reduce single nitrate species agglomerations in solution and to enhance the chemical reactivity between the different nitrate compounds. The glycerol molecule provides a longer chain with hydrogen bonding sites which could conceivably complex different nitrate species in close physical proximity to one another.

The fractional chemical weight distributions for solutions tested were determined using a 212 ratio:

	Ba(NO ₃) ₂	Ca(NO ₃) ₂	Cu(NO ₃) ₂
Ratio	2	1	2
wt%	49.12%	15.49%	35.39%.

a. The Effect of a Water-only Solvent.

Figure 4 shows DTGA spectra for the nitrates when dissolved in water only. Thermogravimetric changes below 200° C are being attributed to water absorbed in the nitrate film by exposure to air. Copper denitration proceeds as before, unaffected by the presence of the other nitrate complexes. Its characteristic spectra in the first derivative is once again observed at 265° C. The percentage weight change observed between 228° C and 369° C was roughly 11%, and is attributed to copper denitration. This is in general agreement with an 11.9% weight differential that would be expected using the fractional weight percentage change observed during Cu₂(OH)₃NO₃ denitration/dehydration between 220° C and 300° C.

In mixed-water solutions Ca(NO₃)₂ and Ba(NO₃)₂ denitration appears to be shifted to lower temperatures. Principal first derivative spectra for the denitration transitions are observed between 375° C and 700° C. This is in rough agreement with the Ca(NO₃)₂ spectra, but is contrary to the findings for Ba(NO₃)₂. It appears as though Ca(NO₃)₂ and Ba(NO₃)₂ denitration is accelerated by each other's presence or by the copper oxides in the films. It is also plausible that Ca(NO₃)₂ and Ba(NO₃)₂ complex together in aqueous solutions. Calculations of the fractional weight percent changes using the individual denitration data predicts a total percentage weight change of 57.56%, in rough agreement with the 54.35% weight change observed in the mixed films. It seems reasonable to assume that in water-only solvents most denitration should be complete above temperatures of 700° C.

b. The Effect of a Water-20% vol Ethanol Solvent.

Figure 5 shows DTGA spectra from the 20%-vol ethanol solution. Spectral signatures in the 0th and 1st derivative spectra are identical, indicating Cu₂(OH)₃NO₃ denitration again proceeds unaffected by the presence of either Ca(NO₃)₂ or Ba(NO₃)₂ in ethanol solvents. An analytical comparison was not possible.

Figure 6 shows the Differential Scanning Calorimetry (DSC) measurements in oxygen on the dried residue of the precursors mixed in water and 20% vol ethanol solution. Strong endothermic peaks are noticeable at temperatures just below outgassing temperatures identified by DTGA. (See Figure 5). This suggests that the individual nitrates are breaking apart seemingly unaffected by each other's presence. The lack of any exothermic peaks in the spectra shows that no latent heats of crystal fusion are being released. Although the use of ethanol may help dissolve Ba(NO₃)₂ and prevent its precipitation from solution, it does not promote the formation of fused crystal microstructures.

Furthermore, the addition of ethanol to the solution reduces the liquid surface tension to such a degree that boiling during the drying process caused liquid drops carrying raw materials powders to spew from the substrate. Ethanol experimentation was discontinued at this point because of the adverse effects splattering would have on stoichiometric control.

c. The Effect of a Water-20% Glycerol Solvent.

Experimentation with glycerol solutions was conducted to try to improve film uniformity. Since glycerol is a chain molecule with many hydrogen bonding sites the individual nitrate species have a better chance of being physically complexed closer to each other if they bind at different sites along the chain. It is intended that the close physical proximity of the individual nitrate species provided by the glycerol chain would improve uniformity, inhibit single species clustering, and enhance the formation of BaCaCuO crystallites. Stoichiometric formation of BaCaCuO crystallites is preferred to CuO crystallites segregated from CaO/BaO polymorphous phases. This will help ensure chemical integrity during subsequent processing and single phase formation during thallium diffusion.

Figure 7 shows that the qualitative character of glycerol-complexed BaCaCu-denitration in oxygen changes substantially. DTGA spectra below 182° C, (the boiling point of glycerol) is due primarily to dehydration. Spectra between 182° C and 250° C is attributed to glycerol outgassing. The most notable feature of this spectra is that $\text{Cu}_2(\text{OH})_3\text{NO}_3$, if it is at all present in the glycerol residue, no longer denitrates by itself. Furthermore, the largest relative change in weight occurs below 500° C. The weight change between 250° and 500° C accounts for roughly 67% of all outgassing above 250° C. This indicates that $\text{Ca}(\text{NO}_3)_2$ and $\text{Ba}(\text{NO}_3)_2$ denitration participates in the copper oxide conversions and that BaCaCu complexes are being formed in solution. Roughly one third of the relative weight change occurs above 500° which can be solely attributed to $\text{Ca}(\text{NO}_3)_2$ and $\text{Ba}(\text{NO}_3)_2$ (complexed) denitration. This data also shows that the microcrystallites formed with a glycerol binder are relatively stable in oxygen at temperatures up to $\approx 900^\circ\text{C}$. Changes in the first derivative spectra above 900° C suggest that the compound could break down at elevated temperature.

Figure 8 shows DSC spectra under oxygen atmospheres for the mixed precursors formed in water/glycerol solvents. Three exothermic peaks are evident at 204° C, $\approx 300^\circ\text{C}$, and 341° C. This data, and the marked change in the DTGA spectra for glycerol solutions is direct evidence that the glycerol molecule chemically binds the individual metallic nitrate precursors, promotes reactivity between the precursors and the formation of microstructural crystallites in the sprayed films after thermal processing. An unusual feature of this spectra is that structural relaxation is not observed at temperatures slightly below the principal outgassing band between 250° and 500° C.

3. Effect of Substrate Temperature on Film Deposition

In chemical spray pyrolysis substrate temperature can affect both surface morphology and film stoichiometry. Thermal mass transfer, convection currents, vapor phase dynamics or evaporative effects and secondary chemical reactions can adversely affect chemical incorporation rates into the films. The thermodynamics of this deposition technique has not yet been fully characterized so process control has to be obtained through empirical study uniquely. To identify suitable substrate temperatures chemical incorporation was studied by spraying 223 BaCaCu-nitrate ratios dissolved in all three solvents at substrate temperatures between 180° and 350° C.

Energy Dispersive X-ray Spectroscopy was performed on the films to evaluate atomic ratios. Figure 9 shows the atomic Ca/Cu and Ba/Cu ratios observed in the films sprayed using an ethanol 20%-vol solvent versus substrate temperature. The Ca/Cu and

Ba/Cu ratios used in solution are also shown. By simple inspection it is apparent that during the spray process both Ca and Cu are not fully incorporated since the Ba/Cu film ratio is always greater than the solution ratio and the Ca/Cu film ratio is always less than the solution ratio.

Figure 10 shows copper and calcium incorporation rates against substrate temperature between 180° and 350° C. Incorporation rates were calculated assuming $\text{Ba}(\text{NO}_3)_2$ is incorporated at 100%. Under this assumption a system of three linearly coupled equations can be constructed for which there are two unknowns. Percentages of Ca and Cu lost can be calculated against Ba incorporation using the ratio of each in the solution. The accuracy of the calculation can be tested by comparing the ratio of Ca/Cu in the films to value obtained through calculation. Figure 11 shows the percentage differences between the calculated and observed values.

A very sharp increase in the copper incorporation and an enhancement in the calcium incorporation was observed at 260° C. This matches the peak denitration temperature for $\text{Cu}(\text{NO}_3)_2$. This would appear to suggest that film incorporation rates for the metallic cations can be quite sensitive to oxidizing conditions and mass transfer phenomena at the substrate surface.

Since substrate temperature has such a strong influence on the resultant stoichiometry in the hydroxynitrate films a hot plate was constructed to control substrate temperature to within 1° C. This construction employs an Omega(TM) Series 2000 Programmable Temperature Controller capable of ramp and soak temperature cycling.

Films prepared from glycerol 20%-vol solvents were far less susceptible to surface reactivity. Scanning Electron Microscopy (SEM) revealed that a 260° C substrate temperature provided the best surface morphologies. Plates 1-3 show surface characteristics of films prepared using water-only, ethanol (20% vol), and glycerol (20% vol) at that substrate temperature. Both the ethanol and water-only films show signs of single species agglomeration as indicated by the DTGA spectra. Although the films prepared with glycerol had the best submicron microstructures, (See Plate 4), they remained quite porous, (Plate 5), with a high density of weak link interconnections between grain granules.

Continued research using glycerol (20% vol)/water solvents sprayed onto substrates heated to 260° C has shown that solution stoichiometries can be reproduced in the films. Table I shows atomic percents measured in a series of films using semiquantitative Energy Dispersive X-Ray Spectroscopic analysis, by Photometrics, Inc., Woburn, MA.. These results indicate that a strong correlation between solution and film stoichiometries can be achieved using these process parameters. Plate 6 is a backscattered scanning electron micrograph of sample 223-02. Good chemical uniformity and small microstructures can be formed using these process conditions.

B. EFFECT OF SUBSTRATES ON THE QUALITY OF ANNEALED FILMS.

Precursor films were prepared on <100> oriented epitaxially polished yttrium-stabilized zirconia (YSZ) and magnesium-oxide substrates. After spraying at a substrate temperature of 260° C in air the films were immediately denitrated by thermal bake out using a temperature cycle determined from thermal analysis measurements.

In both instances microcracking was observed in the oxide precursors. This is a shortcoming to any solution process where the films essentially have to be dried from a slurry and large volumes of reactant by-product is driven from their interior. This results in a generally porous texture. Films sprayed onto YSZ substrate had very poor adhesion to the substrate after the denitration process, and were not suitable for Ti-diffusion. (See Plate 5).

Most of the YSZ-substrate films were damaged during the diffusion step either by film evaporation or flaking.

Films deposited onto MgO substrates had sharply reduced microcrack densities and far superior adhesion. The MgO substrate films did indeed become superconducting after Tl-diffusion when suitable processing parameters were used. No increased microcracking was observed even after electrical characterization in liquid nitrogen. These results suggest very strong suitability of MgO substrates with Tl-Ba-Ca-Cu-O superconducting films prepared using solution processes over a range of temperature from 77 K to 1225 K.

C. THALLIUM DIFFUSION PROCESSING.

The superconductive Tl-Ba-Ca-Cu-O phase is formed from the Ba-Ca-Cu-O precursor by diffusing thallium into the film. This can be done with a pellet of thallium oxide in a small porcelain crucible. The pellet is of sufficient size so that it does not totally evaporate during the short annealing step. The substrate containing the precursor films is suspended over the crucible and the assembly is placed in a quartz tube furnace at 850° C for 15 minutes. During the process, argon, air, oxygen, or a mixture of gasses are flowed over the sample. Only oxygen atmospheres were successful in preventing the sprayed precursor films from evaporating off of the substrate. The gas flow rate is adjusted empirically to optimize the oxygen content of the resulting film and to maintain sufficient oxygen overpressures above the films.

D. ELECTRICAL PROPERTIES OF THE SUPERCONDUCTING FILMS.

Figure 12 shows the R-T curve for the first superconducting sample obtained. The transition is sharp and the zero-resistance temperature is 112 K. While this is not the highest temperature reached by the thallium containing superconductors, it exceeds the highest reported value for sprayed films by 15 K. [3] In all five superconducting films were produced with zero resistance temperatures ranging between 97 K and 112 K.

Preliminary measurements of critical currents at 77 K in these spray pyrolyzed films range between 100 and 250 A/cm². These values are low for high-field magnet applications and result in major part from the porosity of the films, excessive weak link interconnections, poor grain alignment, and nonuniform crystallographic orientation. Many of these deficiencies can be reduced by finer tuning the process.

E. CRYSTALLOGRAPHIC ORIENTATION OF THE CERAMIC.

An important consideration if the construction of useful magnets is the orientation of the material in the films used. To obtain high critical currents needed for high fields, the crystal grains in polycrystalline films should be oriented with the c-axis perpendicular to the substrate so that the current flows in the a-b plane. Thus, it was important for us to determine whether or not films could be deposited with a preferential orientation. After processing, we analyzed our films using XRD and determined that the films grew with the c-axis perpendicular to the substrate surface.

Table II compares the x-ray diffraction patterns of Tl-Ba-Ca-Cu-O bulk powders to an epitaxial thin film prepared by rf-sputtering and the T_c = 112 K film prepared by chemical spray pyrolysis and thallium diffusion. The epitaxial film has total c-axis orientation in the plane of the substrate, and the powder diffraction has completely random orientations. The c-axis oriented patterns are highlighted and the normalized peak intensities are given to show preferential c-axis orientation in the plane of the substrate for the spray pyrolyzed film.

F. SILVER-DOPING EXPERIMENTATION.

Silver doping into the precursor films can be easily achieved using silver nitrate, $\text{Ag}(\text{NO}_3)_2$, which dissolves readily into water. Silver incorporation into the Y-Ba-Cu-O has been shown to greatly enhance critical current densities, ductility and other mechanical properties. For these reasons the feasibility of silver-doping by chemical spray pyrolysis was examined in Phase I.

Three silver-doped films (10%-, 20%-, and 30%-wt) were prepared and each showed negligible microcrack densities after denitration baking, regardless of the substrate used, i.e., YSZ or MgO. Unfortunately in an attempt to phase separate the Ba-Ca-Cu-O precursor from the silver, by annealing at 1000 C, the silver-doped films evaporated. An undoped film was annealed at the same time and it did not completely evaporate which suggests that silver incorporation into the Ba-Ca-Cu-O precursor increases the vapor pressure of the compound.

III. PLANS FOR FUTURE DEVELOPMENT.

The successful demonstration of a deposition process for high- T_c superconducting films which can be applied to the preparation of large-area thick films has now made it possible to consider the manufacture of liquid nitrogen-cooled superconducting wire tape. A cross-section of a prototype design for this construction is given in Figure 13. As diagrammed, a stainless steel strength member copper tape will be used as the base structure. Spray pyrolyzed MgO film will be deposited upon it to provide good adhesion between the superconductor and the support structure. Researchers at the Naval Research Laboratories, Washington, D.C., have successfully demonstrated that spray pyrolysis can be used to deposit 100 oriented MgO films on sapphire, fused silica, and silicon. [4]

Silver-doped TlBaCaCuO films will be sprayed through a mask to form tracks on the MgO-coated base tape. The use of silver is being considered to improve the ceramic's ductility and mechanical workability, [5], as well as to enhance the material's current carrying capability. [6] Applying the superconductor in the wire as tracks should also reduce A.C. losses and improve thermal and electrical shunting of the stored energies and stresses which develop in the films and can quench a superconducting magnetic coil. A silver layer will overlay the superconductor to improve conduction to the copper shunt, and an insulating tape will cap the tape to inhibit high-voltage electrical discharging between windings when the tape is assembled into an operating coil. This design is being considered because it provides sufficient structural support to the mechanical stresses expected from 5-6 Tesla magnetic fields.

A major objective in the successful demonstration of a high-field magnet will be the development of strong flux pinning potentials in the superconducting films. It will be necessary to pin magnetic fluxoids at defect sites with sufficient strength to resist the Lorentz forces induced by the driving currents. The free movement of fluxoids in the superconducting wire tape will dissipate energy and pinch-off critical current densities needed to operate in strong magnetic fields. The value of critical current densities in all type-II superconductors is strongly affected by processing parameters and is not necessarily an intrinsic property of the superconducting system. To achieve this aim significant research will be dedicated to optimizing c-axis orientation of the films by adjusting deposition parameters, and using other salt reactants or chemical binders in fabricating the precursor films. The application of nuclear irradiation [7] and mechanical shock compression [8] can improve flux pinning potentials and will be evaluated in this development as well.

Finally, once large area films have been deposited onto the tape structure which have suitable electrical properties, the spatial characteristics of currents flowing in these films under applied magnetic fields will be measured. These measurements will be crucial to the

determination of the optimal topological surface structure for the high-field magnet. This work will be done with the MIT Francis Bitter National Magnet Laboratory in Cambridge, MA. Once these properties have been assessed, a coil utilizing the wire tape in a pancake, Bitter coil, or hybrid pancake-Bitter coil geometry will be designed to generate a 5-6 Tesla field and tested.

Acknowledgments

The authors are grateful for the contributions made to this paper by Dr. John E.C. Williams and Robert Weggel from the MIT Francis Bitter National Magnet Laboratory, Cambridge, MA.

References

- [1] Kang, J.H., Gray, K.E., Kampworth, R.T., and Day, D.W., *Large anisotropy in the upper critical field of sputtered thin films of superconducting Tl-Ba-Ca-Cu-O*, Appl. Phys. Lett., **53**(25), 2562 (1988).
- [2] Phase II Proposal, Contract #NAS1-19012, National Aeronautics and Space Administration, NASA Langley Research Center, Hampton, VA 23665-5225.
- [3] Barboux, P. Tarascon, J.M., Shokoohi, F., Wilkens, B.J., and Schwartz, C.L., *Thick Films by Solution Processes*, J. Appl. Phys. Lett., **64**, 6382 (1988).
- [4] DeSisto, W.J., and Henry, R.L., *Deposition of (100) oriented MgO films on sapphire by a spray pyrolysis method*, Appl. Phys. Lett., **56**, 2522 (1990).
- [5] Miller, J., Jr., Holder, S.L., and Hunn, J.D., *Improvement of YBa₂Cu₃O_{7-x} Thick films by Doping with Silver*, Appl. Phys. Lett., **54**(22), (1989).
- [6] Dwir, B., Affronte, M., and Pavuna, D., *Evidence for enhancement of critical current by intergrain Ag in YBaCuO-Ag ceramics*, Appl. Phys. Lett., **55**(4), 399 (1989).
- [7] van Dover, R.B., Gyorgy, E.M., White, A.E., Schneemeyer, L.F., Felder, R.J., and Waszczak, J.V., *Critical currents in proton-irradiated single-crystal Ba₂YCu₃O_{7-d}*, Appl. Phys. Lett., **56**(26), 2661 (1990).
- [8] Weir, S.T., Nellis, W.J., Kramer, M.J., Seaman, C.L., Early, E.A., and Maple, M.B., *Increase in the flux-pinning energy of YBa₂Cu₃O_{7-d} by shock compression*, Appl. Phys. Lett., **56**(14), 2042 (1990).

TABLE I

SAMPLE I.D.	DESIRED ATOMIC PERCENTAGES			MEASURED ATOMIC PERCENTAGES			SURFACE UNI- FORMITY
	Ba	Ca	Cu	Ba	Ca	Cu	
223-02	28.57	28.57	42.86	30%±2	28%±2	42%±2	GOOD
233-02	25.00	37.50	37.50	28%±2	41%±2	30%±2	POOR
243-01	22.22	44.44	33.33	22%±1	46%±2	32%±2	GOOD
253-02	20.00	50.00	30.00	20%±1	48%±2	32%±2	GOOD
224-02	25.00	25.00	50.00	29%±2	29%±2	41%±2	POOR
225-01	22.22	22.22	55.56	26%±2	25%±2	48%±2	POOR

Table I. Stoichiometric control achieved by spraying nitrate precursors dissolved in water and 20%-vol glycerol on substrates heated to 260 C.

Table II-XRD orientation

POWDER (hkl) I/Io	PYROLYSIS (hkl) I/Io	RF SPUTTERING (hkl) I/Io
002/5	002/2	002/9
	004/2	004/5
006/5	006/4	006/8
		008/4
	103/5	
	105/1	
0010/9	0010/8	0010/9
107/87	107/3	
	110/2	
200/100		
118/14		
119/5		
205/5		
	0012/100	0012/100
210/17		
212/10		
214/8		
220/47		
	1011/1	
	200/2	
	1112/1	
300/18		
	215/1	
	0018/25	0018/18
316/14		

X-ray diffraction patterns for $Tl_2CaBa_2Cu_2$. The preferential orientations of a spray pyrolyzed film prepared during Phase I is compared to those of an epitaxial rf-sputtered film, (Yolchikawa, et al., Appl. Phys., July 18, 1988), and to the random orientations of a powder sample, (Hermann, PHYS. REV. LETT., Vol. 60, No. 16, 1988).

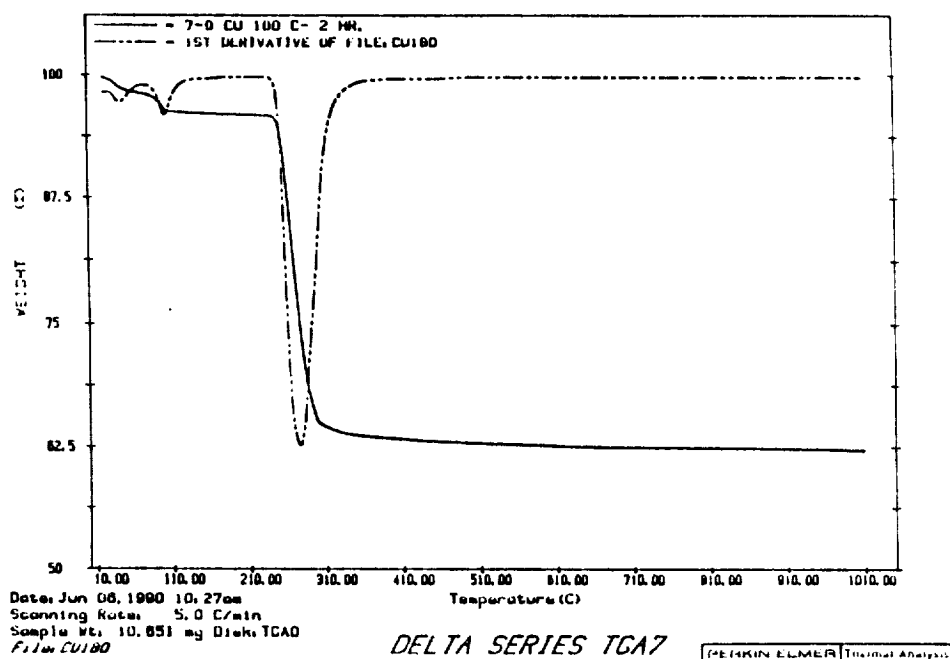


Figure 1. DTGA spectra of $\text{Cu}_2(\text{OH})_3\text{NO}_3$ -the residue of aqueous $\text{Cu}(\text{NO}_3)_2$ dried at 170 C.

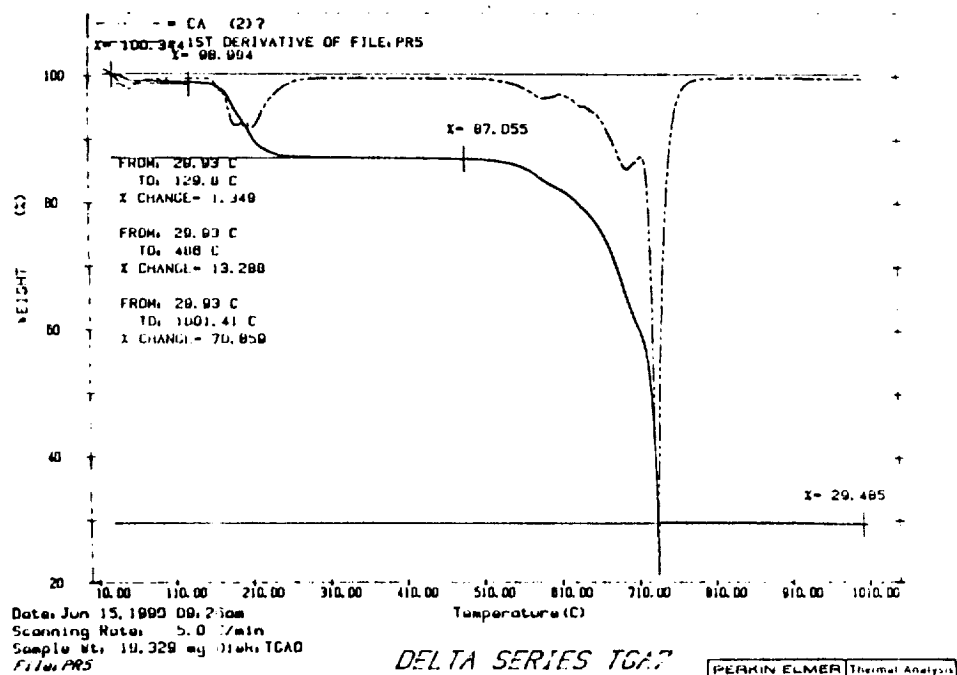


Figure 2. DTGA spectra of aqueous $\text{Ca}(\text{NO}_3)_2$ dried at 170 C.

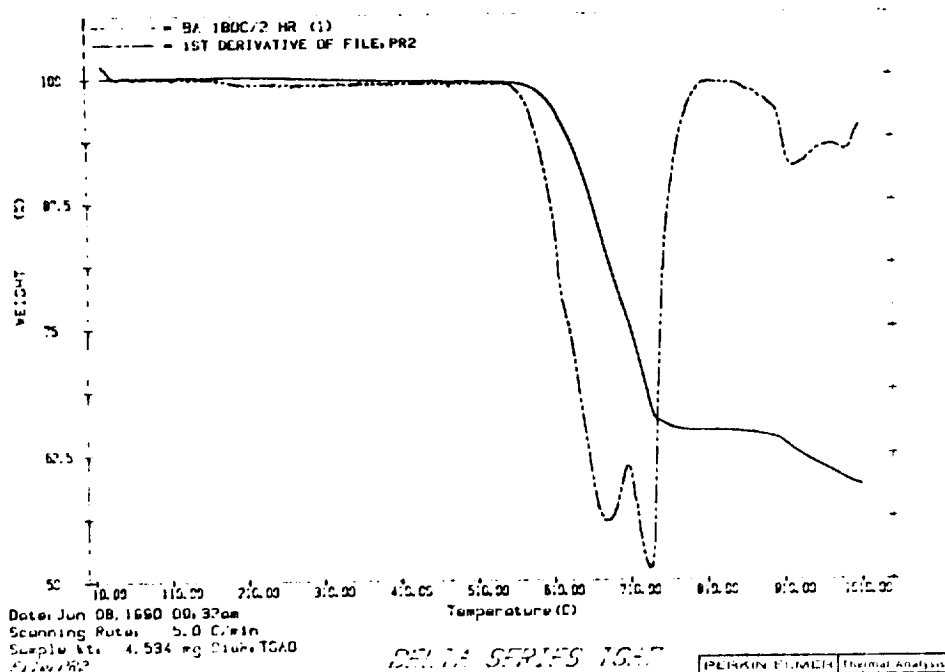


Figure 3. DTGA spectra of aqueous $\text{Ba}(\text{NO}_3)_2$ dried at 170 C.

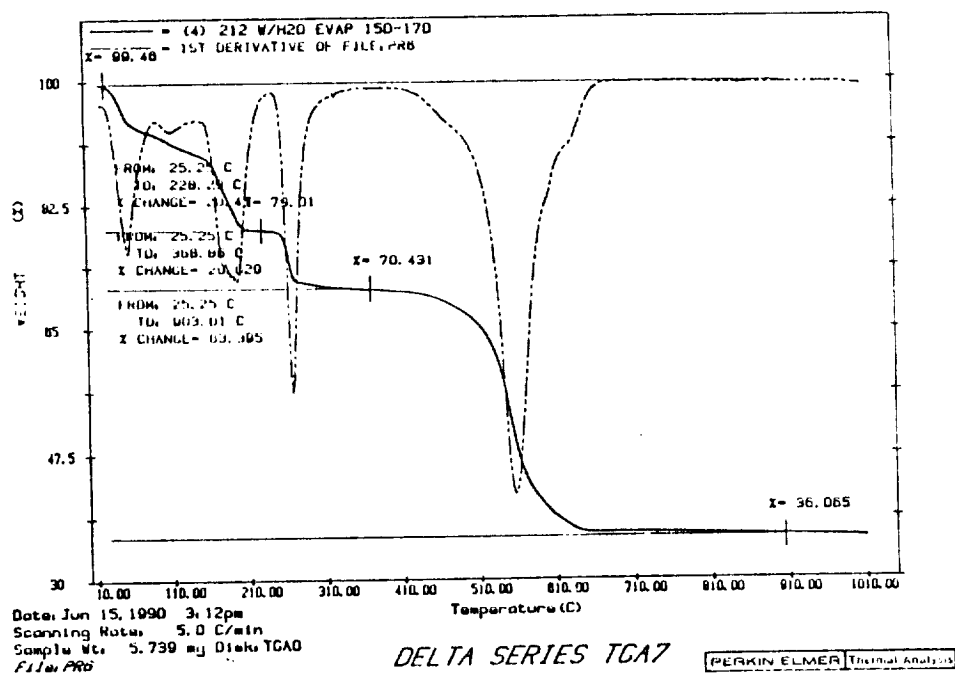


Figure 4. DTGA spectra of mixed 212-Ba-Ca-Cu hydroxynitrates dissolved in water only and dried at 170°C in air.

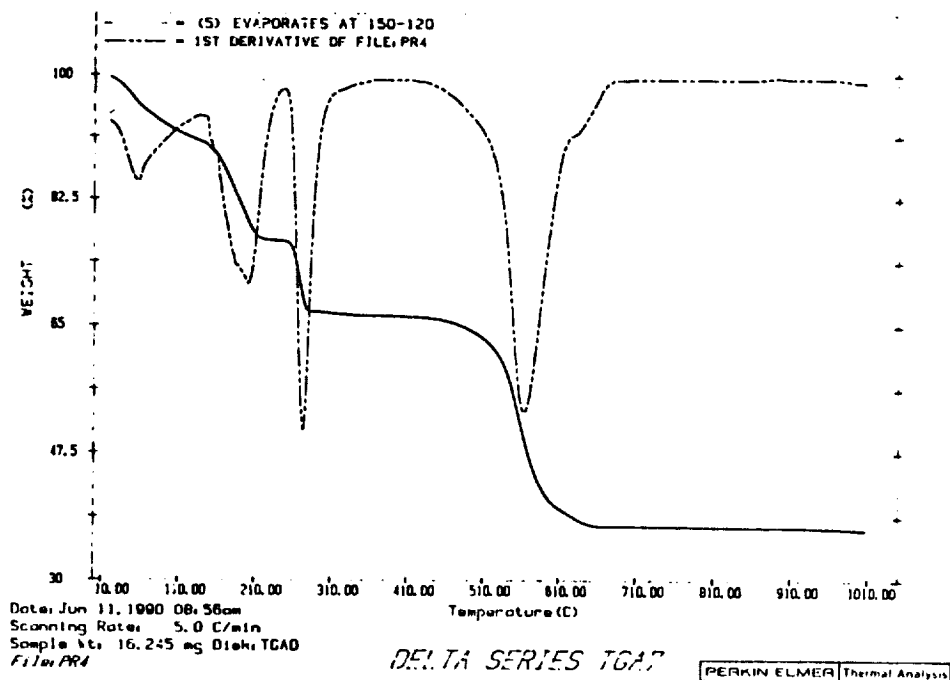


Figure 5. DTGA spectra of mixed 2:1:2-Ba-Ca-Cu hydroxynitrates dissolved in water and ethanol (20% vol) and dried at 120 C in air.

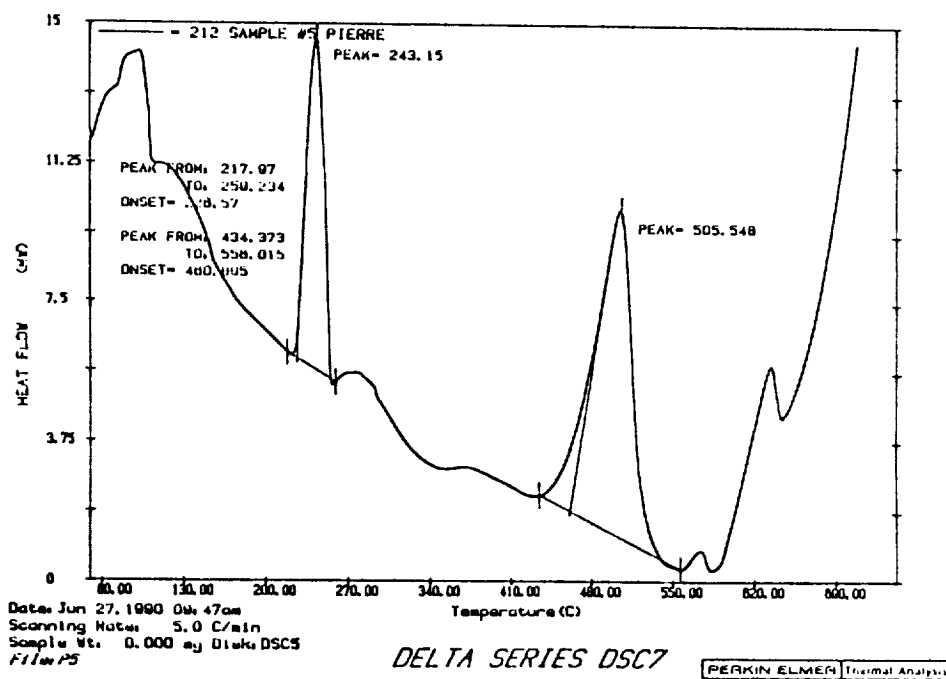


Figure 6. DSC measurement of 2-1-2-Ba-Ca-Cu hydroxynitrate residue mixed in water and 20%-vol ethanol solution in an oxygen atmosphere.

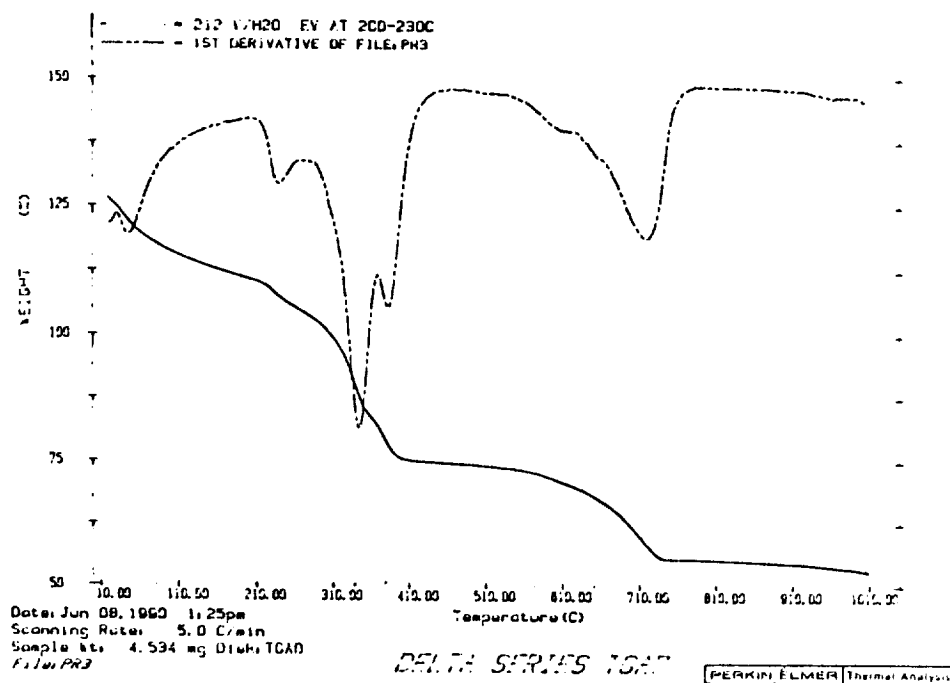


Figure 7. DTGA spectra of mixed 212-BaCaCu hydroxynitrates dissolved in water and glycerol (20% vol) and dried at 210-230 °C.

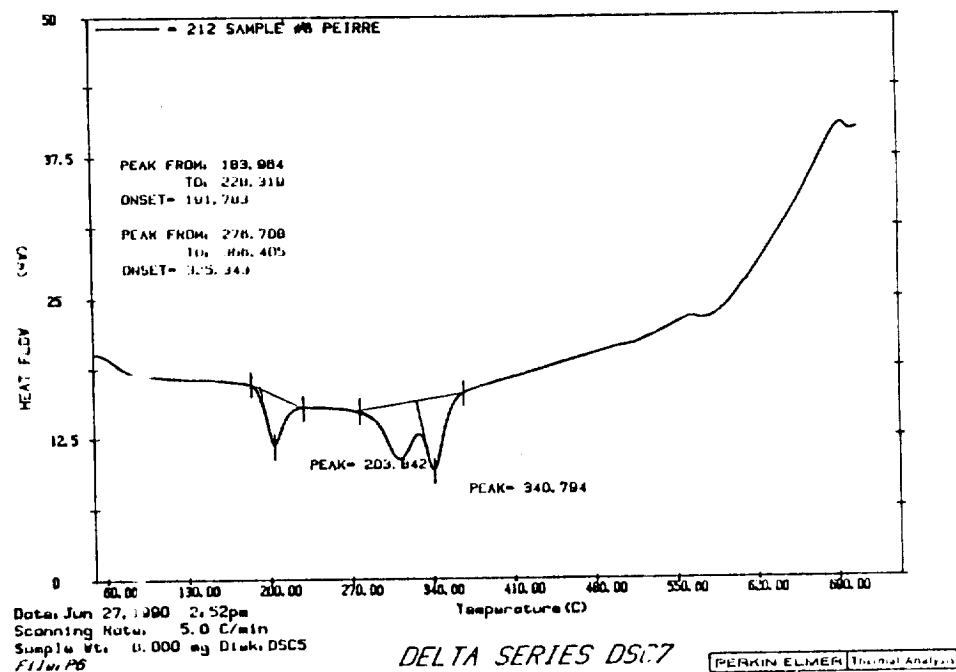


Figure 8. DSC measurement of 2-1-2-Ba-Ca-Cu nitrate residue mixed in water and 20%-vol glycerol solution in an oxygen atmosphere.

Cu/Cu and Ba/Cu Ratios in Film and Solution versus Substrate Temperature

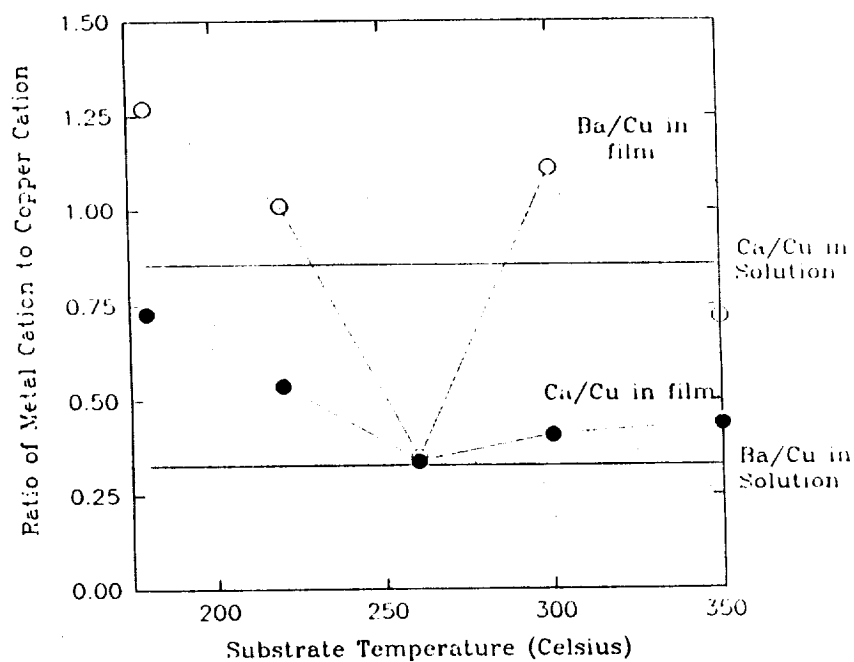


Figure 9. Ba/Cu and Ca/Cu atomic ratios in films sprayed from mixed BaCaCu nitrates dissolved in water and ethanol (20%vol) versus substrate temperature. Ba/Cu and Ca/Cu atomic ratios in solution are marked by the solid lines.

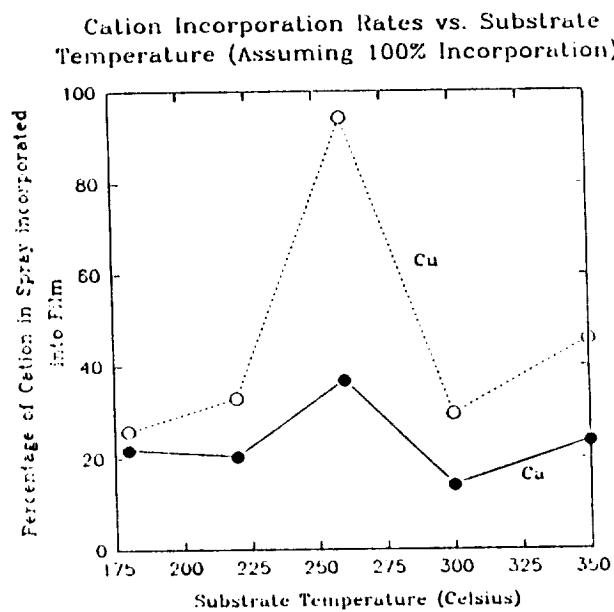


Figure 10. Percent incorporation rates for Ca and Cu sprayed from mixed BaCaCu nitrates dissolved in water and ethanol (20% vol) versus substrate temperature. (Calculated assuming 100% Ba incorporation over substrate temperatures).

Discrepancy between Measured and Calculated Ca/Cu Ratios Assuming 100% Ba Incorporation and Calculated Ca and Cu Incorporation Rates

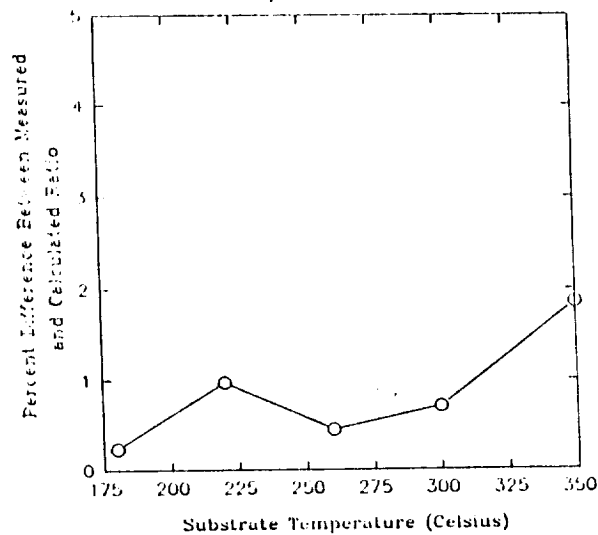


Figure 11. Percentage deviation between Ca/Cu ratios measured in films and Ca/Cu ratios calculated from Ca and Cu loss estimates assuming 100% Ba film incorporation.

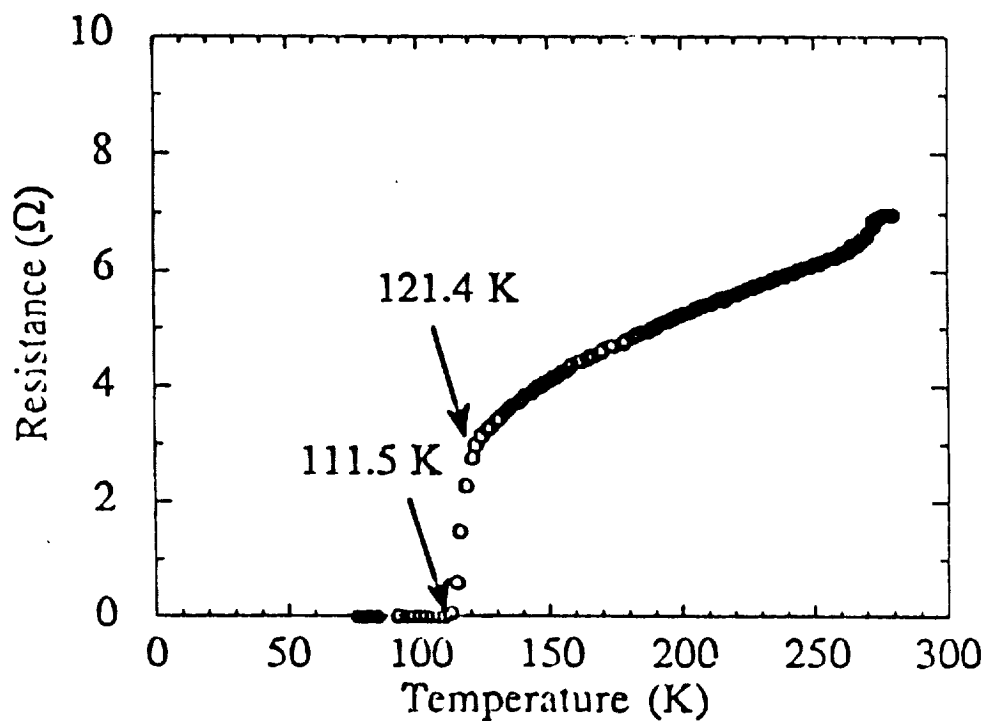


Figure 12. R-T curve for Tl-Ba-Ca-Cu-O superconductor prepared by spray pyrolyzing a Ba-Ca-Cu-O precursor film and thallium diffusion to form the superconductive phase.

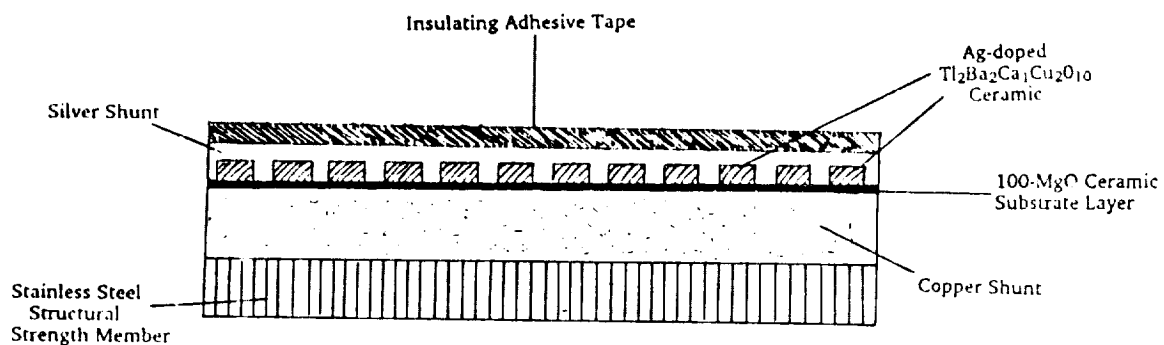


Figure 13. Cross-section of the prototype design of Tl-Ba-Ca-Cu-O wire tape for use in a superconducting magnetic coil. (Not drawn to scale).

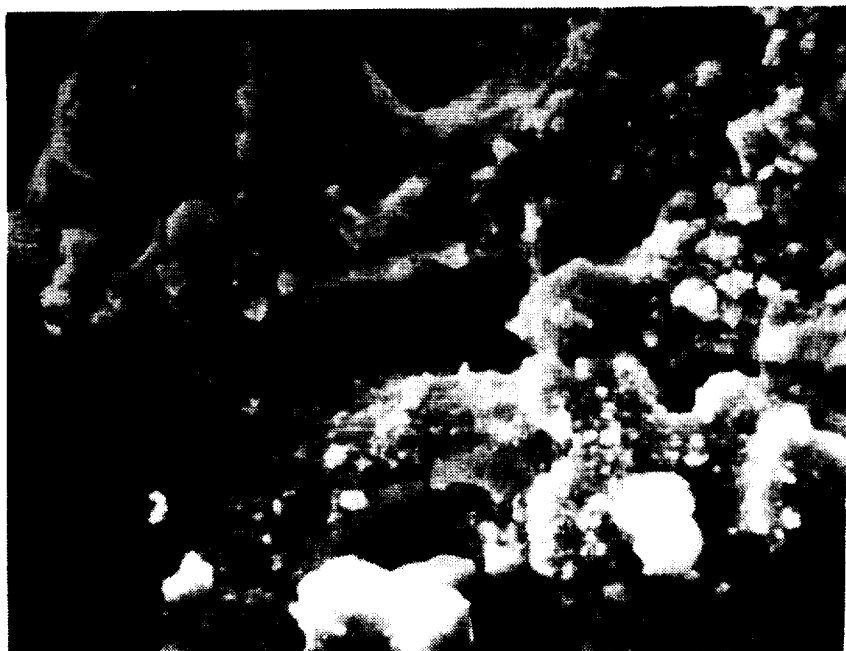


Plate 1. SEM micrograph of a spray pyrolyzed Ba-Ca-Cu-O precursor prepared using a water-only solution. (Magnification 1250 X).

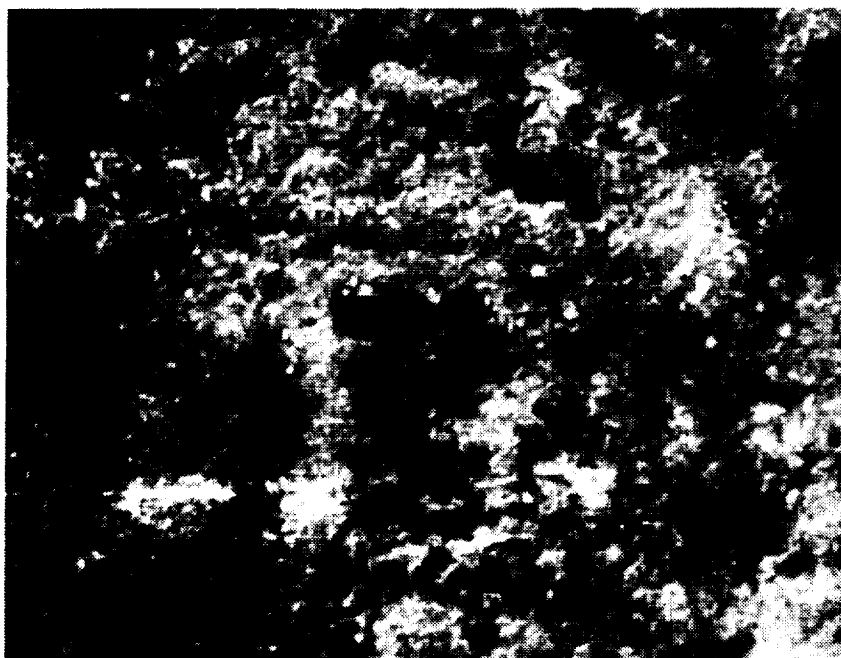


Plate 2. SEM micrograph of a spray pyrolyzed Ba-Ca-Cu-O precursor prepared using a 20%-vol ethanol/water solution. (Magnification 1250 X).

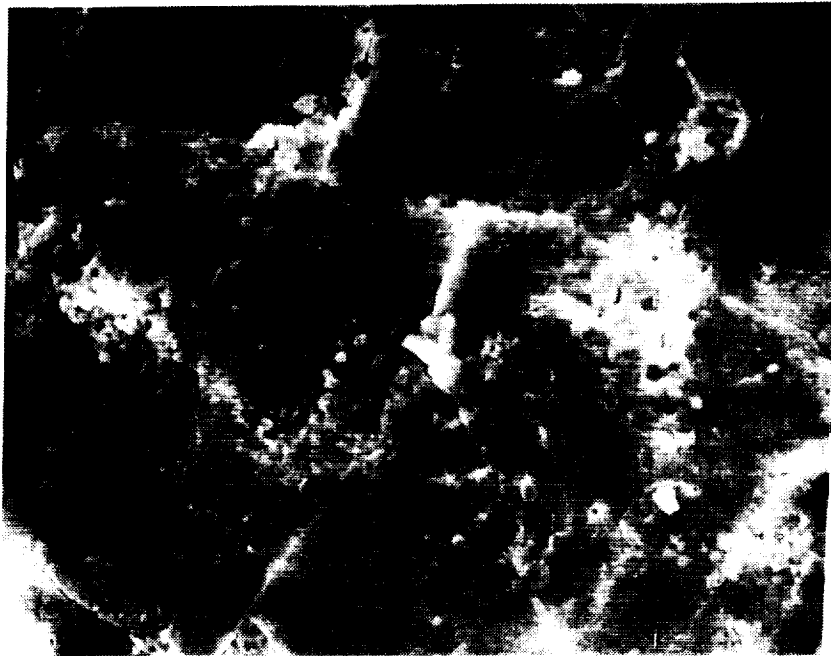


Plate 3. SEM micrograph of a spray pyrolyzed Ba-Ca-Cu-O precursor prepared using a 20%-vol glycerol/water solution. (Magnification 1250 X).

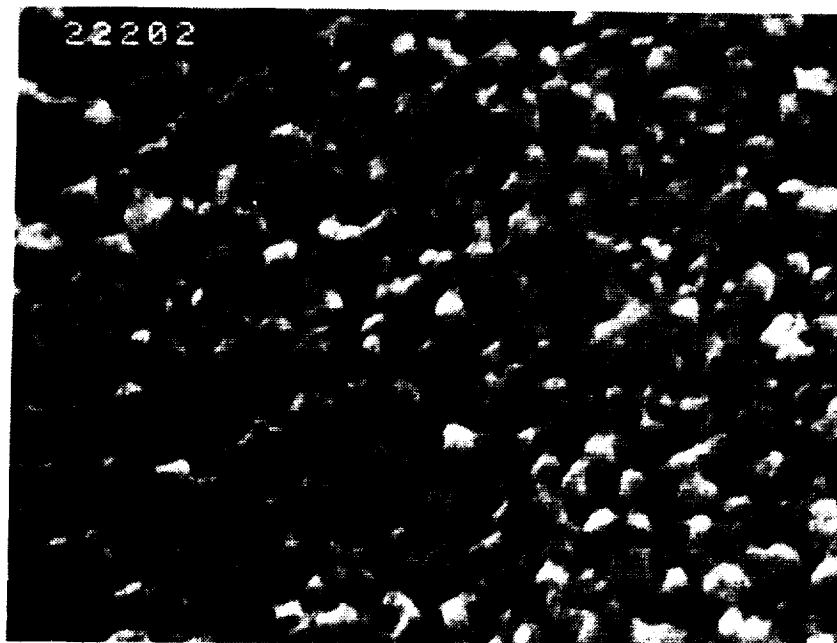


Plate 4. SEM micrograph of the submicron microstructure of the grain granules in a spray pyrolyzed Ba-Ca-Cu-O precursor film prepared using a 20%-vol glycerol/water solution. Weak links connecting granules limit high critical current densities. (Magnification 12.9K X).



Plate 5. SEM micrograph of a crack in a Ba-Ca-Cu-O precursor film lifting off from a yttrium-stabilized zirconia substrate reveals the porosity of the preliminary films. The high density of weak links in the films will have to be reduced to obtain reasonable critical current densities. (Magnification 3.01K X).



Plate 6. Backscattered electron SEM micrograph showing the baseline chemical uniformity of the Ba-Ca-Cu-O precursor film prepared using a 20%-vol glycerol/water solution. (Magnification 321 X).

PANEL DISCUSSION with audience participation -
APPLICATIONS of SUPERCONDUCTIVITY

Chairman - Dantam K. Rao
Mechanical Technology Incorporated
968 Albany-Shaker Road, Latham, NY 12110

Panel Members - Gerald V. Brown
NASA Lewis Research Center
Mail Stop 23-3, Cleveland, OH 44135

Moustafa K. Abdelsalam
Madison Magnetics Incorporated
216 Walnut Street, Madison, WI 53705

David B. Eisenhaure
SatCon Technology Corporation
12 Emily Street, Cambridge, MA 02139-4507

Warren C. Kelliher
NASA Langley Research Center
Mail Stop 416A, Hampton, VA 23665-5225

Dantam Rao

The purpose of this session is to explore the interest of the magnetic bearing community in applying superconductors to magnetic suspension systems and to discuss the issues related to these applications. As most of you probably know, superconductors have good potential, at least theoretically; the current density of superconductors is an order of magnitude or a couple of orders of magnitude higher than the current density of copper. Typical values are about 10 Amps per square millimeter versus about 100 Amps per square millimeter and flux densities are also fairly high. The flux density of copper as used in magnetic bearings is limited by iron to about 2.3 Tesla compared to the flux density of superconductors which could be demonstrated up to about 20 Tesla for short samples but typically about 5 Tesla normally. So this theoretical potential could be translated into some practical applications to improve performance. I think that this is the particular motivation for this session. We have a panel that consists of people who I suppose most of you know. On the right side we have Gerry Brown from NASA Lewis who was in the superconductivity area about 30 years back dealing with superconducting magnets and Dr. Abdelsalam from Madison Magnetics who has been working for the past 10 years on MSBS and associated systems and on the left side we have Dr. Warren Kelliher from NASA Langley who is working in the area of high T_c superconductor development and applications, and on the left most side we have David Eisenhaure, President of SatCon Corporation who has expertise in Low T_c superconducting suspension applications. The way in which we thought we could organize this panel discussion was to give some time to individual panel members to give us their views about the applications and possible potentials of superconductors and then to have audience participation for interactive discussion to identify other potential applications. We'll start with Gerry Brown to talk about his views.

Gerald Brown

As far as applications go, I will note the ones that we are interested in at NASA Lewis where cryogenic temperatures are inherently available, such as turbo pumps for perhaps the Space Shuttle main engines or orbital transfer vehicles. Liquid hydrogen is the most attractive from a temperature viewpoint because its way below the critical temperatures of the superconductors we are talking about and also its perhaps the safer application. I'm not sure whether people are that ready to accept heavy current windings in a lox pump where every metal present can become fuel. We're also interested in vibration isolation in space at Lewis but because of the associated cryogenic support that you would need with high temperature superconductors I don't really see them as being applicable in that area except perhaps if you have a very large coarse isolation stage. For instance if you were going to isolate the entire experiment payload bay; get a rough isolation at that level where you could afford perhaps the cryogenic support system and then provide finer isolation at the experiment level. One of the key problems of high T_c superconductors (many have already been mentioned), current density, looks as if it will come along. I was talking to John Steckly and he mentioned that there had been reports of current densities that rival that of NbTi, Niobium Titanium. Structural integrity of the ceramics is often focused on but this is not a new problem. It has always been assumed that the inter-metallics like Niobium-Tin and that sort of compound would fail if you ever allowed the superconductor to go into tension so it's always a prestressed compressive situation that you want this type of superconductor to be in. So that is not an entirely new problem. The degree of the problem may be different. AC losses seem to me to be a major consideration and these have been beaten for the lower temperature superconductors to the extent that AC coils can be operated at power line frequencies. There are about three different kinds of AC losses and they all respond to making finer filaments and twisting these filaments with ever tighter pitches and transposing these filaments by twisted twist and so forth. Whether you can actually manufacture the ceramic materials in this form is certainly not clear, we don't even have a big bulk superconductor that's usable yet, but if we expect to carry any substantial component of AC current in the superconductors these items will have to be faced up to. On the other hand, it's been suggested by some of the people at the University of Wisconsin, Roger Boom and company,

that perhaps you don't need to carry the highest frequency components in the superconductor itself. If you do have a normal sheath then that part of the Fourier analyzed current that is of high frequency can perhaps be carried in the sheath and what is of low enough frequency to soak in through the skin depths of that conductor could then be carried by the superconductor, so perhaps you don't have to get the entire AC signal or AC current to soak clear into the core superconductor. Then finally just harking back to the days of the old superconductors, it could take a long time. From the time that people started showing really good current densities in short samples of Niobium Titanium and Niobium Tin it was probably 10 years or more before we had decently stable magnets that you could depend upon. So it won't happen over night in my opinion. As far as the thing that's going to work first, I was very pleased to see what Dantam had presented a couple of talks ago. Everybody's attracted to superconductors because they can produce so much field and since force goes as the square of the field, if you can get five times as much field, say 10 Teslas as versus 2, it's very attractive, but the structural problem is substantial when you take that big of an increase so I think that easiest first application is going to be just the replacement of copper by superconductor as Dantam was talking about. In the first place the conductor is not subjected to very much stress, the relative permeability of the iron or iron cobalt core gives some indication of relative stress. In fact I guess it may even go as a square of that but the winding in an iron core system doesn't see that much stress unless you try to bend it around a square corner or something. Furthermore, the AC loss situation would be easier to handle there. One advantage that Dantam didn't go into in his particular study is that you can push the core materials into the saturated range if you have plenty of ampere turns to burn and I think that is an attractive thing that could yield another factor of 2 on the load capacity. One further thing - people that come to this discussion from superconductivity tend to think of big coils running at 10 Tesla and no core and people that come from magnetic bearings tend to think of just replacing the copper windings. One thing about using the cores is that you do not have much in the way of fringe field. The distance that fringe fields go is going to be more in the order of the gap than of the coil diameters. Many applications that we're interested in such as space applications, may be applications where substantial fringe fields are unacceptable. Without a core it's hard to build a compensating set of windings where the field doesn't project a long distance. If you did go with the pure higher temperature windings without a core you can get pressures that rival the best that you can get in oil films. I forget the numbers exactly, more than 2000 psi I'd say would be easy. At least the field strength indicates you could get that much. If you are willing to put coils on the rotors you can not only get attraction but also repulsion but again the fringe fields are worse. I have already mentioned the AC loss but one final thing before you actually go and design a high temperature superconductor winding for liquid hydrogen temperature: I think an analysis should be done to determine whether high purity aluminum could do better. Somebody this morning or yesterday mentioned that you can get resistance ratios between room temperature and hydrogen temperature of 400 or better with very high purity aluminum so you really ought to check where you'd be better off.

Dantam Rao

Thanks, Gerry, I would now like to hand it over to Moustafa to talk about his experience.

Moustafa Abdelsalam

Mine will be easier than Jerry because I'll talk about the Magnetic Suspension and Balance Systems for example. This is where you have to use superconducting magnets for the support system. If you try to use copper magnets the size would become too large and some of the magnets would get away from the model so that you will not be able to use reasonable size magnets for the wind tunnel. So I think the first application of low temperature superconductors would be in large gap magnetic suspension and levitation and there I think that it would be a mistake for somebody to wait for high temperature superconductors to use for those applications, because as Gerry said, and I think that everybody agrees, that development just to make a superconducting solenoid may be 10 years along the road, not something that will happen in the

next couple of years. The gain that you will get there from high temperature superconductors versus low temperature superconductors is not that great. You still have to use a cryogen to cool the magnet and the structural supports are the same, so unless you can make the high temperature superconductor material itself cheaper than low temperature superconductors, the gain there is not necessarily that much. You gain some on the refrigeration power but that is most of what you get. You know the comment about the aluminum for hydrogen temperature - you can use high-grade aluminum. You could actually get down to 2000 resistance ratio for that current density and that, with liquid Hydrogen, might be in the range of somewhere between 2 kiloamps per centimeter squared and 4 kiloamps per centimeter squared depending on the size and where you can get the surface cooling. The only problem that you find there is that the high-grade aluminum is very soft so something has to be done to structurally support it. Another application where you have to, just by nature, use superconductivity is for energy storage where you can just store energy in superconducting coils and for that you can't use any other methods. You know you are forced to use, just by the nature of the problem itself, superconducting material.

Dantam Rao

Thanks, Moustafa. Now I will turn it over to Warren.

Warren Kelliher

Thank you very much. Can I see a showing of hands of the people who attended the Magnetic Suspension Workshop two years ago? Do we have any of the people here? Just a few of you. One of the things that was outstanding to me is comparing the papers and the presentations that we have today versus what we had there two years ago. Because two years ago the announcements of these superconductors had just come out, you had the hype saying that they will solve the world's problems etcetera. Then we went into the dismay of finding that these materials were not that easy to work with and everything else. What we have now is sort of a hard-core group of people who are working with the engineering properties of these materials and putting them into a fabricated shape so they can be put into magnets, both small and large gap type of materials and the work is progressing quite well from what I can see because we've learned an awful lot in those two years about what causes the high J_c s that are necessary for keeping these materials in the superconducting state. We've got up to, in some of the single crystal materials, 10^6 amperes per square centimeter. It shows the possibilities, even in the bulk, of getting into thousands of amperes per square centimeter and that's all we really need for most wire type applications. One of the things that I disagree with a little bit on the MSBS is that we do have an NTF tunnel here and that handles a cryogen and therefore you automatically have the cryogen to run an MSBS system. However, going to a Helium-cooled system causes the cost to become very prohibitive (a million dollars a day or something like that). So high T_c material will provide a very nice MSBS system, at least for the NTF tunnel here, that will be able to support the model and get rid of the interferences associated with the sting. One of the persons that attended two years ago was Dr. Jack Crowe. I was hoping that he would be able to show up this time but he couldn't. He is in Florida state right now and is now Head of the Magnetism Institute. I hope the problem is solved there between Boston and Florida but this is again its thought of focusing some of the activities in the superconductor materials towards the magnetism field and I see much more of that going to take place in the future. The high T_c materials are going to find much more practical use as a magnetic material in the future.

Dantam Rao

Thanks Warren. I think we appreciate your comments on real world applications and how far we are today towards these real world applications. Now, I would like to turn it over to David.

David Eisenhaure

As advertised, I'm Dave Eisenhaure and I am currently employed by SatCon Technology Corporation up in Cambridge, right down the street from the magnet lab that's in question. In fact we can talk to the people during lunch hour and get their views on the whole problem. SatCon specializes in magnetic bearing and suspension systems; we've worked with both conventional magnetic bearings and superconducting bearings and suspensions. In fact the linear optical disc bearing in the back of the room is one of our products - just to get in a little advertisement while I'm up here and got the mike. What I thought I would do, since I didn't bring any viewgraphs, is tell you a little bit about some of our experiences with superconducting magnetic bearings and what drove us down that path and what really created the need. I think our experience may be very typical of other applications. I think it was four and a half years ago when we received a contract to design an electromagnetic actuation system for laser radar mirrors. For people who aren't familiar with them, these are extremely agile mirrors; they weigh several hundred pounds; they take two to three hundred kilowatts to drive them; and they require control frequencies as high as 400 Hertz. The typical approach to that problem is hydraulic. That's the "competition" in this application. The problem is that if you lose a drop or two of that hydraulic fluid you ruin the optical surface in the mirror so there's a lot of need to go to a magnetic suspension and drive system, or there's a lot of belief that going that way will eliminate some of these problems. The difficulty is when you begin to look into that problem you find out that the inertias associated with conventional soft iron magnetics suspending and driving these systems are so high that you can't meet the system performance specifications. You basically can't drive the actuators themselves even without the laser radar mirror attached. We began looking at superconducting magnetic suspensions and drives and these superconducting suspensions and drives were basically superconducting fields coupled with either normal conducting or hyperconducting armatures. What we found out by going down that path was that with normal conducting armatures we could basically beat the specific performance requirements of hydraulics by a little bit and with hyperconducting armatures we could beat them by a lot. Since then we've had several additional hyperconducting laser radar mirror development programs and we've extended that technology to the advanced concept CMG that Jim Downer reported on yesterday. I think one thing to keep in mind is the comment that Pat Wolke made during his talk describing the different kinds of actuators that are available and which can be built for magnetic suspension and torquing systems. I think you know that when you're developing superconducting systems you have the same options. Every one of those actuators has a superconducting analog and perhaps you have even more because it is not necessary to use iron in all of these applications because of the very high current densities. I have been to a number of these magnetic bearing and suspension conferences and now we're kind of talking about a niche within a niche here because we're talking about superconducting magnetic bearings within the general realm of magnetic bearings and suspensions and if you look at magnetic bearings and suspensions in general it's kind of a niche technology. It's emerging and the place that it can attract research and development funds are the areas where it's either an enabling technology (you can't do it any other way) or just has an overwhelming advantage to conventional technologies. It's got to be a lot better than the way it's currently being done or nobody's going to do it and for magnetic bearings you see a few of those places being found right now. It's happening in canned pumps, it's happening in certain specialized kinds of compressors. Some people believe it's happening in attitude control wheels and in some parts of the world it's happening in machine tool spindles for extremely high speed very precise machining. I think by looking at now that's happening with conventional magnetic bearings and suspensions, you can look at the problem and say: where can we really use superconducting suspensions - where they have a unique place in the world and there are some areas. One area is the application that we found for high performance CMGs, laser radar mirrors, those kinds of very high specific performance requirements. That same kind of requirement is what's driving the people that are trying to build Gigawatt size power systems on space or to put multi-thousand horsepower electrical drives in submarines. They want to make them small, compact, and light. On the other side of things, there are some people that want to build rotating machinery with microwatt kinds of

power levels that they're going to send to Neptune or something and maybe the zero resistivity requirements of superconductivity will enable that. Maybe it's hard to build that machinery with conventional technology. There's a couple of things that haven't been mentioned here (Dave Trumper mentioned it a little bit) that is related to very precise positioning systems. One thing you don't usually think about in servo systems, because usually you're being buffeted by everything, is the internal noise in these systems. If you're building a very quiet, very precise positioning system, what you may find is that the Johnson noise in the actuators is the predominant noise source in the system. Well, superconductors give you a mechanism to eliminate that. I think, along the same lines in very many precise stable systems, like perhaps electron microscope slides, where people are talking about positioning accuracies of an angstrom or better, introducing any heat into those systems is a big problem. You don't have the stability in the materials if you're introducing milliwatts or higher levels of heat and superconductivity provides an enabling mechanism for that kind of a problem. I think one of the things that a group like this can do is to provide some guidance to designers like myself as far as what are the applications that are really needed and what are the requirements for those applications. What should we be designing and why and that's all I have to say, Thank you.

Dantam Rao

Thanks, Dave. Now, I have a few words to say about the experience that we have at MTI. We have, of course, had a couple of contracts dealing with superconducting applications from SDI and NASA and basically the object of the study was to identify potential applications in SDI systems where superconductors could form a good marriage with the system requirements. It is a rather difficult study because of the fact that, as you know, most of the SDI systems are politically oriented - they change from day to day and what you see today in the newspaper may not be found the next day. Within that kind of uncertainty we did in fact study the Phase I architecture of SDI systems and found that there is a certain scope where the cryogenic fluids are naturally available within the system. Basically, in the space based engines, that is the power engines where the cryogenic turbo machinery exists and the cryogenic turbo machinery already has liquid hydrogen available as a fuel. That is one potential application. The other applications which we feel are there, as was pointed out earlier, the space shuttle main engine hydrogen turbo pump and similar turbo pumps that are being planned. The liquid hydrogen is already available and there is a good marriage between the requirements of the superconductor with the applications needs. The application demands that the bearing should be very stiff and high load. The high load and the high stiffness requirements are normally met now by rolling element bearings and it is difficult to meet the same requirements by any other bearing other than a very high stiffness superconducting bearing. In addition to that I may digress a little at this stage to say that when I looked into the applications I saw the basic trends in the world and I saw a divergence in the trends between what Japan does and what the United States does. The Japanese, most of the time, focus mostly on the commercial multi-unit kind of applications where the research dollars are spread over a number of units so that the people will benefit. They probably start to identify an application right at a top level where people will use it, mass produce it, and then develop the technology from that state whereas in the United States I see that most of the applications are targeted at one-of-a-kind applications and the research dollars that the government spends are concentrated on that application and there is actually a problem there. Let me assure you that is basically a socio-economic issue which probably some other audience member could comment on. The other applications which we would have in mind - I think most of you are aware of the magnetically levitated trains where superconductors are used by the Japanese to levitate the entire train. You can consider that as basically a 5 degree-of-freedom controlled magnetic bearing except for the fact that the particular device is driven by a linear motor. Instead, the rotary bearings are driven by some prime mover, except for that difference the superconductors are being used there and the advantage of the superconductors there is that they open the gaps quite substantially because of the higher ampere turns that are generated by the superconductors. They use an eddy current levitation mode there and that could be a basic technology which the United States could adopt if the Maglev Trains come around here. The third application I think, which probably some of the members of the

audience are aware of, potentially multi-unit applications, are Cryo-coolers where current Cryo-cooler bearings are right now either rolling element bearings or gas bearings. I believe that there is a potential for the high T_c superconductors playing a role in the sense that they could levitate the rotating shaft permanently. Once it is levitated it could run without contact and that would reduce the wear and the power requirements. Right now the gas bearings they use in the Cryo-coolers are limited by the very short clearances - roughly they are under about a 12 micron clearance. You could see that the wear and tear potential is very high there with the gas bearings and the high T_c passive bearings could be probably be an application there. The other applications which I think some of the members of the audience are already dealing with are the MSBS suspension systems and micro-g isolators. I think there we probably need some participation from the members where we could extend the applications into potential space devices. With this I'll turn over the floor to the members of the audience and invite them to participate in the discussion.

Pat Wolke -Honeywell

Just another chance to editorialize little bit I guess but to reiterate what Dave said these applications have to be enabling technologies, or something where you get a significant performance increase and I would be wary about overselling the capabilities of some of these devices. Maybe in the realm of spacecraft applications we talked about ball bearings having a limited life and wear out mechanisms. One of the key wearout mechanisms is eventual loss of lubrication and I see in superconductivity that you also have effectively a consumable in the cryogen and if we talk about applications where they've got a lot of liquid hydrogen onboard anyway, all for this other stuff, we've got it available for us. Well typically, in control applications where you might be using magnetic bearings, those are operational for the entire life of the spacecraft and the other consumables are sitting ready for a particular application. They don't want to pop the canister for those. Once you pop the can you can't reseal it, it leaks. So that consumable that you have is part of your control system and must be included in calculations of the lifetime of your device, so we have to be careful about overselling these things, getting people too excited and then being basically disappointed at the end. We have to be realistic up front and include all of the things that are necessary in the system.

Dantam Rao

Thanks, Dave, it is your turn to answer the question.

Dave Eisenhaure

I get to answer that? Yes, I agree and I think we see two kinds of things; one thing is people are going to send up satellites that they really need and they are going to get data back from those; the other is the kind of thing we see at SDI and that is where some grandiose Battle Station is going to be built in the sky and that may never happen. I guess there are two levels. My thought was that superconductivity is a niche within a niche. I personally think that for a lot of spacecraft applications, conventional room temperature bearings without superconductors are just fine. It is not at all that clear you need superconductors to do those things. If you go down the path a little bit and you say, "we have some applications where we really need superconductors, we have to build a torquer that weighs 5 pounds and produces 4-5000 foot/pounds of torque in a direct drive application," maybe what we need is a space-rated refrigerator to really use these things. That's what the people that are trying to put superconducting electric drives into ships believe. They believe that one of the critical pieces of equipment they need in order to use these guys is a refrigerator and whether that refrigerator makes 70 degree Kelvin or whether it makes 4, it's a critical part and we don't have it. You can buy it for your lab, but you can't buy one to put in a ship and you certainly don't have one that can fly. Now, maybe magnetic bearings, either superconducting or maybe not superconducting are a part of that system, and you know, I'm a little bit prejudiced and I think that perhaps they are, but you know that's one of the things that has

to be thought about. If this is going to happen, that's one of the pieces that has to be done and someone has to do it and someone has to pay for it.

Dantam Rao

Thanks, Dave. I think that I'm going to offer a small comment on that. I would tend to agree with Pat's comment that there might be a likelihood of overselling, because of the fact that for over the past 50 years of activity in the superconductivity area we have a very few mature applications where the dynamic environment is involved. One particular application where the experience was gathered over 15-20 years that comes to my mind was the superconducting alternator program and the government spent a lot of money on that program and the only comments I heard from the funding agencies were that the multimewatt alternators haven't produced a single watt.

Gerald Brown

Just one quickie, in some missions the cryogen may not be a consumable. If it's supposed to last long enough so that they've found a refrigerator is better than just a certain amount of storage, then you're just using power instead of the fluid.

John Stekly - Intermagnetics General Corporation

I'd just like to make a comment. When you mention the superconducting alternator, I think that this is certainly one area that has been explored. However, magnetic resonance imaging is an area where superconductors are being applied on a commercial basis. It's the largest single commercial application of superconductivity. For those of you who are older you probably know what it's all about, for those younger fellows that don't need to have MRI scans this is a Computer Tomography (CT) type device and you use 1 meter bore superconducting magnets. Now these didn't show up all of a sudden fully developed. You needed to have extremely high uniformity, measured in parts per million. You had to have magnets that didn't decay to better than one part in ten to the seventh per hour and you also needed to have a refrigeration system that was compatible with use in a hospital. Now, I think that this goes back to the system comment, you need all of this in order to make it work, plus you have to have it economical. You can't just have somebody that wants to use superconducting wire for MRI because it just won't work. You have to use the wire that's available with the cryogenics system that exists now with a cryostat and with the costs that it takes to assemble all of this. I think again that this is the reason magnetic resonance imaging is a viable application today. I think that any other application needs all of these elements. The other area that's very successful, again it's not quite as difficult, is high energy physics. They make large accelerators; there's 1000 superconducting magnets that are operating at Fermilab that have been operating for the better part of a decade and there's the supercollider which is just in the process of being started in Texas that will have 12000 superconducting magnets. All very successful applications of superconductivity, but again, it involves cryogenics, it involves magnetic design that is particular to that application and the correct economics, and I think that when you have that the application will work.

Dantam Rao

Would anybody like to add to what John said?

Moustafa Abdelsalam

I think I agree with John, that if you have the application, you don't wait and I think that this was part of that recommendation that I will offer. For example, for MRI, if we waited until we had high temperature superconducting wires to make the magnets, we would still be waiting. And at the same time, we would have lost all the experience that we got along the way. Somebody

else might have built them. For space applications, let me add that since we have hydrogen on the space station, it would make sense to use high temperature superconductor energy storage. Since you are not going to pay for the refrigerant, you know for hydrogen you can actually store it in the system and you can use the magnetic energy storage system instead of batteries in space. There are some studies that use toroids, in that case, you don't have any stray fields on the station and you can actually store energy there and it's weight effective compared to other systems. Another area for the high temperature superconductor that I think can probably be done soon, is the leads for low temperature superconductors. A major part of the losses for low temperature superconductors, especially for magnets, is the leads for those magnets, I'm talking about for example MSBS where you have to have the leads connected all the time for control and then if you can make those leads high temperature superconductor then you can decrease a lot of the refrigeration power that you need for that.

Dantam Rao

Thanks, Moustafa. Regarding John's comment, I think that I would fully agree with what John said, that the current experience of superconducting magnets is quite extensive, that is we have very mature and technologically proven applications; as he pointed out, there are quite a lot of MRI systems which are being used all of the time. The superconducting supercollider is one of the systems that is being projected and an MSBS system could probably be one of the potential applications but what I was trying to point out when I selected the cryo-alternator or superconducting alternator for my comments was that in my mind when we are dealing with magnetic suspensions we are dealing with mechanical devices and when the mechanical devices are rotating or vibrating or whatever, they are distinctly different from steady-state devices like MRI and superconducting supercolliders. Its dynamic machines that we are dealing with and their dynamic environment. The distinct and unique opportunity that the superconducting community had to demonstrate the utility of the superconductors in a dynamic environment was the superconducting alternator and that was the only system I thought could be compatible with the magnetic suspension requirements which the superconductors may face in the future if we think of inserting the superconductors into mechanical systems.

Robert Humphris - University of Virginia

I have a question for the panel concerning superconductivity in magnetic bearings for rotating machinery. In most of the magnetic bearings with rotating machinery today they are using switching amplifiers as the power amplifier, to save power again, and of course these switching amplifiers work at frequencies from 20 kilohertz up to 100 kilohertz, and I can just imagine the AC losses involved at these frequencies. Is this going to be a real problem?

Dantam Rao

Let me comment on that. I think that there are 3-4 ways in which we could see the superconductors inserted into magnetic bearings. One approach was, which Gerry Brown probably feels comfortable with, and I also feel comfortable, was immediate insertion by replacing the copper by superconductors. That is an approach which could be viable. If you do that then you are going to face the problem which you mentioned but there are alternative approaches. That is, instead of trying to expose the superconductors to high frequencies you can design the flux circuit such that the superconductors will act as permanent magnets in persistent current mode and the flux circuit is away from the alternating fields in a decoupled mode. If you do that then you can avoid the problem.

Bob Humphris

In that case, what would be the advantage of superconductivity over a permanent magnet bias?

Dantam Rao

Okay, there I think the answer is that permanent magnets have a maximum flux-density of 1.3 Tesla whereas the magnetic materials saturate at around about 2.3 Tesla. There's a difference of 1 Tesla, so probably the superconductors could play a role by increasing the bias flux-density.

Un-identified Speaker

I'm intrigued by the idea of energy storage that was alluded to a little bit ago. Maybe this is slightly out of the field which you're discussing here, can somebody give me a thumbnail sketch of what you're alluding to?

Moustafa Abdelsalam

Okay, there was a study at the University of Wisconsin, on superconducting magnetic energy storage for space applications, where you can ship toroids, D-shaped toroids, to the space station and use them to store energy. What you do there is like a persistent mode electromagnet, where you have the current flowing all of the time in the electromagnet. You are storing the energy as a magnetic field and you can draw in and take part of that energy, you can charge and discharge the electromagnet. It works much like a battery except that you are storing the energy as a magnetic field not as a chemical reaction and actually there is a Defense Nuclear Agency (DNA) Phase I contract study on building 20 megawatt hour superconducting magnetic energy storage. That's for utility applications where you level the utility power. You charge it over night where you don't have much load for the utility and discharge it during the day when you have a peak load and this way you can level the load on the utility. The first phase of this study was just submitted, I think, in August, beginning of August of this year and DNA is studying two designs and I think that sometime next year DNA will decide which design is going to be built for the next four years so that's Phase II of the study.

Kirk Logsdon

I had a question for the panel. Given the practical limitations of keeping flux contained in the circuit and not spewing all over the place in certain applications, does anyone on the panel feel that research on better soft magnetic materials should be pursued in light of the superconducting coils that we have potentially coming on the scene some day?

Dantam Rao

I don't know, maybe I'll try to answer that question. It depends upon the system which you have in mind. If you have in mind aerospace systems, at least the systems that I have come across - the SDI space systems, most of them are extremely sensitive to flux lines. Let me back up. I think that there are two types of systems in SDI. There are Sensor Systems which sense the oncoming missile where they use infrared detectors. Those systems are very sensitive to magnetic flux lines. There are Weapons Systems which throw the missiles on the oncoming missile and those Weapons Systems may not be that sensitive, like lasers for example. But the Sensor Systems are going to be quite sensitive to flux lines. One way of containing the flux lines is soft magnetic materials as you were suggesting. The other way could be using the superconductor in a diamagnetic mode, which could probably be attractive, I don't know. Probably there is a need to see the system tradeoff between the weight of a diamagnetic shield versus the weight of the

magnetic material shield. I think that is a systems study, every specific system has to be looked at to see which approach looks better. The approach which we thought could be better is to channel the flux, to solve that particular problem using iron, at least right in the beginning.

Don Rote - Argonne National Laboratory

We did a study a couple of years ago on applications of superconductors and high temperature superconductors to transportation, and one of the things that we looked at was the question of SMES, Superconducting Magnetic Energy Storage, and what we found was that in terms of the amount of energy that you could store per unit weight you simply cannot beat a battery for storing energy. There's no way around it, the mechanical stresses are sufficiently great that by the time you include the components necessary to retain the magnet form, and it gets even worse in the case of a toroid, that you simply cannot beat the battery. But there are certain cases under which you can beat a battery and it therefore becomes the same question that was raised before and that is what are the special applications where superconductivity does provide some benefit. It does not provide benefit in terms of energy per unit mass stored, but it does provide benefits in terms of how fast you can charge the system, how fast you can discharge it, how many cycles you can go through. Chemical batteries are very bad, notoriously bad, when you try to charge them very fast, discharge them very fast, or expose them to many deep cycles. If the superconducting coil is properly designed you can charge it fast, discharge it fast, and recycle it many, many times provided the mechanical stresses can be properly accounted for. So there may be applications in the space environment, as there are on the ground, where you can take advantage in that regard, but don't be misled by the notion that you can beat a battery for energy storage per unit mass, because to our knowledge, at least at the present time, it can't be done.

Dantam Rao

Yes, that is an interesting observation, and I think that Moustafa would be the right person to answer the questions raised. I'm aware that the sponsor to the SMES project had the object of demonstrating the trade-off between the energy storage device versus batteries by experiments. Probably Moustafa would be able to add something more to that.

Moustafa Abdelsalam

I tend to agree with you. I'm talking about power per unit mass. If you try to get a certain level of power from batteries, you will not be able to do it. You will have an energy storage magnet to do that. It's not energy per unit mass. I should have mentioned that.

David Eisenhaure

One of the things that hasn't been mentioned too much today and which we hear about in the newspapers is the need to ground-test large space structures and I hear stories about NASA and other agencies flying larger and larger space structures and the question of how these things can be ground-tested and how you simulate a space environment. There hasn't been much discussion of that here and it seems like we're probably at the right NASA Center to discuss that. I was wondering if any of the NASA people could comment on what the needs are and whether some of these large gap suspensions would be applicable to that task?

Dantam Rao

I think the comment is open to NASA personnel here.

Nelson Groom - NASA Langley Research Center

Well, in answer to that question, I think that there are applications for magnetic suspension to ground tests. As you pointed out, ground testing is very important. There are problems testing anything on the ground, as you know, but with large space structures, it is even more so. The less influence that you have on a structure, the better off you are, so the answer is yes.

John Murphy, Rockwell

I'd like to comment on current space vehicle design and currently it's influenced very heavily by the propulsion system and currently we think that the HO propulsion system (Hydrogen-Oxygen) is the best for specific impulse. There are other servicing fluids that we could pick, but for other reasons, the current design is for that. That leads you to hydrogen and oxygen in a cryogenic form or a slush form with high density fuel cells that we currently know about through Air Force technology. It looks like superconducting technology as a complement to that is very applicable to future space vehicle design and I have alluded to this with several of the speakers but it is certainly a fertile area that we should explore for future space vehicle design, specifically for SEI or interplanetary application where maintenance becomes a big problem and in-flight maintenance becomes a reality which you must address.

Dantam Rao

I tend to agree with what we tentatively conclude in our SDI sponsored study - that is basically liquid hydrogen was one of the most abundant fluids in the SDI systems and maybe the applications could target liquid hydrogen temperatures. But instead of targeting an application like that before you start experimenting with liquid hydrogen fluid straight away, maybe you could start gaining experience by conducting demonstrations using liquid nitrogen at a higher temperature, gaining experience then go down to liquid hydrogen. The two-tier approach could be a viable approach to develop and demonstrate the technologies.

Colin Britcher - Old Dominion University

I have a comment. I guess I'm sort of a believer in technology demonstration exercises for their own sake. I think that is a throwback to the early operations of NASA where they built X-Aircraft because they were kind of nifty things to build. (They learned an awful lot on the way of course.) I guess the LGMSS experiment that was described this morning counts as a technology demonstration exercise and I got the impression from Pierre DeRochemont that there was some effort to build a high temperature superconducting magnet with the National Magnet Lab, which may also qualify. Are there other efforts underway or should there be other efforts underway? Is it the right time for people to try to build large magnets that can carry high AC currents, that kind of thing?

Dantam Rao

If I understand your question, I think the question was--are there applications other than the MSBS for the large magnets--am I right?

Colin Britcher

No. The question is: should people be trying to do technology demonstration exercises; build hardware almost for its own sake, just to show the practicality of using superconductors on large scales or for unsteady load applications or for large force applications, that kind of thing.

Dantam Rao

I don't know. My comment may sound personal but the research dollars available are rather stringent unless a specific application is targeted. It will be very difficult to get funding to start demonstrating that High- T_c magnets or Low- T_c magnets could be used for a specific dynamic environment. I think that maybe my comment is to target the application first, to understand the dynamic environment, then try to simulate the dynamic environment, simultaneously keeping in mind that there could be a potential payoff. Payoff is very critical to demonstrate that the dollars are spent wisely. I think that a rather difficult issue is to see that payoff. In superconductors most of the current payoffs come from paper studies but unless it is demonstrated it is difficult to have the continued funding from the government.

David Eisenhaure

I have another perspective on that. If you look at some of this technology, conventional magnetic bearings have been around for about 50 years and you could build quite nice ones for the last 20 and the question is--why aren't they flying? Why can't you get a program manager to put them on his spacecraft or into his submarine or whatever? I think that the other view is you know no one believes paper studies. If you are going to put things in space, put them into real systems. You have to do some demonstrations. I agree with you. I think you've got to build some things and you've got to fail a few times and if you do that, you are really going to demonstrate the technology that people will believe. The question of how you get the research dollars vectored into those programs, I don't know, I think that's an institutional problem and I think you have to figure out a way that all the money just doesn't go into funding, that some of the money is kept out and some of these things we're going to do. So I believe what you said, that's a good thing and it should happen.

John Murphy

David, to comment that the next flight vehicle that is a good candidate for demonstration is the X-30, the NASP experimental vehicle, that is due to come on line in about 1997 to the year 2005, to demonstrate some of the space application for this new complementary technology.

John Stekley

I just wanted to make a comment on the fact that low temperature superconductors have been developed recently with very low filament sizes using matrices that are resistive rather than copper and these have been developed in order to be used at power frequencies, for things like transformers, power control equipment, and again these are available for a few individual magnets and I think certainly for some of the applications here. I think it makes a lot of sense to see how these operate before you get up into very large sizes. I think you need some experience. Generally the losses are frequency dependent, only so much per cycle, and these conductors typically operate reasonably well up to fields of about one Tesla (AC operation).

Dexter Johnson, NASA Lewis

I've only been on board with NASA Lewis for about 4 weeks now and I'm just getting into learning about magnetic applications and so forth but I was a NASA Fellow and I did my Masters thesis research here at NASA Langley. Just to address your inquiry into the suspension of large space structures, earth-bound testing and so forth. My Masters thesis had to do with trying to minimize the dynamics which you have coupling to the suspension system, in which you're doing testing on an earth-bound structure. I see from my experience that most of the work that has been done has been passive applications. My particular work was active, and I could see very well

where magnetic bearings or magnetic actuation could play a part. Some of the other things that have been used have been air tables and that type of thing, although those have caused problems. I'm sure that magnetic suspension could very well be used and it's a big area that magnetic suspension could be applied to.

David Eisenhaure

Where did you do your thesis?

Dexter Johnson

In the Structural Dynamics Branch, but now it's Spacecraft Dynamics Branch here at Langley and I did it with the University of Buffalo.

Dantam Rao

Are there questions? I think we have stretched it a little bit beyond our scheduled time, because it's tea time. Anyway I hope you are very, very thirsty. In conclusion, I would like to thank all of the audience who participated in the discussion and hope we have increased the awareness of superconductors in the magnetic bearing community and that the next time that we meet, we will have the opportunity of listening to more presentations where superconductors have been used in bearings or suspensions or similar devices. Thanks very much.

DEVELOPMENT and DESIGN of a MAGNETIC INERTIALLY REFERENCED ISOLATION
SYSTEM for MICROGRAVITY EXPERIMENTATION

Kirk Logsdon, Carlos M. Grodsinsky
NASA Lewis Research Center
Mail Stop 23-3
Cleveland
OH 44135



Lewis Research Center

SPACE EXPERIMENTS DIVISION

SFSD

Space Flight Systems Directorate

1. Introduction

- Vibration Sources
- Spacecraft Environment

2. Active Magnetic Isolation

- Advantages
- Disadvantages

3. Development of Active Inertial Magnetic Isolation System

- Inertially Referenced Magnetic Control

4. Design of Active Inertial Magnetic Isolation System

- Conceptual Configuration of Isolation Platform
- Prototype System
- Preliminary Results

5. Summary



Lewis Research Center

SPACE EXPERIMENTS DIVISION

SFSD

Space Flight Systems Directorate

Vibration sources present on the Space Transportation System (STS) and in the future the Freedom Station. These sources are categorized by frequency range, from DC up to $> 10^1$ Hz.

Quasi-Static (DC to 10^{-3} Hz)

- Aerodynamic Drag: function of atmospheric conditions and surface area
- Gravity Gradient: function of distance to orbiter center of gravity
- Photon Pressure: function of projected surface area viewing Sun

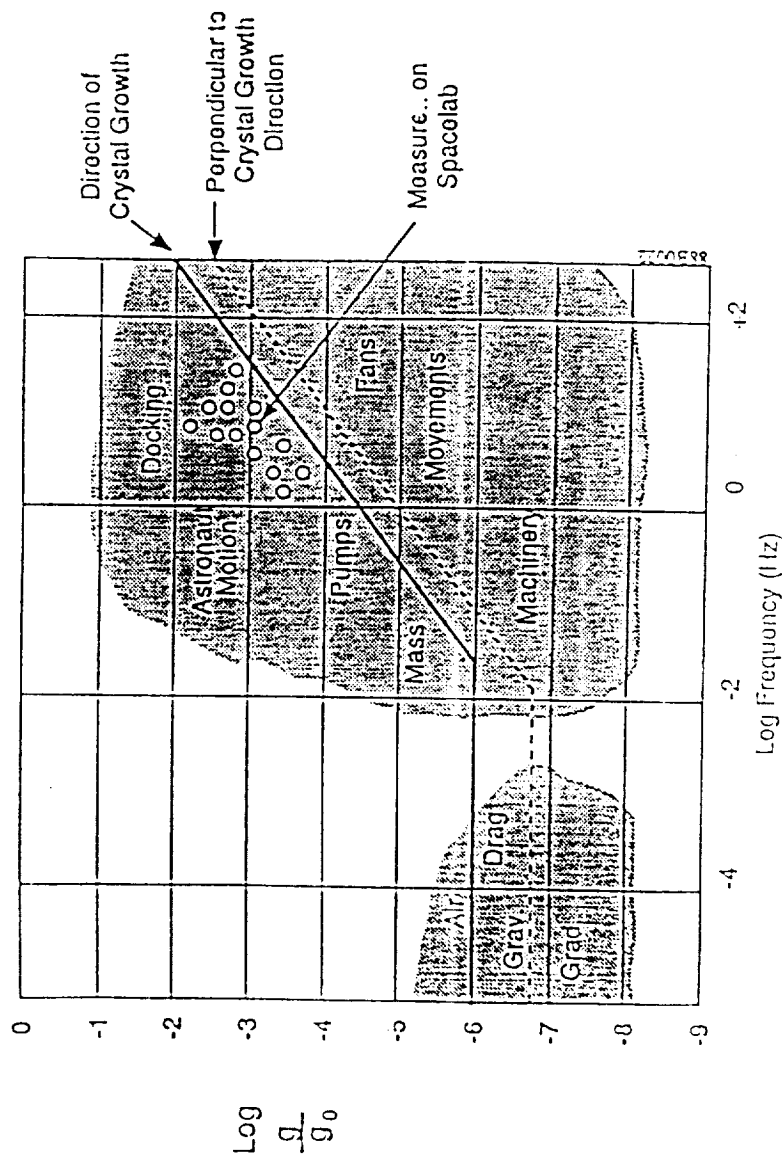
Low Frequency (10^{-3} to 10^1 Hz)

- Large Flexible Elements
 - Solar Arrays
 - Antennae
- Crew Motion
- Attitude Control
- Robotic Motion

Medium-High Frequency ($> 10^1$ Hz)

- On Board Equipment: pumps, motors, and other dynamic facility equipment

G-Level Tolerance for Monochromatic Oscillatory Disturbances (Stuhlinger)



Plot gives magnitudes of various disturbances verses their characteristic frequencies.



Lewis Research Center

SPACE EXPERIMENTS DIVISION

SFSD

Space Flight Systems Directorate

Active magnetic isolation systems advantages in disturbance rejection for sensitive payloads.

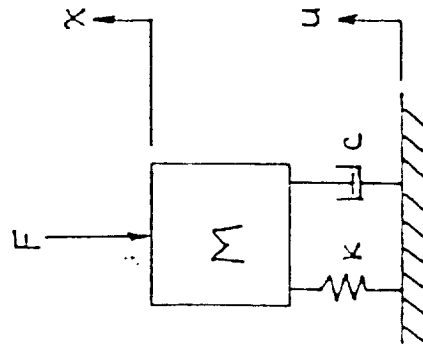
Advantages

- Variable Stiffness and Damping
- "Adaptive" Control Capability
- Isolation of Direct and Base Disturbances
- Adaptable to Various Payload Masses
- Payload Centering Under Load

Disadvantages

- Greater Complexity

One degree-of-freedom differential equation of motion demonstrating the conceptual approach to an inertially referenced isolated payload.



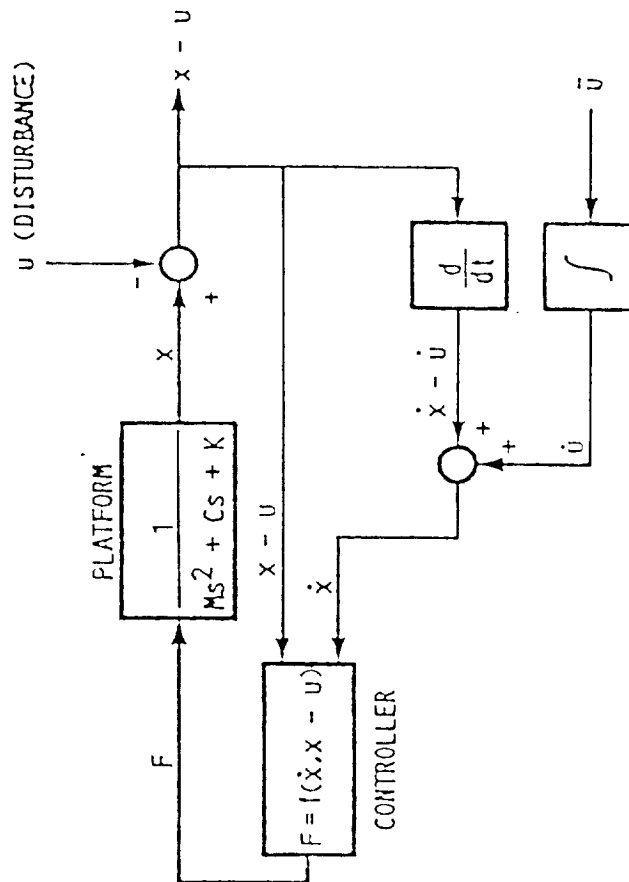
Without Inertial Isolation:

$$m \frac{d^2x}{dt^2} + c \left\{ \frac{dx}{dt} - \frac{du}{dt} \right\} + k(x - u) = 0$$

With Inertial Isolation:

$$m \frac{d^2x}{dt^2} + c \left\{ \frac{dx}{dt} - \frac{du}{dt} \right\} + k(x - u) = 0$$

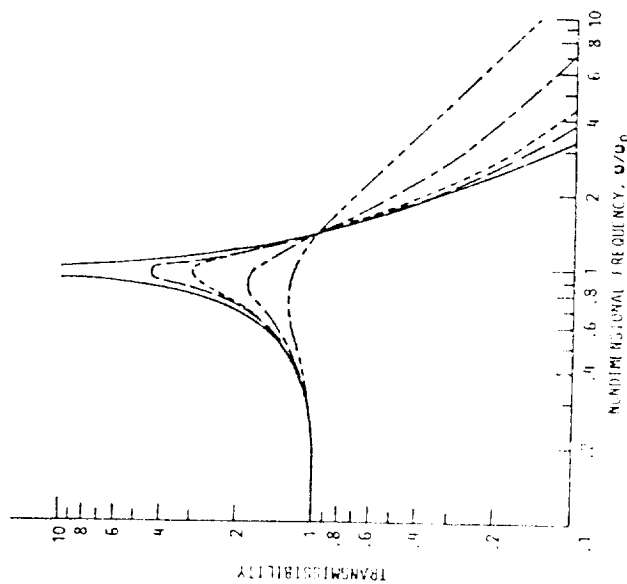
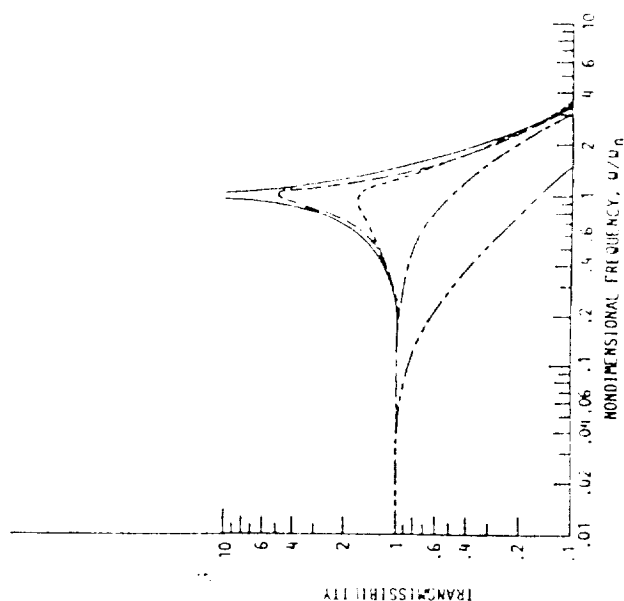
One degree-of-freedom block diagram of inertially referenced payload control system.



Transmissibility curves of an inertially damped one degree-of-freedom control system as compared to a relatively referenced active system.

INERTIAL DAMPING TRANSMISSIBILITY CURVES

RELATIVE FEEDBACK TRANSMISSIBILITY CURVES



NASA

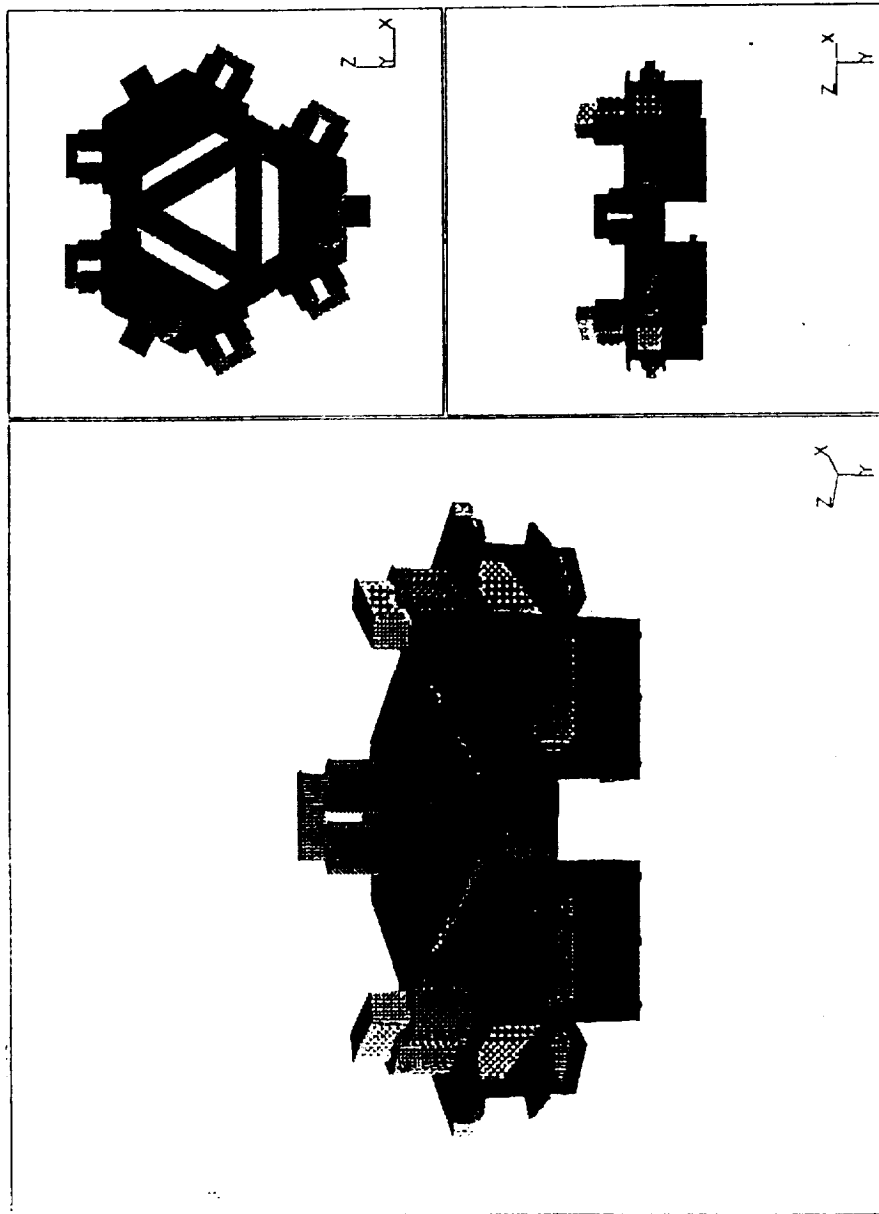
Lewis Research Center

SPACE EXPERIMENTS DIVISION

SFSD

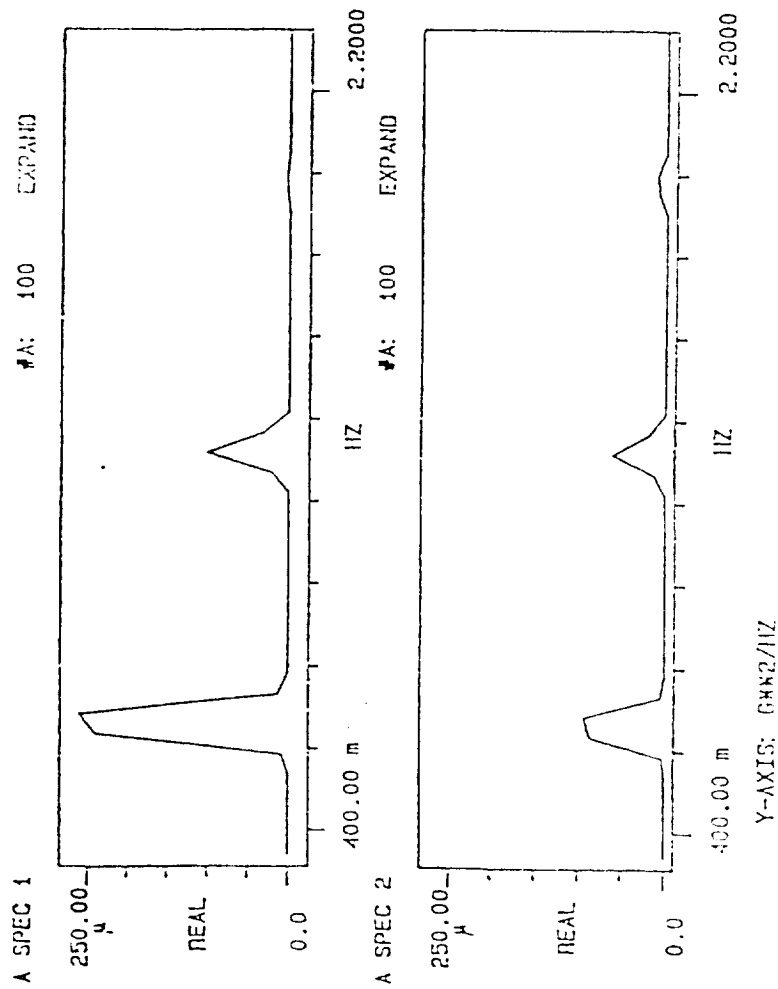
Space Flight Systems Directorate

Conceptual configuration of a six degree-of-freedom isolation platform.



ORIGINAL PAGE IS
OF POOR QUALITY

Preliminary isolation results of a three degree-of-freedom configuration.





Lewis Research Center

SPACE EXPERIMENTS DIVISION

SFSD

Space Flight Systems Directorate

SUMMARY

1. Active magnetic systems can substantially improve isolation at low frequencies.
2. Active magnetic systems can be adaptively controlled to optimally isolate a payload in a random environment.
3. Ability of systems to use inertially sensed information in order to decouple the mass from a dynamic environment.
4. Active isolation systems can be designed for several payload configurations and thus, can be used as a microgravity experimentation support facility.
5. Response of the system can be adapted by using various sensing feedback methods in the feedback control loop.

ACTIVE VIBRATION ISOLATION MOUNTS

H. Ming Chen, Richard Dorman, Donald Wilson
Mechanical Technology Incorporated
968 Albany-Shaker Road
Latham
NY 12110

Active Vibration Isolation Mounts

By

H. Ming Chen

Richard Dorman

Donald Wilson

Abstract

Several approaches toward reduction of vibration from operating machinery to ground through active electromagnet mounts are discussed. The basic approach to active mount design is to take advantage of the force attenuation characteristics of soft mechanical spring mounts and supplement their limitations with an active electromagnetic system. Techniques discussed include vibration cancellation approaches, as well as a method of altering mount stiffness and damping properties at the disturbing frequencies. Analytical and experimental results are presented encompassing the magnitude of force reduction and the stability characteristics of each technique.

Description of Figures

Figure 1

The advantages and capabilities of an active mount are summarized in the tabulation of Figure 1.

Figure 2

The objective of the active mount as summarized in Figure 2 is to isolate machinery or platforms from ground. This is accomplished by sensing the force transmitted to ground to drive an electromagnet.

Figure 3

This figure illustrates a typical mount using an elastomer to support the weight and an electromagnet to provide dynamic forces.

Figure 4

Vibration control techniques to be reviewed include the use of filters to control the stiffness and damping properties of the support (fixed or tracking filters), or the use of an inverse transfer function.

Figure 5

The force transmissibility curve illustrates the reduction in transmitted forces that can be achieved by altering the support stiffness and damping properties. This figure also illustrates that the primary advantages of force attenuation occur at the lower frequency range.

Figure 6

Figure 6 further illustrates the influence of stiffness and damping modifications to the transmissibility of forces through the mount.

Figure 7

Controls of the active mount depend upon adjusting the stiffness and damping of the electromagnet as a function of the transmitted force as detected by a force gage or load cell.

Figures 14, 15

These figures refer to the technique used in developing an inverse transfer function. The test rig is excited with a sinusoidal signal to the electromagnet. The amplitude and phase are recorded at the force gage relative to the excitation. This information comprises the transfer function across the mount. The control technique is to develop a similar amplitude and phase function through a series of filter networks. A 180° phase inversion of this signal will drive in opposition to the force gage signal and cancel the transmitted force.

Figure 16

Figure 15 is a block diagram of the proposed filter network to create the inverse transfer function.

Figures 17, 18

These figures illustrate the constructed circuit to duplicate the characteristics of Figures 14 and 15. Tests are presently in progress to check out the performance of this approach.

Figures 8, 9, 10

These figures illustrate a test rig used to demonstrate force attenuation techniques. In Figure 8, the mount supporting a vibration shaker is shown in the foreground. The control function is performed digitally in a desk-top IBM-PC. The control signal is amplified with a linear amplifier shown as the box alongside the rig. A close-up of the rig in Figure 9 shows the force gage used as the control pickup. In Figure 10, the electromagnet is visible with the mount disassembled.

Figure 11

This figure shows the computer CRT screen and the software control commands.

Figure 12

In this figure, the real time vibration wave is shown above an FFT plot of the vibration as picked up on the force gage. In this figure, the force gage is inactive.

Figure 13

This is a repeat plot of Figure 13 with the active mount activated. The output from the force sensor has been reduced from an amplitude of 0.3151 v. to 0.0252 v., as noted from the value of Y at the bottom of the plots.

Active Isolation Mounts

- Isolate Machinery Base Using Elastomer and Electromagnetic Mount Combination
- Electromagnets React to Dynamic Disturbance
- Attenuation of >20 dB Over Standard Elastomer Mount in Laboratory
- Easily Retrofitted with Most Dynamic Machinery
- Failsafe Design Provides Passive Mount Backup

891704

FIGURE 1

Mechanical Technology Incorporated

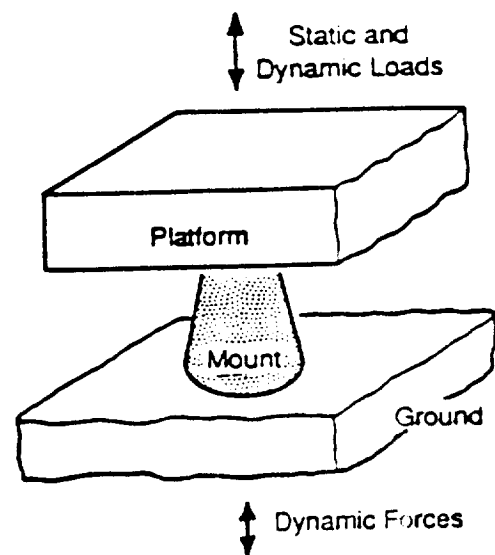
ACTIVE MAGNETIC ISOLATION MOUNTS

Objective:

Isolate Platform from Both Platform Induced and Ground Induced Vibrations

Method:

Sensor Driven, Actively Controlled Electromagnet to Cancel Dynamic Forces



Potential Benefit

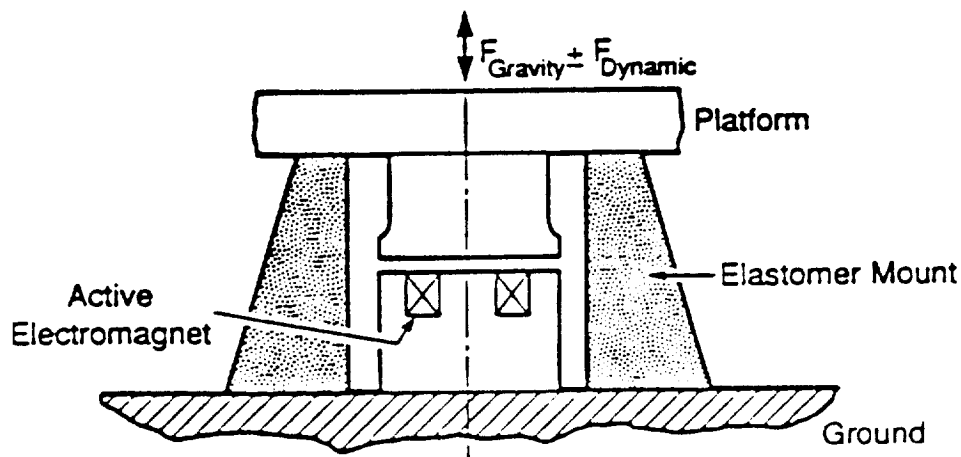
- *15 to 1 Amplitude Reduction*
- *Eliminate Multiple Rafting*
- *Compatible with Current Mount Designs*
- *New or Retrofit Capability*
- *Applicable to a Variety of Platforms*

FIGURE 2

ACTIVE MAGNETIC ISOLATION MOUNTS

Approach:

- Electromagnetic Support in Parallel with Existing Mount
- Elastomer/Spring Mount Carries Gravity Load
- Electromagnet Reacts Dynamic Load Only



Result

Minimize Size, Weight, and Complexity of Active Mount

FIGURE 3

VIBRATION CONTROL TECHNIQUES

- BAND PASS FILTERS
- TRACKING FILTERS (LMS)
- INVERSE TRANSFER FUNCTION

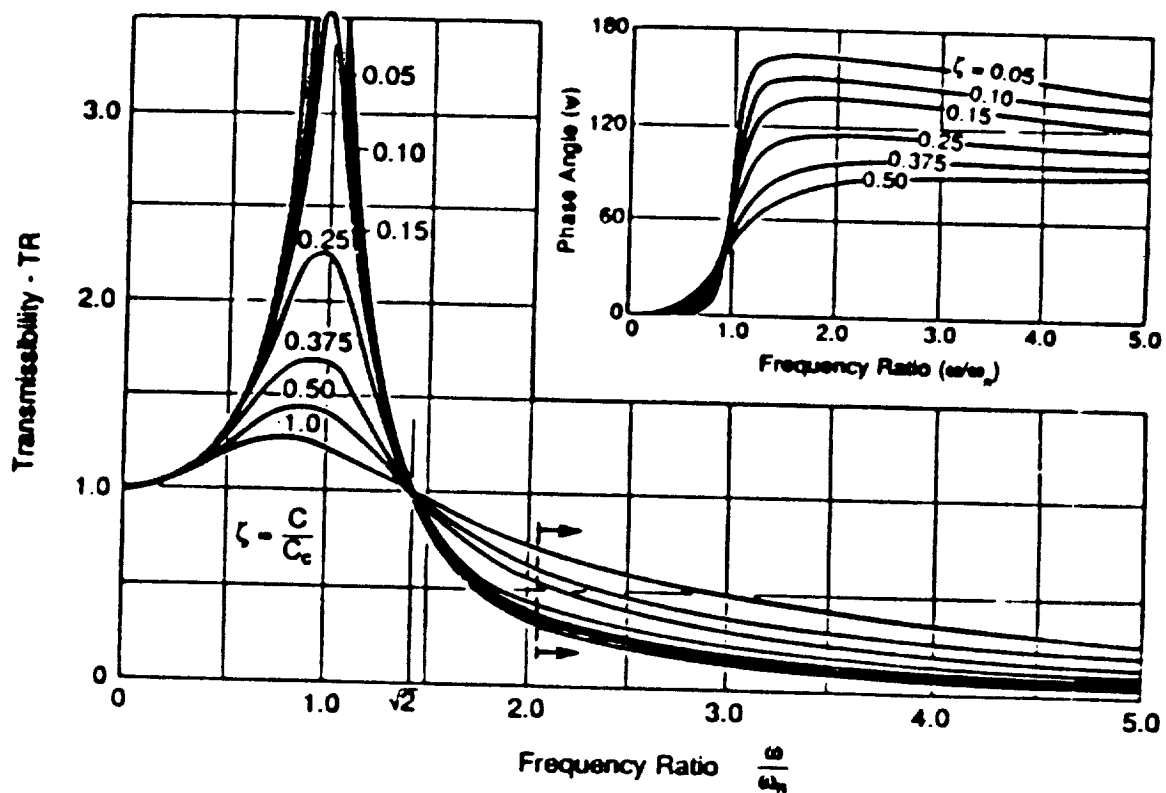
FIGURE 4

Mechanical Technology Incorporated

ACTIVE MAGNETIC ISOLATION MOUNTS

Approach:

Minimize Dynamic Force Transmission
by Actively Altering Support Stiffness and Damping



Result

20 to 30 dB Attenuation
at Discrete Frequencies

FIGURE 5

INFLUENCE OF REDUCED STIFFNESS AND INCREASED DAMPING ON FORCE TRANSMISSION

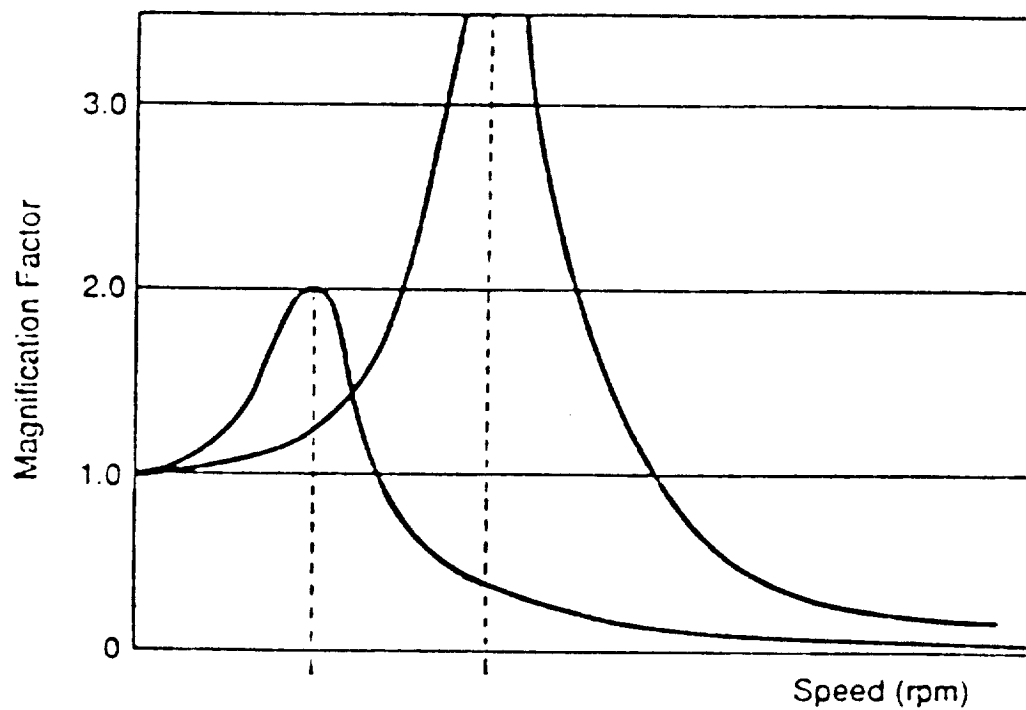


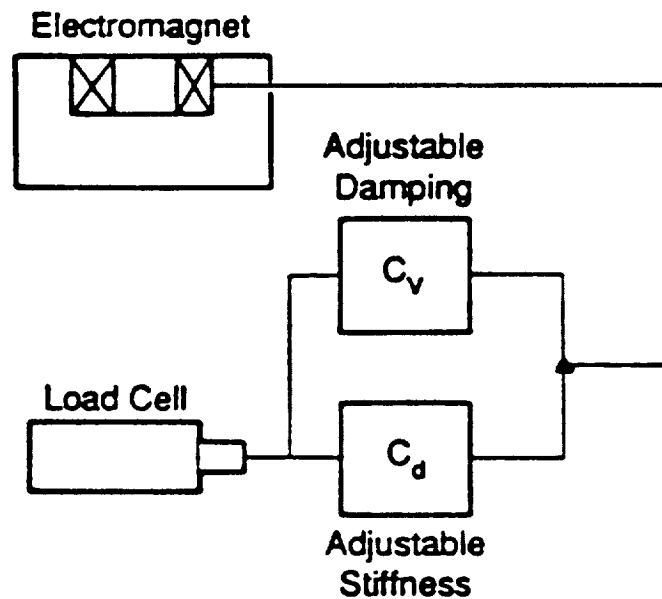
FIGURE 6

Mechanical Technology Incorporated

ACTIVE MAGNETIC ISOLATION MOUNTS

Approach:

Control Circuit Alters Stiffness and Damping



Result

***Control Parameters to Achieve
Reduced Elastomer Stiffness***

FIGURE 7

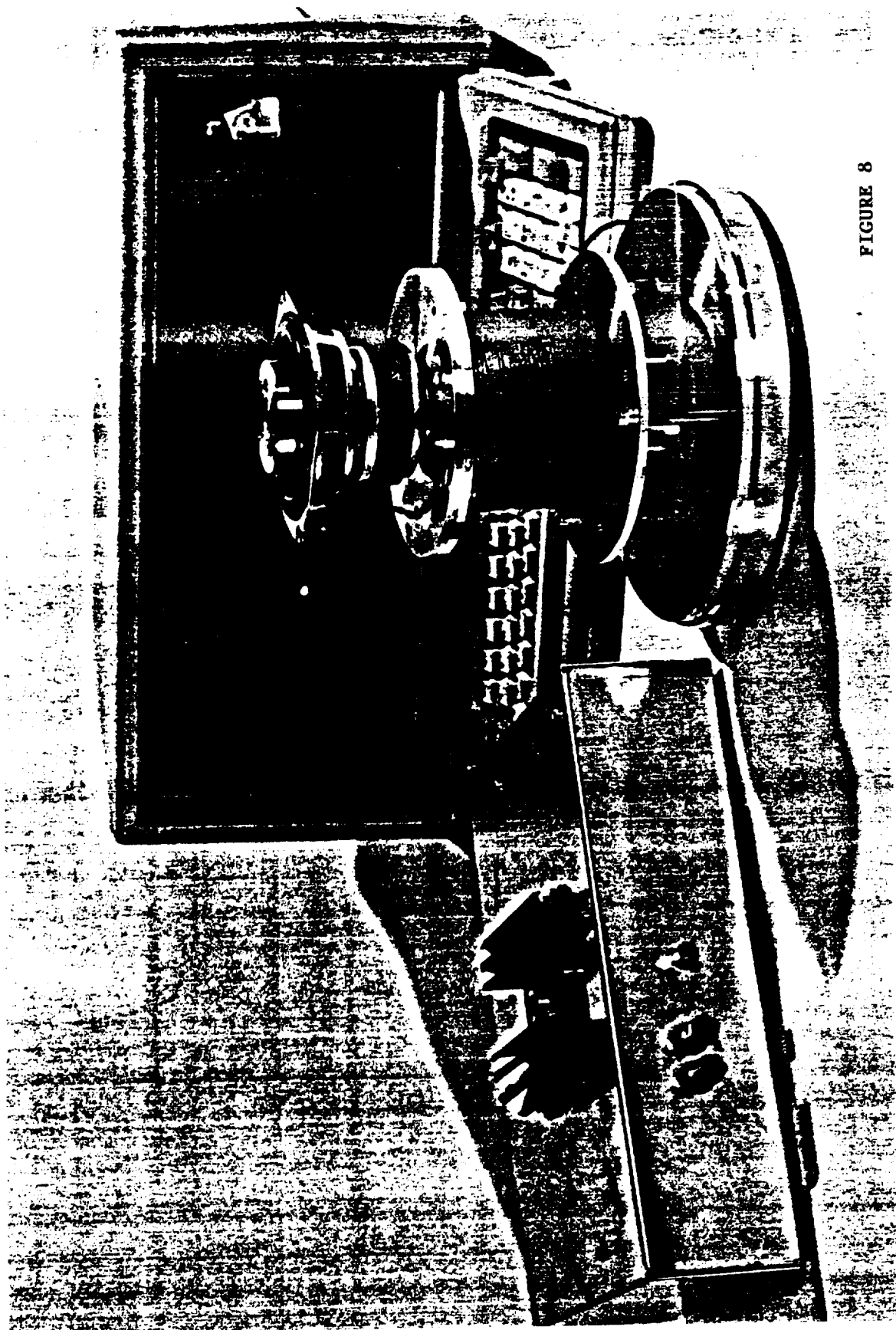


FIGURE 8

FIGURE 9

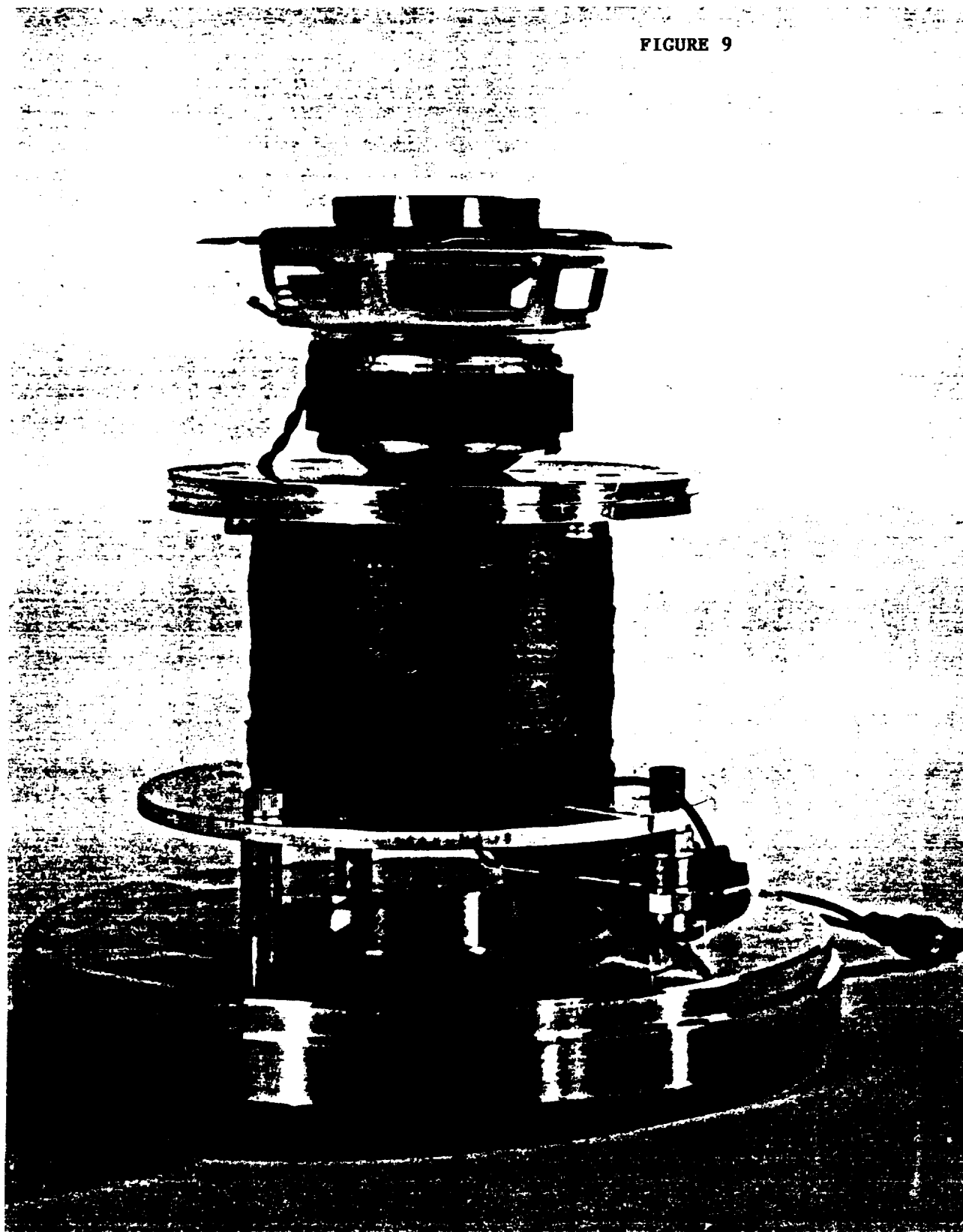
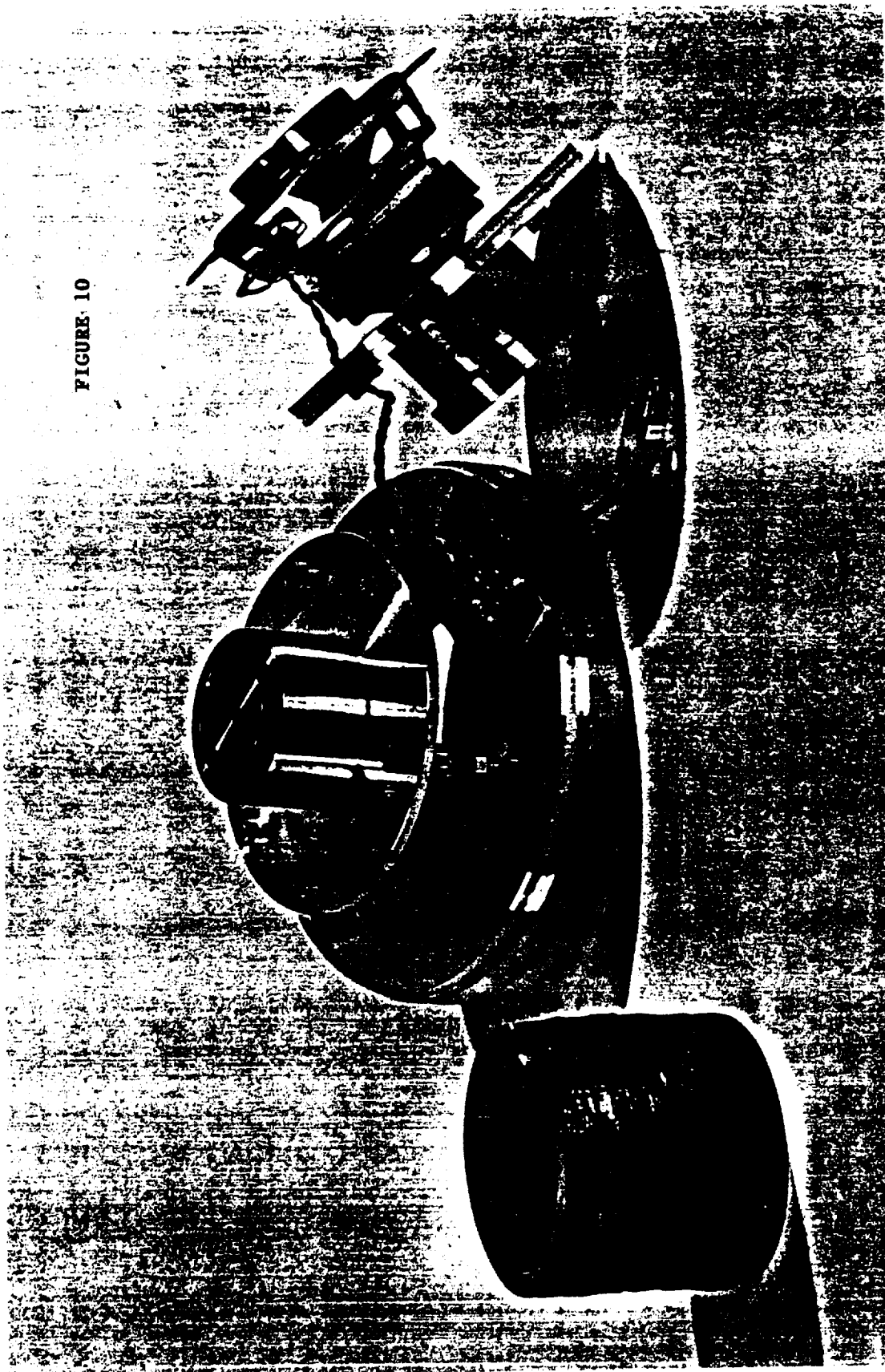
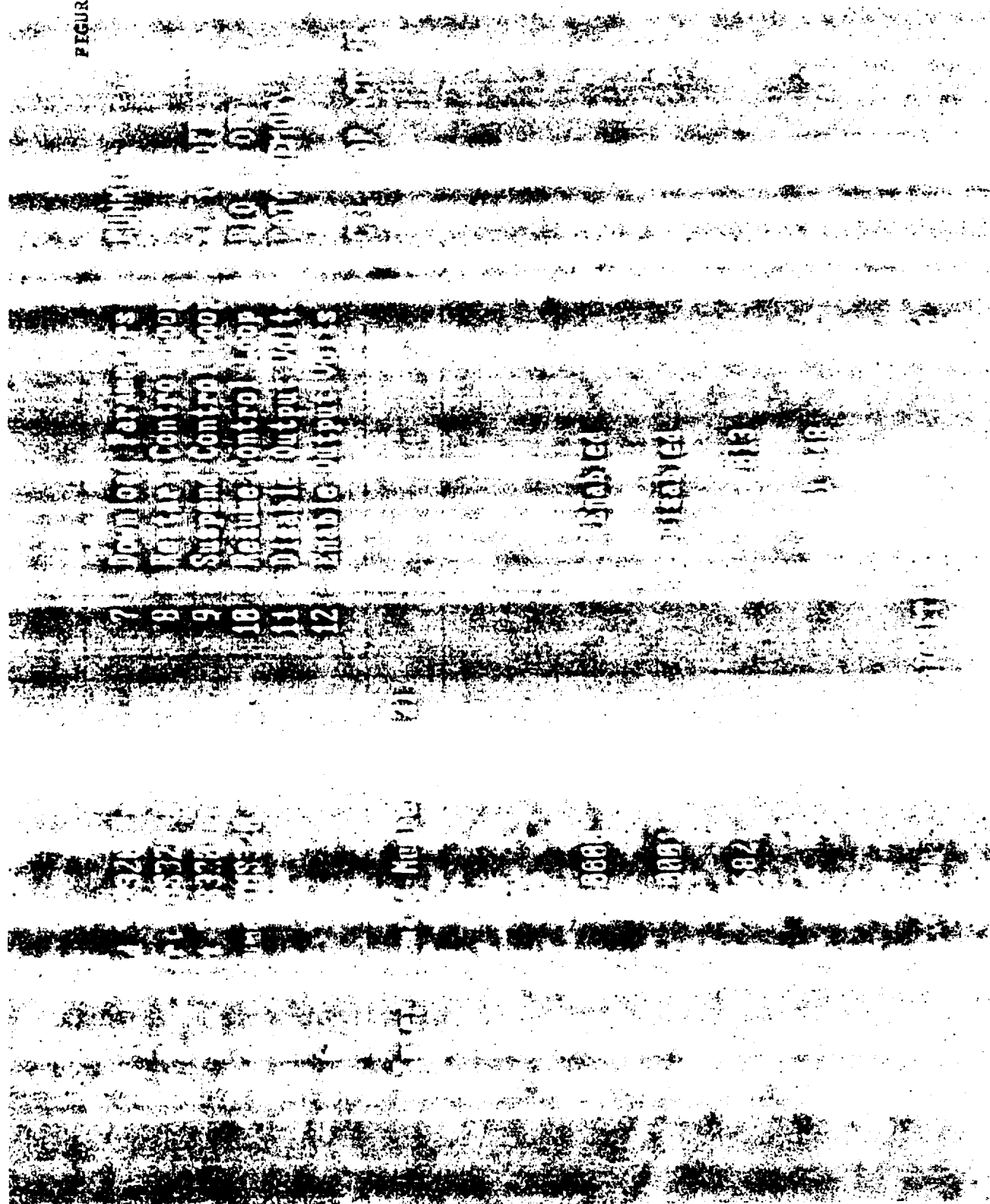


FIGURE 10



ORIGINAL PAGE IS
OF POOR QUALITY

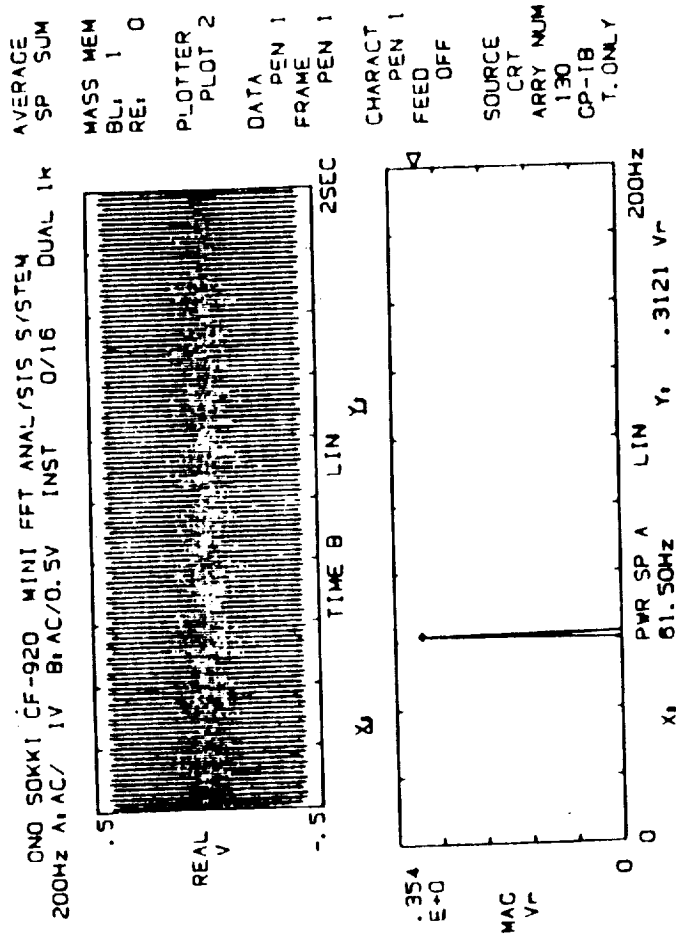
FIGURE 11



Mechanical Technology Incorporated

ACTIVE ISOLATION MOUNT TEST RESULT

-- WITHOUT AIM CONTROL --



89245 A

FIGURE 12

ACTIVE ISOLATION MOUNT TEST RESULT

-- WITH AIM CONTROL --

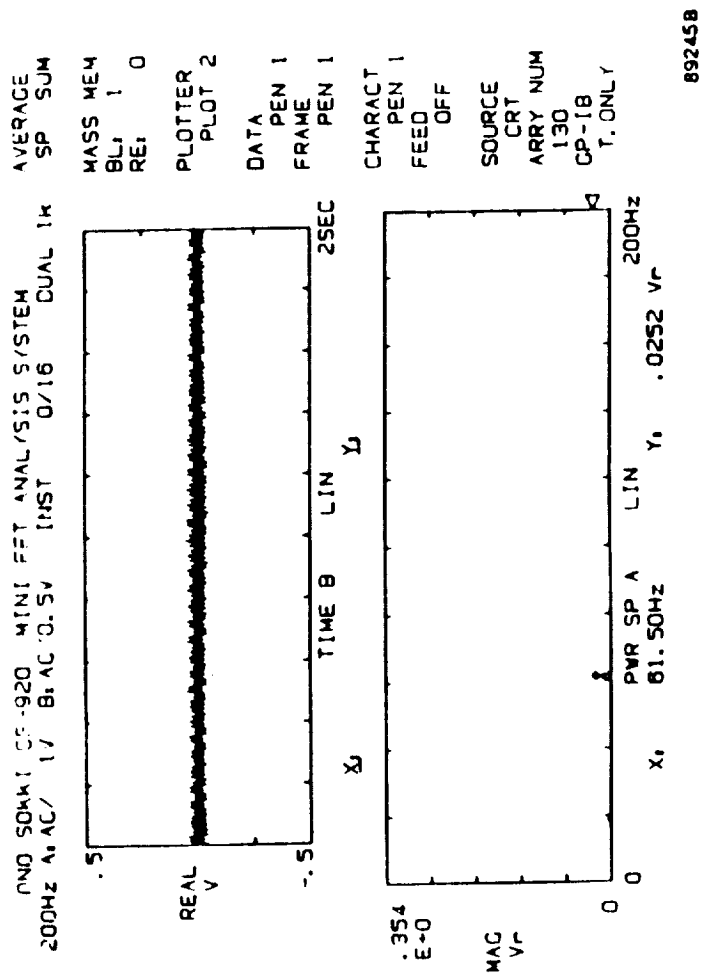
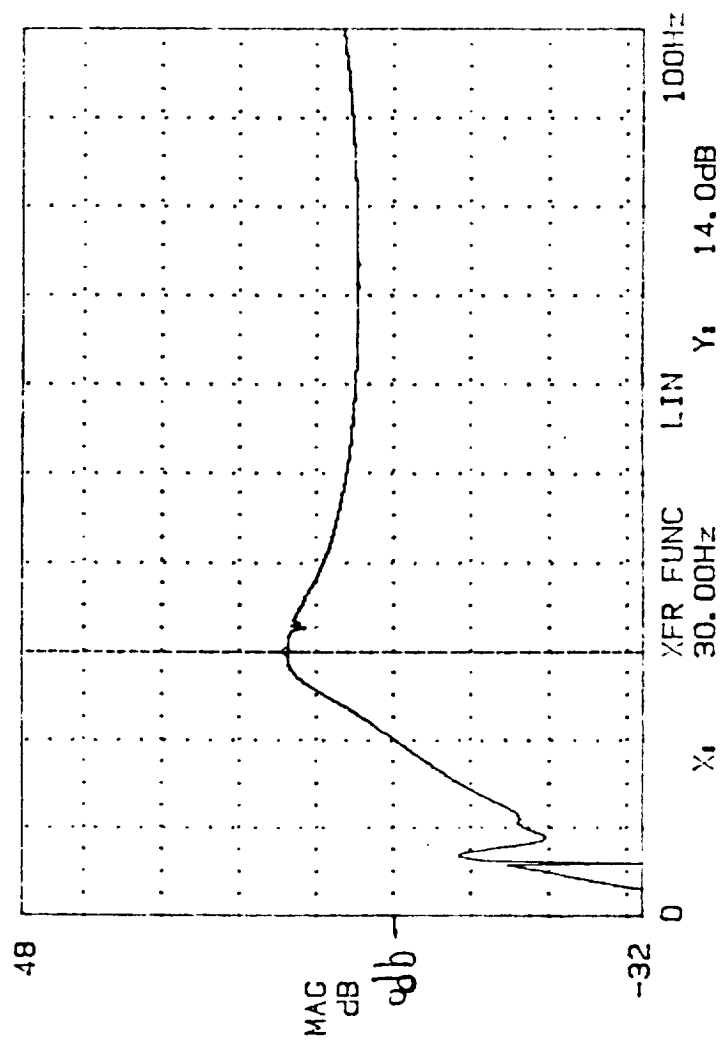


FIGURE 13

OND SOKKI CF-920 MINI FFT ANALYSIS SYSTEM
 100Hz A: DC/0.2V B: DC/0.5V S: SWP 1400/4096 DUAL 1K

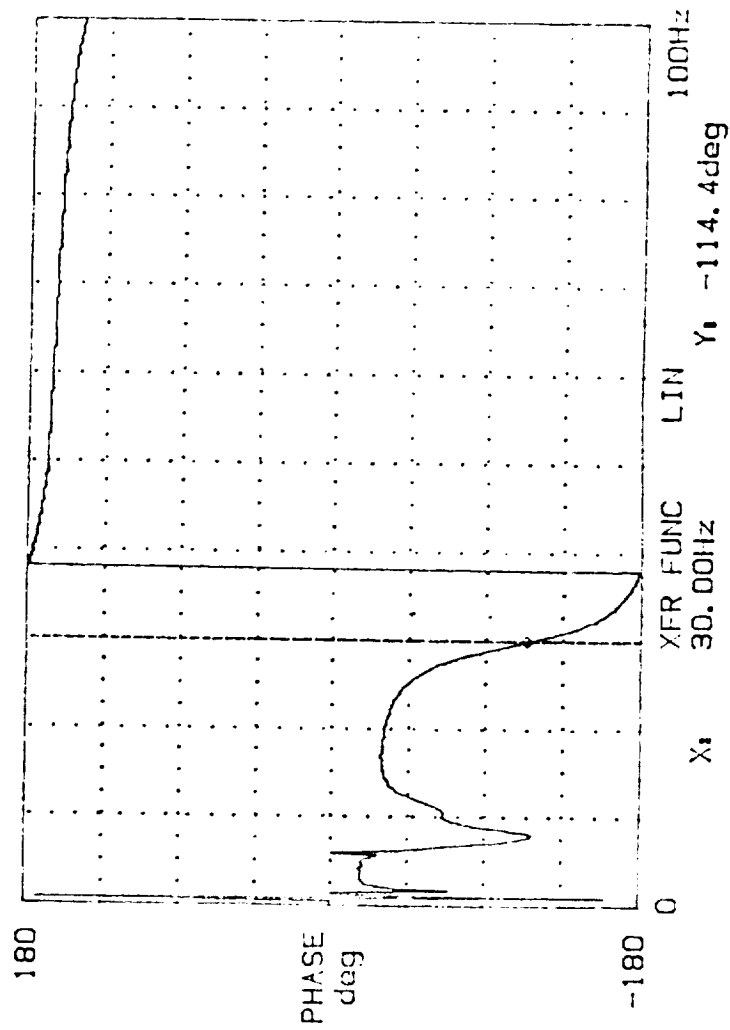


DISPLAY UNIT VIEW TIMER SEQUENCE PLOTTER OPTION 16, 45 etc.

FIGURE 14

STRUCTURAL AMPLITUDE RESPONSE

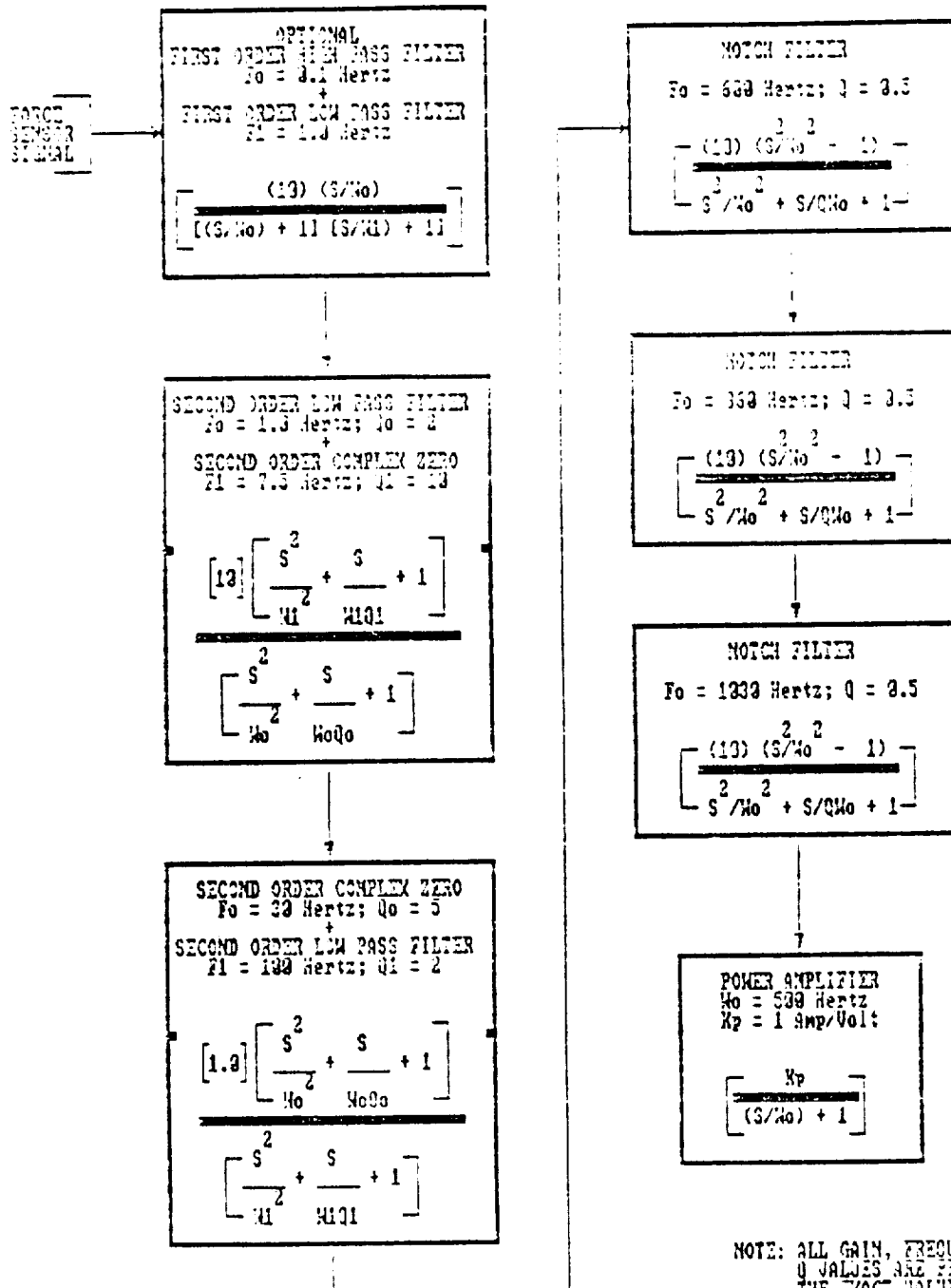
OHIO SOKKI CF-920 MINI FFT ANALYSIS SYSTEM
 100Hz A:DC/0.2V B:DC/0.5V S:SWP 1400/4096 DUAL 1K



16.31
etc.

DISPLAY UNIT VIEW TIMER SEQUENC PLOTTER OPTION

FIGURE 15 - STRUCTURAL PHASE RESPONSE



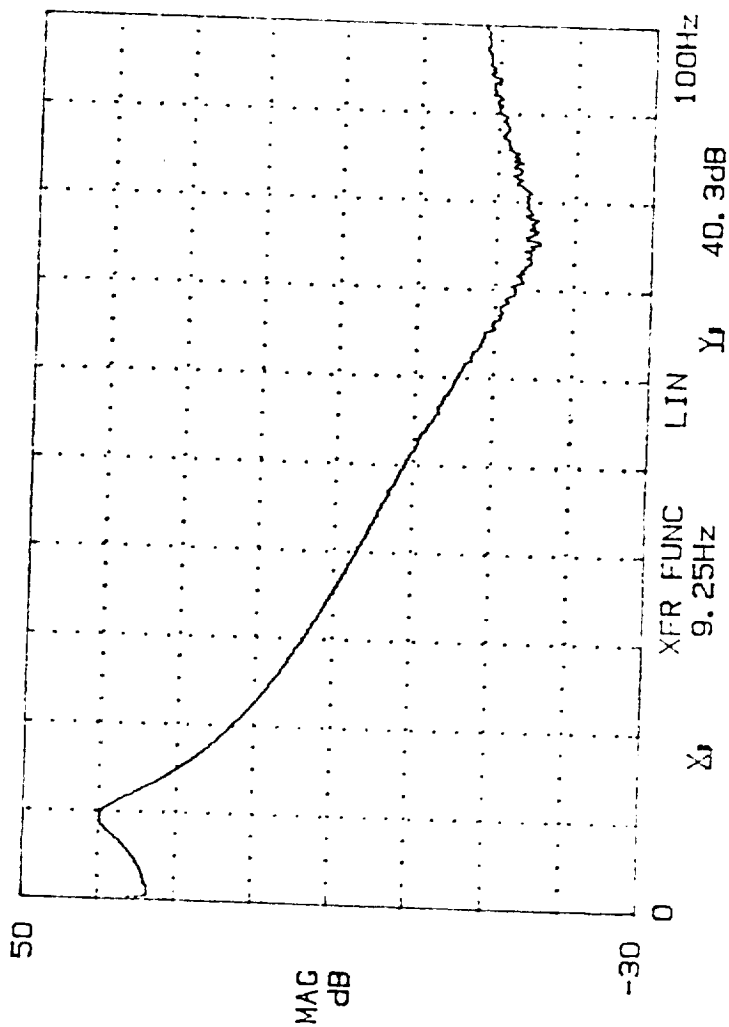
NOTE: ALL GAIN, FREQUENCY, AND Q VALUES ARE PRELIMINARY. THE EXACT VALUES WILL BE DETERMINED BY TESTS ON THE FINAL ACTIVE MOUNT UNITS.

FIGURE 16

R. DOZMAN
5/24/90

PROPOSED COMPENSATION CIRCUIT CLOSED LOOP/FORCE SENSOR

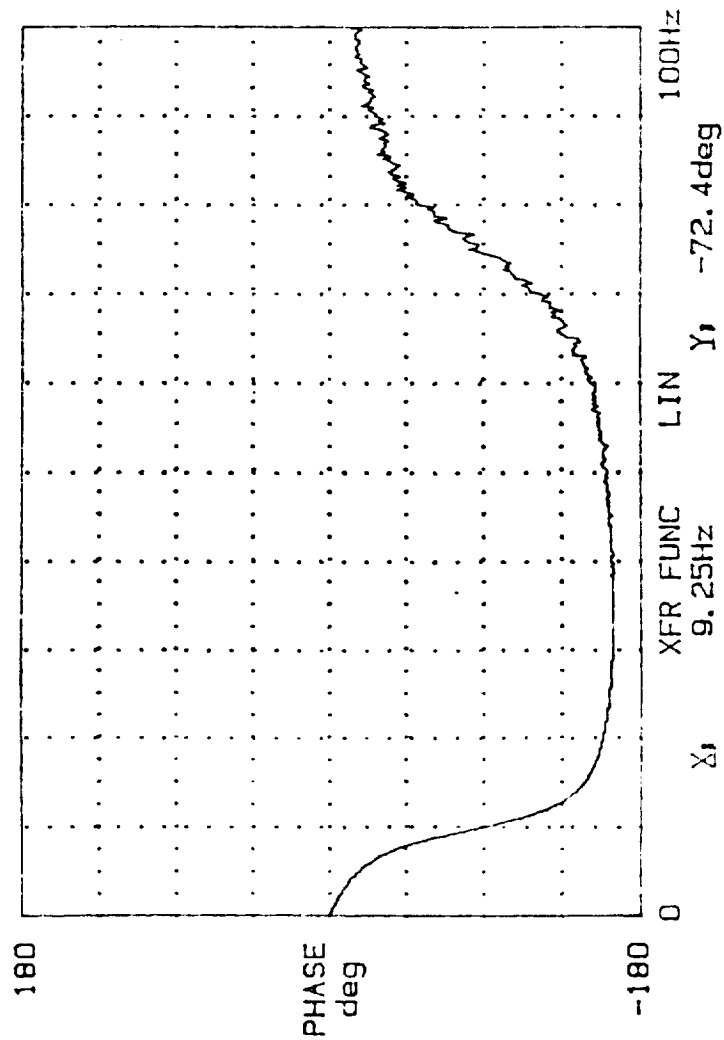
100Hz A, DC/0.2V B, DC/ 20V S, SUM 283/4096 DUAL 1k



DISPLAY UNIT VIEW TIMER SEQUENC PLOTTER OPTION etc. 21.06

FIGURE 17 - AMPLITUDE RESPONSE OF CONTROL CIRCUIT

100Hz A, DC/0.2V B, DC/ 20V S, SUM 283/4096 DUAL 1k



DISPLAY UNIT VIEW TIMER SEQUENC PLOTTER OPTION etc. 21, 09

FIGURE 18 - PHASE RESPONSE OF CONTROL CIRCUIT

VIBRATION ISOLATION of SCIENCE EXPERIMENTS in SPACE
- DESIGN of a LABORATORY TEST SETUP

Bibuti B. Banerjee, Paul E. Allaire, Carl R. Knospe
Department of Mechanical and Aerospace Engineering
University of Virginia
Thornton Hall, McCormick Road
Charlottesville
VA 22901

University of Virginia / NASA Lewis

DISTURBANCE LEVELS

Quasi-Steady or "DC" Accelerations

<u>Relative Gravity</u>	<u>Frequency (Hz)</u>	<u>Source</u>
1E-7	0 to 1E-3	<i>Aerodynamic Drag</i>
1E-8	0 to 1E-3	<i>Light Pressure</i>
1E-7	0 to 1E-3	<i>Gravity Gradient</i>

Periodic Accelerations

<u>Relative Gravity</u>	<u>Frequency (Hz)</u>	<u>Source</u>
2E-2	9	<i>Thruster Fire (orbital)</i>
2E-3	5 to 20	<i>Crew Motion</i>
2E-4	17	<i>Ku Band Antenna</i>

Non-Periodic Accelerations

<u>Relative Gravity</u>	<u>Frequency (Hz)</u>	<u>Source</u>
1E-4	1	<i>Thruster Fire (Attitudinal)</i>
1E-4	1	<i>Crew Push-Off</i>

University of Virginia / NASA Lewis

VIBRATION ISOLATION OBJECTIVES

1. The Problem

- Vibration Causes
 - Thruster fire
 - Machinery operation
 - Crew motion
- Desired Isolation Range
 - $10E-5$ to $10E-6$ g
 - 0 to 10 Hz frequency
- Passive Isolation Capabilities
 - $10E-2$ to $10E-3$ g
 - Not good at low frequencies

2. The Solution

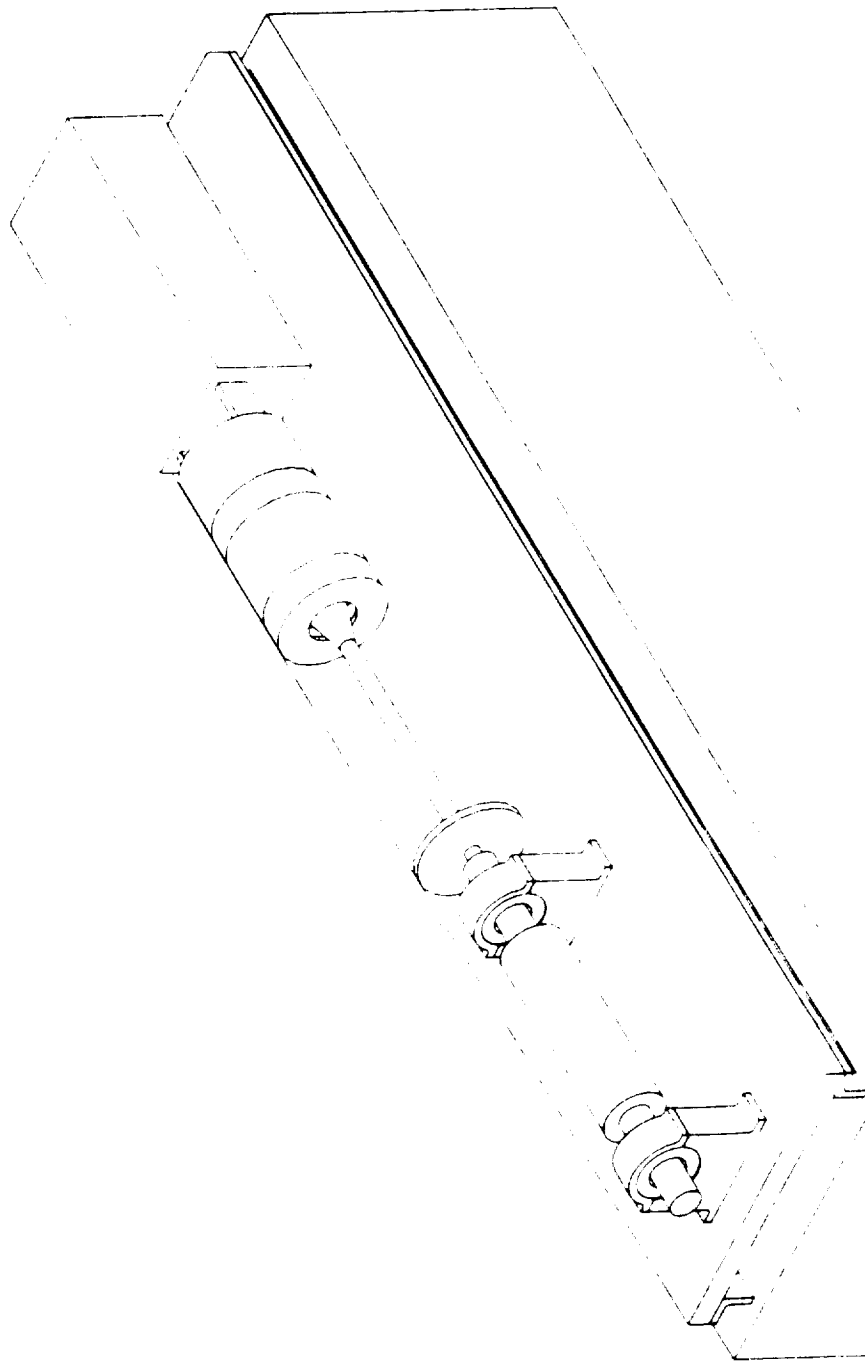
- Active Control Isolation
 - Electromagnetic Actuators
 - Low Frequency Accelerometers
 - Digital Control
 - Effects of Umbilicals

University of Virginia / NASA Lewis

INITIAL EXPERIMENT : 1-D ISOLATION

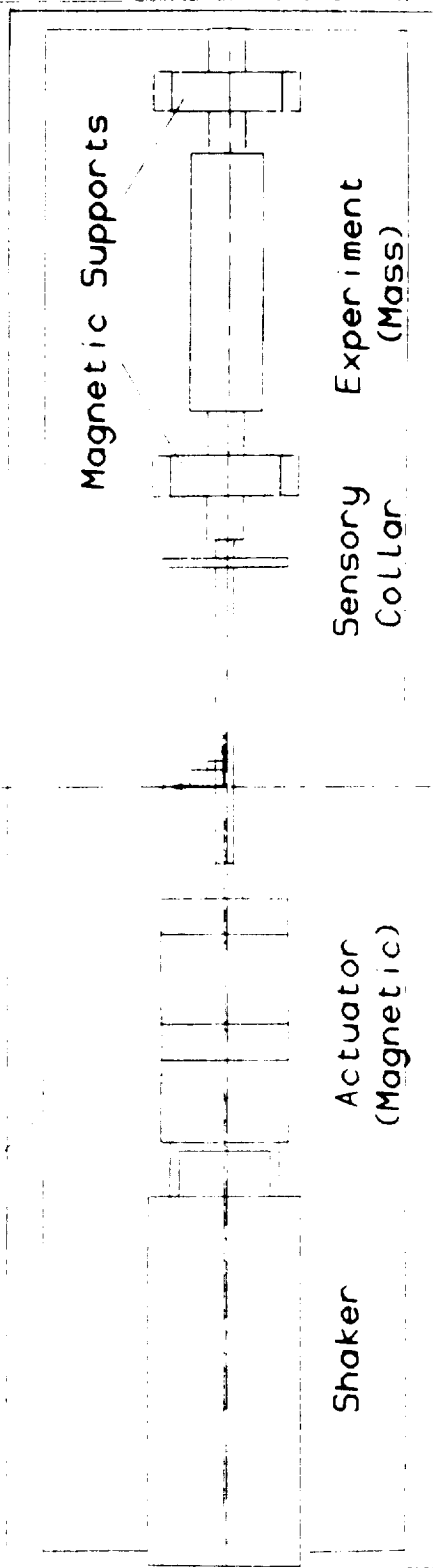
1. Long-stroke Shaker
2. Umbilicals
3. Electromagnetic Actuator
 - Lorentz Type
 - Long Action Magnetic Actuator (LAMA)
4. Sensors
5. "Experiment" Mass
6. Magnetic Supports
7. Base

University of Virginia / NASA Lewis



University of Virginia / NASA Lewis

Steel Plate

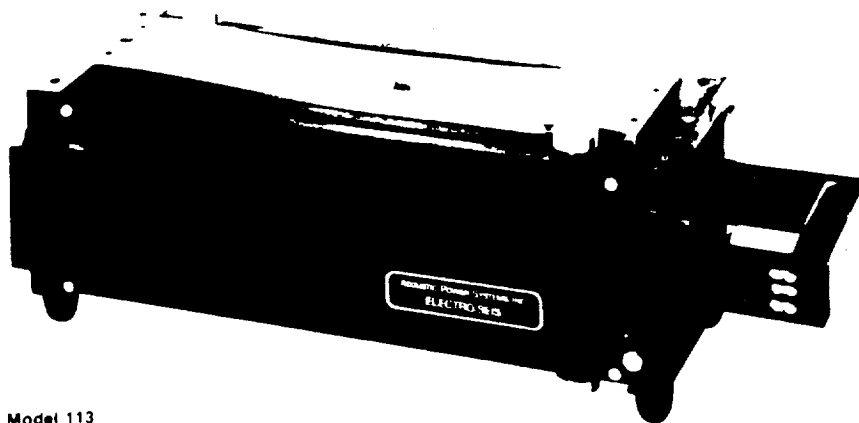


Concrete Base

University of Virginia / NASA Lewis

LONG STROKE SHAKER

6.25-in, 158-mm p-p stroke

**Model 113**

ELECTRO-SEIS

SPECIFICATIONS

Maximum Torque
Maximum Torque
Maximum Torque
Armature Weight
Maximum Overhung Load
Armature Attachment Form
Air Pressure Required
Armature Temperature
Shaft Speed Weight
Shaft Weight
Over Dimensions
Height
Width
Depth
Maximum Power Amplifier
Shaft
Handrail

Model 113

1. 1990年12月24日
 2. 1991年1月10日
 3. 1991年1月10日
 4. 1991年1月10日
 5. 1991年1月10日
 6. 1991年1月10日
 7. 1991年1月10日
 8. 1991年1月10日
 9. 1991年1月10日
 10. 1991年1月10日
 11. 1991年1月10日
 12. 1991年1月10日
 13. 1991年1月10日
 14. 1991年1月10日
 15. 1991年1月10日
 16. 1991年1月10日
 17. 1991年1月10日
 18. 1991年1月10日
 19. 1991年1月10日
 20. 1991年1月10日
 21. 1991年1月10日
 22. 1991年1月10日
 23. 1991年1月10日
 24. 1991年1月10日
 25. 1991年1月10日
 26. 1991年1月10日
 27. 1991年1月10日
 28. 1991年1月10日
 29. 1991年1月10日
 30. 1991年1月10日
 31. 1991年1月10日
 32. 1991年1月10日
 33. 1991年1月10日
 34. 1991年1月10日
 35. 1991年1月10日
 36. 1991年1月10日
 37. 1991年1月10日
 38. 1991年1月10日
 39. 1991年1月10日
 40. 1991年1月10日
 41. 1991年1月10日
 42. 1991年1月10日
 43. 1991年1月10日
 44. 1991年1月10日
 45. 1991年1月10日
 46. 1991年1月10日
 47. 1991年1月10日
 48. 1991年1月10日
 49. 1991年1月10日
 50. 1991年1月10日
 51. 1991年1月10日
 52. 1991年1月10日
 53. 1991年1月10日
 54. 1991年1月10日
 55. 1991年1月10日
 56. 1991年1月10日
 57. 1991年1月10日
 58. 1991年1月10日
 59. 1991年1月10日
 60. 1991年1月10日
 61. 1991年1月10日
 62. 1991年1月10日
 63. 1991年1月10日
 64. 1991年1月10日
 65. 1991年1月10日
 66. 1991年1月10日
 67. 1991年1月10日
 68. 1991年1月10日
 69. 1991年1月10日
 70. 1991年1月10日
 71. 1991年1月10日
 72. 1991年1月10日
 73. 1991年1月10日
 74. 1991年1月10日
 75. 1991年1月10日
 76. 1991年1月10日
 77. 1991年1月10日
 78. 1991年1月10日
 79. 1991年1月10日
 80. 1991年1月10日
 81. 1991年1月10日
 82. 1991年1月10日
 83. 1991年1月10日
 84. 1991年1月10日
 85. 1991年1月10日
 86. 1991年1月10日
 87. 1991年1月10日
 88. 1991年1月10日
 89. 1991年1月10日
 90. 1991年1月10日
 91. 1991年1月10日
 92. 1991年1月10日
 93. 1991年1月10日
 94. 1991年1月10日
 95. 1991年1月10日
 96. 1991年1月10日
 97. 1991年1月10日
 98. 1991年1月10日
 99. 1991年1月10日
 100. 1991年1月10日

APPLICATIONS

- [illegible]

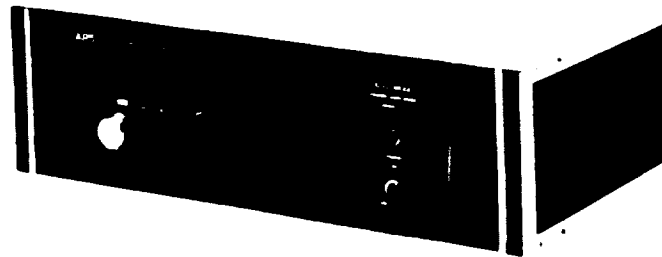
FEATURES

- [illegible]

ORIGINAL PAGE IS
OF POOR QUALITY

University of Virginia / NASA Lewis

Model 114 Power Amplifier



DESCRIPTION

The APS 114 and APS 124 **DUAL-MODE** Power Amplifiers are designed specifically to provide drive power for electrodynamic shakers. The output stage uses proven high reliability power operational amplifiers arranged to produce a balanced output.

The amplifiers have features which make them uniquely suited for studying the dynamic characteristics of structures. They may be operated in either a voltage or current amplifier mode, selectable from the front panel. This operating mode selector switch facilitates shaker drive power interruption in either a current or voltage mode for observation of resonance decay in structures.

The completely self-contained units are packaged in rugged aluminum enclosures suitable for bench or rack mounting. Forced air cooling and massive heat sinks for the output devices insure continuous operation with a shaker delivering rated force into blocked resistive or reactive loads.

A current monitor signal available on the rear panel permits monitoring of the instantaneous output current amplitude and phase. Electronic protection circuitry will detect an output short-to-ground or overload conditions and remove the drive signal.

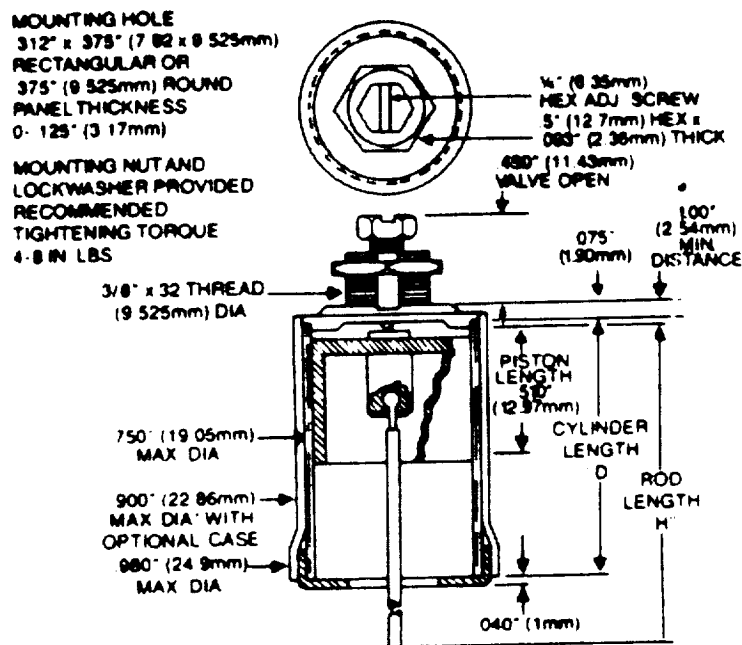
The Model 124-EP features an extended power option which provides higher peak power with the same average power of the basic Model 124.

SPECIFICATIONS

	Model 114
Average Output into shaker reactive load	125 V A rms
Peak Output into shaker reactive load	250 V A rms
Current Output peak (random noise)	6.0 A peak
Current Output continuous	4.0 A rms
Frequency Range	2-2000 Hz
Input Signal Voltage	2 V peak
Input Impedance	100 K ohm
Noise referred to max. output	-90 dB
Current Monitor output	250 mV A
Input Power	120 V 50-60 Hz 300 W 220-240 V optional
Rear Panel Connectors	
Power Output	WK3-315 Cannon
Input Current Monitor	BNC Type 3-Pa
AC Power	Std 3-Pin Receptacle
Weight	25 lb (11.3 kg)
Size HxWxD	5.22 x 17 x 13.25 inches 133 x 432 x 235 mm

University of Virginia / NASA Lewis

DASHPOT SERIES 160



Bore:

.627" (16.0mm)

Damping Coefficient:

Regular damping: 2.5#/in./sec.

Super damping: 10#/in./sec.

Maximum Pull Force:

4# (1.8kg.)

Maximum Friction Force:

Less than 1gm.

Operating Temperature

Range:

-75°C to +150°C

Approximate Piston

Weight:

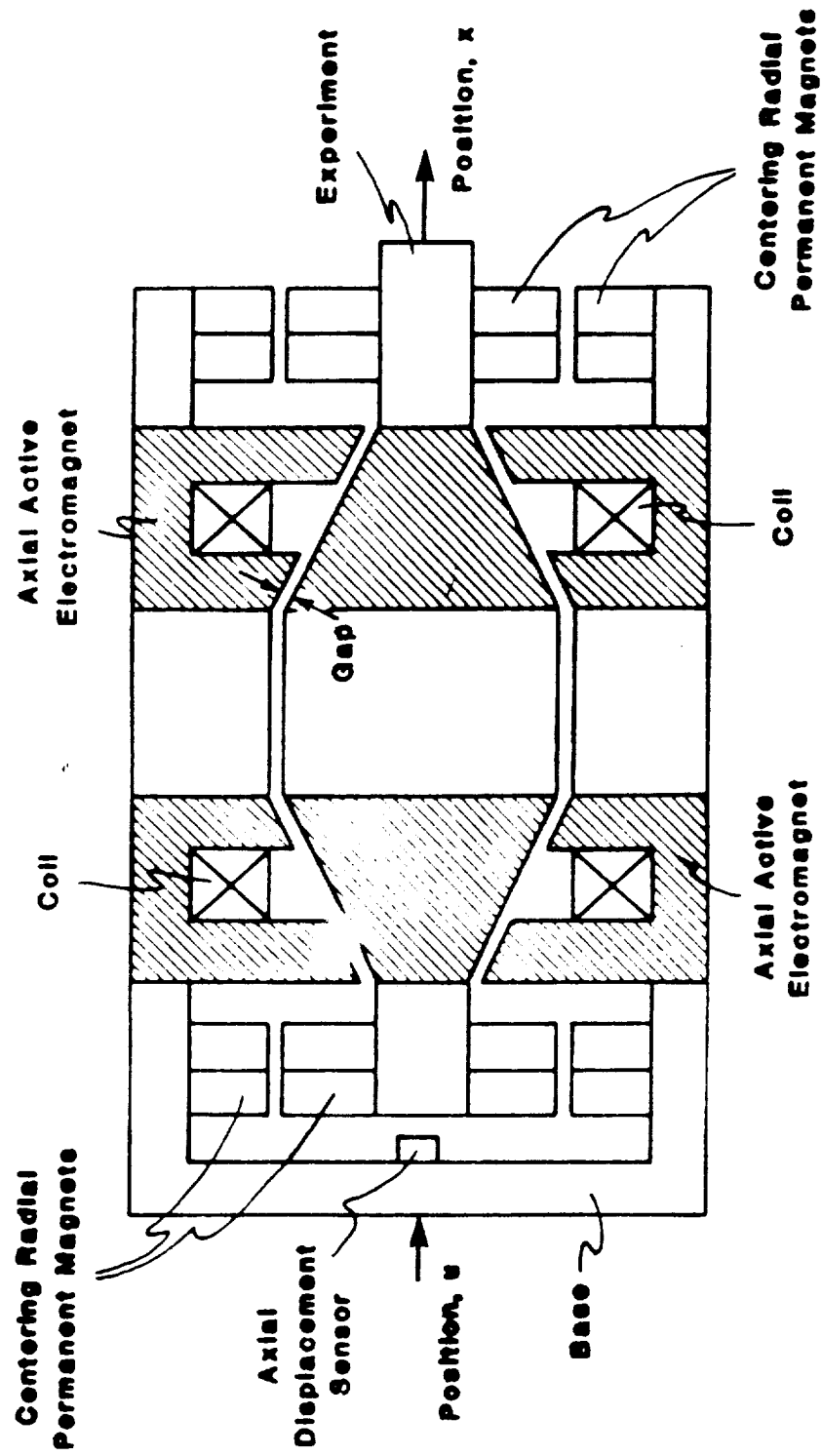
3gm.

Cylinder Weight: 1st inch:

8gm.

Each additional inch:

3.6gm.



Long Action Magnetic Actuator (LAMA) Diagram

University of Virginia / NASA Lewis

QA-700

SUNDSTRAND DATA CONTROLS
Q-FLEX® SERVO ACCELEROMETER



Features

- Cost-Effective High Accuracy
- Field-Adjustable Voltage Sensitivity and Range
- Consistently Repeatable Accuracy and Stability
- Self-Contained Sensor and Electronics in One Small Hermetic Package
- Better than 1 micro g Threshold and Resolution
- Dual Built-In Test Capability
- Wide Dynamic Range
- Internal Temperature Sensor Thermal Modeling

QA-700 Technical Data

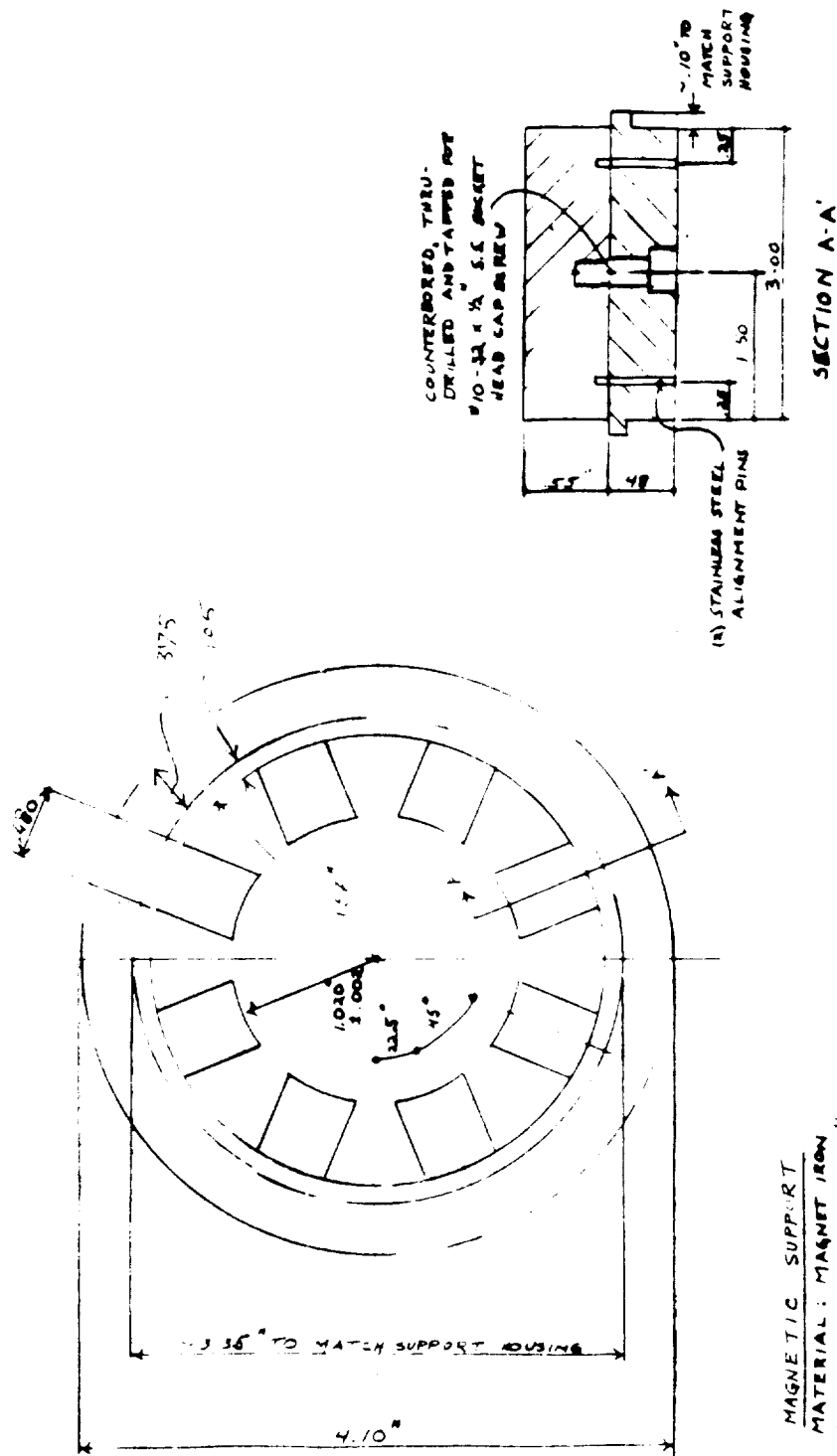
PERFORMANCE

Output Range	$\pm 30g$
Bias	8mg max
Bias Thermal Coefficient	$70\mu g/^{\circ}C$ max
Current Scale Factor	$\pm 3mA/g$ com
Scale Factor Thermal Coefficient	200 ppm/ $^{\circ}C$ com
Linearity Error	$48\mu g/g$ max
Input Axis Misalignment	$\pm 1^{\circ}$ rad
Resolution Threshold	$1\mu g$ max
Frequency Response	
0-10 Hz	$\pm 0.1\%$ max
10-200 Hz	$\pm 0.5\%$ max
200-300 Hz	$\pm 1.0\%$ max
Natural Frequency	300 Hz
Damping Ratio	0.3 to 0.8

ELECTRICAL

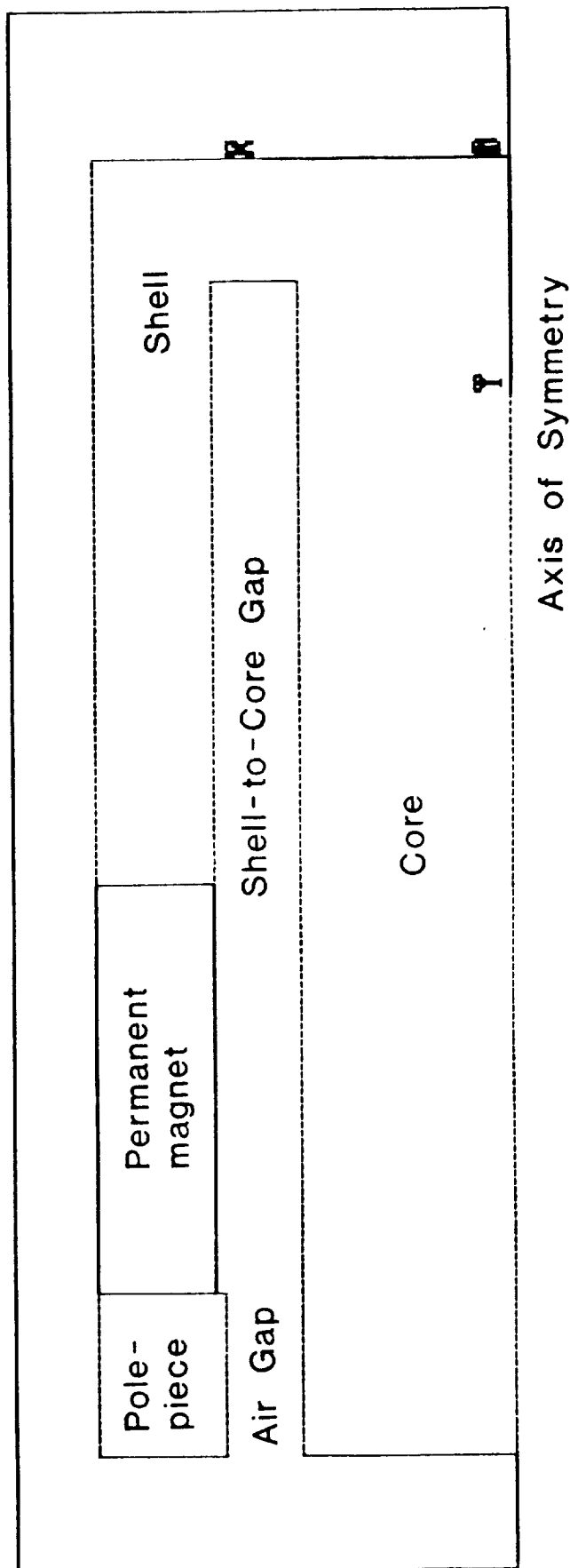
Input Voltage	$\pm 13 VDC$ to $\pm 18 VDC$
Quiescent Current max	20mA per supply
Isolation (case to all pins)	10 megohms at 50 VDC
Temperature Sensor Output*	$1\mu A/^{\circ}K$

ORIGINAL PAGE IS
OF UNKNOWN QUALITY



MAGNETIC SUPPORT
 MATERIAL: MAGNET IRON
 DIMENSIONS: ± .001"
 ± .005"
 UNLESS NOTED

MODEL: lrntz1 DATE: SEP-14-90



Axisymmetric Section of Lorentz Actuator

University of Virginia / NASA Lewis

LORENTZ ACTUATOR : DESIGN EQUATIONS

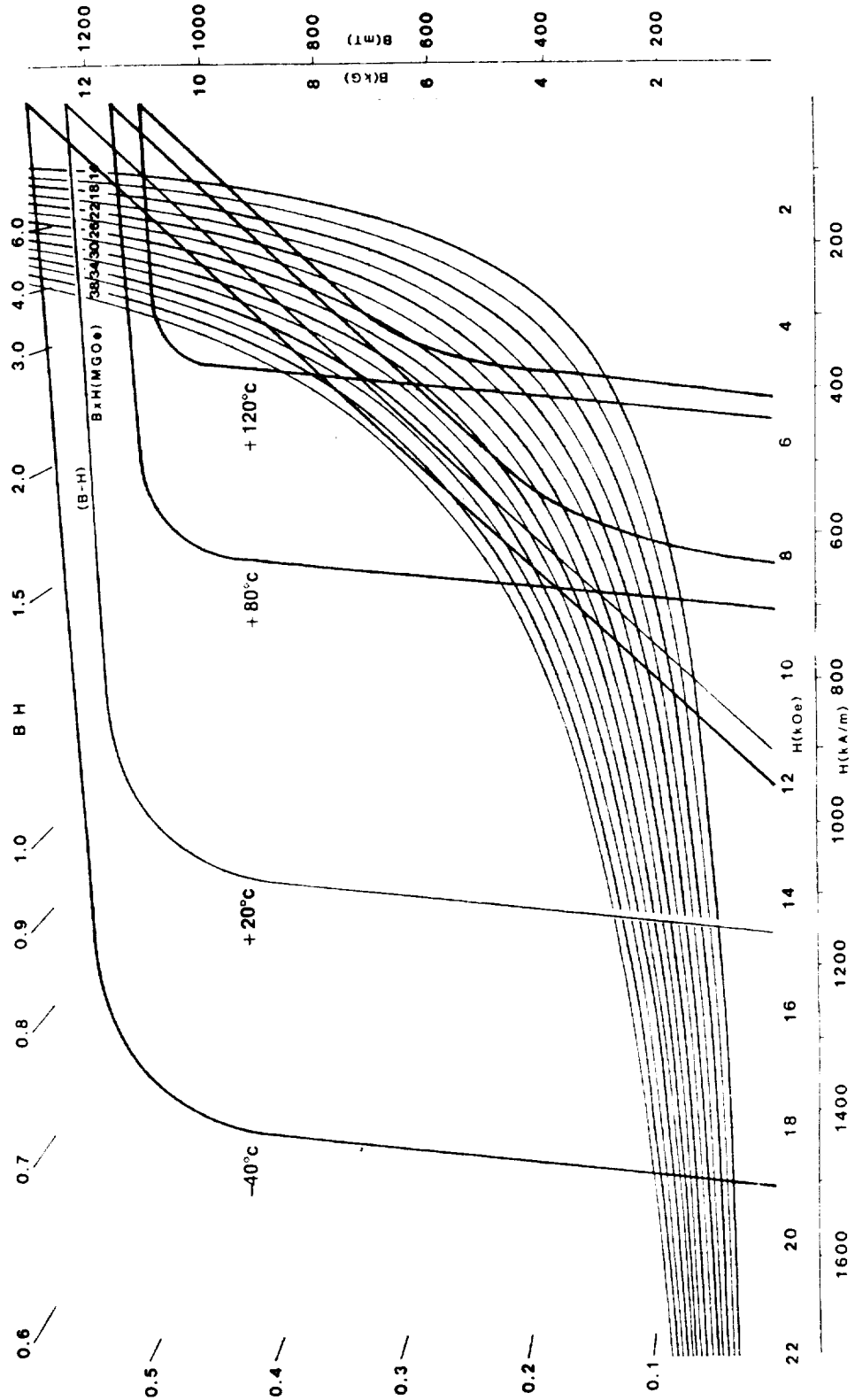
1. Assume permanent magnet operating point for maximum energy product : $(-H_1, B_1)$.
2. Compute magnet flux, $f_m = B_1 * A_m$.
3. Compute circuit flux, $f_c = H_1 * L_m / R$, where R is the circuit reluctance.
4. Compare f_m and f_c .
5. Adjust operating point until $f_m = f_c = f$, when actual operating point has been found. (In case of saturation, f = saturation flux in saturated circuit segment.)
6. Calculate air gap flux density, $B_g = f / A_g$.
7. Compute force capability, $F = i * l * B_g$, where i is the actuator current and l is the total length of coil wire in the air gap.
8. Change actuator geometry or circuit / magnet material until desired force level is achieved.

Crumax 355

Demagnetization Curve and Energy Product Values

COMPARISON DATA

	Br(kG)	Hc(kOe)	Hci(kOe)	BH max(mega-G-Oe)
CRUMAX 261	10.4	10.0	20	26
CRUMAX 282	10.8	10.1	17	28
CRUMAX 301	11.0	10.6	20	30
CRUMAX 315	11.5	10.9	14	31
CRUMAX 322	11.6	10.8	17	32
CRUMAX 355	12.3	11.3	14	35



University of Virginia / NASA Lewis

LORENTZ ACTUATOR : INITIAL DESIGN

Total length	= 3.17 in
Magnet outer diameter	= 3.20 in
Magnet inner diameter	= 2.10 in
Magnet length	= 1.00 in
Shell outer diameter	= 2.80 in
Shell base thickness	= 0.30 in
Pole-piece thickness	= 0.40 in
Core diameter	= 1.10 in
Air gap	= 0.17 in
Shell-to-core gap	= 0.50 in
Gap ratio	= 1 : 2.94
Coil wire diameter	= 26.67 mils
Number of layers	= 4
Total number of turns	= 450
Maximum coil current	= 2.52 A
Air gap flux density	= 0.50 T
Saturation flux density	= 1.20 T
Maximum force generated	= 2.33 lbf
Actuator weight (excl. coil)	= 4.12 lbf

University of Virginia / NASA Lewis

LORENTZ ACTUATOR : COMPACT DESIGN

Total length	= 3.17 in
Magnet outer diameter	= 1.95 in
Magnet inner diameter	= 1.40 in
Magnet length	= 1.00 in
Shell outer diameter	= 1.95 in
Shell base thickness	= 0.30 in
Pole-piece thickness	= 0.40 in
Core diameter	= 1.00 in
Air gap	= 0.17 in
Shell-to-core gap	= 0.20 in
Gap ratio	= 1 : 1.18
Coil wire diameter	= 26.67 mils
Number of layers	= 4
Total number of turns	= 450
Maximum coil current	= 2.52 A
Air gap flux density	= 0.45 T
Saturation flux density	= 1.20 T
Maximum force generated	= 1.93 lbf
Actuator weight (excl. coil)	= 2.18 lbf

University of Virginia / NASA Lewis

LORENTZ ACTUATOR: FINITE ELEMENT ANALYSIS

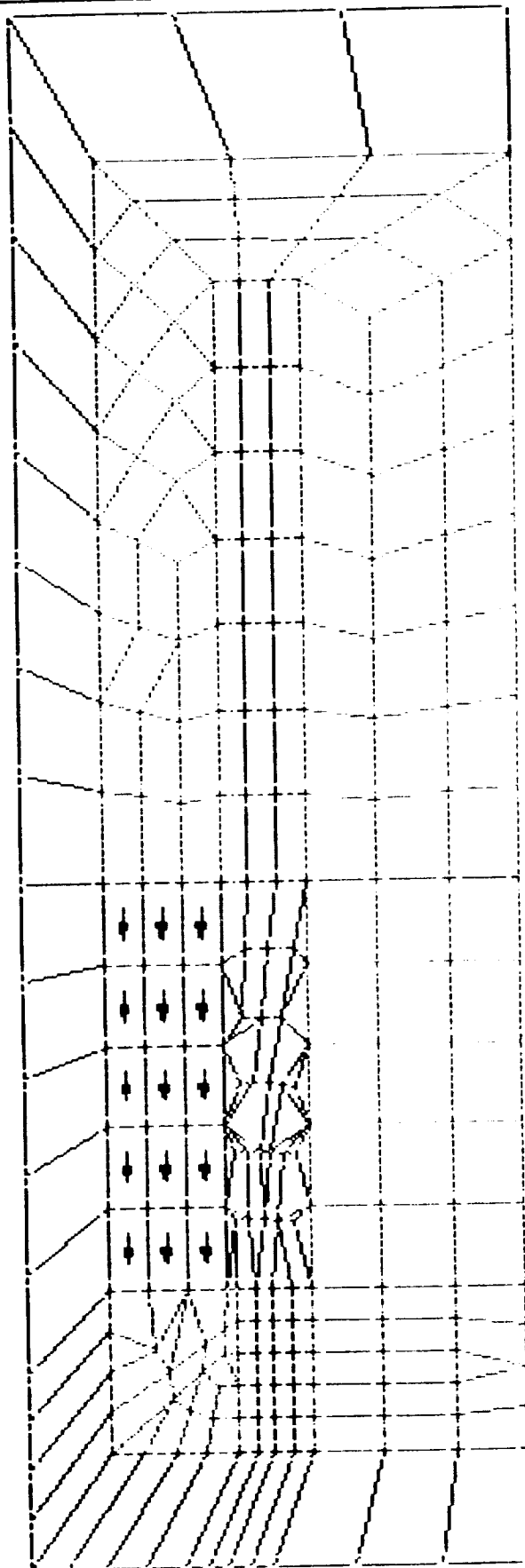
Motivation

- Different geometric configurations
- Leakage across shell-to-core gap
- Saturation in core
- Minimum weight
- Reasonable cost
- Circuit materials with different saturation levels
- Effect of current-carrying coil on air gap flux
- Fringing

Other Considerations

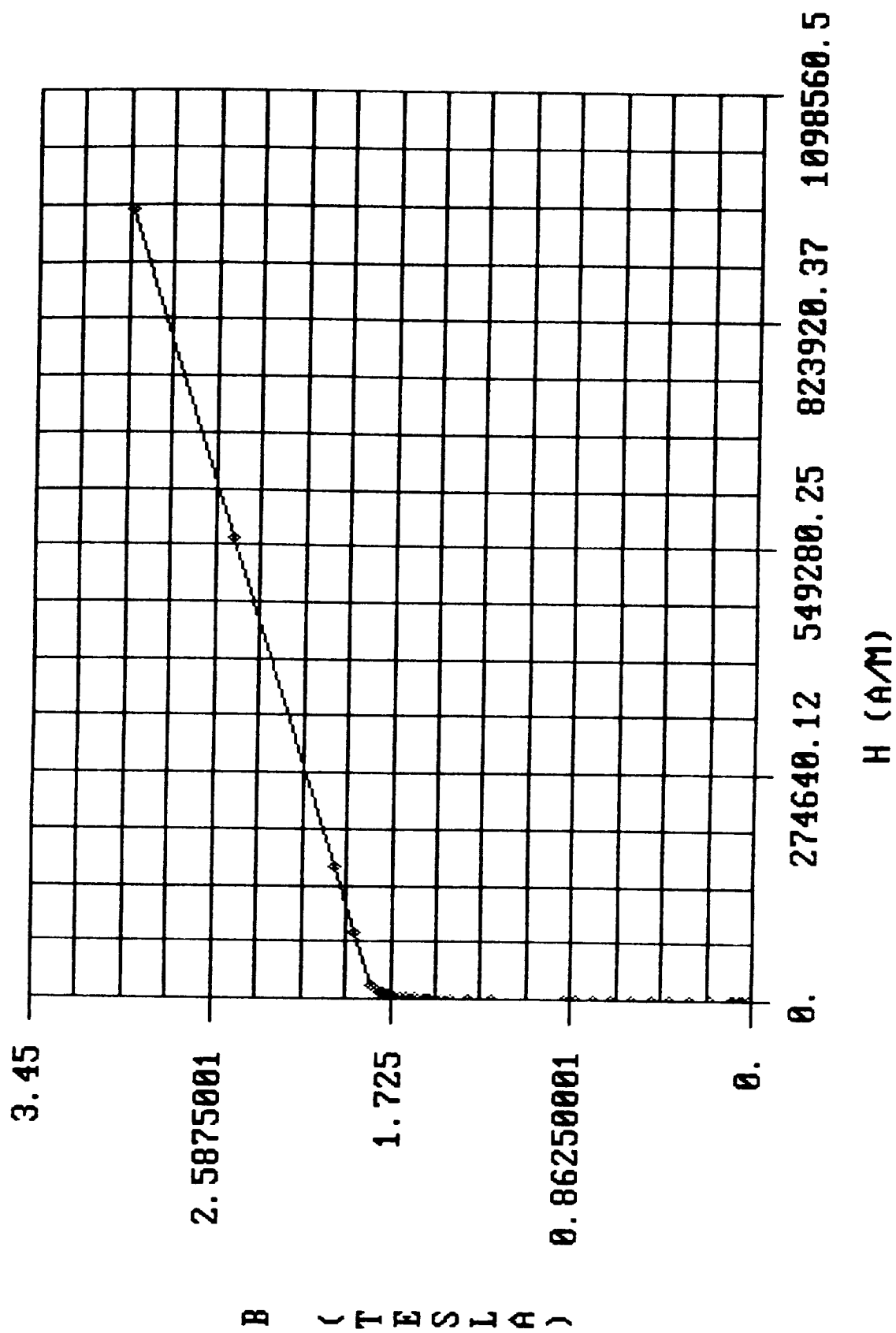
- Mesh effects (coarse/fine)
- Nonlinear analysis (B-H curves)
- High gradient regions

MODEL: lrntz1 DATE: SEP-14-90



Finite Element Mesh for Lorentz Actuator

B vs. H TABLE ID 11 (Carbon Steel)



MODEL: lorentz

DATE: SEP-19-90

MAGNETIC FLUX DENSITY (TESLAS)

MAXIMUM = 1.456

1.456

1.214

0.9710

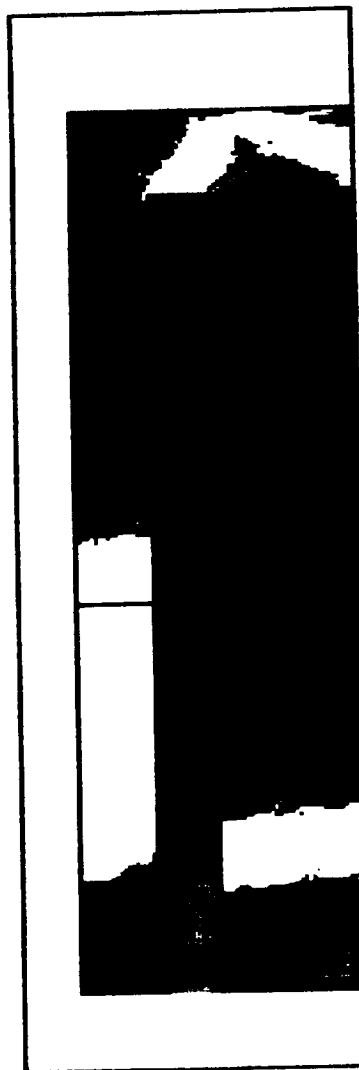
0.7282

0.4855

0.2427

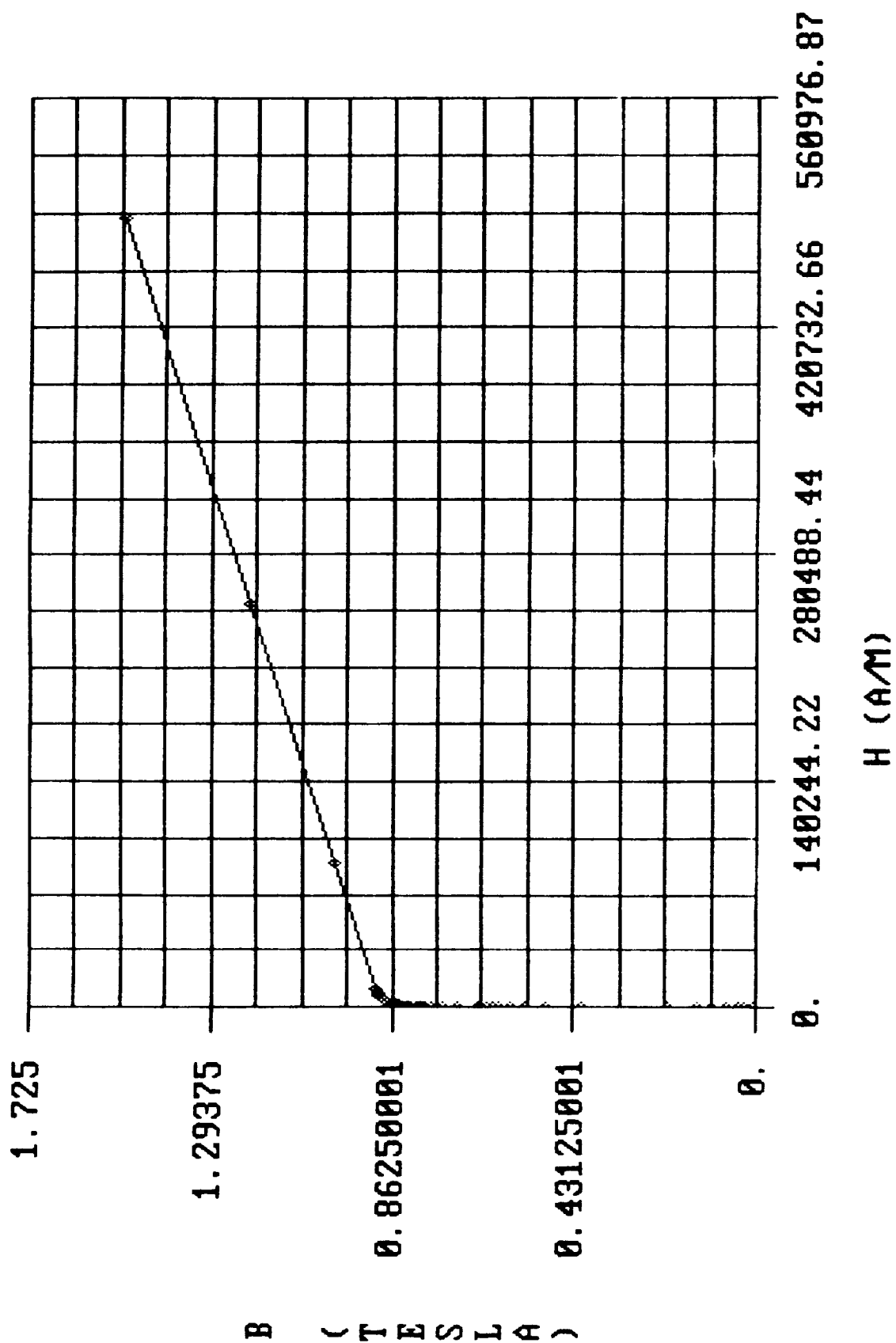
0.0000E+00

MINIMUM = 0.0000E+00



Case 1 : Circuit Material -- Carbon Steel;
No Current in Coil

B vs. H TABLE ID 13 (HYMU 80)



MODEL: lrntz1

DATE: SEP-17-90

MAGNETIC FLUX DENSITY (TESLAS)

MAXIMUM = 1.050

1.050

0.8751

0.7001

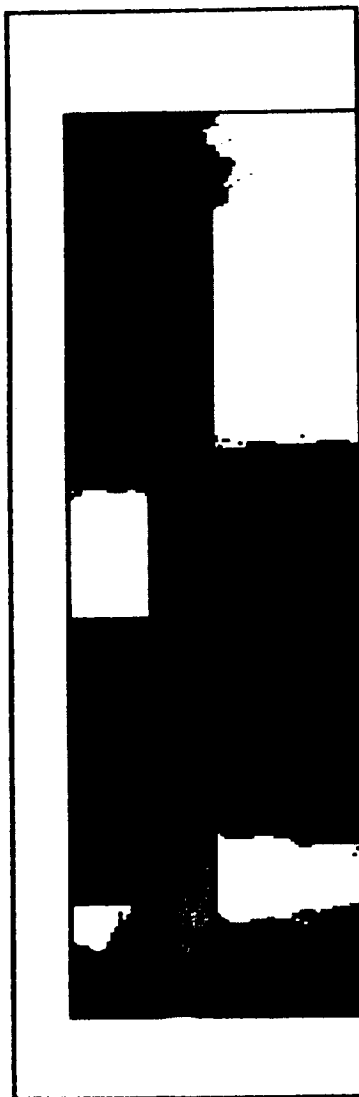
0.5251

0.3500

0.1750

0.0000E+00

MINIMUM = 0.0000E+00



Case II : Circuit Material -- HYMU 80;

No Current in Coil

MODEL: lrntz2

DATE: SEP-17-90

MAGNETIC FLUX DENSITY (TESLAS)

MAXIMUM = 1.024

0.8529

0.6823

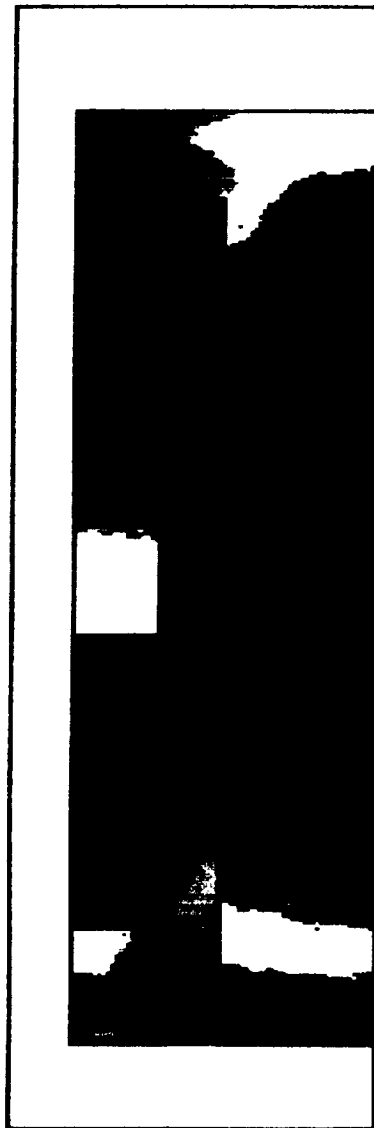
0.5118

0.3412

0.1706

0.0000E+00

MINIMUM = 0.0000E+00



Case III : Circuit Material -- HYMU 80;
2.52 A in Coil, at 0 degree Phase

MODEL: lrrntz3

DATE: SEP-19-90

MAGNETIC FLUX DENSITY (TESLAS)

MAXIMUM = 1.018

0.8485

0.6788

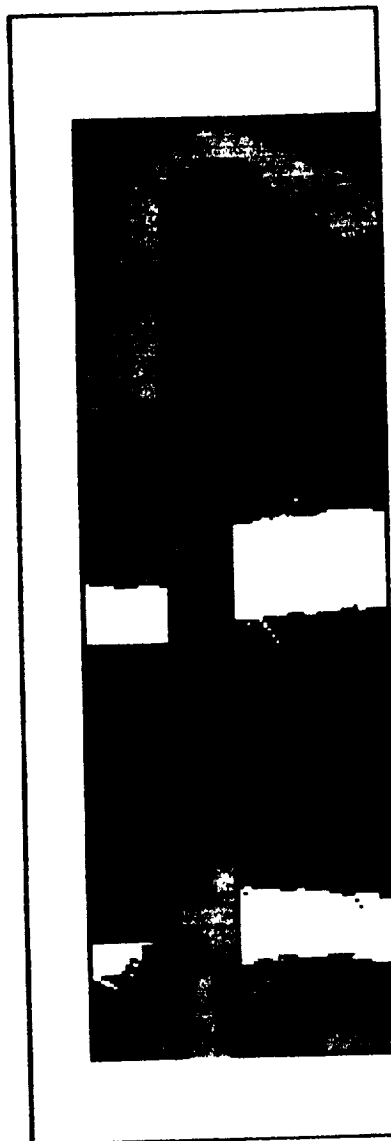
0.5091

0.3394

0.1697

0.0000E+00

MINIMUM = 0.0000E+00



Case IV : Circuit Material -- HYMU 80;
2.52 A in Coil, at 180 degrees Phase

University of Virginia / NASA Lewis

CONCLUSIONS

- Design complete
 - Experiment
 - Lorentz Actuator
- Construction in progress
 - Concrete base in place
 - Shaker and its amplifier bought
 - Magnetic supports under construction
 - Data acquisition system being developed
- Experiment operational by late 1990
 - Background vibration measurements
 - Testing with "disturbances" generated by the shaker

DEVELOPMENT of a SUITABLE INDUCTIVE SENSOR for MAGNETIC BEARINGS

David P. Plant
FARE Incorporated
4716 Pontiac Street, Suite 304
College Park
MD 20740

Ronald B. Zmood
Royal Melbourne Institute of Technology

James A. Kirk
University of Maryland

DEVELOPMENT OF A SUITABLE INDUCTIVE DISPLACEMENT SENSOR FOR MAGNETIC BEARINGS

David P. Plant
FARE, Inc.

Dr. Ronald B. Zmood
Royal Melbourne Institute of Technology

Dr. James A. Kirk
University of Maryland

I. ABSTRACT

The work presented in this paper covers the recent developments in the area of non-contacting displacement sensors for a 500 Watt-hour magnetically suspended flywheel energy storage system. "Pancake" [permanent magnet, PM, and electromagnet, EM] magnetic bearings are utilized to suspend the flywheel. The work includes a detailed review of commercially available non-contacting displacement sensors and their suitability of operating with magnetic bearings. In addition, several non-contacting displacement sensors were designed and constructed for this magnetic bearing application. The results will show, currently available, commercial non-contacting displacement sensors will not function as desired and that an inductive sensor was developed to operate within this magnetic bearing.

II. INTRODUCTION

A prototype 500 Wh flywheel energy storage system is being built for the NASA Goddard Space Flight Center. This energy storage system is targeted for spacecraft applications, for it exhibits high specific energy densities and can be used for attitude control. A conceptual view of the 500 Wh energy storage system can be seen in Figure 1. The energy storage system incorporates three key technologies, interference assembled multi-ring composite flywheel, high efficiency brushless motor and generator, and magnetic bearings. This paper focuses on displacement transducers, which are a vital element in the suspension of flywheels, via magnetic bearings. These transducers or sensors detect the displacement of the flywheel relative to the stator portion of the magnetic bearing. This displacement is referred to as the measurand. In practice, measurement systems seldom respond directly to the measurand. More often, for ease in measuring, it is desirable to

convert from one physical quantity to another by means of a transducer. The conversion in this case is from displacement to a voltage level which is proportional to the displacement of the flywheel. Next this voltage signal is feedback through the control system, compared to a reference voltage, and a control current is applied to the electromagnetic coils, in the magnetic bearings, to center the flywheel.

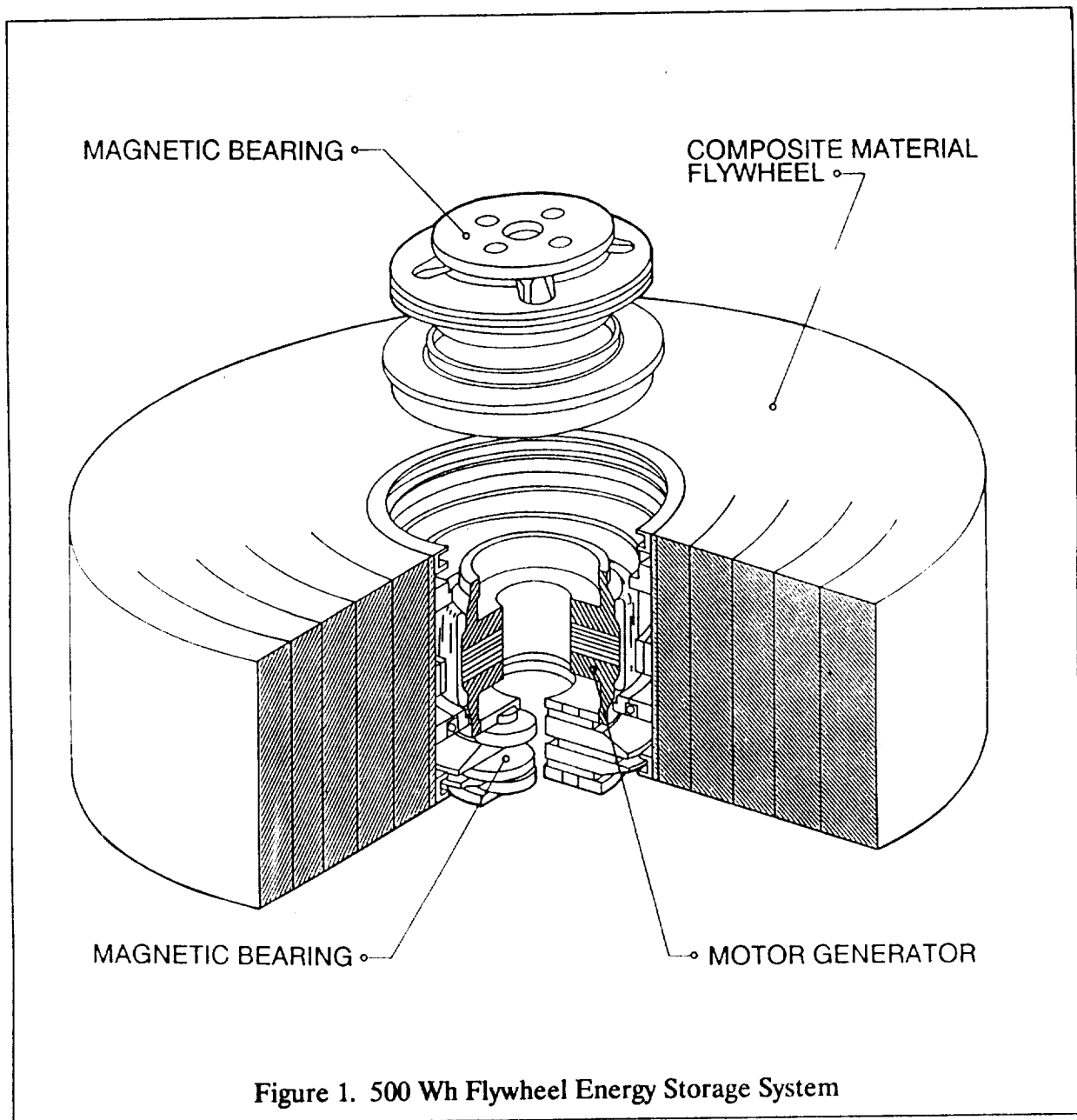


Figure 1. 500 Wh Flywheel Energy Storage System

In selecting a non-contacting displacement transducer for a magnetic bearing application, requirements for these sensors must be specified. The requirements include, the nominal linear range, the resolution, the sensitivity, the frequency response, the size of the transducer, the wire bend radius of the sensor's lead wire, and the power consumption. The main performance requirements of the displacement transducer for the 500 Wh energy storage system are listed in Table 1. For this 500 Wh energy storage system the displacement transducers were to be moved from sensing the outside periphery of the flywheel to sensing the inside surface of the flywheel. The initial location chosen for the sensor was on the inside of the magnetic bearing.

Linear Range:	20 mils
Sensitivity:	60 V/in.
Resolution:	20 μ inches
Power Consumption:	less than 40 mW
Size:	Must fit on inside of a magnetic bearing 0.250" dia. 1.000" length
Operating Environment:	Must operate in strong magnetic fields

Table 1. Sensor Specifications for 500 Wh Energy Storage System

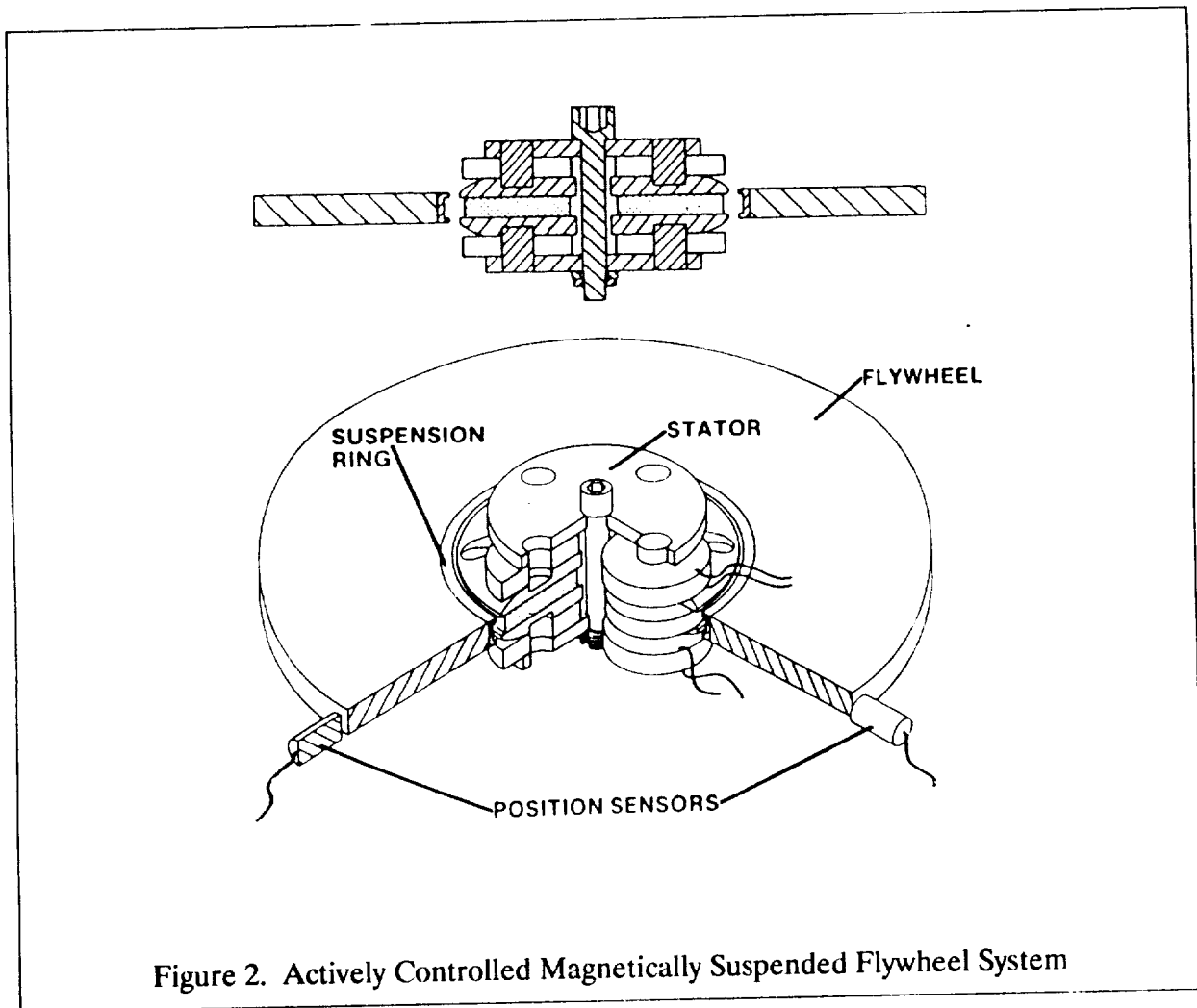
III. BACKGROUND ON COMMERCIALY AVAILABLE TRANSDUCERS

Some of the types of non-contacting displacement transducers presently accessible are inductive, capacitive, and optical transducers. Although there are other types of non-contacting displacement transducers, such as radiation, ultrasonic, and air gauging, only inductive, capacitive, and optical types were investigated. The general advantages and disadvantages [for use in the 500 Wh energy storage system] of the inductive, capacitive, and optical sensors are presented next. Inductive sensors have adequate frequency response, small size, and have a relatively large linear range. The main disadvantage of the inductive sensor was uncertainty of operating in a strong magnetic field. Also the inductive sensor produced a sensing area that was the shape of a cone protruding from the sensor's probe tip. Any conducting material that would intersect this conical sensing field would affect the output of the sensor. The capacitive sensor could be custom sized to tailor fit the 500 Wh energy storage system, due to several companies that build custom designed capacitive sensors. Problems of low frequency response, very high cost, and stray capacitance fields basically prohibited the use of capacitive sensors in the 500 Wh energy system. The optical sensors were quite promising with very high frequency responses, large linear ranges, very low cost, and very small probe size with the use of fiber optics. The only disadvantage of the optical sensor was the problem of non-uniform surface reflectivity of the target surface.

A survey, of the commercial vendors, was conducted to locate a displacement sensor that could be utilized with the 500 Wh energy storage system. From the search, several potential displacement transducers were identified and several sensors were obtained for testing with the 500 Wh energy storage system.

IV TRANSDUCER TESTING

The experimental testing of each displacement transducer was separated into two parts. The first consisted of voltage output of the transducer versus target displacement testing and the second dealt with performing experimental tests using the displacement transducer in an actively controlled magnetically suspended flywheel system. This test system utilized one magnetic bearing, see Figure 2. In the following paragraphs the results of several of the sensors tested are presented.



Two different model sensors (KD-2400 and the KD-2300-1SU) were tested from Kaman Instrumentation Corporation of Colorado Springs, CO. The KD-2400 sensor was an inductive type sensor and was the sensor used in the previous magnetic bearing systems built at the University of Maryland. The voltage output curve for this sensor is shown in Figure 3. This sensor was able to meet all of the stack system's sensor requirements except for the size requirement. The sensor's probe was too large to fit on the inside of a magnetic bearing. This sensor was tested for the reason that it was readily available and worked successfully in previous magnetic bearing systems. The other Kaman sensor, KD-2300-1SU, passed all requirements for the stack system and proved to be very versatile. The voltage output versus

displacement curve is shown in Figure 4. The sensitivity was easily adjustable to 60 volts per inch. The linear range for the KD-2300-1SU was only approximately 40 mils for an aluminum target and 35 mils for a stainless steel target. An advantage of this sensor was that it did not detect ferromagnetic materials.

The last sensor tested was the SPOT optical sensor designed and built at the University of Maryland. This sensor's voltage output versus displacement curve is shown in Figure 5. Optical sensors produce voltage output versus displacement curves that have two linear portions, these portions are named the front slope and the back slope. Since this sensor was built in-house it proved to be quite flexible. The sensitivity and linear range were easily adjustable to match the required specifications of the stack system.

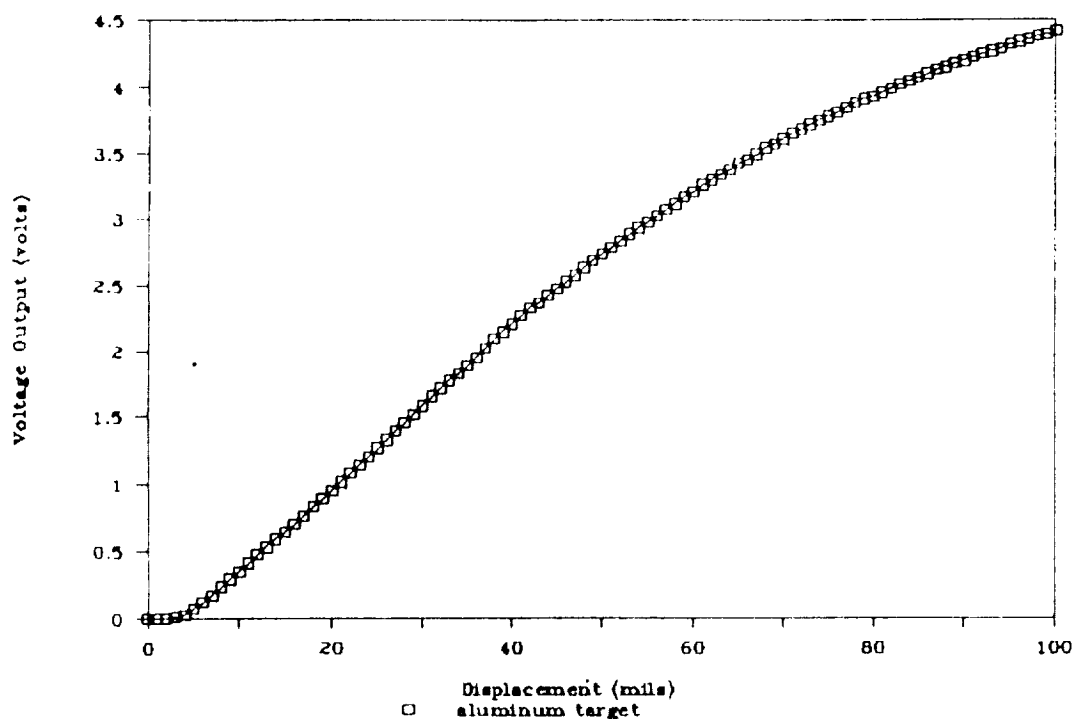


Figure 3. Voltage Versus Displacement for Kaman KD-2400 Sensor

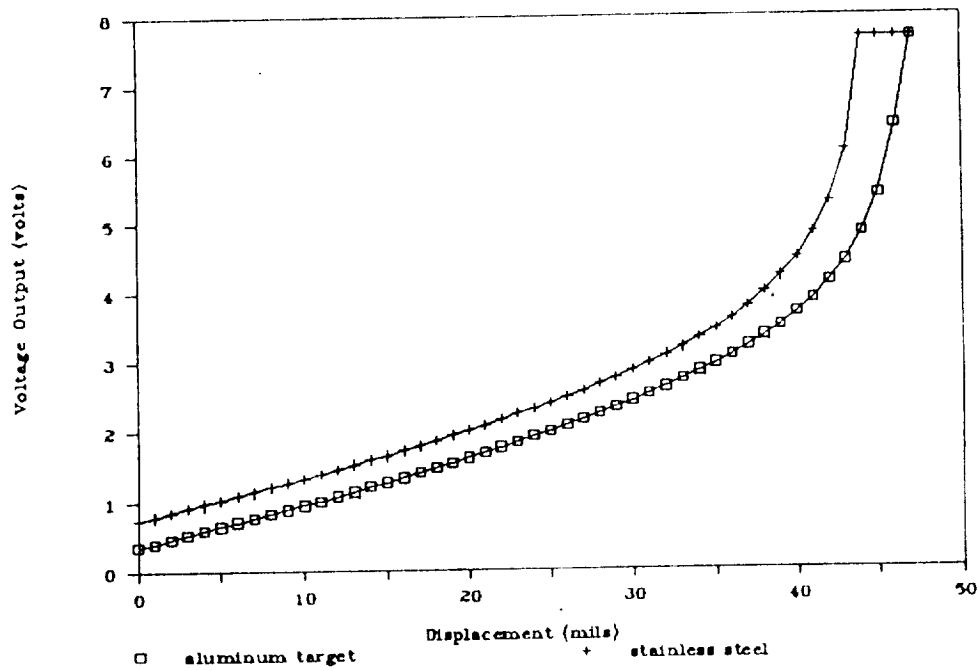


Figure 4. Voltage Versus Displacement for Kaman KD-2300-1SU Sensor

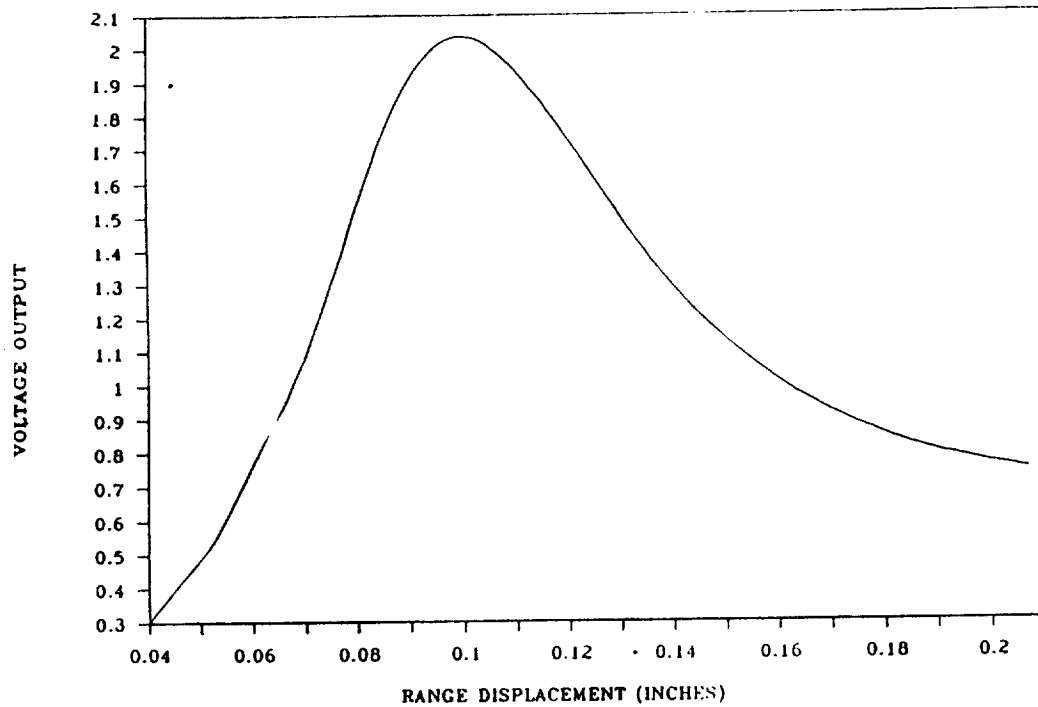


Figure 5. Voltage Versus Displacement for SPOT Sensor

Once all the displacement transducer's sensitivities were calibrated to 60 volts per inch, further experiments on the sensors were performed to reveal if these sensors could function on the inside of a magnetic bearing. The first experiment that was performed on all displacement transducers was to substitute one of the displacement transducer being tested with an existing Kaman KD-2400 inductive sensor in an existing magnetic bearing. All of the displacement transducers passed this test except for the SPOT optical transducer. The SPOT displacement transducer failed the test because of the target's non-uniform surface reflectivity. The target in this case was the outside surface of the magnetic bearing system's flywheel which is constructed of aluminum. The problem of non-uniform surface reflectivity was documented in Figure 6. This figure displays the voltage output of the SPOT and Kaman KD-2400 transducers versus time for a flywheel speed of 100 rpm. The peak to peak displacement of the Kaman KD-2400 sensor was approximately 0.05 volts, which translates at 60 volts per inch to 0.8 mils. The peak to peak displacement of the SPOT sensor was approximately 0.14 volts or 2.3 mils. In an attempt to eliminate the non-uniform surface reflectivity problem, different colored target surfaces and polished target surfaces were utilized. All these types of surfaces did not correct the problem. For this reason the SPOT sensor was dropped from further consideration.

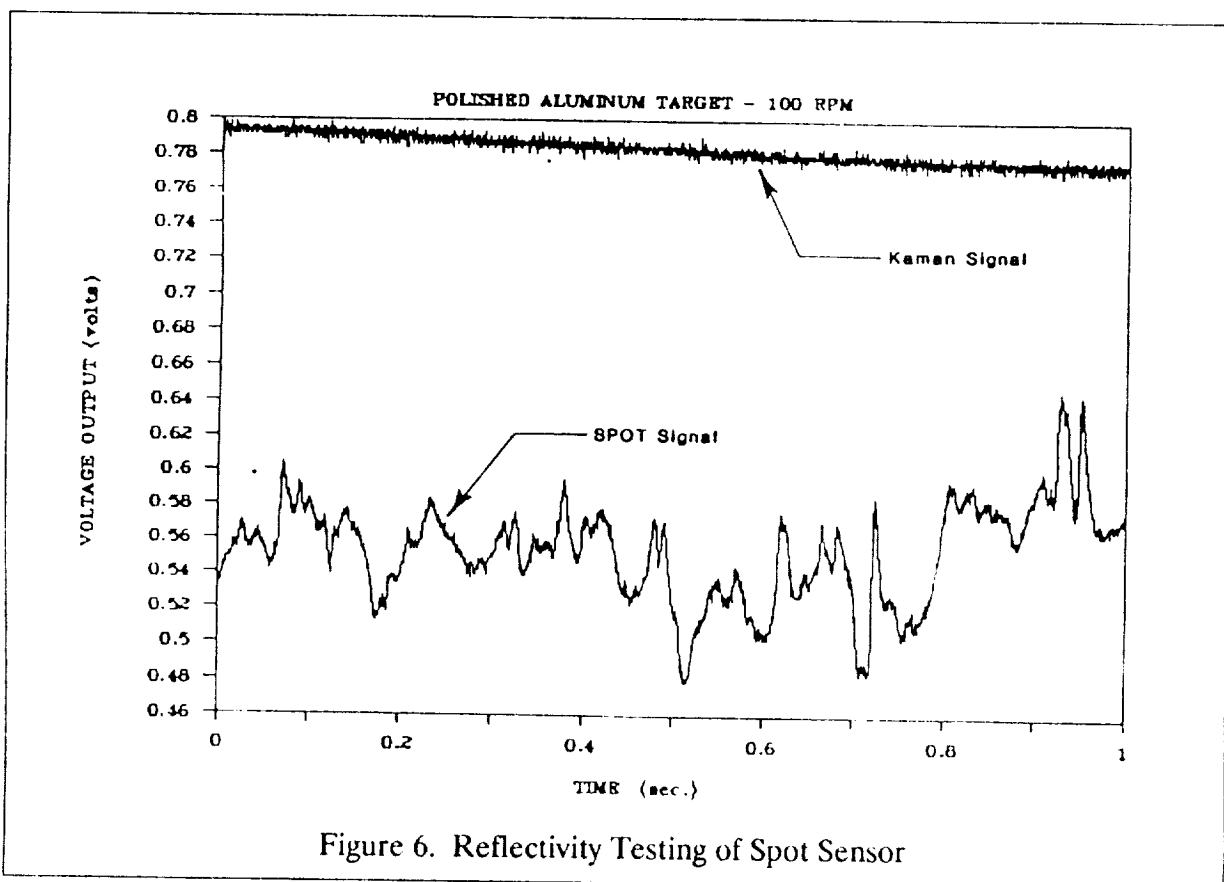
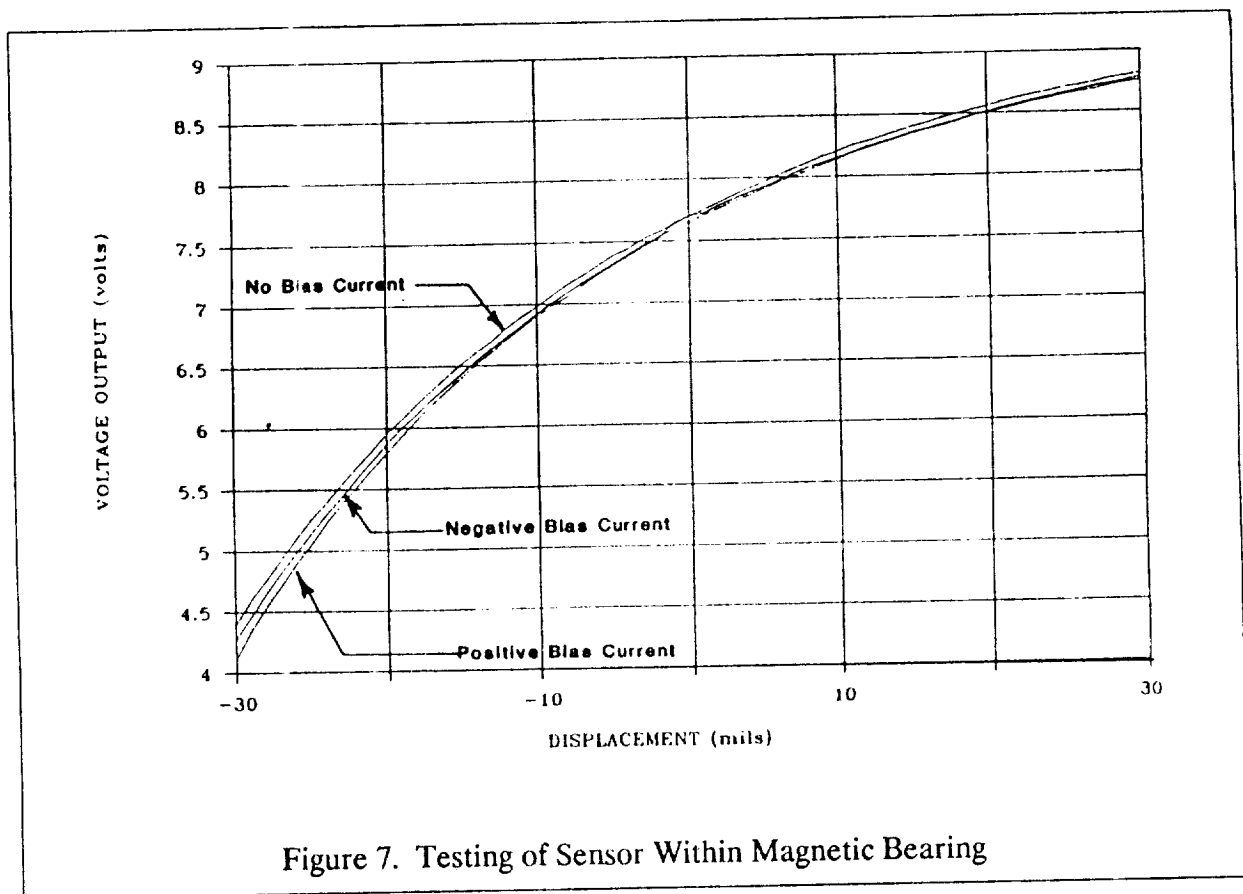


Figure 6. Reflectivity Testing of Spot Sensor

All the inductive sensors passed the suspension test. To conduct further experiments it was necessary to design and fabricate a mechanical fixture to house the displacement transducers within the magnetic bearing. Once the sensors were placed in the magnetic bearing two experiments were conducted, a voltage output versus displacement experiment and a suspension test. The voltage output versus displacement test was conducted using both the Scientific Atlanta and Kaman KD-2300-1SU sensors. For this experiment, an aluminum ring had to be placed on the inside of the return ring to provide the sensors with an aluminum target to detect. Figure 7. shows the curves created by the Scientific Atlanta sensor. There are three curves in Figure 7., one curve for no current applied to the EM coils and two curves with different currents applied to the EM coils. These three curves show that an inductive sensor can still function within a static magnetic field. For both the Kaman and

Scientific Atlanta sensors the sensitivity of the sensor decreased once inside the magnetic bearing. This change in sensitivity was due to the large magnetic fields originating from the magnetic bearing. The sensors were recalibrated to 60 volts per inch for the next test of suspension with the inside sensor. The flywheel was rotated to a low speed of a few hundred revolutions per minute and the output signals from the Scientific Atlanta and Kaman KD-2400 sensors were compared. The Scientific Atlanta sensor was tested on the inside of the magnetic bearing and the voltage output of this sensor was compared to the voltage output of one of the Kaman KD-2400 sensors, which was used to suspend the flywheel. The output signal of the Scientific Atlanta sensor did not match the signal produced by the Kaman sensor. The reason why these two graph do not correspond was because the Scientific Atlanta sensor was affected by the dynamic magnetic fields produced when the magnetic bearing was actively suspending the flywheel. To confirm this hypothesis a second experiment was run. This experiment produced a strong alternating electromagnetic field directly in front of the Scientific Atlanta sensor. The sensor was fixed relative to the target which was the iron pin at the center of the EM coil. The output of the sensor was monitored and found to vary although the sensor and target were fixed. This test concluded that inductive sensors were affected by varying magnetic fields and could not be utilized within the magnetic bearing. This test was also conducted on the Kaman and Bently Nevada sensors and similar results were obtained.



Since inductive transducers rely upon magnetic effects they are particularly prone to interference from external magnetic fields generated by the magnetic bearings actuators. Subsequent experimental investigation of one commercial transducer has shown the probable cause to be due to the transducer sensor casing. This casing is manufactured from a stainless steel which is mildly, but sufficiently, ferromagnetic so that the transducer calibration is affected by changes in the saturation level of the steel when it is immersed in an external magnetic field.

V. UOMD, RMIT & FARE TRANSDUCER DEVELOPMENTS

From the above experimental work, it was concluded that the displacement transducers tested could not be adapted to the inside of the magnetic bearing. Commercial inductive sensors will not work because of the alternating magnetic fields and the optical sensors have problems with non-uniform surface reflectivity. It is for this reason that effort has been devoted to developing suitable position transducers for 500 Wh flywheel energy storage system, which meet fairly stringent requirements of reliability, simplicity of concept, robustness, and ease of application. In this work attention has been largely concentrated on inductive transducers.

Both the inner and outer bores of the flywheel grow significantly as it spins from zero to a maximum speed of 80,000 rpm. In the case of the inner bore the radial growth has been estimated to be 0.43 mm [17 mils] at a speed of 80,000 rpm. On the other hand the rotor translational motion is limited by the touchdown bearings to ± 0.15 mm [6 mils] about its nominal center position, which it is observed is significantly less than the radial growth. Consequently any rotor position measuring system which senses the position, of either the flywheel outer rim or its inner bore, must be able to differentiate between displacements due to these two sources. To overcome this difficulty differential transducers need to be used. In the case of inductive elements positioned to sense on diametrically opposite sides of the flywheel inner bore. If these inductors are connected in an electrical bridge circuit the bridge balance will be unaffected by radial growth, and will only sense changes in inductance due to translational motion.

Experience has shown that sensitivities in the range 2 to 40 V/mm are achievable with acceptable output signal-to-noise ratios, but the sensitivities are usually limited in applications to the range 2 to 4 V/mm. Commercially available inductive transducers typically operate with carrier frequencies of 1 to 2 Mhz, and sense physical displacement signals having bandwidths up to 10 khz.

Inductive transducers require a metallic target, and if they are to sense displacement on the flywheel outer rim then it must have a metallic surface attached by some means. The limited strength of metals combined with the very high surface speed of the flywheel makes this a difficult task. While the difficulty of attaching a metal surface to the outer rim may possibly be overcome, mounting the position transducers so as to sense displacement on the outer rim of the flywheel is not recommended for other reasons. Firstly, there are problems in maintaining concentricity between the flywheel outer rim and its inner bore, both during manufacture and especially when it is running at high speed. The latter situation arises due to the effects of large rotor growth with increase in rotor speed, and the inhomogeneity of the composite structure causing an eccentricity to develop between the flywheel outer rim and the inner bore which changes as a function of speed. Secondly, the transducer sensors need to be rigidly and accurately fixed to the flywheel outer support structure which in turn must be accurately positioned with respect to the bearing stator; a complicated manufacturing problem. Thus for both manufacturing and operational reasons it is sensible to mount the position sensor internally so as to measure the displacement of the flywheel inner bore relative to the magnetic bearing stator.

VI. RELATIONSHIP TO MAGNETIC BEARINGS

The remainder of this discussion will center on how inductive sensors may be used in electrical bridge networks to solve the collocation problem by ensuring the effective displacement sensing planes are along the bearing actuator planes of symmetry. Four possible arrangements for the inductive sense coils of the transducers are shown in Figure 8. The most ideal arrangement is shown in Figure 8(a) where the coils are mounted between the pole faces, as this enables direct displacement measurement in the bearing planes $X_A X_A'$ and $X_B X_B'$. For practical reasons this arrangement is difficult to implement and so will not be considered further.

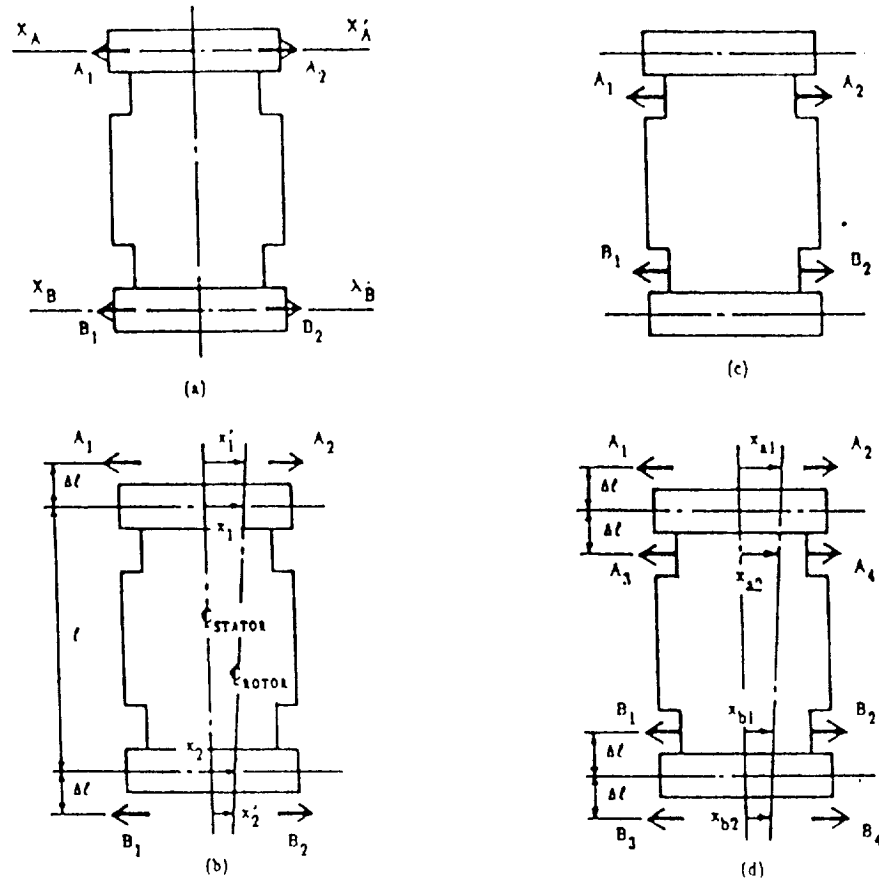


Figure 8. Alternative Location for Sensors. Sensor Positions Indicated by Arrows

The remaining possible arrangements can measure the displacements in the bearing planes of symmetry provided it is assumed that the bearing actuators and the motor/generator are rigid bodies. For example, let us consider the alternatives shown in Figures 8(b) and (c) where the inductive sense coils are shown by the arrow bars in each case. From simple geometry the displacements x_1 and x_2 can be calculated from measurements x_1' and x_2' and for the case shown in Figure 8(b) are given by

$$(1) \quad x_1 = x_1' \left[\frac{\ell + \Delta \ell}{\ell + \frac{\Delta \ell}{2}} \right] + x_2' \left[\frac{\Delta \ell}{\ell + \frac{\Delta \ell}{2}} \right]$$

and

$$(2) \quad x_2 = x_1' \left[\frac{\Delta \ell}{\ell + \frac{\Delta \ell}{2}} \right] + x_2' \left[\frac{\ell + \frac{\Delta \ell}{2}}{\ell + \frac{\Delta \ell}{2}} \right]$$

As long as $\Delta \ell / \ell$ is small the error due to uncertainties in $\Delta \ell$ can be neglected and the computed values of x_1 and x_2 can be used in place of their exact values in the respective bearing controllers.

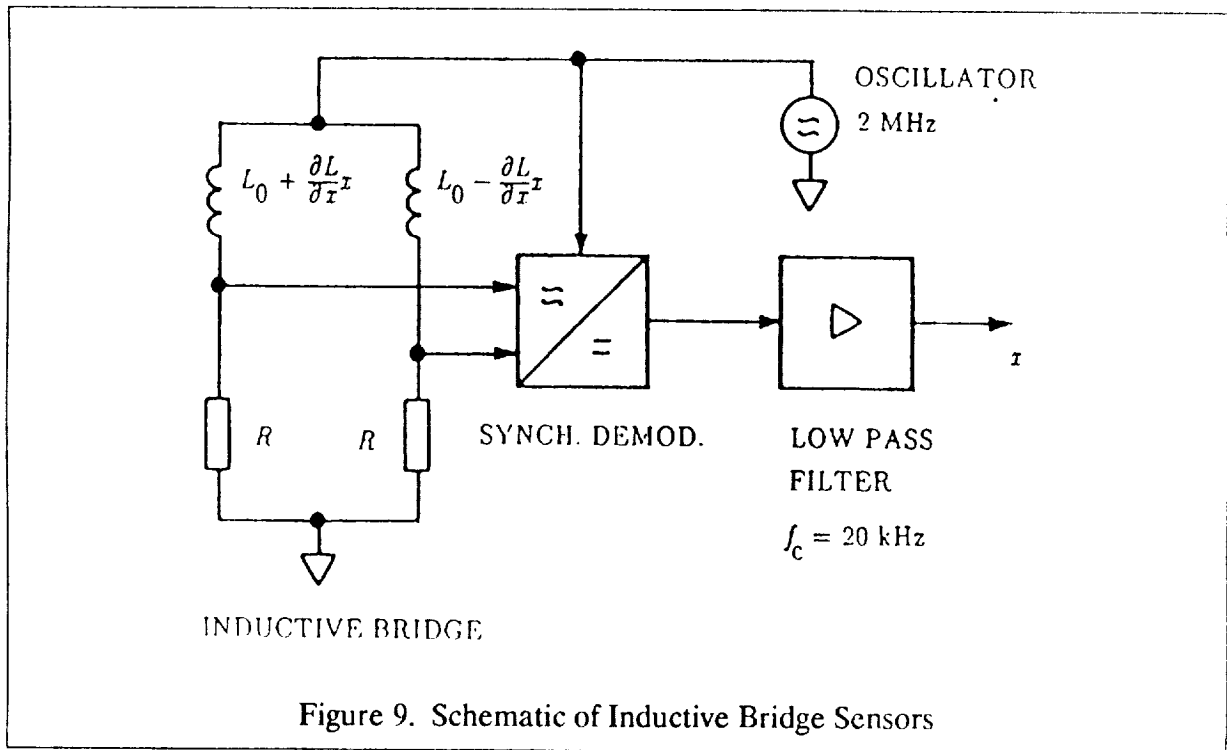
If the motor cannot be considered to be rigid then the arrangement shown in Figure 8(d) needs to be used. Here the sense coils A_1, A_2 , coils A_3, A_4 , coils B_1, B_2 and coils B_3, B_4 are separately connected in a series. Since these coils are symmetrically displaced about the bearing planes of symmetry the transducer outputs will be x_1 and x_2 , where

$$(3) \quad x_1 = \frac{x_{a1} + x_{a2}}{2}$$

and

$$(4) \quad x_2 = \frac{x_{b1} + x_{b2}}{2}$$

In Figure 9. is shown a simplified schematic of the experimental inductive bridge transducer, which can be used with any of the mechanical arrangements shown in Figure 8. The sensor inductors are connected in a Maxwell impedance bridge whose output is fed to a synchronous demodulator. The output of the demodulator passes through a low pass filter which filters the residual high frequency modulation products as well as any extraneous noise induced into the circuitry. The filter output is an analog signal whose magnitude is proportional to the displacement.

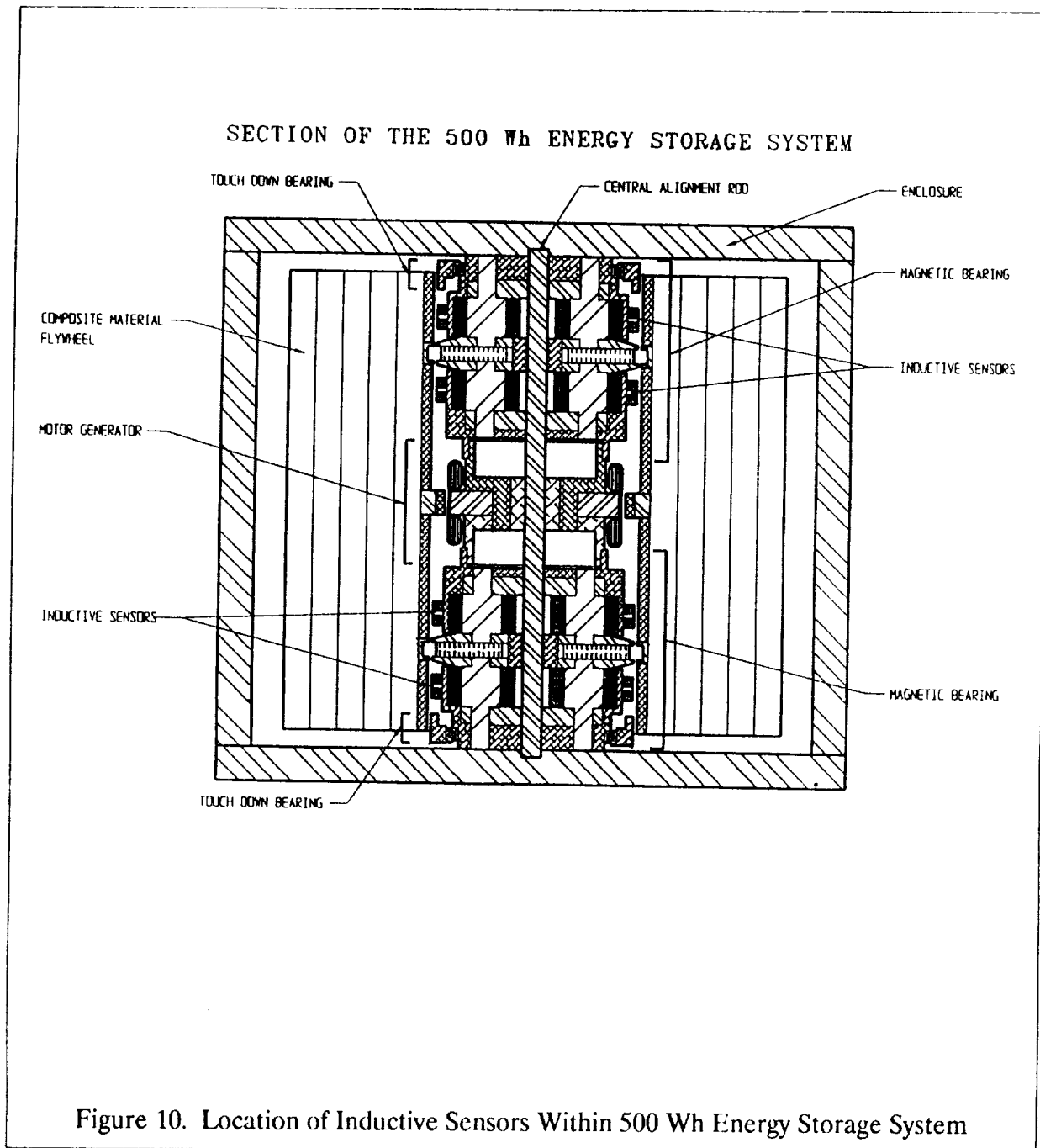


From the remarks given above concerning the use of stainless steel in commercial inductive sensors care was taken to only use non-ferrous materials, such as aluminum in the construction of the experimental sensors. Aluminum was also used for the transducer target. Experiments showed that using this construction made the transducers insensitive to changes in external magnetic fields.

The inductive sensors describe above will be utilized with the magnetic bearings in the prototype 500 Wh energy storage system. The specifications of this inductive sensor are presented in Table 2. A view of the location of these sensors within the 500 Wh energy storage system is shown in Figure 10.

Operating Principle:	Differential eddy current induction
Linear Range:	80 mils. Can be increased to 200 mils
Sensitivity:	60 V/in. Maximum exceeds 130 V/in.
Resolution:	20 μ inches at 60 V/in. sensitivity
Frequency Response:	5 kHz (3dB)
Output Range:	± 10 V (offset can be adjusted to zero output)
Mounting:	Sensors remote from signal conditioning (0 - 4 ft)
Target:	Metallic - non-ferrous
Adjacent Metal:	Insensitive to external magnetic fields
Coil Inductance Range:	50 μ H to 130 μ H

Table 2. Inductive Sensor Specifications



VII. CONCLUSIONS AND RECOMMENDATIONS

The research conducted, showed that commercially available displacement sensors could not work with the 500 Wh flywheel energy storage system. Optical sensors were too sensitive to the non-uniform surface reflectivity and the inductive sensors were affected by the dynamic magnetic fields produced by the magnetic bearings. These conclusions led to the development of an inductive sensor, which was built and tested with the 500 Wh magnetic bearings. The placement of this inductive sensor within the 500 Wh energy storage system was altered and several sensors were used in a differential arrangement. The sensors will soon be incorporated with the final 500 Wh energy storage system.

VIII. REFERENCES

1. Anand, D.K., Kirk, J.A., Zmood, R.B., Studer, P.A., and Rodriguez, G.E., "*System Considerations for a Magnetically Suspended Flywheel*", Proceedings of the 21st Intersociety Energy Conversion Engineering Conference, August 25-29, 1986, San Diego, California, pgs. 2.449-2.453
2. Kirk, J.A., Studer, P.A. and Evans, H.E., "*Mechanical Capacitor*", NASA TND-8185, March 1976.
3. Kirk, J.A. and Huntington R.A., "*Energy Storage - An Interference Assembled Multi-ring Super-Flywheel*", Proceedings of the 12th Intersociety Energy Conversion Engineering Conference, Sept. 2, 1977, Washington, D.C., pgs. 517-524
4. Evans, H.E. and Kirk, J.A., "*Inertial Energy Storage Magnetically Levitated Ring-Rotor*", Proceedings of the 20th Intersociety Energy Conversion Engineering Conference, August 18-23, 1985, Miami Beach, Florida pgs. 2.372-2.377
5. Kirk, J.A., Anand, D.K., and Khan, A.A., "*Rotor Stresses in a Magnetically Suspended Flywheel System*", Proceedings of the 20th Intersociety Energy Conversion Engineering Conference, August 18-23, 1985, Miami Beach, Florida, pgs. 2.454-2.462
6. Plant, D.P., Anand, D.K., Kirk, J.A., "*Prototype of a Magnetically Suspended Flywheel Energy Storage System*", Proceedings of the 24th Intersociety Energy Conversion Engineering Conference, August 7 to August 11, 1989, Washington, D.C.
7. Jeyaseelan, M., Anand, D.K. and Kirk, J.A., "*A CAD Approach to Magnetic Bearing Design*", Proceedings of the 23rd Intersociety Energy Conversion Engineering Conference, July 31 to August 5, 1988, Denver Co., Volume 2, pgs. 87-91.
8. Plant, D.P., Jayaraman, C.P., Frommer, D.A., Anand, D.K., Kirk, J.A., "*Prototype Testing of Magnetic Bearings*", Proceedings of the 22nd Intersociety Energy Conversion Engineering Conference, August 10-14, 1987, Philadelphia, Pennsylvania.
9. Plant, D.P., Anand, D.K., Kirk, J.A., Calomeris, A.J., Romero, R.L., "*Improvements in Magnetic Bearings for Flywheel Energy Storage*", Proceedings of the 23rd Intersociety Energy Conversion Engineering Conference, July 31-August 5, 1988, Denver, Colorado.
10. Plant, D.P., "*Prototype of a Flywheel Energy Storage System*", Master of Science Thesis, University of Maryland, 1988.
11. Zmood, R.B., Pang, D., Anand, D.K., and Kirk, J.A., "*Improved Operation of Magnetic Bearings for Flywheel Energy Storage System*", Proceedings of the 25th Intersociety Energy Conversion Engineering Conference, August 12-17, 1990, Reno, NV.
12. Horn, D., "*Optical Fibers, Optimal Sensors*", Mechanical Engineering, September, 1988. pp. 84-88.
13. Norton, H.N., "*Handbook of Transducers for Electronic Measuring Systems*", Prentice-Hall, Inc., Chapters I and 3, 1969.

The NEW ELECTRO-OPTICAL DISPLACEMENT MEASURING SYSTEM for the 13 inch MSBS

Timothy D. Schott, Ping Tchong

Mail Stop 238

NASA Langley Research Center

Hampton

VA 23665-5225

A NEW ELECTRO-OPTICAL DISPLACEMENT MEASUREMENT SYSTEM FOR THE 13 INCH MSBS

Timothy D. Schott
Engineering Technician

Ping Tcheng, Ph.D.
Senior Research Engineer

Langley Research Center, NASA
Hampton, Virginia 23665

ABSTRACT

The development of a five channel electro-optical model position measurement system is described. The system was developed for the 13 Inch Magnetic Suspension and Balance System (MSBS) located at NASA Langley Research Center. The system consists of five linear photodiode arrays which are illuminated by three low power HeNe lasers, an assembly of lenses and mirrors for shaping the beams, and signal conditioning electronics. The system is mounted to a free standing, pneumatic isolation table to eliminate vibration susceptibility. Two distinct channels are used for sensing vertical displacement and pitch, providing an angle of attack (AOA) measuring range of 40 degrees with a ± 0.02 degree precision.

INTRODUCTION

The 13 Inch MSBS was originally constructed by Arnold Engineering and Development Center in 1965 and was relocated to NASA LaRC in 1979 [1]. Model position was sensed by a system of X-ray sources and detectors which produced an analog signal proportional to their exposure to the beams. Four beams were directed diagonally across the test section at the model to detect pitch and yaw, while a fifth vertical beam detected axial motion. A suspended model would partially block the X-ray beams, leaving a portion of the detector unexposed, or shadowed. Although the X-ray system was suited for detecting model position through the aluminum test section, the potential safety hazard prompted development of an optical system. The optical system operated on the same principle of blocking a portion of a laser beam (light sheet) with the wind tunnel model and sensing position using light sensitive detectors. A new subsonic wind tunnel with a transparent test section was designed to accommodate the optical system.

The original optical system design was dictated by existing hardware used for mounting of the X-ray system. A series of poles

surrounding the test section allowed fore and aft sliding of the detectors for different lengths of models. Many custom adapters were required to mount the optical system components to the existing structure. The optical components themselves, were limited to very short focal lengths in order to fit in confined areas.

Installation of this system was completed in 1986 and it was successfully used for several years with minimal modifications. The system did suffer some deficiencies, however. Building vibrations were parasitic because of the critical optical alignment. The position sensors were mounted to precision translators partially constructed of magnetic materials. Magnetic field intensity variations would sometimes vibrate the position sensors into a resonance. Optical realignment for various models was tedious and time consuming, often consuming an entire day. The limited AOA range of ± 8 degrees did not meet the requirements of the 13 Inch MSBS, initiating design improvements.

SYSTEM DESCRIPTION

The original system consisted of five identical channels using the same 1-inch position sensors. The new system uses longer position sensors for two of the channels to improve the AOA range, resulting in a combination of two separate subsystems. In addition, a new mounting system for the optics and sensors has been implemented. The following is a detailed description of the new system components.

Position Sensors

Linear, self-scanning photodiode arrays (PDA) were chosen to detect model position. A pair of 1-inch arrays are used for sensing position in side and yaw while a third senses axial position. Each of the 1-inch PDAs contains 1024 individual elements on 25 micron centers. Each device is mounted to a 3 inch square factory supplied circuit board. The circuit boards contain all necessary clock circuits for operation. Modifications allowed the circuits to be operated in a master-slave configuration, driving the arrays with the same 500 KHz clock.

A pair of 2.4-inch arrays are used to detect vertical and pitch position. Each of these arrays contains 4096 elements on 15 micron centers. The commercially available units are presently driven by modified factory circuit boards. A master-slave configuration with a 1.1 MHz clock is also used for these units. The 13 Inch MSBS system computer provides a 256 Hz scan initiate signal, which is synchronized with both of the PDA sampling clocks.

Light Sheet Generating Optics

Two different light sheet generating methods are used for PDA

illumination to accommodate different requirements for each subsystem. The method used to illuminate the 1-inch PDAs is less critical since these are normally operated in saturation. While the device is saturated, it is not sensitive to small intensity variations along its aperture. Minor scratches on the test section windows and dust on the optics generally do not degrade the system operation.

A 5mw HeNe laser beam is fanned by using a 4mm diameter glass rod as a high power cylindrical lens. This quickly expands the beam into a wide angle, reducing the optical path length and saving space. The sheet is then collimated by a 50mm diameter plano-convex cylindrical lens with a focal length of 150mm. Since this combination loses very little power, two PDAs can be illuminated by use of a plate beamsplitter. Figure 1 illustrates how the two side and yaw detectors are illuminated in this manner. The axial array is on its own axis and is, therefore, illuminated by its own 2mw laser and associated optics for simplicity.

The two 2.4-inch arrays used for detecting lift and pitch are not operated in saturation and are very sensitive to intensity variations along the aperture. Several different lens combinations for beam expansion, including commercially available units, were evaluated before satisfactory results were obtained. A double glass rod expander, which spreads a section of the first light sheet a second time to overcome the Gaussian profile was successful but very inefficient since the resulting light sheet is many times wider than the diameter of the collimating lens. A plano-convex cylindrical collimating lens was believed to be necessary to avoid increasing the thickness of the light sheet. A lens was custom ground to meet size and focal length requirements without realizing the effects of distortion on the system accuracy. A laboratory calibration revealed that the collimating lens caused large errors due to spherical aberration and was replaced by a spherical achromatic doublet of longer focal length. Construction of a second light sheet by inserting a plate beamsplitter caused diffraction patterns, ghost images, and added to the intensity variations.

Figure 2 illustrates the present light sheet generation for the two vertical sensors. The expanding optics are basically Keplerian design so that a spatial filter may be used. A 5mw multimode laser was found to improve the uniformity of the light sheet due to its flatter profile. A single plano-convex cylindrical lens with a 6.4 mm focal length spreads the beam while a plano-convex spherical lens with a focal length of 600mm and diameter of 95mm performs the collimation. The inherently small spherical aberration of the high f-number lens reduces system errors at the expense of a long optical path length. Errors may be further reduced with a substantial increase in component cost. Unlike a cylindrical lens, the spherical collimating lens causes the light sheet to change thickness over the path length. If the PDA is located near the focus of the lens, the resulting line will be extremely narrow, making alignment more critical. The greater the distance between

the detector and the lens focus, the thicker the light sheet. A small amount of spreading is desirable to make the system less susceptible to vibration.

Several advantages are gained by splitting the laser beam prior to expansion using a cube beamsplitter. The cube beamsplitter does not rely on uniform metallic deposition and the splitting process has no direct effect on the quality of the light sheets. Although a duplicate set of components is required, the height of the two optical channels may be independently adjusted to the required optical axis. By rotating the beamsplitter about the laser beam axis, the reflected beam angle is varied without affecting the original beam. This feature allows a much higher AOA when equal positive and negative angles are not required during the same test.

Signal Conditioning Electronics

Two signal conditioning schemes are used for each of the PDA types to accommodate two different video signal formats. The 1-inch arrays are operated in saturation and produce a serial train of pulses proportional in amplitude to the exposure of each of the 1024 photodiodes sampled during a scan. The 2.4-inch arrays produce a sample and hold analog signal. The longer array is also more likely to encounter two shadow edges, resulting in two level transitions on the video signal. Detecting two shadow edges and their location requires more sophisticated electronics. The following will describe the two signal processing schemes.

The pulse video signal is carried by coaxial cable to the signal conditioner where a voltage comparator with an adjustable threshold level shapes the signal into TTL compatible rectangular pulses. The pulses are fed to binary ripple counters which count the total number of pixels exceeding the threshold level. The total number of illuminated pixels is then retained by latches for the duration of the following scan. The actual location of the shadow edge is easily determined by the system computer since one end of the PDA must always remain illuminated.

As with the pulse video processing, a voltage comparator is used at the input of the sample and hold video signal conditioner. The comparator transforms the video signal into a clean TTL level pulse by triggering on the voltage level changes occurring at the shadow edges. The comparator's hysteresis band along with various timing delays of other components help reject the diffraction effects on the video signal level transitions. Polarity sensitive monostable multivibrators are used to detect light-dark and dark-light transitions.

The location of a shadow edge is determined by counting PDA sampling clock pulses during each scan. The count is continuously fed to two separate registers during the scan. At the occurrence of a video level change, the appropriate register is enabled, temporarily storing the data until the end of the scan. The data is then shifted to the output registers, where it remains for the

duration of the following scan. An output enable pulse from the system computer controls which tri-state register will be accessed, requiring only one set of lines for both outputs. A balanced, optically isolated, line driver/receiver system is used for signal transfer between the computer and signal conditioner. The 256 Hz scan initiate pulse from the system computer is used for various resetting and clock synchronization. Shown in Figure 3 is a block diagram for one of the two channels.

Mechanical Assembly

An aluminum framework was designed for mounting the position sensors and a portion of the optical components. The mounting system basically consists of two arches joined by two sets of poles allowing fore and aft translation of the three 1-inch PDAs. Precision linear translators allow fine lateral positioning of the 1-inch arrays. The arches were designed to fit between the test section and the electro-magnets. Optical rails mount to either side of the assembly, supporting the entire optical system for the vertical sensing channels. The 2.4-inch PDAs are mounted to custom built aluminum translators for vertical adjustment. The framework assembly is attached to a commercially available 36" X 24" optical breadboard on which the remaining optical components are mounted. The aluminum breadboard provides flexibility of optical layout as well as accepting a broad range of optical holders. Ambient building vibration and magnetic field induced vibrations are minimized by floating the entire system on a pneumatic isolation table. The table, which suppresses vibration above 2 Hz at a rate of 12 db/octave, physically isolates the position sensors from the electro-magnet structure. Figures 4 and 5 are photographs of the optical system before and after installation.

CONCLUSIONS

A new model position detection system has been installed and demonstrated at the 13-Inch MSBS. System AOA range and general reliability is superior to that of the original system while meeting cost and development time requirements. Although the system has not been calibrated in the test environment, separate laboratory calibrations of the 2.4-inch and 1-inch systems were performed [2], [3]. Overall precisions of ± 0.002 and ± 0.0005 were displayed in linear measurements while angular precisions of ± 0.02 degrees and ± 0.015 degrees were exhibited by the 2.4-inch and 1-inch systems respectively. Mechanical difficulties remain to be a primary shortcoming. The physical size of the factory circuit boards limit the vertical adjustment range of the 2.4-inch PDAs, directly affecting the AOA range. Smaller clock-generating circuit boards are currently under development to alleviate this problem.

REFERENCES

- [1] Mathews, R.K.; Brown, M.D.; Langford, J.N., "Description and Initial Operation of the AEDC Magnetic Model Suspension Facility: Hypersonic Wind Tunnel (E)", AEDC-TR-70-80, May 1970.
- [2] Tcheng, P. and Schott, T.D., "A Five Component Electro-Optical Positioning System", ICIASF '87 Record. International Congress on Instrumentation in Aerospace Simulation Facilities, pp. 322-337.
- [3] Schott, T.D., and Tcheng, P., "A High Resolution Electro-Optical Displacement Measurement System", Proceedings of the 35th International Instrumentation Symposium, Instrument Society of America, 1989, pp. 441-454.

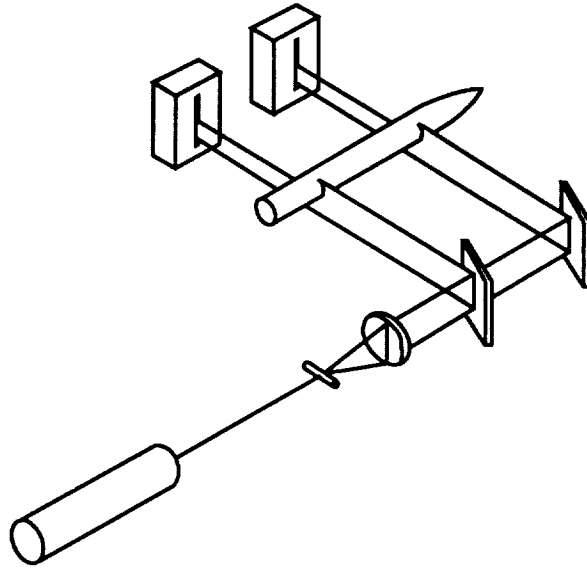


Figure 1

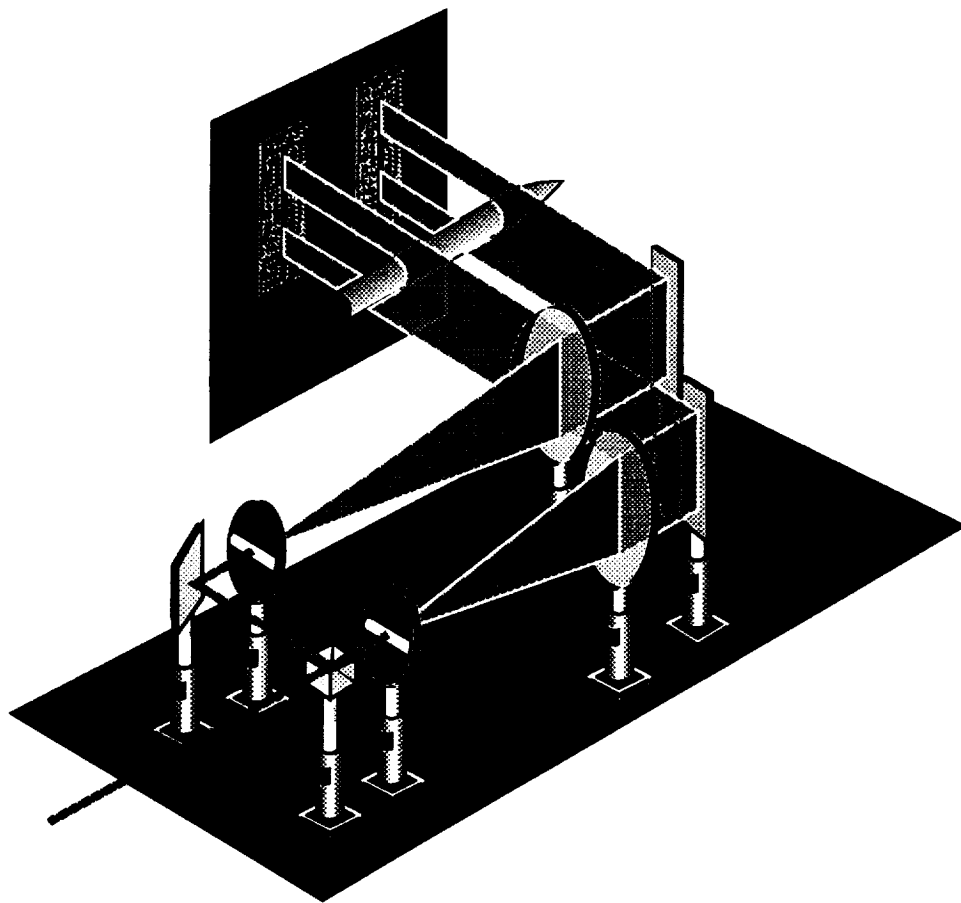


Figure 2

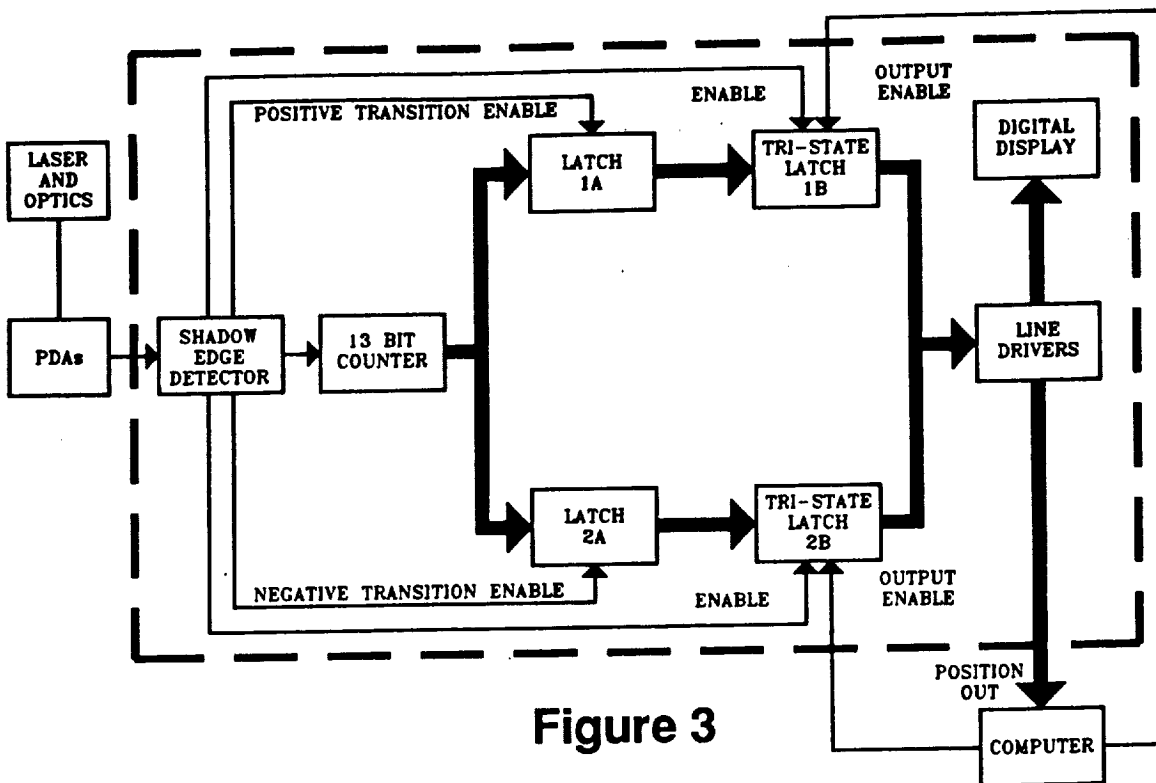


Figure 3

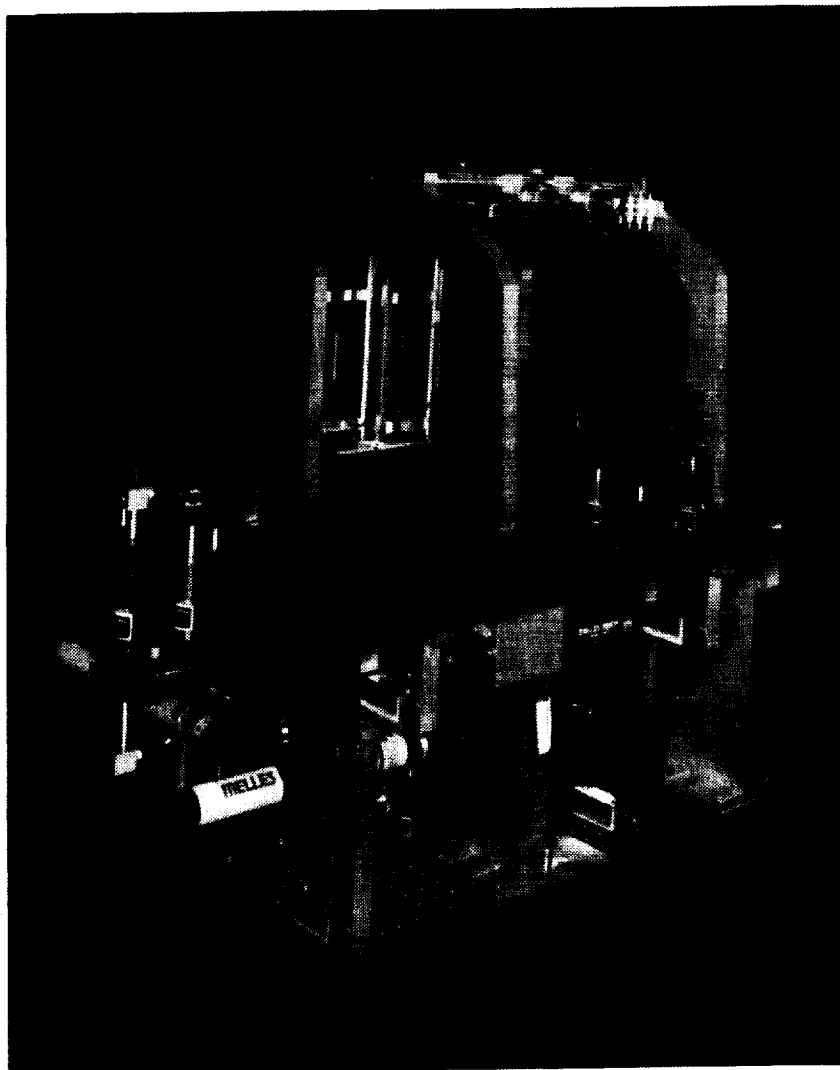


Figure 4

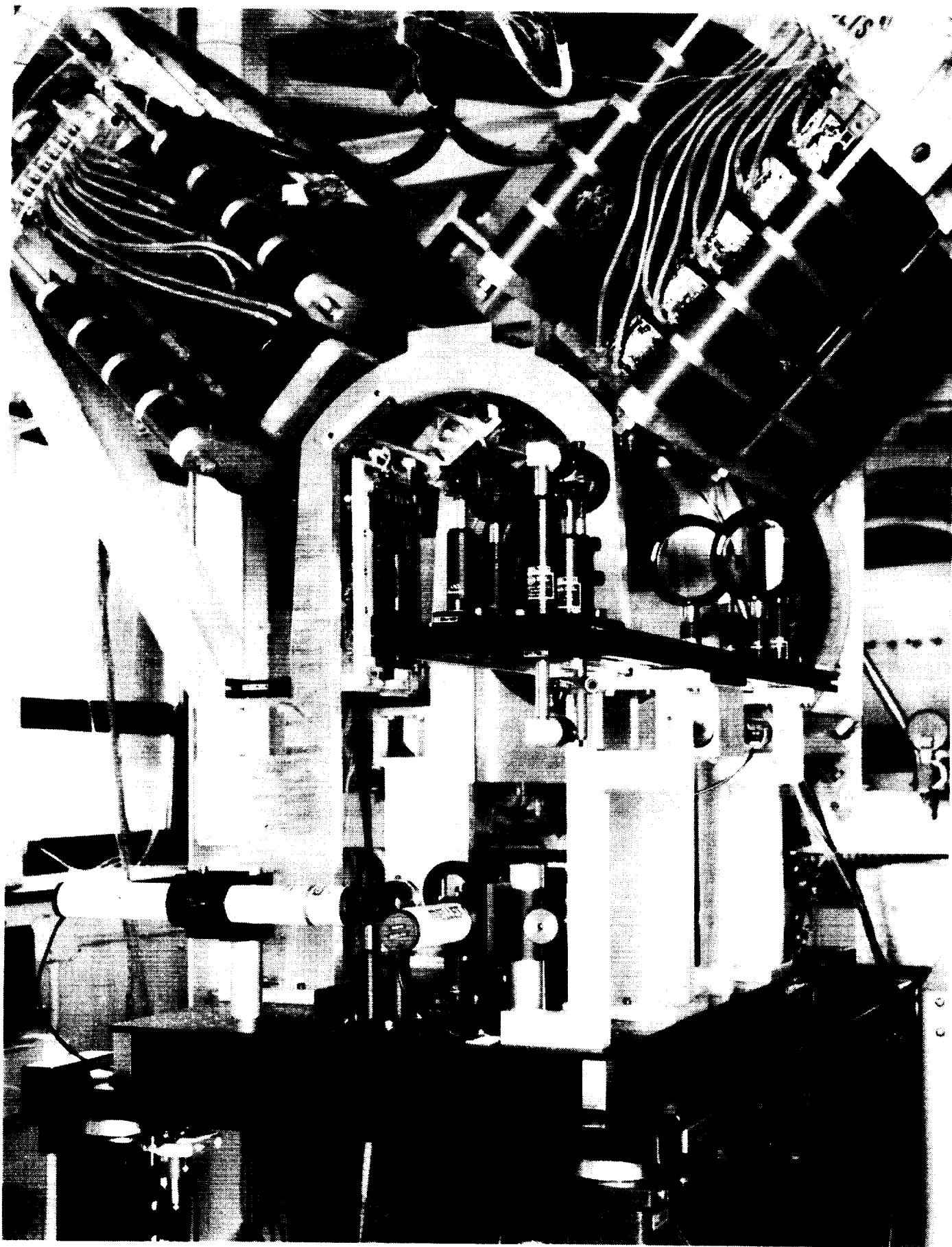


Figure 5

**The OPTICAL POSITION MEASUREMENT SYSTEM for a LARGE-GAP MAGNETIC
SUSPENSION SYSTEM (LGMSS)**

**Sharon S. Welch
Mail Stop 161
NASA Langley Research Center
Hampton
VA 23665-5225**

**James I. Clemmons Jr.
Vigyan Research Associates
30 Research Drive
Hampton
VA 23665**

Summary

A photogrammetric optical position measurement system is currently being built as part of the NASA Langley Research Center Large-Gap Magnetic Suspension System (LGMSS). The LGMSS is a five degree-of-freedom, large-gap magnetic suspension system to be built in the Advanced Controls Test Facility (ACTF). The LGMSS consists of a planar array of electromagnets which levitate and position a model containing a permanent magnet core. Information on model position and attitude is required to control the position of the model and stabilize levitation. The optical position measurement system determines the position and attitude of a levitated model in six degrees of freedom and provides this information to the system controller. Eight optical sensing units positioned above the levitated model detect light emitted by small infrared Light Emitting Diodes (LEDs) embedded in the surface of the model. Each LED target is imaged by a cylindrical lens on a linear Charge Coupled Device (CCD) sensor. The position and orientation of the model are determined from the positions of the projected target images. A description of the position measurement system, tracking algorithm, and calibration techniques, as well as simulation and preliminary test results of the position measurement system will be presented.

Introduction

A Large-Gap Magnetic Suspension System (LGMSS) is currently being built at NASA Langley Research Center to test control laws for magnetic levitation for vibration isolation and pointing. A photogrammetric optical position measurement system has been designed and is currently being fabricated at NASA Langley as a part of the LGMSS. The optical position measurement system will measure the position and attitude of a levitated body in six degrees of freedom and supply this information to the LGMSS control system. This paper will describe the requirements for the position measurement system, and present the design of the system as well as some preliminary test results on a prototype sensor. A high level description of the system will first be presented. This will be followed by a discussion of the tracking and calibration techniques. Lastly, details of the system design will be presented and some conclusions about the performance of the optical sensing system.

Presentation Outline

Position Measurement System Requirements

Overview of the Sensing System

Tracking and Calibration Techniques

Closeup of the Sensing System

Experimental Results

Position Sensing Requirements

The requirements for the position measurement system are derived from the requirements for the LGMSS. There are three fundamental requirements for the position measurement system. These requirements are: 1) that the sensing system be able to track the levitated body to an accuracy consistent with the accuracy requirements for the LGMSS; 2) that the position information supplied by the sensing system be supplied at a high enough rate that the LGMSS can stabilize levitation of the model; and 3) that the measurement made by the sensing system not interfere with the function of the LGMSS.

To meet the three requirements specified above, a photogrammetric optical sensing approach was selected. Small point targets embedded in the surface of the levitated body are detected by multiple cameras positioned about the model. The locations of the projected target images are determined and triangulation techniques are used to determine the position and attitude of the model from this information. The accuracy requirement for the optical sensing system is set by the accuracy requirement for the LGMSS. The LGMSS is required to position a levitated model to an accuracy of ± 0.01 inches in x, y, and z, and ± 0.02 degrees in yaw, pitch, and roll (defined by the Euler angles psi, theta, and phi). The optical sensing system is allowed thirty percent of the error budget and thus the required accuracy for the sensing system is ± 0.003 inches in x, y, and z, and ± 0.006 degrees in psi, theta, and phi. The frequency response for the optical sensing system is 20 samples/second. This is not a fast update rate, but is fast enough that the LGMSS can control the levitation of the model to the accuracy specified for the system.

Position Sensing Requirement

Position Measurement Accuracy

+/- 0.003 inches xcm, ycm, zcm

+/- 0.006 degrees in psi, theta, phi

Frequency Response

20 samples/second

Noninvasive Measurement

Overview of the Optical Sensing System

In figure 1 is a block diagram of the optical sensing system. Eight infrared light emitting diode (LED) targets are embedded in the surface of the levitated model. The targets are multiplexed in time for target identification. As each target is flashed on, it is detected by sixteen linear charge coupled device (CCD) array sensors. A cylindrical lens, positioned in front of the detector focuses the light emitted by a target as a line of light on the detector array. Each array has 2048 photosensitive elements. A voltage signal is output from the array which is proportional to the light falling on each element or pixel. (figure 2) The location of each target image along the CCD array is determined by calculating the location of the centroid of the light distribution falling on the detector. The analogue video signal output of each CCD sensor is digitized and stored in a random access memory (RAM) which can be accessed by a high speed digital signal processor (DSP). There are a total of sixteen analogue to digital converters (one for each sensor), and sixteen DSPs (Texas Instruments TMS320C30s). The location of the centroid of light is calculated by the DSP and stored in a central memory. The locations of the target images in the sensors are used to determine the position and attitude of the levitated model. Data flow from the DSPs to the central memory is controlled by a 68000 based microcontroller. The calculation of model position and attitude is performed in an I860 based array processor. The array processor resides on a VME bus and is controlled by a SUN computer.

Optical Sensing System

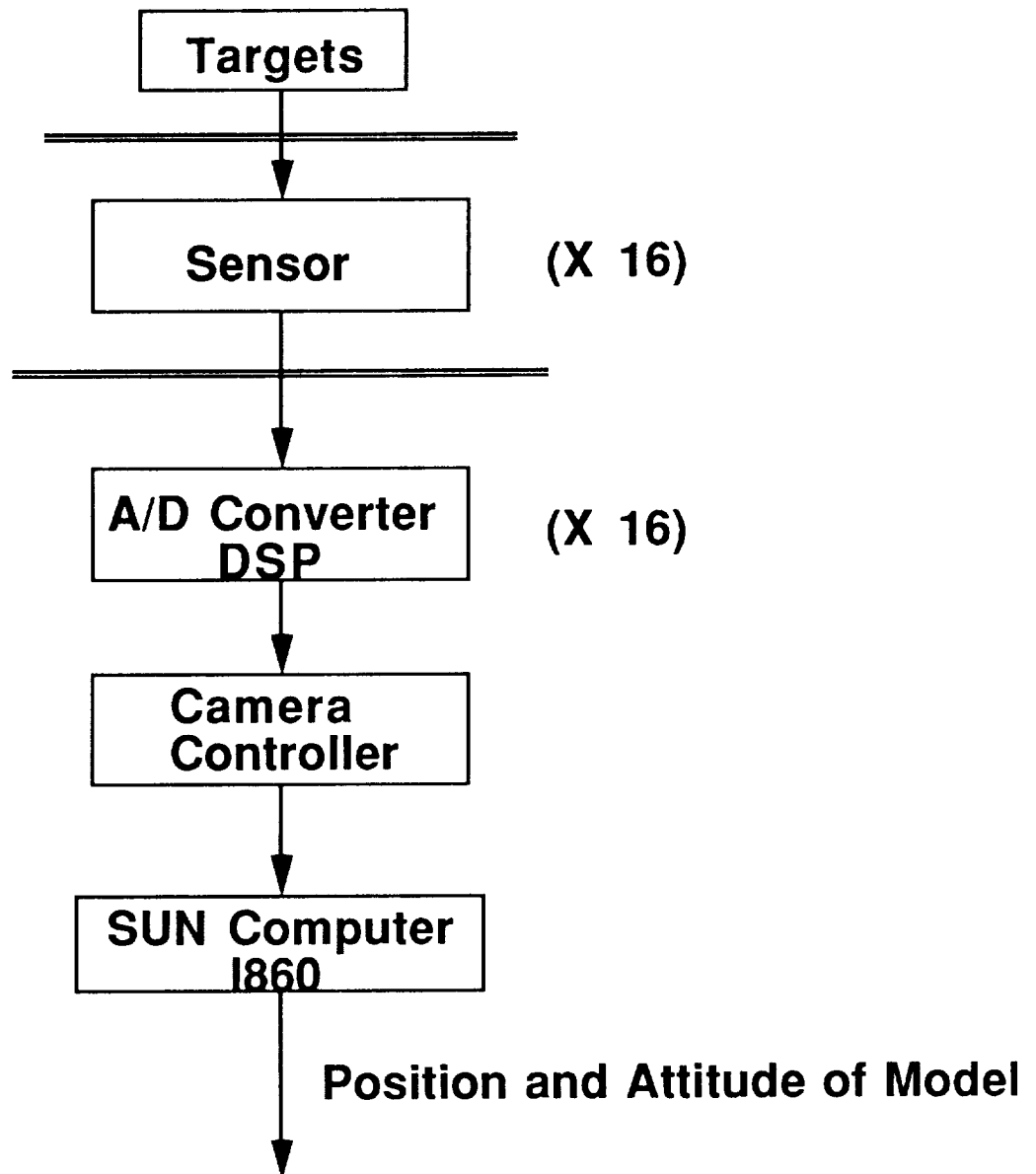
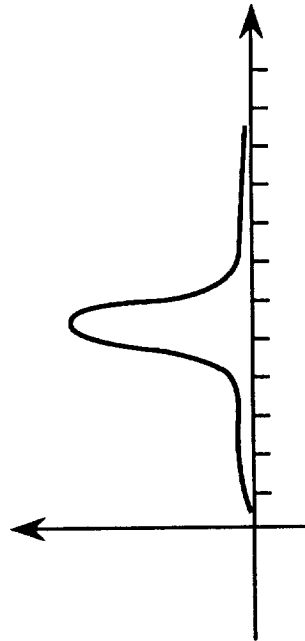


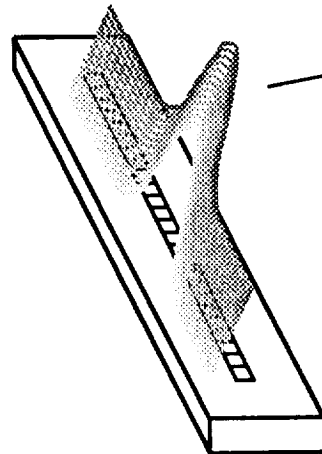
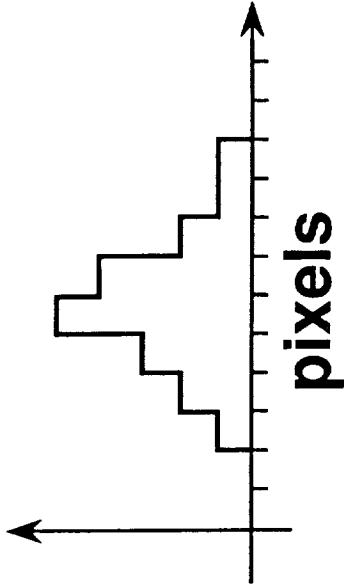
Figure 1. Block diagram of the optical sensing system showing signal flow.

LIGHT DISTRIBUTION

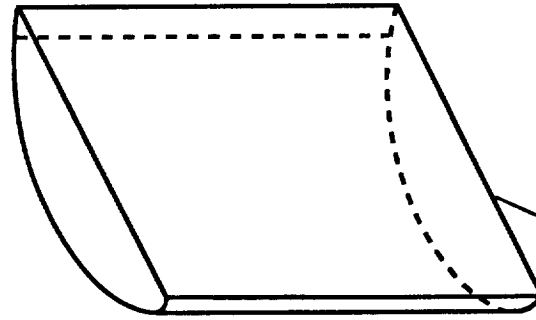
Light intensity
incident on array



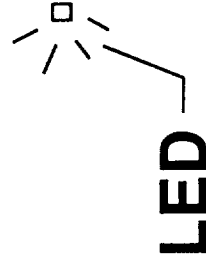
Voltage output
of CCD sensor



Light
distribution



Cylindrical
lens



LED

Figure 2. Drawing showing the light distribution incident on the Charge Coupled Device (CCD) detector and the CCD detector output.

Sensing Unit

Eight sensing units are located symmetrically about, and approximately five feet above the levitated model. Each sensing unit consists of two linear CCD sensors oriented orthogonally with respect to one another.(figure 3) The output of each sensing unit is thus an x and y camera location for each projected target image. Each sensing unit is mounted to the sensing system support structure. The sensing unit mount allows the orientation of the sensing unit to be adjusted in two angular directions as well as the verticle direction.(figure 4)

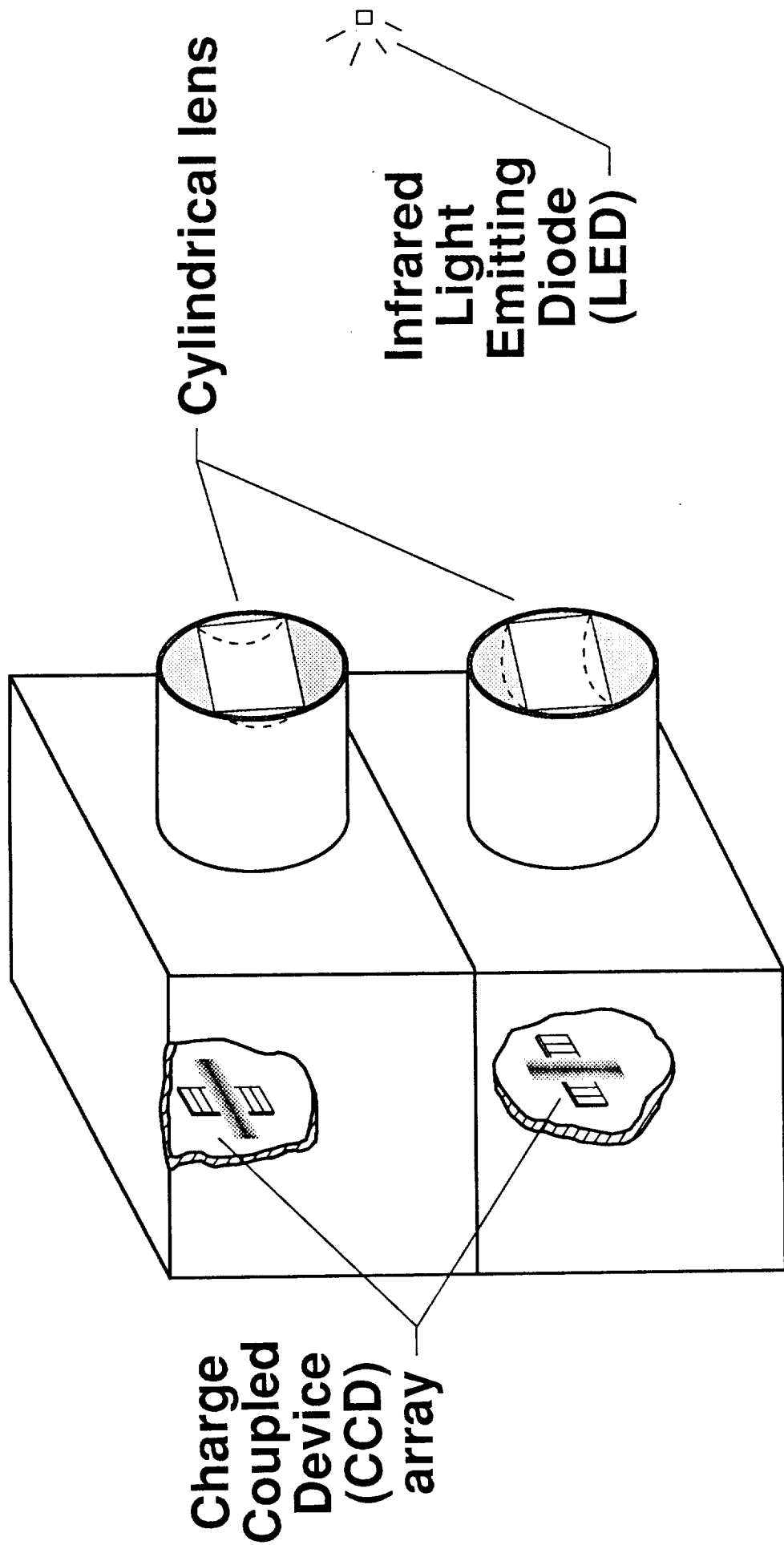


Figure 3. Drawing of a sensing unit. Each sensing unit consists of two CCD cameras oriented orthogonally.

DIAGRAM OF SENSING UNIT MOUNT

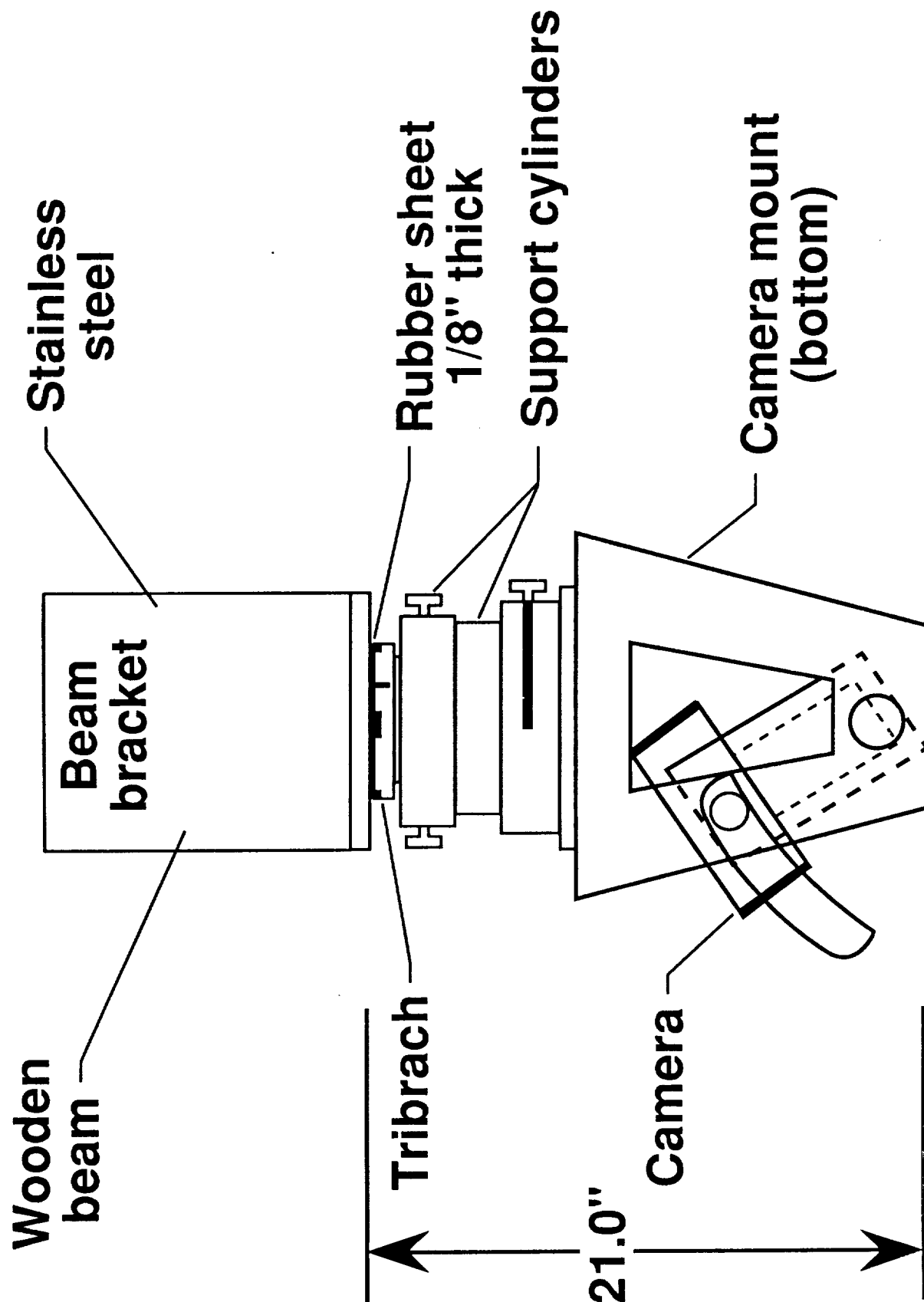


Figure 4. Drawing of sensing unit mount.

Coordinate System Definition

The coordinate system for the LGMSS and position measurement system is a right hand cartesian coordinate system.(figure 5) The z axis points up. The position of the levitated model is defined by the x, y, and z position of the origin of a body fixed reference frame in the laboratory (or fixed) reference frame. The orientation of the model is defined by the Euler angles ψ , θ , ϕ (yaw, pitch, roll). The rotation sequence is yaw, pitch, and roll.

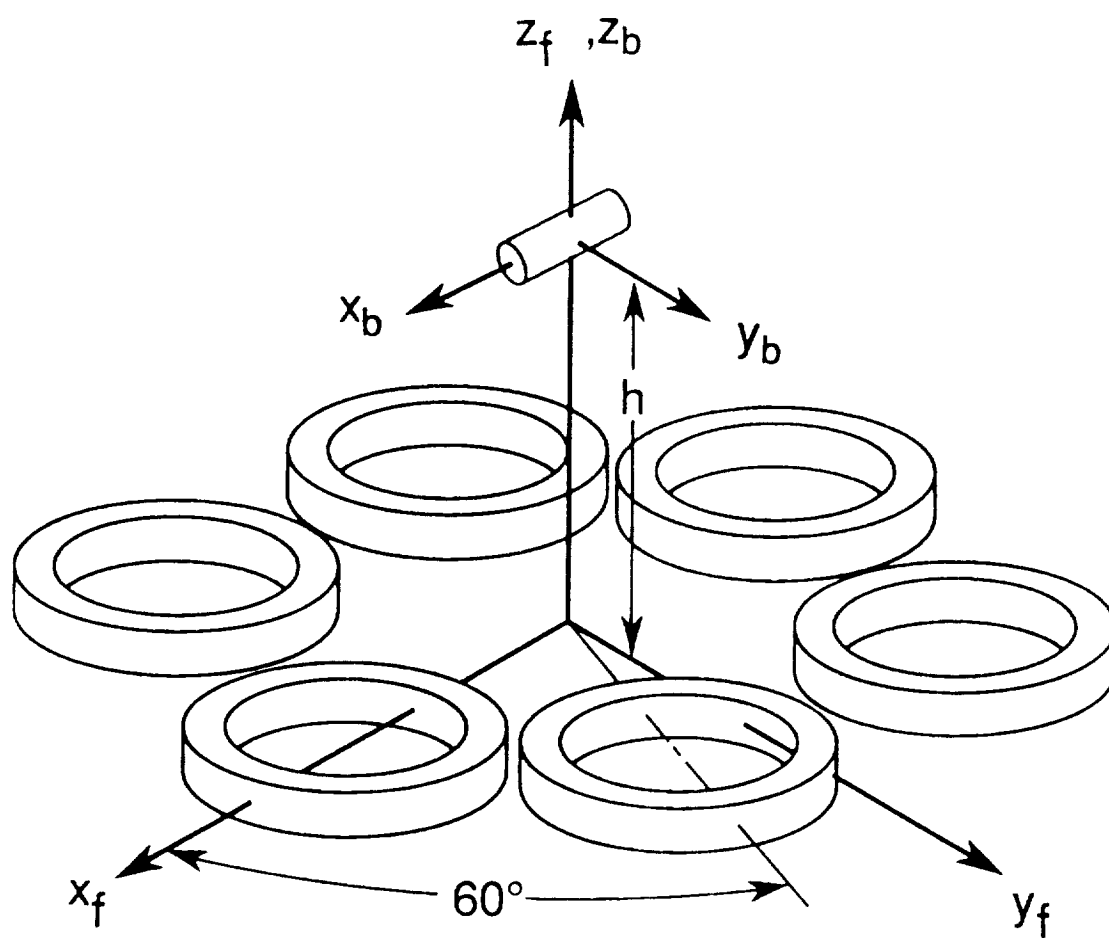


Figure 5. Diagram showing cylindrically shaped model levitated by a six coil magnetic suspension system. Coordinate systems of body and suspension system indicated by subscripts b and f, respectively.

Transformation Equations

The position and orientation of the model are determined by solving a set of nonlinear equations which relate the measured x and y camera coordinates of each target to the six parameters, x_{cm} , y_{cm} , z_{cm} , ψ , θ , and ϕ . Two sets of transformation equations are listed below. The first set of transformation equations describe the transformation from body fixed reference frame coordinates (x_b , y_b , z_b) to laboratory or fixed reference frame coordinates (x_f , y_f , z_f) in terms of the coordinates of the origin of the body frame in the laboratory frame (x_{cm} , y_{cm} , and z_{cm}) and the orientation of the body frame with respect to the fixed frame, given by the sines and cosines of the Euler angles psi (ψ), theta (θ), and phi (ϕ). The second set of transformation equations describe the transformation from laboratory reference frame coordinates for the j th target (x_{fj} , y_{fj} , z_{fj}) to the i th camera (x_{ij} , y_{ij}) in terms of the x , y , z position of the perspective center of each camera in the laboratory reference frame, denoted by X_i^c , Y_i^c , and Z_i^c , and the orientation of each camera with respect to the laboratory reference frame. In the second set of equations, the m_{ij} are elements of the rotation matrix and are functions of the camera pointing angles. The terms x_{pi} and y_{pi} are the principal points for the i th camera, and $f_{x,yi}$ is the focal length of camera i . The positions and orientations of each camera are determined by an independent survey and through calibration.

Substituting the first set of transformation equations below into the second produces a set of nonlinear equations which describes the dependence of the x_{ij} and y_{ij} positions of the projected images of target diode j in sensing unit i in terms of the position and orientation of the model. The position and orientation of the model are given by the six parameters x_{cm} , y_{cm} , z_{cm} , ψ , θ , ϕ . With eight targets and eight sensing units, 128 equations are thus generated. These equations are linearized and solved using an iterative technique (Newton's Method).

$$x_{fj} = x_{cm} + x_{bj}(\cos(\theta)\cos(\psi) + y_{bj}(-\cos(\phi)\sin(\psi) + \sin(\phi)\sin(\theta)\cos(\psi)) + z_{bj}(\sin(\phi)\sin(\psi) + \cos(\phi)\sin(\theta)\cos(\psi))$$

$$y_{fj} = y_{cm} + x_{bj}(\cos(\theta)\sin(\psi) + y_{bj}(\cos(\phi)\cos(\psi) + \sin(\phi)\sin(\theta)\sin(\psi)) + z_{bj}(-\sin(\phi)\cos(\psi) + \cos(\phi)\sin(\theta)\sin(\psi))$$

$$z_{fj} = z_{cm} + x_{bj}(-\sin(\theta)) + y_{bj}(\sin(\phi)\cos(\theta)) + z_{bj}(\cos(\phi)\cos(\theta))$$

$$x_{ij} = x_{pi} + f_{ix} \left[\frac{m_{11}(x_{fj} - X_{xi}^c) + m_{12}(y_{fj} - Y_{xi}^c) + m_{13}(z_{fj} - Z_{xi}^c)}{m_{x31}(x_{fj} - X_{xi}^c) + m_{x32}(y_{fj} - Y_{xi}^c) + m_{x33}(z_{fj} - Z_{xi}^c)} \right]$$

$$y_{ij} = y_{pi} + f_{iy} \left[\frac{m_{21}(x_{fj} - X_{yi}^c) + m_{22}(y_{fj} - Y_{yi}^c) + m_{23}(z_{fj} - Z_{yi}^c)}{m_{y31}(x_{fj} - X_{yi}^c) + m_{y32}(y_{fj} - Y_{yi}^c) + m_{y33}(z_{fj} - Z_{yi}^c)} \right]$$

Targets

As stated previously, eight infrared light emitting diode targets are embedded in the top surface of the model. Each target consists of an LED chip soldered into a small parabolic reflector.(figure 6) The wavelength of the light is 850 nm. The diameter of the reflector is 0.047 inches. Figures 6 - 11 show a diagram of the cross section of a target, a picture of a target compared to a dime, a graph of the spatial distribution of the light output from an LED target, a picture of a cylindrical model with the targets embedded in the surface, a picture of the circuit board for the target driver electronics, and a diagram showing the timing pulses. The larger diameter shown in diagram 6 is a heat sink. Special bonding techniques had to be developed which would provide adequate heat conduction when the diodes are driven at high current levels. The materials which are used to bond the LED and leads to the reflector are noted in diagram 6.

The driver electronics and power supply for the targets are all located on the model. The size of the driver electronics package is about 1 inch in diameter and 0.25 inches in thickness. Two nickel cadmium (rechargeable) batteries are provided. The dimensions of the batteries are 1 inch in diameter and about 1 inch in length. These batteries can provide sufficient power to operate for about 2 hours.

In addition to the target diodes, two additional strobe diodes, located on the bottom surface of the model are used to time the sensor acquisition of each target and detect the flashing of the first of the eight targets (or the beginning of frame). Diagram 11 shows the timing pulses for the prototype model. The timing diodes are separated from the target diodes in wavelength. The photodetectors used to detect these diodes, which are located beneath the levitated model, are filtered..

During tracking of the model, each of the eight target diodes is turned on in sequence for a period of time which may range from approximately 1.25 ms to 3.75 ms. (The length of time is determined by resistor values which are set in driver circuitry located in the model.) During this time, the CCD sensors integrate the light falling on the array. Following integration, the signal is read out and the centroid location is determined. After all eight diodes have been illuminated they are turned off during the time the sensing system is calculating the position and attitude of the model. The length of time required to calculate the position and attitude of the model is 15 ms. Following the calculation, the computed position and attitude information is sent to the LGMSS controller and a new frame is begun.

LIGHT EMITTING DIODE TARGET

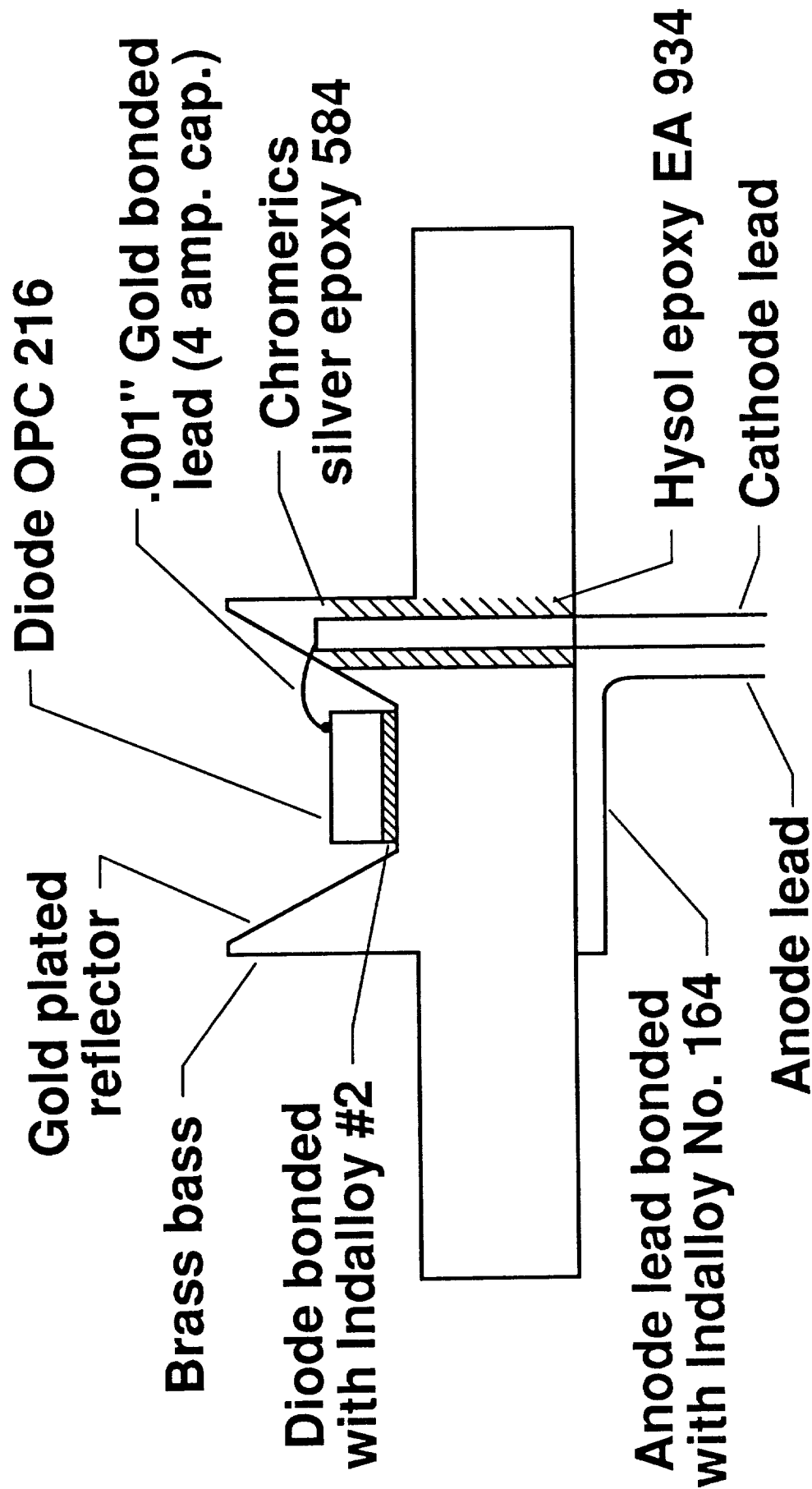


Figure 6. Drawing of a Light Emitting Diode (LED) target cross section.

ORIGINAL PAGE
BLACK AND WHITE PHOTOGRAPH



Figure 7. Picture of a target LED next to a dime.

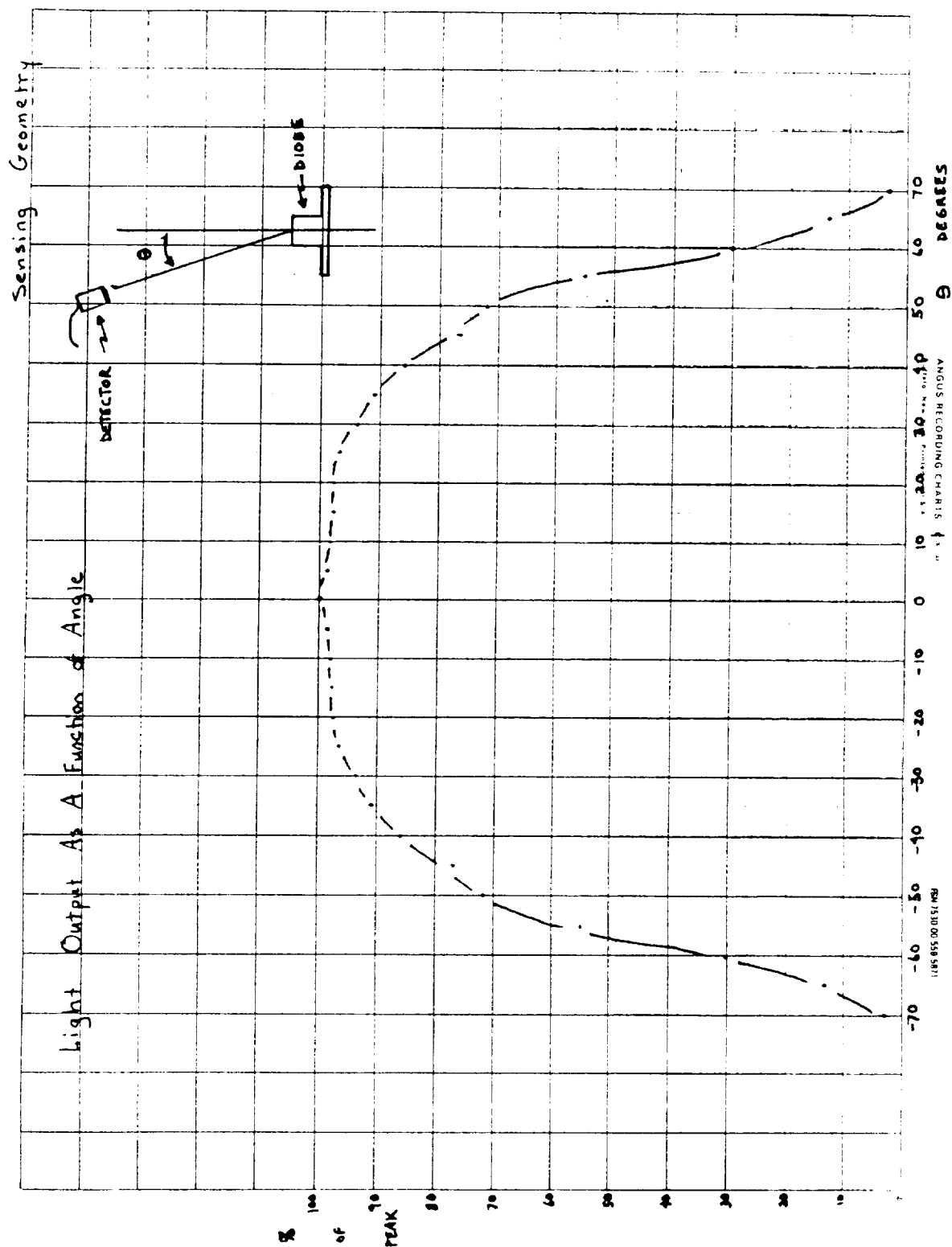


Figure 8. Graph of spatial distribution of light emitted by LED target.

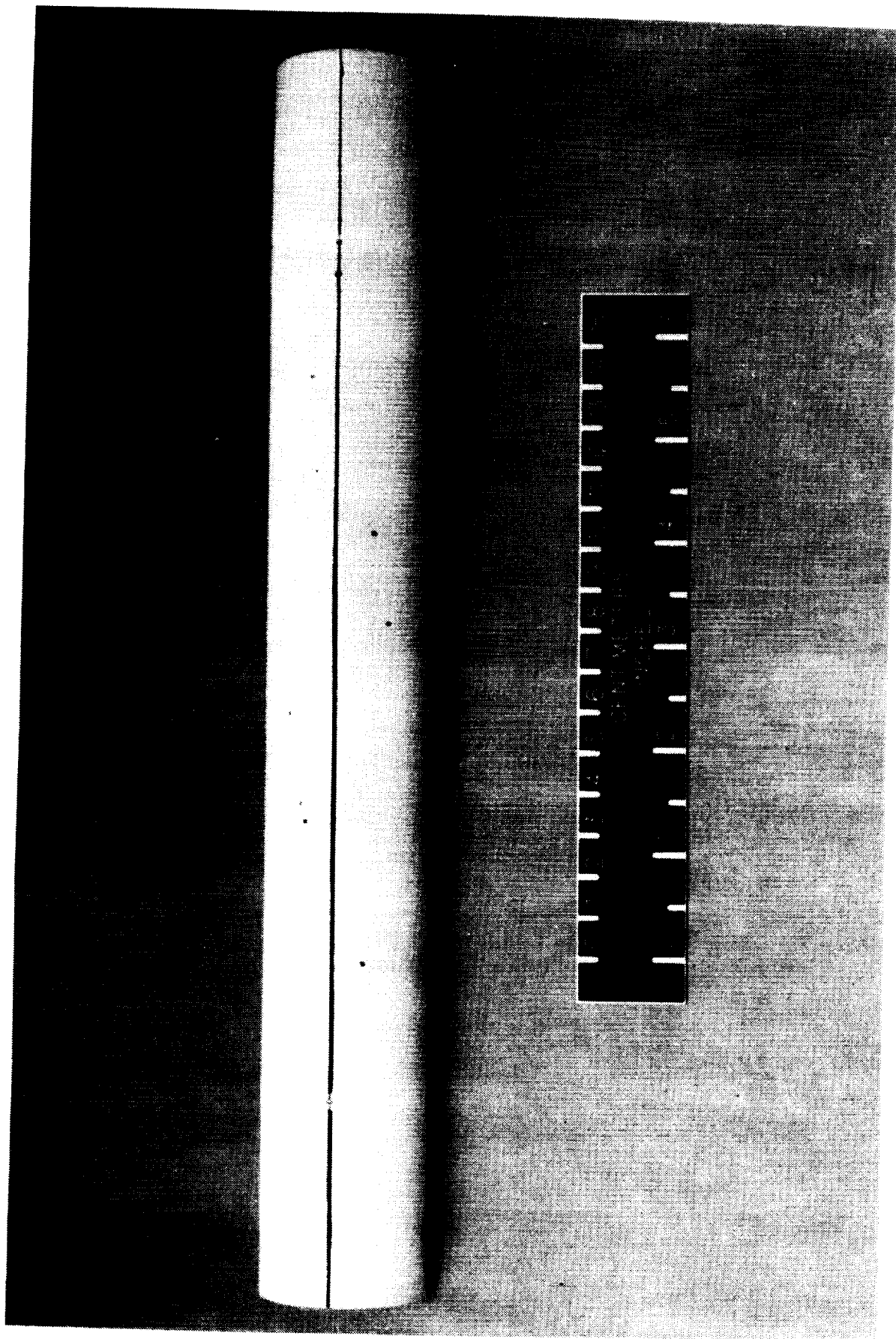


Figure 9. Picture of cylindrical model with targets embedded in the surface.

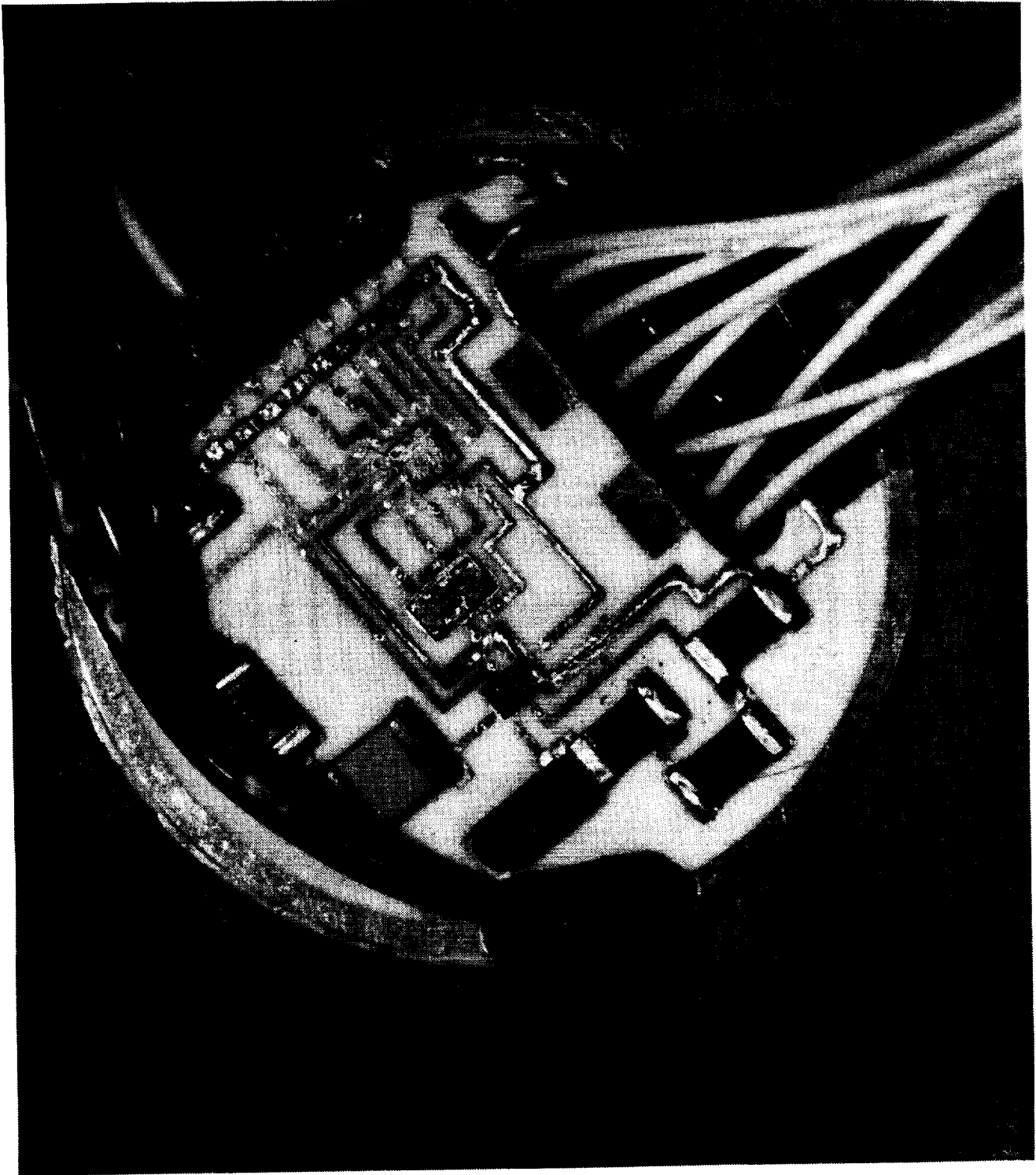
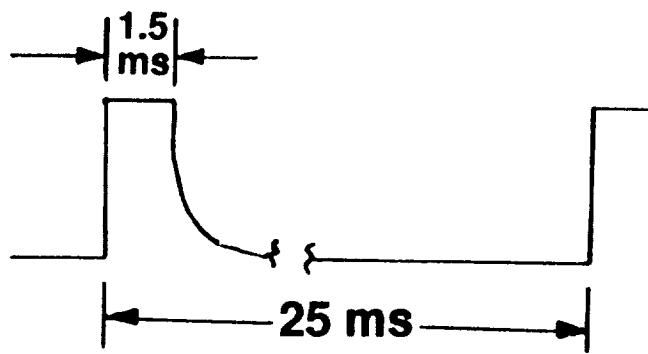


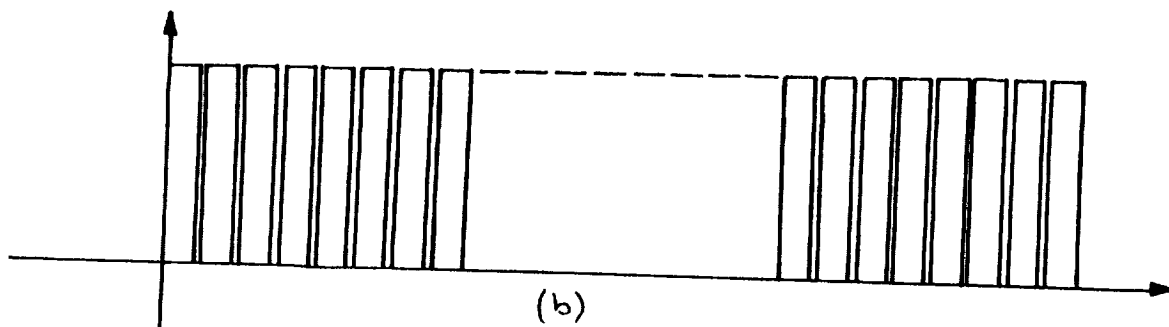
Figure 10. Picture of LED target driver electronics circuit board.

ORIGINAL PAGE
BLACK AND WHITE PHOTOGRAPH

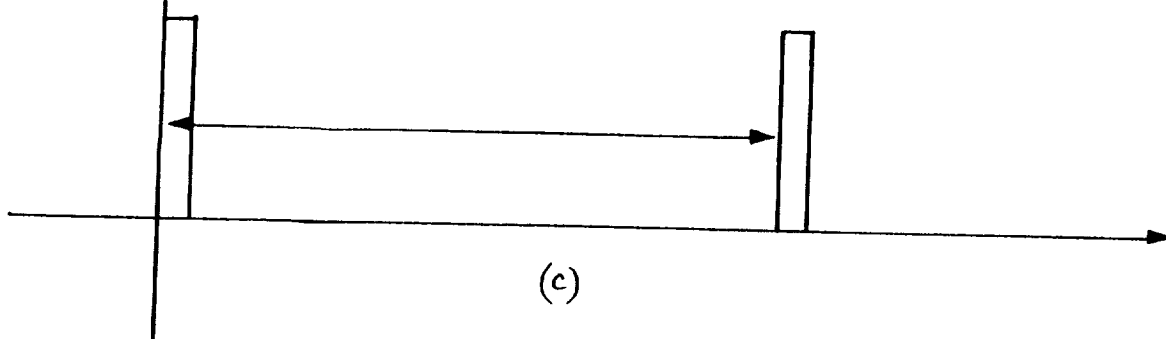
ORIGINAL PAGE IS
OF POOR QUALITY



(a)



(b)



(c)

Figure 11. Diagram of the timing pulses for beginning of frame and acquisition of a single target. a) Pulse for a single diode. b) Pulses generated by strobe diode for timing. c) Pulses generated by strobe diode for timing the beginning of a set of eight diodes.

Sensor Electronics

Figures 12 - 14 show pictures of the various sensor components. Figure 12 shows the front and back view of the camera board. Also shown is the thermoelectric cooler circuitry. Some of the components on the camera board are being operated at high clock speeds. As a result, without active cooling, these parts will overheat and be destroyed. A thermoelectric cooler is provided to actively cool these parts. A thermoelectric cooler was used to avoid inducing vibrations which could disturb the optical measurement. Figures 13 and 14 show pictures of the analogue to digital converter and digital signal processor boards, respectively.

ORIGINAL PAGE
BLACK AND WHITE PHOTOGRAPH

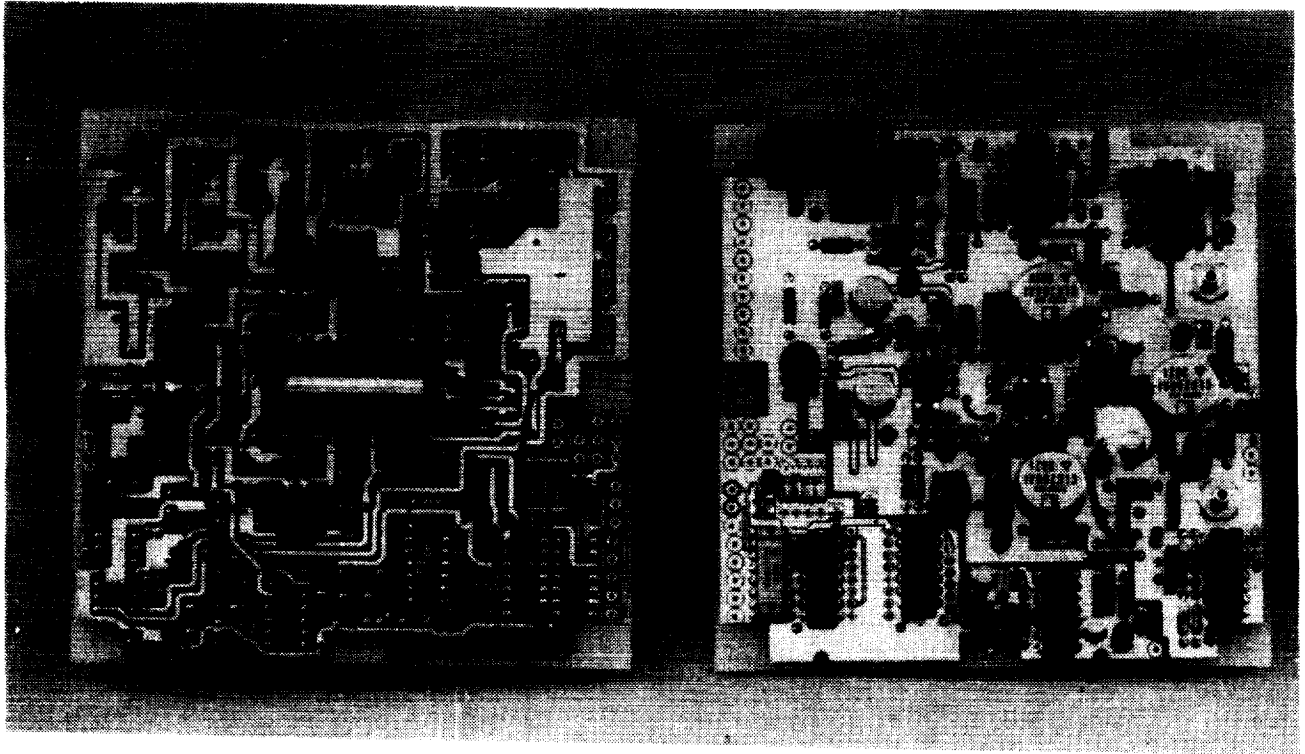


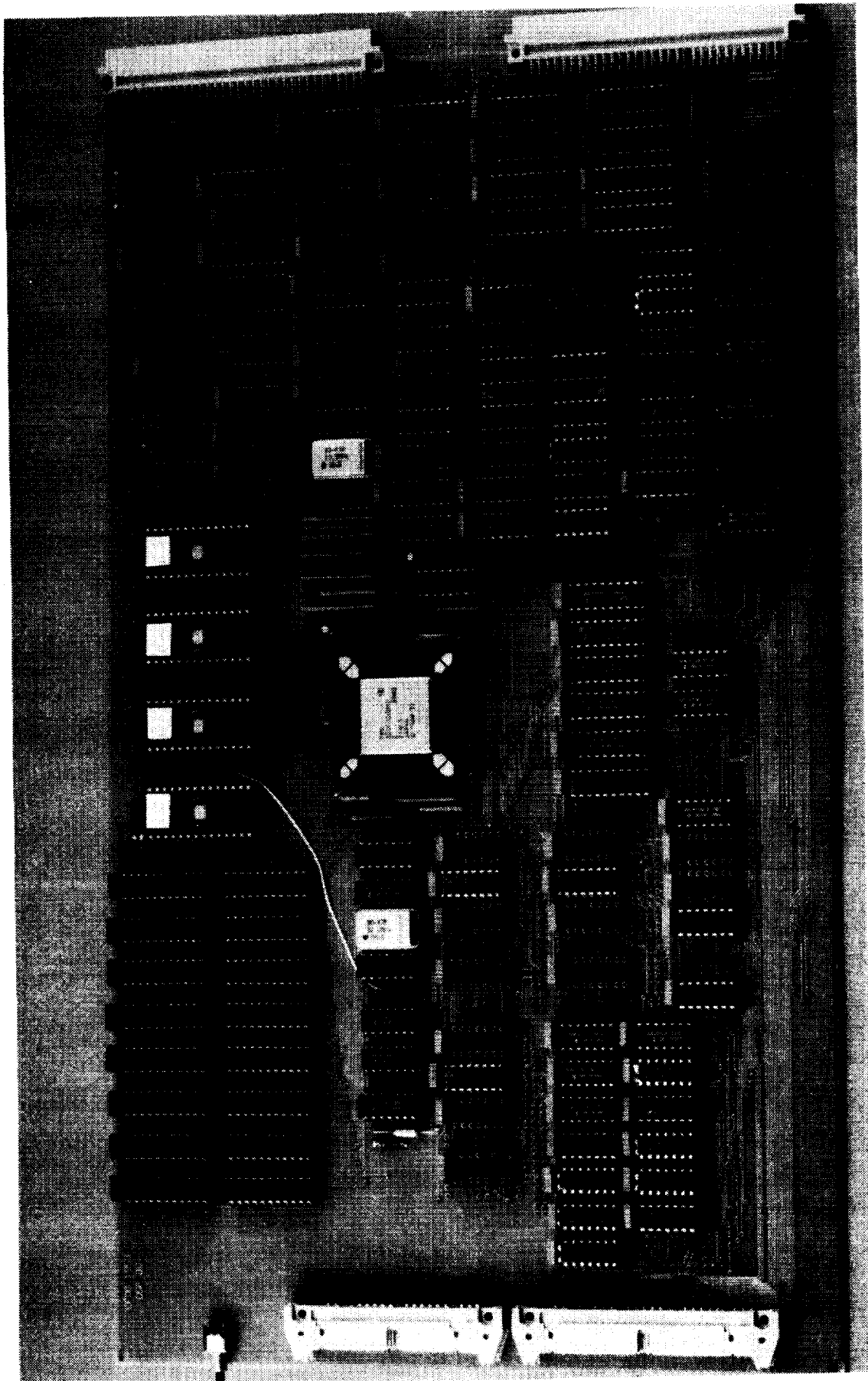
Figure 12. Pictures of camera board (front and back view) and thermoelectric cooler board.



Figure 13. Shown in this picture is the analogue-to-digital (A/D) converter board. The A/D is a 10 bit flash capable of a maximum data conversion rate of 20 megasamples/second.

Figure 14. On the following page is a picture of the digital signal processor (DSP) board. The DSP is a Texas Instruments TMS320C30. The clock speed is 32 mHz which yields an instruction cycle time of approximately 60 ns. The total time to perform the calculation of the centroid, background, and signal-to-noise ratio is about 1 ms.

ORIGINAL PAGE
BLACK AND WHITE PHOTOGRAPH



Graphs of Output of Prototype Sensor

Figure 15 is a graph showing the digital output of a prototype CCD sensor when imaging the cylindrical model of figure 9. The integration time of the camera was set to integrate over the entire frame time of all eight targets. Figure 16 is a graph of a portion of the digital output of a camera when imaging a single LED target. The light distribution spans approximately 11 pixels.

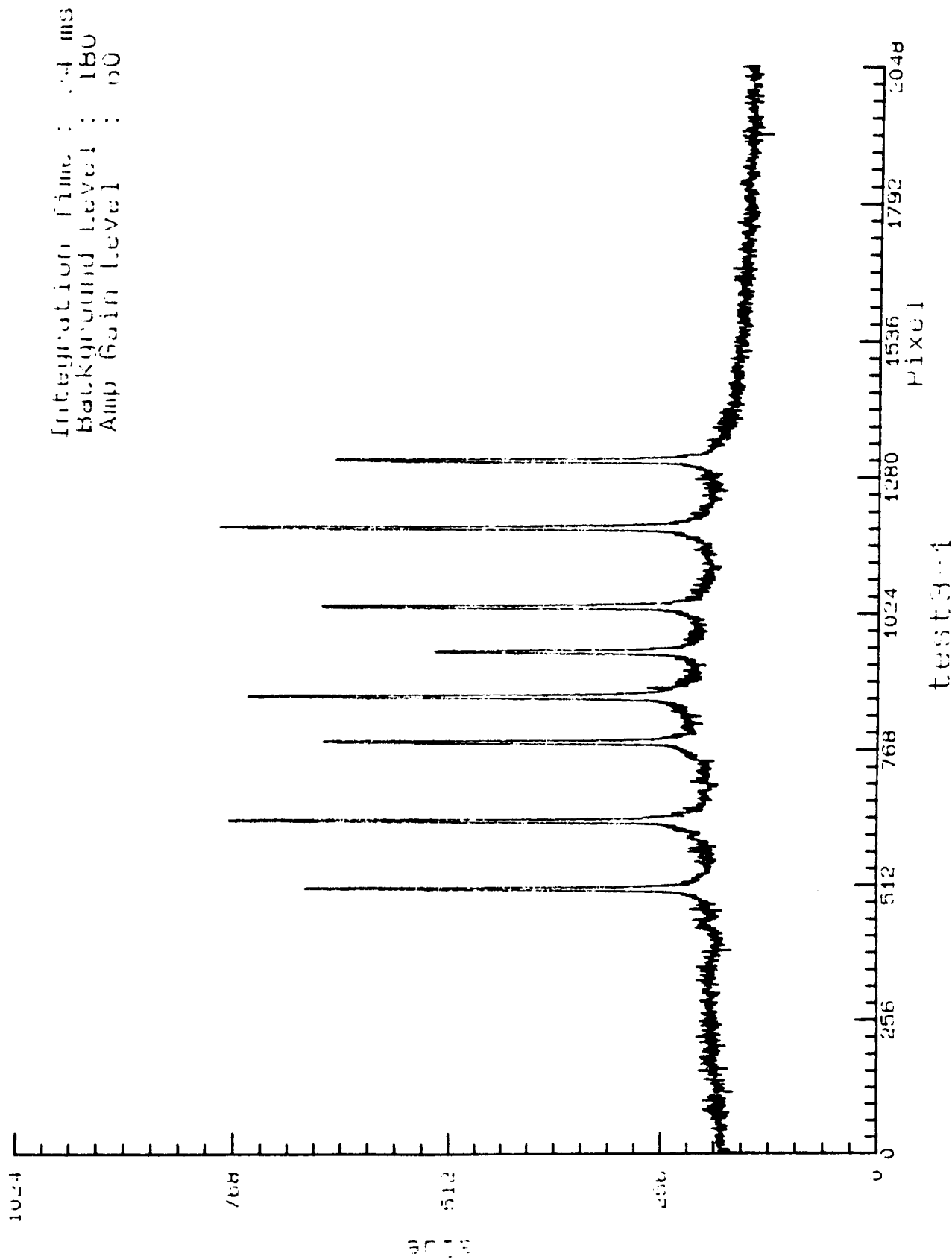


Figure 15. Graph of digital signal output of camera when imaging cylindrical model with eight targets.

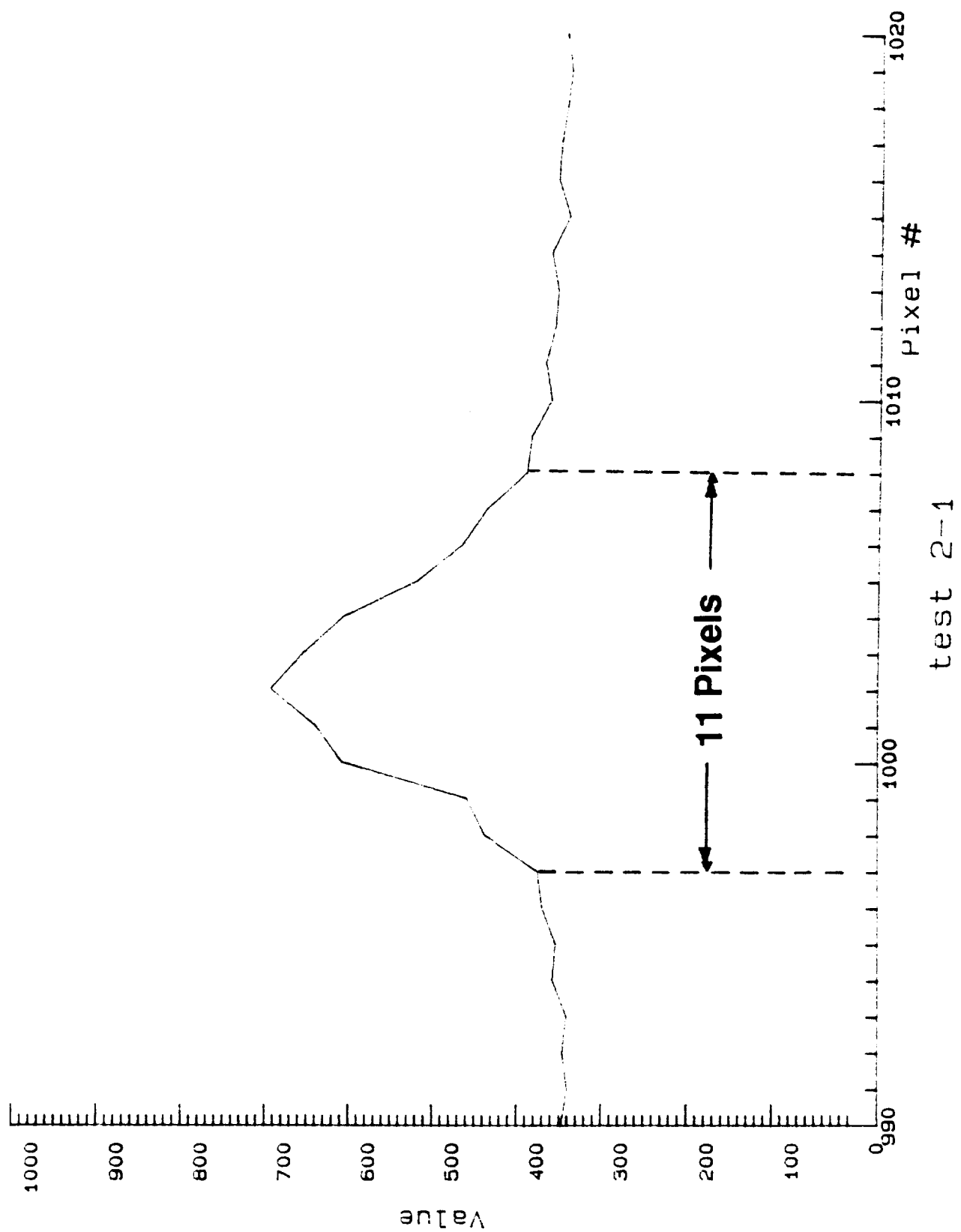


Figure 16. Graph of digital output of a camera for a single LED target.

Conclusions

Early simulation results were used to determine the level of signal-to-noise which would be needed to achieve the accuracy specified for the position measurement system. No model dynamics were taken into account in the simulation. Rather, the model was assumed to be stationary over the total 10 ms time in which the target locations were being sensed. The signal-to-noise ratio required to achieve the specified accuracy for the sensing system has been demonstrated. Also, it appears that a sample rate in excess of 20 samples/second can be achieved. However, further tests are required before it is known how much faster the system can track.

Conclusions

- * Simulation and test results indicate that the accuracy requirements for the sensing system will be met**
- * Software is being streamlined to improve the frequency response, should be possible to sample > 20 samples/sec**

APPENDIX

LIST OF ATTENDEES

Paul E. Allaire
University of Virginia
Mechanical Engineering Department
Thornton Hall
Charlottesville, VA 22901
Bus. Phone: (804) 924-3292

Dr. Willard W. Anderson
NASA Langley Research Center
Mail Stop 479
Hampton, VA 23665

Bus. Phone: (804) 864-1718

Bill G. Asbury
NASA Langley Research Center
MS 904
Hampton, VA 23665-5225

Bus. Phone: (804) 865-1018

Bibhuti Banerjee
University of Virginia
ROMAC Labs, Mech & Aero Engrg
Thornton Hall, McCormick Road
Charlottesville, VA 22901
Bus. Phone: (804) 924-3292

Mr. David A. Barnes
Honeywell, Inc.
13350 U. S. Hwy 19 North
Clearwater, FL 34624-7290

Bus. Phone: (813) 539-4030

James G. Batterson
NASA Langley Research Center
MS 161
Hampton, VA 23665-5225

Bus. Phone: (804) 864-4059

Michael C. Beale
Newport News Shipbuilding Co.
4101 Washington Avenue
E-78/B600
Newport News, VA 23607
Bus. Phone: (804) 688-9896

Fred B. Beck
NASA Langley Research Center
Mail Stop 490
Hampton, VA 23665-5225

Bus. Phone: (804) 864-1829

Vaughn D. Behun
NASA Langley Research Center
MS 904
Hampton, VA 23665-5225

Bus. Phone: (804) 865-1018

Leo Blecher
Intermagetics General Corp.
P. O. Box 566 Charles Park
Guilderland, NY 12084

Bus. Phone: (518) 456-5456

Robert W. Bosley
Allied-Signal Aerospace Comp.
2525 West 190th Street
P. O. Box 2960
Torrance, CA 90509-2960
Bus. Phone: (213) 323-9500

Mr. Rich Boyden
NASA Langley Research Center
Mail Stop 287
Hampton, VA 23665-5225

Bus. Phone: (804) 864-5160

Colin P. Britcher
Old Dominion University
Dept. of Mechanical Engg.
Norfolk, VA 23529-0247

Bus. Phone: (804) 683-3720

Dr. Gerald V. Brown
NASA Lewis Research Center
MS 23-3
Cleveland, OH 44135

Bus. Phone: (216) 433-6047

Thomas G. Campbell
NASA Langley Research Center
Mail Stop 490
Hampton, VA 23665

Bus. Phone: (804) 864-1772

Ms. Michelle L. H. Chun
The Pentagon
Industrial Activities Office, OASD
Washington, DC 20310-0440

Bus. Phone: (703) 834-3779

James H. Connelly
Charles Stark Draper Laboratory
555 Technology Square
MS#37
Cambridge, MA 02139
Bus. Phone: (617) 258-4729

Mr. L. P. de Rochemont
Radiation Monitoring Devices, Inc.
44 Hunt Street
Watertown, MA 02172

Bus. Phone: (617) 926-1167

Thomas C. Britton
Lockheed Engg.
NASA Langley Research Center
MS 161
Hampton, VA 23665-5225
Bus. Phone: (804) 864-6619

Gary Brown
NASA/Goddard Space Flight Center
MS 716.2
Greenbelt, MD 20771

Bus. Phone: (301) 286-3964

Ingrid Carlberg
NASA Langley Research Center
MS 416A
Hampton, VA 23665-5225

Bus. Phone: (804) 864-4174

James Clemmons
Vigyan Associates
NASA Langley Research Center
MS 383
Hampton, VA 23665-5225
Bus. Phone: (804) 864-4466

Taumi S. Daniels
NASA Langley Research Center
Mail Stop 238
Hampton, VA 23665-5225

Bus. Phone: (804) 864-4659

Jorge H. Decanini
TRW
One Space Park
R9/2181
Redondo Beach, CA 90278
Bus. Phone: (213) 814-6307

Capt. Ted A. Doederlein
Astronautics Laboratory
AL/VSSS
Edwards, CA 93523-5000

Bus. Phone: (805) 275-5483

Dr. James R. Downer
SatCon Technology Corporation
12 Emily Street
Cambridge MA 02139

Bus. Phone: (617) 661-0540

David B. Eisenhaure
SatCon Technology Corporation
12 Emily Street
Cambridge, MA 02139-4507

Bus. Phone: (617) 661-0540 Ext 201

Gerald K. Foshage
Honeywell Satellites Systems Div.
Box 52199
Phoenix, AZ 85072-2199

Bus. Phone: (602) 561-3178

Carlos M. Grodsinsky
NASA Lewis Research Center
21000 Brookpark Rd., MS500-205
Cleveland, OH 44135

Bus. Phone: (216) 433-2664

Mike Hagopian
NASA/Goddard Space Flight Center
Greenbelt, MD 20771

Bus. Phone: (301) 286-7854

Mr. Richard Dorman
Mechanical Technology, Inc.
968 Albany Shaker Rd.
Latham, NY 12110

Bus. Phone: (518) 785-2224

Mr. David Dress
NASA Langley Research Center
Mail Stop 287
Hampton, VA 23665-5225

Bus. Phone: (804) 864-5126

Karl Flueckiger
Charles Stark Draper Laboratory
MS 4C
555 Technology Square
Cambridge, MA 02139
Bus. Phone: (617) 258-3850

Melvin C. Gilreath
NASA Langley Research Center
Mail Stop 490
Hampton, VA 23665-5225

Bus. Phone: (804) 864-1817

Nelson J. Groom
NASA Langley Research Center
Mail Stop 161
Hampton, VA 23665

Bus. Phone: (804) 864-6613

David Hampton
University of Virginia
ROMAC Labs, Mech & Aero Engrg
Thornton Hall, McCormick Road
Charlottesville, VA 22901
Bus. Phone: (804) 924-3767/3292

Steven D. Harrah
NASA Langley Research Center
MS 490
Hampton, VA 23665-5225

Bus. Phone: (804) 864-1805

David H. Hibner
Pratt & Whitney
400 Main Street
MS 163-09
East Hartford, CT 06108
Bus. Phone: (203) 565-2238

Neil Holmberg
NASA Langley Research Center
Mail Stop 442
Hampton, VA 23665-5225

Bus. Phone: (804) 864-6970

R. R. Humphris
University of Virginia
Dept. of Mech & Aero Engineering
Thornton Hall
Charlottesville, VA 22901
Bus. Phone: (804) 924-3292

Mr. Ken Jacobs
NASA Langley Research Center
Mail Stop 442
Hampton, VA 23665-5225

Bus. Phone: (804) 864-6967

Dr. Bruce G. Johnson
SatCon Technology Corporation
12 Emily Street
Cambridge, MA 02139

Bus. Phone: (617) 661-0540

Michael J. Hennessy
Intermagnetics General Corp.
P. O. Box 566 Charles Park
Guilderland, NY 12084

Bus. Phone: (518) 456-5456

Richard Hockney
SatCon Technology Corporation
12 Emily Street
Cambridge, MA 02142

Bus. Phone: (617) 661-0540 X206

Mr. Stuart Hsu
Honeywell, Inc.
19019 N. 59th Avenue
Glendale, AZ 85308

Bus. Phone: (602) 561-3485

James D. Hurley
Mechanical Technology Inc.
968 Albany Shaker Rd.
Latham, NY 12110

Bus. Phone: (518) 785-2177

Dexter Johnson
NASA Lewis Research Center
21000 Brookpark Rd., MS 23-3
Cleveland, OH 44135

Bus. Phone: (216) 433-6046

Mr. V. O. Jones
Newport News Shipbuilding Co.
4101 Washington Ave.
E-78/B600
Newport News, VA 23607
Bus. Phone: (804) 688-9896

Dr. Prakash B. Joshi
Physical Sciences Inc.
20 New England Business Center
Andover, MA 01810

Bus. Phone: (508) 689-0003

Mr. Haig Kalfaian
Allied-Signal Aerospace Co.
Route 46
Teterboro, NJ 07608

Bus. Phone: (201) 393-3061

Mr. John M. Keesee
Magnetic Bearings Inc.
609 Rock Road
Radford, VA 24141

Bus. Phone: (703) 731-4983

Dr. Robert A. Kilgore
NASA Langley Research Center
Mail Stop 285
Hampton, VA 23665-5225

Bus. Phone: (804) 864-5020

Dr. R. Gordon Kirk
Virginia Polytech. & State Univ.
Dept. of Mechanical Engg.
Randolph Hall
Blacksburg, VA 24061
Bus. Phone: (703) 231-7478

Carl Knospe
University of Virginia
Dept. of Mechanical & Aerosp. Engg.
Thornton Hall, McCormick Rd.
Charlottesville, VA 22901
Bus. Phone: (804) 982-2603

Dr. Suresh M. Joshi
NASA Langley Research Center
Mail Stop 230
Hampton, VA 23665

Bus. Phone: (804) 864-6608

Claude R. Keckler
NASA Langley Research Center
Mail Stop 479
Hampton, VA 23665

Bus. Phone: (804) 864-1716

Warren C. Kelliher
NASA Langley Research Center
Mail Stop 416A
Hampton, VA 23665-5225

Bus. Phone: (804) 864-4172

Ronald W. Kipp
Kingsbury, Inc.
10385 Drummond Rd.
Philadelphia, PA 19154

Bus. Phone: (215) 824-4887

Josiah D. Knight
Duke University
Dept. of Mech. Engg. and Mat. Science
Durham, NC 27706

Bus. Phone: (919) 660-5337

Peter J. LaRocca
Charles Stark Draper Laboratory
555 Technology Square
Cambridge, MA 02139

Bus. Phone: (617) 258-1555

Pierce L. Lawing
NASA Langley Research Center
Mail Stop 267
Hampton, VA 23665-5225

Bus. Phone: (804) 864-5137

Mr. Duncan C. McCallum
Charles Stark Draper Laboratory
M. S. #4C
555 Technology Square
Cambridge, MA 02139
Bus. Phone: (617) 258-2426

Mr. James M. Michael
Lockheed Engg & Sciences Co.
NASA Langley Research Center
MS 444
Hampton, VA 23665-5225
Bus. Phone: (804) 864-7062

Mark Motter
NASA Langley Research Center
MS 442
Hampton, VA 23665-5225
Bus. Phone: (804) 864-6978

Mr. Stuart J. Olstad
FluiDyne Engineering Corp.
5900 Olson Memorial Hwy.
Minneapolis, MN 55422

Bus. Phone: (612) 544-2721

David P. Plant
FARE, Inc.
4716 Pontiac Street, Suite 304
College Park, MD 20740

Bus. Phone: (301) 982-2093

Mr. Kirk A. Logsdon
NASA Lewis Research Center
21000 Brookpark Rd.
MS 500/217
Cleveland, OH 44135
Bus. Phone: (216) 933-2836

Edward B. McCaul
Duke University
Dept. of Mech. Engg. and Mat. Science
Bldg. 144-A
Durham, NC 27706
Bus. Phone: (919) 660-5311

William E. Michaud
Magnetic Bearings, Inc.
609 Poquonnock Road
Groton, CT 06340

Bus. Phone: (203) 445-4005

John V. Murphy
Rockwell International, Sp. Sys. Div.
P. O. Box 21086
Kennedy Space Center, FL 32815

Bus. Phone:

Lloyd A. Ormon
Newport News Shipbuilding
4101 Washington Ave.
Newport News, VA 23607

Bus. Phone: (804) 380-4795

Dr. Douglas B. Price
NASA Langley Research Center
Mail Stop 161
Hampton, VA 23665-5225

Bus. Phone: (804) 864-6605

Rhonda R. Raffi
SatCon Technology Corporation
12 Emily Street
Cambridge, MA 02139

Bus. Phone: (617) 661-0540

Mr. Dharamendra N. Rawal
Virginia Polytechnic & State Univ.
Dept. of Mechanical Engg.
Blacksburg, VA 24060

Bus. Phone: (703) 361-3798

Dr. Donald Rote
Argonne National Laboratory
Bldg. 362
9700 S. Cass Ave.
Argonne, IL 60439
Bus. Phone: (708) 972-3786

Kevin Shelton
Lockheed Engg.
NASA Langley Research Center
MS 383
Hampton, VA 23665-5225
Bus. Phone: (804) 864-4470

Dr. Jag J. Singh
NASA Langley Research Center
Mail Stop 235
Hampton, VA 23665-5225

Bus. Phone: (804) 864-4760

John Stekly
Intermagnetic General Corporation
6 Eastern Road
Acton, MA 01720

Bus. Phone: (508) 264-4099

Dantam K. Rao
Mechanical Technology Inc.
968 Albany Shaker Road
Latham, NY 12110

Bus. Phone: (518) 785-2689

Lewis Rosado
DoD - Air Force
WRDC/POSL
WPAFB, OH 45433-6563

Bus. Phone: (513) 255-1286

Raouf Selim
Christopher Newport College
Physics Department
50 Shoe Lane
Newport News, VA 23601
Bus. Phone: (804) 599-7192

Dr. Thomas A. Shull
NASA Langley Research Center
Mail Stop 488
Hampton, VA 23665

Bus. Phone: (804) 864-1837

Dr. Michael R. Squillante
Radiation Monitoring Devices, Inc.
44 Hunt Street
Watertown, MA 02172

Bus. Phone: (617) 926-1167

Mr. Stuart S. Stephens
FluiDyne Engineering Corp.
5900 Olson Memorial Hwy
Minneapolis, MN 55422

Bus. Phone: (612) 544-2721

Mr. Richard A. Swendsen
TRW
One Space Park
Bldg. R9/1885
Redondo Beach, CA 90278
Bus. Phone: (213) 814-6092

Anil Trivedi
Allied-Signal Aerospace
2525 West 190th Street
P.O. Box 2960, M/S T-41; Dept. 93190

Bus. Phone: (213) 512-4231

Mr. John Ukstins
Allied Signal Corp.-Bendix Guid. Sys.
Dept. 6401 MS 2/13
Teterboro, NJ 07608

Bus. Phone: (201) 393-2567

Bertice E. Walker
Newport News Shipbuilding
4101 Washington Ave.
Newport News, VA 23607

Bus. Phone: (804) 688-2285

Robert C. Whitestone
David Taylor Research Center
Code 2712
Annapolis, MD 21402

Bus. Phone: (301) 267-3458

Patrick Wolke
Honeywell Satellite Systems Group
19019 North 59th Ave.
Glendale, AZ 85308-9650

Bus. Phone: (602) 561-3553

Robert S. Tamosaitis
Dupont
Experimental Station 304/C118
P. O. Box 80304
Wilmington, DE 19880
Bus. Phone: (302) 695-1752

David L. Trumper
Univ. of North Carolina at Charlotte
Dept. of Electrical Engineering
Charlotte, NC 28223

Bus. Phone: (704) 547-4324

Erik Vedeler
NASA Langley Res. Center
MS 490
Hampton, VA 23665-5225

Bus. Phone: (804) 864-1825

Sharon S. Welch
NASA Langley Research Center
Mail Stop 161
Hampton, VA 23665

Bus. Phone: (804) 864-6611

Stephanie Wise
NASA Langley Research Center
MS 474
Hampton, VA 23665-5225

Bus. Phone: (804) 864-

Belle L. Wood
NASA Langley Research Center
MS 444
Hampton, VA 23665-5225

Bus. Phone: (804) 864-7257

Dr. Kamal Youcef-Toumi
Massachusetts Institute of Technology
77 Massachusetts Avenue
Cambridge, MA 02139

Bus. Phone: (617) 253-2216

W. Robert Young
NASA Langley Research Center
MS 490
Hampton, VA 23665-5225

Bus. Phone: (804) 864-1824

Millard A. Zydron
Newport News Shipbuilding Co.
4101 Washington Avenue
E-52/B600
Newport News, VA 23607
Bus. Phone: (804) 688-8693



Report Documentation Page

1. Report No. NASA CP-10066, Part 2		2. Government Accession No.		3. Recipient's Catalog No.	
4. Title and Subtitle Aerospace Applications of Magnetic Suspension Technology				5. Report Date March 1991	
				6. Performing Organization Code	
7. Author(s) Nelson J. Groom and Colin P. Britcher, Editors				8. Performing Organization Report No.	
9. Performing Organization Name and Address NASA Langley Research Center Hampton, VA 23665-5225				10. Work Unit No. 590-14-11-02	
				11. Contract or Grant No.	
12. Sponsoring Agency Name and Address National Aeronautics and Space Administration Washington, DC 20546-0001				13. Type of Report and Period Covered Conference Publication	
				14. Sponsoring Agency Code	
15. Supplementary Notes Nelson J. Groom: Langley Research Center, Hampton, Virginia. Colin P. Britcher: Old Dominion University Research Foundation, Norfolk, Virginia.					
16. Abstract In order to examine the state of technology of all areas of magnetic suspension with potential aerospace applications, and to review related recent developments in sensors and controls approaches, superconducting magnet technology, and design/implementation practices, a three-day Workshop on Aerospace Applications of Magnetic Suspension Technology was held at the Langley Research Center in Hampton, Virginia, on September 25-27, 1990. A total of 28 papers were presented covering the areas of pointing and isolation systems, microgravity and vibration isolation, bearing applications, wind tunnel model suspension systems, large gap magnetic suspension systems, controls, rotating machinery, science and applications of superconductivity, and sensors. In addition to the presentations, there was a panel discussion on applications of superconductivity. A copy of each paper presented at the workshop and an edited transcript of the panel discussion is included. A list of attendees is presented in an Appendix.					
17. Key Words (Suggested by Author(s)) Magnetic Bearings, Magnetic Suspension, Large Gap Magnetic Suspension, Small Gap Magnetic Suspension, Sensors, Superconducting Magnetic Suspension Systems, Control Systems			18. Distribution Statement Unclassified - Unlimited Subject Category 18		
19. Security Classif. (of this report) Unclassified		20. Security Classif. (of this page) Unclassified		21. No. of pages 407	
				22. Price A18	

